National Technical University of Athens
School of Applied Mathematics &
Physical Sciences
Department of Physics

European Oragnisation for
Nuclear Research
The n_TOF collaboration

Dissertation
for the degree of
Doctor of Philosophy

Study of the ^{240}Pu(n,f) and ^{237}Np(n,f) reaction cross sections at the new experimental area (EAR2) of the CERN n_TOF facility

Stamatopoulos N. Athanasios

Advisory committee : Kokkoris Michael
Professor, National Technical University of Athens

Vlastou Rosa
Professor, National Technical University of Athens

Lagoyannis Anastasios
Principal Investigator, NCSR “Demokritos”

March 2019

National Technical University of Athens
School of Applied Mathematics &
Physical Sciences
Department of Physics

European Organisation for
Nuclear Research
The n_TOF collaboration

Study of the ^{240}Pu(n,f) and ^{237}Np(n,f) reaction cross sections at the new experimental area (EAR2) of the CERN n_TOF facility

Stamatopoulos N. Athanasios

Examining committee :

Kokkoris Michael
Professor, National Technical University of Athens, Greece

Lagoyannis Anastasios
Principal Investigator, NCSR "Demokritos", Greece

Chiaveri Enrico
Spokesperson of the n_TOF collaboration, CERN, Switzerland

Colonna Nicola
Principal Investigator, INFN Bari, Italy

Diakaki Maria
Reasearcher, CEA-Cadarache, France

Patronis Nikolaos
Associate Professor, University of Ioannina, Greece

Stoulos Stylianos
Associate Professor, Aristotle University of Thessaloniki, Greece

March 2019

Στην Αντιγόνη...

ACKNOWLEDGEMENTS

Yet another journey, quite a long and fascinating one, is about to reach its destination. Fortunately, many travel companions were aboard and shed the light when this expedition had to face stormy seas. The journey matters more than the destination itself, preach the wise, therefore the comrades with whom I sailed in parallel routes, were the ones who undoubtedly made travelling to be a once-in-a-lifetime experience, each one in his own particular way therefore the order of appearance in the succeeding lines is rather random.

First of all, I would like to thank **Maria Kastriotou** and **Lefteris Skordis** for their invaluable help and hospitality during the first months of my stay at CERN. If it had not been for them, my everyday life would have been tremendously more difficult.

Valentina Paneta deserves a special thank you for the long supportive and caring emails in the very first weeks of my PhD life, which helped me focus on what needed to be focused on.

Mr. **Vasilis Papadakis**, is the host who transmitted the pathogen that caused me to suffer from the incurable disease called Physics. As a high-school physics teacher, was the ideal person that a student can come across to satisfy his curiosity.

Twenty-one months in total, perhaps a bit more, were spent at the n_TOF facility at CERN, a unique place with unique people one of which is the spokesperson of the n_TOF collaboration, **Enrico Chiaveri**. Enrico's outstandingly unlimited drive and ideas in putting the n_TOF collaboration as much forward as possible, has been an inspiration and most of all a free course, that will accompany me the years to come.

The first persons I met at n_TOF were **Christina Weiss** and **Carlos Guerrero**, two bright people which share a lot in common. Their practical way of thinking and knowledge sharing, to name a few, has been a source of inspiration to many n_TOF "youngsters" and I feel very lucky to have met and been influenced by them.

"La famiglia italiana", **Mario Mastromarco** and **Massimo Barbagallo** have been an island of sunshine despite the long rainy days, both figuratively and literally, and as proper "fratelli", always there to keep you on the right track.

Daniela Macina and **Federica Mingrone**, the female part of the n_TOF Italian

family, have always been around acting as manna from heaven in times when everything seemed impossible. Most impressively, they made impossible seem easy. I would like to thank you for being around.

One of the most active collaborators within n_TOF, is without a shadow of a doubt, **Nicola Colonna**. Nicola is of those people whose passion in whatever they do, is an inspiration for the young generation. He was very close to me from the start, during the setting-up of the $^{240}Pu(n,f)$ experiment, till the end of this journey, by being a member in the examination committee. His strong belief and trust in me and the data analysis, along with our innumerous meetings in which he freely shared his knowledge, ideas, expertise, advice and most importantly passion, were amongst the most dominant factors in continuing torturing the recorded data. *"Nicola, there are no words to properly express my gratitude towards you, for the help, support and motivation you freely provided...Grazie mille! "*

The limitless knowledge you realise quite a few people in this field posses, will always be an example to follow and definitely acts as a strong motivation. I consider myself lucky to have met such people within the n_TOF collaboration. **Frank Gunsing**, **Laurent Tassan-Got** and **Peter Schillebeeckx** were among those people and one common thing they share is their great skills as educators. Frank and Laurent were the n_TOF scientific coordinators during the first and last two years, that the present thesis was in progress, respectively. Frank's politeness and patience when being asked questions which might had obvious answers was unmatched. Not only did he provided the answers, but he had a unique way to put the answers right to ones head.

Laurent is the kind of person that will try to feed the scientific hunger of (not only) young people, even though he might be involved in a ton of other obligations. He will skip sleeping, just to prepare a document with the answers he provided a few hours ago, in order to help in the most significant extend.

Peter, even though he is amongst the most highly regarded people in neutron physics, he is the type of person that believes : "we all learned the most from asking questions and making mistakes". This is a small proof of the encouragement he spreads in the young generation and I am totally grateful towards him for the immediate answers he provided in my innumerous questions he received."*Peter, I would like to thank you for opening a new world to me and helping me in trying to find answers!*"

Everything would have definitely been dull without P.T.B., the Princess, the Troll and the Bully. As an honourable Troll, I would like to thank you **Marta Sabatè-Gillarte** and **Michael (Michi) Bacak**, for just being around. Seems simple, but the simple are what matter in life. I am sure that the PTB will always find ways to connect.

The disarming honesty and sincerity of **Petar Zûgec**, virtues which most often than not are misunderstood, have been a beacon throughout this journey. His principles, moral values, great sense of humour and endless discussion gave me an insight to his extremely complicated mind. I will forever cherish the afternoon visits to the chocolate department of the super-market.

Once I have met **Nicolas Patronis** I misunderstood his sense of humour. Once I got to him, I surprisingly discovered that I was wrong. Nicolas, is the kind of people that they care a lot about understanding the concepts of what they are cur-

rently working on. Such a person would repeatedly ask questions, will try to dig in deep, and will not quit unless he has an answer. Observing this scientific culture, helped me in realising that in the end science is about helping others, which can occur by a deep understanding of every step involved in the process. Apart from that, I would like to express my sincere gratitude to Nikolas, for the endless discussions, moments of laughter and ideas that he shared with me, during the last two summers at CERN.

An great amount of gratitude is saved for the people in the nuclear physics group of the department of Physics at the National Technical University of Athens. The strong force that holds this group together and the help that each and every in it is willing to provide, even if not asked for, is impressive. The fellow senior PhD students **Antigoni Kalamara**, **Filothei Pappa** and **Kostas Preketes-Sigalas** make the silent force that trains and guides younger students and their advice and guidance was always on the spot. The junior PhD students **Veatriki Michalopoulou** and **Eleni Ntemou** are the transition bridge between the senior PhD students and the younger ones and always thrilled to take initiative and complete difficult tasks. The Master students **Sotiris Chasapoglou** and **Fotis Maragkos** offered invaluable help during the preparation of the PhD defence hence a huge "Thank you" goes to them. The entire group that additionally consists of the Master students **Eleni Mitsi**, **George Alamanos**, **Eleni Alvanou**, **Natalia Bligoura**, **Thymios Daoulas**, **Nick Dimitrakopoulos**, **Sofia Pantousa**, **Kallia Tsampa** and the undergraduate ones **George Gatis**, **Evi Mourati**, **Artemis Tsantiri**, **Dimosthenis Vougioukas** and **Anastasia Ziagova**, stand as a single unit and are always ready and prepared to help in every situation. Your help and advice during the extensive preparatory talk a few days before the defence is greatly appreciated.

A special thank you, is reserved for **Mary Diakaki**, who in my eyes is a scientific butterfly and flies over flowers to transmit ideas. Upon take-off, these ideas turn into fireworks and enlighten the dark sky. Mary is the kind of person, that will get involved in many discussions and provide ideas that will turn out to be simple yet so well-targeted that will eventually solve the issue. If it hadn't been for Mary, the present thesis would have definitely been different.

A crime usually has a mastermind behind it. **Andrea Tsinganis**, had he been involved in criminal activities, he would definitely be the one who would make the perfect crime a reality. Andrea, who is the man who got me by the hand and walked me through this unimaginatively charming world of neutron physics, has been and will always be a source of inspiration. One of the first advice he gave me was : "Let your work speak of you". It was the first time I realised that so far I was really doing wrong. He was there in the most difficult times of my PhD life, not only due to scientific reasons, and he managed to sooth any socially uncomfortable reactions and made me see clearer through situations, especially in the very beginning. His overall education, character and charisma in explaining in the most simplest way possible, difficult to comprehend concepts, has been an inspiration, certainly an example to follow and an invaluable help in completing the following thesis. If it hadn't been Andrea's contribution through his guidance, advice, pressure, planning and most importantly passion and *meraki* for science, this thesis would have never been completed. *"Andrea, thank you so much for putting up with me the last years. The ideas you inspired, made me realise that carrying on, either scientifically or*

not, requires modesty. I am thankful I have met you and I feel that I've managed to read a few lines of the splendid volume of philosophy that the Sirian left telling everything about everything."

A special paragraph is devoted to two very special people whom I can consider family. I would like to express that I am and always will be eternally grateful towards **Mike Kokkoris** and **Rosa Vlastou**, who supervised me during the last four creative years and made difficult seem easy. The phrase "eternally grateful" cannot echo the level of happiness, honour, joy and respect these two people brought to my life. Their morality, both scientific and social, principles and most of all love and passion for science and research will always remain at a very special pedestal in my heart. They manage, in nonideal circumstances, to share their passion, pass down to the next generation a high-standard perception of research and lead by example a quite productive group by using loyalty, trust, honesty and encouragement as building pillars. *"Mike and Rosa, thank you so much for treating me like an offspring, helping me in achieving my goals, inspiring and encouraging me along the way and most of all for being there everyday... I will forever treasure the years I spent in our group..."*

Last but certainly not least, I feel the need to express my happiness and joy of having spent the last years in office 212 with **Anigoni Kalamara**. Our lunch and coffee breaks were anticipated everyday along with the moment she quietly was entering the office and smiling "Καλημέεεεερααα". Above all, I would like to thank her for spending her life with me and sharing it with mine. I will forever cherish and treasure these years of our life and I hope that we will grow grey together and share a plethora of experiences. Among the most difficult tasks in life is to find people who accept you for who you are, even though you are quite far from perfect. "*Thank you for being such a person...*"

August 2018,
Mont Blanc

Contents

Prologue

The nuclear disintegration of heavy nuclei was firstly observed in the late 1930s, by Otto Hahn and Fritz Strassmann. Even though 80 years have passed by, the mechanism that the fission process is governed by, is not yet fully understood and in some cases the developed theoretical models are quite far from accurate predictions. Despite the absence of a well-defined global theoretical description for the phenomenon, fission has been in the service of mankind through the means of energy production, providing 10% of the global energy consumption.

The use, however, of nuclear energy, apart from its benefits, resulted in the formation of nuclear waste, which cannot be used as a fuel, therefore their management is still an open issue. To accommodate the aforementioned concern, the development of advanced nuclear systems such as Gen-IV reactors and Accelerator Driven Systems (ADS), which can be operated with a fast neutron spectrum and offer reduced safety margins and fuel recycling capabilities, has been thought through.

The optimum design and safe operation of such systems, though, requires the most accurate possible knowledge of neutron-induced fission reactions of actinides, such as the $^{240}Pu(n,f)$ and $^{237}Np(n,f)$ ones, which were studied in the present work. On average 60 kg per thermal reactor unit of ^{240}Pu are annually produced, hence it is considered to be one of the most important among nuclear waste products. ^{237}Np on the other hand, is used as a reference reaction in feasibility studies of advanced nuclear systems, on account of its low fission threshold and moderate activity. As a result, both reactions are considered to be of high priority and the accurate knowledge of the fission cross sections will significantly assist in the challenging task of designing and operating advanced nuclear systems.

In this respect, the ^{240}Pu fission cross-section was initially studied at the 180 m flight of CERN's n_TOF facility, most commonly referred to as EAR1, however, the high activity of the samples, in combination to the moderate neutron flux, caused an irreversible radiation damage to the detection system, which consisted of a Micromegas assembly. To address similar issues of studying short-lived, low mass and/or high activity samples, a new vertical flight path (EAR2) which sits 19 m above the lead spallation target was commissioned. The second experimental area,

features good resolving capabilities, a higher neutron flux than EAR1 and due to the shorter time-of-flights involved, significantly better background suppression.

For these reasons, the $^{240}Pu(n,f)$ reaction was successfully studied in EAR2, inaugurating the experimental launching of the newly commissioned EAR2. The data analysis, yielded a cross-section that spanned over more than 9 orders of magnitude in energy, from 9 meV up to 6 MeV. In addition, the high sample masses and neutron beam intensity, lead to appreciably high counting rates in the MeV region, which were resolved by the development of a relevant counting-loss correction methodology. The availability of useful experimental data in literature, for sub-threshold fission was quite limited, therefore the present work can provide input to future evaluations. The derived cross-section was theoretically investigated over a broad energy range through means of resonance analysis incorporating the $\mathfrak{R}$-Matrix formalism (`SAMMY` code) as well as with nuclear reaction codes (`TALYS-1.9` and `EMPIRE-3.2`).

The $^{237}Np(n,f)$ reaction, was additionally studied, in order to address the discrepancies observed by previous n_TOF data obtained in EAR1, in the MeV range. Although data was recorded from sub-thermal energies up to 15 MeV, the analysis revealed a contamination in the ^{237}Np samples, which has a significant impact in the sub-threshold data. Therefore, fission data will be reported from 100 keV up to 15 MeV, which is nevertheless the energy range of high priority interest.

The information previously described, is discussed in detail in the present manuscript which is divided in six chapters. In the beginning, an introduction to the importance of providing nuclear data in general is given, while at the same time the motivation behind the two studied reactions, is presented.

The first chapter, provides details on the experimental conditions and apparatus used during the experimental campaigns. More specifically, the n_TOF facility is briefly described along with its new experimental area (EAR2), while a detailed discussion is put into the time-of-flight technique. Technical details are also provided regarding both the fission foils and the detection systems used in the campaigns.

Monte-Carlo simulations were performed by coupling the `GEF` and `FLUKA` codes and are presented in the second chapter. The main goal was to estimate the fraction of rejected fission signals due to the application of an amplitude threshold in the analysis. In addition, the self-absorption of fission fragments within the volume of the samples was studied, thus providing information on the overall detection efficiency of the Micromegas assembly used during the measurements.

Data at n_TOF was recorded by flash-ADC's and therefore stored in waveforms, which in turn were analysed using pulse shape analysis techniques. The signal handling required the use of average detector pulse shapes which were extracted by computational routines, developed in the framework of the present work, which have also been used in the data analysis of other experimental campaigns within n_TOF.

The data analysis procedure is described in the fourth chapter along with the results for the derived cross sections concerning both reactions. Since the study of the $^{240}Pu(n,f)$ reaction was the first experiment performed in EAR2, the analysis revealed several significant issues which were successfully addressed, such as the high counting losses, which have already been mentioned. In this respect, this

manuscript was written as a means to provide detailed information concerning the analysis of fission data recorded at EAR2.

The last chapter of the present thesis, describes the concepts of fission and its theoretical description from the Liquid Drop Model to the double-humped fission barrier. The basic concepts of neutron-induced reactions are discussed along with a brief description of the $\mathfrak{R}$-Matrix and Hauser-Feshbach formalisms, which were used to investigate the $^{240}Pu(n,f)$ cross-section. Resonance analysis was performed up to 10 keV, yielding resonance kernels for 30 resonances up to ~ 2.7 keV which were included in current evaluations and 9 additional ones in the $\sim 2.7 - 10.2$ keV range, which can provide input to future evaluations. The statistical nuclear model calculations, performed with the `TALYS-1.9` and `EMPIRE-3.2` codes, although adequately reproduced all open neutron channels, did not manage to successfully investigate the structures observed in the vicinity of the fission threshold. Therefore the development of theoretical models concerning the second well of the fission potential has to be thought through.

Εκτεταμένη περίληψη

Η παρούσα διδακτορική διατριβή αφορά στη μέτρηση ενεργών διατομών αντιδράσεων σχάσης στα πλαίσια του πειράματος n_TOF στο CERN. Πιο συγκεκριμένα οι αντιδράσεις $^{240}Pu(n,f)$ και $^{237}Np(n,f)$ μελετήθηκαν στη νέα πειραματική γραμμή EAR2 η οποία κατασκευάστηκε για τη μέτρηση αντιδράσεων στις οποίες εμπλέκονται στοιχεία με υψηλή ενεργότητα. Τα τελικά αποτελέσματα, καθώς και επιλεγμένα σημεία της ανάλυσης των δεδομένων θα περιγραφούν συνοπτικά.

Κίνητρα μελέτης αντιδράσεων σχάσης

Τα τελευταία χρόνια περίπου το 10% της παγκόσμιας κατανάλωσης ενέργειας προέρχεται από πυρηνικούς αντιδραστήρες [1] μέσω αντιδράσεων σχάσης. Η χρήση όμως της πυρηνικής ενέργειας, παρά τα πολλαπλά οφέλη, ακολουθείται από την συσσώρευση καταλοίπων, που είναι γνωστά ως *πυρηνικά απόβλητα*. Τα εν λόγω απόβλητα είναι ραδιενεργά με μεγάλους χρόνους ζωής, συνεπώς η διαχείρισή τους αποτελεί ένα μείζον ζήτημα για την σύγχρονη κοινωνία.

Μια αποδοτική επίλυση, αποτελεί η ανακύκλωση των πυρηνικών αποβλήτων σε νέου τύπου αντιδραστήρες, οι οποίοι θα χρησιμοποιούν αυτό που έως τώρα θεωρούταν κατάλοιπο, ως πυρηνικό καύσιμο. Με αυτόν τον τρόπο επιτυγχάνεται αφενός η μετατροπή των μακρόβιων καταλοίπων σε βραχύβια και αφετέρου δίδεται η δυνατότητα να παραχθεί ενέργεια λόγω του επιπρόσθετου διαθέσιμου πυρηνικού καυσίμου.

Η λειτουργία των εν λόγω νέου τύπου αντιδραστήρων (4ης γενιάς [2,3] και Σύστημα Οδηγούμενο από Επιταχυντή-ADS [4,5]) θα επιτυγχάνεται με την χρήση φάσματος ταχέων νετρονίων, συνεπώς η ακριβής γνώση των ενεργών διατομών σχάσης είναι ύψιστης σημασίας και προτεραιότητας, όπως αντικατοπτρίζεται στην Λίστα Αιτημάτων Υψηλής Προτεραιότητας (High Priority Request List [6]) που έχει θεσπιστεί από την Υπηρεσία Πυρηνικής Ενέργειας (The Nuclear Energy Agency-NEA, [7])και τον Οργανισμό Οικονομικής Συνεργασίας και Ανάπτυξης (Organisation for Economic Co-operation and Development-OECD, [8])

Επιπρόσθετα της διαχείρισης των πυρηνικών αποβλήτων, η λειτουργία των νέου τύπου αντιδραστήρων είναι σημαντική καθώς τα διαθέσιμα κοιτάσματα Ουρανίου, το οποίο αποτελεί το πυρηνικό καύσιμο του σήμερα, αναμένονται είτε να στερέψουν ή να είναι ασύμφορη η εξόρυξή τους μέχρι το έτος 2050 [9], συνεπώς εναλλακτικοί κύκλοι πυρηνικού καυσίμου πρέπει να χρησιμοποιηθούν.

Τέλος, τα μελλοντικά εργοστάσια πυρηνικής ενέργειας οφείλουν να διακρίνονται από μειωμένα περιθώρια ασφαλείας, τόσο κατά την λειτουργία τους όσο και ως προς επιθέσεις τρίτων με σκοπό την αρπαγή των πυρηνικών αποβλήτων για χρήση τους σε εκρηκτικές συσκευές. Οι νέου τύπου αντιδραστήρες, είναι σχεδιασμένοι να λειτουργούν σε υποκρίσιμες συνθήκες συνεπώς δεν τίθενται ζητήματα υπερκρισιμότητας. Επιπλέον, τα ραδιενεργά κατάλοιπα, δεν θα απομακρύνονται από τον πυρήνα του αντιδραστήρα αφού η καύση τους θα πραγματοποιείται εντός του κατά την δημιουργία τους, συνεπώς θα είναι αδύνατη η αρπαγή τους.

Οι αντιδράσεις $^{240}Pu(n,f)$ και $^{237}Np(n,f)$

Το σχετικά μακρόβιο ^{240}Pu, με χρόνο ημιζωής 6561 χρόνια, προκύπτει εντός του πυρήνα ενός αντιδραστήρα ως παραπροϊόν διαδοχικών συλλήψεων νετρονίων από το ^{238}U. Περίπου 60 kg ^{240}Pu παράγονται ετησίως ανά αντιδραστήρα, ποσότητα που θεωρείται αρκετά σημαντική ώστε να θεωρηθεί ως εναλλακτική πηγή πυρηνικού καυσίμου [10], γεγονός που δικαιολογεί την ύπαρξή του στην Λίστα Αιτημάτων Υψηλής Προτεραιότητας [11], στην οποία ζητείται η ενεργός διατομή της σχάσης σε ένα εύρος ενεργειών από 500 eV - 6 MeV, με ακρίβεια από 3 – 13%.

Το ^{237}Np, λόγω του μεγάλου του χρόνου ημιζωής (2.1 εκατομμύρια χρόνια), χρησιμοποιείται ως στόχος αναφοράς σε πειράματα σχεδιασμού των νέου τύπου αντιδραστήρων, συνεπώς η όσο το δυνατόν ακριβέστερη γνώση της ενεργού διατομής του, για ενέργειες νετρονίων 200 keV - 20 MeV αποτελεί ύψιστη προτεραιότητα για την μελέτη της λειτουργίας των εν λόγω αντιδραστήρων, γεγονός που αντικατοπτρίζεται στην Λίστα Αιτημάτων Υψηλής Προτεραιότητας [12] όπου ζητείται η γνώση της ενεργού διατομής σχάσης με αβεβαιότητα μικρότερη από 3%.

Πειραματική διάταξη

Η μελέτη των εν λόγω αντιδράσεων πραγματοποιήθηκε στα πλαίσια της διεθνούς συνεργασίας n_TOF στο CERN στην νέα πειραματική γραμμή EAR2, η οποία βρίσκεται $19m$ πάνω από την κυλινδρική πηγή νετρονίων. Η κυλινδρική πηγή, με διάμετρο $60cm$ και μήκος $40cm$ είναι κατασκευασμένη από μονολιθικό μόλυβδο και περιβάλλεται από νερό το οποίο δρα ως επιβραδυντής νετρονίων και ψυκτικό μέσο ενώ τα νετρόνια παράγονται μέσω αντιδράσεων θρυμματισμού κατά την πρόσκρουση πρωτονίων ενέργειας $20GeV/c$. Μια σχηματική αναπαράσταση της εγκατάστασης n_TOF φαίνεται στο σχ. 1 όπου είναι εμφανής η οριζόντια πειραματική γραμμή EAR1 η οποία είναι εγκατεστημένη $185m$ από το κέντρο του στόχου μολύβδου. Το νετρονικό φάσμα που προκύπτει καλύπτει ένα μεγάλο ενεργειακό εύρος από θερμικές ενέργειες

(meV) έως μερικές δεκάδες MeV, όπως φαίνεται χαρακτηριστικά στο σχ. 2.

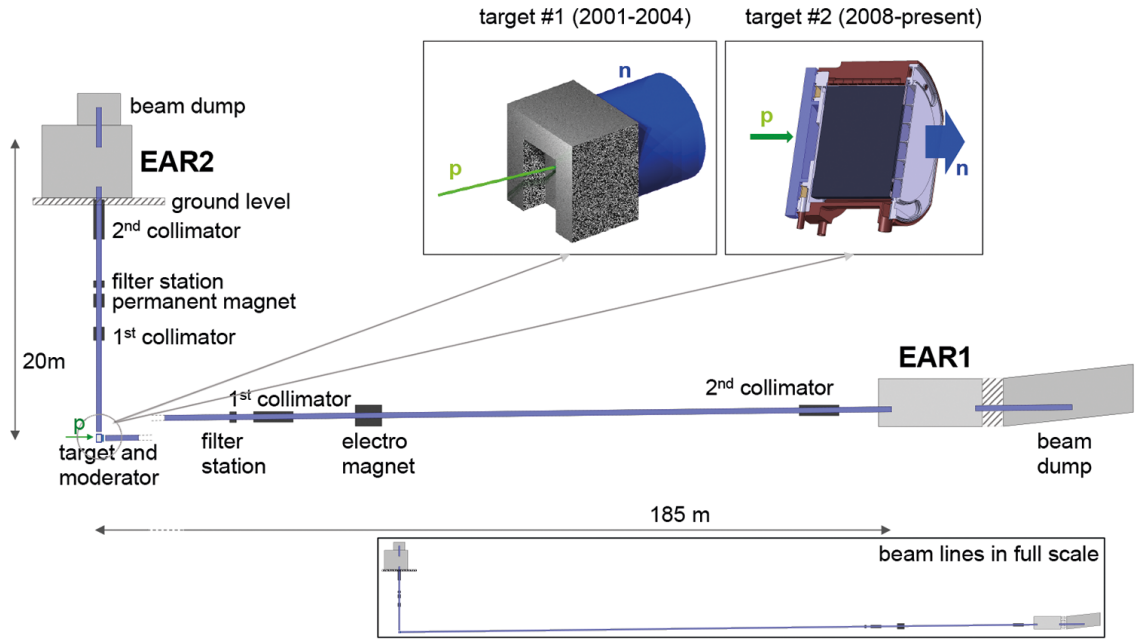

***Σχήμα 1**: Γραφική αναπαράσταση της εγκατάστασης n_TOF η οποία διαθέτει δύο πειραματικές γραμμές, μια οριζόντια και μια κατακόρυφη οι οποίες βρίσκονται $185m$ και $20m$ από το κέντρο της κυλινδρικής πηγής νετρονίων.*

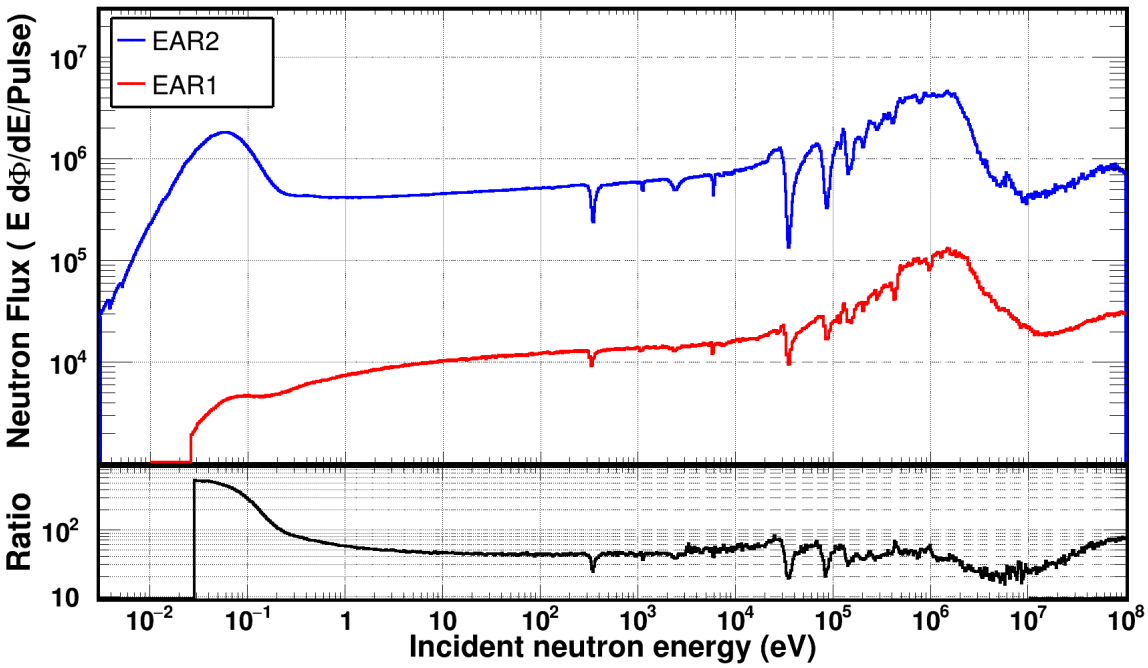

***Σχήμα 2**: Το ενεργειακό φάσμα των νετρονίων στην εγκατάσταση n_TOF , εκτείνεται από θερμικές ενέργειες νετρονίων έως μερικές δεκάδες MeV.*

Στόχοι σχάσης

Για την μελέτη των αντιδράσεων σχάσης, χρησιμοποιήθηκαν υπέρλεπτοι στόχοι που κατασκευάστηκαν στο εργαστήριο JRC-Geel . Οι στόχοι είχαν διάμετρο $3cm$ και τυπικό πάχος μερικών δεκάδων nm. Συγκεκριμένα στην περίπτωση του πειράματος $^{237}Np(n,f)$ ένας στόχος δόθηκε από το εργαστήριο IPN-Orsay με στόχο την ελαχιστοποίηση συστηματικών αβεβαιοτήτων. Στους πίνακες 1 και 2 δίδονται τα χαρακτηριστικά των προς μέτρηση στόχων καθώς και των στόχων αναφοράς (^{238}U και ^{235}U).

***Πίνακας 1**: Βασικά χαρακτηριστικά των στόχων που χρησιμοποιήθηκαν στην μελέτη της αντίδρασης $^{240}Pu(n,f)$.*

Στοιχείο	Αριθμός Αναφοράς	Ενεργότητα (kBq)	Μάζα (mg)	Επιφανειακή πυκνότητα (mg/cm^2) ($\times 10^{-7}$ $atoms/b$)		Ατομική περιεκτικότητα (%)
^{240}Pu	$TP2010-011-01$ $TP2010-011-03$ $TP2010-011-04$	6.016(23) 6.793(26) 6.410(25)	0.7163(28) 0.809(3) 0.763(3)	0.1017(4) 0.1148(5) 0.1223(5)	2.55(1) 2.88(1) 2.72(1)	^{238}Pu : 0.0733(29) ^{239}Pu : 0.0144(18) ^{240}Pu : 99.8915(18) ^{241}Pu : 0.00041(31) ^{242}Pu : 0.02027(41) ^{244}Pu : 0.000046(88)
Σύνολο		**19.219**	**2.2883**	**0.3248**	**8.15**	
^{235}U	$SP3576\_1$	40.5 Bq	0.563(11)	0.0912(17)	2.34(5)	^{234}U : 0.1698 ^{235}U : 99.475 ^{236}U : 0.0273 ^{238}U : 0.3277
^{238}U	$TP2011-008-03$	9.38(19) Bq	0.745(15)	0.1070(22)	2.71(6)	$^{238}U > 99.9$

***Πίνακας 2**: Βασικά χαρακτηριστικά των στόχων που χρησιμοποιήθηκαν στην μελέτη της αντίδρασης $^{237}Np(n,f)$.*

Στοιχείο	Αριθμός Αναφοράς	Ενεργότητα (kBq)	Μάζα (mg)	Επιφανειακή πυκνότητα (mg/cm^2) ($\times 10^{-7}$ $atoms/b$)		Ατομική περιεκτικότητα (%)
^{237}Np (JRC)	$TP2015-005-01$ $TP2015-005-02$ $TP2015-005-03$ $TP2015-005-04$	11.114(42) 11.780(45) 11.939(45) 11.845(56)	0.4270(21) 0.4526(23) 0.4587(23) 0.4551(26)	0.0604(9) 0.0640(9) 0.0649(9) 0.0644(9)	1.52(2) 1.61(2) 1.63(2) 1.62(2)	^{237}Np : 100
Σύνολο		**46.678**	**1.7934**	**0.2537**	**6.38**	
^{237}Np (IPN)	$Npt-nTOF-2016$	38.56	1.48	0.266	6.75	^{237}Np : 99.988 ^{238}Pu : 0.001 ^{239}Pu : 0.011
^{235}U	$TP2015-006-03$	40.58(25) Bχ	0.508(3)	0.0718(11)	1.84(3)	^{234}U : 0.035973(75) ^{235}U : 99.9336(14) ^{236}U : 0.009629(53) ^{238}U : 0.02073(14)
^{238}U	$TP2015-007-04$ $TP2015-007-05$	23.4(3) Bq 23.32(28) Bq	1.883(25) 1.875(23)	0.266(4) 0.265(4)	6.73(1) 6.71(1)	^{234}U : 0.000000592(18) ^{235}U : 0.0007668(14) ^{236}U : 0.000009266(42) ^{238}U : 99.999223(15)

Ανιχνευτική διάταξη

Η ανίχνευση των θραυσμάτων σχάσης επιτεύχθηκε με χρήση ανιχνευτών αερίου Micromegas, μια σχηματική αναπαράσταση του οποίου φαίνεται στο σχ. 3. Ο εν λόγω ανιχνευτής αποτελείται από δύο περιοχές οι οποίες διαχωρίζονται από ένα αγώγιμο μικροπλέγμα πάχους $5\mu m$: την περιοχή ολίσθησης με πλάτος $5mm$ και την περιοχή ενίσχυσης πλάτους $50\mu m$. Στις εν λόγω περιοχές εφαρμόζονται ηλεκτρικά πεδία τάξης μεγέθους $1kV/cm$ και $50kV/cm$, αντίστοιχα. Οι στόχοι σχάσης, οι οποίοι αποτελούν μέρος του ανιχνευτή, τοποθετήθηκαν με τους ανιχνευτές σε έναν κυλινδρικό θάλαμο στον οποίο υπήρχε μείγμα αερίου $Ar : CF_4 : iC_4H_{10}$ σε αναλογία όγκου $88 : 10 : 2\%$ σε ατμοσφαιρική πίεση. Η σειρά των στόχων φαίνεται στο σχ. 4.

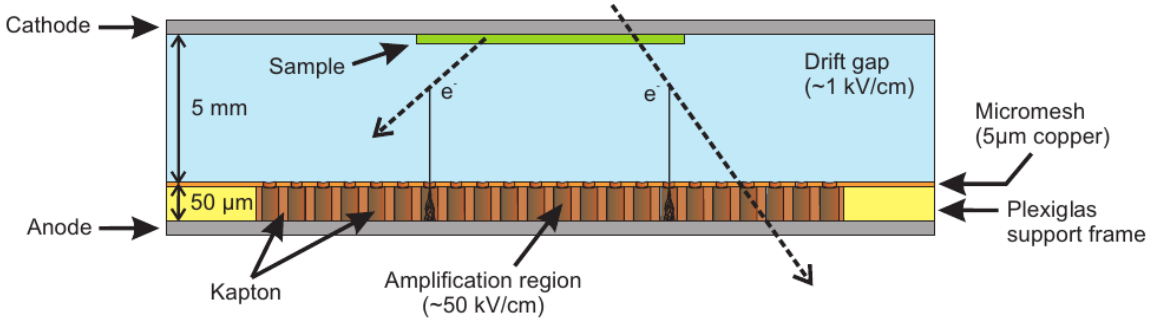

***Σχήμα 3**: Σχηματική αναπαράσταση του ανιχνευτή αερίου Micromegas , συστοιχία του οποίου χρησιμοποιήθηκε για την ανίχνευση των θραυσμάτων σχάσης [13].*

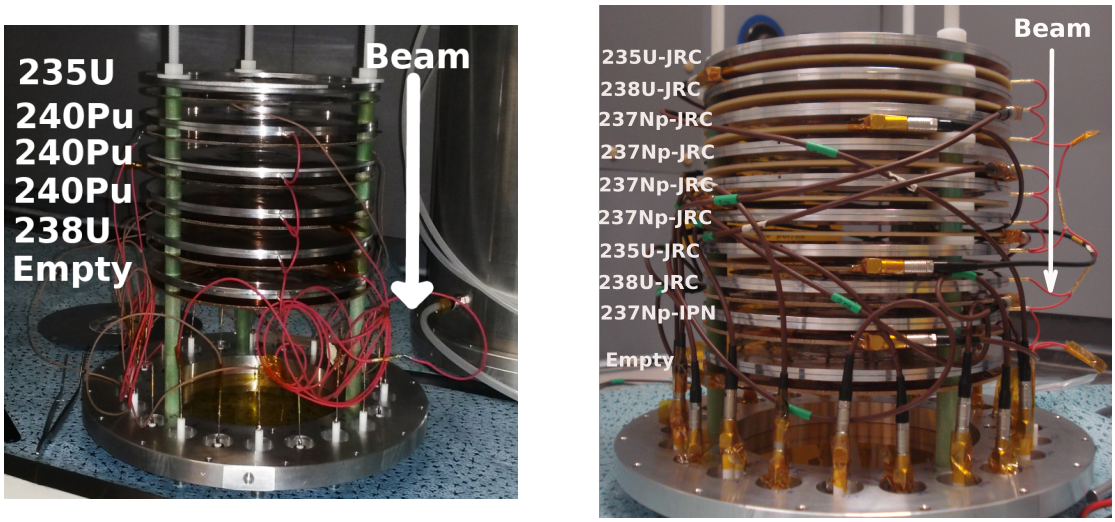

(α') ^{240}Pu ***(β')*** ^{237}Np

***Σχήμα 4**: Οι συστοιχίες ανιχνευτών-στόχων για τα πειράματα $^{240}Pu(n,f)$ (αριστερά) και $^{237}Np(n,f)$ (δεξιά). Το βέλος υποδηλώνει την κατεύθυνση της δέσμης των νετρονίων.*

Τεχνική χρόνου πτήσης

Ο καθορισμός της ενέργειας των νετρονίων E, πραγματοποιήθηκε με την χρήση της τεχνικής χρόνου πτήσης t, σύμφωνα με την κλασικιστική εξίσωση (1), όπου L είναι το μήκος πτήσης, m η μάζα του νετρονίου και v η ταχύτητά του. Μια περισσότερο ρεαλιστική περιγραφή περιλαμβάνει τις σκεδάσεις που λαμβάνουν χώρα εντός του στόχου και συνεπώς το πραγματικό μήκος πτήσης είναι μεγαλύτερο από το γεωμετρικό L κατά ένα ισοδύναμο μήκος λ το οποίο υπόκειται σε στατιστικές διακυμάνσεις και είναι διαφορετικό για κάθε ενέργεια νετρονίου. Η κατανομή των ισοδύναμων μηκών $\lambda(E)$ υπολογίστηκε από προσομοιώσεις Monte-Carlo από την συνεργασία n_TOF με την χρήση του κώδικα FLUKA [14, 15] και για την περίπτωση της EAR2 η εν λόγω κατανομή φαίνεται στο σχ. (5).

$$E(eV) = \frac{1}{2}mv^2 = \frac{1}{2}m\left(\frac{L}{t}\right)^2 \approx \left(72.298\frac{L(m)}{t(\mu s)}\right)^2 \tag{1}$$

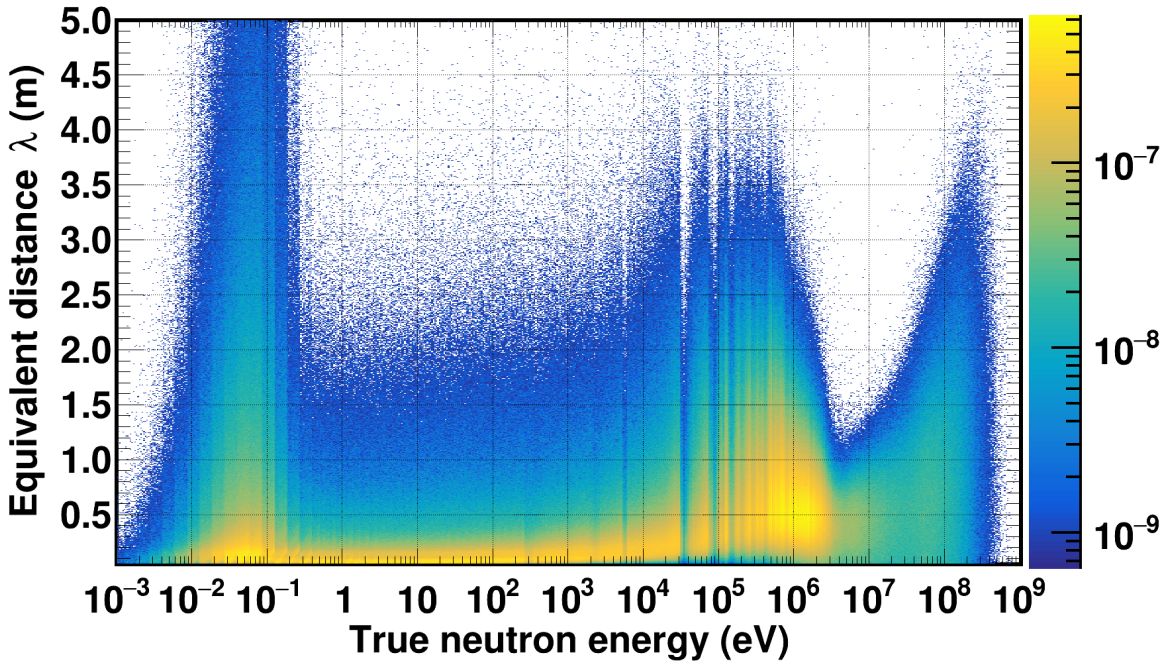

***Σχήμα 5**: Οι προσομοιώσεις για το ισοδύναμο μήκος λ, το οποίο αποκαλείται συνάρτηση απόκρισης του φασματομέτρου χρόνου πτήσης, πραγματοποιήθηκαν με χρήση του πακέτου Monte-Carlo, FLUKA .*

Ο προσδιορισμός του χρόνου πτήσης περιλαμβάνει την αναγνώριση δύο οικογενειών παλμών : (α) του επονομαζόμενου "γ-flash" το οποίο αποτελείται από φωτόνια που δημιουργούνται από τις αντιδράσεις κατακερματισμού των πυρήνων του μολύβδου και (β) των παλμών που δημιουργούνται από τα θραύσματα σχάσης, τα οποία δημιουργήθηκαν από το εισερχόμενο νετρόνιο. Η πρώτη οικογένεια αποτελεί την έναρξη (START) της καταγραφής του χρόνου πτήσης ενώ η δεύτερη το τέλος (STOP) της. Η διαφορά των δύο παλμών αποδίδει τον χρόνο πτήσης του εισερχόμενου νετρονίου.

Ανάλυση σήματος παλμών

Ο ακριβής προσδιορισμός του χρόνου πτήσης πραγματοποιήθηκε μέσω ανάλυσης σήματος παλμών και των σχετικών κωδίκων που αναπτύχθηκαν στη συνεργασία n_TOF . Κατά τη διάρκεια των πειραμάτων, η καταγραφή και αποθήκευση παλμοσειρών διάρκειας 16 *ms* έκανε δυνατή την ύστερη επεξεργασία των παλμών. Η αναγνώριση των χρήσιμων σημάτων βασίστηκε στον υπολογισμό της πρώτης παραγώγου και στην εφαρμογή κατάλληλων κριτηρίων ώστε να ελαχιστοποιηθεί η αναγνώριση θορύβου. Ένα παράδειγμα αναγνώρισης σήματος φαίνεται στο σχ. 6.

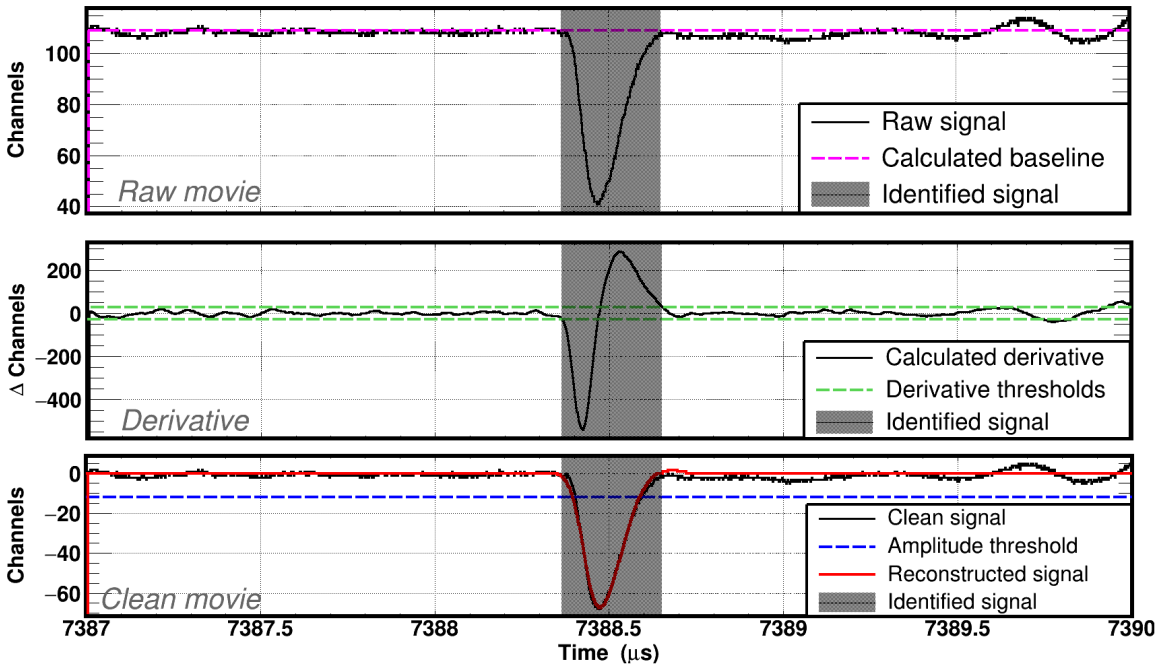

***Σχήμα 6**: Η αναγνώριση σήματος από την αποθηκευμένη παλμοσειρά (πάνω σχήμα) βασίστηκε στον υπολογισμό της πρώτης παραγώγου (μεσαίο σχήμα). Η τελική παλμοσειρά (κάτω σχήμα) υπολογίζεται μετά την αφαίρεση του υποβάθρου.*

Μέρος των εν λόγω κωδίκων αναπτύχθηκε στα πλαίσια της παρούσης διατριβής και περιλαμβάνει την εύρεση μέσων παλμών σχάσης και γ-flash . Ο υπολογισμός μέσων σημάτων, ο οποίος πραγματοποιήθηκε μέσω της συσσώρευσης αποθηκευμένων πειραματικών παλμών, υπήρξε καθοριστικής σημασίας στην ανίχνευση σημάτων που αντιστοιχούν σε σχάση προκαλούμενη από νετρόνια υψηλής ενέργειας. Χαρακτηριστικά παραδείγματα μέσων παλμών φαίνονται στα σχήματα 7 και 8.

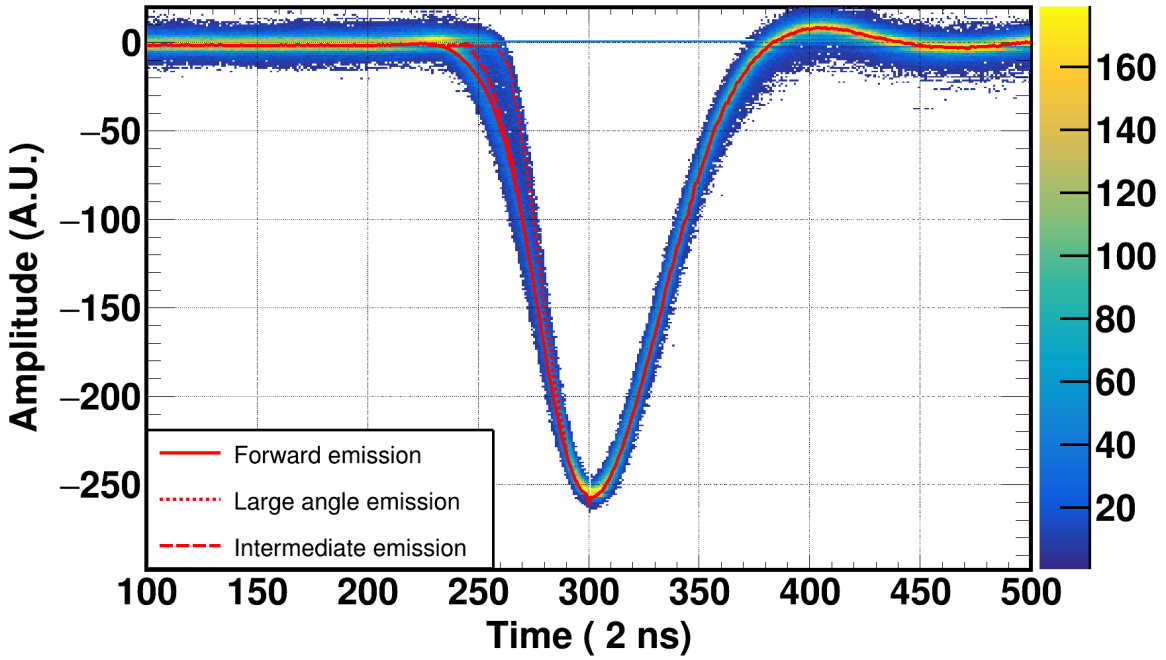

***Σχήμα 7**: Ο υπολογισμός των μέσων παλμών θραυσμάτων σχάσης πραγματοποιήθηκε μέσω της συσσώρευσης των αποθηκευμένων πειραματικών παλμών. Τα 3 διαφορετικά μέσα σήματα αντιστοιχούν σε διαφορετικές γωνίες εκπομπής των θραυσμάτων σχάσης.*

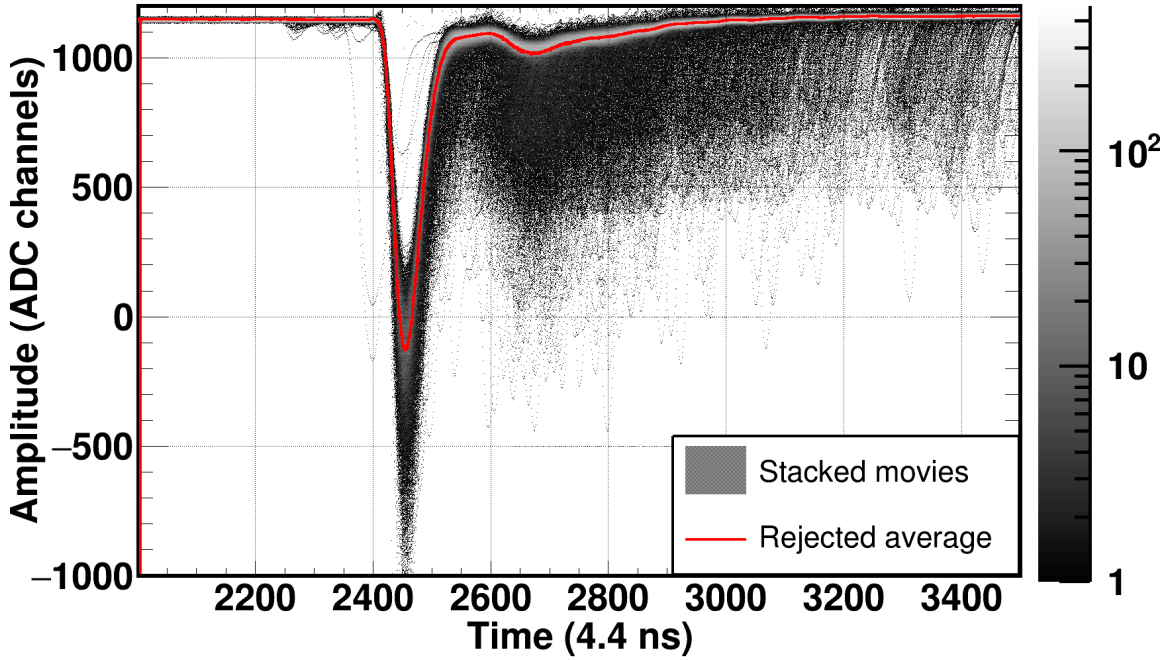

***Σχήμα 8**: Ο υπολογισμός των μέσων παλμών γ-flash πραγματοποιήθηκε μέσω της συσσώρευσης των αντίστοιχων αποθηκευμένων πειραματικών παλμών. Κατά την εύρεση των μέσων γ-flash, τα σήματα σχάσης δεν λήφθηκαν υπόψιν.*

Υπολογισμός της ενεργού διατομής

Η ενεργός διατομής σχάσης σ των δύο αντιδράσεων υπολογίζεται εν γένει με βάση την παρακάτω εξίσωση

$$\sigma = \frac{C}{C^{(\mathrm{ref})}} \frac{\prod_i f_i}{\prod_i f_i^{(\mathrm{ref})}} \frac{n^{(\mathrm{ref})}}{n} \frac{\Phi^{(\mathrm{ref})}}{\Phi} \sigma^{(\mathrm{ref})} \tag{2}$$

όπου τα καταγεγραμένα γεγονότα C διορθώθηκαν, στα εν λόγω πειράματα μέσω των παραγόντων f_i για τις κάτωθι συνεισφορές

1. Μη καταμέτρηση γεγονότων σχάσης λόγω της εφαρμογής κατωφλίου ύψους σημάτων (f_{amp})
2. Παρασιτικά γεγονότα από προσμίξεις στους στόχους (f_{imp})
3. Μη καταμέτρηση παλμών εξαιτίας του υψηλού ρυθμού παραγωγής γεγονότων σχάσης (f_{DT})
4. Ενδοαπορρόφηση των θραυσμάτων σχάσης στους στόχους (f_{abs})
5. Απορρόφηση των νετρονίων από τα υλικά της διάταξης (f_{shield})
6. Γεγονότα αυθόρμητης σχάσης (f_{SF})
7. Γεγονότα αυθόρμητης εκπομπής πυρήνων μεσαίου βάρους (f_{CD})
8. Παρασιτικά γεγονότα σχάσης προκαλούμενης από φωτόνια ($f_{\gamma f}$)

Οι παράγοντες n και Φ αντιστοιχούν στο πλήθος των πυρήνων του εκάστοτε στόχου και της νετρονικής ροής, αντίστοιχα ενώ ο δείκτης (ref) αφορά στους στόχους αναφοράς. Τέλος η εξ. (2) μετατρέπεται στην εξ. (3), στην οποία βασίστηκε ο υπολογισμός των ενεργών διατομών νετρονικής σχάσης. Στην συνέχεια θα περιγραφούν συνοπτικά οι τρεις πρώτοι διορθωτικοί παράγοντες.

$$\sigma = \frac{C}{C^{(\mathrm{ref})}} \frac{f_{\mathrm{amp}}}{f_{\mathrm{amp}}^{(\mathrm{ref})}} \frac{f_{\mathrm{imp}}}{f_{\mathrm{imp}}^{(\mathrm{ref})}} \frac{f_{\mathrm{DT}}}{f_{\mathrm{DT}}^{(\mathrm{ref})}} \frac{f_{\mathrm{abs}}}{f_{\mathrm{abs}}^{(\mathrm{ref})}} \frac{f_{\mathrm{shield}}}{f_{\mathrm{shield}}^{(\mathrm{ref})}} \frac{f_{\mathrm{SF}}}{f_{\mathrm{SF}}^{(\mathrm{ref})}} \frac{f_{\mathrm{CD}}}{f_{\mathrm{CD}}^{(\mathrm{ref})}} \frac{f_{\gamma f}}{f_{\gamma f}^{(\mathrm{ref})}} \frac{n^{(\mathrm{ref})}}{n} \frac{\Phi^{(\mathrm{ref})}}{\Phi} \sigma^{(\mathrm{ref})} \tag{3}$$

Κατώφλι ύψους παλμών

Το πειραματικό φάσμα σχάσης, περιλαμβάνει εκτός από τα θραύσματα, την ενδογενή ραδιενέργεια του εκάστοτε στόχου, όπως φαίνεται στο σχ. 9. Η εφαρμογή του εν λόγω κατωφλίου, οδηγεί στην απόρριψη ενός μέρους των θραυσμάτων σχάσης το οποίο μπορεί να εκτιμηθεί μέσω προσομοιώσεων Monte-Carlo οι οποίες πραγματοποιήθηκαν μέσω των κωδίκων GEF [16] και FLUKA [14, 15] . Η αναπαραγωγή του πειραματικού φάσματος σχάσης και ο προσδιορισμός του ποσοστού του ολοκληρώματος που βρίσκεται κάτω από το κατώφλι, αποτελεί τον διορθωτικό παράγοντα f_{amp} ο οποίος έχει τιμή περί το 10%, όπως φαίνεται στο σχ. 10.

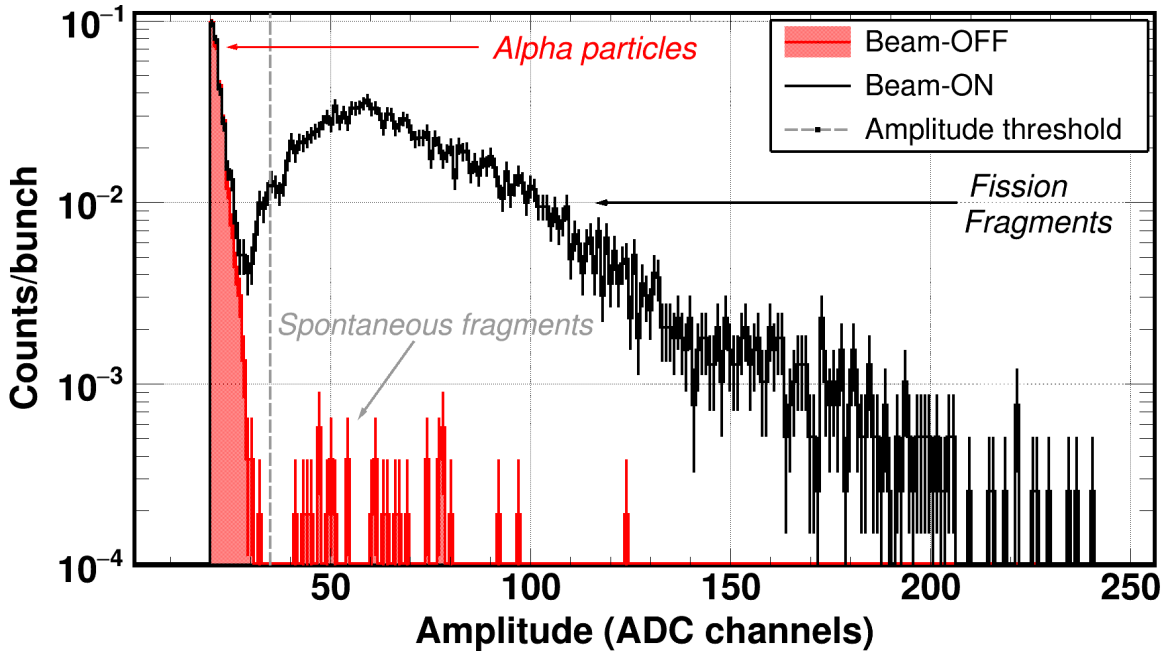

***Σχήμα 9**: Κατά τη διάρκεια των πειραμάτων, εκτός από τα σήματα σχάσης καταγράφονται σήματα που αντιστοιχούν σε σωματίδια α, από την ενδογενή ραδιενέργεια του εκάστοτε στόχου. Τα σήματα αυτά δεν απορρίπτονται κατά τον υπολογισμό της ενεργού διατομής μέσω της εφαρμογής ενός κατωφλίου.*

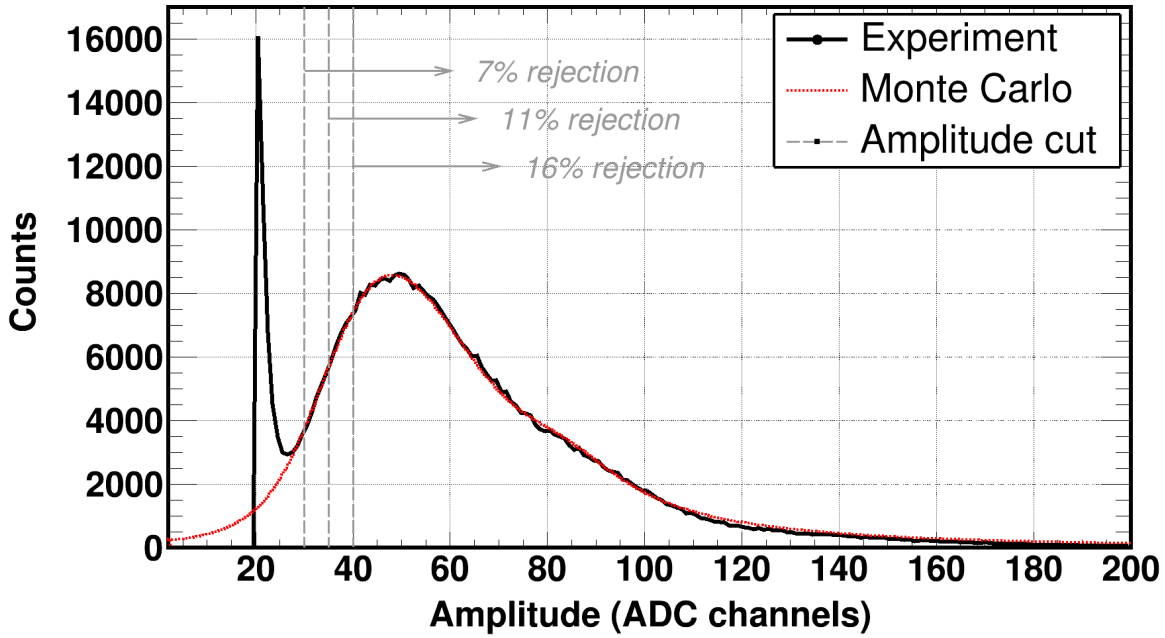

***Σχήμα 10**: Πειραματικό και προσομοιωμένο φάσμα από έναν στόχο ^{240}Pu (#5). Τρία διαφορετικά κατώφλια ύψους εφαρμόστηκαν ώστε να ελεγχθεί η ευαισθησία της διόρθωσης. Για κάθε κατώφλι δίδεται το ποσοστό απόρριψης γεγονότων σχάσης.*

Προσμίξεις στόχων

Όπως φαίνεται στους πίνακες 1 και 2, οι στόχοι που χρησιμοποιήθηκαν περιείχαν προσμίξεις οι οποίες συνεισφέρουν στα καταγεγραμμένα γεγονότα σχάσης. Η αφαίρεση των εν λόγω συνεισφορών πραγματοποιήθηκε μέσω του υπολογισμού της ενεργού διατομής της εκάστοτε πρόσμειξης $\sigma^{(i)}$ πολλαπλασιασμένης με την ατομική της ποσόστωση στο στόχο $f^{(i)}_{abun}$ ($\sigma^{(i)}_w$), όπως φαίνεται στην εξ. (4).

$$\sigma^{(i)}_w = f^{(i)}_{\text{abun}} \cdot \sigma^{(i)} \tag{4}$$

Ο διορθωτικός παράγοντας f_{imp} προκύπτει ως ο λόγος του υπό μέτρηση ισοτόπου (π.χ. ^{240}Pu) ως προς το άθροισμα του γινομένου των εκάστοτε ενεργών διατομών με την αντίστοιχη ποσόστωσή τους, όπως φαίνεται στην εξ. (5).

$$f_{\text{imp}} = \frac{\sigma_w^{^{240}Pu}}{\sum_i \sigma^{(i)}_w} \tag{5}$$

Ένας χαρακτηριστικός διορθωτικός παράγοντας για την περίπτωση του ^{240}Pu φαίνεται στο σχ. 11 (πάνω γράφημα). Στο κάτω γράφημα, φαίνεται η συνολική αβεβαιότητα στον διορθωτικό παράγοντα.

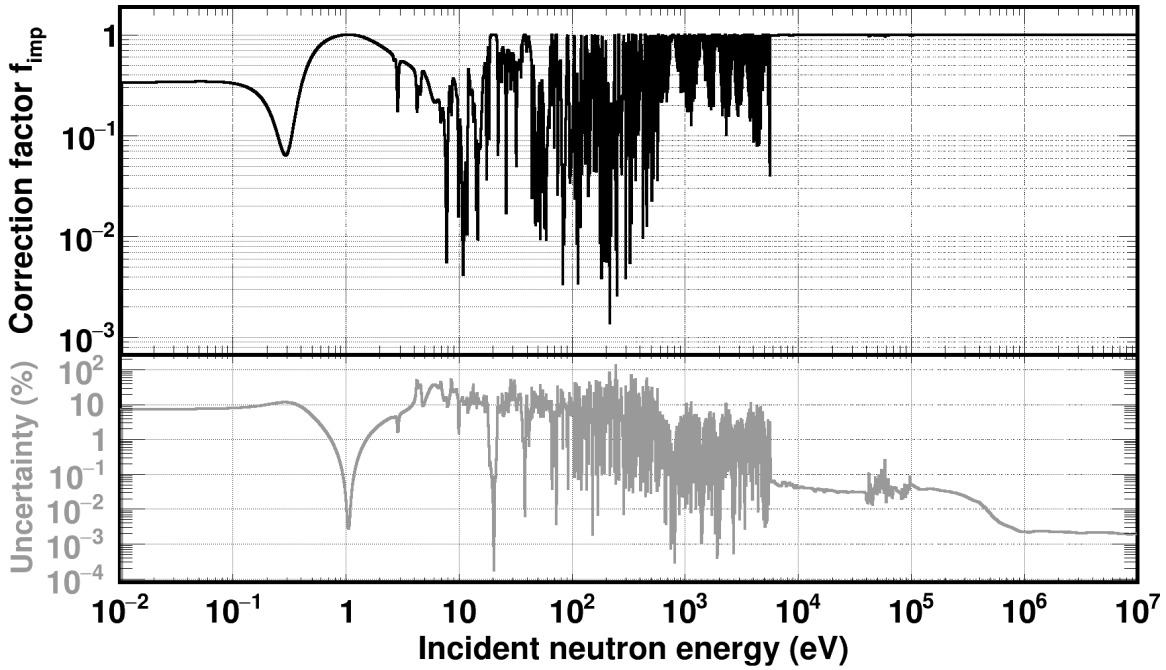

***Σχήμα 11**: Ο διορθωτικός παράγοντας f_{imp} (πάνω γράφημα) που εφαρμόστηκε στην περίπτωση του ^{240}Pu συναρτήσει της ενέργειας. Η διόρθωση είναι σημαντική σε χαμηλές ενέργειες νετρονίων. Στο κάτω γράφημα φαίνεται η συνολική εκτιμώμενη αβεβαιότητα στον διορθωτικό παράγοντα.*

Απώλειες γεγονότων λόγω του υψηλού ρυθμού καταγραφής

Σε περιπτώσεις όπου οι μάζες των στόχων σε συνδυασμό με την ενεργό διατομή μιας αντίδρασης και την προσπίπτουσα ροή είναι τέτοιες ώστε να προκαλέσουν υψηλούς ρυθμούς καταγραφής, η πιθανότητα απώλειας γεγονότων αυξάνεται. Αυτό παρατηρήθηκε στα δύο πειράματα όπου οι στόχοι του ^{240}Pu και ο στόχος ^{237}Np που κατασκευάστηκε στο εργαστήριο IPN-Orsay είχαν μεγάλη μάζα.

Στην ενεργειακή περιοχή άνω του 1 MeV η νετρονική ροή και η ενεργός διατομή σχάσης αυξάνεται με αποτέλεσμα την αύξηση του ρυθμού παραγωγής θραυσμάτων σχάσης και κατ΄ επέκταση την απώλεια καταγραφής τους. Για να θεραπευτεί η εν λόγω αδυναμία, μια νέα μεθοδολογία αναπτύχθηκε στα πλαίσια της παρούσης διατριβής η οποία βασίστηκε στην κατασκευή των κατανομών των χρονικών διαφορών μεταξύ διαδοχικών παλμών και στην μίμηση του ανιχνευτικού συστήματος από μια γεννήτρια παλμών [17].

Κατανομές χρονικών διαφορών

Η κατανομή των χρονικών διαφορών μεταξύ διαδοχικών παλμών αποδεικνύεται ότι είναι εκθετική. Η αντίστοιχη πειραματική όμως, παρατηρείται να αποκλίνει από την εκθετική συμπεριφορά σε μικρές χρονικές διαφορές, λόγω της περιορισμένης χρονικής διακριτικής ικανότητας του ανιχνευτικού συστήματος, όπως φαίνεται στο σχ. 12. Η εκθετική προσαρμογή των πειραματικών σημείων και η επέκτασή της μέχρι την τομή με τον άξονα των y δίνει τον διορθωτικό παράγοντα f_{DT} ως το ολοκλήρωμα που βρίσκεται μεταξύ των πειραματικών σημείων και της επέκτασης της προσαρμογής.

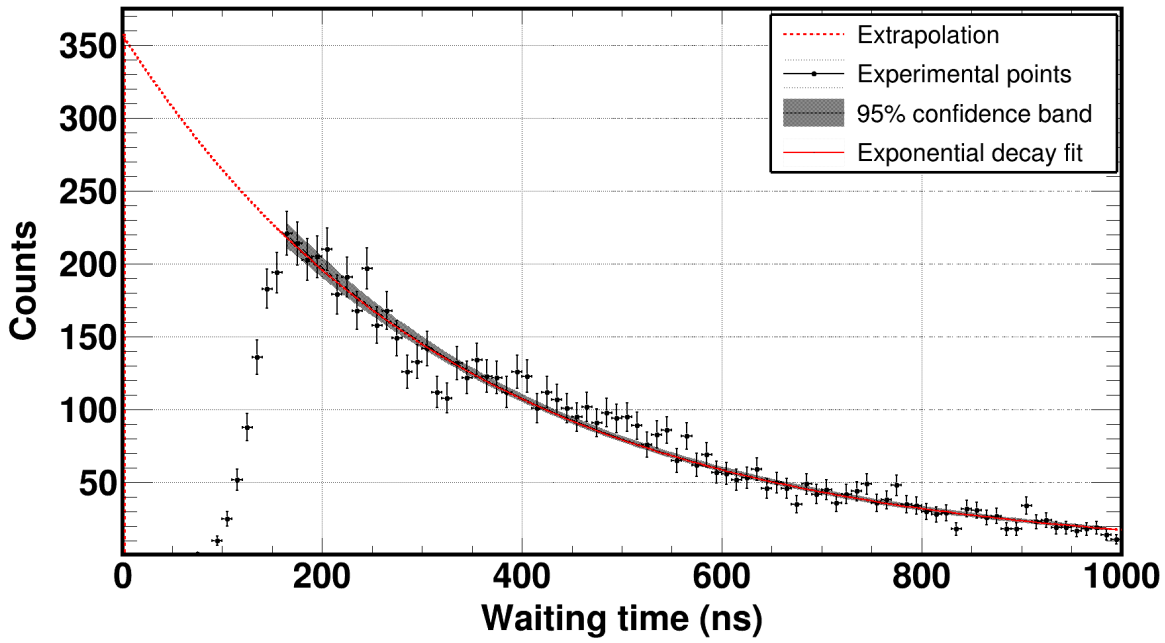

***Σχήμα 12**: Η κατανομή των χρονικών διαφορών μεταξύ διαδοχικών παλμών ακολουθεί τον νόμο εκθετικής πτώσης. Σε μικρούς χρόνους, όμως παρατηρείται απόκλιση από την αναμενόμενη συμπεριφορά.*

Μίμηση του ανιχνευτικού συστήματος

Ένας δεύτερος τρόπος να εκτιμηθεί το ποσοστό των απωλειών λόγω του υψηλού ρυθμού καταγραφής, αποτελεί την μίμηση του ανιχνευτικού συστήματος μέσω γεννητριών παλμών. Πιο συγκεκριμένα, τα πειραματικά σήματα, δίδονται στην εν λόγω γεννήτρια η οποία τα κατανέμει σύμφωνα με την κατανομή Poisson σε συχνότητες που καθορίζονται από τον χρήστη. Έπειτα ακολουθεί η ανάγνωση των παλμών από το σύστημα καταγραφής στο οποίο πραγματοποιήθηκε το πείραμα. Σειρά έχει η αναγνώριση των παλμών από τις ρουτίνες που χρησιμοποιήθηκαν στην ανάλυση των δεδομένων και ο υπολογισμός του πειραματικού ρυθμού καταγραφής. Ο λόγος μεταξύ της καθορισμένης από τον χρήστη και της πειραματικής συχνότητας, δίνει τον διορθωτικό παράγοντα f_{DT}.

Όπως φαίνεται στο σχ. 13, ο υπολογισμός της ενεργού διατομής της αντίδρασης $^{238}U(n,f)$ η οποία αποτελεί αντίδραση αναφοράς, αναπαράγεται ικανοποιητικά με τους δύο τρόπους διόρθωσης. Τα μπλε σημεία, αντιστοιχούν στη μέχρι πρότινος πρότυπη μεθοδολογία που εφαρμοζόταν για την διόρθωση λόγω απωλειών καταγραφής [18, 19].

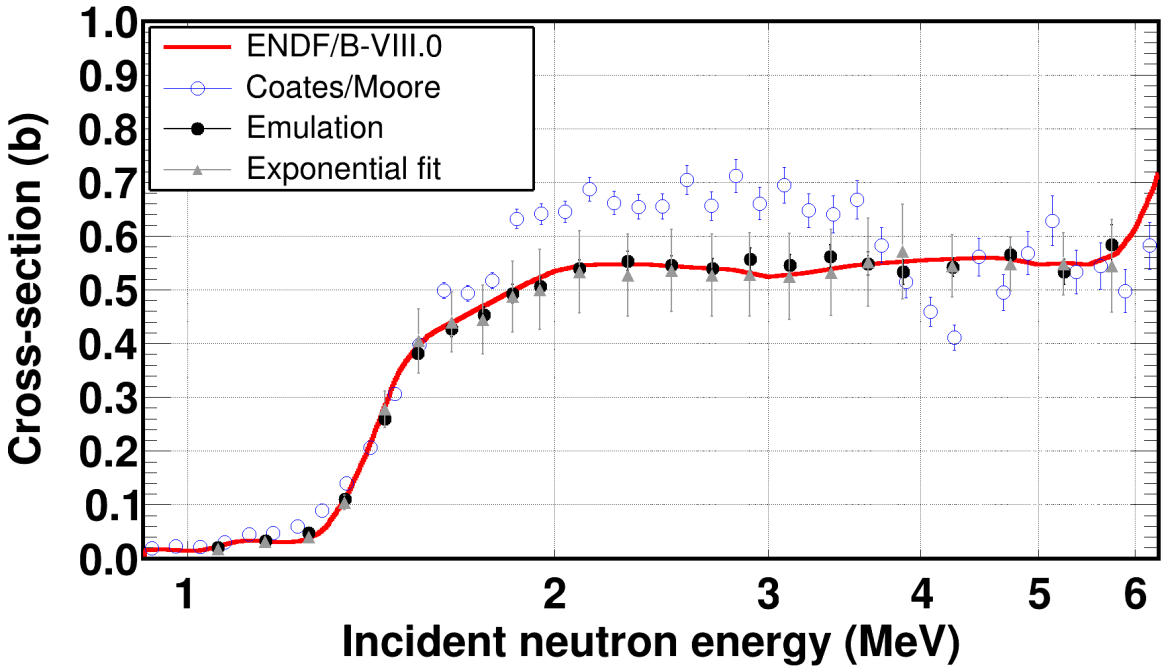

***Σχήμα 13**: Η ενεργός διατομή της αντίδρασης αναφοράς $^{238}U(n,f)$ αναπαρήχθη ικανοποιητικά εντός 5% με τους δύο προτεινόμενους τρόπους διόρθωσης. Τα μπλε σημεία αντιστοιχούν στις μεθοδολογίες που προτάθηκαν από τους Moore [18] και Coates et al. [19].*

Αποτελέσματα

Η ενεργός διατομή σχάσης υπολογίσθηκε στο ενεργειακό εύρος 9 meV - 6 MeV για την περίπτωση της αντίδρασης $^{240}Pu(n,f)$ ενώ για την $^{237}Np(n,f)$ λόγω της παρουσίας προσμίξεων που δεν έχουν ακόμη προσδιορισθεί, το ενεργειακό εύρος

περιορίστηκε μεταξύ 200 keV και 14 MeV, όπως φαίνεται στα σχήματα 14 και 15 που ακολουθούν.

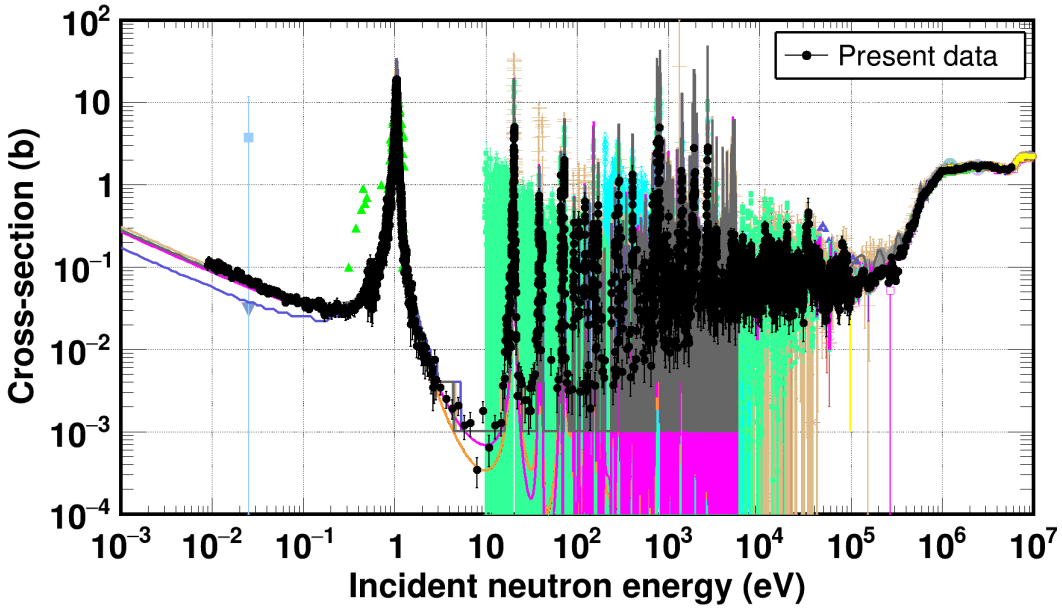

***Σχήμα 14**: Η ενεργός διατομή της αντίδρασης $^{240}Pu(n,f)$, που αποτελεί το πρώτο πείραμα στην EAR2 , υπολογίστηκε στο ενεργειακό εύρος 9 meV - 6 MeV, υπερκαλύπτοντας μια ενεργειακή περιοχή μεγαλύτερη από 9 τάξεις μεγέθους.*

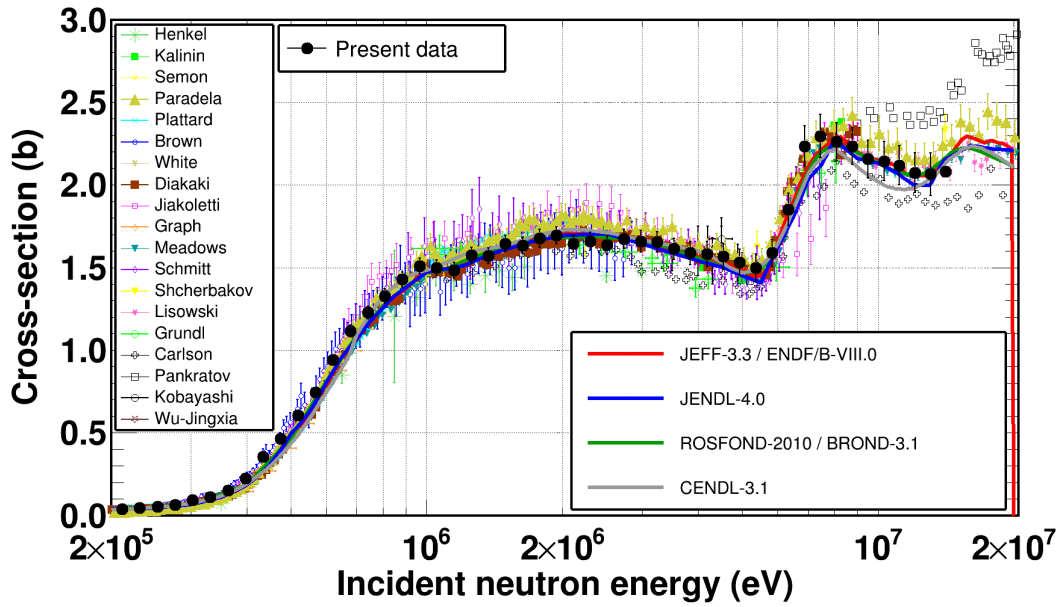

***Σχήμα 15**: Η ενεργός διατομή της αντίδρασης $^{237}Np(n,f)$ υπολογίστηκε στο ενεργειακό εύρος 200 keV - 14 MeV*

Στα επόμενα σχήματα, παρουσιάζεται η ενεργός διατομή της αντίδρασης $^{240}Pu(n,f)$ στα επιμέρους ενεργειακά τμήματα.

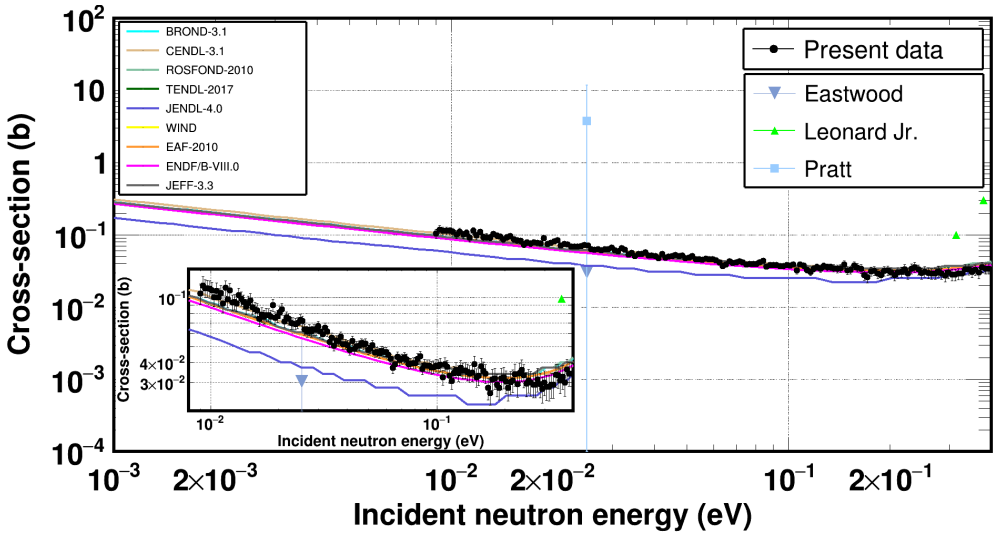

(α′) $9-400\ meV$

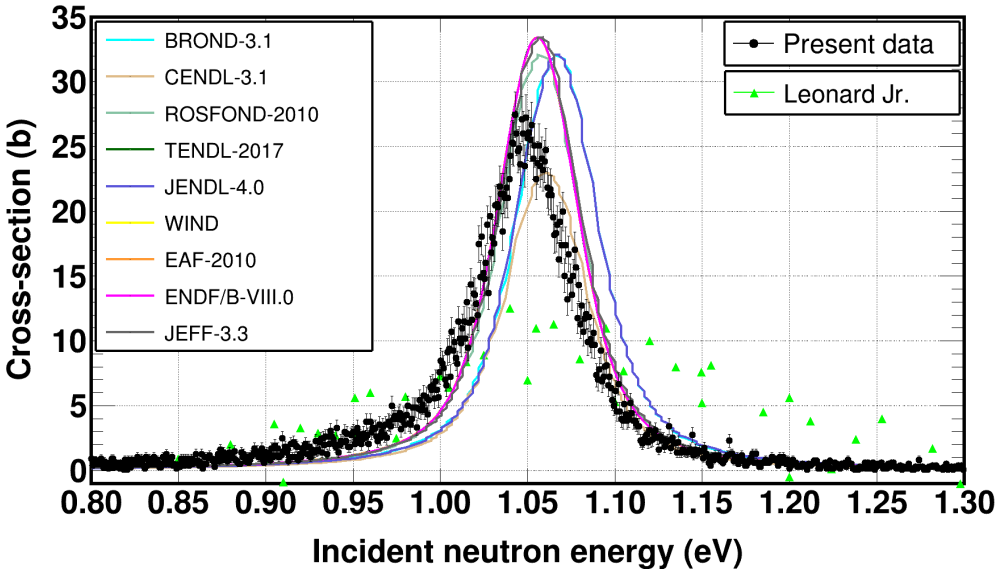

(β′) $0.8-1.3\ eV$

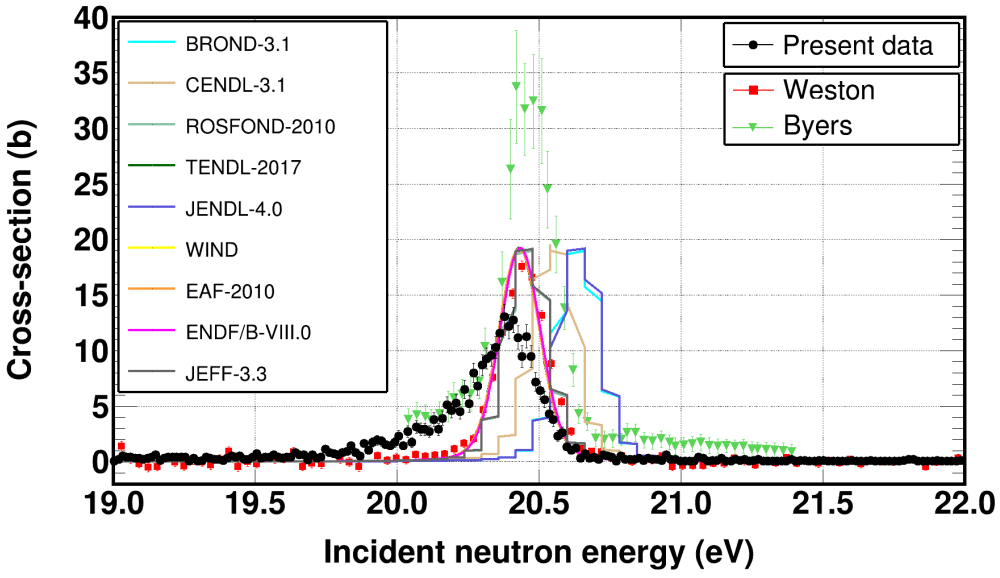

(γ′) $19-22\ eV$

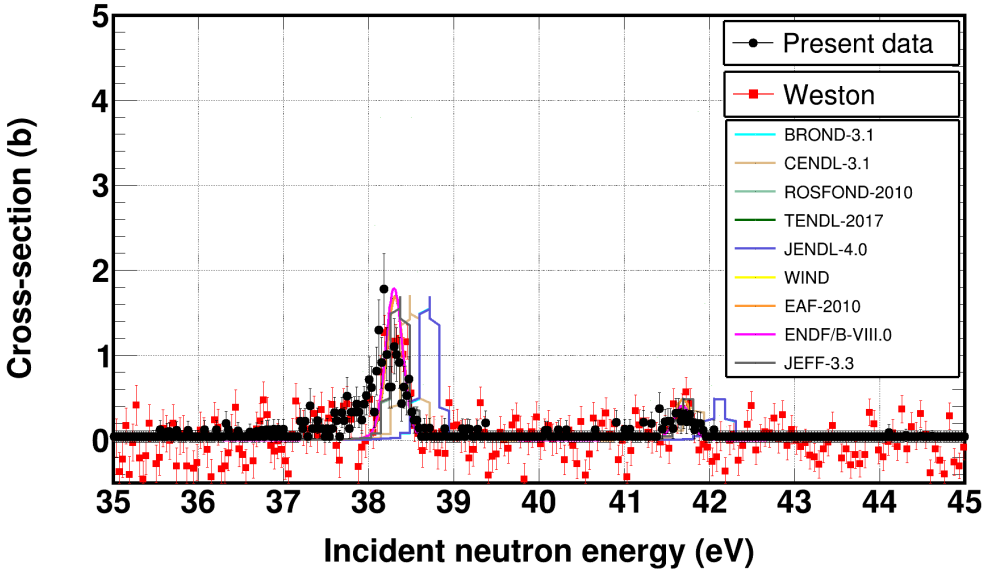

(δ') $35 - 45\ eV$

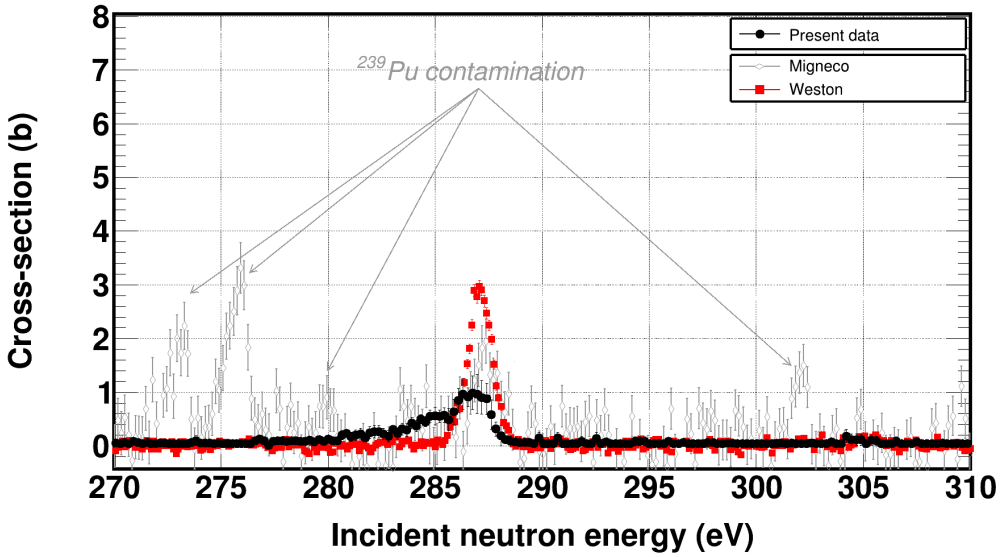

(ε') $270 - 310\ eV$

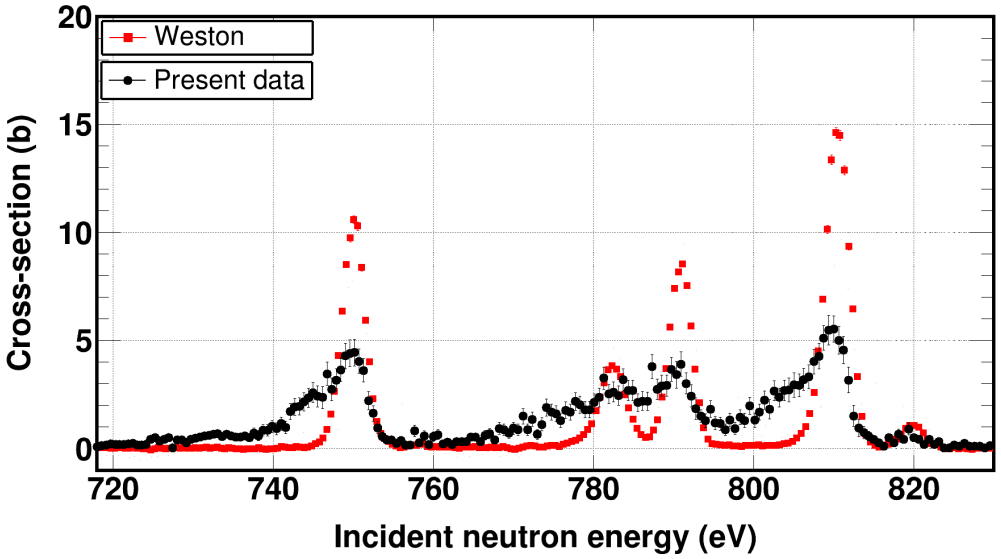

(ς') $720 - 830\ eV$

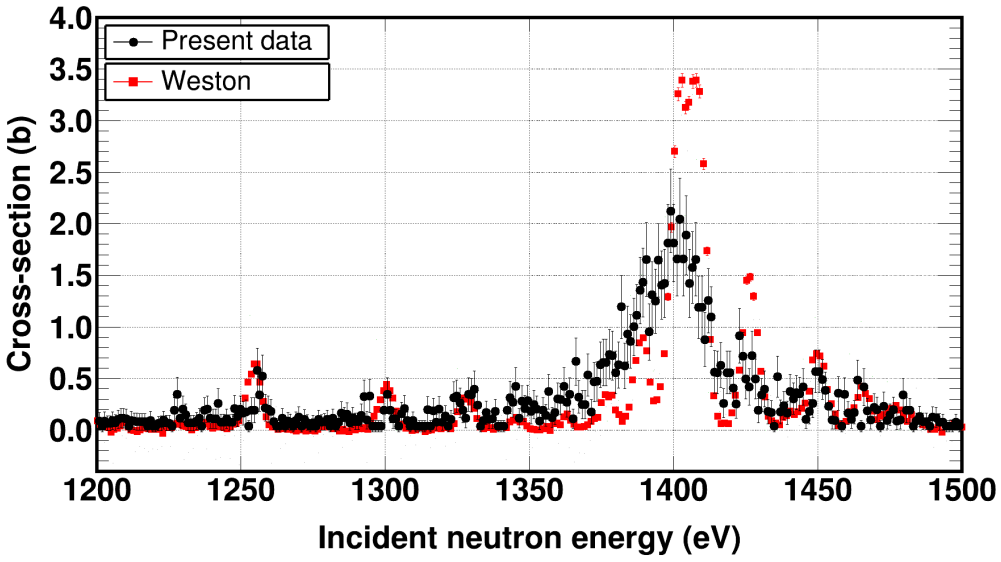

(ζ) $1200-1500\ eV$

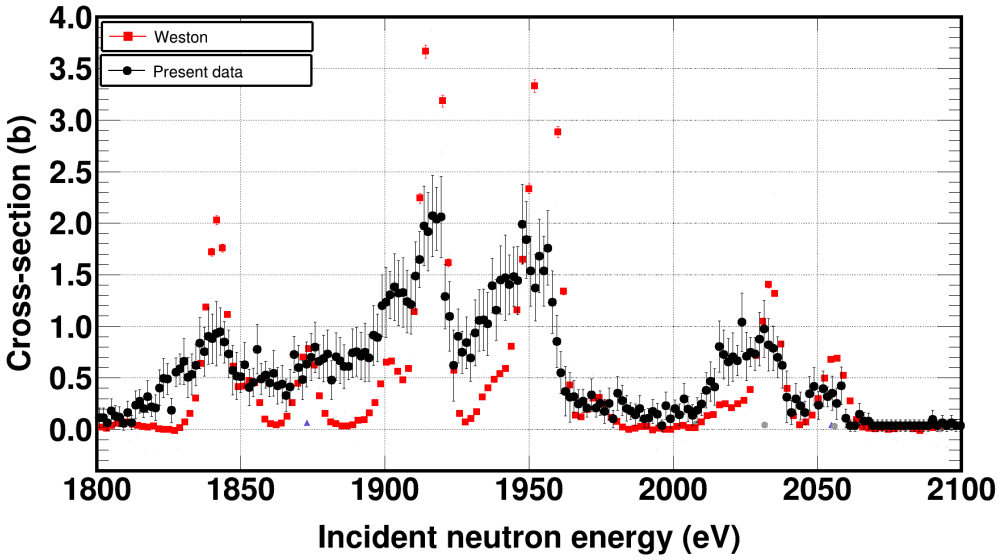

(η) $1800-2100\ eV$

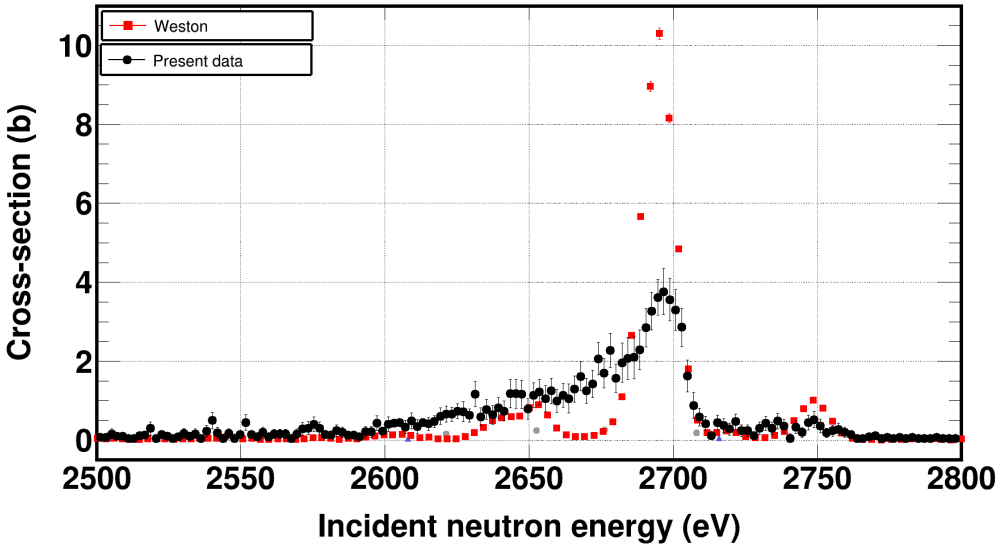

(θ) $2500-2800\ eV$

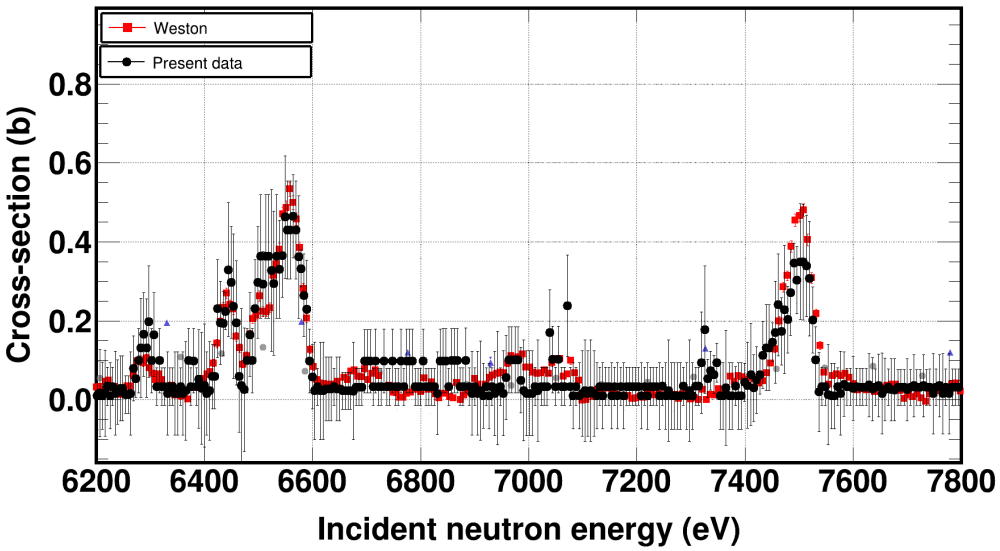

ι΄) $6200 - 7800\ eV$

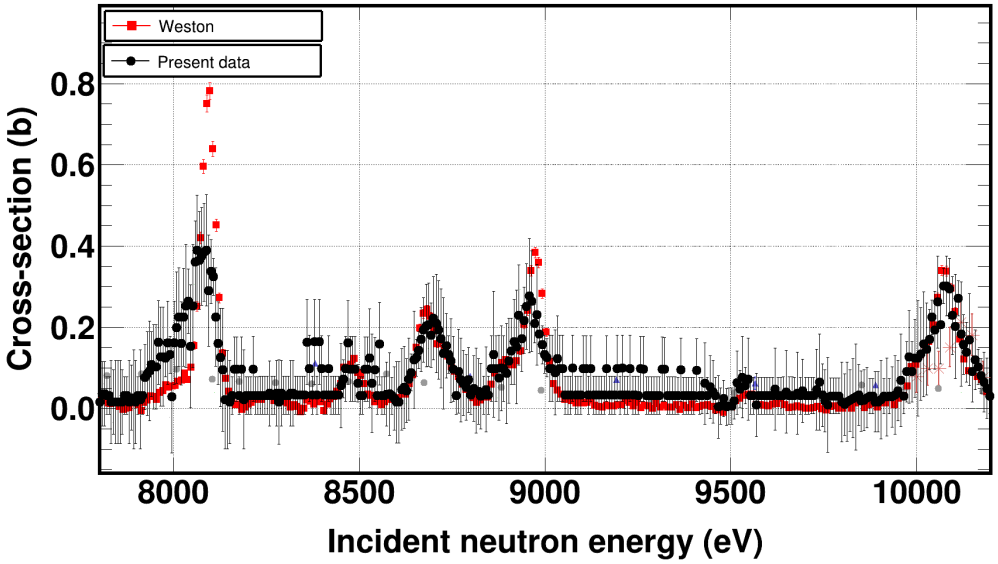

ια΄) $7750 - 10200\ eV$

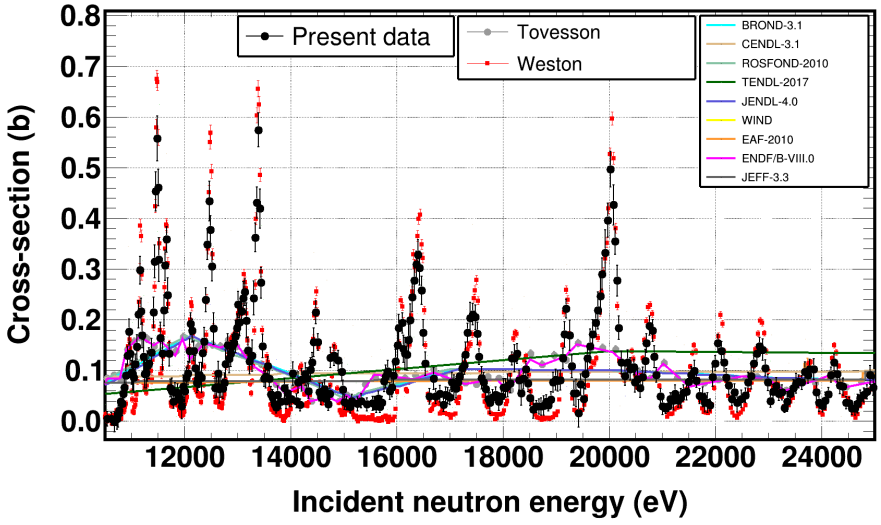

ιβ΄) $11 - 25\ keV$

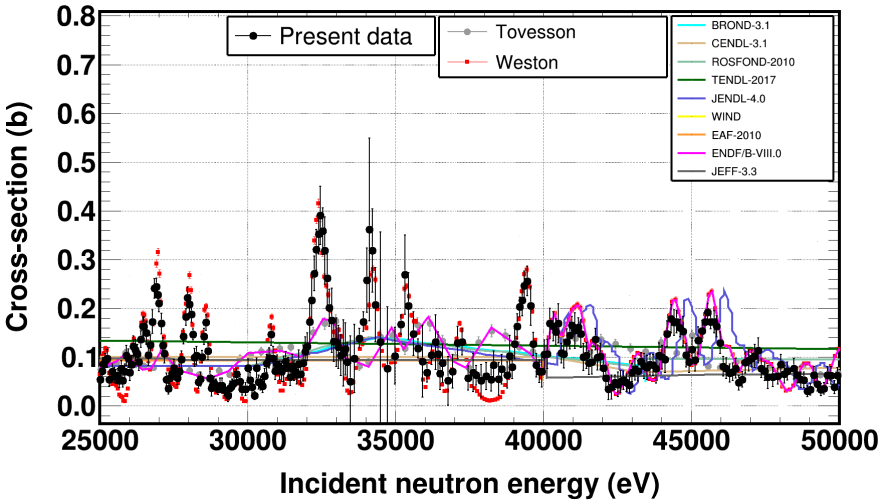

(ιγ') $25 - 50\ eV$

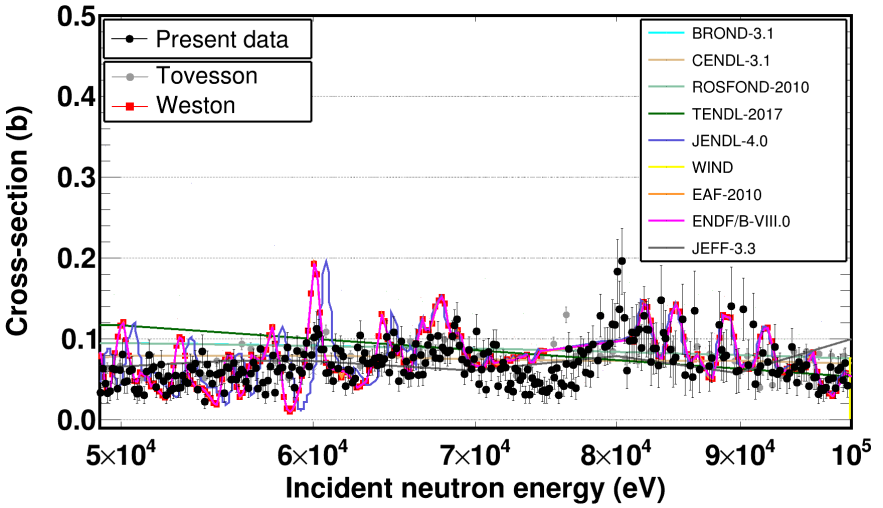

(ιδ') $50 - 100\ keV$

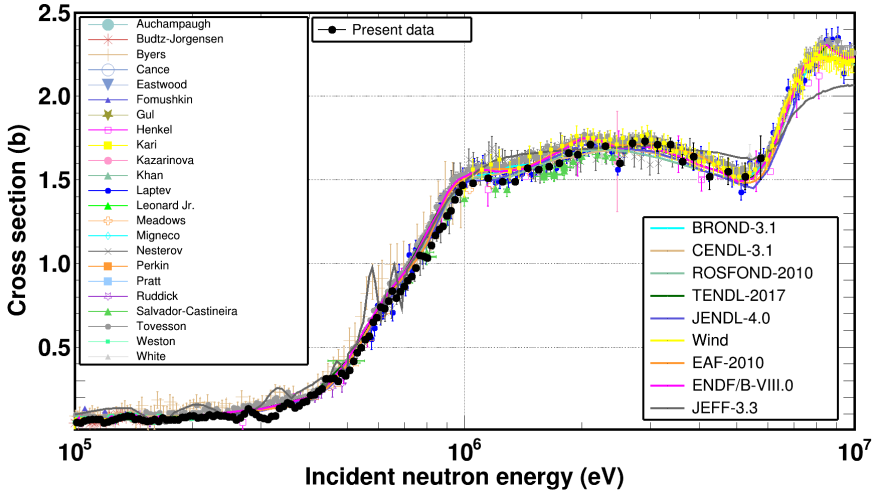

(ιε') $100\ keV - 6\ MeV$

Σχήμα 16: *Η ενεργός διατομή της αντίδρασης* $^{240}Pu(n,f)$ *σε σύγκριση με τα υπάρχοντα πειραματικά δεδομένα και τις βιβλιοθήκες αξιολόγησης στις επιμέρους ενεργειακές περιοχές.*

Θεωρητικοί υπολογισμοί

Ο υπολογισμός της ενεργού διατομής στην περίπτωση της $^{240}Pu(n,f)$ περιλαμβάνει την ενεργειακή περιοχή των συντονισμών, μεταξύ 1 eV και ~ 10 keV. Συνολικά αναλύθηκαν 39 συντονισμοί σχάσης, με χρήση του κώδικα SAMMY και του φορμαλισμού Reich-Moore , το ολοκλήρωμα $\Gamma_n\Gamma_f/\Gamma$ των οποίων δίδεται στον πίνακα 3.

***Πίνακας 3**: Ολοκληρώματα ($\Gamma_n\Gamma_f/\Gamma$) των 39 συντονισμών όπως υπολογίστηκαν από την ανάλυση R-Matrix στην ενεργό διατομή της αντίδρασης $^{240}Pu(n,f)$.*

Ενέργεια συντονισμού (eV)	$\Gamma_n\Gamma_f/\Gamma$ (meV)	Ενέργεια συντονισμού (eV)	$\Gamma_n\Gamma_f/\Gamma$ (meV)
1.06	$4.240\,10^{-4}$	1902.74	1.145
20.56	$9.256\,10^{-3}$	1913.20	4.426
38.45	$3.373\,10^{-3}$	1937.75	1.969
41.88	$1.087\,10^{-3}$	1945.34	7.135
66.73	$5.285\,10^{-3}$	1957.29	12.00
73.03	$1.663\,10^{-2}$	2034.24	2.319
122.26	$1.435\,10^{-2}$	2037.75	$1.491\,10^{-2}$
152.00	$1.986\,10^{-2}$	2054.03	3.788
170.09	$2.809\,10^{-2}$	2688.63	33.97
287.92	$5.365\,10^{-2}$	2700.36	3.66
405.31	$1.206\,10^{-1}$	2746.25	5.342
749.93	3.217	6540.00	28.25
795.22	1.197	7460.13	18.42
808.18	4.240	7502.21	19.46
1400.51	8.587	8059.46	20.95
1412.08	1.855	8090.72	20.08
1423.93	2.044	8721.60	18.88
1842.16	1.578	8903.75	20.65
1853.57	1.645	10082.37	47.55
	$\longrightarrow$	10201.16	18.75

Στα σχήματα που ακολουθούν, παρουσιάζονται τα αποτελέσματα της ανάλυσης R-Matrix .

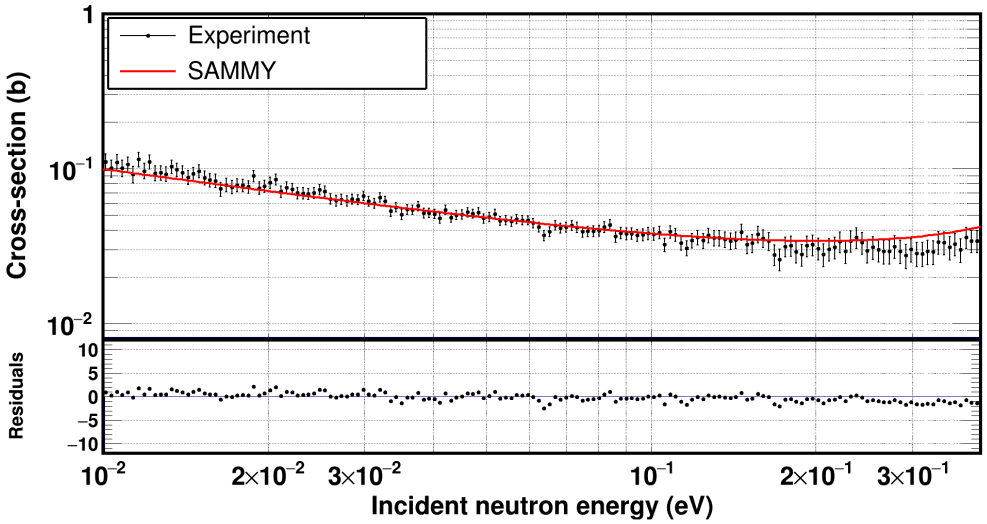

(α′) $10 - 400\ meV$

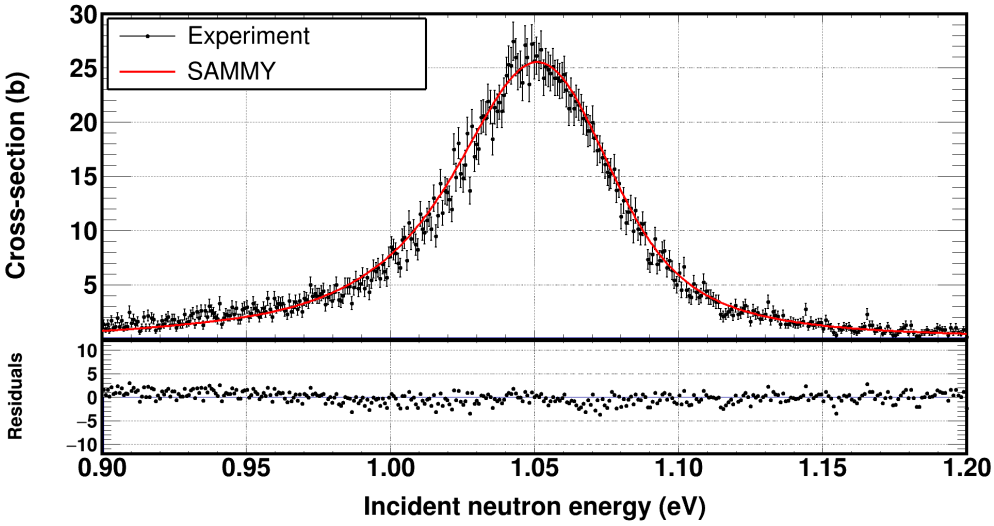

(β′) $900meV - 1.2\ eV$

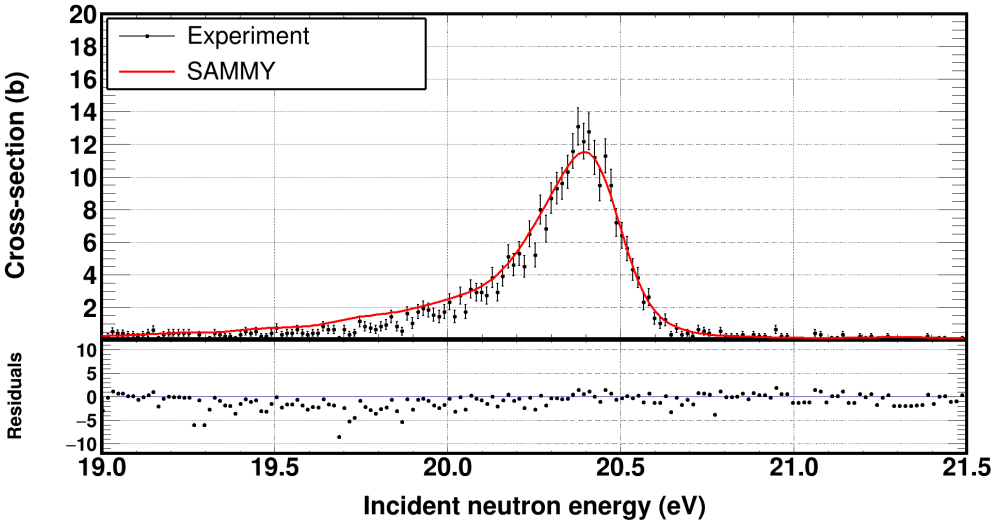

(γ′) $19 - 21.5\ eV$

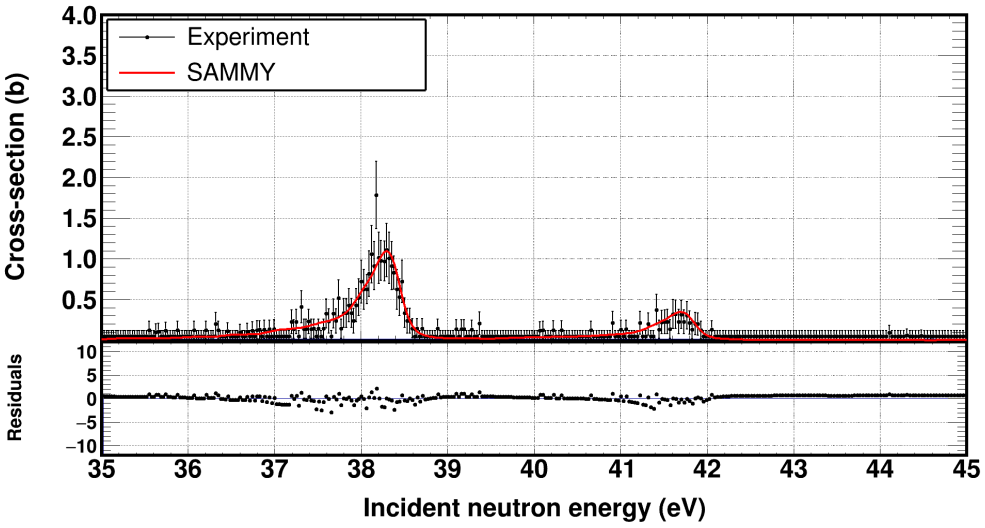

(δ΄) $35-45\ eV$

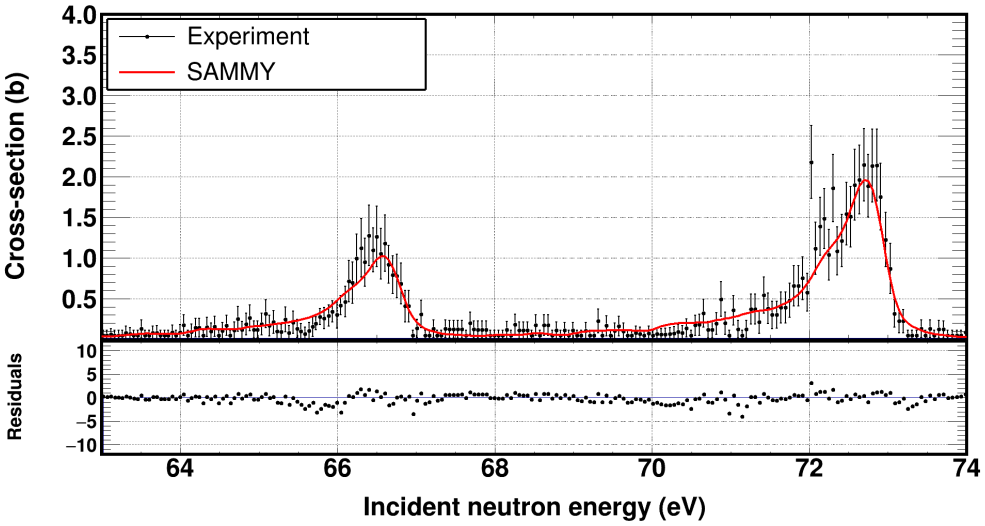

(ε΄) $63-74\ eV$

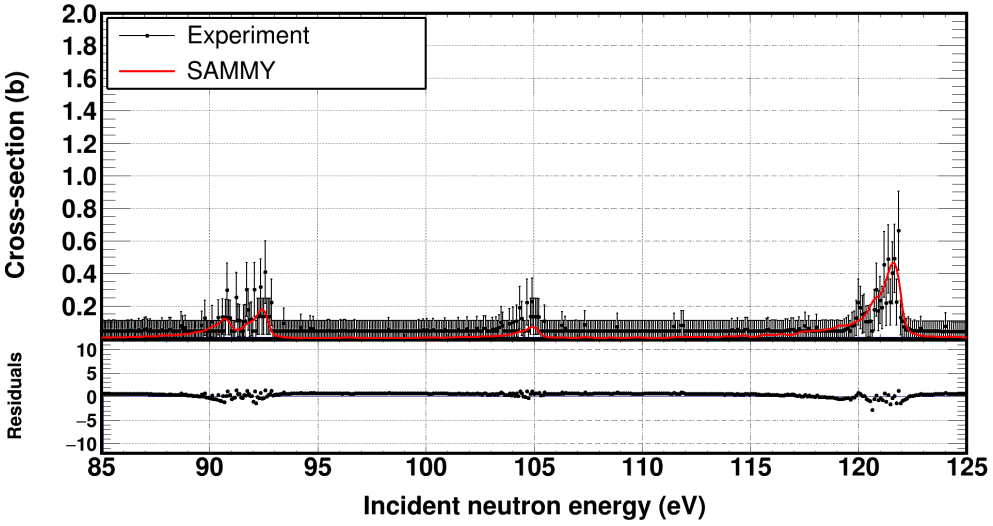

(ς΄) $85-125\ eV$

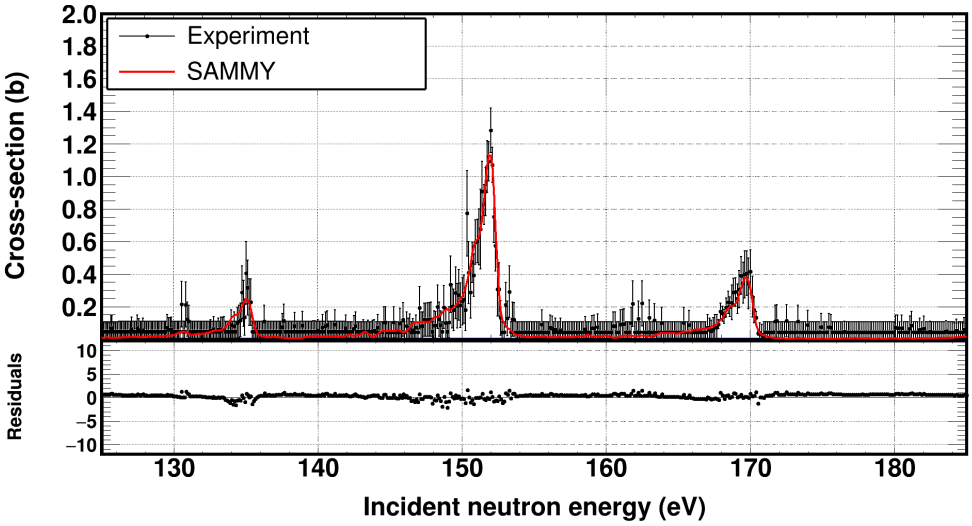

(ζ) $125 - 185\ eV$

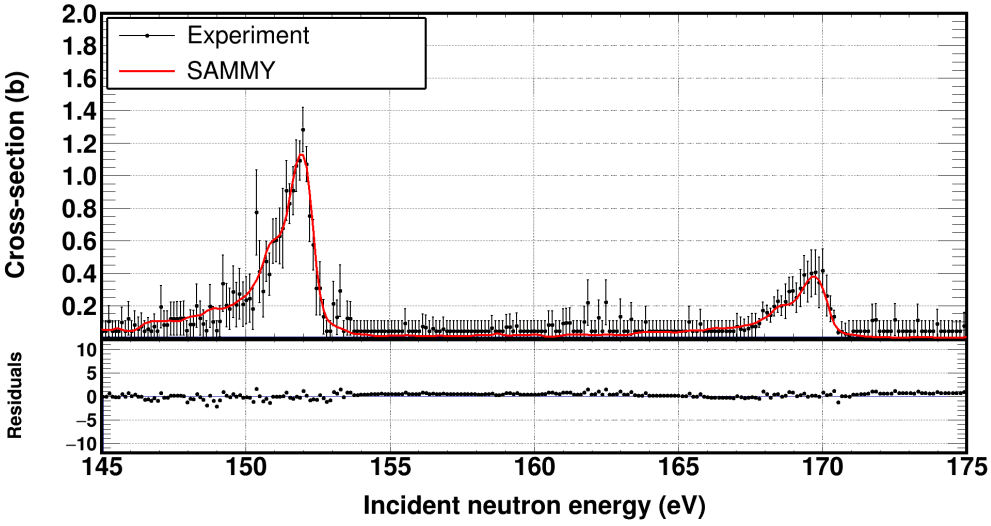

(n′) $145 - 175\ eV$

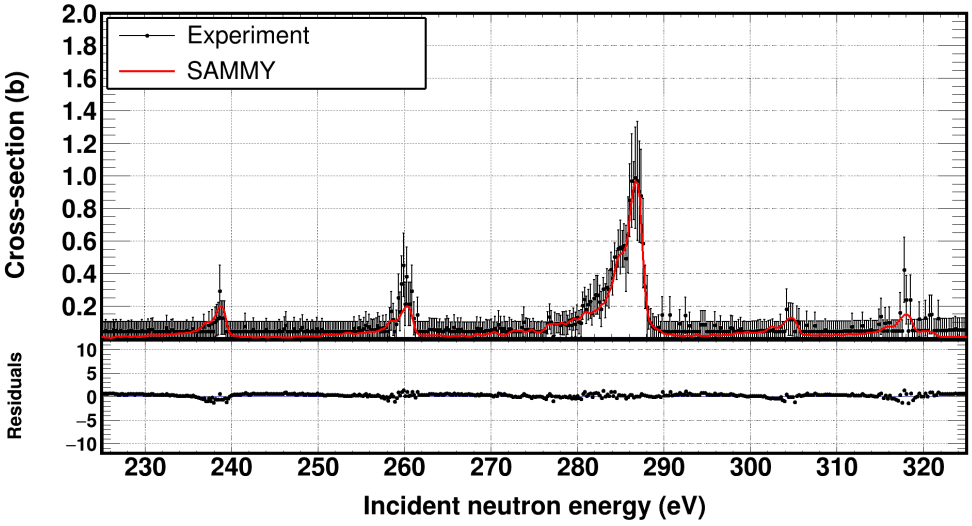

(ϑ′) $225 - 325\ eV$

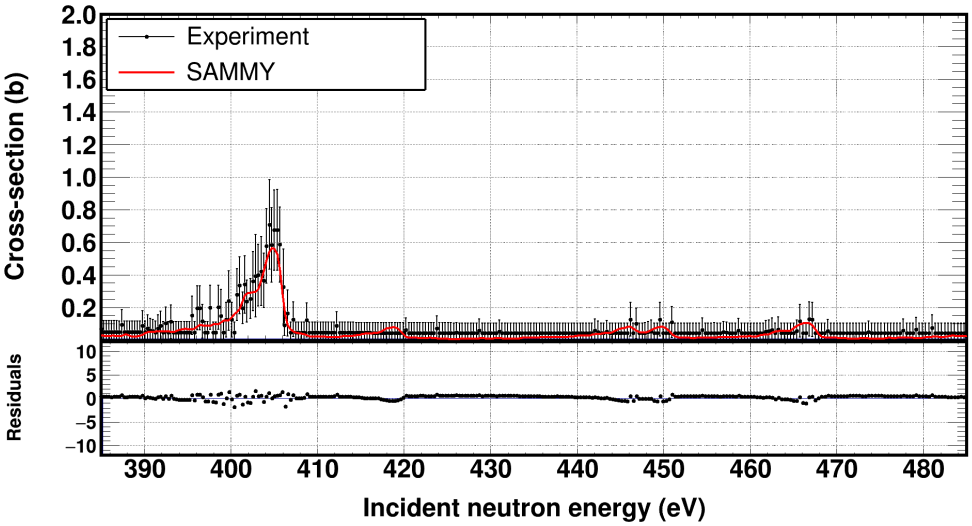

ι΄) $385 - 485\ eV$

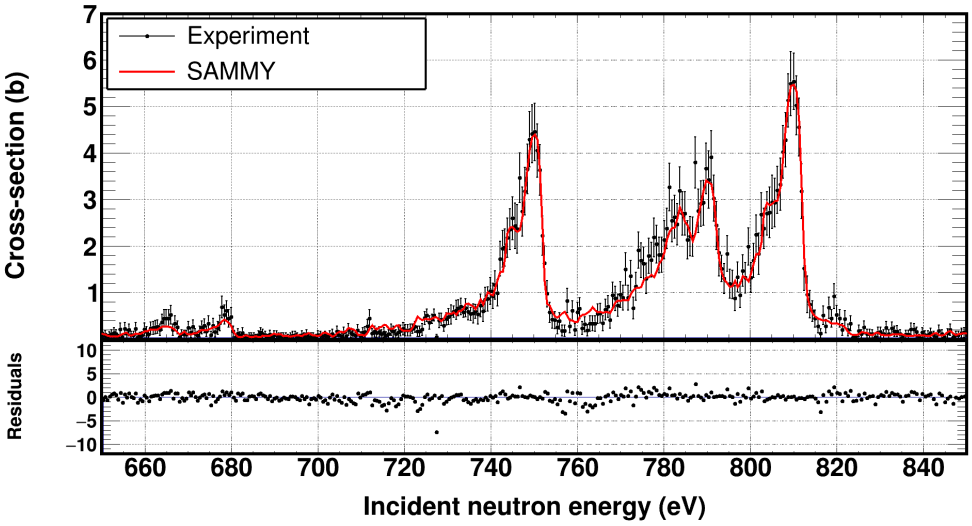

ια΄) $650 - 850\ eV$

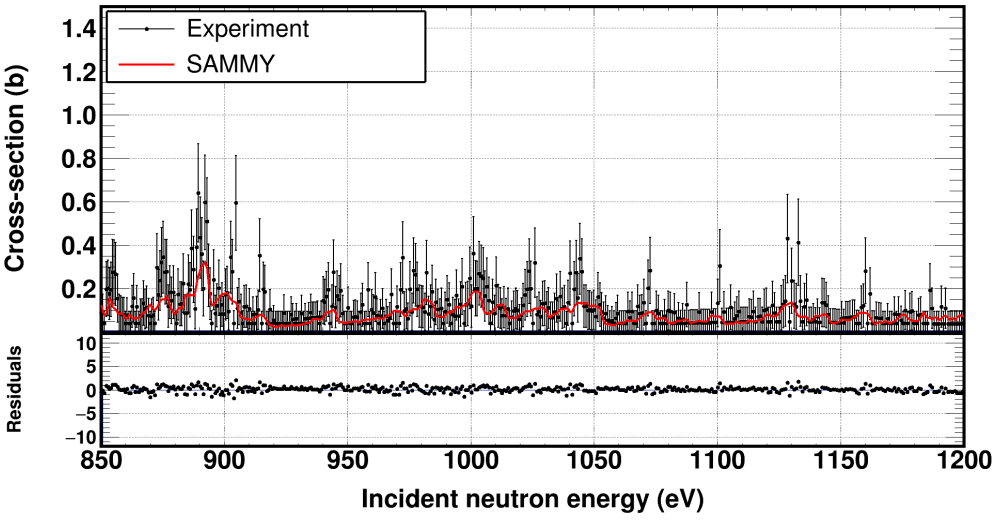

ιβ΄) $850 - 1200\ eV$

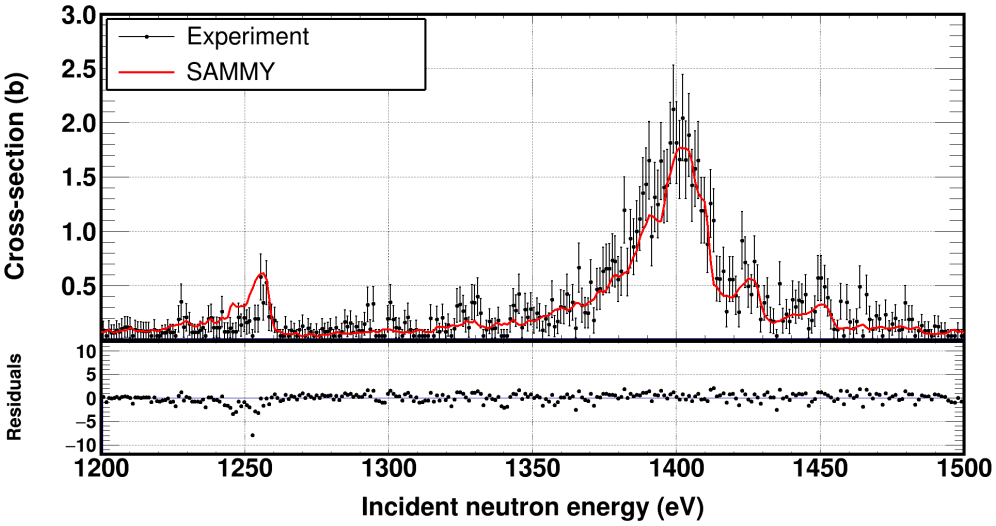

(ιγ′) $1200 - 1500\ eV$

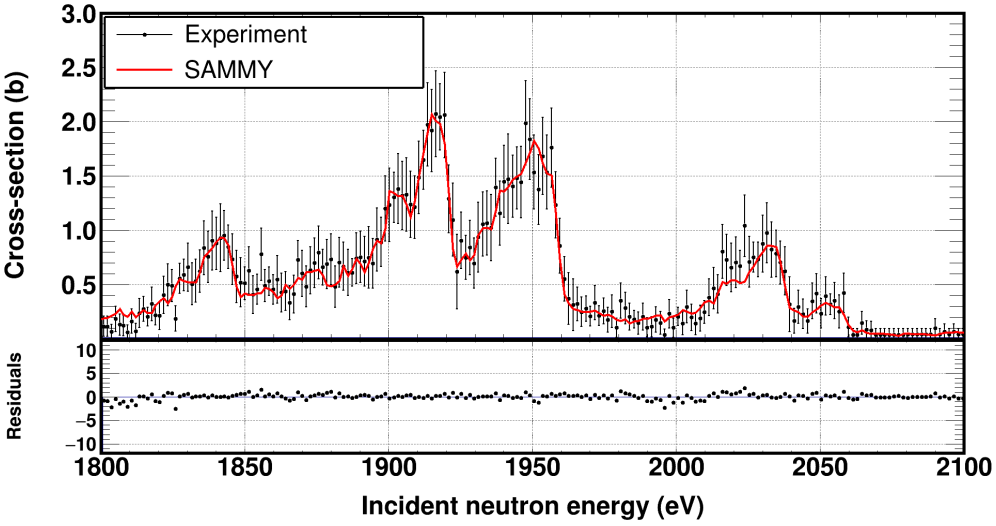

(ιδ′) $1800 - 2100\ eV$

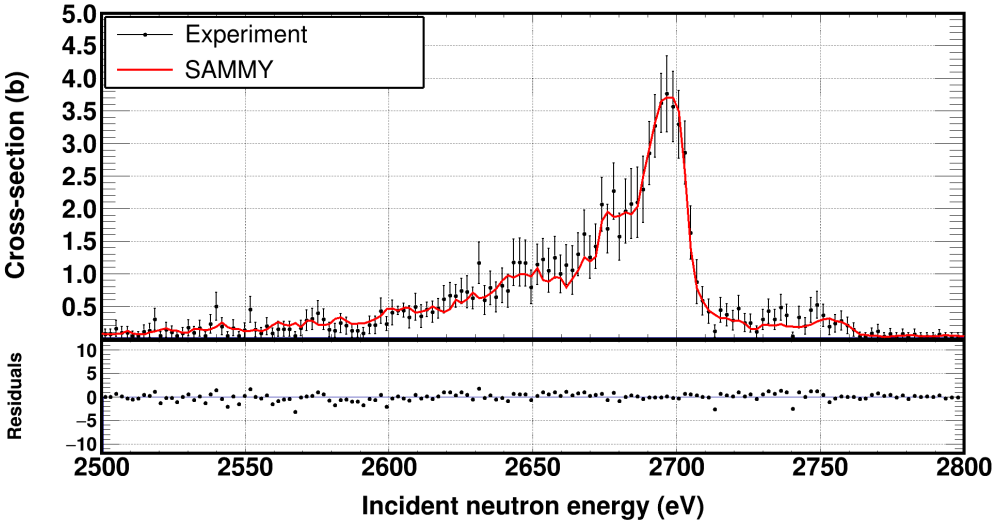

(ιε′) $2500 - 2800\ eV$

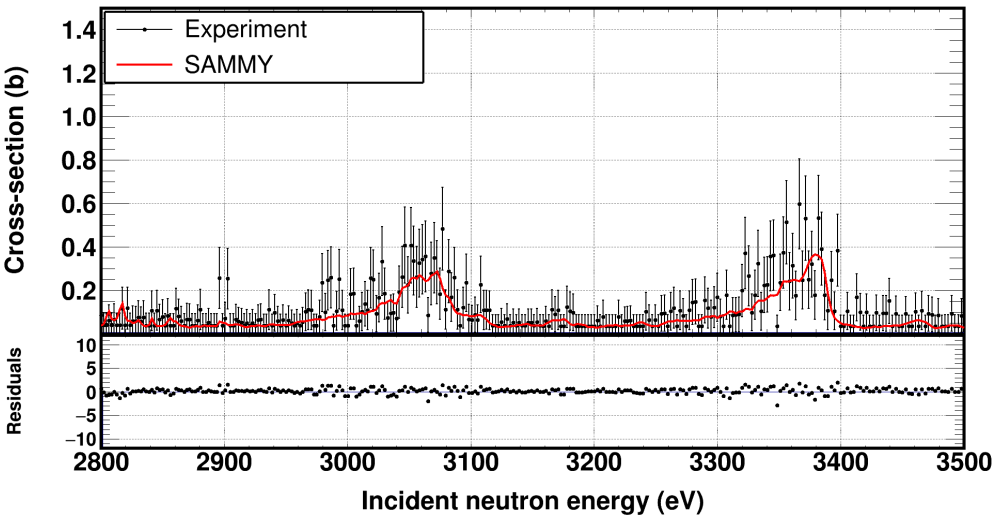

ιϛ′) $2800 - 3500\ eV$

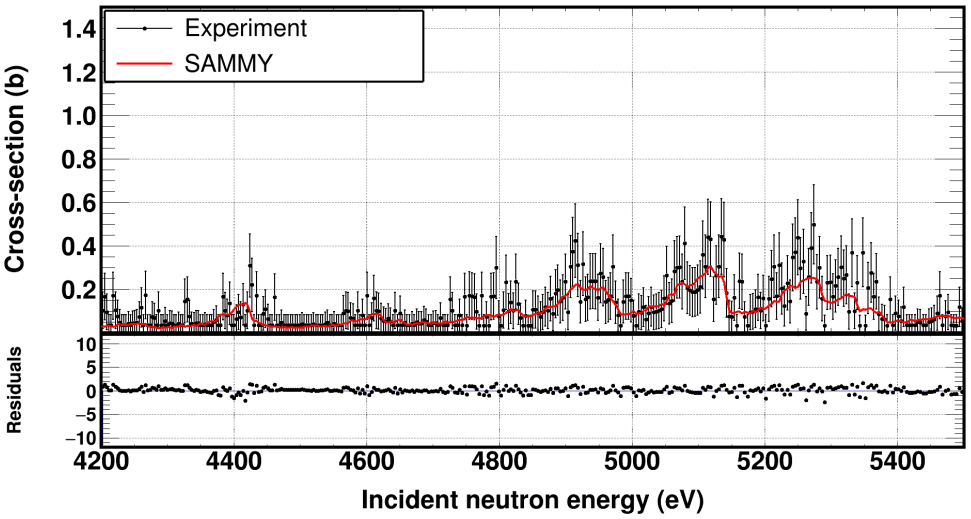

ιζ′) $4200 - 5500\ eV$

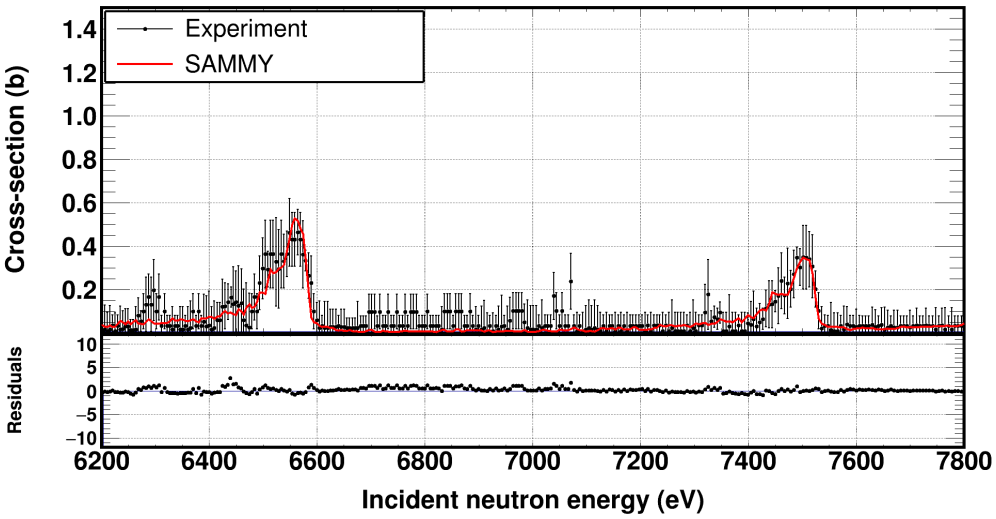

ιη′) $6200 - 7800\ eV$

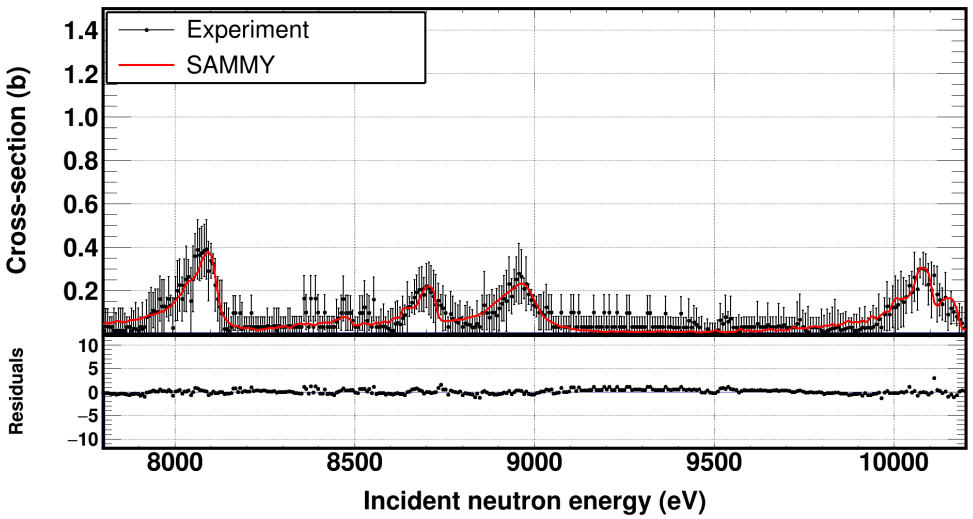

(αʹ) $7800 - 10200\ eV$

Σχήμα 17*: Η προσαρμογή που πραγματοποιήθηκε με τον κώδικα* `SAMMY` *στην ενεργό διατομή της αντίδρασης* $^{240}Pu(n,f)$ *στο ενεργειακό εύρος* $10\ meV$ *έως* $10.2\ keV$.

Τέλος, πραγματοποιήθηκαν υπολογισμοί βασισμένοι στον φορμαλισμό Hauser - Feshbach με χρήση των θεωρητικών κωδίκων `EMPIRE-3.2` και `TALYS-1.9` χρησιμοποιώντας Βελτιωμένο Γενικευμένο Μοντέλο Υπερευστού και το Γενικευμένο Μοντέλο Υπερευστού, αντίστοιχα για τις πυκνότητες ενεργειακών καταστάσεων. Και στις δύο περιπτώσεις, το δυναμικό που περιγράφει την σχάση επιλέχθηκε να είναι διπλό, με ύψος $V_a = 6.650\ MeV$ και $V_b = 5.150\ MeV$ για το πρώτο και το δεύτερο πηγάδι αντίστοιχα για τον πυρήνα ^{241}Pu. Οι τελικοί υπολογισμοί που πραγματοποιήθηκαν φαίνονται στα παρακάτω σχήματα.

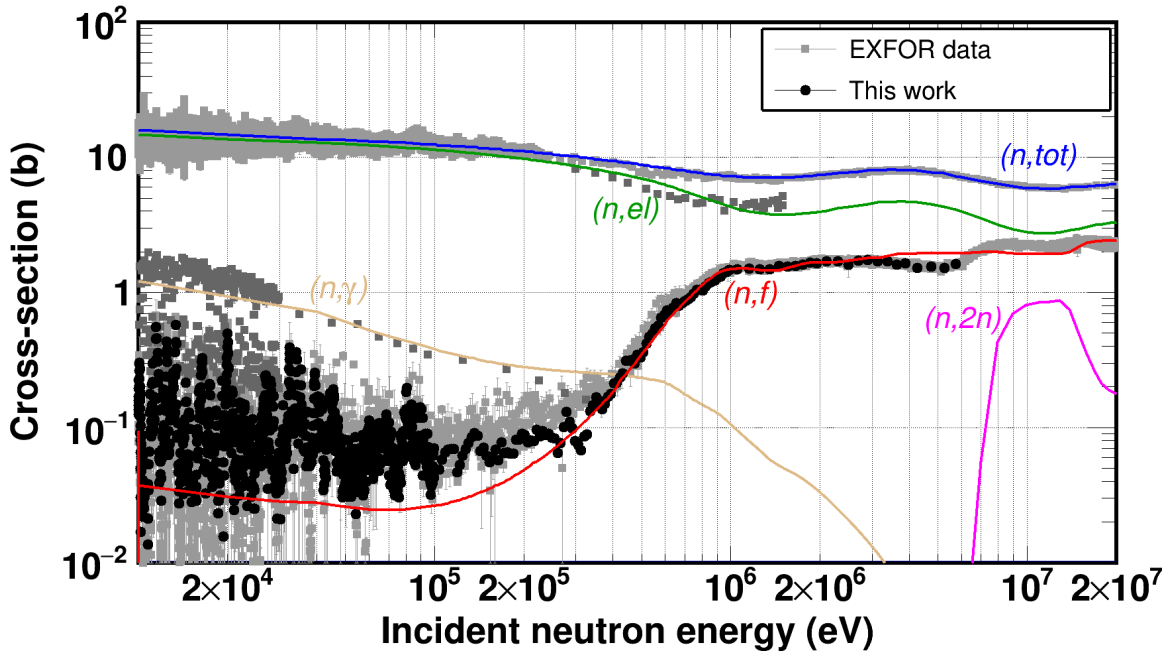

Σχήμα 18: *Οι υπολογισμοί που πραγματοποιήθηκαν με τον κώδικα* `EMPIRE-3.2` *αναπαράγουν ικανοποιητικά τις αντιδράσεις* $(n,tot),(n,el)$ *και* (n,γ). *Στην περίπτωση της* (n,f) *η τιμή της ενεργού διατομής στο κατώφλι της σχάσης ήταν ικανοποιητική, αλλά κάτω από τα* $300\ keV$, *παρατηρήθηκε υποεκτίμηση της.*

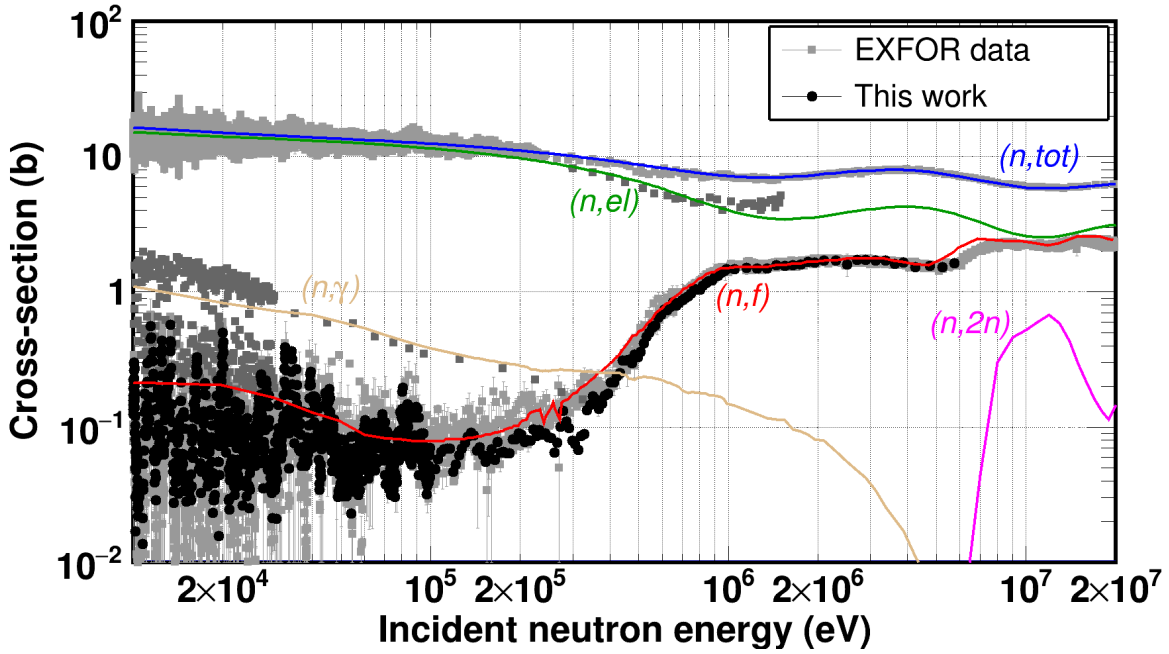

Σχήμα 19: *Οι υπολογισμοί που πραγματοποιήθηκαν με τον κώδικα* `TALYS-1.9` *αναπαράγουν ικανοποιητικά τις αντιδράσεις* $(n,tot),(n,el)$ *και* (n,γ). *Στο κατώφλι της σχάσης η ενεργός διατομή υπερεκτιμάται ενώ κάτω από αυτό οι θεωρητικοί υπολογισμοί συμβαδίζουν με τις πειραματικές τιμές, αλλά όχι με την μορφή της ενεργού διατομής.*

Introduction

Nuclear disintegration: The new nuclear process

Following the major and important discoveries of radioactivy by Henri Becquerel in 1896 [20], the electron by Joseph John Thomson one year later [21], the nuclei by Ernest Rutherford and his students Hans Geiger and Ernest Marsden in 1906 [22, 23], which set the fundamentals and initialised the study of nuclear matter, the discovery of the neutron by James Chadwick in 1932 [24] gave birth to a new era of research concerning this exotic, as considered to be at that time, uncharged particle.

Its lack of charge made the neutron the most suitable particle to bombard naturally abundant elements with, since there is no Coulomb barrier to be overcome, as an attempt to create heavier nuclei and study their behavior. Already in 1934, Enrico Fermi and his collaborators had performed neutron activation experiments using Radon-Beryllium sources with maximum 800 mCi (30 GBq) activities in a great variety of elements ranging from Hydrogen up to natural Uranium [25]. Especially in the case of heavy nuclei, such as Uranium, Fermi et al. [26] were able to observe four different decay constants, two of which were attributed to transuranic elements, while the remaining ones were left unidentified.

It was not until 1939 when Otto Hahn and his student Fritz Strassmann, who was an expert in analytical chemistry, identified Barium after bombarding Uranium with neutrons [27, 28], being therefore the first who experimentally observed the new nuclear process that is known today as neutron-induced fission. The formation of elements with such lower mass than Uranium had been rejected for physical reasons until that time in 1939 when Lise Meitner and her nephew Otto Robert Frisch gave the first explanation of the new phenomenon named nuclear disintegration, by resembling the heavy nucleus to a liquid drop whose decreased surface tension following the absorption of a neutron causes its break-up into two parts [29].

Niels Bohr and John Archibald Wheeler gave a more detailed explanation in 1939 on the mechanism of fission [30] based on the liquid drop model in which they predicted, among others, that without bombardment by neutrons, the fission

rate of uranium should be negligible. Konstantin Petrzhak and Georgy Flyorov decided to confirm that prediction in 1940 only to discover that the spontaneous fission rate of Uranium was in fact non negligible [31].

The aforementioned observation along with the complexity of this nuclear process itself set the demand of a descriptive model with predictive capabilities, high. It took forty years to develop a nuclear potential, named as double-humped fission pottential by S. Bjørnholm and J. E. Lynn [32] in 1980 which, along with the Bohr-Wheeler model are considered to describe accurately the salient features of the phenomenon, up to the present day.

From nuclear fission to nuclear energy

The disintegration of heavy nuclei, as astonishing a phenomenon is thought to be from the time it was discovered up to the present day apart from the interest to understand the physics laws that govern the fission process, gave rise to the beginning of a new era of energy production. Once fission occurs, the sum of the individual binding energies per nucleon BE_{FF} of the remaining nuclei is greater than the binding energy per nucleon BE of the heavy nucleus that has undergone disintegration, as can be seen in fig. 20. Enrico Fermi tried to tame the energy released from this new exothermic nuclear process by producing the first nuclear chain reaction in 1942 [33] in a chain reacting pile, which was the first form of what is known nowadays as a nuclear reactor, that consisted of Uranium as nuclear fuel, embedded in graphite for moderation purposes.

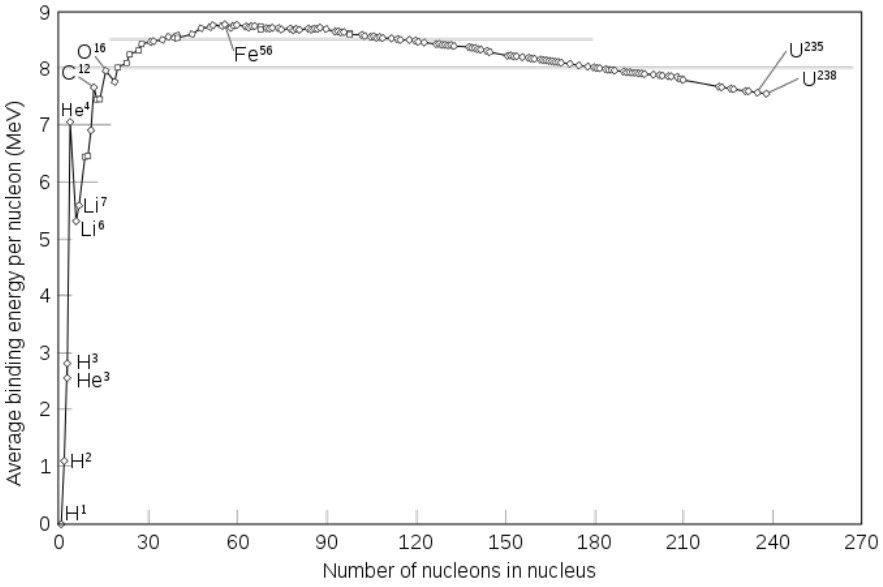

Figure 20: *Average binding energy per nucleon with respect to the mass number Z. It is evident that fission of heavy nuclei with mass numbers greater than 100 is an exothermic reaction and results in the formation of lighter nuclei with higher binding energies per nucleon.*

This first nuclear chain reaction ushered the nuclear age so at the present day 450 nuclear reactors are in operation worldwide, as seen in fig. 21 and provide 10%

of the global energy consumption [1]. There are, however, three major concerns that puzzle both authorities and society regarding the use of nuclear energy, that arise from incidents occurred the past years: (i) the safety of their operation taking into account the nuclear accidents that took place at Three Mile Island, USA in 1979, at Chernobyl, USSR in 1986 and at Fukushima, Japan in 2011, (ii) the efficient nuclear waste management and (iii) the proliferation of nuclear material that is being accumulated over the past fifty years of power plant operation and its potential use in military or terrorist related activities as has already occurred in the cases of numerous nuclear exercises, the atomic bombings of Hirosima and Nagasaki in Japan and in vulnerability attacks on various nuclear installations.

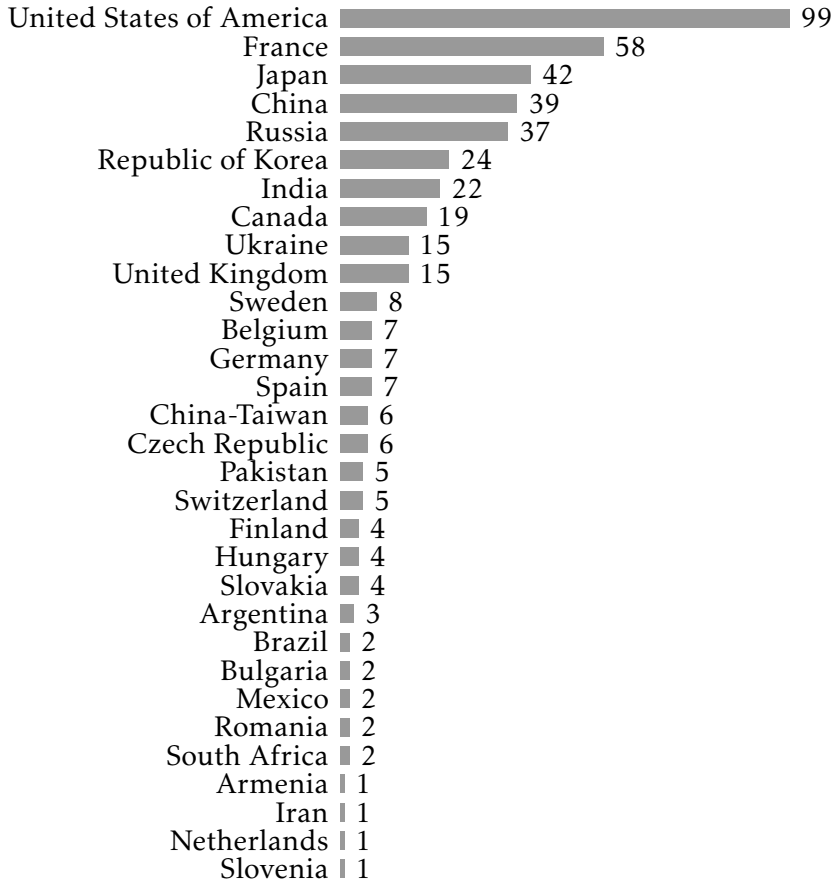

Figure 21: *Number of operational nuclear power plants worldwide in 2018. In total* 450 *nuclear reactors provide* $\sim$ 400 GW_e *of electric power that corresponds to* 10% *of the total global energy consumption [1].*

In this respect, a possible solution to address the aforementioned chief concerns is the development of low operation risk nuclear systems with reduced safety margins and nuclear fuel recycling capabilities. Such an infrastructure will minimise the risk of future accidents and attacks since what is considered up to today to be nuclear waste, will be used as renewable nuclear fuel inside the reactor vessel making additionally the nuclear waste management more efficient.

In order to study the feasibility and development of such reactors, the Generation-IV Forum (GIF) was founded in 2000 [2] to evaluate all possible solutions and fi-

nally to select the one(s) that deemed more suitable to address the aforementioned needs. After almost twenty years of studies and research, 6 out of 130 reactor solutions were found to be the most appropriate to be considered as the successors of the currently in operation reactors. These reactors include the Gas-cooled Fast Reactor (GFR), the Lead-cooled Fast Reactor (LFR), the Molten Salt Reactor (MSR), the Supercritical Water-cooled Reactor (SCWR), the Sodium-cooled Fast Reactor (SFR) and the Very High Temperature Reactor (VHTR).

The new generation-IV reactors, which will be hybrids of thermal and fast reactors, are expected to have more efficient burn-up capabilities and most importantly use waste from currently operating reactors as nuclear fuel [3]. This nuclear waste that is planned to be used consists mainly of minor actinides, whose neutron-induced fission cross sections exhibit an effective threshold above 1 MeV incident neutron energies.

An alternative option for nuclear systems that meet the criteria described above are the sub-critical Accelerator Driven Systems (ADS) [4, 5]. Their operation is based on the production of high energy neutrons via spallation caused when charged particles, usually electrons and protons, are accelerated at high energies (~ 1 GeV) by LINACs or cyclotrons, and impinge on high atomic mass targets, such as Tungsten, depleted Uranium, Lead etc. A prominent advantage of these systems is the ability to efficiently control the chain reaction that powers the reactor on, as well as the possibility to operate in sub-criticality since the neutron spectrum that is injected in the reactor after the spallation can be instantly cut-off, by simply switching the accelerator off. In addition, the fast neutron spectrum of ADS makes them the most suitable solution at the present day, to incinerate and transmute long-lived nuclear waste, such as Plutonium and Neptunium isotopes, by using the nuclear waste of conventional reactors as fuel.

An additional limiting factor in the production of electricity by the use of nuclear resources, is the amount and availability of today's most widely nuclear fuel: Uranium. According to a recent publication by S. Gabriel et al. in 2013 [9], the remaining 7.1 Mt of Uranium resources would be just enough to meet the current demand until 2050, therefore an alternative approach must be considered.

In this respect, a viable solution would include the use of Thorium based fuels, which is found in larger than Uranium quantities on Earth. Natural Thorium consists of 99.98% of the stable ^{232}Th, which although not fissile itself, if combined with ^{235}U and/or ^{239}Pu can be sufficient to retain a nuclear chain reaction and therefore be used as nuclear fuel. In addition, neutron capture in ^{232}Th forms ^{233}Th which in turn undergoes two β-decays to produce the fissile Uranium isotope ^{233}U, which can enhance the efficiency of the nuclear fuel cycle by 30% more efficiently than ^{239}Pu does at the conventional uranium cycle, taking into account both the higher ^{232}Th than ^{238}U neutron capture cross-section and the comparable ^{233}U to the ^{239}Pu fission cross-section at the thermal point, as can be seen in fig. 22
.

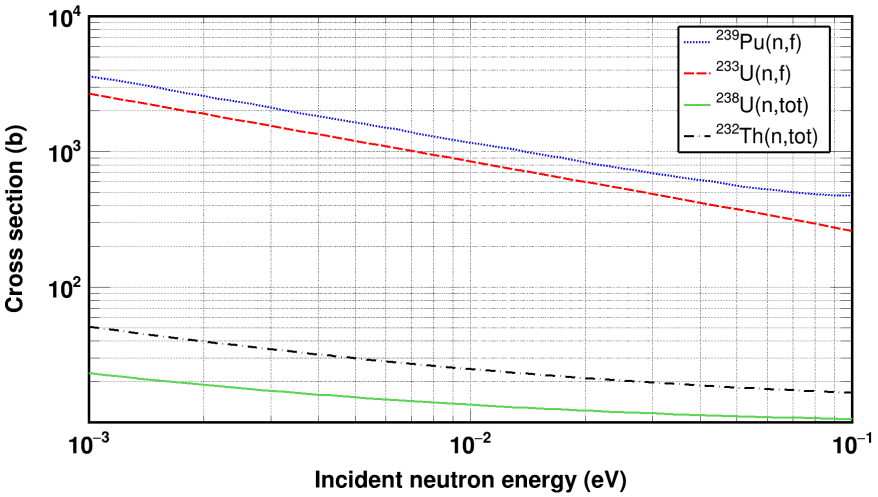

Figure 22: *Total neutron capture cross-sections for ^{232}Th and ^{238}U along with neutron-induced fission cross-sections of ^{233}U and ^{239}Pu in the thermal region as obtained from the JEFF-3.3 evaluation library [34].*

Additional benefits of the use of a Th/U based nuclear cycle include the limited production of long-lived actinides compared to the conventional U cycle as well as its intrinsic proliferation resistance due to the high γ-activity of the daughter nuclei of the short-lived ^{232}U (mainly ^{212}Bi and ^{208}Tl) which is formed from $(n,2n)$ reactions on ^{232}Th. This high and strong emission of γ-radiation is considered to utilise the burn-out products of Th/U fuel as unattractive carriers of highly enriched Uranium and weapons grade Plutonium and therefore avoids the proliferation for non-peaceful purposes [35].

On the way to more accurate nuclear data on actinides

For the reasons and concerns discussed previously, it is of vital importance for the feasibility and sensitivity studies of next generation nuclear reactors to obtain accurate nuclear data on a variety of actinide isotopes, for various neutron-induced reactions at neutron incident energies that range from thermal up to tens of MeV [36]. As an example of the importance of accurate nuclear data, the Nuclear Energy Agency (NEA) [7], a specialised agency within the Organisation for Economic Cooperation and Development (OECD) [8] has introduced the High Priority Request List (HPRL) [6] in which numerous neutron-induced cross-sections are listed for various applications along with their target accuracies.

Among other minor actinides reaction cross-sections, $^{240}Pu(n,f)$ is included in HPRL from 2008 [11] and up to the present day the target accuracies, seen in table 4 [37] have not been met. ^{240}Pu, which is produced in conventional nuclear reactors as a by-product from neutron capture on ^{239}Pu, is a long-lived non-fissile Plutonium isotope and therefore builds-up inside a thermal reactor. The amount of Plutonium output that a typical commercial thermal reactor discharges, is approximately 28 kg per Terawatt-hour-electric (TWhe) or about 245 kg per year [10]. The

fissionable ^{240}Pu isotope constitutes about a quarter of the total Plutonium output, which is a significant quantity that can be transmuted in new generation reactors that operate with a fast neutron spectrum, serving as nuclear fuel.

Table 4: *Summary of current and requested target uncertainties of the neutron-induced fission cross-section of ^{240}Pu from incident neutron energies 454 eV up to 6.07 MeV for five types of reactors: Sodium-cooled fast reactor (SFR), European fast reactor (EFR), Gas-cooled fast reactor (GFR), Lead-cooled fast reactor (LFR) and Accelerator-Driven Minor Actinides Burner (ADMAB).*

Energy Range	Initial Uncertainty (%)	Target Uncertainties (%)				
		SFR	EFR	GFR	LFR	ADMAB
454 eV - 2.03 keV	22	13	-	9	-	-
498 keV - 1.35 MeV	6	2	4	2	2	2
1.35 MeV - 2.23 MeV	6	3	-	3	3	3
2.23 MeV - 6.07 MeV	5	3	-	3	3	-

For these reasons several recent experimental data sets have been added to the existing ones. The data sets found in the Experimental Nuclear Reaction Data library (EXFOR) [38] are dating from 1956 up to 2015. An extensive list of all the data found in EXFOR can be seen in table 5 and the reported cross-sections are seen in fig. 23, where discrepancies can be seen that reach up to 60% in the resolved resonance region between 454 eV- 2.03 keV (fig: 23a) and up to 30% in the energy range 498 keV - 6.07 MeV (fig: 23b).

At the same time the impact of the $^{237}Np(n,f)$ cross-section is equally high since it is frequently used as a reference reaction in many measurements related to feasibility and design studies for advanced nuclear systems, on account of its low fission threshold and moderate activity therefore it is also included in HPRL since 2015 with 2 – 3% target accuracies in the energy region 200 keV - 20 MeV [12]. In addition, the International Atomic Energy Agency (IAEA) [39] has realised that Neptunium could be used for nuclear explosive devices if available in sufficient quantities, therefore a monitoring scheme was approved to keep track of receipts and exports of separated ^{237}Np [40]. In this case as well, the most efficient means to minimise proliferation includes the use of ^{237}Np as a nuclear fuel in advanced fast reactors. To achieve these goals however, more accurate data sets than the ones already available in EXFOR, which are listed in table 6, are needed. Finally, in fig. 24 the available in literature data can be seen, where discrepancies exist that reach up to 25% in the energy range 200 keV - 1 MeV (fig. 24a) while smaller but still in need to be resolved 10% discrepancies can be seen in the first chance fission plateau between 1 - 6 MeV (fig. 24b) where even the two latest measurements by Diakaki et al. [41–43] and Paradela et al. [44] at the time that the present thesis was written show discrepancies up to 7%.

In order to meet the requirements on the requested target accuracies, the best possible estimations on the aforementioned cross-sections need to be made which

arise from evaluating available in literature data sets. A complimentary variety of data from several facilities that employ different experimental set-ups and techniques, using various detection systems and different reference reactions is deemed necessary to minimise and eventually eliminate systematic uncertainties of the experimental observables.

In view of all the above, the $^{240}Pu(n,f)$ and $^{237}Np(n,f)$ reactions have been extensively studied at the newly commissioned experimental area 2 (EAR2) at the neutron time-of-flight facility (n_TOF) at the European Center for Nuclear Research (CERN), which features a 19.5 m flight path, for neutron energies that span from thermal to a few MeV, using detection set ups based on the Micromegas detector.

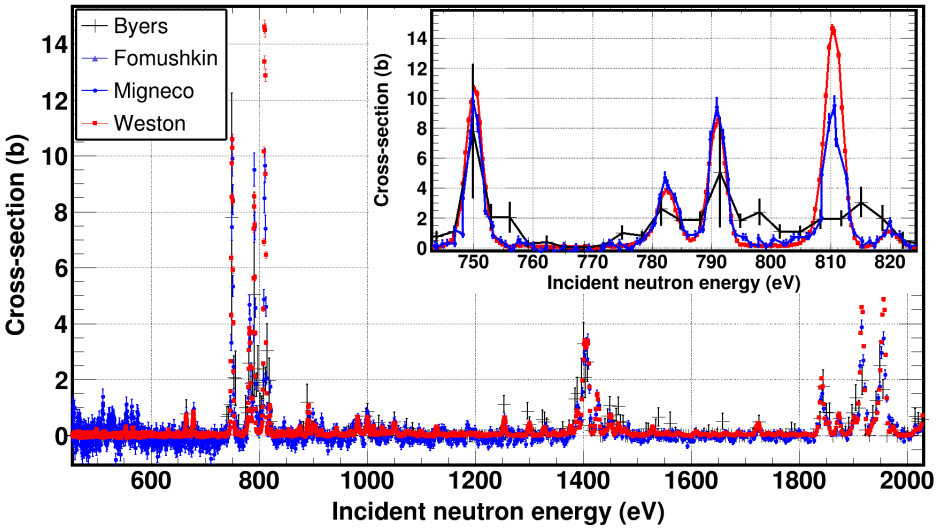

(a) *454 eV - 2.03 keV. In the inset the cross-section is shown in the 740 – 830 eV region where large discrepancies were observed.*

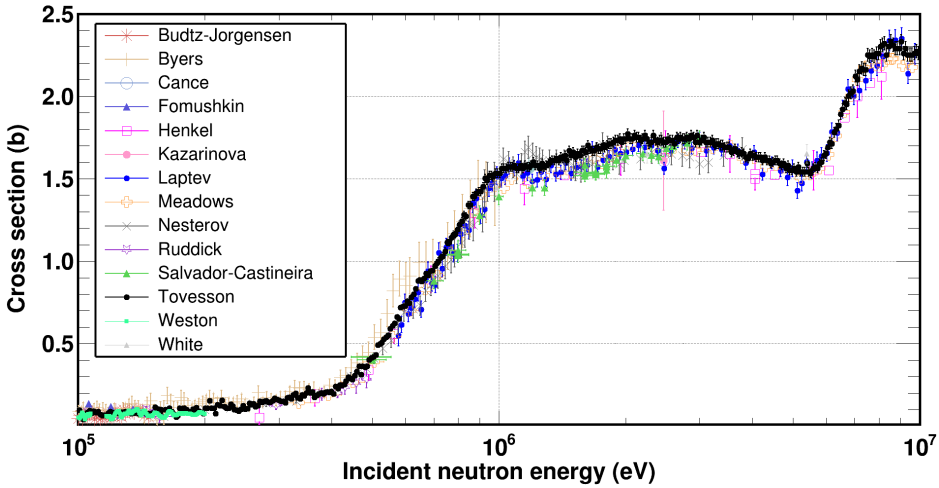

(b) *100 keV - 10 MeV*

Figure 23: *Experimental data set found in EXFOR concerning the $^{240}Pu(n,f)$ reaction. Discrepancies can be seen that reach up to 60% in the resolved resonance region between 454 eV-2.03 keV (top image) and up to 30% in the energy range 498 keV - 6.07 MeV (bottom image).*

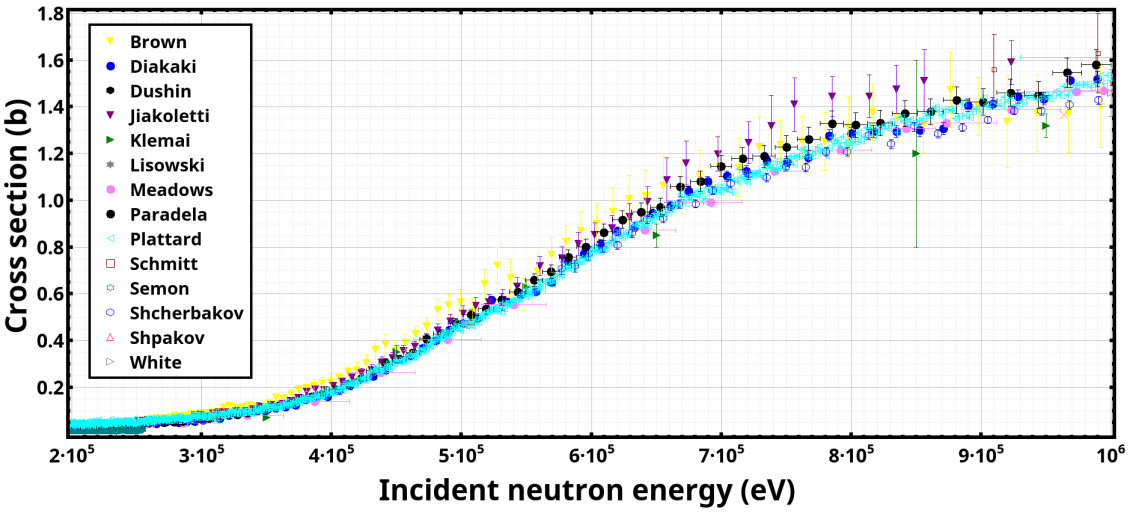

(a) 200 *keV* - 1 *MeV*

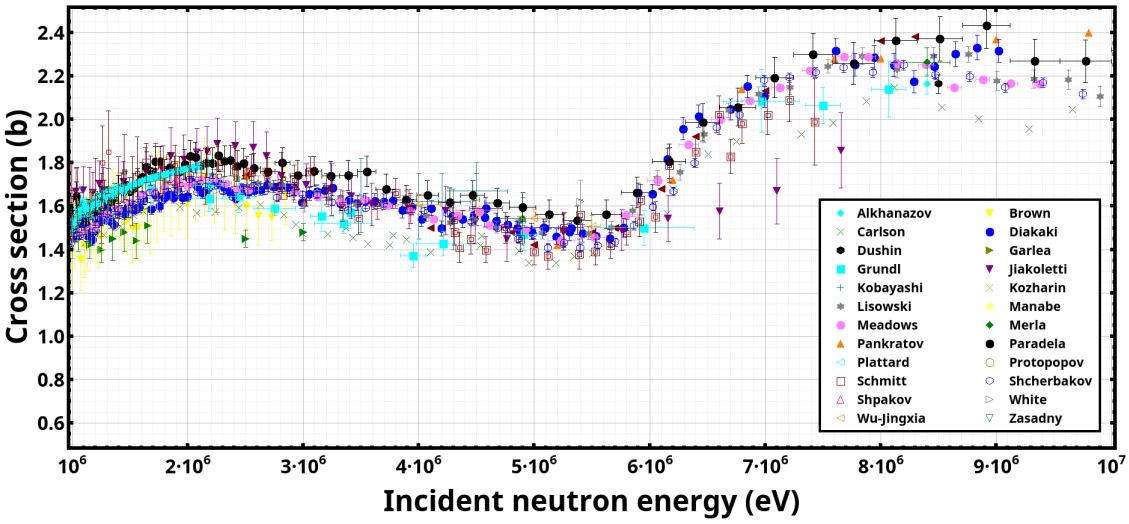

(b) 1 - 10 *MeV*

Figure 24: *Experimental data set found in EXFOR regarding the* $^{237}Np(n,f)$ *reaction. Discrepancies can be seen that reach up to* 25% *in the energy region between* 200 *keV*- 1 *MeV (top image) and up to* 10% *in the energy range* 1 - 10 *MeV (bottom image).*

Table 5: *List of experimental data-sets found in EXFOR regarding the neutron-induced fission cross-section of ^{240}Pu. The list contains information on the year that the manuscript was published, (1^{st} column), the first author's name (2^{nd} column), the energy range of each measurement (3^{rd} column) and finally, a link to the reference for each measurement (4^{th} column). The entries are sorted in descending chronological order.*

Year	Name	Energy Range	Reference
2015	P. Salvador-Castineira	$1.60 \cdot 10^6 - 3.00 \cdot 10^6$	[45]
2015	P. Salvador-Castineira	$5.00 \cdot 10^5 - 1.80 \cdot 10^6$	[45]
2015	P. Salvador-Castineira	$5.00 \cdot 10^5 - 3.00 \cdot 10^6$	[45]
2009	F. Tovesson	$2.01 \cdot 10^3 - 1.98 \cdot 10^8$	[46]
2007	A.B. Laptev	$5.77 \cdot 10^5 - 1.96 \cdot 10^8$	[47]
1986	K. Gul	$1.47 \cdot 10^7$	[48]
1984	L.W. Weston	$9.73 - 2.00 \cdot 10^5$	[49]
1983	B.M. Aleksandrov	$1.20 \cdot 10^6$	[50, 51]
1982	M. Cance	2.47×10^6	[52]
1981	J.W. Meadows	$3.35 \cdot 10^5 - 9.60 \cdot 10^6$	[53]
1981	C. Budtz-Jorgensen	$1.00 \cdot 10^4 - 1.49 \cdot 10^5$	[54]
1980	N.A. Khan	$1.48 \cdot 10^7$	[55, 56]
1978	K. Kari	$1.00 \cdot 10^6 - 2.12 \cdot 10^7$	[57–60]
1975	G.F. Auchampaugh	$7.71 \cdot 10^2 - 1.98 \cdot 10^3$	[61]
1975	E.F. Fomushkin	$1.77 \cdot 10^3 - 1.51 \cdot 10^5$	[62]
1968	E. Migneco	$2.00 \cdot 10^2 - 7.99 \cdot 10^3$	[63]
1967	P.H. White	$1.00 \cdot 10^6 - 1.41 \cdot 10^7$	[64]
1966	D.H. Byers	$2.00 \cdot 10^1 - 9.78 \cdot 10^5$	[65]
1965	J.L. Perkin	$2.40 \cdot 10^4$	[66]
1964	P. Ruddick	$6.10 \cdot 10^4 - 4.85 \cdot 10^5$	[67]
1960	V.G. Nesterov	$4.00 \cdot 10^4 - 3.79 \cdot 10^6$	[68]
1960	M.I. Kazarinova	$2.50 \cdot 10^6$	[69]
1960	M.I. Kazarinova	$1.46 \cdot 10^7$	[69]
1958	T.A. Eastwood	$2.53 \cdot 10^{-2}$	[70]
1957	R.L. Henkel	$2.70 \cdot 10^5 - 8.12 \cdot 10^6$	[71]
1956	W.W. Pratt	$2.53 \cdot 10^{-2}$	[72]
1956	B.R. Leonard Jr.	$3.05 \cdot 10^{-1} - 1.30$	[73]

Table 6: *List of experimental data-sets found in EXFOR regarding the neutron-induced fission cross-section of ^{237}Np. The list contains information on the year that the manuscript was published, (1^{st} column), the first author's name (2^{nd} column), the energy range of each measurement (3^{rd} column) and finally, a link to the reference for each measurement (4^{th} column). The entries are sorted in descending chronological order.*

Year	Name	Energy Range	Reference
2016	M. Diakaki	$1.49 \cdot 10^5 - 2.00 \cdot 10^6$	[41]
2016	M. Diakaki	$2.04 \cdot 10^6 - 9.02 \cdot 10^6$	[41]
2013	M. Diakaki	$4.58 \cdot 10^6 - 5.32 \cdot 10^6$	[42,43]
2010	C. Paradela	$9.77 \cdot 10^2 - 1.00 \cdot 10^9$	[44]
2010	C. Paradela	$1.00 \cdot 10^0 - 1.00 \cdot 10^4$	[44]
2002	O. Shcherbakov	$5.77 \cdot 10^5 - 1.96 \cdot 10^8$	[74]
1994	A.D. Carlson	$5.17 \cdot 10^0 - 5.13 \cdot 10^3$	[75,76]
1992	I. Garlea	$1.48 \cdot 10^7$	[77]
1991	K. Merla	$4.90 \cdot 10^6 - 1.85 \cdot 10^7$	[78]
1991	K. Merla	$1.47 \cdot 10^7$	[78]
1988	J.W. Meadows	$1.47 \cdot 10^7$	[79]
1988	P.W. Lisowski	$1.00 \cdot 10^6 - 1.98 \cdot 10^7$	[80]
1988	F. Manabe	$1.35 \cdot 10^7 - 1.49 \cdot 10^7$	[81]
1986	K. Gul	$1.47 \cdot 10^7$	[82]
1986	V.V. Kozharin	$2.53 \cdot 10^{-2}$	[83]
1986	V.I. Shpakov	$1.90 \cdot 10^6$	[84,85]
1984	G.F. Auchampaugh	$3.50 \cdot 10^1 - 1.30 \cdot 10^2$	[86,87]
1984	K.R. Zasadny	$1.46 \cdot 10^7$	[88,89]
1984	Wu Jingxia	$4.00 \cdot 10^6$	[90]
1984	I. Garlea	$1.48 \cdot 10^7$	[91]
1983	J.W. Meadows	$1.31 \cdot 10^5 - 9.37 \cdot 10^6$	[92,93]
1983	V.N. Dushin	$8.50 \cdot 10^6$	[94,95]
1983	I.D. Alkhazov	$8.40 \cdot 10^6 - 1.47 \cdot 10^7$	[96]
1982	M. Cance	$2.47 \cdot 10^6$	[97]
1981	R. Arlt	$1.47 \cdot 10^7$	[98–100]
1979	D.J. Grady	$7.70 \cdot 10^5 - 9.64 \cdot 10^5$	[101]
1979	A.D. Carlson	$1.11 \cdot 10^6 - 1.89 \cdot 10^7$	[102]
1977	I.D. Alknazov	$1.48 \cdot 10^7$	[103]
1976	M.D. Semon	$2.01 \cdot 10^1 - 2.55 \cdot 10^5$	[104]
1975	S. Plattard	$9.99 \cdot 10^4 - 2.10 \cdot 10^6$	[105–107]
1973	K. Kobayashi	$3.50 \cdot 10^6 - 4.90 \cdot 10^6$	[108,109]
1973	S. Plattard	$2.72 \cdot 10^0 - 3.52 \cdot 10^4$	[107,110]
1972	R.J. Jiacoletti	$2.00 \cdot 10^5 - 7.66 \cdot 10^6$	[111]
1971	W. Kolar	$2.01 \cdot 10^1 - 5.21 \cdot 10^1$	[112,113]
1970	W.K. Brown	$3.16 \cdot 10^1 - 2.18 \cdot 10^3$	[114]
1970	W.K. Brown	$1.00 \cdot 10^5 - 2.85 \cdot 10^6$	[115]
1969	R.H. Iyer	$1.41 \cdot 10^7$	[116]
1967	J.A. Grundl	$1.07 \cdot 10^6 - 8.07 \cdot 10^6$	[117]

continued ...

. . . continued

Year	Name	Energy Range	Reference
1967	P.H. White	$1.00 \cdot 10^6 - 1.41 \cdot 10^7$	[64]
1965	J.L. Perkin	$2.40 \cdot 10^4$	[66]
1965	P.H. White	$4.00 \cdot 10^4 - 5.05 \cdot 10^5$	[118]
1963	V.M. Pankratov	$2.50 \cdot 10^6 - 2.64 \cdot 10^7$	[119, 120]
1960	V.M. Pankratov	$9.60 \cdot 10^6 - 2.18 \cdot 10^7$	[121–123]
1959	B.R. Leonard Jr.	$4.12 \cdot 10^{-2}$	[124, 125]
1959	H.W. Schmitt	$9.10 \cdot 10^5 - 7.43 \cdot 10^6$	[126]
1959	B.M. Gokhberg	$1.20 \cdot 10^4 - 1.50 \cdot 10^6$	[127]
1958	A.N. Protopopov	$1.46 \cdot 10^7$	[128]
1958	S.P. Kalinin	$2.50 \cdot 10^6 - 8.30 \cdot 10^6$	[129]
1952	R.L. Henkel	$4.60 \cdot 10^5 - 7.45 \cdot 10^6$	[130]
1947	E.D. Klema	$2.50 \cdot 10^5 - 3.00 \cdot 10^6$	[131]

CHAPTER 1

Experimental details

In nuclear physics experiments, where induced cross-sections are studied, the use of a facility that provides a projectile beam with which the nuclear system under study gets excited, is mandatory. The excited system (or target nucleus) de-excites by the emission of a particle (referred to as ejectile) which is detected by a detection assembly. The ejectile interacts with the detector material and causes the formation of a pulse. This pulse, usually small to be directly recorded, is amplified and fed to an acquisition system for subsequent analysis. In view of all the above, apart from the beam facility, a sample material, a detection system and read-out chain are deemed necessary to perform such studies.

1.1 The n_TOF facility at CERN

The history of the n_TOF facility started in the years between 1995 and 1997 when its predecessor, the TARC experiment (Transmutation by Adiabatic Resonance Crossing) [132,133], was established in the framework of the Energy Amplifier [134,135], in an attempt to study the feasibility of transmuting long-lived fission fragments in Accelerator Driven Systems (ADS) using the Adiabatic Resonance Crossing (ARC) [136]. It deserves a dedicated note, that the mastermind behind these creative ideas is the Nobel Prize laureate, Carlo Rubbia. These activities led to an accumulation of knowledge and technical know-how on the neutron production via spallation on high-Z materials, using high-energy and high-luminosity ion beams. Therefore the vision of a neutron facility to measure neutron cross-sections from the eV to the MeV regime was born: In 2001 the n_TOF facility at CERN had its first physics beam delivered [137].

The experimental programme at n_TOF [138, 139] is mainly focused on measurements of neutron-induced cross-sections for three main categories of reactions:

(i) fission reactions which are important for the development of advanced nuclear systems for nuclear energy production [140], (ii) radiative capture reactions which are of great interest to nuclear astrophysics and for the design and operation of nuclear reactors [141] and (iii) charged particle reactions which are relevant to medical applications [142], such as Boron Neutron Capture Therapy and nuclear astrophysics as well [143].

Since its first beam in 2001, n_TOF has evolved through three main phases of operation, as summarised in table 1.1 and it currently offers two beam lines: A horizontal with high-resolution and moderate flux at 185 m flight path and a newly commissioned vertical one with high-flux and moderate resolution at 19.5 m, which are referred to as Experimental Area 1 (EAR1) and Experimental Area 2 (EAR2), respectively. A graphical representation of the facility that includes both experimental areas can be seen in fig. 1.1

Table 1.1: *The three phases of operation of the n_TOF facility at CERN from 2001 till 2018. The running period, the new features and the measured reactions in each phase are also shown. The gaps between phases are due to, either commissioning purposes regarding the facility itself, or long shutdowns at CERN for the upgrade of the accelerator complex.*

Phase	Period	Upgrade	Reaction		
			(n,γ)	(n,f)	(n,cp)
I	2001 - 2004	Original Design	25	11	-
II	2009 - 2010	New target	14	3	2
	2010 - 2012	Borated water as moderator			
III	2014 - 2018	Construction of EAR2	14	4	4

1.1.1 The neutron source

Neutrons at n_TOF are produced via spallation when 20 GeV/c proton bunches from CERN's Proton Synchrotron (PS) impinge on a 40 cm in length and 60 cm in diameter monolithic cylindrical Pb spallation target. The proton bunch intensity varies from $\sim 3\times10^{12}$ (referred to as parasitic bunches) up to $\sim 8\times10^{12}$ protons (referred to as dedicated bunches) due to the maximum power allowed to be delivered on target before reaching a radiation monitor alarm, while the nominal proton bunch has an intensity of 7×10^{12} protons. The small repetition rate, which does not exceed 0.8 Hz (1.2 s between consecutive bunches) and the small width of the proton bunch (7 ns RMS in dedicated and 20 ns in parasitic mode) allows for well separated neutron bunches delivered in both experimental areas while avoiding any overlap between them. The average of ~ 300 total neutrons released per incident proton make n_TOF one of the brightest neutron sources that exist, as far as the instantaneous flux is concerned, and therefore ideal for the measurement of low cross-sections, highly radioactive samples and isotopes available in small masses in

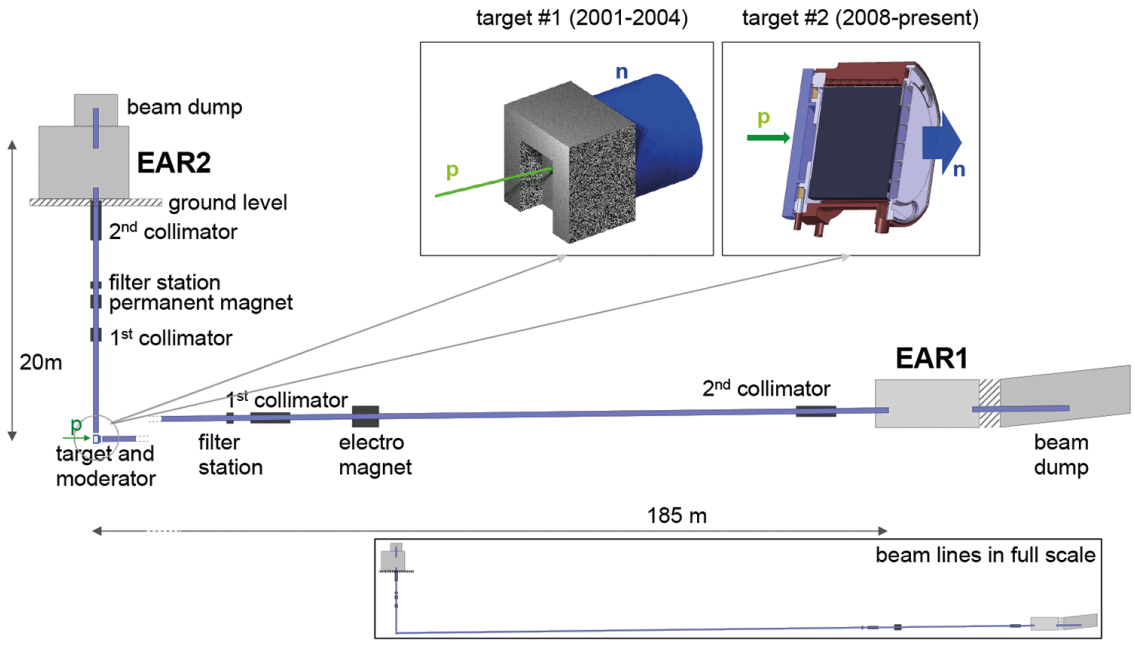

Figure 1.1: *Graphical representation of CERN's n_TOF facility that features two flight paths: A horizontal, high-resolution, moderate flux one at* 185 *m (EAR1) and a newly commissioned vertical high-flux, moderate resolution one at* 20 *m (EAR2). Both spallation targets used from the initial operational phase, are also shown [144].*

combination with the good energy resolution and background supression. A characteristic example is the recent cross-section measurement of $^{7}Be(n,\alpha)$ [143] over a wide neutron range at EAR2.

The spallation target, is surrounded by a 1 cm thick circulating layer of cooling water, as well as an additional 4 cm thick layer of borated water in the horizontal direction, as seen in fig. 1.2 for moderation purposes. The use of 1.28% boric acid (H_3BO_3) enriched in ^{10}B, diluted in water, enhances the probability that the vast majority of thermal neutrons produced are captured via the $^{10}B(n,\alpha)$ reaction. Thus, the emission of 2.2 MeV γ-rays from the radiative neutron capture on hydrogen is considerably suppressed. This has also an effect on the neutron spectrum by suppressing the number of thermal neutrons that reach the experimental hall. Since borated water is only present in the proton beam direction, the effect is only visible in EAR1 as can be seen in the evaluated fluxes for EAR1 and EAR2, in fig. 1.3 [145].

In the same figure certain structures are present which are worth to be mentioned and discussed.

1. *Sub thermal region*: The two peaks seen in the flux in EAR2 below 10 meV are attributed to phonon dispersions in the lead target from neutron inelastic scattering [146, 147] .
2. *Thermal point (25.3 meV)*: The water, that is used as a coolant and moderator, enhances the flux at the vicinity of the thermal point. However, for reasons discussed previously, this is the case only for EAR2. For EAR1, the use of borated water practically removes the thermal peak.
3. *Epithermal Region (1 eV - hundreds of keV)*: a nearly isolethargic behavior is

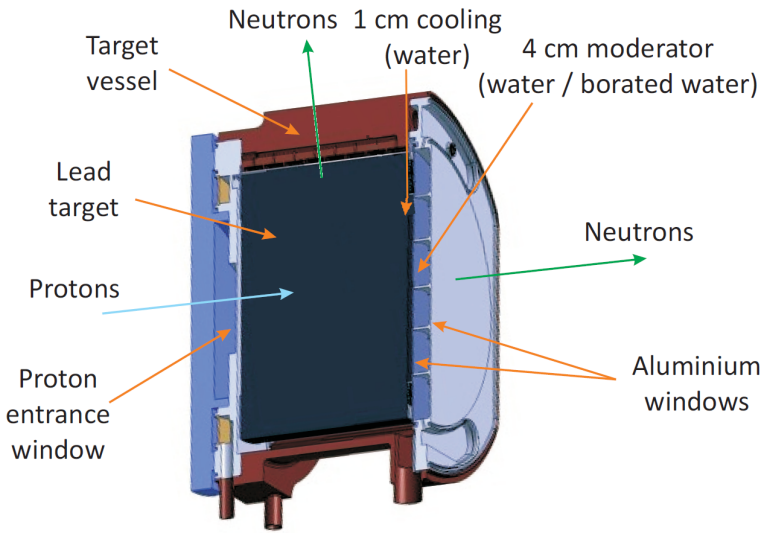

Figure 1.2: *The lead spallation target used at n_TOF during Phases II and III. The presence of borated water suppresses the γ-rays emitted from radiative capture on hydrogen. In addition the emission of thermal neutrons is suppressed in the case of EAR1 [13].*

observed.

4. The observed dips are transmission dips due to structural materials in the target (i.e. aluminum neutron window, traces of Mn within the spallation target) as well as the oxygen that is present in the moderator. More specifically, each individual dip is attributed to:
   - 341 eV $\rightarrow$ ^{55}Mn
   - 1.1 keV $\rightarrow$ ^{55}Mn
   - 2.4 keV $\rightarrow$ ^{55}Mn
   - 6 keV $\rightarrow$ ^{27}Al
   - 35.4 keV $\rightarrow$ ^{55}Mn,^{27}Al
   - 87.6 keV $\rightarrow$ ^{55}Mn,^{27}Al
   - $>$ 400 keV $\rightarrow$ ^{16}O
5. 1 *MeV region*: Neutron evaporation peak which is attributed to the neutrons produced via either fission or evaporation of spallation products.
6. 100 *MeV*: The bump seen in the region of 100 MeV is usually referred to as the spallation peak and it is associated with neutrons produced via the intranuclear cascade, following the spallation process.

Finally, the neutron spectrum at n_TOF covers a wide neutron energy range from the thermal region up to several tens of MeV [145]. As seen in fig. 1.3, the flux peaks at $\sim$ 1 MeV where $\sim 10^2$ and $\sim 5\times10^3$ neutrons/cm^2/nominal pulse reach EAR1 and EAR2, respectively. To calculate the number of neutrons per surface per energy bin (right y-axis) from the isolethargic flux (left y-axis), the flux value (dΦ) per bin is multiplied by the width of the corresponding energy bin (dE) and divided by the central neutron energy (E) in each individual bin as seen in eq. (1.1).

$$\text{neutrons (E)} = \mathrm{d}\Phi(E)\cdot\frac{\mathrm{d}E}{E} \tag{1.1}$$

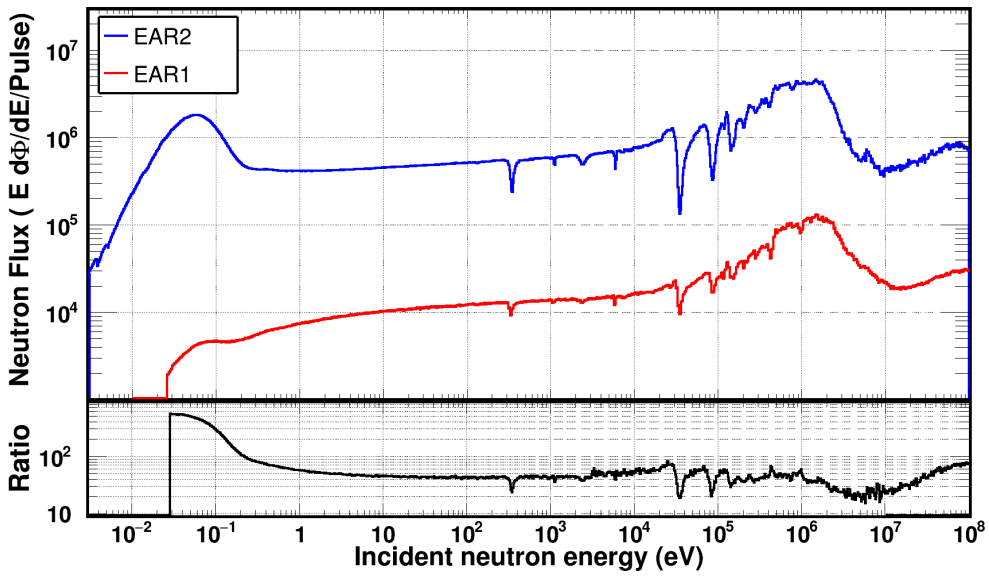

Figure 1.3: *The neutron flux regarding the capture collimator for EAR1 and EAR2 (top panel) spans from the thermal region up to several tens of MeV. The overall shape of the flux is explained in the text. The flux ratio between EAR2 and EAR1 is also shown (bottom panel) for comparison. An isolethargic binning of* 100 *bins per energy decade is used.*

1.1.2 The second experimental area - EAR2

The measurements of the reactions studied in the framework of the present thesis took place at the newly commissioned experimental area 2 (EAR2), therefore a few details will be given concerning only this experimental hall. More information on EAR1 and its performance can be found in numerous resources (i.e. [13, 148–150]).

The second experimental area lies between 18.16 (floor level) and 24.73 (beam dump) m above the spallation target as can be seen in fig. 1.4. The beam-line, which is kept under vacuum at $\sim 10^{-2}$ mbar, consists of stainless steel tubes with 31.7 cm inner diameter. At the level of the spallation target the beam line has a polygonal section to match the polygonal opening on the support vessel, as seen in fig: 1.5. This polygonal neutron window allows for the lowering of a vacuum chamber from the vertical beam line down to the level of the target.

The neutron collimation system consists of two collimators: the first collimator, which is made of iron (Fe) is installed at a 7.4 m distance above the spallation target, has a length of 1 m and an inner diameter of 20 cm. The second collimator rests 15.04 m above the Pb target, inside a vacuum vessel. Its outer diameter is 68 cm, while for the inner one there are two possibilities offered, namely: 2.2 cm for capture measurements and 6 cm for fission. Apart from the first 2 m of Fe, the second collimator consists of an additional meter of borated polyethylene (B-PE) while its last 40 cm have a core of boron carbide (B_4C) cylinders. The collimation system results in a neutron beam profile that diverges by 1 mm over 1 m after the exit of the second collimator and a focal point at 1.08 m above the floor level.

To diverge charged particles originating from the spallation process in the target, a permanent magnet is placed at 10.4 m above the target along the neutron beam line. The 1.13 m long dipole magnet features a magnetic field of 253 mT in

the center and a total integrated magnetic field of 0.287 Tm which is greater by ~ 44% with respect to the 0.2 Tm calculated by simulations as being sufficient to diverge the maximum expected proton momentum of 1.205 GeV/c, at the magnet's position [151].

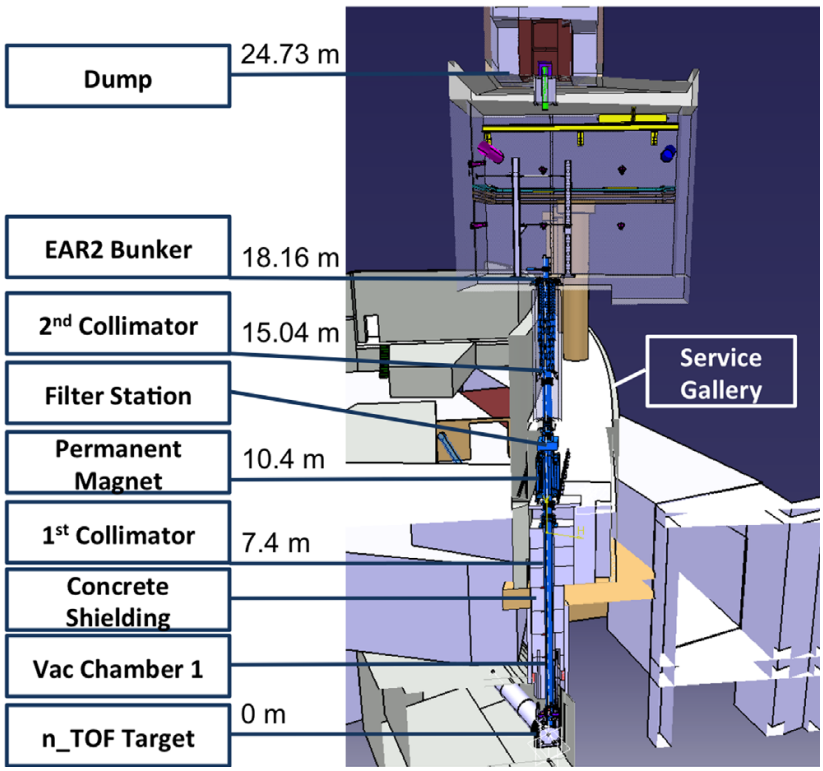

Figure 1.4: *Schematic layout of the beam-line components from the spallation target, which is located at the bottom part of the figure, on the way up to the beam dump in EAR2. [151]*

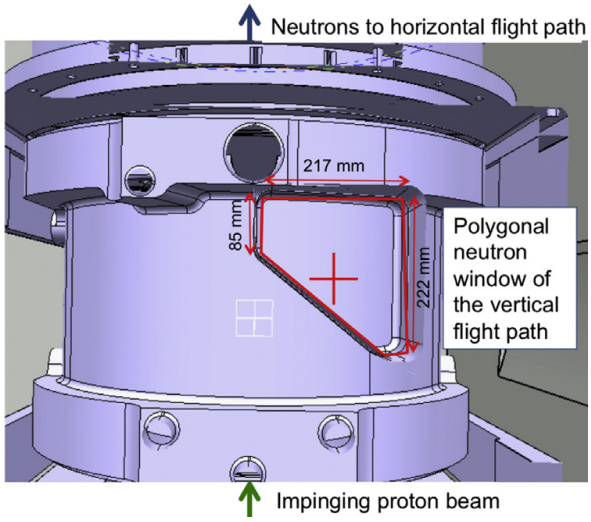

Figure 1.5: *The polygonal exit window from the spallation target towards EAR2, allows for the lowering of a vacuum chamber from the vertical beam line down to the level of the target. The red cross indicates the center of the neutron beam. [151]*

A filter station is located at 11.4 m above the spallation target which is equipped with 8 neutron filters. Each filter can be inserted in the beam line either individually, or as a group of two or more in order to suppress different neutron energies from the beam based on the neutron absorption in energies near big resonances (so called dark resonances) on the cross-section of the (n, tot) reaction. A list of the available filters along with their thicknesses and the corresponding dark resonances is seen in table 1.2.

Table 1.2: *A list of the available neutron filters installed in the filter box in EAR2 along with the thickness and the energies of the dark resonances. Each filter can be used individually or in combination with other filter(s) and the selection of filters can be remotely controlled from the control room.*

Slot #	Filter	Thickness (mm)	Resonance energy (eV)
	Mo	10	45
1	W	8	4,19,184
	Co	0.25	132
2	Ag	0.5	5.2
3	Bi	50	800, 2300
4	Cd	0.5	Thermal
5	Al	30	35, 100, 5900
6	Al	80	35, 100, 5900
7	Pb	20	γ attenuation
8	Pb	10	γ attenuation

Finally, the construction of the second experimental area extends the experimental capabilities of the existing infrastructure and enables the study of a wider range of challenging cross-sections that concern short-lived isotopes, highly radioactive materials and samples that are available in small masses. A characteristic example is the first measurement performed in EAR2 and concerns the measurement of the $^{240}Pu(n, f)$ cross-section, which was originally attempted in EAR1 [13, 152] but the high intrinsic α-activity of the samples led to detector deterioration and therefore could not provide results. The higher flux and the shorter time of flights involved in EAR2 offer a significantly stronger suppression of sample-induced background as can be seen in fig. 1.6, where the comparison of pulse height spectra proves the more efficient α to fission fragments separation.

1.2 The time of flight technique

As mentioned above, the white n_TOF neutron spectrum covers more than 10 orders of magnitude in energy which is determined using the time of flight technique. In its simplest form, the time of flight t of a neutron with mass $m = 939.55$ MeV/c^2

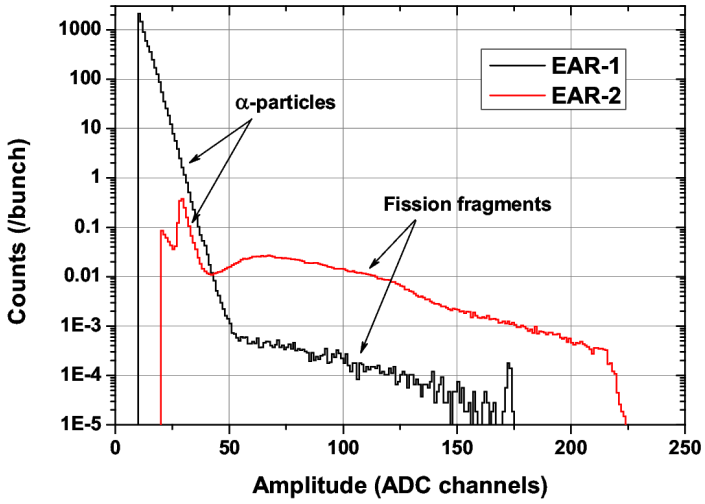

Figure 1.6: *Pulse height spectra obtained from the $^{240}Pu(n,f)$ campaigns in EAR1 and EAR2. The higher flux and the shorter time of flights involved in EAR2 offer a significantly stronger suppression of sample-induced background, therefore the α to fission fragments separation is more efficient [153].*

travelling along a geometrical flight path L after exiting the target and interacting within the sample, is directly related to its energy E, considering the classical expression seen in eq. 1.2 or the relativistic one seen in eq. 1.3, in which γ represents the Lorentz factor and c is the speed of light. The relativistic effect can be neglected for at least up to 100 MeV, as can be seen in fig. 1.7 where the relation between t and E is calculated for both experimental areas.

$$E(eV) = \frac{1}{2}mv^2 = \frac{1}{2}m\left(\frac{L}{t}\right)^2 \approx \left(72.298\frac{L(m)}{t(\mu s)}\right)^2 \tag{1.2}$$

$$E = mc^2(\gamma - 1) = mc^2\left(\frac{1}{\sqrt{1-\left(\frac{L}{tc}\right)^2}} - 1\right) \tag{1.3}$$

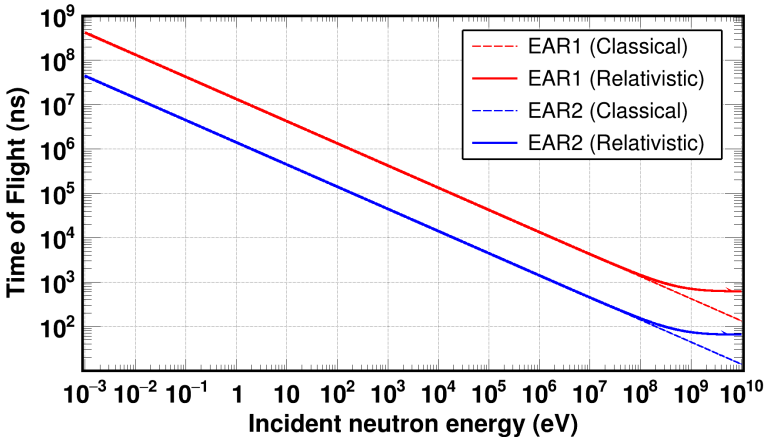

Figure 1.7: *Classical and relativistic relation between the time of flight t and the incident neutron energy E in the case of EAR1 ($L = 185$ m) and EAR2 ($L = 19.5$ m). It can be seen that for neutron energies below 100 MeV, the relativistic effect can be neglected.*

In practice though, the extraction of the neutron energy E is more complicated. First of all, prior to the arrival of neutrons, the emission of a prompt γ component takes place, which is subject to a time distribution related to the width of the proton bunch. This component is related to the spallation process and is commonly referred to as γ-flash. The γ-flash arrives at the experimental hall at a time $t_\gamma = t_0 + L/c$ where t_0 is the time when the proton bunch impinged on the Pb target or the start signal (fig. 1.8) and is provided experimentally by beam monitors. In the case of n_TOF the start signal is given from two beam monitor detectors: a beam current transformer (BCT) and a pick-up wall current monitor (PKUP). After the γ-flash, neutrons reach the sample, interact with its nuclei and produce signals which are read-out from the detector. The interaction in the sample, in the case of a compound reaction like fission, is considered to be instantaneous compared to the timing properties of the read-out system, therefore the arrival of a neutron in the sample at a time t_s takes into account the interaction time. In this simple case the measured time of flight t_m is calculated from eq. 1.4. It has to be noted that in the calculations the time delay due to cables is ignored since it doesn't change the calculation of the time of flight; it is simply the same offset in t_s and t_γ.

$$t_m = t_s - t_\gamma + \frac{L}{c} = t_s - t_0 \tag{1.4}$$

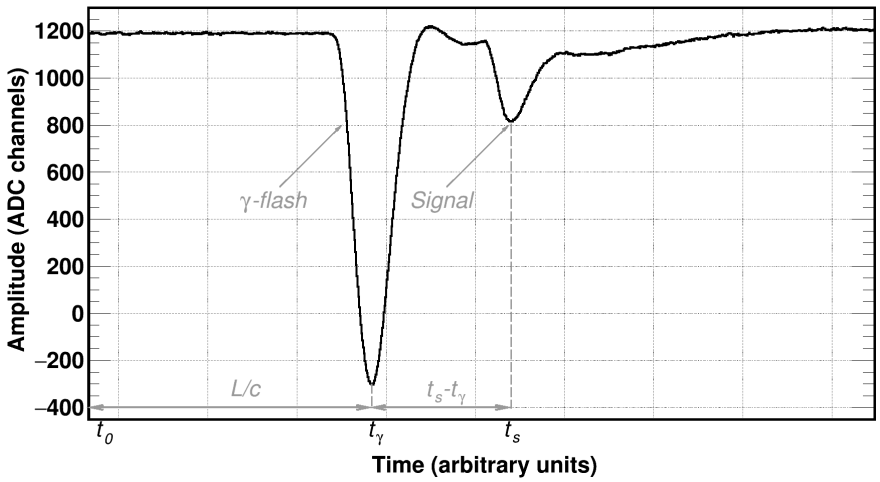

Figure 1.8: *Time-frame of a typical γ-flash followed by a fission signal. The calculation of the measured time of flight t_m is based on the subtraction between the arrival time of the fission signal (t_s) and the γ-flash arrival time (t_γ) taking into account the photon flight time (L/c) along a flight path L (eq. 1.4).*

1.2.1 Response of a time of flight spectrometer

In reality, however, there is not a unitary conversion from a measured time of flight t_m to the true neutron energy E. This is mainly attributed to the fact that the proton bunch is subject to a time distribution (7 ns RMS in the case of PS) and most importantly to the time t_t a neutron spends inside the target-moderator assembly,

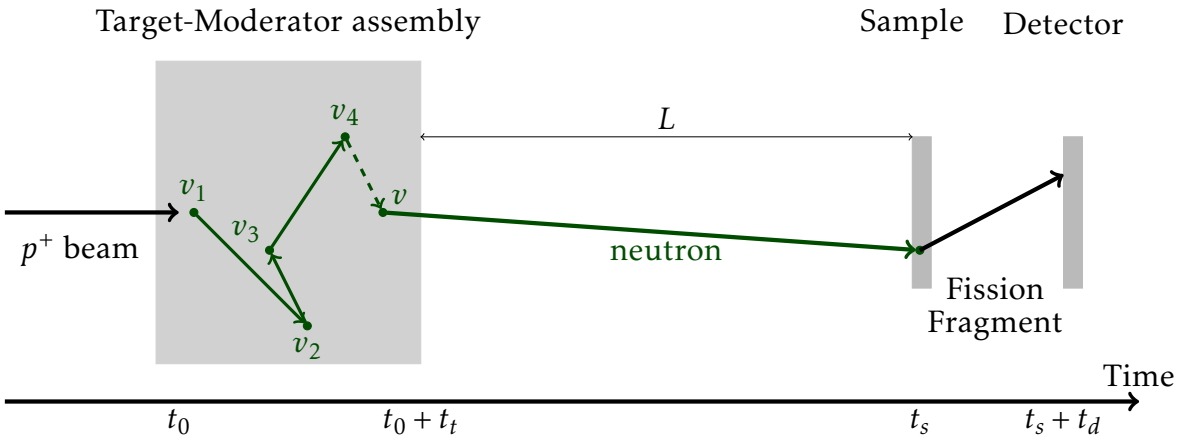

Figure 1.9: *A spallation neutron spends a time t_t inside the target-moderator assembly due to scattering before exiting the target with a velocity v and reaching the sample at the time t_s, travelling a geometrical distance L. The time t_0 corresponds to the time the proton bunch impinged on the target.*

as illustrated in fig. 1.9. Each neutron is initially produced with a velocity v_1[1] and undergoes inelastic scattering before exiting the target at a velocity v. The real time of flight t therefore, has to be corrected for t_t and subtracted from the measured t_m as calculated in eq. 1.5, where t_d denotes the time needed for the neutron transport in the sample-detector assembly and the additional time needed until the particle detection. The neutron transport in the case of a thin sample can be neglected, therefore t_d accounts only for the difference between the time of detection and the moment the neutron enters the sample.

$$t = t_m - t_t - t_d \tag{1.5}$$

It goes without saying that the neutron transport inside the target-moderator assembly is subject to a probability distribution, therefore the t_t has a distribution for each neutron energy $R(t_t, E)$ which is commonly referred to as the response function (RF) of a time-of-flight spectrometer. An example of such a distribution of t_t times with respect to the true neutron energy E can be seen in fig. 1.10 where the RF at a scoring plane 37.2 cm above the spallation target on the way up to EAR2 is shown. The RF was calculated from Monte Carlo simulations using the FLUKA general transport code [14, 15] by the n_TOF collaboration.

The moderation time, although it represents an intrinsic feature of a facility, it is not always a convenient quantity to instantiate the response function of a TOF spectrometer since, as can be seen in fig. 1.11a, it strongly depends on the neutron energy. A more convenient quantity to be used is the equivalent moderation distance λ and is expressed through a simple transformation of variables between the true neutron velocity v and the moderation time t_t, as seen in eq. (1.6). This transformation results in probability distributions which are much less dependent on the neutron energy, as can be seen in fig. 1.11b. An example of a distribution of

[1] To simplify the equations that will follow, instead of the neutron energy E, its velocity v will be used.

the equivalent distance λ with respect to the neutron energy E can be seen in fig. 1.12 where the FLUKA simulated RF $R(\lambda(t_t), E)$ for EAR2 is shown.

$$\lambda = v t_t \tag{1.6}$$

Taking all these factors into account, the final energy response or resolution of

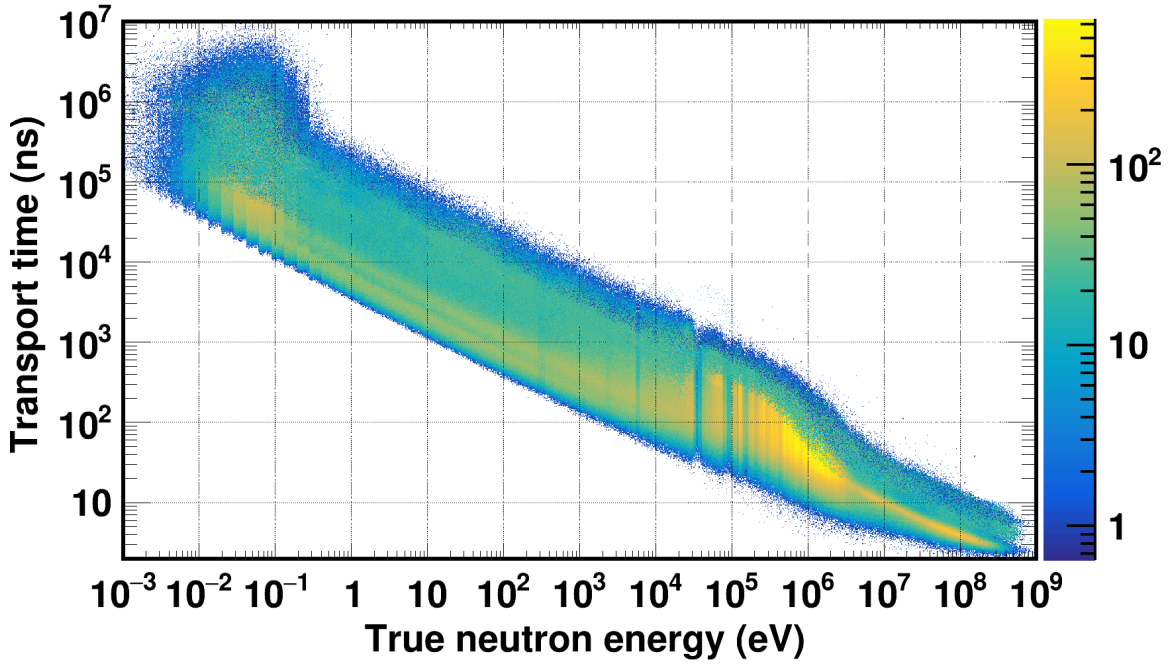

Figure 1.10: *FLUKA simulation for the response function $R(t_t, E)$ of EAR2 at n_TOF 37.2 cm above the center of the spallation target. For every real neutron energy E there is a distribution of the neutron transport time t_t within the target-moderator assembly. Both quantities are given in an isolethargic binning of 100 bins per energy decade. The values shown in the z-axis represent arbitrary units.*

a spallation time of flight spectrometer $\Delta E/E$ can be considered as a convolution of the following quantities:

1. The duration of the primary beam bunch (7 ns RMS in the case of n_TOF) which affects t_0 (Δt_0).
2. Time resolution of detection system that is dominated by time jitters and the overall read-out and affects t_s (Δt_s).
3. Neutron transport in the target-moderator assembly (Δt_t or $\Delta\lambda$).
4. Neutron transport in the sample-detector which affects t_d (Δt_d).

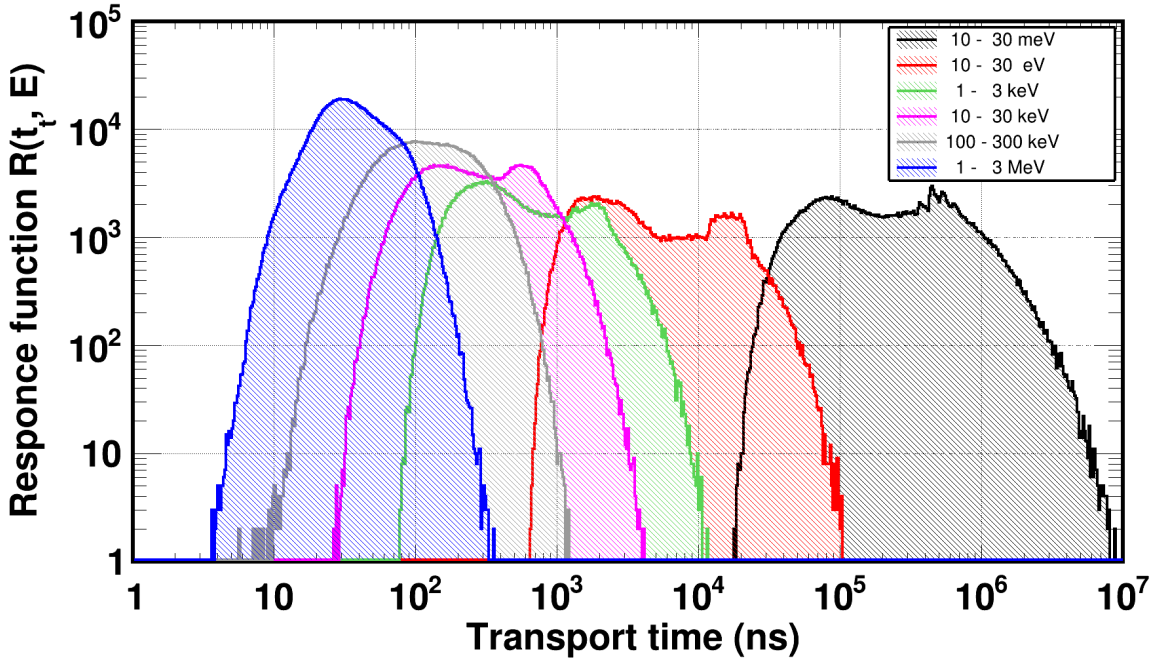

(a) *The response function $R(t_t)$ or moderation time t_t of EAR2 for various neutron energies strongly depends on the true neutron energy E and spans almost seven order of magnitudes from* 5 *ns to* 10 *ms.*

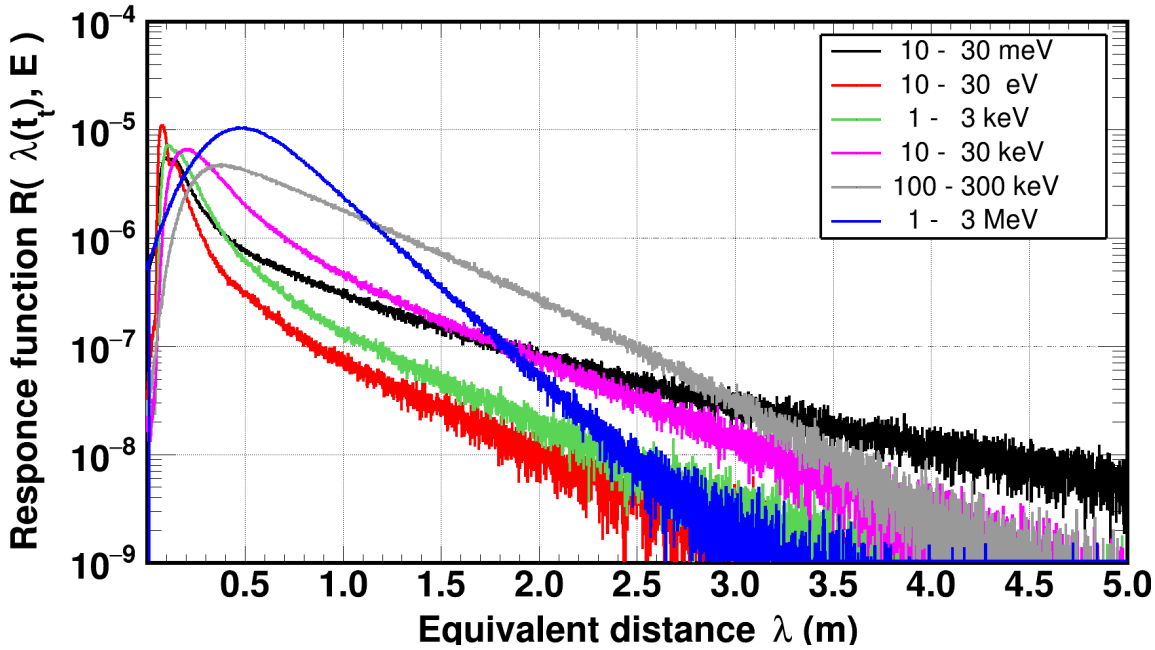

(b) *The response function $R(\lambda(t_t))$ or equivalent distance $\lambda(t_t)$ of EAR2 for various neutron energies does not strongly depend on the true neutron energy E and ranges from* 1 *cm up to* 5 *m.*

Figure 1.11: *Distribution of the moderation time t_t and equivalent distance $\lambda(t_t)$ for various neutron energies from thermal up to the MeV region.*

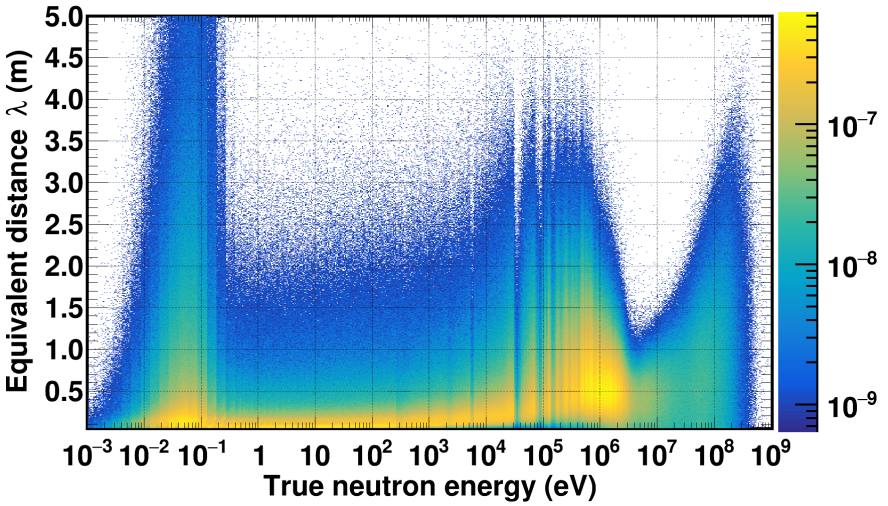

Figure 1.12: *FLUKA simulation for the response function $R(\lambda(t_t), E)$ of EAR2 at n_TOF. For every real neutron energy E there is a distribution of the neutron equivalent distance λ within the target-moderator assembly. The neutron energy E is given at an isolethargic binning of 20 bins per energy decade and the equivalent moderation distance λ at a linear binning of 1 mm. The values shown in the z-axis represent arbitrary units.*

The first two components are independent of the neutron energy and can be adequately represented simply by a normal distribution, while the Δt_s can be neglected since t_s is considered negligible in the thin target approximation, which is valid for fission samples. The same is valid for the fourth component as well in the case of fission at least up to a few MeV since there is no experimental evidence that the energy spectrum of fission products strongly depends on the energy of the incident neutron, therefore Δt_d can also be represented by a normal distribution. The most dominant factors are thus the distribution of the transport time t_t or the equivalent transport distance λ and the duration of the pulsed beam. The total energy resolution can be calculated using eq. (1.2) as seen in eq. (1.7), assuming in the first order approximation a normal distribution for the moderation length of 15 cm. Each individual contribution can be calculated by considering the rest to be equal to zero and can be seen in fig. 1.13.

$$\frac{\Delta E}{E} \approx 2\frac{\Delta v}{v} = 2\sqrt{\frac{\Delta t}{t}^2 + \frac{\Delta L}{L}^2} = 2\sqrt{\frac{\Delta t_0}{t}^2 + \frac{\lambda}{L}^2} \tag{1.7}$$

Finally, the classical expression to determine the true neutron energy E taking into account the neutron transports in the target moderation assembly t_t, in the sample t_s and in the detector can be expressed as follows:

$$E = \frac{1}{2}m\left(\frac{L+\lambda(E)}{t_s - t_\gamma + L/c - t_d}\right)^2 \tag{1.8}$$

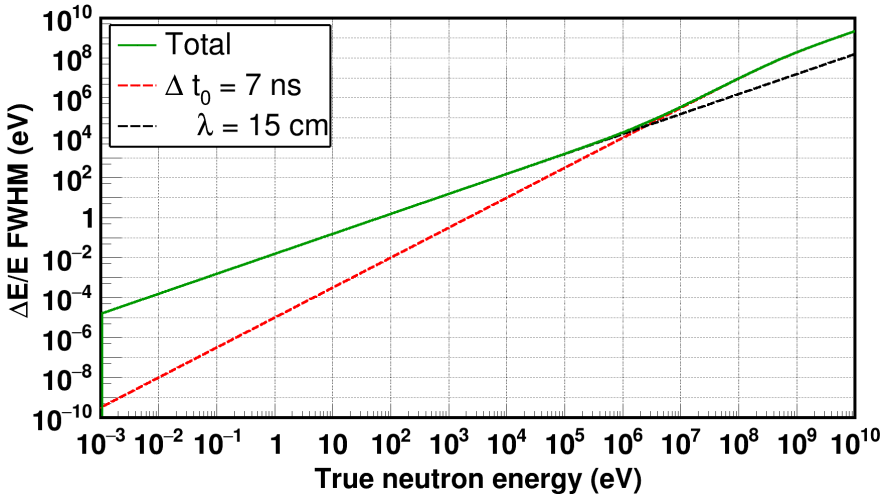

Figure 1.13: *Resolution of a TOF spectrometer assuming a flight path L = 19.5 m, a time spread Δt_0 = 7 ns of the primary proton pulse and a constant equivalent moderation length λ = 15 cm. It can be seen that in neutron energies greater than a few MeV the time spread of the primary beam plays an important role whereas in lower energies can be considered insignificant.*

1.3 Fission foils

In fission experiments, in order to avoid extensive self-absorption of fragments, which are high-Z, highly energetic charged particles, the samples are typically foils with a thickness of the order of a few tens of nm. In the framework of the present thesis, thin samples for both experimental campaigns were manufactured at the Joint Research Center in Geel, Belgium (JRC-Geel[2]). The technique used to produce the samples was the so-called molecular plating of the material on 0.25 mm thick and 5 cm in diameter aluminium backings, while the deposits had a diameter of 3 cm. Their activities were determined by α-particle counting while for the atomic abundances of the contaminants, thermal ionisation mass spectroscopy was used. In fig. 1.14 the yellowish deposits on the aluminium backings of ^{240}Pu and ^{237}Np can be seen.

1.3.1 The plutonium samples

In the case of the $^{240}Pu(n,f)$ experimental campaign three ^{240}Pu samples in total, were used with deposits in the form of plutonium dioxide (PuO_2) [154]. The total ^{240}Pu mass was $\sim$ 2.29 mg, the total α-activity was found to be $\sim$ 19.4 MBq while, despite the high 99.89% purity, other plutonium isotopes were found as contaminants. In table 1.3, a list with the characteristics of the fission foils is provided.

In addition to the ^{240}Pu samples, two reference foils were used, namely a ^{235}U one to cover the energy region from thermal to MeV neutron energies and a ^{238}U one to be used above 1 MeV. The areal density of the ^{235}U sample, which was found as a UF_4 chemical compound, was 91.2 $\mu gr/cm^2$ while its α-activity was measured

[2]Formerly known as Institute for Reference Materials and Measurements, EC-JRC-IRMM

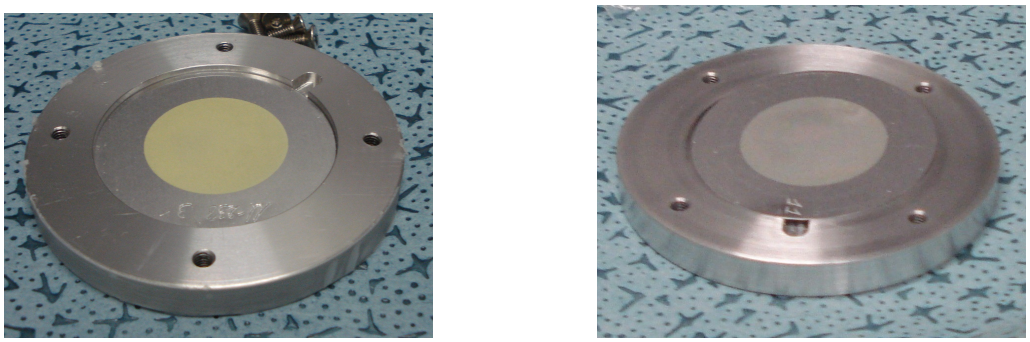

(a) ^{240}Pu *sample* ***(b)*** ^{237}Np *sample*

Figure 1.14: *Photographs of a* ^{240}Pu *and a* ^{237}Np *sample used in the experiments. The* 3 *cm in diameter yellowish deposits sit on the* 5 *cm in diameter aluminium backings. The fission foils are still in their containers. The photographs were taken during the sample manipulation and installation on the Micromegas chamber in a Class-A lab in the ISOLDE facility at CERN.*

to be 40.5 Bq. The ^{238}U sample, found in uranium oxide form ($U(OH)_4$), had an areal density of 107 $\mu gr/cm^2$ while its α-activity in this case was six orders of magnitude less, compared to the ^{240}Pu one and reached 9.38 Bq.

Table 1.3: *List of the main characteristics, and stated impurities of the samples used in the* $^{240}Pu(n,f)$ *experimental campaign along with the estimated uncertainties as given by JRC-Geel. The activities in the* ^{240}Pu *samples (lot BC01269) as well as the level of contamination were determined on May 2011. For the* ^{235}U *sample the activity and levesl of contamination were determined on January 1981 while for the* ^{238}U *one (lot 2677) on February 2012.*

Sample	Reference Number	Activity (MBq)	Mass (mg)	Areal density (mg/cm^2) (×10^{-7} atoms/b)		Atomic abundances (%)
^{240}Pu	TP2010-011-01 TP2010-011-03 TP2010-011-04	6.016(23) 6.793(26) 6.410(25)	0.7163(28) 0.809(3) 0.763(3)	0.1017(4) 0.1148(5) 0.1223(5)	2.55(1) 2.88(1) 2.72(1)	^{238}Pu : 0.0733(29) ^{239}Pu : 0.0144(18) ^{240}Pu : 99.8915(18) ^{241}Pu : 0.00041(31) ^{242}Pu : 0.02027(41) ^{244}Pu : 0.000046(88)
Total		**19.219**	**2.2883**	**0.3248**	**8.15**	
^{235}U	SP 3576_1	40.5 Bq	0.563(11)	0.0912(17)	2.34(5)	^{234}U : 0.1698 ^{235}U : 99.475 ^{236}U : 0.0273 ^{238}U : 0.3277
^{238}U	TP2011-008-03	9.38(19) Bq	0.745(15)	0.1070(22)	2.71(6)	$^{238}U > 99.9$

1.3.2 The neptunium samples

In the case of the $^{237}Np(n,f)$ experimental campaign five ^{237}Np samples were used in total: four with a total mass of ~ 1.8 mg and a total activity of ~ 46.7 kBq, found in the chemical compound of Neptunium Hydroxide (H_5NpO_5) provided by JRC-Geel and one with a mass of 1.48 mg and a total activity of ~ 38.6 kBq prepared

at the IPN-Orsay. The reason for using two different batches of materials was to eliminate systematic uncertainties. More specifically, as already mentioned, the two latest measurements by Diakaki et al. and Paradela et al. showed discrepancies that reached 7%. The sample used in the latter measurement was also prepared at IPN-Orsay from the same batch as the one used here, therefore a conclusion could be drawn regarding the resolving of the discrepancies. In table 1.4 the characteristics of the samples used in the $^{237}Np(n,f)$ experiment are listed.

Apart from the ^{237}Np samples three reference uranium samples in total were used in the form of Uranium Hydroxide deposits (H_6O_6U): a ^{235}U with a 508 μg to cover the energy region from thermal neutron energies up to the MeV range and two ^{238}U samples featuring a total mass of $\sim$ 3.8 mg to cover the MeV range, where the need to solve the aforementioned discrepancies was high.

Table 1.4: *List of the main characteristics, and stated impurities of the samples used in the $^{237}Np(n,f)$ experimental campaign along with the estimated uncertainties as given by JRC-Geel. In the case of the IPN-Orsay samples, no estimated uncertainty was provided. The activities in the JRC ^{237}Np samples (lot 9005) as well as the levels of contamination, were determined on May 2015, while for the IPN one, the determination took place on September 2016. For the ^{235}U sample (lot 680) the activity and levels of contamination were determined on June 2015 while for the ^{238}U ones (lot 2677), on April 2015.*

Sample	Reference Number	Activity (kBq)	Mass (mg)	Areal density (mg/cm^2) ($\times 10^{-7}$ atoms/b)		Atomic abundances (%)
^{237}Np (JRC)	TP2015-005-01	11.114(42)	0.4270(21)	0.0604(9)	1.52(2)	^{237}Np : 100
	TP2015-005-02	11.780(45)	0.4526(23)	0.0640(9)	1.61(2)	
	TP2015-005-03	11.939(45)	0.4587(23)	0.0649(9)	1.63(2)	
	TP2015-005-04	11.845(56)	0.4551(26)	0.0644(9)	1.62(2)	
Total		**46.678**	**1.7934**	**0.2537**	**6.38**	
^{237}Np (IPN)	Npt-nTOF-2016	38.56	1.48	0.266	6.75	^{237}Np : 99.988 ^{238}Pu : 0.001 ^{239}Pu : 0.011
^{235}U	TP2015-006-03	40.58(25) Bq	0.508(3)	0.0718(11)	1.84(3)	^{234}U : 0.035973(75) ^{235}U : 99.9336(14) ^{236}U : 0.009629(53) ^{238}U : 0.02073(14)
^{238}U	TP2015-007-04	23.4(3) Bq	1.883(25)	0.266(4)	6.73(1)	^{234}U : 0.000000592(18) ^{235}U : 0.0007668(14) ^{236}U : 0.000009266(42) ^{238}U : 99.999223(15)
	TP2015-007-05	23.32(28) Bq	1.875(23)	0.265(4)	6.71(1)	

1.4 Detectors and fission chamber

For the detection of the fission fragments in both experimental campaigns, a detection set-up based on the Micromegas (Micro-mesh gaseous structure) detector [155–157] was employed housed in a cylindrical aluminium chamber. In addition to the fission set-up, four silicon padded detectors (SiMon2) were used to monitor the neutron fluence before the fission chamber (FIMG).

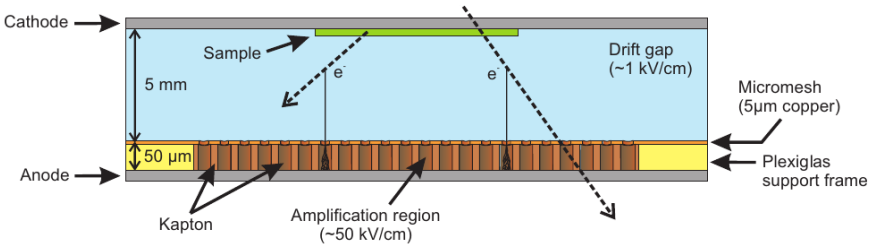

Figure 1.15: *A graphical illustration of the Micromegas detector whose gas volume is divided into two parts by a thin 5μm conductive micro-mesh. The primary electrons created by a fission fragment that escapes the sample, which is part of the detector's cathode, drift towards the micromesh and are multiplied inside the amplification region [13].*

1.4.1 The Micromegas detector in fission measurements

The Micromegas detector belongs to the relatively new MPGD (Micro-pattern gaseous detectors) family [158–160] which has grown greatly over the last 2 decades. The special case of neutron experiments, in which the minimum possible quantity of material is required to reduce the background, has been addressed by the low mass Microbulk Micromegas variant [161–163]. The 9.5 cm in diameter active volume of such a detector is divided into two parts by a thin 5 μm copper micromesh, with 35 μm diameter holes and a pitch of 50 μm: (a) the drift region or conversion gap and (b) the amplification region or gap. The drift region, in which the primary radiation ionises the gas and primary electrons are created, lies between the detector's cathode (or drift) and the micromesh. The fission foils are typically part of the detector's cathode as can be seen in fig. 1.15. Typical electric fields applied in this region are of the order of ~ 1 kV/cm while the distance between the two terminals was 5 mm in both fission experiments. The ~ 5 MeV α-particles emitted from the ^{240}Pu and ^{237}Np samples, have a range of the order of 30 mm, while fission fragments[3] need to travel ~ 20 mm to deposit their entire energy.

The primary electrons are created in the conversion gap and drift towards the micromesh with a typical drift velocity of the order of $10\,cm/\mu s = 0.1\,mm/ns = 100\,\mu m/ns$ depending on the circulating gas mixture used, which in the case of fission experiments at n_TOF is $Ar : CF_4 : iC_4H_{10}$ at 88 : 10 : 2% volume fraction at atmospheric pressure. The amplification gap, which is made of a 50 μm thick and 10 cm in diameter Kapton foil with its holes being filled in with the gas mixture, lies between the micromesh and the anode or pad of the detector that is usually grounded through a 50 Ω termination. Typical electric fields applied in this region are of the order of 50 kV/cm, therefore the primary electrons further ionise the gas through avalanche multiplication. The field lines in the two regions can be seen in fig. 1.16.

[3] The typical range was calculated for ^{94}Sr with a kinetic energy of 100 MeV, using the SRIM code [164, 165].

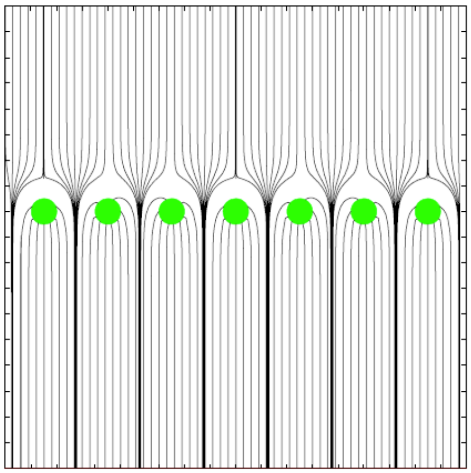

Figure 1.16: *Simulated electric field in the region near the micromesh. The field lines at the conversion gap (top half) focus electron trajectories on the amplification region (bottom half) through the center of the holes. [166]*

In fission experiments where a Micromegas detector assembly is employed, the voltage configuration is usually set to collect argon ions at the micromesh, therefore negative voltages are applied to the micromesh and the cathode. The flight time of a fission fragment inside the gas volume is of the order of 1 ns, the mean drift time of the electrons in the drift region is of the order of 50 ns while roughly ~ 100 ns, also referred to as collection time, is required by the Argon ions to travel a $50\,\mu m$ distance under the influence of a 50 kV/cm electric field inside the gas mixture used, given their $1.25\,cm^2/Vs$ mobility [167]. The signal in a Micromegas detector filled with the gas used at n_TOF and read-out by the n_TOF preamplifiers, has a duration of the order of 250 ns in FWHM or 500 ns in full width and varies depending on the emission angle of the fission signal and the characteristics of the preamplifier module.

More specifically, taking into account three general cases of fragment emission (forward, large angle and intermediate) as seen in fig. 1.17, the signal shapes in the forward and intermediate emissions are not expected to significantly differ since the charge collection begins as soon as the nearest to the micromesh electron initiates the avalanche and the first ions are collected. This process takes place immediately after the passage of the fission fragment, therefore the signal formation starts with practically zero delay. On the contrary, electrons produced from fission fragments emitted in large angles, almost parallel to the micromesh, produce signals with sharper rise times and delays equal to their drift time. The special case of such emission angles that the trajectory of the fission fragment intercepts the support frame of the micromesh, results in considerably smaller delays since the nearest to the micromesh electron needs to drift towards it but still is quite close to the neighboring region.

The signal's rise time, measured from $0-100\%$ of the amplitude, is of the order of 200 ns due to the drift time of electrons in the conversion gap and the collection time of argon ions in the micromesh. The decay time, measured from $100-0\%$ of the signal's amplitude, in the case of both experimental set-ups was of the order of 300 ns duration which is attributed to the decay constant of the preamplifier.

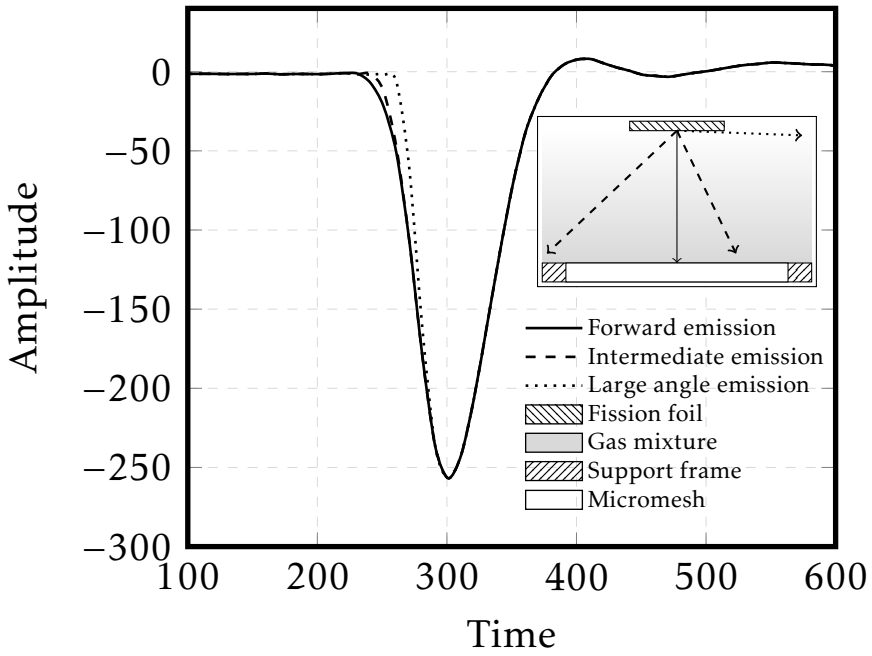

Figure 1.17: *Signal shapes are not expected to vary appreciably in the case of forward and intermediate emission since the charge collection begins at the the same time instance for the two cases. On the contrary, the large angle emission introduces a time delay in the charge collection equal to the electron drift time on the drift region. The inset contains a graphical representation of the emission inside the detector's volume.*

The detectors used in the experiments were also characterised in order to achieve the optimum operational conditions for the fission fragment/α-particle separation. More specifically, the detectors were operated at the maximum relative electron transparency, which is a quantity that represents the ratio of electrons that reach the amplification gap with respect to the ones initially created, which was found to correspond to a drift field between $0.7-1$ kV/cm as can be seen in fig. 1.18. In low drift fields the electrons do not acquire enough kinetic energy and as a result they are captured by the surrounding ions (recombination effect). In very high electric fields, the field lines converge to the micromesh, therefore the electrons do not pass towards the amplification region and are collected on the mesh. In between these two regions, the maximum transparency is reached. The characterisation was performed with fission foils from both campaigns (^{235}U from the $^{240}Pu(n,f)$ experiments and ^{237}Np (IPN) from the $^{237}Np(n,f)$ one) by following the centroid of the deposited energy by the intrinsic α-particles of each sample when changing the applied voltage on the cathode, while keeping the voltage on the micromesh constant, using a typical preamplifier-amplifier-ADC read-out chain.

The same procedure was followed to confirm the exponential detector gain with an increasing electric field. In this case the voltage on the cathode was kept at a constant value and the voltage on the mesh was varied. The results shown in fig. 1.19 validate the proper exponential electron/ion collection on the mesh.

While the detector characterisation showed a well expected behavior, the high frequency noise present in EAR2 , led to an upgrade of the read out adapters on the detector. Prior to the $^{237}Np(n,f)$ experiment the standard read-out line was

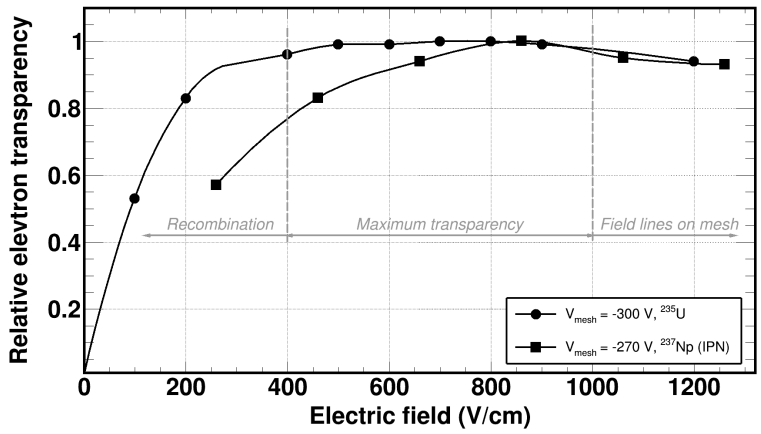

Figure 1.18: *Relative electron transparency as measured in the ^{235}U sample from the $^{240}Pu(n,f)$ campaign and the ^{237}Np (IPN) sample from the $^{237}Np(n,f)$ one with respect to the applied electric field in the drift region. The curves are normalised to 1.*

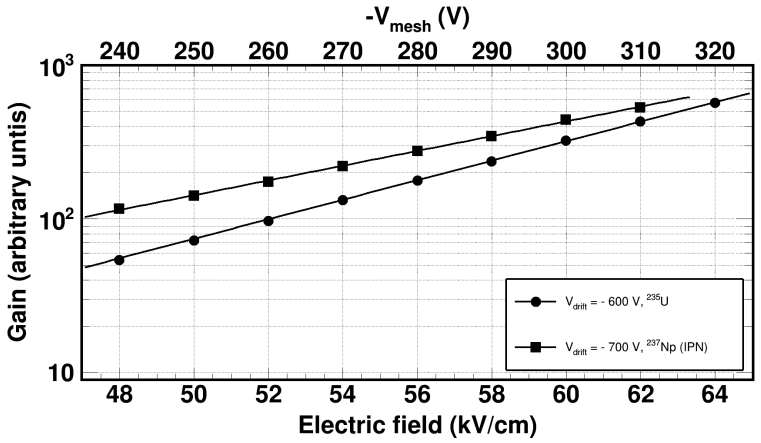

Figure 1.19: *Exponential gain curves as measured with the ^{235}U sample used in the $^{240}Pu(n,f)$ measurements and the ^{237}Np (IPN) used in the $^{237}Np(n,f)$ ones. The black lines represent exponential fits on the experimental points.*

a soldered single-core cable on the detector, a cabling set-up which is sensitive to electromagnetic interference (EMI). In an attempt to minimise the effect of this high frequency noise, LEMO adapters were soldered instead on the detectors, as well as on the chamber's feed-through flange, in the framework of the present thesis, and the signal was transferred to the read-out system through a LEMO co-axial cable (fig. 1.20).

Finally, the Micromegas detectors were housed in a cylindrical aluminium gas chamber, whose entrance and exit windows were made of 25 μm thick and 15 cm in diameter Kapton foils. Apart from the fission foils described in section 1.3, a cathode with a sample backing without deposited material was used to monitor possible -neutron or photon induced- proton or α recoils from the detector materials. The procedure of manipulating and installing the radioactive samples inside the chamber, took place at a certified class-A laboratory at the ISOLDE facility at CERN, inside a constantly ventilated glass box. A photograph of the Micromegas assembly used in both measurements can be seen in fig. 1.21.

(a) LEMO adapter on the detector. *(b)* LEMO adapters on the feed-through flange.

Figure 1.20: *In the $^{237}Np(n,f)$ campaign, LEMO adapters were soldered on the detectors and the chamber's feed-through flange to minimise the high frequency noise that was present in EAR2. For the signal transfer co-axial LEMO cables were used.*

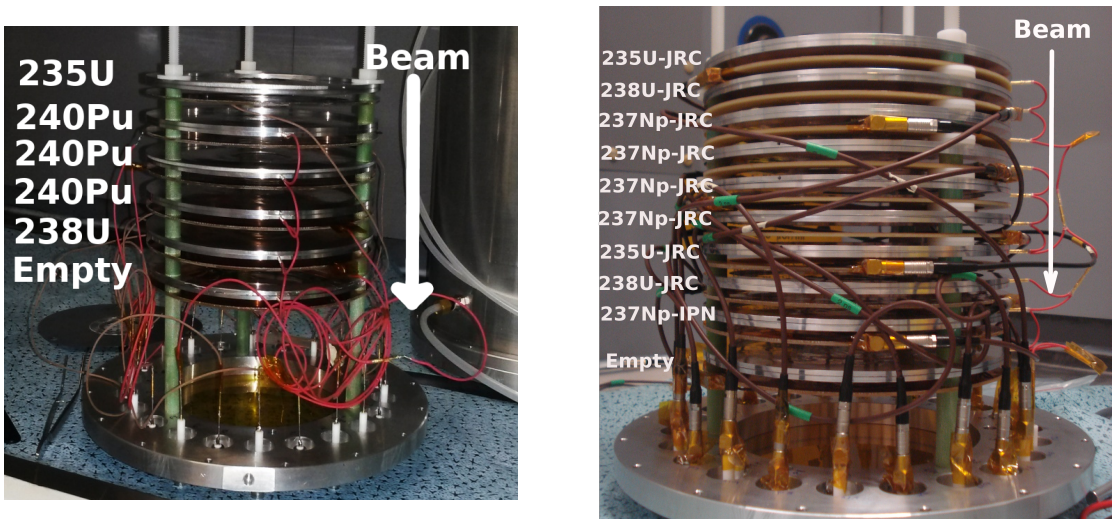

(a) ^{240}Pu *(b)* ^{237}Np

Figure 1.21: *Photographs of the $^{240}Pu(n,f)$ (left) and $^{237}Np(n,f)$ (right) set-ups after the completion of the target manipulation that took place in a certified class-A laboratory in ISOLDE facility at CERN. Apart from the ^{240}Pu /^{237}Np targets and the reference samples, empty frames were added to monitor any possible proton or alpha recoils from the surrounding materials. The arrow indicates the beam direction.*

1.4.2 Beam monitors

The intensity of the proton beam that impinged on the n_TOF target was monitored through a Beam Current Transformer (BCT) and a Wall Current Monitor (PKUP). For the neutron beam monitor, a set-up made of silicon detectors is located along the beam line on the entrance to EAR2.

1.4.2.1 Neutron beam monitors and alignment

To monitor the neutron beam flux, a low-mass silicon detector assembly (SiMon2) has been installed in the beam line at a distance of 19.2 m above the spallation target [168] and below the Micromegas fission chamber. The neutron detection is made possible by the use of the $^6Li(n,t)\alpha$ reaction and a neutron ^6LiF conversion foil with a surface density of $420\,\mu g/cm^2$, which is placed inside a vacuum chamber held at a $\sim 10^{-2}$ mbar pressure. The tritons and α-particles produced by the $^6Li(n,t)\alpha$ reaction are detected by four $300\,\mu m$ in thickness and $3\times3\,cm^2$ in surface, silicon single padded detectors provided by Micron Semiconductors (MSX09-300) which are not placed directly in-beam, as can be seen in fig. 1.22, but are tangent to a sphere with a radius of 3 cm and centered around the ^6LiF foil, at an angle of 45° degrees with respect to the beam direction. In this way, the neutron beam, which is 2.2 cm in diameter using the capture set-up can cross the flux monitor without touching the edges of the detectors.

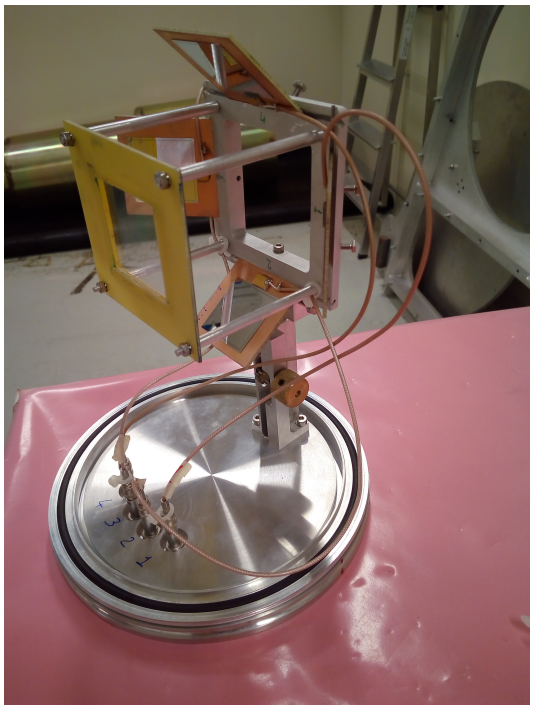

Figure 1.22: *The neutron beam monitor of EAR2 consists of four silicon single padded detectors (reflective squares) placed at 45° with respect to the beam direction. A stable ^6LiF salt is used as a neutron converter to monitor the neutron flux via the $^6Li(n,t)\alpha$ reaction and the detection of tritons and α-particles. The neutron beam travels from the left hand to the right hand side of the image.*

The fission chamber was aligned with respect to the neutron beam by the use of the Gafchromic-EBT^3 self-developing dosimetry film. A pair of Gafchromic foils were placed on the top and bottom part of the chamber, respectively, shadowing the Kapton windows. An eight-hour exposure time in the neutron beam with the capture collimator in place, is adequate to provide information on the geometrical

profile of the neutron beam. The foils are then scanned with a typical image scanner and a basic image processing helps to enhance the contrast between the irradiated and unaffected by the beam area of the film. A sample pre- and post-processed Gafchromic film from the $^{237}Np(n,f)$ campaign can be seen in fig. 1.23.

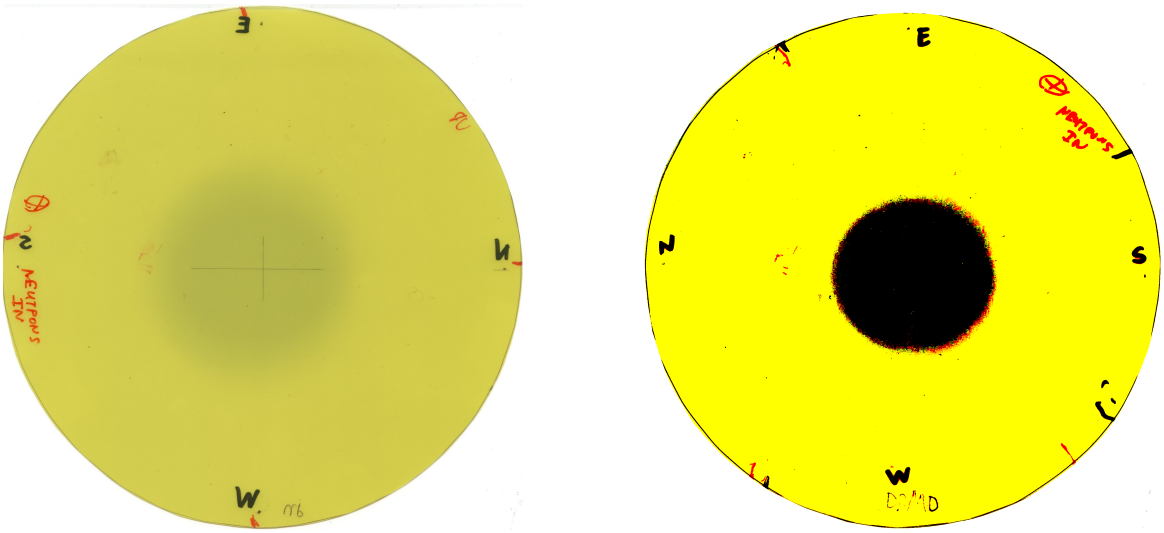

(a) Pre-processed *(b)* Post-processed

Figure 1.23: *Self-developing Gafchromic foils were placed on the top and bottom of the fission chamber for the alignment with respect to the neutron beam. A scanned image of a film used in the $^{237}Np(n,f)$ campaign can be seen before and after processing.*

Finally, in fig. 1.24 the final configuration installed in EAR2 in the $^{240}Pu(n,f)$ campaign can be seen. It has to be noted that the set-up in the $^{237}Np(n,f)$ experimental campaign was identical to the $^{240}Pu(n,f)$ one.

1.4.2.2 Proton beam monitors

A beam current transformer, located at 6 m before the lead spallation target on the extraction line that leads to n_TOF (FTN line) and passively monitored the proton beam intensity. Right after the BCT, a resistive wall current monitor has been installed, whose signal was directly injected to the n_TOF acquisition system in order to be used in the online analysis for timing purposes or to directly monitor the proton beam intensity [169].

1.5 From detector signals to data buffers

The charge collected in the micromesh results in the formation of signals which are amplified by the use of current sensitive preamplifiers before being fed in the n_TOF data acquisition system and then stored at CERN's advance storage manager

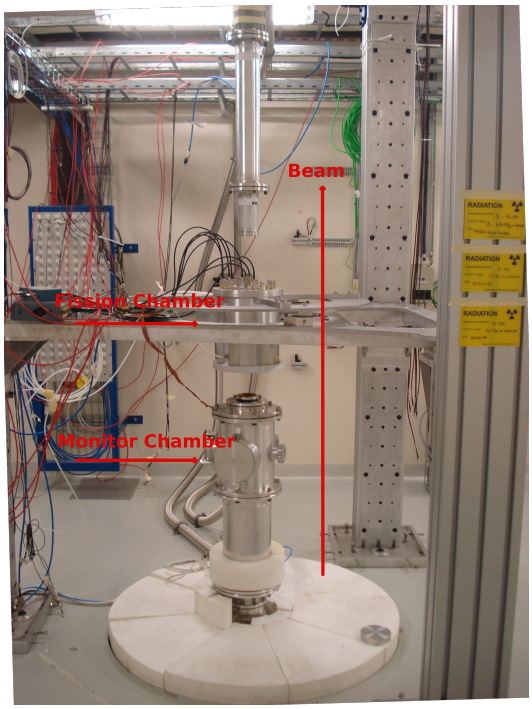

Figure 1.24: *The final set-up in the $^{240}Pu(n,f)$ campaign at EAR2. The vertical neutron beam on its arrival to EAR2, meets the monitor chamber that houses four silicon detectors and a ^{6}LiF conversion foil before it passes through the fission chamber that houses the Micromegas detectors and the fission foils. The set-up in the $^{237}Np(n,f)$ experiment was identical to the $^{240}Pu(n,f)$ one.*

(CASTOR) for further off-line processing.

More specifically, the read-out consisted of current sensitive preamplifiers, provided by INFN-Bari, which followed the leading edge of the charge collection from the detector while avoiding any further time-wise lengthy shaping. In the case of the $^{240}Pu(n,f)$ measurement the preamplifier set-up consisted of a multi-channel module, with insufficient shielding and therefore sensitive to EMI. In the case of the $^{237}Np(n,f)$ campaign, the single module was replaced by twin-channel modules, an upgrade which along with the single-core cable replacement inside the chamber, improved the quality of the recorded signals as will be discussed later.

The signals were then fed to the analogue-to-digital converters, namely Signal Processing Devices (SPDevices) which offer high sampling rates from 14 up to 1800 MS/s, a resolution up to 14-bits, a dynamic range from ±0.2 to ±5 V and a total acquisition time of 100 ms per duty cycle (usually referred to as *bunch*), which is enough to reach down to thermal neutron energies. In the case of the $^{240}Pu(n,f)$ measurement an 8-bit resolution system was available and the sampling rate used was 500 MHz, while the full scale ranged between 0.5 and 2 V, depending on the gain of the detectors. The reason lies to the fact that detectors coupled with low-activity samples can be operated at higher gains since the space charge within the gas volume is small enough to reach the Raether limit (maximum charge $< 10^6 - 10^7 e^-$) at high electric fields. In the $^{237}Np(n,f)$ experiment the SPDevices were operated at a sampling rate of 225 MHz and a 12-bit resolution. The detectors were operated at higher gains therefore the full scale range in this case was 5 V.

To minimise the data collection rate and the recording of useless noise sequences, a zero-suppression algorithm was employed. Based on a user-defined amplitude threshold, data is stored only at times when this threshold is crossed and consequently the data acquisition is triggered. The waveforms were stored between two consecutive threshold crossings with the addition of a user defined pre- and post-sample in order to ensure that the whole time-trace (usually referred to as *movie*) is stored. In the case of high counting rates, where a signal can cause a threshold crossing within the post-samples, the acquisition is extended until the next crossing occurs. Since the γ-flash results in baseline distortions and useful information can be hidden within, the zero-suppression can be set to be initialised after a user-defined time span.

Finally, the recorded data are stored on tape in binary files at CERN's advanced storage manager, so-called CASTOR, in segments of bunches for further off-line processing and analysis. In the case of the $^{240}Pu(n,f)$ measurement each segment consisted of one bunch, while a different approach was used two years later during the $^{237}Np(n,f)$ experimental campaign, when each segment consisted of twenty bunches.

CHAPTER 2

Monte Carlo simulations

To better understand the detectors in terms of the energy deposition of fission fragments on the gas volume, Monte Carlo simulations were performed. More specifically, the fission specialised Monte Carlo code GEF, was used to produce distributions of fission products which were then fed to the generalised Monte Carlo code, FLUKA where the interaction of these heavy ions with the gas molecules was studied. The simulations were performed on the scope of drawing conclusions on the self-absorption of fragments on the fission foils as well as to estimate the portion of fission fragments that were discarded during the analysis, for reasons that will be discussed later in the text.

2.1 GEF: A general description of fission observables

To study the fission process in an empirical level the GEF code [16], which implements the GEF model, was used. The General Description of Fission model (GEF) is based on the implementation of a phenomenological model of fission, which treats the fission of user requested fissioning nuclei with a set of global collective parameters [16]. Despite the absence of quantum-mechanical features, the macroscopic treatment of GEF provides quantitative predictions of fission observables which are in good agreement with experimental data. Among its predictions, information on fission product properties such as the atomic number Z, the mass A and the total kinetic energy released per simulated fission event were provided before and after the neutron evaporation.

The fission product properties that were requested for the four fissioning nuclei used in the experiments, namely for the ^{236}U, ^{238}Np, ^{239}U and ^{241}Pu were then used as the primary ionising beam in the FLUKA simulations. However, prior sensitivity studies were performed in order to better understand the importance of certain

variables such as the incident neutron beam and grasp basic concepts of the fission process through the study of predicted distributions of the fission products (i.e. mass, atomic number, kinetic energy).

2.1.1 Dependence on the incident neutron spectrum

GEF provides the possibility to produce fragment distributions for various incident neutron beams, either a monoenergetic one or a neutron spectrum. To study the effect of the energy of the incident beam on the production of fission products, mass distributions were reconstructed for neutron beams of 1 meV, 1 eV, 1 keV, 100 keV and 1 MeV incident energy as well as for the neutron spectrum of EAR2. The selection of these energies was such to cover a wide range from thermal ones up to the fission threshold as well as to simulate a realistic production of fragments using the EAR2 neutron flux. As seen in fig. 2.1, where the mass probability distributions of $^{240}Pu(n,f)$ are shown for different incident neutron spectra, the distribution of fission products did not heavily depend on the energy of the incoming neutrons as indicated by the most probable values of the distributions, therefore the calculations that follow assumed a monoenergetic neutron beam at 1 MeV incident energy, for computational time minimisation reasons. It has to be mentioned that the calculations performed for the remaining fissioning nuclei, led to the same conclusion, therefore in all cases an incident neutron beam of 1 MeV was used.

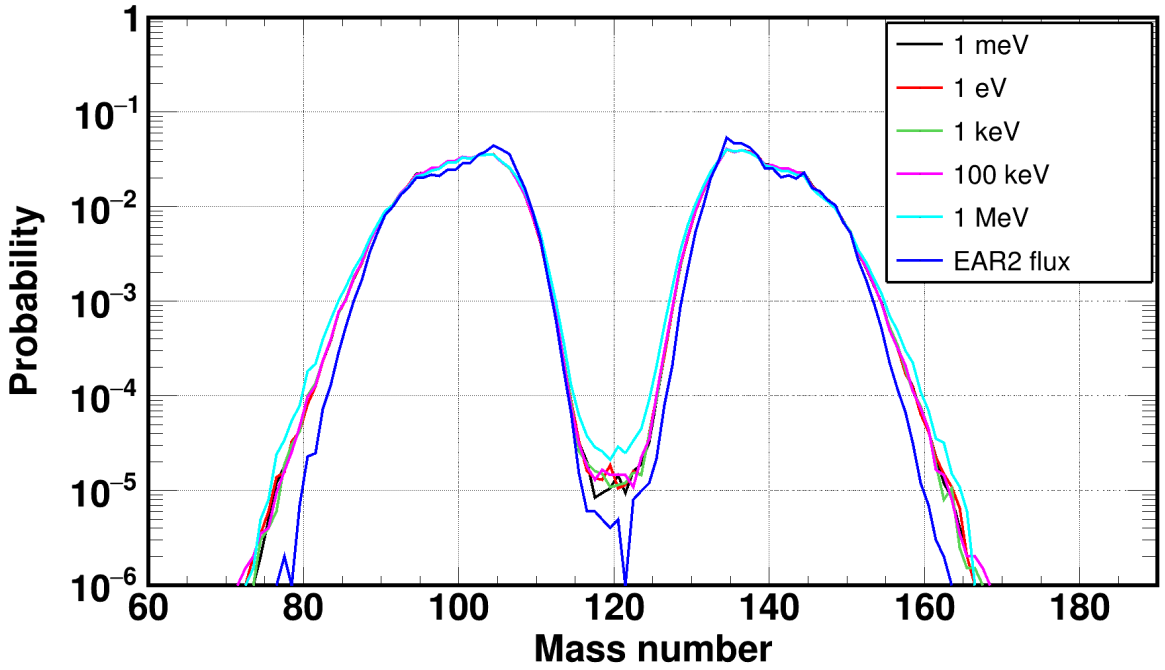

Figure 2.1: *Calculated mass distribution of fission products occurring from the $^{240}Pu(n,f)$ reaction. It is notable that the incident neutron energy did not affected the distribution of fission fragments. The calculations were performed with the use of the GEF code.*

2.1.2 Distributions of fission products

An important information that was extracted from calculations performed with GEF, regards the distribution of certain properties of fission products such as the mass and atomic number (A and Z, respectively) as well as the kinetic energy (K) post neutron evaporation. The study of these distributions was an asset in better understanding the concept of the fragment production as well as their interaction with the gas of the Micromegas detector system. An example of the mass number of fission fragments against their kinetic energy, which is commonly referred to as "fission-lungs", obtained from GEF is shown in fig. 2.2 where the calculation was performed for the ^{241}Pu compound nucleus for a neutron beam at 1 MeV incident energy.

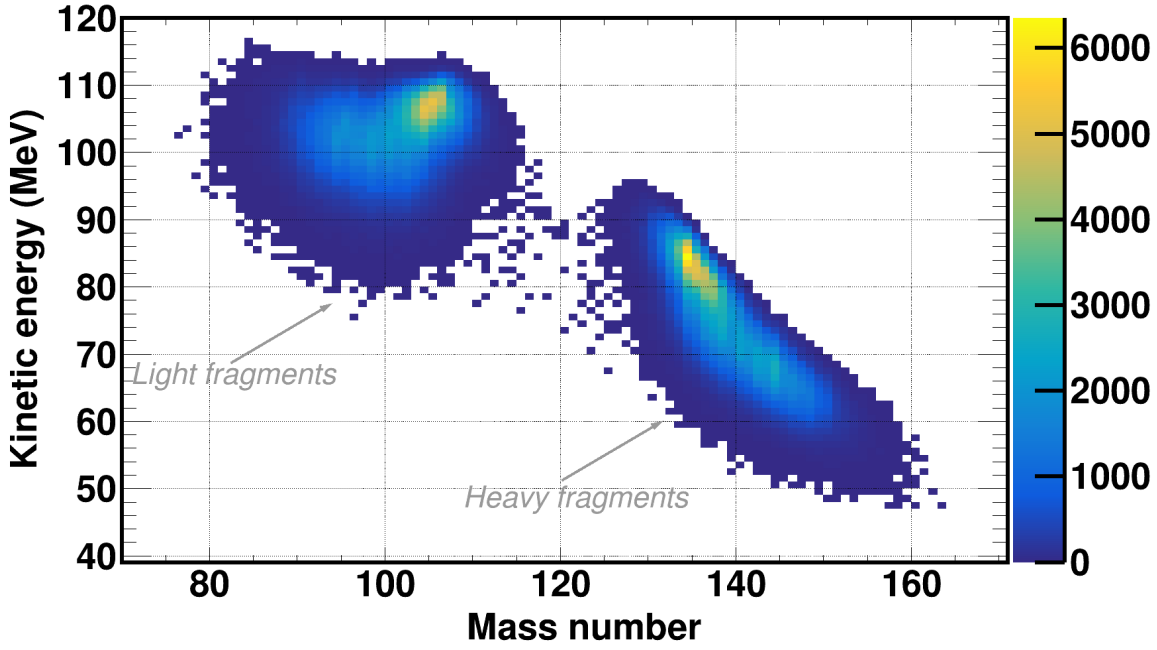

Figure 2.2: *Mass number of fission products against their kinetic energy, as obtained from GEF for the case of the $^{240}Pu(n,f)$ reaction induced by a 1 MeV monoenergetic neutron beam. This distribution is commonly referred to as the "fission lungs".*

A projection of the previous distribution on the x-axis, would provide the mass distribution of the fragments produced during the fission process. A closer examination of these distributions for the reactions studied in the framework of the present thesis, revealed an interesting characteristic of the fission process. As can be observed in fig. 2.3, where the predicted mass distributions of fission fragments induced by a 1 Mev neutron beam for the $^{240}Pu(n,f)$, $^{237}Np(n,f)$, $^{238}U(n,f)$ and $^{235}U(n,f)$ reactions are plotted, the heavy fragments have almost identical mass distribution independently of the fission reaction. On the contrary, the distribution of light fragments had a dispersion and more specifically the heavier the compound nucleus, the heavier the light fragments were, which could eventually lead to the merging of light and heavy fission fragment mass distributions with increasing compound mass. It has to be mentioned that the previous conclusion is not

valid for lighter nuclei ($A < 210$) where symmetric fission is more probable [170].

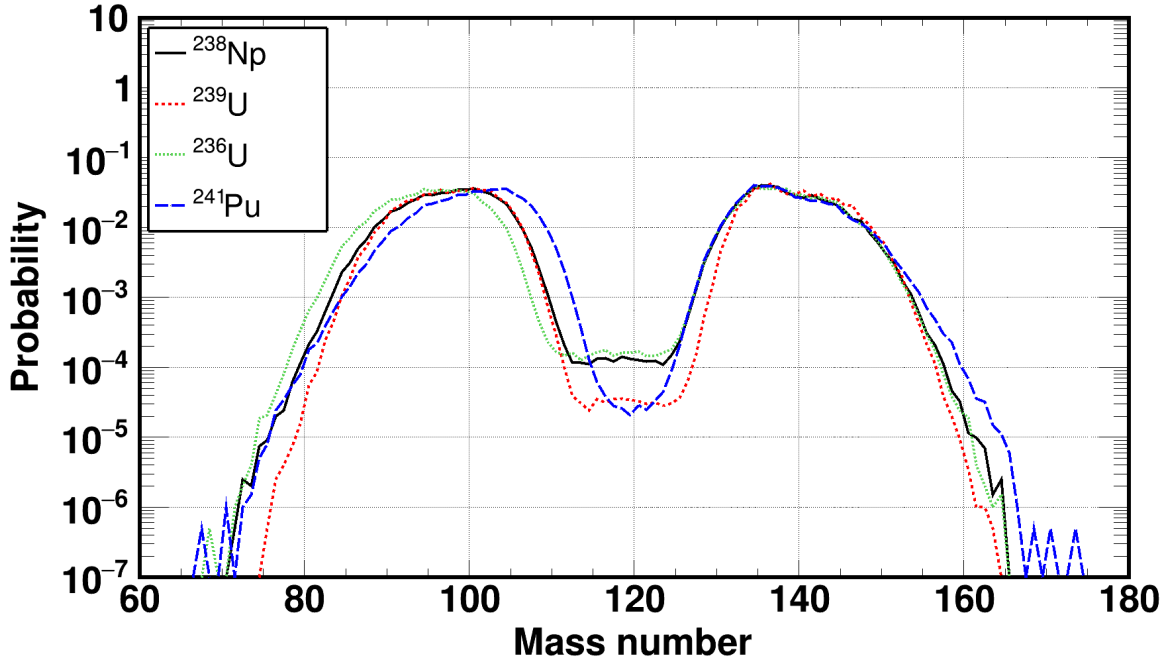

Figure 2.3: *Mass number distributions of fission products occurring from the reactions studied in the present thesis as calculated from* GEF *for incident neutrons of* 1 *MeV. It is evident that the mass of the heavy fragments does not depend on the fissioning nucleus whereas the heavier it is, the largest the most probable mass of the light fragments becomes.*

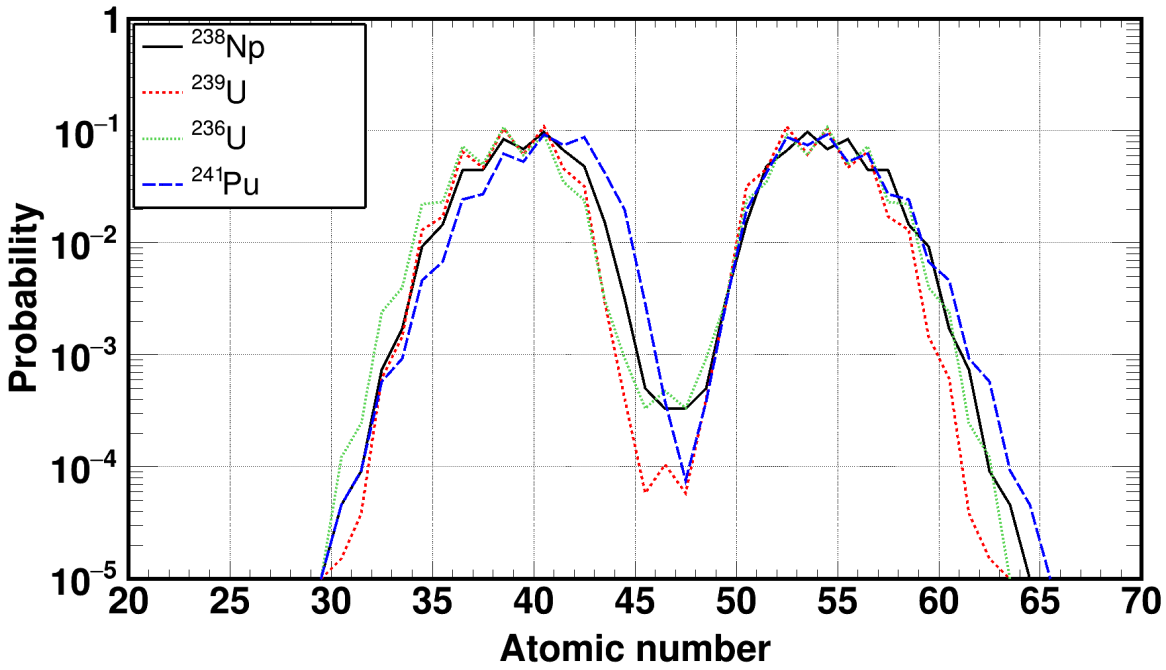

Figure 2.4: *Atomic number distributions of fission products occurring from the reactions studied in the present thesis as calculated from* GEF *for incident neutrons of* 1 *MeV. It is evident that the produced heavier elements are independent of the induced reaction whereas the light fragments are heavier elements for heavier compound nuclei.*

This observation was attributed to shell effects which occur at the scission point, where the fissioning system is highly unstable and has to cool down. The easiest way to do so, is to get rid of a considerably big amount of energy by fissioning and splitting into two unequal parts. It seems that there is a prominent preference in the formation of nuclei with an atomic number around 52 – 54, as can be seen in fig. 2.4, regardless of the fissioning nucleus. This tendency can be justified by examining the Nilsson diagram, seen in fig. 2.5b, where for large quadrupole deformations ϵ_2 there is a closed shell around Z > 50. While the compound nuclear system, which has initially 92 – 94 protons, is about to fission, it prefers to do so in the least expensive way, energy-wise, therefore the formation of a fragment with 50 or less protons would require a huge energy leap, as the heavy fragment is created from top to bottom. This implies that the remaining ~ 40 protons will form the light fragment and as seen in fig. 2.5a they can be arranged between the $2p_{1/2}$ and $1f_{5/2}$ states which have a similar excitation energy E.

2.1.3 On the expected separation between light and heavy fragments

The calculated fragment distributions indicate that the heavier the compound nucleus, the worse the separation between light and heavy fission fragments. The energy loss of charged particles on a medium can be described by the Bethe-Bloch equation [171] seen in (2.1)

$$-\frac{dE}{dx} = 2\pi N_A r_e^2 m_e c^2 \rho \frac{Z}{A}\frac{z^2}{\beta^2}\left[\ln\left(\frac{2m_e c^2\beta^2\gamma^2 W_{max}}{I^2}\right) - 2\beta^2 - \underbrace{\delta(I,\eta)}_{\substack{density\\ correction}} - \overbrace{2\frac{C(I,\eta)}{Z}}^{\substack{Shell\\ correction}}\right] \quad (2.1)$$

where

- $2\pi N_a r_e^2 m_e c^2 = 0.1535\ MeV\ cm^2/gr$
- r_e: The electron radius
- m_e: The electron mass
- N_A: The Avogadro constant
- c: The speed of light
- ρ: The density of the medium
- z: The charge of the incident ion (in e^- units)
- A: The mass number of the medium
- Z: The atomic number of the medium
- β: The velocity v/c of the incident particle
- γ: The γ relativistic factor $(1/\sqrt{1-\beta^2})$
- W_{max}: The maximum energy transfer on a collision
- I: The mean ionisation potential
- N_e: The electron density of the medium
- δ: The density correction factor
- C: The shell correction factor

The important dependence is the energy deposition of an ion to its charge z and it velocity v, on a first order approximation. The charge z of a fission fragment

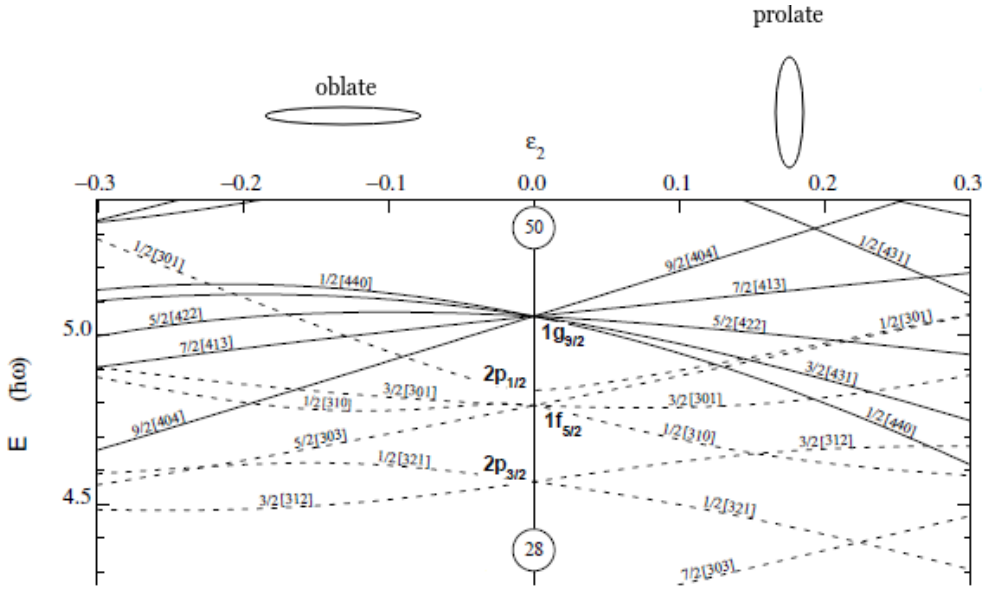

(a) *Around* $Z = 40$

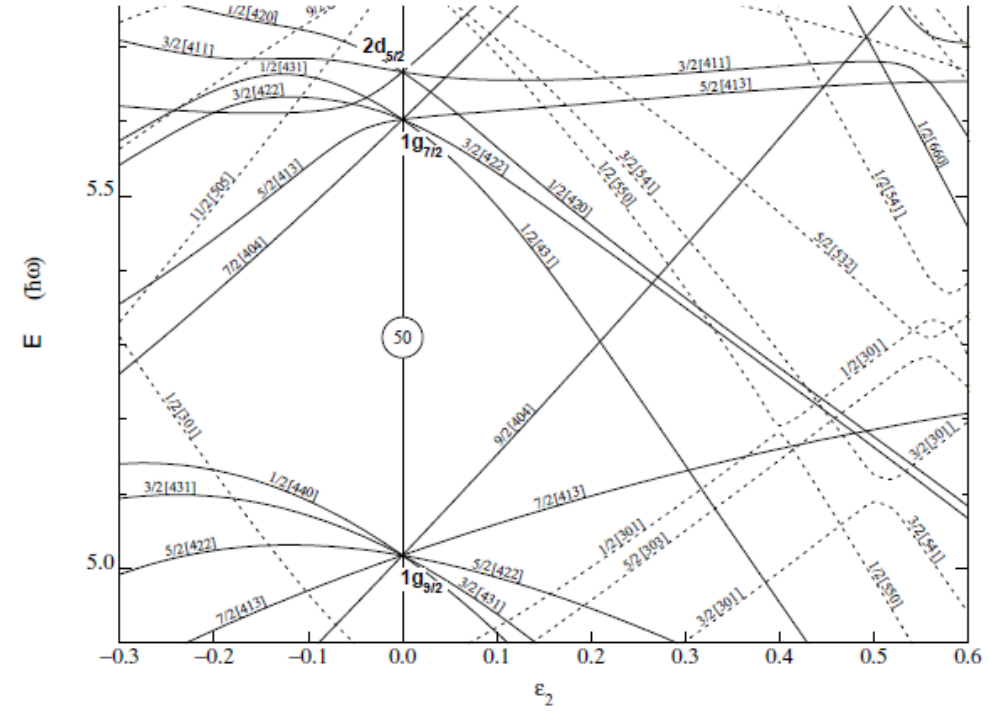

(b) *Around* $Z = 50$

Figure 2.5: *Nilsson diagrams for protons in the regions around* $Z = 40$ *(top panel) and* $Z = 50$ *(bottom panel). The big energy gap at* $Z = 50$ *favours the formation of nuclei with* $52-54$ *protons (heavy fragments) while the remaining* ~ 40 *out of the initial* $92-94$ *form the light fragments.*

during the whole process of its interaction with the gas, can be assumed to be its atomic number Z and its velocity is related to its kinetic energy K therefore

$$-\frac{\mathrm{d}E}{\mathrm{d}x} \propto \frac{AZ^2}{K} \tag{2.2}$$

where the mass number A is assumed to be proportional to the mass of the fission fragment. GEF calculations provided these properties of the fission products and as seen in fig. 2.6, it is evident that the separation between heavy and light fission fragments is much poorer in the case of $^{240}Pu(n,f)$ compared to the one in the $^{235}U(n,f)$ reaction. This simple calculation will be useful in interpreting the reconstructed amplitude spectra, as will be discussed later in the text.

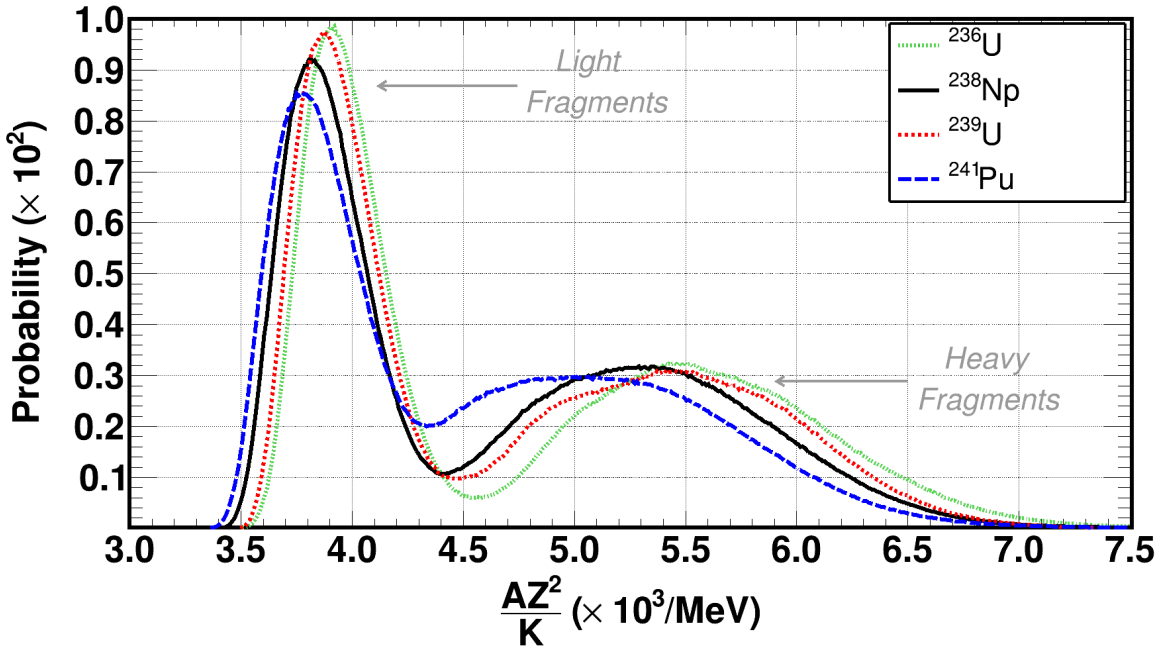

Figure 2.6: *Expected energy deposition (in arbitrary units) in the same arbitrary medium of fission fragments produced by GEF for the $^{235}U(n,f)$, $^{238}U(n,f)$, $^{237}Np(n,f)$ and $^{240}Pu(n,f)$ reactions. It is evident that the heavier the fissioning nucleus, the poorer the separation between heavy and light fission fragments.*

2.2 Energy deposition of fission products

The fission product distributions that were calculated by means of the GEF model, were used as a heavy ion source inside the corresponding fission foil and were propagated along a cylindrical gas volume, whose composition was the one used in the measurements. To simulate the energy deposition of the fragments on both the fission foils and the gas, the general purpose Monte-Carlo code, FLUKA [14, 15] was used.

2.2.1 Heavy ion source

To propagate the fission fragments towards the gas volume, a dedicated source routine had to be implemented. This routine used the properties of the fission fragments calculated by GEF (Z, A, K) and propagated randomly the heavy or the light fragment towards the gas. The fragment that was not selected, was discarded to save processing time. The points within the actinide foil from which the fragments were generated, were also randomly selected in such a way to have a uniform particle generation. Finally, the directional cosines of the emitted fragments were created in a way to generate a uniform 2π emission towards the gas volume.

2.2.1.1 Generation points

To ensure that the generation points were randomly distributed within the sample volume, their (x, y, z) coordinates were stored in order to examine any possible biasing. The geometry of the simulated sample-gas assembly can be seen in fig. 2.7 where the fission sample (brown cylinder) had a radius of $r_s = 1.5$ cm and a $\tau_s = 100$ nm thickness while the gas volume (magenta cylinder) had a $r_g = 4.75$ cm radius and a thickness of $\tau_g = 7$ mm. The propagation of the fission fragments took place along the cylinders' axis, which in the present geometry was considered to be the z-axis, while the bases were assumed to lie on the $x-y$ plane. It has to be noted that the contact surface between the two cylinders lied at the origin of the coordinate system.

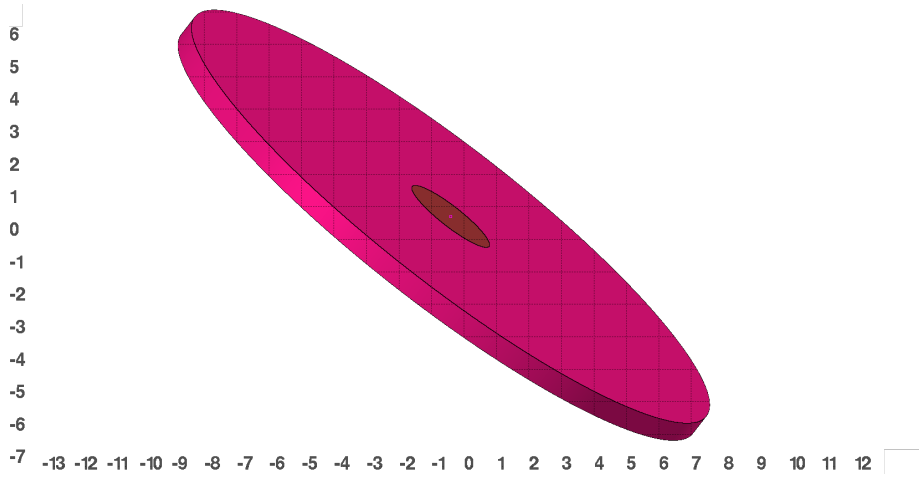

Figure 2.7: *Geometry of the FLUKA simulations as seen on FLAIR [172] interface. The fission foil can be seen in the center while the large cylinder corresponds to the gas volume of the detector. The axes seen on the geometry correspond to metric cm.*

The fission fragments were produced within the actinide cylindrical sample, randomly using FLUKA's embedded random generator FLRNDM() which produces random number in the range $[0, 1)$. The (x, y) coordinates were assigned using a polar reference system (ρ, θ) where $x = \rho\cos\theta$ and $y = \rho\sin\theta$. The polar angle θ was randomly selected in the $[0, 2\pi)$ range by generating a number i with the

formula seen in eq. (2.3)

$$i = 2\pi \cdot \texttt{FLRNDM()} \tag{2.3}$$

To properly produce a uniform distribution of a number i along the radius of the sample (r_s), the following modus operandi was used

$$i = r_s \cdot \sqrt{\texttt{FLRNDM()}} \tag{2.4}$$

The selection of $\sqrt{\texttt{FLRNDM()}}$ instead of simply `FLRNDM()` produces a uniform distribution of points on a circular surface as can be seen in fig. 2.8

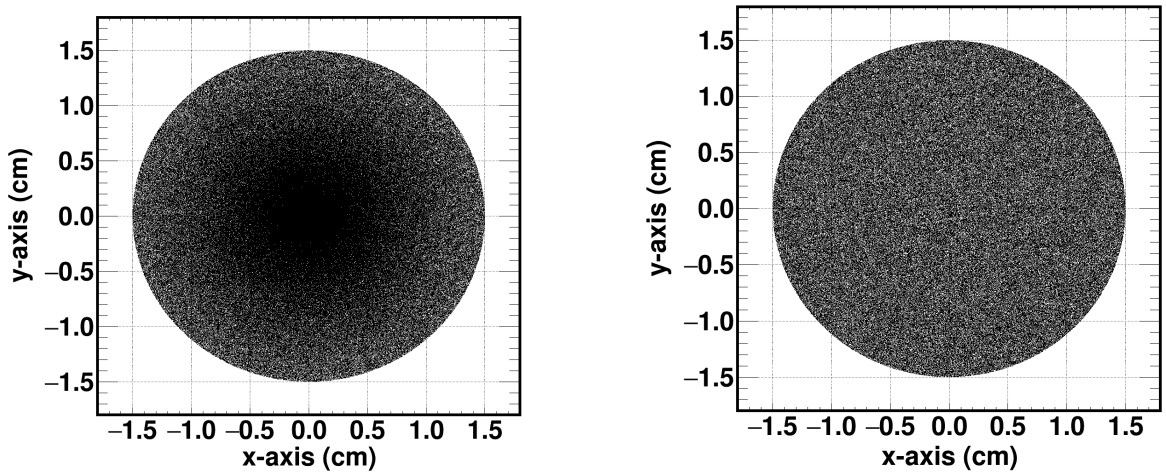

(a) `FLRNDM()` *(b)* $\sqrt{\texttt{FLRNDM()}}$

Figure 2.8: *Comparison of generating randomly distributed points on a circular surface with (right panel) and without (left panel) the use of the square root of the pseudo-random generator* `FLRNDM()`*. It is evident that the use of* $\sqrt{\texttt{FLRNDM()}}$ *results in a uniform distribution of points.*

Finally, the z-position of the generation point was randomly selected to lie between $[-\tau_s, 0)$ since the sample lies on the negative octants of the coordinate system. A uniform distribution was properly achieved, as seen in fig. 2.9 by generating numbers i using the following formula

$$i = \tau_s \cdot \texttt{FLRNDM()} \tag{2.5}$$

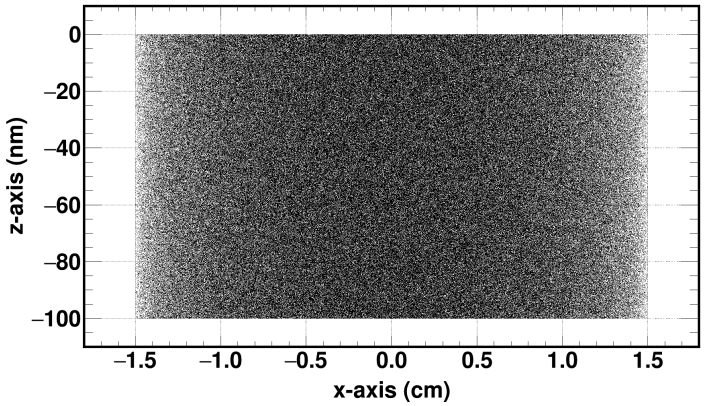

Figure 2.9: *Fission fragments were generated randomly within the sample volume using* `FLUKA`*'s* `FLRNDM()` *embedded random number generator function. The* $x - z$ *plane is shown.*

2.2.1.2 Emission angles

Once the generation points were generated uniformly within the fission foils, a 2π emission had to be simulated. FLUKA uses the directional cosines $\cos x, \cos y, \cos z$ to define the direction of a vector $\vec{v} = (v_x, v_y, v_z)$ on a (x, y, z) coordinate system, as seen in eq. (2.6)

$$\vec{v} = \underbrace{\frac{v_x}{\sqrt{v_x^2 + v_y^2 + v_z^2}}}_{\cos x}\hat{x} + \underbrace{\frac{v_y}{\sqrt{v_x^2 + v_y^2 + v_z^2}}}_{\cos y}\hat{y} + \underbrace{\frac{v_z}{\sqrt{v_x^2 + v_y^2 + v_z^2}}}_{\cos z}\hat{z} \tag{2.6}$$

where x, y, z are the angles between the vector $\vec{v}$ and the $x-, y-$ and $z-$axis, respectively. As mentioned previously, the surface of the sample sits on the $x - y$ and the beam was propagated along the z-axis therefore to simulate a 2π emission the angles x and y were varied in the range $[0, \pi)$, while the angle z was assigned values in the $[0, \pi/2)$ region. As seen in fig. 2.10 where a thousand directions are shown produced from FLUKA within the angle limits described previously, the fission fragment emission was uniform along the positive $z-$axis.

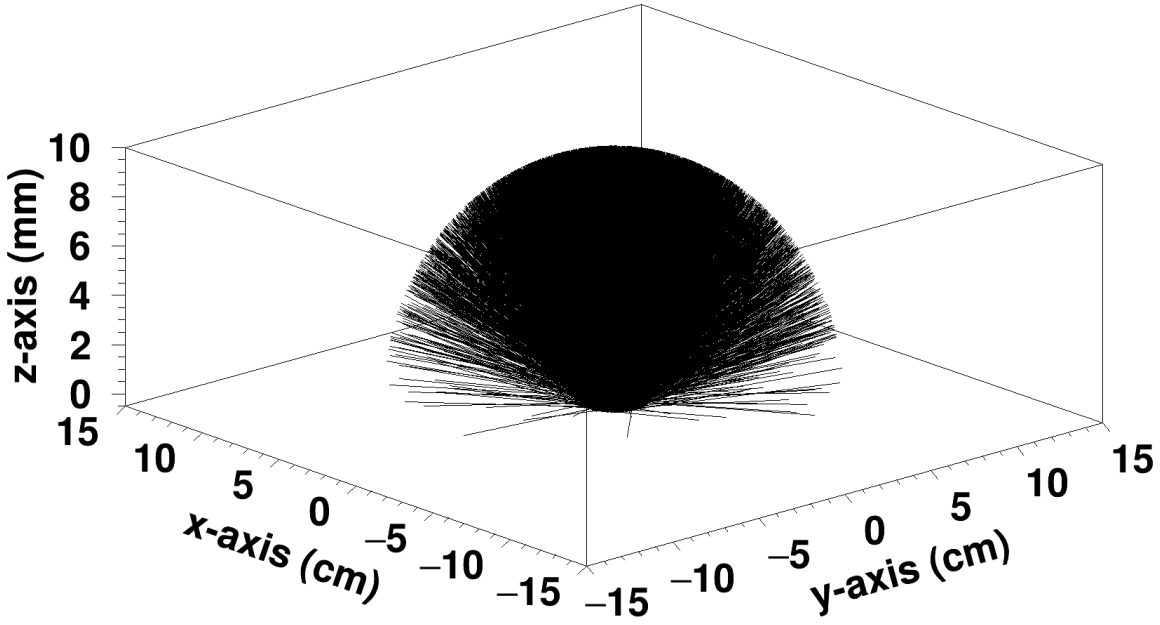

Figure 2.10: *Initial directions of a thousand fission fragments as generated by FLUKA. The particles were propagated along the positive z–axis at a 2π solid angle while the source cylinder was placed at the $x - y$ plane.*

2.2.2 Simulation set-up

The set-up, apart from the heavy ion source, consisted of two cylindrical volumes that represented the gas and the fission foil, whose geometrical attributes were described previously in the text. The gas used in the measurements (Ar:CF_4:iC_4H_10,

at 88 : 10 : 2% volume fraction) was implemented in the simulations at a 1.637×10^{-3} gr/cm^3 density. Since the drift region is the key element in the energy deposition, the amplification gap was not included in the simulation, therefore a total length of 7 mm and a diameter of 9.5 cm were used, as discussed previously in the text.

The fission foils were fabricated according to the materials described in section 1.3. While the diameter was straightforward to be implemented, the assigned thickness of the samples had to be put into further consideration. The reason lies on the fact that the density of the foils cannot be accurately known, given the molecular plating manufacturing process. What was accurately known, nonetheless was the surface density (s), the total mass (m) and therefore the total number of nuclei in each sample (N). This information was used at a sensitivity study of the effect of different thickness-density pairs on the energy deposition in the gas. The areal (s) and mass density (ρ) are related to the thickness (τ) as seen in eq. (2.7)

$$s = \rho \cdot \tau \tag{2.7}$$

Different combinations of (ρ, τ) were used to understand the sensitivity on the energy deposition in the gas, keeping always the surface density, constant. This sensitivity study was performed on a ^{240}Pu sample with a surface density of 101.7 μgr/cm^2. Typical mass densities for actinide foils are around ~ 10 gr/cm^3, therefore the starting point was a density of 10.17 gr/cm^3 which given the areal density mentioned before, yielded a thickness of 10^{-5} cm = 100 nm which was a rather realistic scenario. To stretch the study, unrealistic densities of 1, 1017 and 10^{-5} gr/cm^3 and thicknesses of 1.017μm, 1nm and 10.17 cm, respectively were also simulated. As seen in fig. 2.11, the density practically did not play an important role and the energy deposition is identical in each case, as long as the correct number of nuclei in the sample was accounted for. However, at a very small density, which yields an unrealistically large thickness, the energy deposition distribution differs significantly from the rest due to solid angle effects: the probability to exit the sample at an angle in which there will be no or limited interaction with the gas, is dramatically increased.

As a conclusion, in Monte-Carlo simulations, where usually the density of a compound material is requested, it does not matter if it is not accurately known, as long as a material with the same number of nuclei is modelled. However its dimensions should remain at realistic levels, in order to avoid dramatic solid angle effects. Finally, in simulating the energy deposition in all samples, a thickness of 100 nm was used and the mass density was appropriately varied.

2.2.3 Reproducibility of the simulations

An important check that has to be made when dealing with Monte-Carlo simulations, is the reproducibility of the requested simulated quantities. In this respect, `FLUKA` provides the possibility to run the exact same simulations, multiple times or in different cycles while changing the initial seed. Ideally, calculated results from different cycles should be identical to each other, which was confirmed as fig. 2.12 proves.

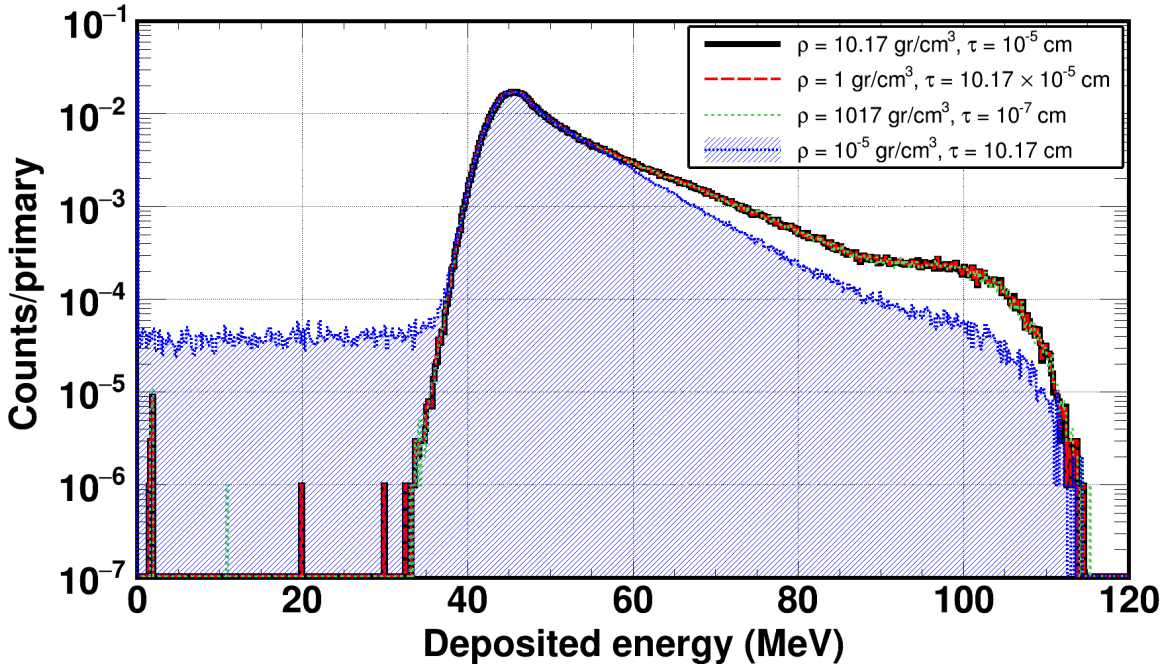

Figure 2.11: *Simulated energy deposition of fission fragments from a ^{240}Pu sample with areal density 101.7μ gr/cm^2 on the gas volume of the detector. Different combinations of thickness τ and mass density ρ were used to illustrate that in Monte-Carlo simulations, the critical parameter in defining a material is the surface density of particles, rather than its thickness, however solid angle considerations have to be taken into account.*

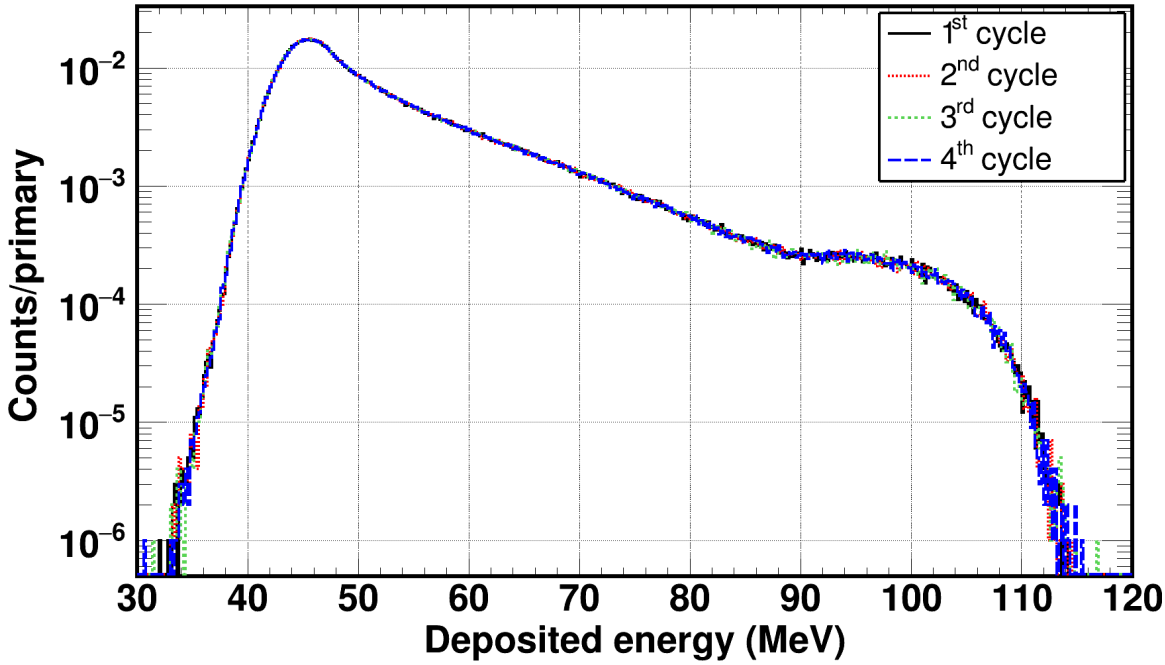

Figure 2.12: *Simulated energy deposition of fission fragments for different initial seeds. The agreement between the distributions in the four cycles is satisfactory.*

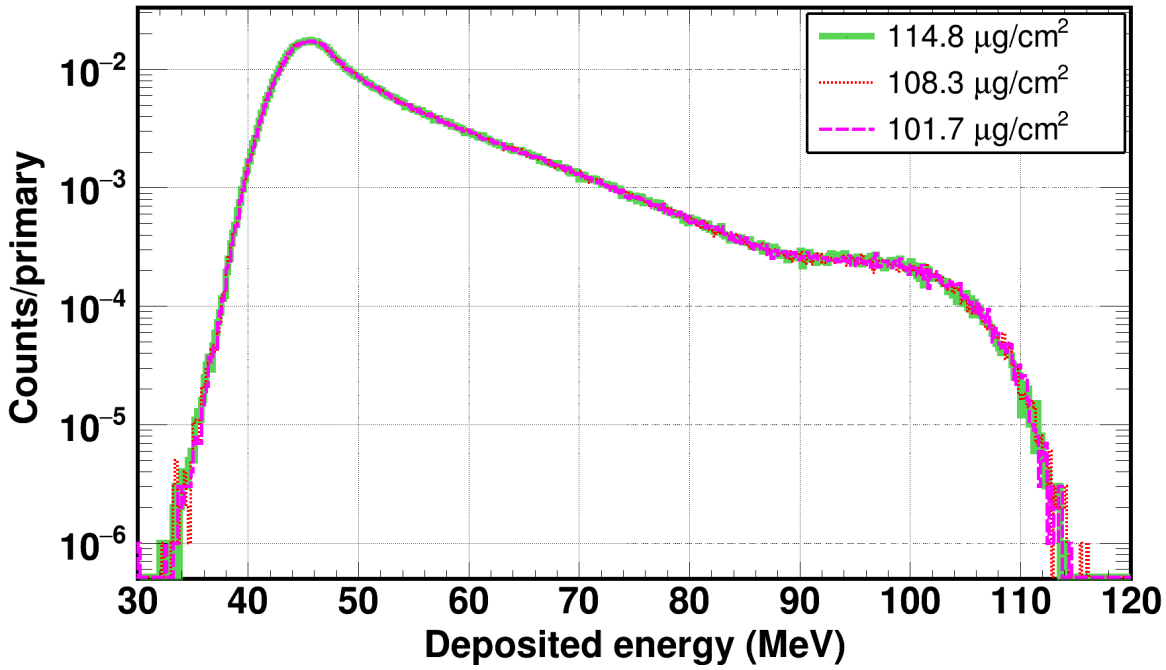

Figure 2.13: *Simulated energy deposition of fission fragments for different masses concerning a cylindrical plutonium source. As expected, a ∼ 15% difference on the mass of a fission foil, did not play a significant role on the energy deposition in a gas volume.*

2.2.4 Effect of the foil mass on the energy deposition

Another effect that was studied, concerned the dependence of the sample mass on the energy deposition in the gas. Since the fission samples used in the measurements were thin ones, a 15% difference in mass was not expected to have a significant effect on the energy deposition on the gas. This was proved from the simulations, as fig. 2.13 shows where the energy deposition from three plutonium cylinders with different masses was simulated.

2.2.5 Energy deposition of heavy and light fragments

To better understand how differently heavy and light fragments interact with the gas, separate simulations were carried out. So far the source routine, randomly selected one of the two fragments, either the heavy or the light, therefore the resulting energy deposition was a convolution of the individual energy depositions.

For the present study, a dedicated source routine was constructed where only one fission fragment family is propagated towards the gas per run. The results of these simulations, can be seen in fig. 2.14, where the energy deposition of heavy and light fragments are shown. For comparison the simulated energy deposition is also plotted in the case where randomly one of the fragments is propagated towards the gas. This study helped identifying that the peak seen in high energy depositions is attributed to the light fission fragments, which was an information used in reproducing the experimental amplitude spectra, as will be explained later in the text.

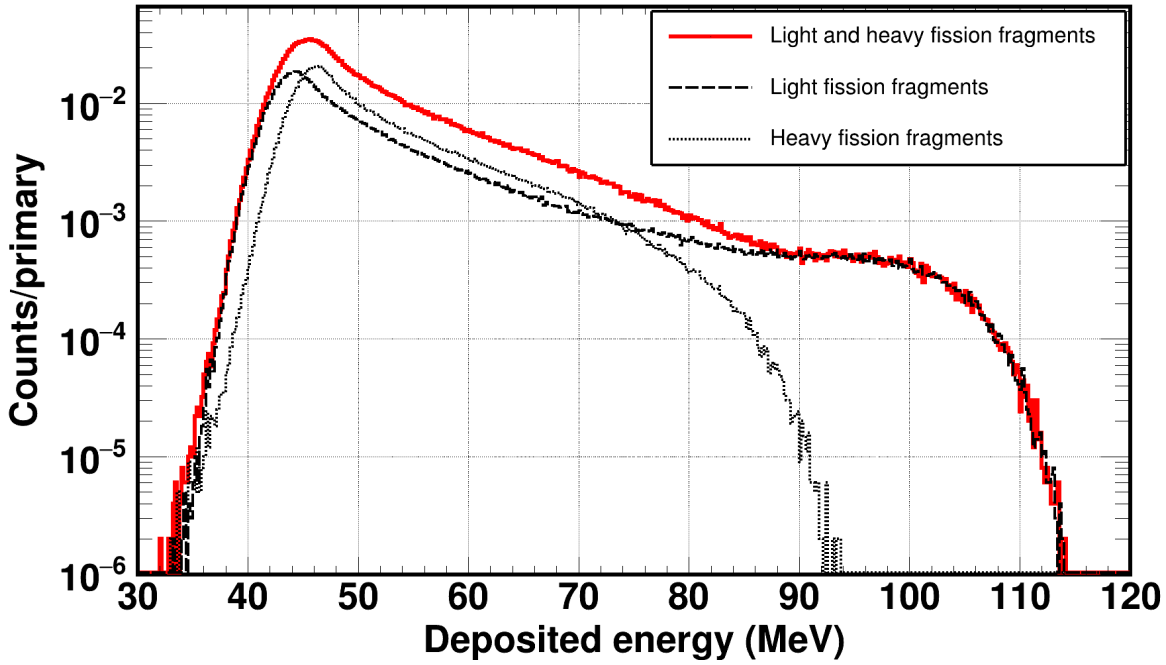

Figure 2.14: *Simulated energy deposition of heavy and light fission fragments from the $^{240}Pu(n,f)$ reaction. For comparison the energy deposition is shown in the case where randomly one of the fragments is propagated towards the gas.*

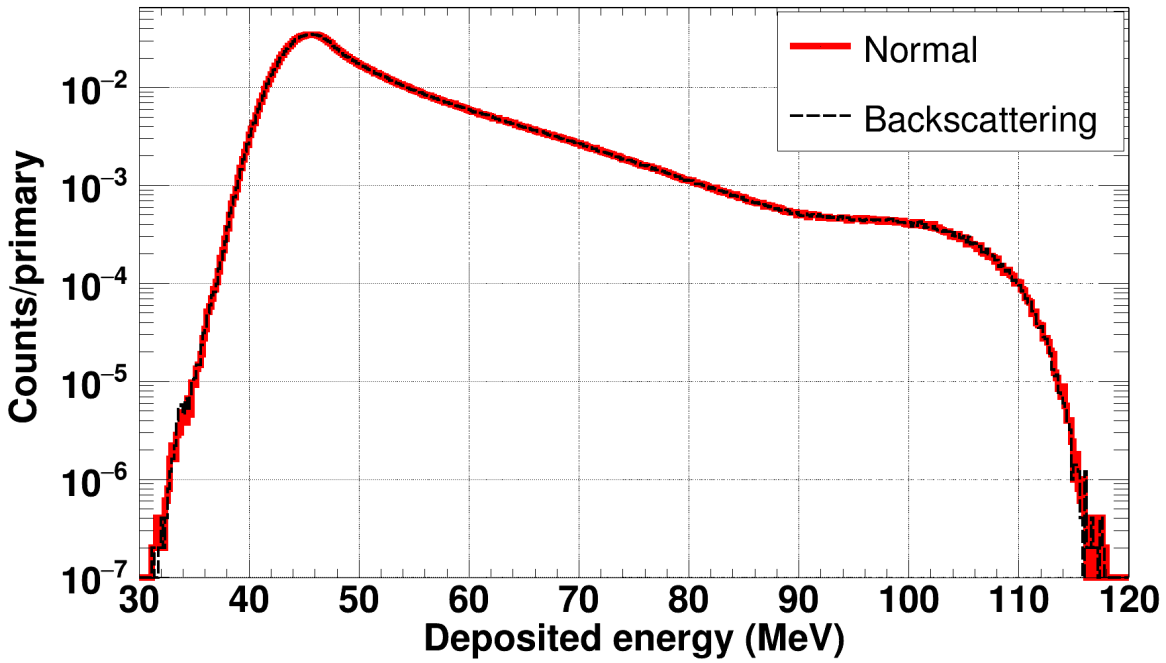

Figure 2.15: *Comparison of the simulated energy deposition of fission fragments from the $^{240}Pu(n,f)$ reaction between the enabling of backscattering within the sample volume or not. As expected since fission samples are ultra thin, the effect if negligible.*

2.2.6 On the backscattering of fission fragments

So far only one of the two fragments was emitted towards the gas at a 2π solid angle. This, although not terribly inaccurate, did not take into account the interaction of the pair fragment with the fission foil itself, which could potentially lead to its backscattering inside the gas and create additional fission signals and consequently lead to an overestimated cross-section.

To study whether there is non-negligible effect, a dedicated routine was again employed which in the present case both fragments were generated at the same point within the sample volume. The light fragment was propagated randomly at a 4π emission angle whereas the heavy was assigned an emission angle supplementary to the one of the light. The energy deposition of both fragments in the gas volume was scored. Since the samples used in the experiments and were properly modelled in the simulations, were thin foils, the effect of the backscattering compared to the "normal" treatment was negligible, as seen in fig. 2.15.

2.2.7 Effect of the angular distribution of fission fragments

Experimental evidence indicates that at incident neutron energies above the fission threshold, fragments can be produced at an angular distribution, as described in various published works such as the ones seen in [173–175]. To study the effect of the angle emission of fragments towards the gas, a dedicated source routine was developed in which the fission products were emitted at an angle z with respect to the z-axis. Several angles were simulated ranging from $0° - 90°$ and the energy deposition on the gas was stored.

The quantum efficiency of a Micromegas detector is practically 100%, if the deposited energy is greater than the average energy required to created an electron-ion pair in a gas, the so called W-value (~ 25 eV for argon). Given that, an energy deposition smaller than the W-value would regard the fission fragment as undetectable therefore for the different emission angles the fraction of particles with zero energy deposition with respect to the number of primary ones would provide an estimation on whether the angular distribution could have an effect. It was found that for emission angles up to 89° there was no particular effect on the number of particles that deposit energy below the W-value, therefore the effect of the angular distribution, if any, was considered to be negligible.

2.2.8 Effect of the chemical composition of the samples

The use of the Monte Carlo method to extract information that is impossible or difficult to do so otherwise, is by default an approximation because the exact reproduction of the experimental conditions is not possible. Such an approximation usually regards the chemical composition of materials used in the simulations.

In the case of the present simulations, the chemical composition of the actinide foils, although known from the preparation procedure, might not have been precisely modelled in the simulations. The main reason lies in the fact that humidity

could have been accumulated in the samples, thus increasing the concentration of oxygen and hydrogen. To validate whether such an occasion played an important role in the extracted information, auxiliary simulations were performed in which different chemical compositions were used.

The most extreme case scenario regards the ^{238}U samples used in the $^{237}Np(n,f)$ campaign since the 70% mass fraction of uranium in $U(OH)_6$ was the lowest one found in the samples used in both campaigns while at the same time these foils were the most massive ones. A small mass fraction indicates a higher sensitivity in deviations from the nominal composition whereas a high mass enhances energy struggling effects. In this respect, three different samples were simulated: (a) a pure uranium; (b) the nominal $U(OH)_6$ and (c) a roughly 60% higher (OH) concentrated $U(OH)_{10}$. As seen in fig. 2.16, the main difference was observed in small energy depositions where as the concentration of hydrogen and oxygen gets higher, the energy deposition distribution was shifted towards the left and the more intense struggling caused it to broaden. However, the fraction of the integrals from zero energy deposition up to the most probable value with respect to the total integral were found to be 31.0, 32.2 and 32.0% in the case of U, $U(OH)_6$ and $U(OH)_{10}$ sample compositions, respectively which implied that the exact knowledge of the chemical composition of the fission foils was not expected to play a significant role in the amplitude cut correction which, as mentioned earlier in the text, was the main motivation of the simulations.

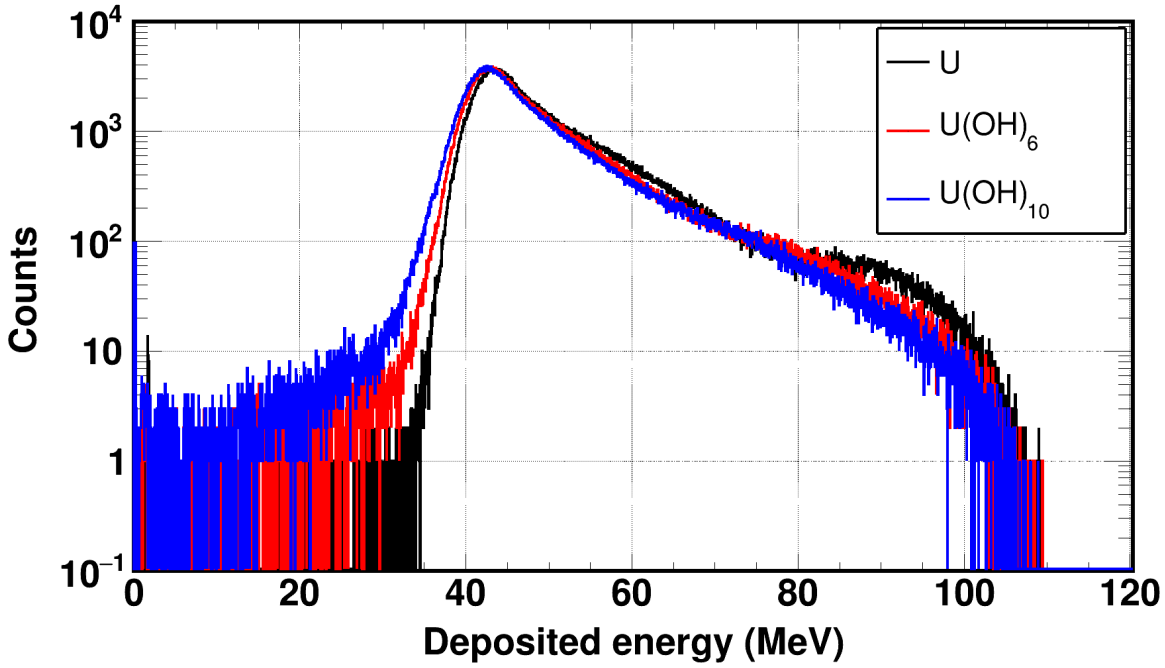

Figure 2.16: *Comparison of the simulated energy deposition of fission fragments from the $^{238}U(n,f)$ reaction for different chemical compositions regarding the ^{238}U sample from the $^{237}Np(n,f)$ campaign. Despite the different energy deposition distributions, the integrals in the three cases from zero deposition up to the most probable value were in agreement within 3%.*

2.3 Reproduction of experimental amplitude spectra

The basic scope of the preceding simulations was to quantitatively determine the fraction of fission fragments that are absorbed on the fission foil as well as to estimate the fraction of fission counts that overlap with the counts occurred from the α-particles.

While the former is easy to calculate, since the absorbed fragments are the ones that did not deposit energy in the gas, the latter requires an additional consideration: The broadening due to the detection set-up i.e. the detector and the shaping performed by the electronics.

The deconvolution of the distribution of an experimental observable, such as the amplitude of a signal which is proportional to the energy deposition of the particle that caused its formation, is an ill-posed problem and although numerical recipes do exist, a different approach was used instead. Although the response function of the detection set-up was not known, a realistic skewed Gaussian one was assumed which was used as a convolution function on the simulated energy deposition distribution.

More specifically, the simulated energy distribution was properly shifted so that the energy deposition was converted to amplitude (in ADC channels) and then each bin, which can be assumed to be a Dirac-like function at $\bar{E}$, was broadened along the deposited energy axis E with the function seen in (2.8)

$$y(E) = y_0 + \frac{A}{\sqrt{\frac{2\pi}{\left(\sigma/\sqrt{E}+a/E^2\right)}E}} \exp\left\{-\frac{\log^2 E/\bar{E}}{2\left(\sigma/\sqrt{E}+a/E^2\right)^2}\right\} \tag{2.8}$$

The parameters y_0, A, σ and a were left free and initially varied until there was a nice reproduction of the experimental amplitude spectrum by means of the least squares method. This assisted in finding the correct order of magnitude of the value of the parameters which were then fine tuned by minimising the depression of the residuals between the simulated curve and the experimental points.

An important note that has to be made is that it was empirically observed that this convolution technique was applied separately to the light and heavy fission fragment energy deposition distributions which were then summed and compared to the experimental amplitude spectra. This, although did not play a significant role in the extraction of the information the simulations were set-up for, helped in reproducing more realistically the experimental amplitude spectra.

Finally, the same procedure was applied for all actinide samples. An example of a ^{240}Pu and ^{237}Np experimental amplitude spectra along with the simulations can be seen on in fig. 2.17 where the reproduction of the experimental points is quite satisfactory.

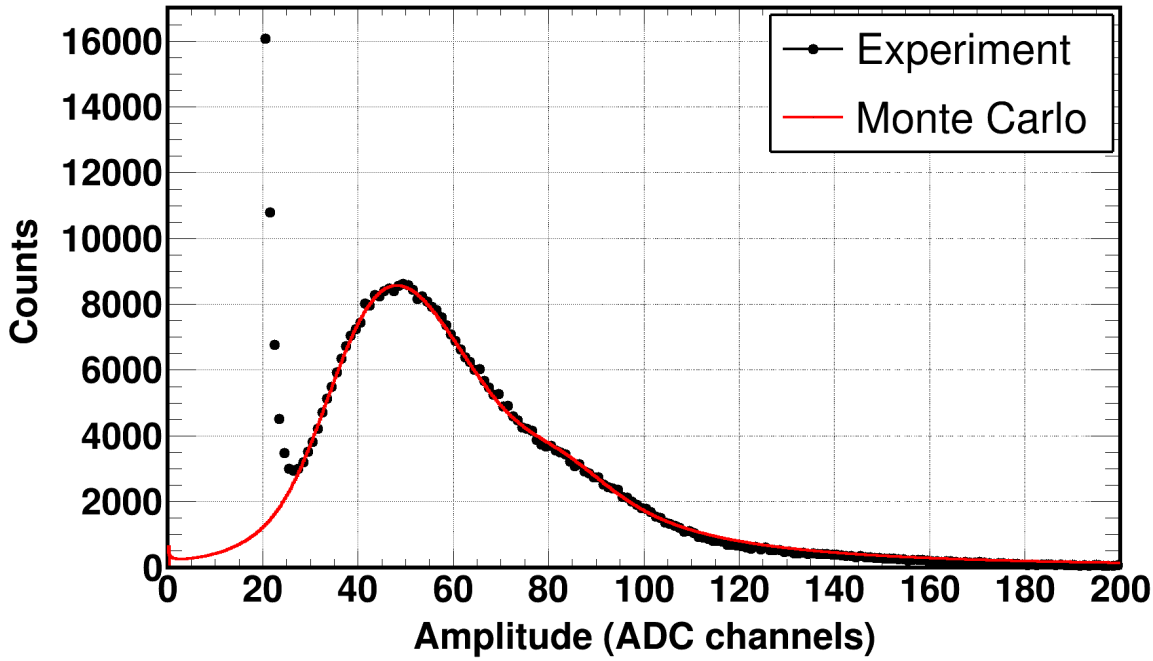

(a) ^{240}Pu - #5

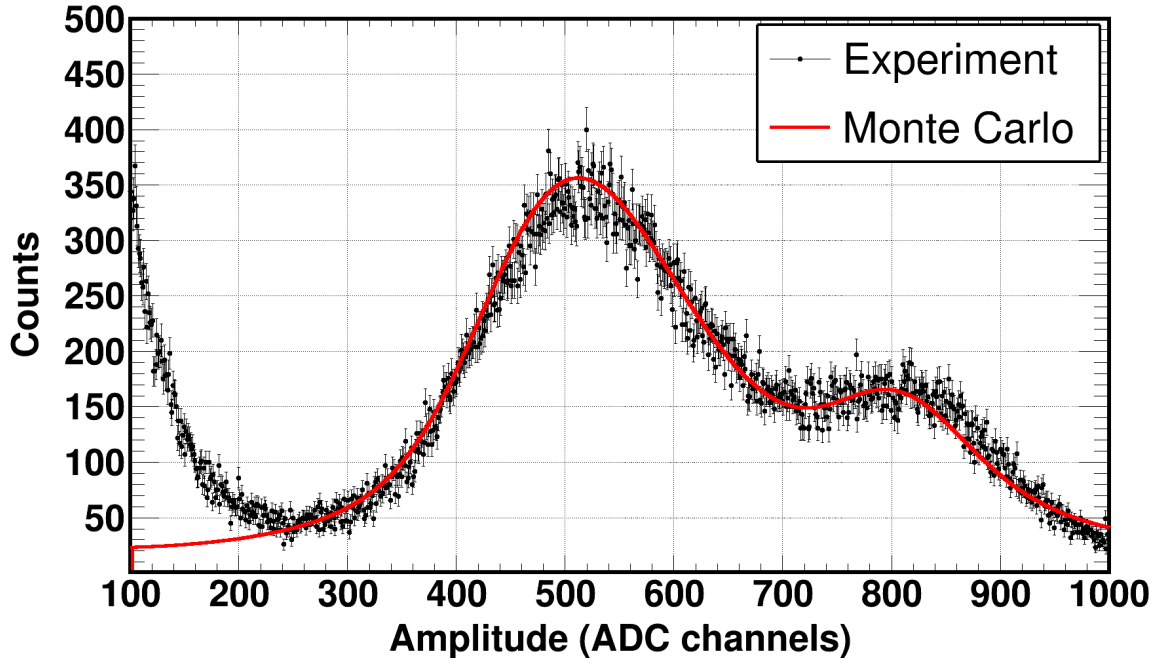

(b) ^{237}Np - #6

Figure 2.17: *Comparison between experimental and simulated amplitude spectra. The reproduction of the experimental points is quite satisfactory.*

2.4 Study of the quality of the simulated spectra

Although the reproductions of the experimental amplitude spectra shown in fig. 2.17 were quite satisfactory, additional studies were carried out not only to validate how realistic the simulated energy distributions were but to quantitatively estimate systematic effects, if any at all.

2.4.1 Reproduction of the total energy deposition distribution

The simulations did not have to take into account the intrinsic α-activity of the samples since the α and the fission fragment peaks were well separated, however the good reproduction of the fission part of the spectrum might not be convincing enough. A possible means of accommodating that, is to add an appropriately normalised beam-off spectrum, to the simulation curve and compare it to the experimental amplitude distribution. As seen in fig. 2.18, the sum between the beam-off spectrum and the simulation curve, reproduced quite nicely the experimental beam-on amplitude distribution, indicating that the performed simulations indeed realistically reproduced the recorded experimental spectra.

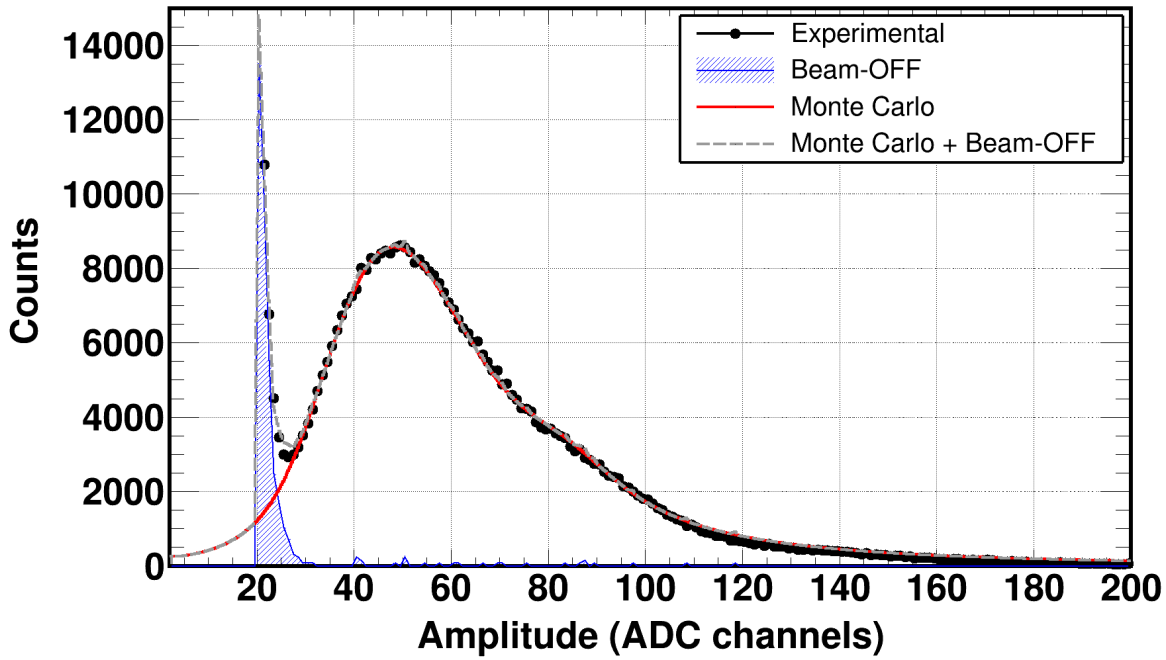

Figure 2.18: *Comparison between a ^{240}Pu amplitude spectrum and the sum of an experimental beam-off amplitude distribution and the simulated curve. The reproduction of the experimental points is quite satisfactory.*

2.4.2 Validation of the simulations on a compressed background region

In cases where the sample activity is high (i.e. the ^{240}Pu samples), the simulated spectra might deviate from reality especially in the overlap region between the α and the fission part of the spectrum. This can be addressed, to a certain extend, by reproducing the experimental amplitude spectra recorded for neutron energies in the region of the 1.05 eV fission resonance, where the high cross-section ensures a strong α-background suppression. As seen in fig. 2.19, apart from the significantly suppressed α-background, it can be claimed that still the reproduction of the experimental spectra, is quite satisfactory. It has to be noted that the parameters (y_0, σ and a seen in eq. (2.8)) used in the reproduction of the resonance amplitude spectrum were identical to the ones used to reproduce the total one. The only parameter that was changed was the scaling factor A, which makes this quality check a strong validation methodology.

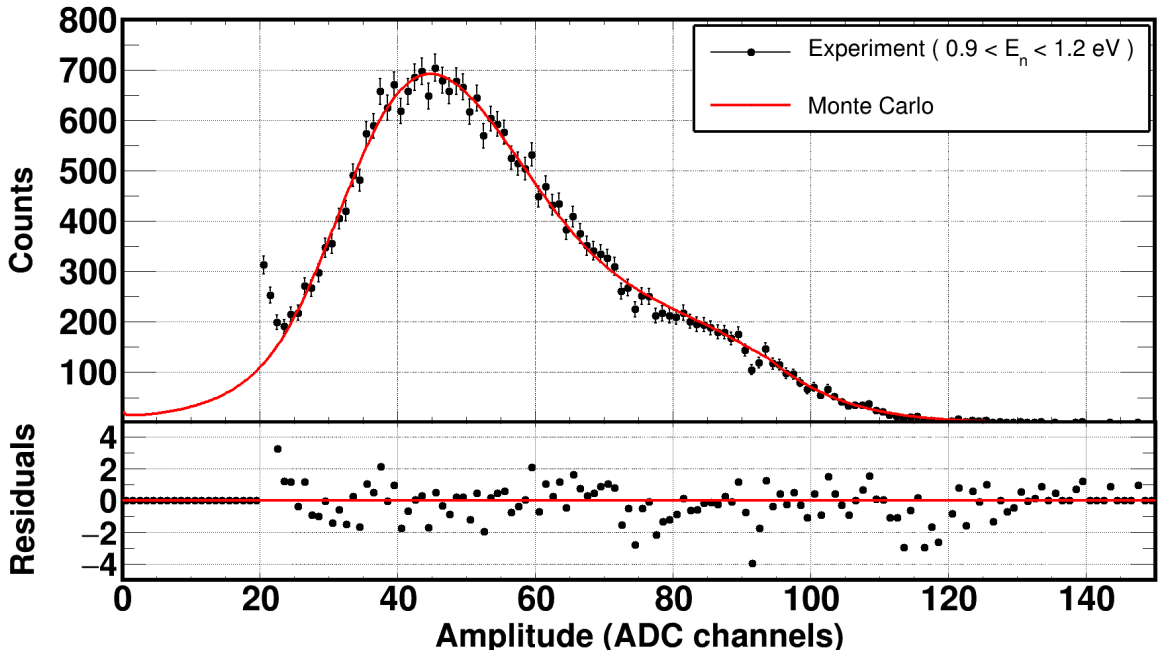

Figure 2.19: *Comparison between a ^{240}Pu amplitude spectrum (#5) recorded for incident neutron energies around the 1.05 eV fission resonance and the simulated energy deposition. The reproduction was quite satisfactory within 1.5σ on average as the residuals indicate.*

2.4.3 Estimation of systematic uncertainties

As described previously, the simulations were performed in order to provide a correction factor for the rejected fission signals due the amplitude threshold that was introduced in the analysis. The study of any systematic effects is therefore crucial, since the impact on the cross-section could be high.

A means of estimating the impact of such effects was to use a spectrum which did not contain any contribution from either α-counts or residuals from the γ-flash

subtraction and thus consisted solely of fission signals. In addition, ideally such a spectrum should be composed of low frequency signals, since pile-up effects distort the amplitude distribution, as will be explained later in the text.

Such a spectrum was available in both measurements from the ^{238}U samples in the energy region from 1.5 - 3 MeV. In this specific region, which corresponds to a time of flight window of approximately 330 ns, the probability to detect an alpha event, given an activity of the order of 10 Bq was calculated from poissonian statistics to be of the order of 10^{-6}, therefore can be considered negligible. In addition, the γ-flash subtraction in this region was well performed and no residuals were expected. Finally the counting rate was low enough (less than one pulse per bunch) to avoid pile-up effects therefore this quality check could be performed. As seen in fig. 2.20, the simulation nicely reproduced the vast majority of the amplitude spectrum. In the low amplitude region however, an inconsistency was observed, since the simulated spectrum was systematically underestimated, to a small extend. The total systematic uncertainty was estimated to be of the order of 5% on the correction factor and, as will be explained in detail later in the text, since the cross-section was calculated with reference to the $^{235}U(n,f)$ reaction, the systematic effects cancelled out.

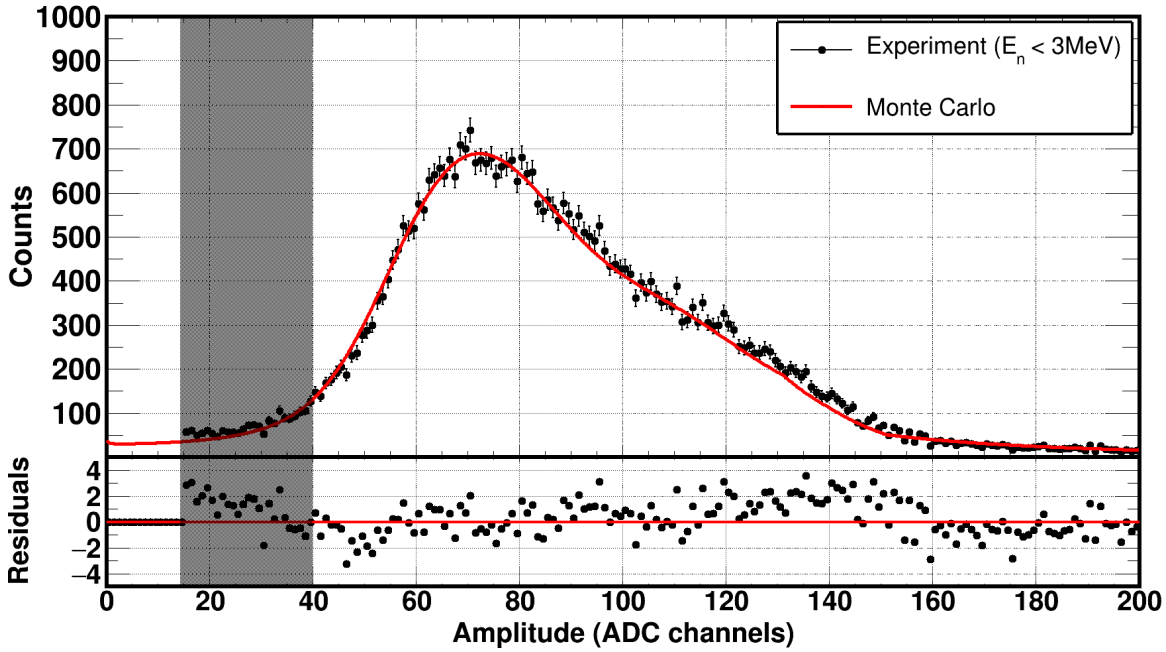

Figure 2.20: *Comparison between a ^{240}Pu amplitude spectrum (#5) recorded for incident neutron energies around the 1.05 eV fission resonance and the simulated energy deposition. The reproduction was quite satisfactory within 1.5σ on average as the residuals indicate.*

CHAPTER 3

Signal treatment and data selection

Signals recorded from the micromesh of each detector-sample module were fed to the acquisition system and then stored in data buffers for later off-line processing and analysis. Briefly, raw data were processed using pulse shape analysis algorithms and then stored in so-called list-mode files which contained basic attributes of each identified signal such as its amplitude, rise-time, time of flight etc. Further data quality checks and selection were performed prior to the estimation of correction factors, in order to accurately calculate the reaction cross-section for each isotope under study.

3.1 Signal handling

Data at n_TOF is processed off-line using the generic n_TOF pulse shape analysis routine [176] that was recently developed. The pulse recognition is based on the first derivative calculation in each movie, as seen in fig. 3.1 along with other user defined elimination criteria referred to as user input parameters (i.e. amplitude, minimum and maximum width, minimum and maximum area to amplitude ratio etc.). It has to be noted that a detailed description of the processing routines is not of relevance in this text, therefore only a basic description will be provided.

3.1.1 From raw waveforms to clean signals

To begin with, the first derivative (fig. 3.1, middle panel) of the raw movie (fig. 3.1, top panel) is calculated as the difference between a user defined set of points N, which is referred to as the step-size. Then the movie's RMS is calculated and a value of $\pm 3.5\times$ RMS is used as the pre-defined derivative thresholds (fig. 3.1, mid-

dle panel, green dashed lines), but there is a possibility to be adjusted by the user. A consecutive quadruple derivative threshold, where the first one occurs at negative values and the fourth in positive ones, indicates a signal candidate and once all eliminating conditions are met the candidate is considered as a real event, whose beginning and ending boundaries are estimated to be at the position where the first and fourth threshold crossings occur, respectively (fig. 3.1, shadowed area).

Once the pulse is identified, the baseline calculation follows. Close to the γ-flash region, which is specified by the user, different options for an adaptive baseline are available, while away from it, a constant one is assumed. The constant baseline (fig. 3.1, top panel, magenta dashed line) is calculated as the average of the raw signal points between the identified pulses, making the calculation unaffected by the actual pulses.

The final step is to calculate the clean signal (fig. 3.1, bottom panel) by subtracting the baseline and applying the eliminating conditions. The final waveform reconstruction (fig. 3.1, bottom panel, red line) takes also into account a user defined amplitude threshold (fig. 3.1, bottom panel, blue dashed line) as an eliminating condition to discriminate real events from noise.

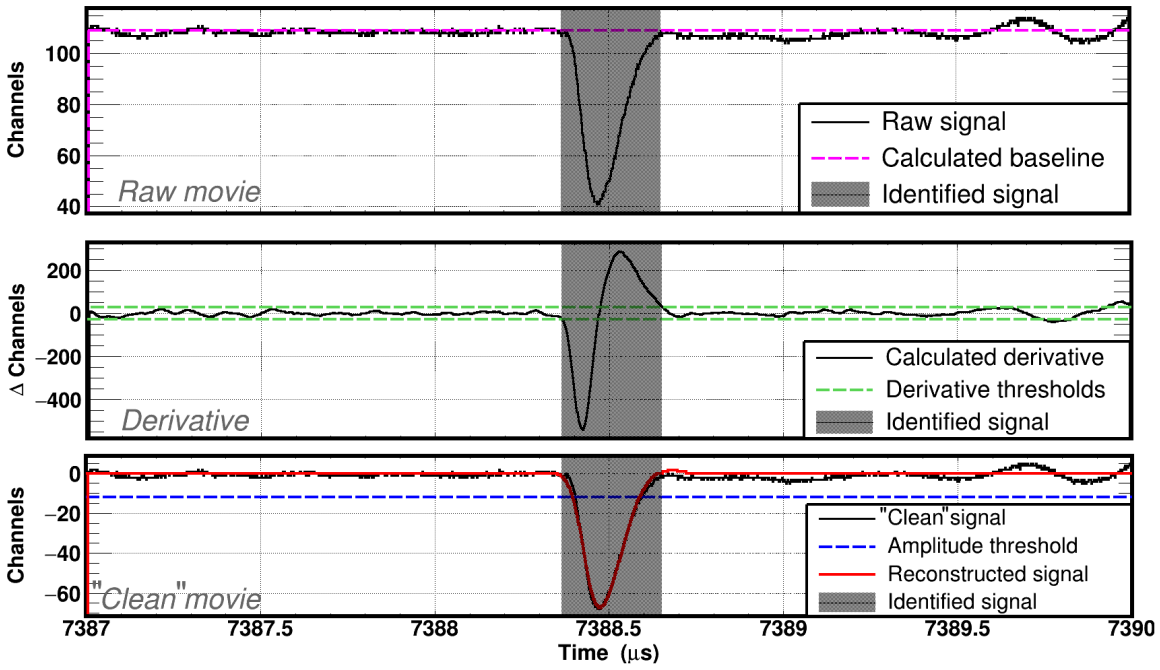

Figure 3.1: *Signal recognition from the raw input (top panel) is based on the calculation of the first derivative (middle panel). The "clean" signal (bottom panel) is then calculated after the subtraction of the baseline. This sample signal regards a fission event from a ^{240}Pu sample.*

3.1.2 Pulse shape analysis

The n_TOF pulse recognition framework provides the possibility to perform numerical pulse shape fitting in each identified signal given a user specified pulse shape. This option is considered to be mandatory for high counting rates, where the signal overlapping is frequent, since the amplitude and timing information can

be extracted much more reliably as can be seen in fig. 3.2. More specifically, two identical signals are shown with a time difference short enough to cause pile-up. It is evident that the amplitude of each signal would be overestimated unless a pulse shape fitting is used. The same is valid for the reconstruction of the peak time of each signal, where the preceding one would be considered to arrive later than in reality while the succeeding one, earlier. To avoid such effects, in both experimental campaigns average pulse shapes were calculated off-line using real signals recorded from the detectors to be used as inputs in the reconstruction routine using the pulse shape fitting option.

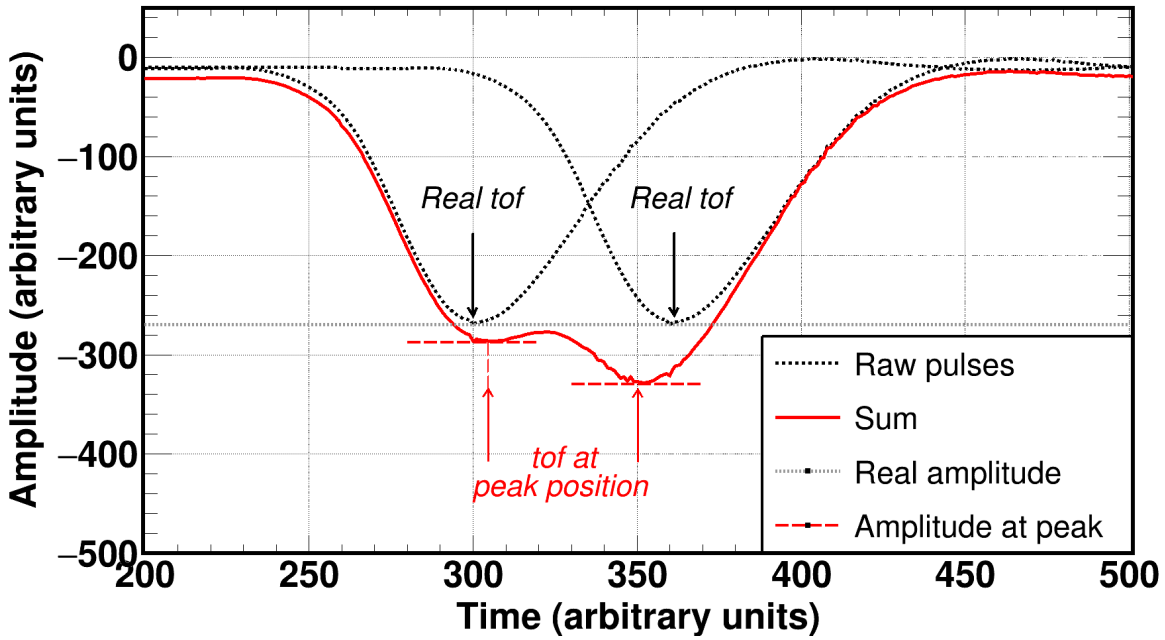

Figure 3.2: *Example case of signal overlapping from two identical pulses. The amplitude and the time of flight would be inadequately reconstructed if pulse shape fitting was not introduced.*

Prior to the calculation of the pulse shapes that were provided to the reconstruction routine, the number of different signals present needed to be estimated. The reconstruction routine provided the possibility to identify signals based on the detection of the maximum amplitude. This first approach, although not optimal for high counting rate cases, can provide a good estimation of the number of individual recorded pulse shapes by correlating the amplitude and the area of the identified signals, as can be seen in fig. 3.3 where at least two clusters are present.

These clusters, as will be discussed shortly, correspond to forward and large angle emissions. In addition the cluster seen for constant amplitudes around 230 ADC channels and areas in the $2.8-3.5\times10^4$ range, is related to electric discharges that occurred during the measurement. A more detailed explanation on the electric discharges and the effect on the data, will be provided later in the text.

To calculate the average signals to be used in the pulse shape analysis, raw movies from fission events were stored and a constant baseline was calculated left and right of the signal's edges. Each fission signal was normalised in amplitude

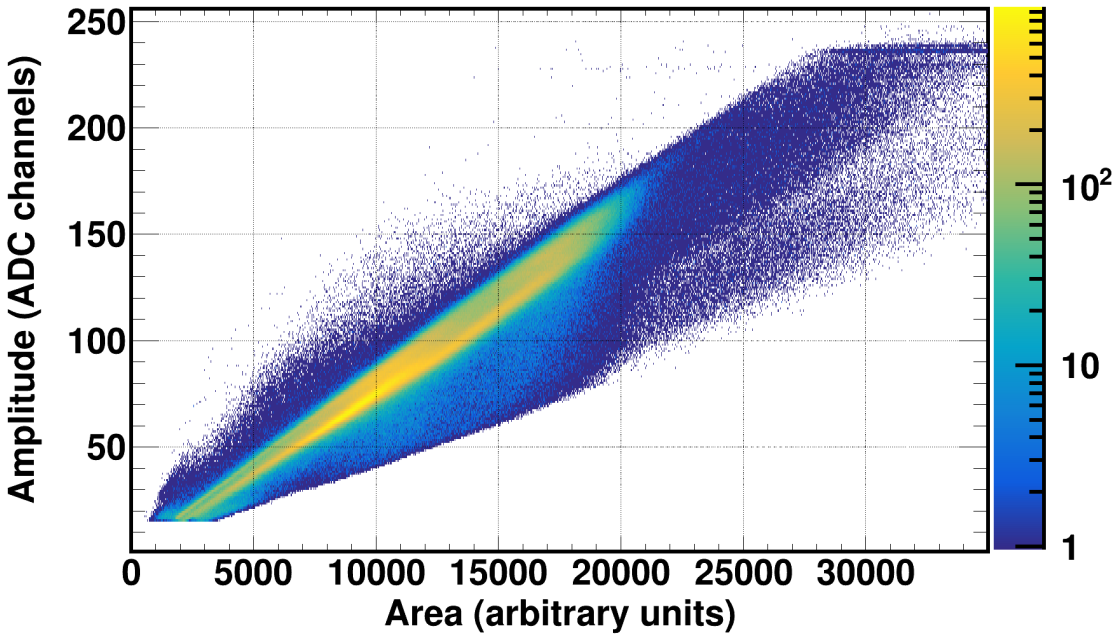

Figure 3.3: *Distribution of the amplitude and area of the identified signals for the ^{235}U sample from the $^{240}Pu(n,f)$ campaign based on the recognition of the maximum amplitude, an option which was provided by the reconstruction routine. At least two clusters are clearly evident, which is an estimation of the number of individual pulse shapes that were fed in the reconstruction routine using the pulse shape fitting option.*

to the value of the maximum ADC channel (256 in the case of the $^{240}Pu(n,f)$ experiment and 4094 in the case of the $^{237}Np(n,f)$ one), aligned in time so that the peak position rests at the same point in time and stacked one on top of each other to form a two-dimensional distribution between time and amplitude as seen in fig. 3.4. The z-axis values represent the relative frequency of each (time, amplitude) combination and it is evident that two main families are present which correspond to forward and large angle emission respectively, as discussed in subsection 1.4.1.

The pulses in between correspond to emission angles in the range of $\sim 85° - 89°$ which reflect particle trajectories that escape the active gas volume. The 85° angle limit was calculated given the geometrical characteristics of the sample-detector assembly and corresponds to the emission from the far edge of the sample towards the opposite edge of the micromesh.

The pulse shapes used as inputs in the reconstruction routine in the $^{240}Pu(n,f)$ case can be seen in fig. 3.4 as red individual signals and were calculated by averaging the two-dimensional distribution, while focusing on each separate region by applying appropriate thresholds in the z-axis. The same procedure was followed in the case of the ^{237}Np signals and similar pulse shapes were calculated.

Finally, fig. 3.5 shows a typical case recorded from a ^{237}Np sample where the pulse shape analysis routine, given a set of properly established user input parameters was able to successfully reconstruct a quintuple pile-up event. It has to be mentioned that in addition to the fission detectors, both proton (PKUP) and neutron (SiMon2) monitors were analysed, however pulse recognition in these cases is straightforward, therefore there is no need for a detailed discussion in this respect.

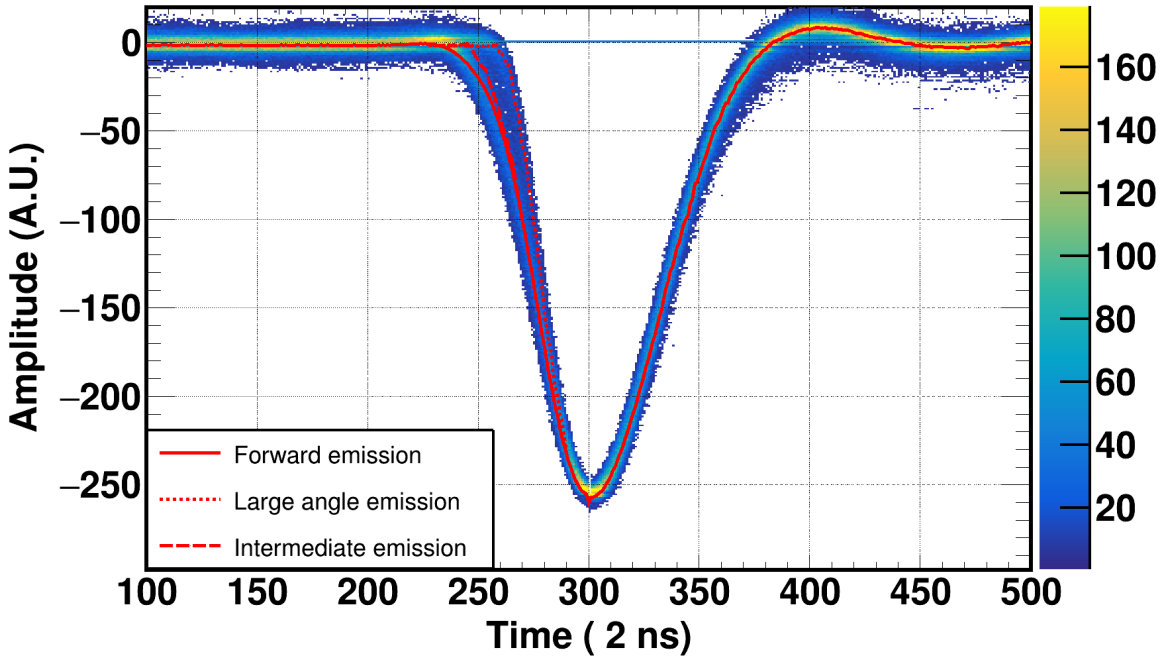

Figure 3.4: *Stack of amplitude normalised and time aligned fission signals from the $^{240}Pu(n,f)$ measurement. Two main pulse shape families are visible, which correspond to forward and large angle emissions. The red pulses correspond to the three pulse shapes used for the numerical fitting.*

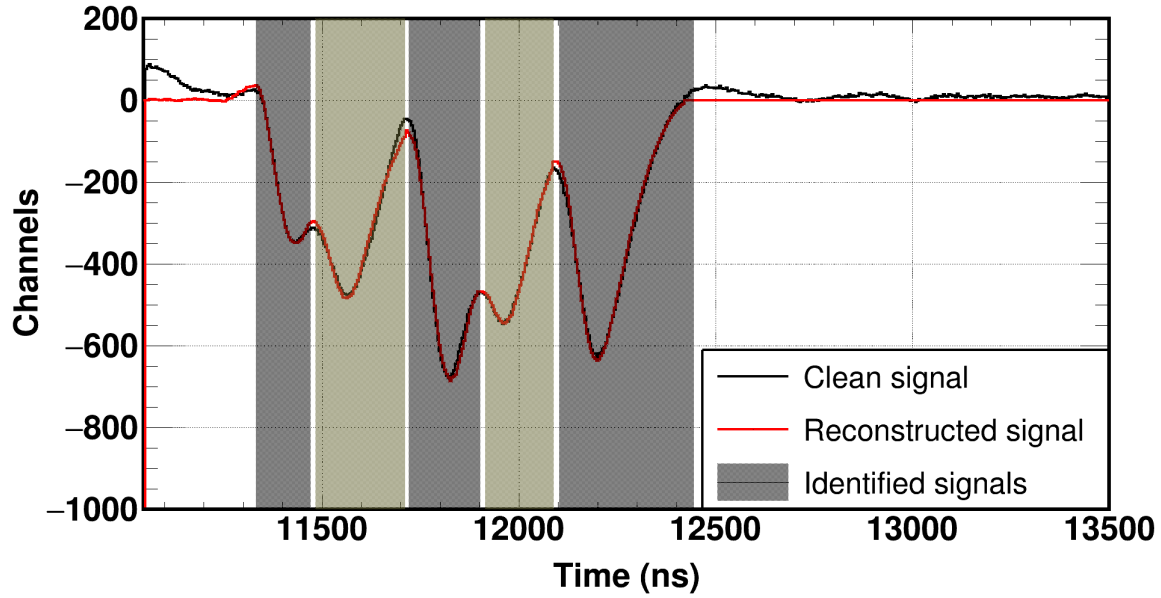

Figure 3.5: *Case of a successful reconstruction of a quintuple event from a ^{237}Np sample. The establishment of user input parameters along with the proper estimation of average pulse shapes provides a satisfactory signal reconstruction.*

To cross-check that the pulse shape fitting procedure was properly applied, apart from checking the χ^2 of the fits for inconsistencies and examining the signal reconstruction in several movies, amplitude spectra that were reconstructed using pulse shape fitting were put in comparison to the corresponding ones made by registering the highest point of the signal as its amplitude. It goes without saying, that this comparison had to be made when certain circumstances were met: (a) a low counting rate had to be ensured in order to avoid pile-up and so that the latter amplitude reconstruction could be trusted and (b) a handful of pulse shapes had to be provided in order to study the behavior of the reconstruction routine when deciding on which was the most proper pulse shape to be fitted in each occasion.

In view of the above, three pulse shapes were provided to fit recorded signals from the ^{235}U sample in the $^{237}Np(n,f)$ campaign. Despite the high cross-section of the ^{235}U (n,f) reaction, the exclusion of high intensity bunches in addition to the rejection of signals in the thermal and MeV regions ensured a pile-up free counting rate, yet sufficient enough to reconstruct the amplitude spectra with adequate statistics.

Firstly the amplitude spectra were reconstructed separately for the corresponding pulse shape that was chosen by the reconstruction routine, as seen in fig. 3.6. More specifically, the routine reported the identity number of the pulse shape that was used in each identified signal therefore these amplitude spectra were reconstructed by gating on this identity. Apart from the best pulse shape used to describe each raw signal, the amplitude of its highest point was also reported, therefore a second family of amplitude spectra were reconstructed similarly to what would be recorded by a typical ADC and were compared to the ones seen in fig. 3.35. The agreement seen in fig. 3.7 is quite satisfactory and indicates that the pulse shape selection is properly done therefore pulse shape fitting was chosen for the signal reconstruction during the analysis of data acquired in both experimental campaigns.

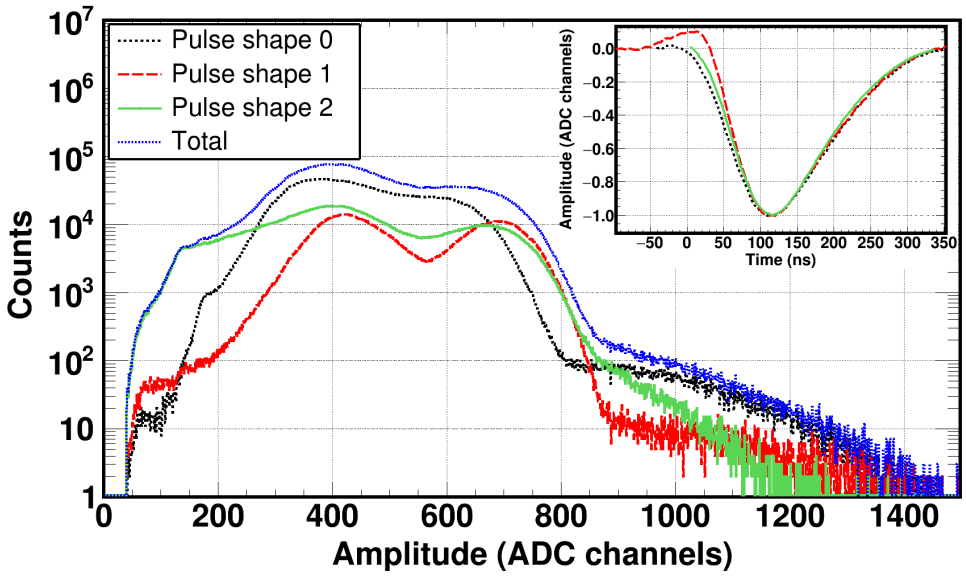

Figure 3.6: *Amplitude spectra reconstructed for the ^{235}U sample in the $^{237}Np(n,f)$ experimental campaign. Each spectrum was reconstructed by gating on the corresponding pulse shape that was used by the routine in each identified signal. The three pulse shapes used in this study are illustrated in the inset.*

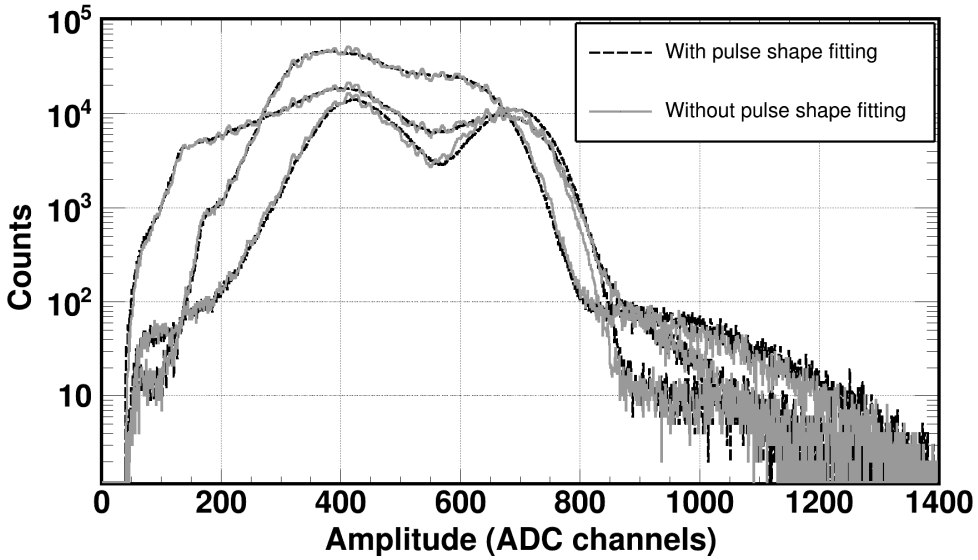

Figure 3.7: *Comparison between amplitude spectra reconstructed by the application of pulse shape fitting (dashed black lines) and highest point in each identified signal. The agreement between the two methods is quite satisfactory.*

3.1.3 Treatment of the γ-flash

A similar procedure was adopted for the γ-flash. The main difference lies on the fact that the rebound that follows the γ-flash was found to be independent of the actual signal's amplitude, as can be seen in fig. 3.8, therefore the stacked signals were not normalised in amplitude. This helps to calculate a well-defined estimate of the average of the constant rebound in order to individually subtract it from each pulse. This procedure results in resolving signals that sit either on the falling edge of the γ-flash or on the oscillatory rebound and thus extending the limit of the highest analysable neutron energy.

3.1.3.1 Calculation of the average γ-flash

To estimate the average three methods were used: (a) the direct average, (b) the most frequent value and (c) the average after rejecting signals that distort the rebound. Since the fission rate is maximum for small time of flights (or similarly high neutron energies), due to the high (n, f) cross-section and the peak of the neutron flux, an increased number of signals was observed, as can be seen in fig. 3.8. The calculation of a direct average (fig. 3.8, green line) in this case would lead to an underestimation of the baseline and a subsequent loss of low amplitude signals after the subtraction from the raw movie. Instead, the next reasonable step is to calculate the most frequent value, however, as seen in fig. 3.9, it is not smooth enough to adequately describe the rebound. The application of a threshold in the z-axis, alternatively, prior to the calculation of the average, can provide a proper reconstruction of the oscillatory rebound and this approach was used to estimate average γ-flash shapes in both experimental campaigns for each detector individually.

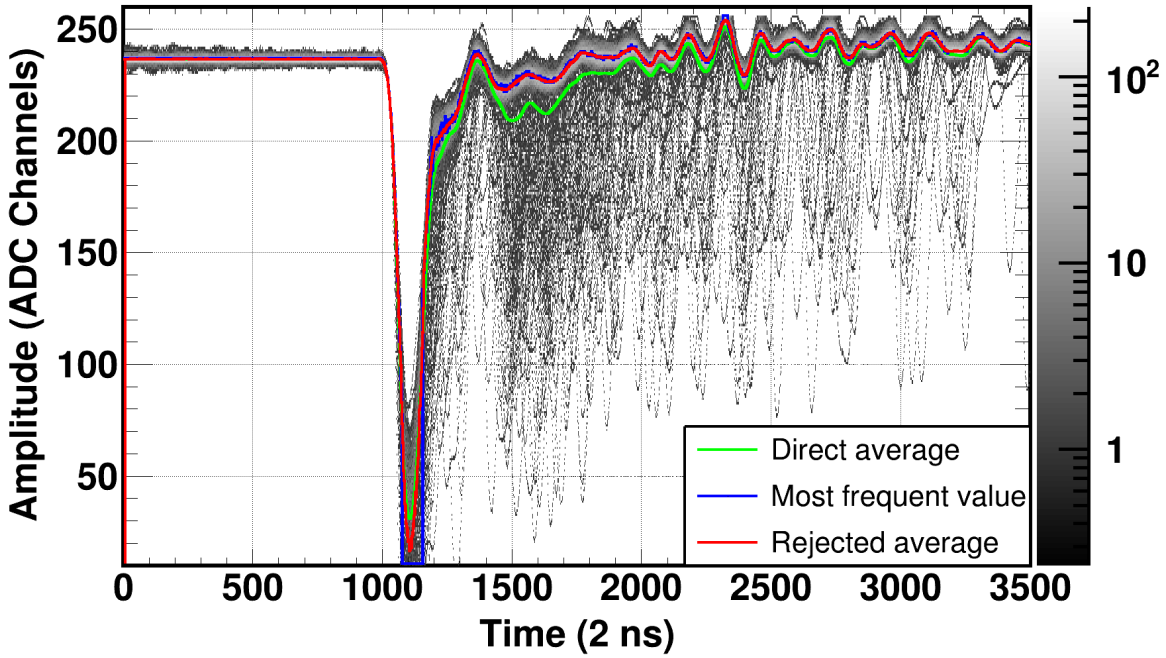

Figure 3.8: *Stack of γ-flash signals for a ^{240}Pu sample. It is evident that the amplitude of the oscillatory rebound is independent of the γ-flash amplitude. The average shapes that were calculated with different methods are also shown (see text for details).*

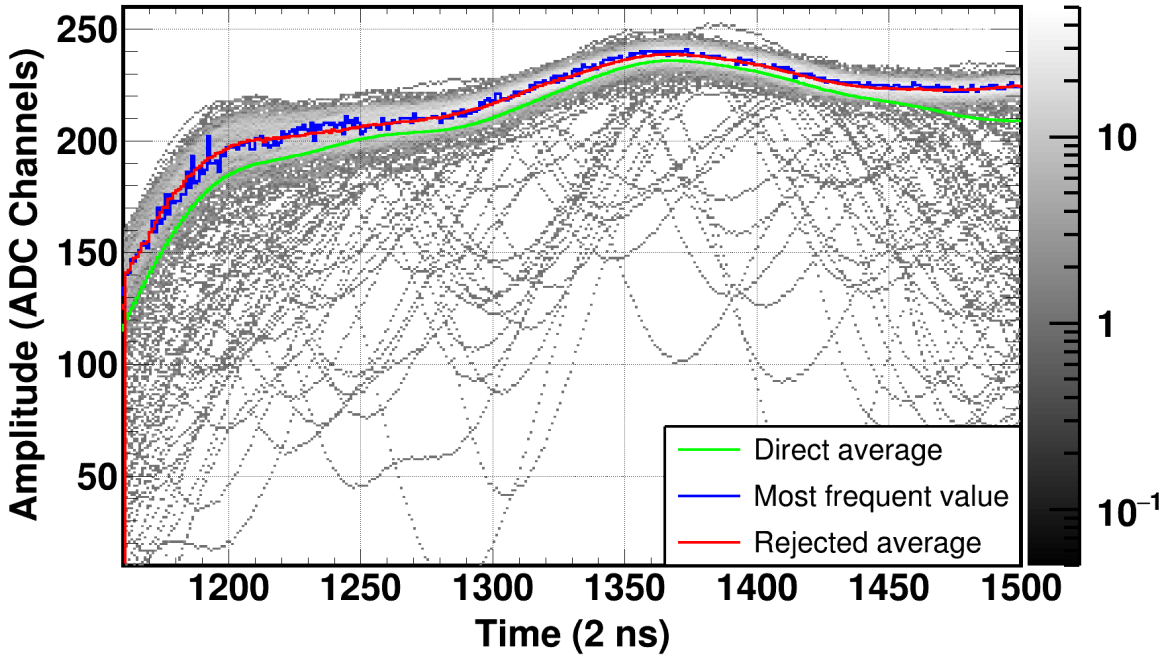

Figure 3.9: *Zoom of stacked ^{240}Pu γ-flash signals. The direct average underestimates the baseline, while the most frequent value is not smooth enough to properly describe the rebound. The calculation of the average after the application of a threshold in z-axis is adequate to reconstruct the constant rebound that follows the γ-flash .*

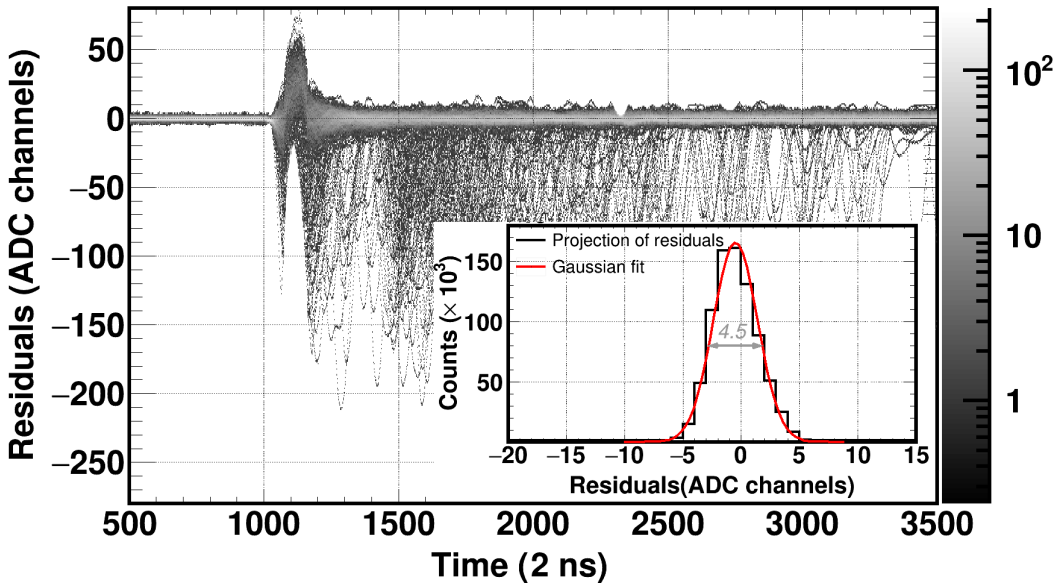

Figure 3.10: *Residuals from the γ-flash subtraction fluctuate around the zero amplitude channel. For times* > 2560 *ns which correspond to a neutron energy of* 5 *MeV, the residuals fluctuate around zero amplitudes with a dispersion of* 4.5 *ADC channels.*

To estimate the limitation and the accuracy of the followed procedure, the estimated average γ-flash shape was subtracted from each individual movie. The residuals from the subtraction, illustrated in fig. 3.10, show that the estimation of the mean γ-flash was adequate since they fluctuate around zero. In addition, the residuals fluctuate with large dispersion (> ±10 ADC channels) between the 1025 and 1280 × 2 ns range, which corresponds to a time of flight of the order of 650 ns and a neutron energy of approximately 5 MeV. This can be defined as the upper limit of the neutron energy that can be safely reconstructed given the aforementioned γ-flash treatment.

The FWHM of 4.5 ADC channels can be considered to have a systematic effect in the rejection of signals with respect to the amplitude threshold introduced in the analysis, as illustrated in fig. 3.11. More specifically, signals with amplitudes near the amplitude threshold could be rejected if the baseline is underestimated (fig. 3.11, green baseline). On the contrary, overestimated baselines only lead to an amplitude overestimation and consequently the event is not lost (fig. 3.11, blue baseline). As a result, losses in the former cases are negligible, as will be discussed later, while in the latter are zero therefore the γ-flash subtraction procedure is considered accurate and does not add systematic uncertainties up to at least an incident neutron energy of 5 MeV.

Finally, the estimated average γ-flash shapes for every detector were fed in the reconstruction routine and were individually subtracted on a bunch-by-bunch basis. A user defined portion of the raw movie was initially fitted and then subtracted from the estimated shapes while the rest was bluntly subtracted in order to keep the rebound intact. An example of a γ-flash subtraction where a fission event from the ^{235}U sample in the $^{237}Np(n,f)$ campaign sits on the falling edge of the γ-flash and is successfully recognised can be seen in fig. 3.12, along with other fission events that occurred at later times.

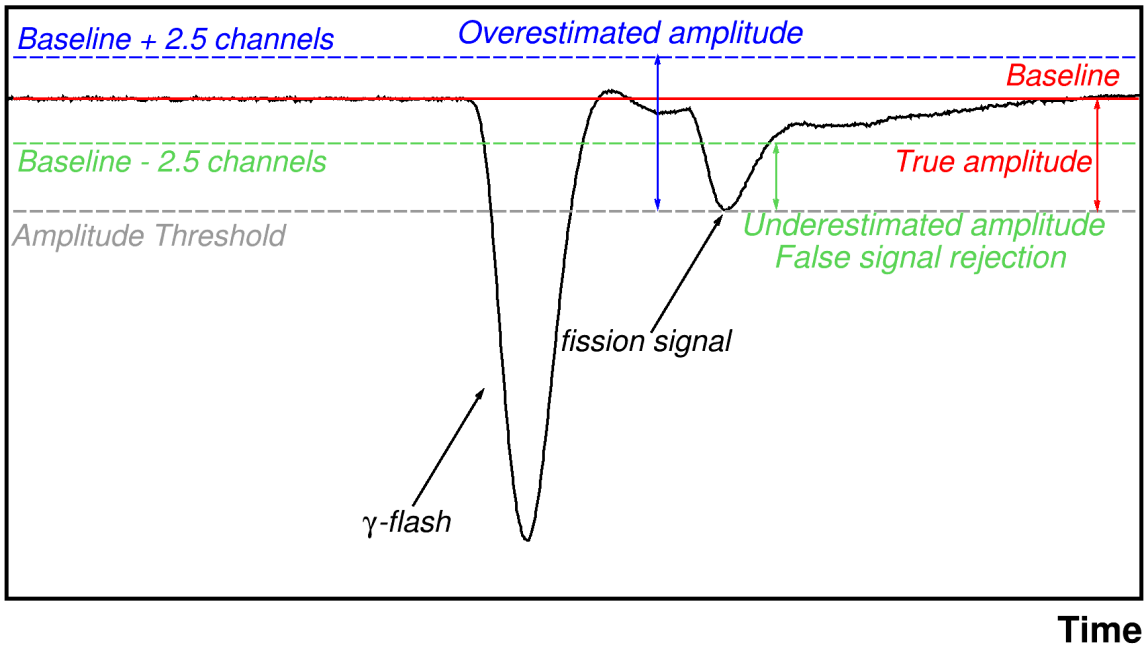

Figure 3.11: *Example case of an over/under-estimation of the baseline. The effect in the case of the underestimation is negligible, while the overestimation cannot lead to false signal rejection with respect to the amplitude threshold.*

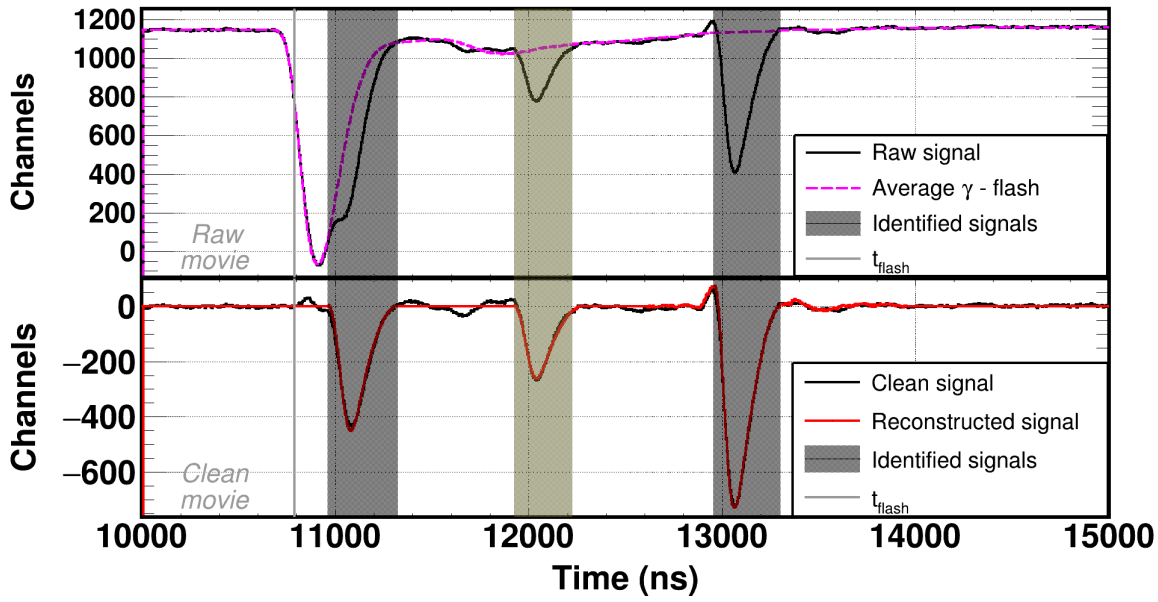

Figure 3.12: *Example case of a γ-flash subtraction which helps to discriminate and successfully reconstruct a fission signal that sits on the falling edge of the γ-flash . This case was recorded at the ^{235}U sample from the $^{237}Np(n,f)$ experimental campaign.*

3.1.3.2 Optimisation of the γ-flash rebounds

The rebounds that follow the γ-flash seen in fig. 3.8 could potentially lead to losses of signals with small amplitudes. Although in the $^{240}Pu(n,f)$ measurement the effect was negligible, since the detectors operated with such gains that the signals could be easily discriminated, a study has been made in order to eliminate the oscillatory rebound for future measurements.

The frequency spectrum of the average γ-flash for a ^{240}Pu sample from the $^{240}Pu(n,f)$ campaign, shown in fig. 3.13, has been calculated by means of the Discrete Fourier Transform seen in eq. 3.1, using the FFTW 3.3.8 library [177]. Apart from the white noise which is dominant for bandwidths above 100 MHz, discrete frequencies were observed.

$$x_n = \frac{1}{N}\sum_{k=0}^{N-1} X_k e^{-j2\pi kn/N} \tag{3.1}$$

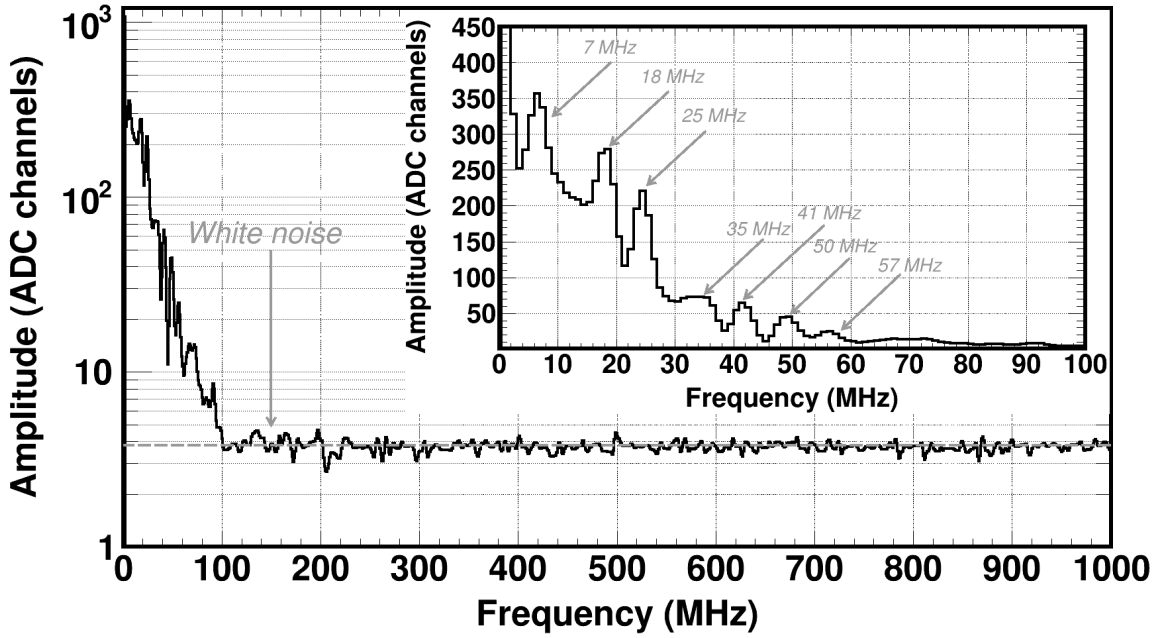

Figure 3.13: *Fourier transform of the average γ-flash of a ^{240}Pu sample from the $^{240}Pu(n,f)$ campaign. Frequencies that correspond to the fundamental frequencies of different modes of a standing wave in EAR2. The inset shows the frequency spectrum up to 100 MHz.*

In particular, the peaks seen in the frequency spectrum above 20 MHz, correspond to the oscillations that succeed the γ-flash and are attributed to the standing waves trapped inside the bunker in EAR2. Treating the experimental hall as a cavity with a length [1] $L = 6.57$ m, a width $W = 6.56$ m and a height $H = 5.85$ m, and the γ-flash as a wave propagating through an aperture with the speed of light c inside the bunker, the fundamental frequencies F_{mnp} of the propagation modes (mnp) can

[1] The length is considered along the propagation of the γ-flash from the floor to the ceiling of EAR2.

be calculated from the Rayleigh-Jeans formula, seen in eq. 3.2. It is evident that a few characteristic fundamental frequencies were seen in the frequency spectrum and correspond to different modes of propagation: $F_{001} = 25.6$, $F_{011} = 34.4$, $F_{111} = 41.3$, $F_{002} = 51.3$, $F_{211} = 57.1$ MHz. In addition, the peak seen at 7 MHz corresponds to the emission frequency of a radio antenna installed in close proximity to EAR2, from the amateur radio club at CERN, while the 18 MHz peak might be attributed to the PS booster whose operating bandwidth covers frequencies from 0.6−18 MHz, however, this has not been confirmed.

$$F_{mnp} = \frac{c}{2}\sqrt{\left(\frac{m}{L}\right)^2 + \left(\frac{n}{W}\right)^2 + \left(\frac{p}{H}\right)^2} \tag{3.2}$$

To eliminate the distortion of the γ-flash rebound which is present due to the pick-up of radio frequencies, a proper shielding of the read-out electronics is necessary. In this respect, the pre-amplifier modules have been shielded using a thick aluminium case, while the single-clone read-out cables, housed inside the fission chamber, have been replaced by co-axial ones, as described in subsection 1.4.1. The effect of these changes, can be seen in the signals recorded during the $^{237}Np(n,f)$ experiment, where the oscillatory rebound was no more present in the average γ-flash , as seen in fig. 3.14.

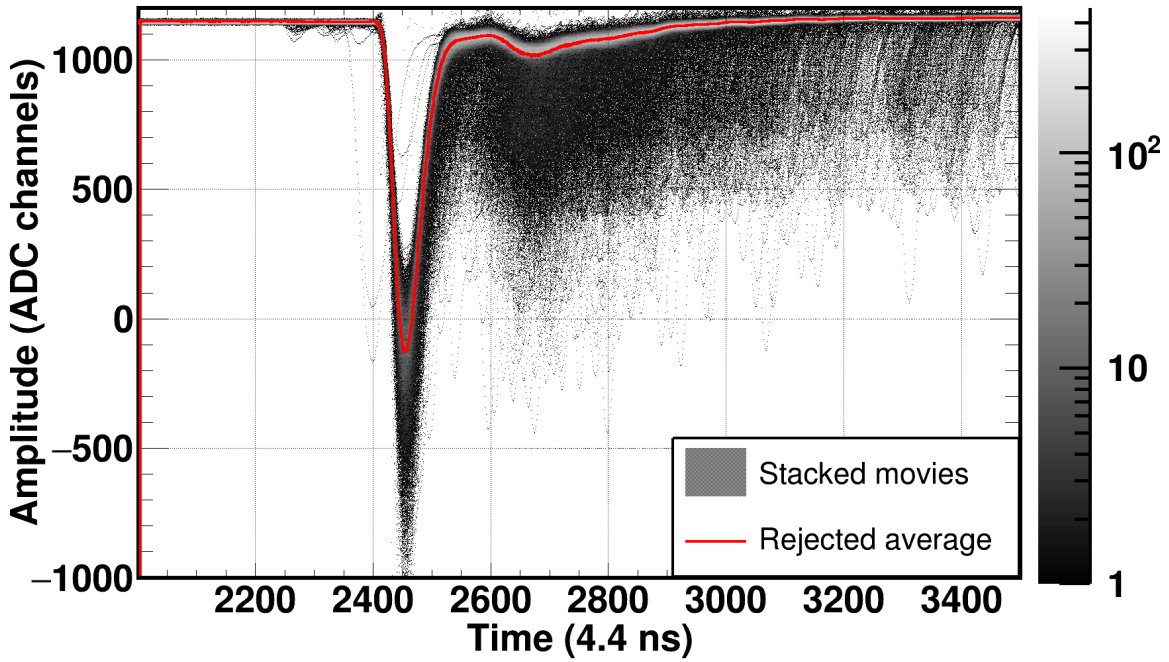

Figure 3.14: *Stack of γ-flash signals for the ^{235}U sample from the $^{237}Np(n,f)$ campaign, along with the estimated average. It is evident that the oscillatory rebound is no longer present in comparison to the ^{240}Pu γ-flash signals.*

3.2 Data quality checks and applied gates

Prior to the calculation of the cross-section and the corresponding correction factors, the parameters used by the reconstruction routine have been established in order to sufficiently identify fission signals and reject noise. The data produced by the routine after the application of γ-flash subtraction and pulse shape fitting has been checked in terms of false signal recognition that would contribute to fission counts and overall quality in general terms. Additional checks have been performed to address the radiation damage induced in the detectors by the high intrinsic activity of the same fission foils in a similar measurement in EAR1 a few years ago.

3.2.1 Effects of intrinsic activity on the fission detectors

An important check that had to be made prior to data analysis, concerned the effect of the intrinsic activity on the detectors which, if severe, would make the data analysis pointless. To investigate whether the detectors suffered any radiation damage which affects their stability, amplitude spectra without the neutron beam, so called beam-off, have been reconstructed. Any possible radiation damage would be indicated as a gain shift in these spectra, therefore the worst case scenario has been studied: beam-off runs from the very beginning and ending of the $^{240}Pu(n,f)$ campaign have been compared concerning the most massive plutonium target. In fig. 3.15 it is evident that the highest energy deposition of α-particles corresponds to channel 35 both in the beginning and the ending of the experiment which implies that the intrinsic activity did not cause any critical damage to the detectors. It has to be noted that both spectra have been normalised to the total number of triggers acquired. The same check has also been performed for all detectors in both campaigns, none of which seemed to have suffered from serious radiation damage, since gain shifts were not observed.

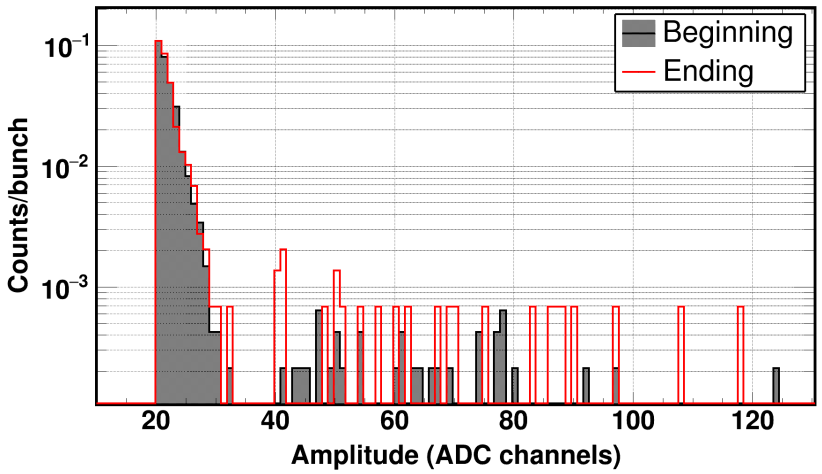

Figure 3.15: *Trigger normalised beam-off spectra as reconstructed from data taken at the very beginning and ending of the $^{240}Pu(n,f)$ campaign. The tails of the α-particles remain at the same position indicating that radiation damage induced in the detectors was not visible. The counts observed in higher amplitudes are attributed to spontaneous fission events.*

3.2.2 Stability of the beam monitors

An essential check which ought to be made concerns the stability of beam monitors; both the proton (PKUP and BCT) and neutron (SiMon2) ones. In this respect PKUP and SiMon2 were analysed using the pulse shape analysis routine framework and the corresponding reconstruction parameters have been established, while for BCT the only information that was available concerned the proton charge and was provided by the PS.

3.2.2.1 Proton beam monitors

Both proton beam monitors are expected to be stable throughout the measurements and be linearly related in terms of the total charge injected from the PS to the spallation target and the total charge induced from the proton beam to the PKUP. The former charge, referred to as BCT value or pulse intensity, was provided from the PS and was stored in the data files while the latter was calculated as the area of the reconstructed PKUP signals.

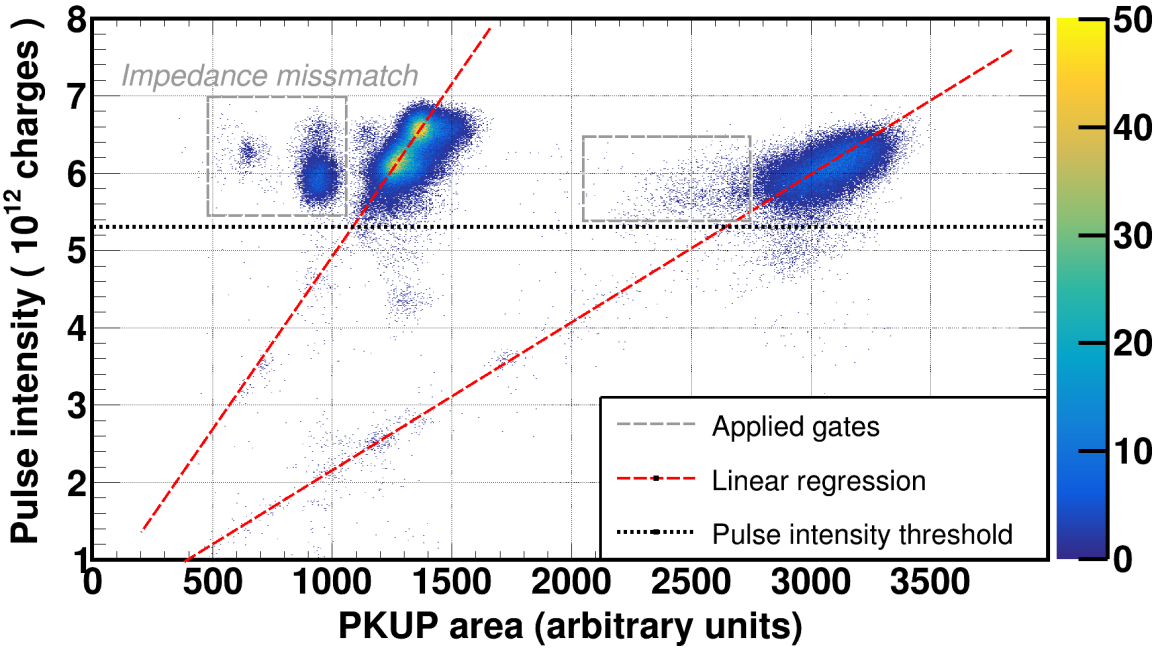

Figure 3.16: *Relation between the PKUP area and the pulse intensity. The two clusters marked with dashed red lines correspond to proton pulses with expected characteristics whereas the cluster marked with dashed gray rectangles correspond to bad quality PKUP which were rejected during the analysis.*

During the $^{240}Pu(n,f)$ campaign, which was the first physics measurement performed in EAR2, a part of the newly constructed experimental beam line commissioning took place, therefore numerous issues had to be addressed. The PKUP read-out was one of them, as reflected in fig. 3.16, where clusters that diverged

from the expected linear regression, marked with dashed gray rectangles, corresponded to an impedance mismatch between the PKUP and the read-out electronics, as can be seen in fig. 3.17 and were rejected in the analysis. In addition smaller clusters were also observed for pulse intensities below 5.3×10^{12} which were also rejected in the analysis by the application of a global threshold. The two different linear regressions that are visible in fig. 3.16 were attributed to different gains in the PKUP read-out amplifier, but there is no obvious reason to reject either one of them, therefore both were taken into account in the analysis.

The stability of the proton monitors was in better condition in the $^{237}Np(n,f)$ campaign as the similar checks showed, therefore there is no need for further discussion in this matter.

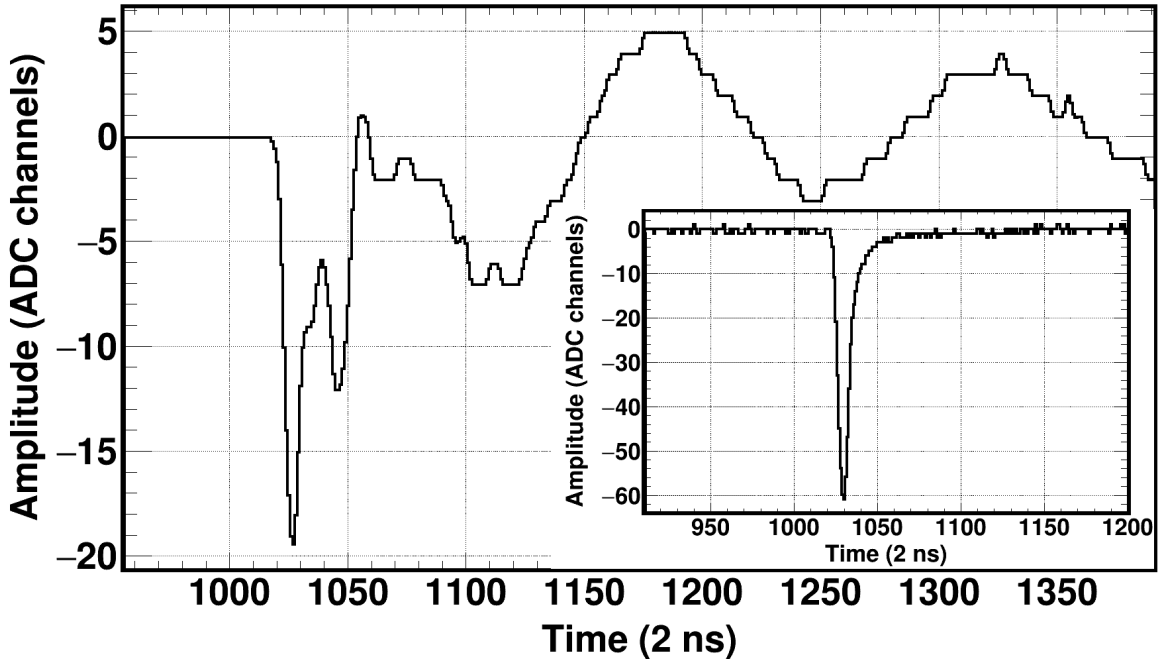

Figure 3.17: *Example case of a bad quality PKUP signal, due to an impedance mismatch between the detector and the read-out chain. A nominal PKUP signal is shown in the inset.*

3.2.2.2 Neutron beam monitor

As discussed previously, the neutron beam monitor consists of four $300-\mu$m thick silicon detectors and is based on the detection of tritons and α-particles with energies 2.73 and 2.05 MeV, respectively, produced by the $^6Li(n,t)\alpha$ reaction. Data were analysed by the four silicon detectors and were also checked in terms of quality and stability.

Firstly, the time of flight of each recognised event has been calculated using eq. 1.4 and has been correlated to the reconstructed amplitude of each individual event. Since the cross-section of the $^6Li(n,t)\alpha$ reaction follows a $1/v$ behaviour, a higher counting rate is expected in higher time-of-flights compared to low ones. In addition, since both products from this direct neutron-induced reaction deposit all their energy in the silicon buffers, the clusters that correspond to tritons and α-particles are expected to be well separated. As a final remark, since the Q-value

of the reaction is approximately 4.8 MeV, roughly the same energy deposition is expected, therefore the same signal amplitude or area, is expected for low neutron energies of the order of 100 keV or less, which correspond to high time-of-flights of the order of a few tens of μs. On the contrary, for small time-of-flights or consequently higher incident neutron energies, the kinetic energy of tritons and α-particles is increasing and, therefore, the amplitudes are expected to increase as well. However, since silicon detectors are heavily affected by the γ-flash , the data cannot be trusted above a few hundreds of keV. All these remarks are reflected in fig. 3.18, where the amplitude is plotted with respect to the logarithm of base 10 of the time-of-flight in ns[2] for one silicon detector from the $^{237}Np(n,f)$ campaign. The other three behave similarly well and this occurred in the $^{240}Pu(n,f)$ experiment as well, therefore no additional discussion is required.

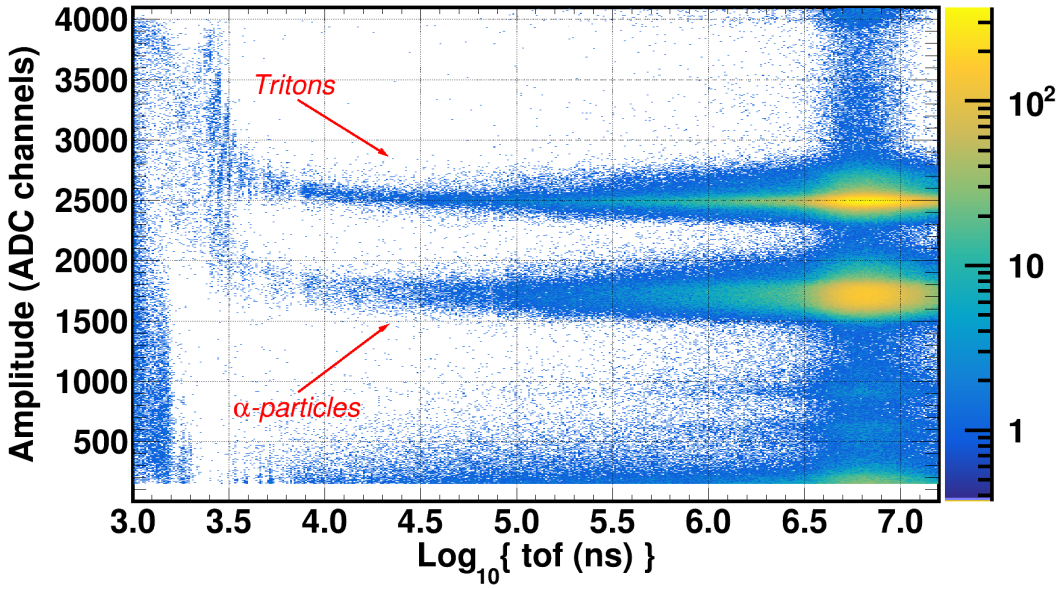

Figure 3.18: *Distribution of amplitude and the logarithm of base* 10 *of the time-of-flight (in ns) for one out of four silicon detectors from the* $^{237}Np(n,f)$ *campaign. Tritons and* α*-particles can be quite well discriminated between each other and the low amplitude noise as well.*

Since the detectors seemed to behave as expected on a run-to-run basis, a stability benchmarking test had to be performed. A similar approach was followed in accordance to the Micromegas detectors: area distributions from beam-on runs acquired in the beginning and the ending of the campaigns were compared in terms of gain shift from possible neutron damage, although not directly in-beam. As seen in fig. 3.19, the area distributions from a single detector from the $^{237}Np(n,f)$ measurement, normalised to the total number of bunches impinging on the Pb target for times-of-flight that correspond to neutron energies below 10 keV, do not indicate any gain shift but are rather identical. In addition to that, the leakage current was monitored throughout the measurements and was found to show only small variations, smaller than 3% around 25 nA.

[2]The values in the x-axis represent the power of 10 of the time-of-flight: A value of 5 for instance, represents a time-of-flight of 10^5 ns.

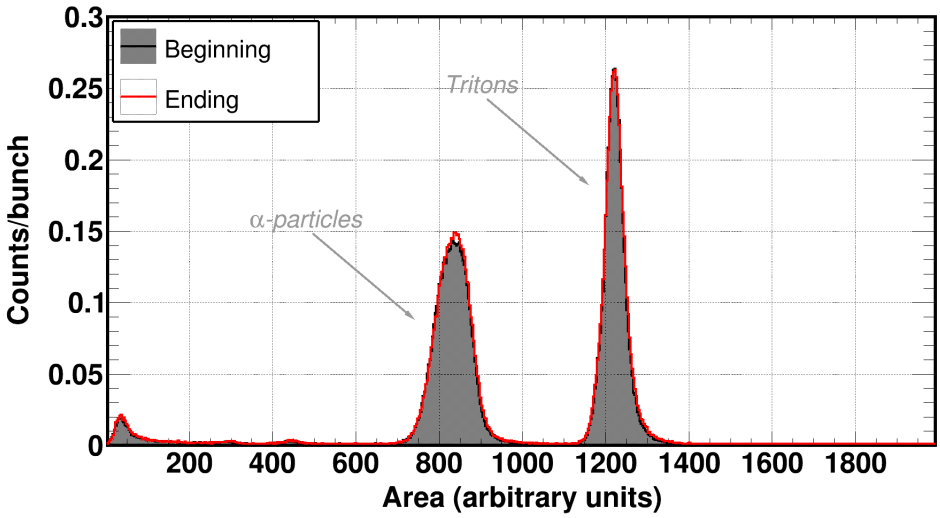

Figure 3.19: *Area distributions from events induced by neutrons with energies below* 10 *keV reconstructed at the beginning and ending of the* $^{237}Np(n,f)$ *campaign for a silicon detector illustrate that no significant neutron damage was induced in the detectors throughout the measurement.*

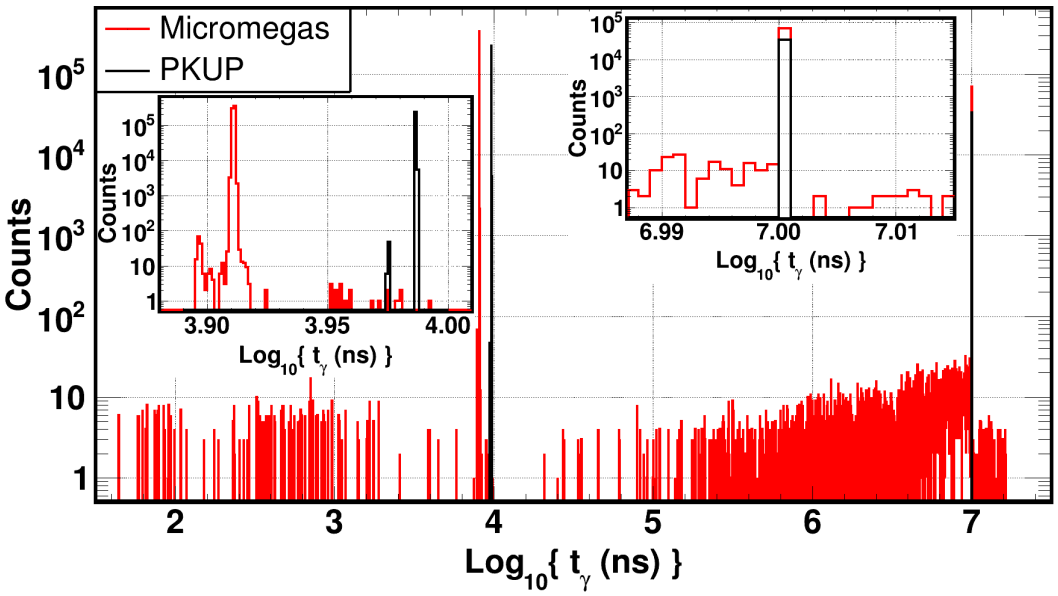

Figure 3.20: *The distribution of the reconstructed* t_γ *for the PKUP was cleaner than the Micromegas detector for a* ^{240}Pu *sample during the* $^{240}Pu(n,f)$ *campaign. The counts observed were attributed to fission events from neutrons produced from proton pre-pulses coming from the PS.*

3.2.3 Recognition of the γ-flash arrival

In time-of-flight measurements an accurate reconstruction of the time characteristics of the detected signals is of vital importance. In this respect the arrival time of the γ-flash , which is used as the start signal of the time-of-flight calculation, has to be properly reconstructed. This was achieved by the establishment of the proper

parameters in the pulse shape analysis routine, in which the γ-flash was identified, prior to the subtraction, as the first signal that crossed a specified amplitude threshold and had a larger width than a given, user defined value. The distribution of t_γ was expected to be narrow and lied around a specific value. As seen in fig. 3.20, the t_γ distribution of a Micromegas detector in the $^{240}Pu(n,f)$ campaign expanded between 10^2-10^7 ns. Two main peaks were observed in times around $10^{3.91} = 8000$ ns and 10^7 ns which were attributed to a change in the delay of the data acquisition system which was in a commissioning phase during the measurement.

Although the two distributions do not affect the reconstruction of the time-of-flight because the latter is calculated as a time difference, the observed counts around them needed further investigation. In this respect, the movies that correspond to these counts were backtracked and an example can be seen in fig. 3.21 where a fission signal is falsely recognised as the γ-flash due to their similar characteristics. It is worth mentioning that these fission signals are generated from neutrons produced by proton pre-pulses coming from the PS as can be seen in fig: 3.22, where a PKUP signal is shown along with smaller (in amplitude) ones. The spacing of these signals is of the order of 240 ns, which corresponds to the extraction frequency of the PS and indicates proton beam losses during the $^{240}Pu(n,f)$ experiment.

Despite the small fraction of these events which were not expected to have a severe effect in the calculated cross-section, it was considered important to discard them by gating only in events with t_γ close to the two main distributions. Another possibility that does not discard any data, would be to take advantage of the PKUP's t_γ distribution, which did not contain any tails whatsoever, and ad hoc assign the t_γ of the fission detectors (t_γ^{FIMG}) in each individual bunch based on the t_γ from the PKUP (t_γ^{PKUP}). This approach was adopted during the data analysis of the $^{240}Pu(n,f)$ data, while for the $^{237}Np(n,f)$ data there was no need to do so, since the t_γ distributions were the expected ones. To use t_γ^{PKUP}, though, the time difference between that and t_γ^{FIMG} had to be known. This constant difference per detector was estimated as the central value from the t_γ $^{(\mathrm{PKUP})} - t_\gamma$ $^{(\mathrm{FIMG})}$ distributions that can be seen in fig. 3.23.

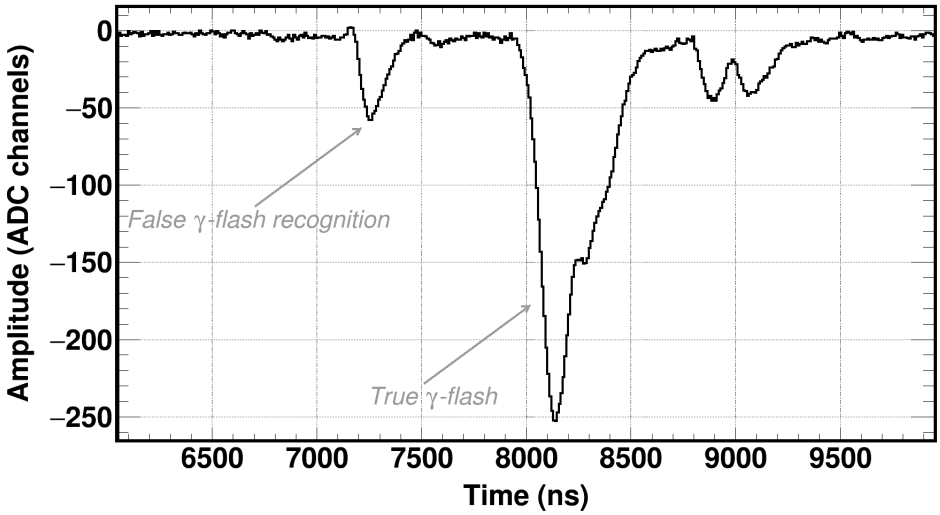

Figure 3.21: *Example case of a signal attributed to neutron induced fission from a proton pre-pulse which results in a false γ-flash recognition.*

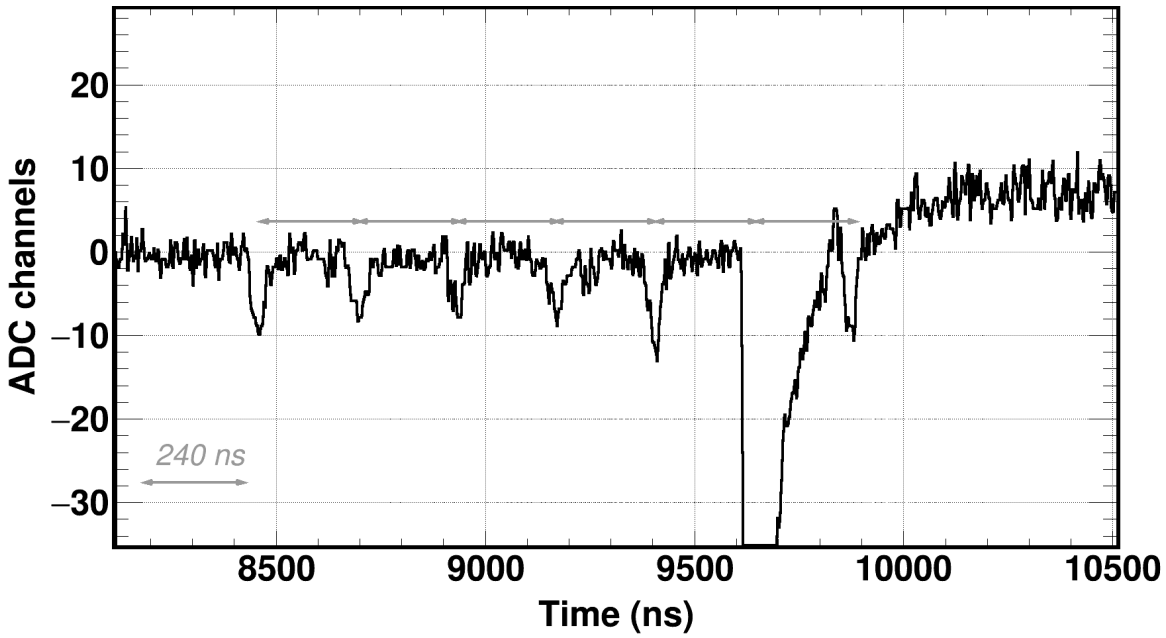

Figure 3.22: *Example case of beam losses from the PS: The main PKUP signal seen at $\sim 9.6\mu s$ arrives between smaller in amplitude signals which correspond to extracted proton buckets from the PS.*

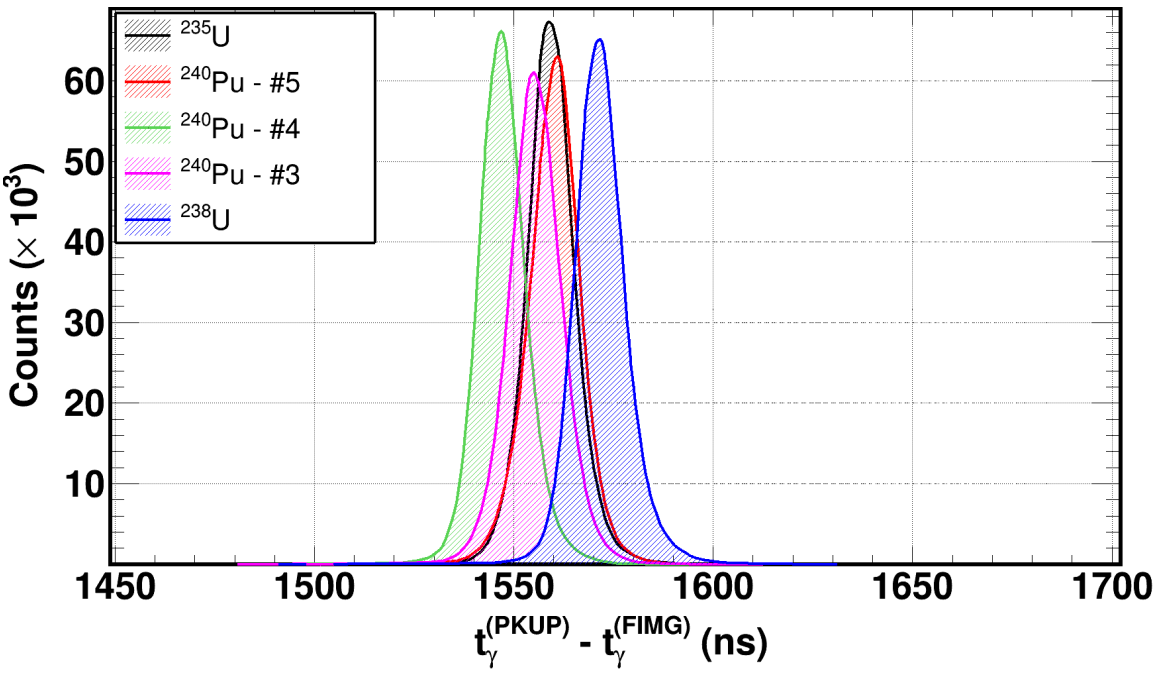

Figure 3.23: *Distributions of the t_γ difference between the PKUP and each individual fission detector (FIMG). The central values correspond to the constant offset assigned to PKUP's t_γ in order to reconstruct t_γ in the FIMG detectors.*

3.2.4 Rejection of sparks

An important check that has to be made when dealing with high gain gaseous detectors concerns the rejection of events that produce a considerable amount of space charge within the gas volume where an electric field is applied. This excess charge, if greater than the Raether limit, causes electrostatic discharges as a result of dielectric breakdown between the detector's micromesh and anode across the volume defined by the gas mixture. Such events lead to an infinite dead-time with respect to the width of the signals and a saturation of the read-out electronics therefore the affected bunches were rejected from the analysis (1.5% and 0% in the $^{240}Pu(n,f)$ and $^{237}Np(n,f)$ campaign, respectively). An example event can be seen in fig. 3.24 where a spark event was recorded for the detector coupled to the ^{238}U sample during the $^{240}Pu(n,f)$ campaign.

3.2.5 Rejection of α-particle counts

Alongside the acquisition of fission events, counts attributed to the intrinsic α-activity were recorded. These counts contribute to the total recorded fission yield, unless rejected during the analysis. Thus the overlap of the fission and α-particle spectra, despite the well-defined separation, has to be taken into account. In this respect, a total α-count rejection strategy was adopted.

More specifically, amplitude thresholds were introduced in the analysis in such a way to completely reject α-counts, while the fission counts lost that lie below the

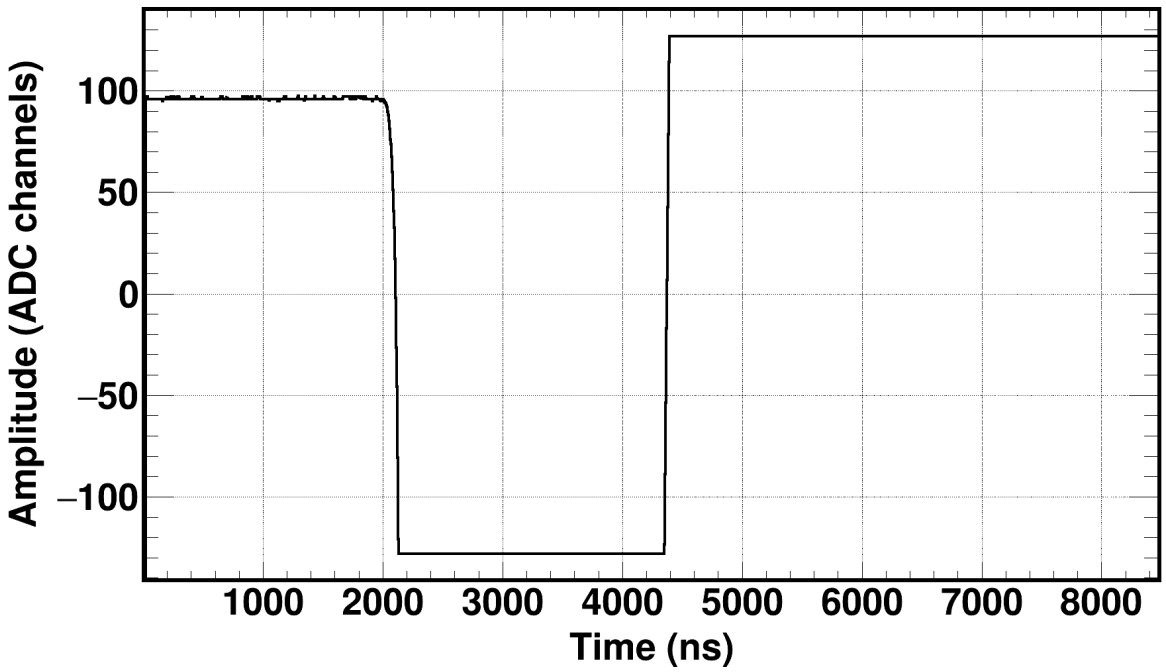

Figure 3.24: *Example case of a spark event recorded from the Micromegas detector coupled to the ^{238}U sample during the $^{240}Pu(n,f)$ campaign.*

α-spectrum were appropriately estimated using Monte Carlo simulations, as will be discussed later. To properly select the amplitude thresholds for each individual detector in both campaigns, reconstructed amplitude spectra from beam-on and beam-off runs were normalised to the total number of bunches and compared with respect to the channel number in which the tail of each α-spectrum ends, so that α-counts were not visible any more, as can be seen in fig. 3.25 in the case of a ^{240}Pu sample.

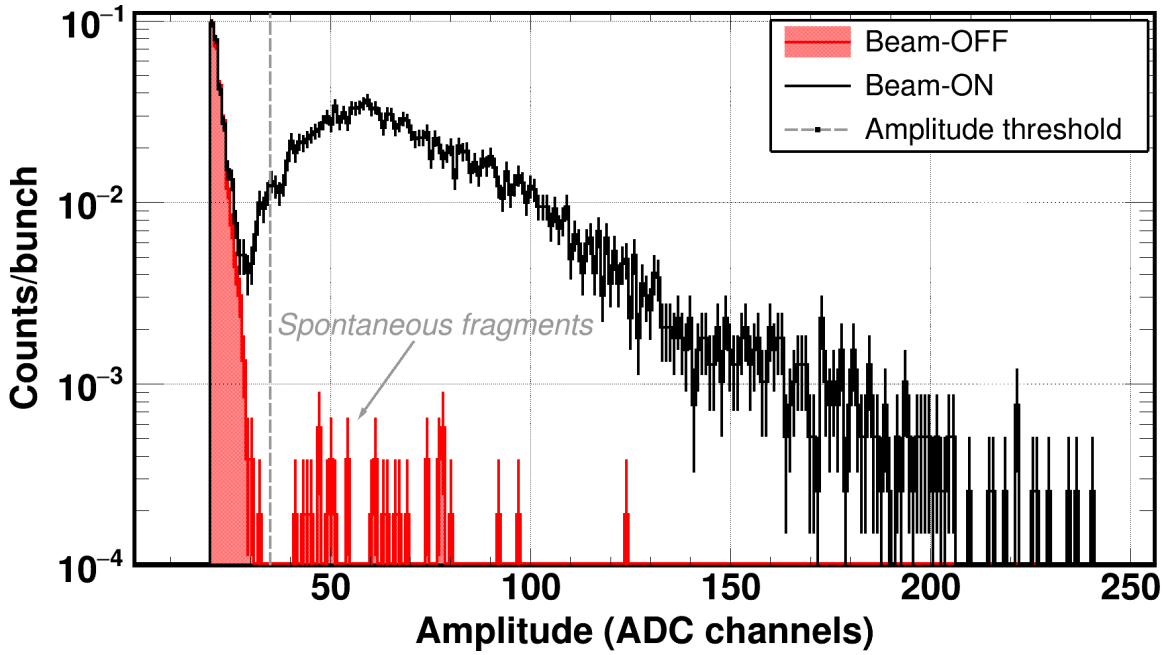

Figure 3.25: *Bunch normalised beam-on and beam-off spectra for a ^{240}Pu sample recorded from ~ 4000 bunch runs. A well defined separation between fission fragments and α-particles was observed. The amplitude threshold was selected based on the tail of the α-particle spectrum, and corresponds to the ADC channel where no α-counts were recorded.*

The strategy of a fixed amplitude threshold was adopted in both experimental campaigns across the whole neutron energy range and for all samples, even for the low activity ^{235}U and ^{238}U ones. The recorded α-counts are expected to decrease for small time-of-flights, or equivalently for higher neutron energies, as shown and marked with a red triangle in the distribution of amplitudes and time-of-flights for a ^{240}Pu sample in fig. 3.26. This behaviour is observed simply because for smaller values of the time-of-flight, the time frame is much more compressed in comparison to greater ones due to the parabolic relation between the incident neutron energy and the time-of-flight. For example, a given difference in the power of time-of-flight corresponds to a much higher time difference in large time-of-flights than in small ones (or in small neutron energies than in high ones). Despite that, clusters were still present in high neutron energies and small amplitudes (red rectangle, fig. 3.26), and were attributed to residuals from the γ-flash subtraction and false recognition of electronic noise as pulses. In this respect, a fixed amplitude defined by simultaneously rejecting the vast majority of what is considered background and minimising the rejection of fission signals, was introduced in the analysis in all detectors in both campaigns. In the case of the distribution seen in fig. 3.26, an amplitude threshold of 35 ADC channels was applied. The additional clusters seen between 850 keV and 1 eV in figures 3.26 and 3.27 correspond to resonances in the neutron induced fission cross-sections.

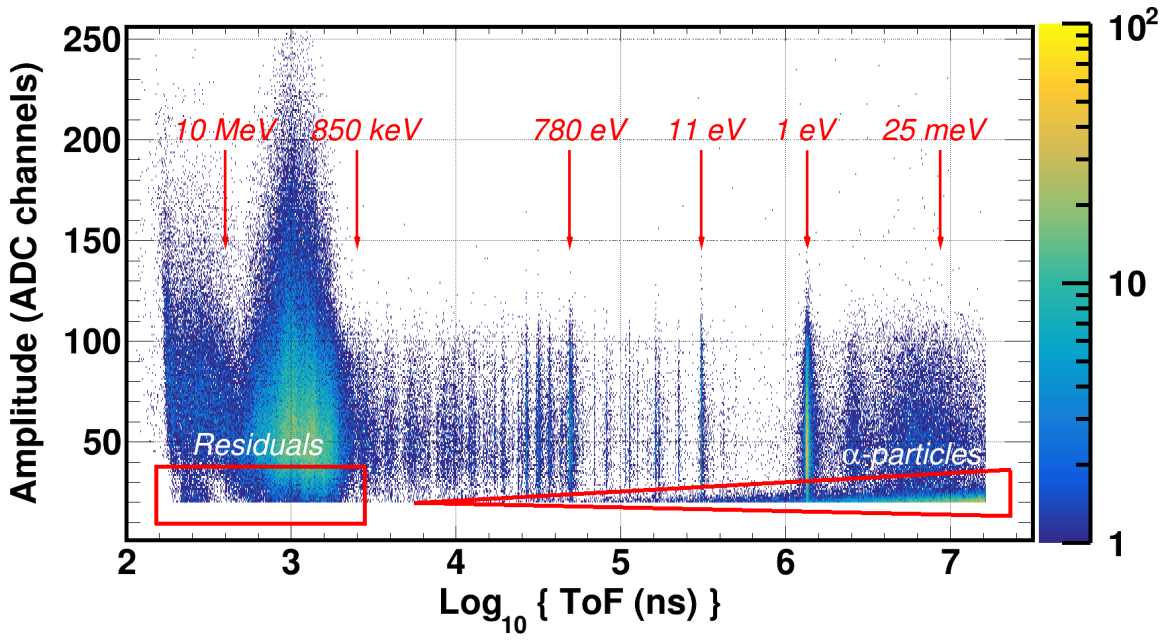

Figure 3.26: *Distribution of amplitude vs time-of-flight for a* ^{240}Pu *sample. The counts induced by the* α*-activity and the residuals from the* γ*-flash subtraction in addition to false recognition of electronic noise can be seen inside the triangle and the rectangle, respectively. For a simple interpretation of the graph, a few incident neutron energies calculated at a flight path of* 19.2 *m are marked with red arrows.*

For the low activity reference samples, although the expected α-counting rate per bunch, given the maximum 40.58 Bq activity of the ^{235}U sample in the $^{237}Np(n,f)$ campaign, was 0.65 counts at maximum, a fixed amplitude threshold was introduced as well, in order to reject residuals from the γ-flash subtraction and falsely recognised electronic noise as true events, as well as for compatibility reasons, so as to introduce systematic uncertainties in the correction of the rejected fission signals. An example case of the time-of-flight vs amplitude distribution can be seen in fig. 3.27 for the ^{235}U sample from the $^{240}Pu(n,f)$ campaign in which it is evident that the α-activity is practically invisible, however a cluster of pulses of small amplitudes was observed in small time-of-flights, which justifies the application of an amplitude threshold, which in this case was selected to be 30 ADC channels. Finally, the much higher fission yield observed in lower neutron energies (high time-of-flights) is attributed to the high neutron induced fission cross-section of the fissile ^{235}U .

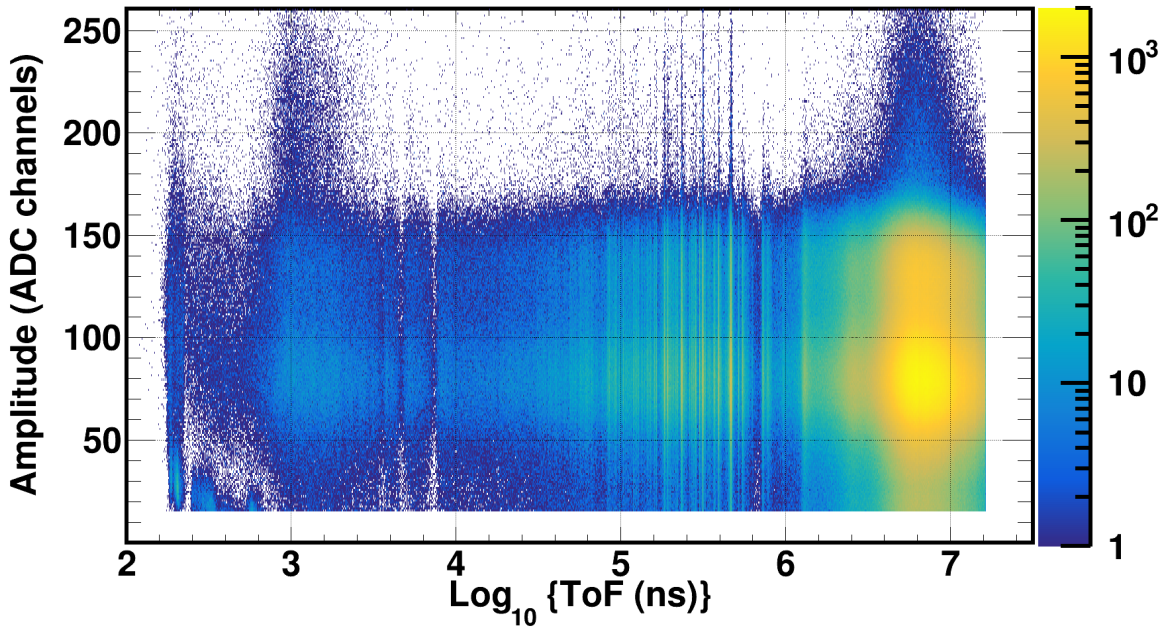

Figure 3.27: *Distribution of amplitude vs time-of-flight for the ^{235}U sample in the $^{240}Pu(n,f)$ campaign whose α-activity is practically invisible. In addition, the clusters seen for time-of-flights in the $10^5 - 10^6$ ns range, correspond to ^{235}U (n,f) resonances which are visible with a rather high resolution.*

3.2.6 Rejection of noise: A brief discussion

Although "noise" is in general interpreted as electronic noise, in cases where pulse shape analysis is applied, falsely recognised pulses contribute to noise. To reject these unwanted signals that would contribute to the recorded fission yield, distributions of various signal attributes, such as amplitude, rise-time, FWHM, area, FWTM, the χ^2 of the fit etc. were thoroughly investigated in an attempt to locate deviations from the expected behaviour.

For instance, since the reconstruction routine accepts pulse shapes in numerical format, the area to amplitude ratio is constant, therefore the amplitude vs area distribution is expected to be linear and whatever deviates from this linearity has to be considered as noise. Similar combinational checks were performed in all detectors in both campaigns for the different signal attributes and consequently, falsely recognised events were rejected. A comprehensive discussion on the numerous performed checks on all detectors will be avoided, since it would not provide any additional information. However, for the sake of principle, an example case can be seen in fig. 3.28, where the FWHM vs amplitude distribution for the ^{235}U sample in the $^{237}Np(n,f)$ campaign is shown.

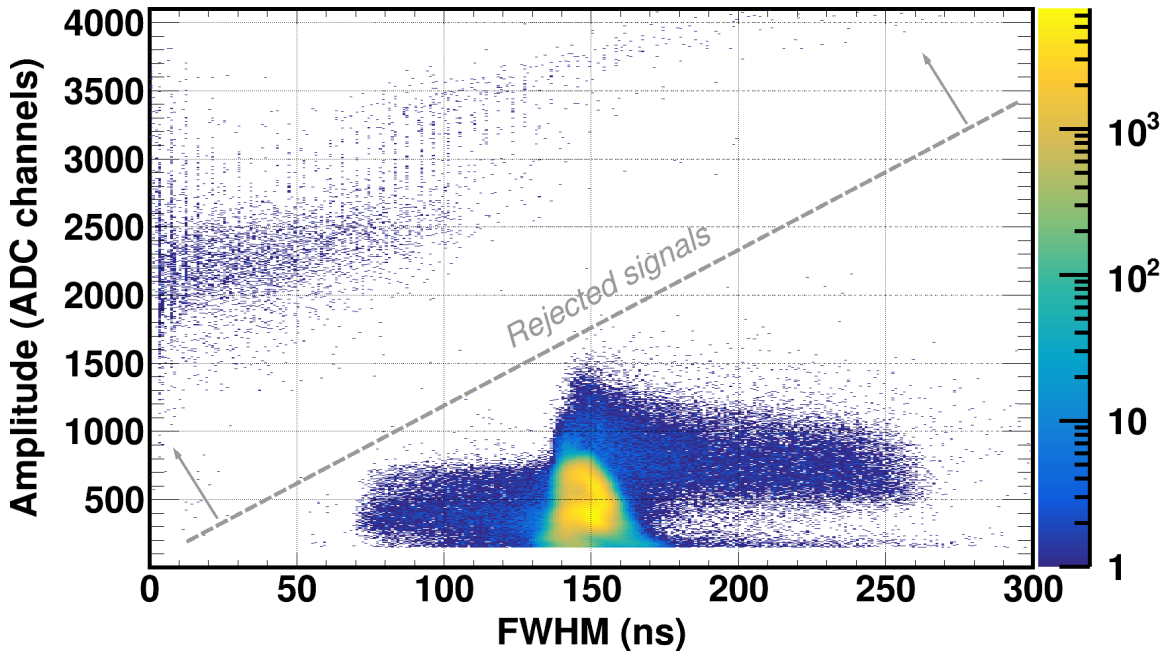

Figure 3.28: *Amplitude vs FWHM distribution for the ^{235}U sample from the $^{237}Np(n,f)$ campaign. A main cluster was observed in FWHM around 150 ns, which was extended in smaller values where piled-up pulses were successfully reconstructed. The signals identified in high FWHM and amplitude values were attributed to unresolved pile-up and falsely reconstructed signals, respectively. The dashed line represents the rejection gate that was applied during the analysis.*

Prior to deciding on what was considered to be noise, the expected behaviour had to be proclaimed: Signals with a constant FWHM were expected, regardless of the amplitude and this can be seen in fig. 3.28, where a dominant FWHM was observed around 150 ns. The signals reconstructed with a smaller FWHM were attributed to cases where two pulses occurred close in time to each other, resulting in resolved pile-up, as can be seen in fig. 3.29.

The higher than 150 ns FWHM, corresponded to unresolvable pile-up cases, in which at least two signals were recorded so close to each other, that practically formed a single one, as can be seen in fig. 3.30. This results in counting losses, which were taken into account, as will be explained later on.

Additionally, high amplitude signals (> 1500 ADC channels) were also reconstructed. These formed a well-separated cluster from the main one, as illustrated in fig. 3.28. The signals observed above the dashed line correspond to a false recognition of high frequency and high amplitude noise as seen in fig. 3.31. Such kind of behaviour was simultaneously observed only in detectors from the $^{237}Np(n,f)$ campaign that were coupled to the new pre-amplifier units described in subsection 3.1.3 and was attributed to small instabilities of the low voltage power supply unit.

The same procedure was repeatedly carried out with several distributions and it was adopted in the analysis of both data-sets. Reconstructed signals, which formed clusters that deviated from the nominal behaviour in the various distributions that were investigated, were backtracked and rejected off-line in the case of false recognition. Other cases in which the signal reconstruction was inefficient, the user input parameters in the processing routine were fine-tuned accordingly. This procedure

was iteratively performed until the distributions could be fully interpreted. This was an indication of high control and understanding of the recorded data.

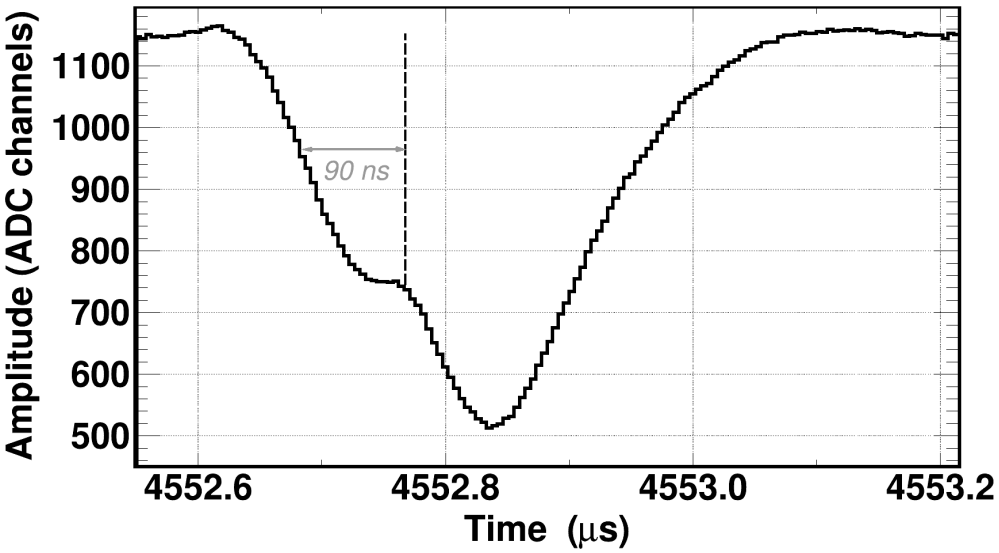

Figure 3.29: *Example case of a resolvable pile-up case recorded from the ^{235}U sample during the $^{237}Np(n,f)$ experiment, in which the FWHM of the left pulse was reported, by the reconstruction routine, to be* 90 *ns.*

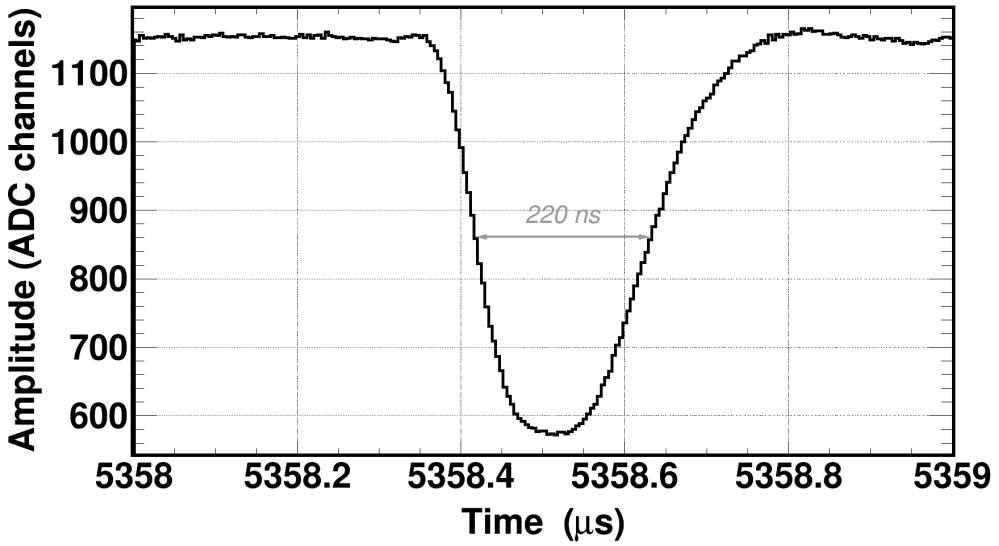

Figure 3.30: *Example case of an unresolvable pile-up case recorded from the ^{235}U sample during the $^{237}Np(n,f)$ experiment, in which at least two signals were formed close in time to each other. The reconstructed waveform resulted in a FWHM of* 220 *ns, a value which is greater than the main* 150 *ns one.*

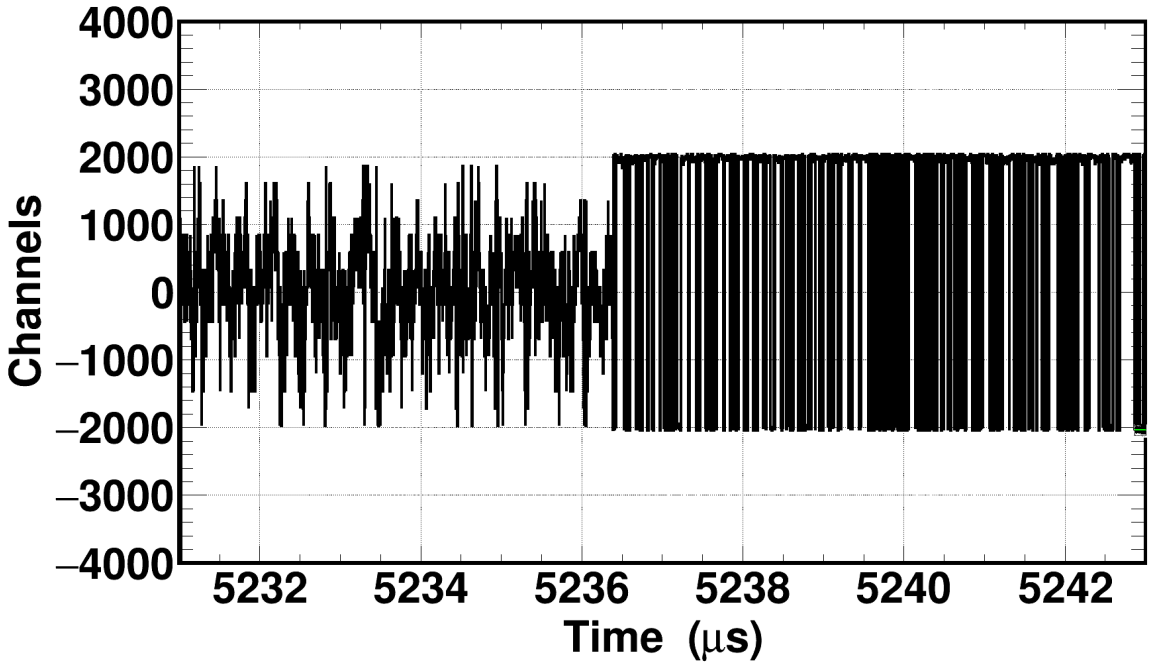

Figure 3.31: *Example case of noise oscillations recorded during the $^{237}Np(n,f)$ measurement that were mistakenly registered as signals. These pulses, that were attributed to instabilities of the low voltage supply unit that powered four pre-amplifiers, were rejected during the analysis.*

Finally, signals that did not fulfil the proper criteria were rejected in order to reconstruct the amplitude spectra only from fission fragments that escaped the fission foils as can be seen in fig. 3.33 for a set of ^{235}U -^{240}Pu and ^{235}U -^{237}Np samples from the $^{240}Pu(n,f)$ and $^{237}Np(n,f)$ measurement, respectively. In the spectra of both ^{235}U samples the light and heavy fission fragment families were evident, as was the pile-up for incident neutron energies when the fission rate was increased. In addition, the α-particle region was well separated from the fission fragments in both the ^{240}Pu and ^{237}Np amplitude spectra, as a consequence of the high background rejection capabilities offered by EAR2.

It has to be noted that during the $^{240}Pu(n,f)$ campaign, where an upgrade of the data acquisition system was taking place, issues were observed related to the counting of the proton intensity and number of bunches. In this respect, in order to ensure a proper normalisation of the recorded data to the proton charge among all sample-detector modules, proton bunches in which a bad event was reconstructed from a single detector, were discarded for all the other detectors as well. The elimination of bad events was based on a 2D map (bunch vs run number) which was filled whenever a specific combination of run/bunch a bad event was tagged. During the off-line analysis, combinations between runs and bunches were checked and whenever the 2D map had a non-zero entry the entire stack of events was discarded. Such a map can be seen in fig. 3.32. On the contrary, during the $^{237}Np(n,f)$ campaign such issues were solved, therefore the rejection was performed on a detector-by-detector basis taking correctly into account the number of registered protons that impinged on the spallation target.

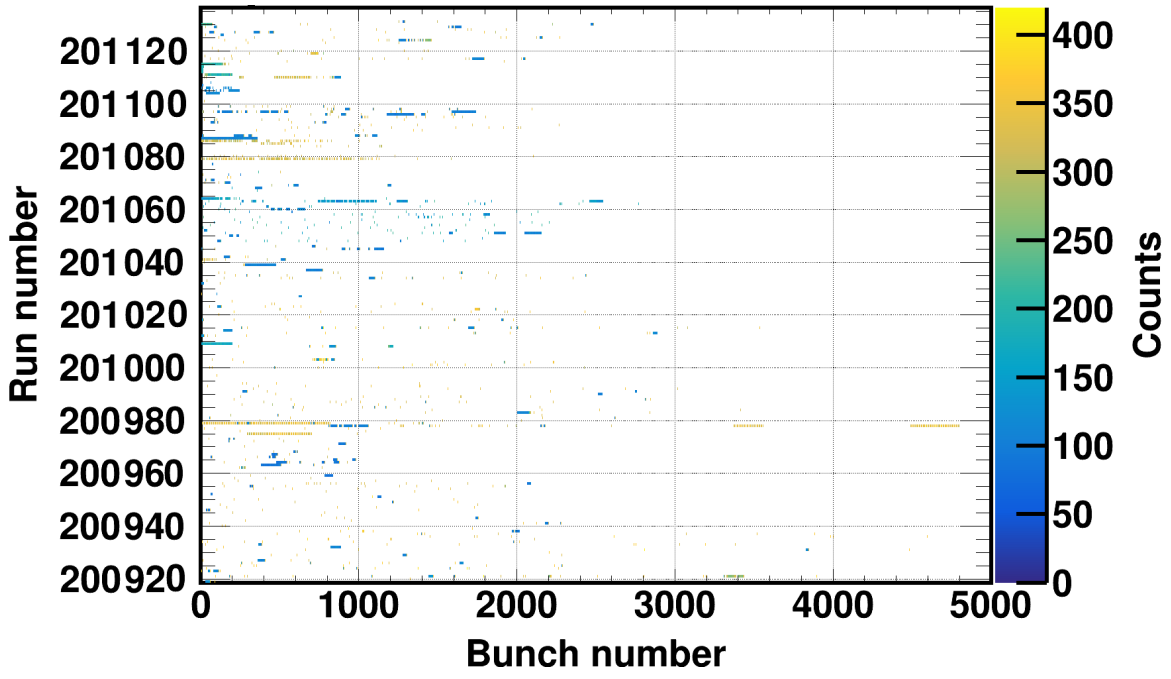

Figure 3.32: *Bad events were mapped according to the bunch and run number that were recorded at, in order to be discarded during the off-line analysis whenever the combination had a non-zero entry.*

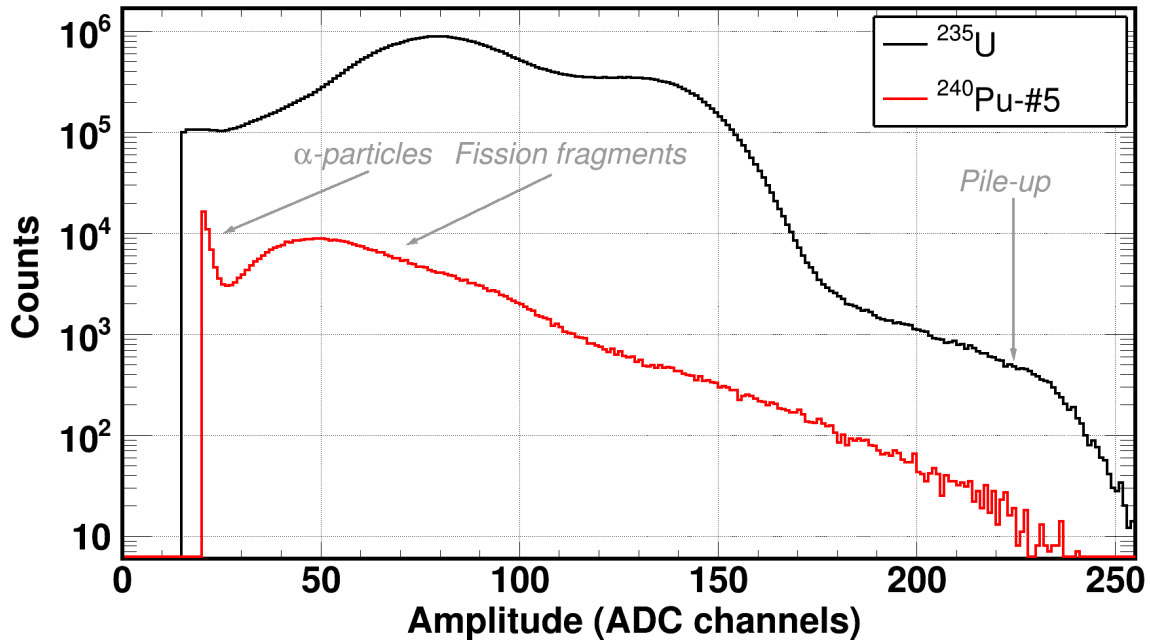

(a) $^{240}Pu(n,f)$

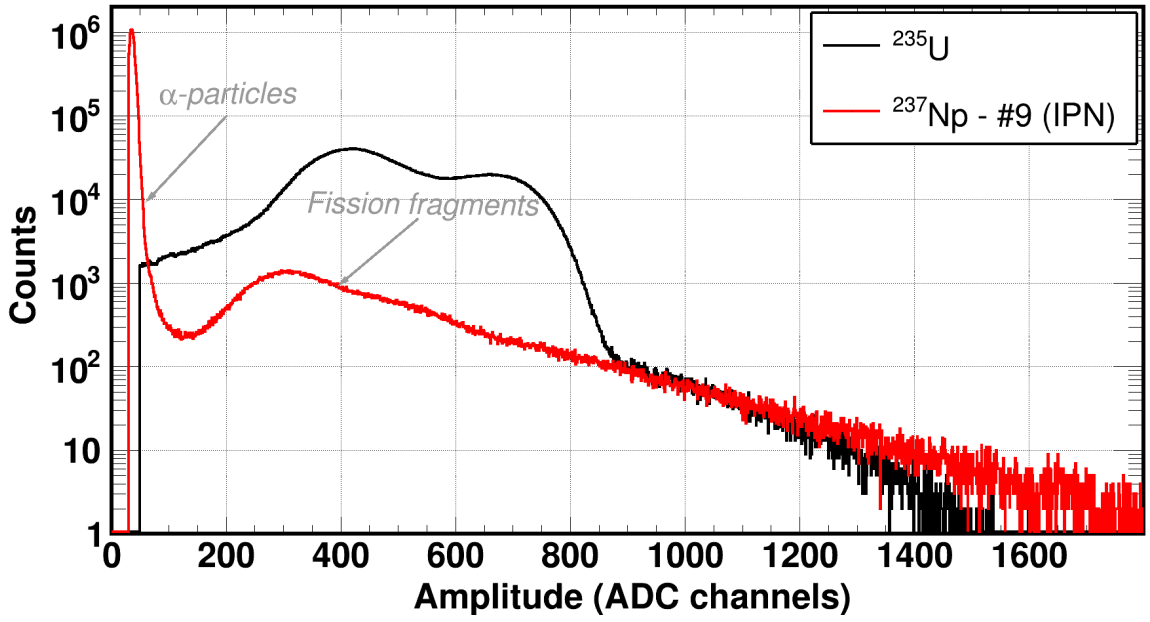

(b) $^{237}Np(n,f)$

Figure 3.33: *Amplitude distribution of the* ^{235}U *and the most massive* ^{240}Pu *and* ^{237}Np *samples, reconstructed from the data acquired and properly selected during the* $^{240}Pu(n,f)$ *and* $^{237}Np(n,f)$ *campaign, respectively. The heavy and light fission fragment families are evident in the* ^{235}U *amplitude spectra whereas the counts attributed to the intrinsic α-activity of* ^{240}Pu *and* ^{237}Np *are well separated from the fission events.*

3.2.7 A study of the energy resolution of the detection system

A reasonable question could be raised concerning the amplitude spectra seen in fig. 3.33 and the appreciably different energy resolution between the ^{235}U samples and the rest of the actinides. In this respect, to ensure that what was reconstructed could be interpreted to a certain extent, a resolution study was performed, whose findings were that it depends on the following:

1. The distributions of fission fragments
2. The activity of each sample
3. The electronics used in the read-out
4. The thickness of the fission foil

It has to be noted that this study was performed in order to better understand the operation of the detection system coupled with the specific read-out system used in the experiments. It was not by any means a detector study therefore its findings have to be confirmed by future Monte Carlo simulations. Moreover, fission cross-section measurements at n_TOF do not require a high resolution, therefore the calculated cross-section did not depend on the this attribute of the detection system. It goes without saying that the conclusions made in the present study, are open to potential discussions; possible explanations were deducted which could help in future interpretations of dedicated detector studies at n_TOF.

The least important issue, yet still with an effect on the energy resolution, con-

cerns the distribution of the produced fragments after the neutron evaporation. As was previously explained in the text, the use of the GEF code made possible the calculation of fission fragment properties, such as the atomic number Z, whose distribution can be seen in fig. 3.34 for the compound nuclei studied in the present thesis. In fig. 3.34 it is evident that the atomic number distribution of heavy fragments is independent of the fissioning nucleus, due to shell effects as was previously explained in the text. On the contrary, the residual mass will be shared between the evaporated neutrons and the light fission fragment whose atomic number distribution exhibits a dependence on the corresponding fissioning nucleus: The heavier the compound, the heavier the light fragments. Consequently, the mean energy deposition per unit length $\mathrm{d}E/\mathrm{d}x$, which is proportional to Z^2, is expected to be identical up to a certain extent for heavy fragments regardless of the actinide sample, whereas the variation of Z calculated for the light ones, will result in a non-identical energy deposition, thus opting for poorer resolution in heavier samples. As an example, the mean Z of light fragments was estimated to be 41 and 38 for ^{241}Pu and ^{236}U, respectively which results in $\sim 15\%$ difference in the energy deposition taking also into account the energy straggling of the fragments.

Quite an important factor in the energy resolution of a Micromegas detector is the activity of each sample. A high activity sample results in the presence of a constant-in time-electron cloud within the gas volume which can alter the motion of primary electrons produced by fission fragments. In fact, the electrons produced by fission products on an electron rich environment, are subject not only to drifting but to diffusion as well therefore the drift velocity is expected to be lower thus enhancing the probability for recombination and loss of deposited energy information. In addition, below the maximum transparency, which occurs when the ratio ξ between the electric fields in the drift and amplification region is 50 [155], the lower the drift velocity the slower the charge collection therefore the induced signal is expected to be wider in cases where the sample activity is high. This in addition to what was described in the previous paragraph, was the main reason why the resolution in the amplitude spectrum of ^{240}Pu in fig. 3.33a is poorer than the ^{235}U one.

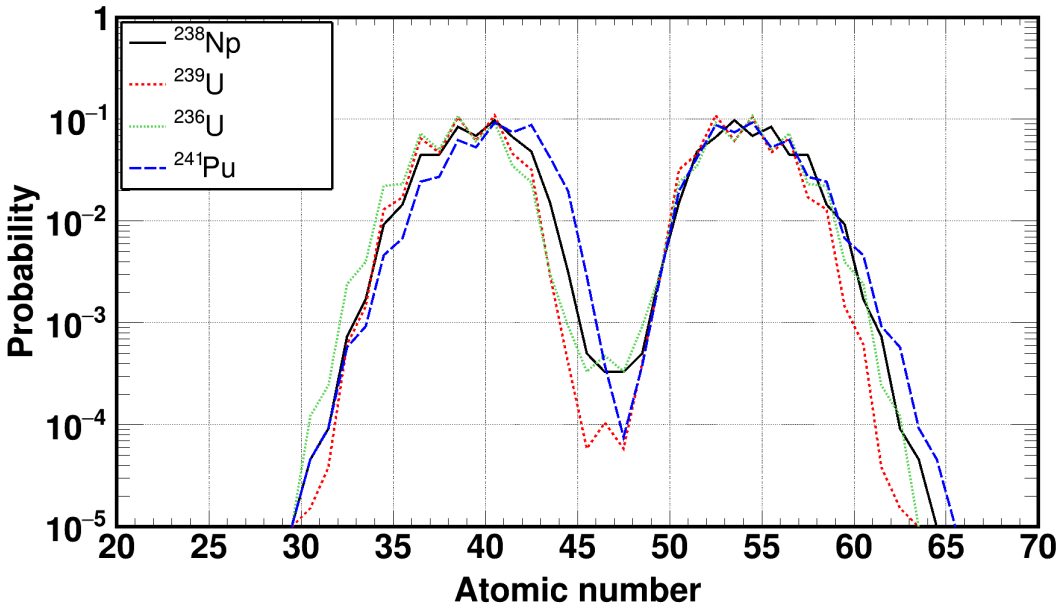

Figure 3.34: *Distribution of the atomic number of post-neutron evaporation fission fragments for the compound nuclei that the present thesis deals with. The distributions were calculated using the specialised Monte Carlo code GEF.*

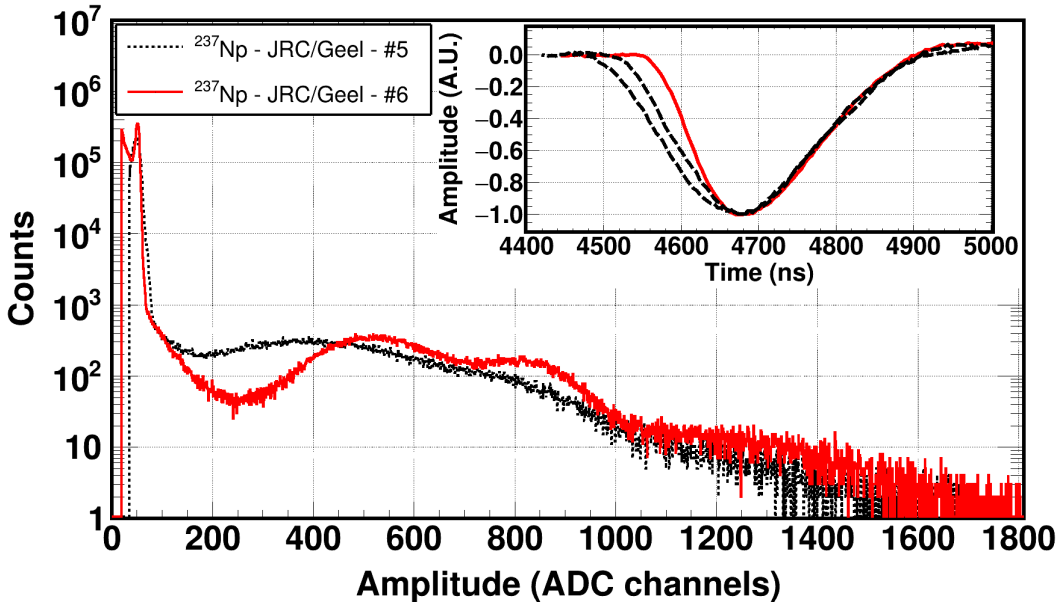

Figure 3.35: *Amplitude spectra of two ^{237}Np samples. The difference in the energy resolution is attributed to the pulse width: A wider pulse (black dashed line) will result in a poorer resolution compared to a faster one (solid red line).*

Furthermore, the characteristics of the read-out system contribute decisively in the energy resolution of the Micromegas detection system used at n_TOF fission experiments. A characteristic example can be seen fig. 3.35, where the amplitude spectra of two ^{237}Np samples are shown. The energy resolution obtained in the case of sample #6 was far different from the one of sample #5, the main difference being a different preamplifier unit. Sample #6 was coupled to a new module with better

time characteristics than the older multi-channel unit sample #5 was coupled to, that was also used in the $^{240}Pu(n,f)$ campaign. This difference was attributed to a better performance of the reconstruction routine when fitting narrower signals.

In addition, although both detector-sample modules were operated at exactly the same conditions, it was observed that the amplitude distribution of the module with the better resolution was gain shifted. To justify this experimental fact, simple calculations were made using a triangular pulse with a width w, a height h and an area s as seen in fig. 3.36.

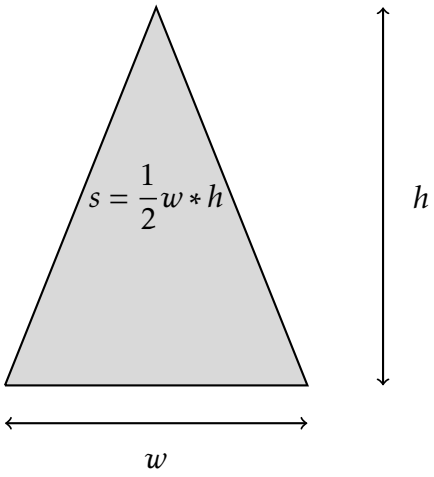

Figure 3.36: *A triangular pulse with width w, height h and area s was used to understand the gain shift that was observed in the amplitude spectrum of ^{237}Np -#6 compared to the corresponding one of ^{237}Np -#5.*

The area of a pulse is proportional to the energy deposited in the detection medium. Assuming an area s of 10 arbitrary units and two cases of wide and narrow pulses with widths w of 2 and 1 arbitrary units, respectively the amplitude h of each pulse was calculated to be 10 and 20 units in the former and the latter case, respectively, thus justifying the observed gain shift in the case of a faster pulse. It has to be noted that the previous discussion was an attempt to justify the observed gain shift. It goes without saying that a gain shift does not necessarily improve the resolution of a detection system.

Finally, the thickness of the actinide foil, affects the kinetic energy of the fragment, at the time it enters the gas volume. The higher the thickness, the higher the effect of energy straggling which results in an increasingly fuzzy amplitude spectrum. A characteristic example can be seen in fig. 3.37, where the amplitude spectrum in the case of a ^{238}U sample had a substantially poorer resolution than the one from the ^{235}U , although the fission fragment distributions and the intrinsic activities did not vary appreciably. The electronics used in both samples were the same as well whereas the ^{238}U samples had a 4 time bigger mass compared to the one of ^{235}U , in order to compensate for the low cross-section and increase the acquired statistics.

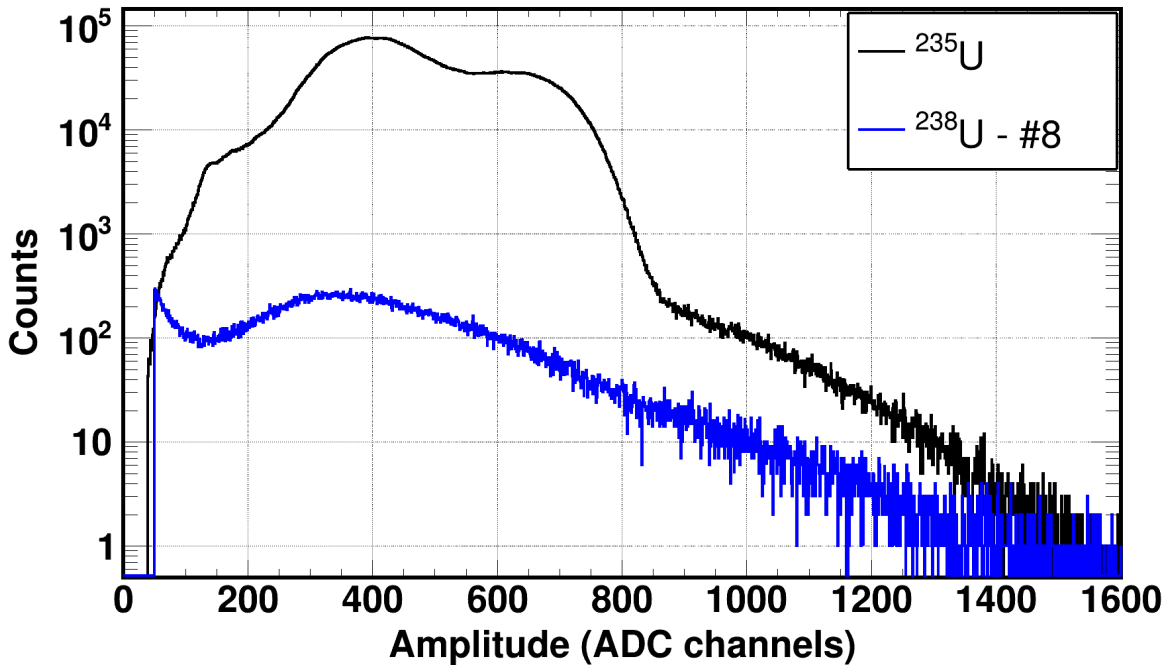

Figure 3.37: *Amplitude spectra of a ^{238}U and the ^{235}U samples reconstructed during the $^{237}Np(n,f)$ campaign. The difference in the energy resolution was attributed to the thickness of the ^{238}U samples, a factor the enhances the energy struggling of fragments inside the fission foil thus affecting the kinetic energy as they enter the detector volume.*

CHAPTER 4

Data analysis and cross-section determination

Once the signal quality was checked and the distributions of the experimental observables were in accordance to what was expected and could be fully interpreted, the necessary corrections were applied to the reconstructed counting spectra in order to determine the neutron induced fission cross-sections of ^{240}Pu and ^{237}Np from thermal energies up to a few MeV.

4.1 Data reduction

As described previously, the recorded movies at n_TOF were digitised, compressed on-line by the application of a zero-suppression algorithm and then stored in binary files, on tape for long term storage. These movies were analysed off-line using the n_TOF pulse shape analysis routines in a way that every portion of the stored waveform that fulfilled certain user defined criteria, was identified as signal and stored in an n-tuple file, in list mode which is a convenient binary format.

A data reduction and selection program was written in C++ using the object-oriented framework and library developed by CERN, ROOT [178], to convert the list-mode data into distributions published in histograms. The routine looped over the entries of all detectors, selected the proper signals based on the applied thresholds, calculated the time-of-flight of each signal, applied all the necessary corrections and finally calculated the $^{240}Pu(n,f)$ and $^{237}Np(n,f)$ cross-sections.

The data reduction routine was organised in three subroutines: a) the conversion routine, which read raw data files and converted them into useful user-defined distributions, b) the correction routine, which was applying the necessary corrections to the raw data and c) the calculation routine which was calculating several

quantities (i.e. flux, cross-section) from the distributions of the corrected observables. The subroutines, were also sharing a library which contained the necessary configuration data (i.e. user-defined thresholds, histogram binning information, values of constants etc.), along with a collection of functions that were used in the reduction routine whose execution was automated through a Linux shell script.

4.2 Derivation of the cross-section

In the context of the present text, only neutron induced reactions will be considered therefore the nuclear reaction r refers to the (n,r) reaction. In addition f and tot refer to the (n,f) and (n,tot) reactions, respectively.

The fission yield (Y_f) on the other hand, describes the probability itself for the fission reaction to occur, thus its values lie within the $[0,1]$ range and can be calculated with the use of the transmission coefficient T, as seen in eq. (4.1).

$$Y_f = (1-T)\frac{\sigma_f}{\sigma_{tot}} \tag{4.1}$$

The transmission of a beam which carries an intensity I_0 through a sample with areal density n is related to the transmission coefficient T which can be expressed from the Beer-Lambert law seen in eq. (4.2)

$$T = \frac{I(n)}{I_0} = e^{-n\sigma_{tot}} \tag{4.2}$$

where $I(n)$ describes the attenuated beam intensity at the sample exit. In the approximation of a thin sample where its thickness or equivalently its surface density is so small that the neutron mean free path is much larger than the sample thickness, eq. (4.2) can be reduced to eq. (4.3) using Taylor series expansion

$$T \approx 1 - n\sigma_{tot} \tag{4.3}$$

The fission yield Y_f therefore becomes proportional to the neutron induced fission cross-section σ_f with the areal density n being the proportionality factor, as seen in eq. (4.4)

$$Y_f = n\sigma_f \tag{4.4}$$

In addition, the reaction yield is nothing more than the ratio between the number of the corresponding reactions that took place N_R to the total integrated neutrons impinged on the sample Φ, however during an experiment the recorded number of reactions C is smaller or equal to N_R, therefore a set of correction factors f_i must be introduced in order to get the best estimation of N_R. This leads to eq. (4.5)

$$Y_f = \frac{N_R}{\Phi} = \frac{C \cdot \prod_i f_i}{\Phi} \tag{4.5}$$

Equations (4.4) and (4.5) can be combined to provide the expression for the fission cross-section seen in eq. (4.6)

$$\sigma_f = \frac{C \cdot \prod_i f_i}{n\Phi} \tag{4.6}$$

In the present work the $^{240}Pu(n,f)$ and $^{237}Np(n,f)$ cross-sections were derived with reference to the $^{235}U(n,f)$ one, above $\sim 2keV$, in order to eliminate systematic effects. In this case the derivation of the cross-section was based on the formula seen in eq. (4.7)

$$\sigma = \frac{C}{C^{(\mathrm{ref})}} \frac{\prod_i f_i}{\prod_i f_i^{(\mathrm{ref})}} \frac{n^{(\mathrm{ref})}}{n} \frac{\Phi^{(\mathrm{ref})}}{\Phi} \sigma^{(\mathrm{ref})} \tag{4.7}$$

The correction factors f_i are generally different, depending on the experiment, thus in the present case the recorded counts C were corrected for the:

1. Self-absorption of fission fragments within the fission foils (f_{abs})
2. Rejected fission signals that lied below the introduced amplitude threshold (f_{amp})
3. Parasitic counts that contributed to the recorded yield and were attributed to fission reactions from contaminants or impurities present in the fission foils (f_{imp})
4. Counting losses occurring due to pile-up and dead-time effects (f_{DT})
5. Neutron self-shielding of the various material layers on the detector-sample stacks (f_{shield})
6. Spontaneous fission events (f_{SF})
7. Cluster decay events (f_{CD})
8. Parasitic counts that contributed to the recorded fission yield from photo-fission reactions ($f_{\gamma f}$)

Finally, the derived cross-sections will be given from the formula seen in eq. (4.8)

$$\sigma = \frac{C}{C^{(\mathrm{ref})}} \frac{f_{\mathrm{abs}}}{f_{\mathrm{abs}}^{(\mathrm{ref})}} \frac{f_{\mathrm{amp}}}{f_{\mathrm{amp}}^{(\mathrm{ref})}} \frac{f_{\mathrm{imp}}}{f_{\mathrm{imp}}^{(\mathrm{ref})}} \frac{f_{\mathrm{DT}}}{f_{\mathrm{DT}}^{(\mathrm{ref})}} \frac{f_{\mathrm{shield}}}{f_{\mathrm{shield}}^{(\mathrm{ref})}} \frac{f_{\mathrm{SF}}}{f_{\mathrm{SF}}^{(\mathrm{ref})}} \frac{f_{\mathrm{CD}}}{f_{\mathrm{CD}}^{(\mathrm{ref})}} \frac{f_{\gamma f}}{f_{\gamma f}^{(\mathrm{ref})}} \frac{n^{(\mathrm{ref})}}{n} \frac{\Phi^{(\mathrm{ref})}}{\Phi} \sigma^{(\mathrm{ref})} \tag{4.8}$$

It has to be noted that the aforementioned quantities, areal density (n) excluded, do not refer to a single incident neutron energy in the case of the present work but are energy depended factors, however for simplicity reasons the energy dependence $\sigma = \sigma(E)$ is not explicitly stated.

Below 2 keV, where the ^{235}U(std, f) does not contain broadening due to the response function of the time-of-flight spectrometer and exhibits a strong resonant behaviour that can cause artefacts when multiplied with C/C^{ref}, the cross-section was derived through the use of the EAR2 evaluated flux, normalised to the experimentally determined flux on the ^{235}U position, at the thermal point.

4.3 Time-of-flight determination

To properly reconstruct the incident neutron energy, an accurate determination of the neutron time-of-flight is deemed necessary. The observable in such measurements is not the time-of-flight itself, but rather the absolute arrival time of a signal, as explained previously in section 1.2, therefore the time-of-flight was calculated off-line.

Calculation of the time-of-flight

The time-of-flight calculation was based on the use of eq. (1.5), however for the time being the transport time t_t within the target-moderator assembly is neglected, therefore the time-of-flight t, was calculated as shown in eq. (4.9):

$$\begin{aligned} t &= t_m - t_d \\ &= \left(t_s - t_\gamma + \frac{L}{C}\right) - t_d \end{aligned} \tag{4.9}$$

where, as explained in section 1.2, t_s and t_γ refer to the times where each identified signal and the γ-flash arrived, respectively, L is the flight path, C the speed of light and t_d takes into account the neutron transport in the target-detector assembly and any possible detection delay.
The arrival time t_s was determined from the reconstruction routine as the time where the identified signal reached its peak point. As explained previously in subsection 1.4.1, in the case of a large angle emission, the charge collection was delayed, which could be taken into account in the time-of-flight determination by subtracting an average drift time of the order of 50 ns. However, since the arrival time was chosen to be the time where the signals peaked, the charge collection time was subtracted instead. This time, which can be considered to be t_d, practically corresponds to the point in time when the fission fragment escaped the sample and the signal's leading edge started to rise. In a gaussian-like signal shaping, this time can be estimated by subtracting the FWHM of the average pulse shape in the forward emission case, from the time in which the signal peaked therefore t_d, in the present notation, is actually the full width at the signal's half maximum Γ_{FIMG}, therefore eq. (4.9) becomes:

$$t = \left(t_s - t_\gamma + \frac{L}{C}\right) - \Gamma_{\text{FIMG}} \tag{4.10}$$

As discussed in subsection 3.2.3, in the case of the ^{240}Pu data, the arrival time of the γ-flash (t_γ^{FIMG}) was assigned based on the time when the proton beam impinged on the spallation target as recorded by the PKUP (t_γ^{PKUP}) taking into account the constant offset t_{offset} between the PKUP and each FIMG detector, seen in fig. 3.23. The times t_γ were determined by the reconstruction routine, at the point in time where the γ-flash signals peaked, in order to be consistent with the assignment of t_s. For the same consistency reasons, the FWHM of the γ-flash Γ_{flash}, was subtracted from the reconstructed t_γ . In the case of the $^{237}Np(n,f)$ data, there was not an evident need to use the PKUP, therefore t_γ was directly derived from the reconstruction routine.

Finally, the calculation of the time-of-flight t was based on eq. (4.11a) and (4.11b) for the $^{240}Pu(n,f)$ and $^{237}Np(n,f)$ data, respectively.

$$t = \begin{cases} (t_s - \Gamma_{\text{FIMG}}) - \left(t_\gamma^{\text{PKUP}} - t_{\text{offset}} - \Gamma_{\text{flash}}\right) + \dfrac{L}{C} & \text{(4.11a)} \\[2ex] (t_s - \Gamma_{\text{FIMG}}) - \left(t_\gamma^{\text{FIMG}} - \Gamma_{\text{flash}}\right) + \dfrac{L}{C} & \text{(4.11b)} \end{cases}$$

Uncertainty in the time-of-flight determination

The time of flight of flight determination is subject to uncertainties, as is the case with quantities which are derived from observables. Throughout the present determination, the following three parameters mainly affect the uncertainty in the time-of-flight:

i. The time reconstruction from the routine itself
ii. The t_γ assignment
iii. Uncertainty in the flight path length

As far as (i.) is concerned, the pulse shape fitting performed by the reconstruction routine along with the established parameters, provides an accurate determination of the arrival time. However, as stressed out in subsection 3.1.2, a high counting rate can lead to pile-up. The reconstruction routine was designed in such a way that it did not perform a double fit in the recognised pulses, but rather fitted the preceding pulse in the first iteration and then the remaining residual. To estimate the effect on the arrival time reconstruction of this approach, high and low counting rate data from the $^{237}Np(n,f)$ campaign were compared. In particular, time-of-flight spectra recorded from the ^{235}U sample for dedicated and parasitic bunches, were scaled and the position in time of resonances was compared. As seen in fig. 4.1a, for large time of flights/low neutron energies, the resonances that were resolved are perfectly aligned in time concerning dedicated and parasitic pulses that differ by an average factor of 2 in intensity. The same was observed for small time-of-flights and high neutron energies, as can be seen in fig. 4.1b where in this case as well, the oxygen structures observed in the recorded counting spectra, are aligned in time. It can be assumed therefore that the reconstruction routine did not introduce any additional systematic uncertainties.

It was previously pointed out that t_γ was assigned based on the PKUP. As seen in fig. 3.23, the distributions of the difference between t_γ^{FIMG} and t_γ^{PKUP} had a FWHM Γ of 14 ns. Assuming a gaussian dispersion, the uncertainty δt_γ in the assignment of t_γ was estimated to be 6 ns and was calculated using eq. (4.12).

$$\delta t_\gamma = \frac{\Gamma}{2\sqrt{2\ln 2}} \tag{4.12}$$

The determination of the flight path L, is also subject to uncertainties, as will be explained later in the text. However, even an uncertainty of the order of 0.3 m in the region of 19.5 m results in a difference of merely 1 ns in the calculation of t_γ , which is smaller than the sampling time, therefore the uncertainty of the flight path L was considered negligible.
Finally, the total estimated uncertainty in the time-of-flight determination was ascribable to the t_γ assignment from the PKUP and had a constant value of 6 ns. Assuming an effective flight path of 19.5 m, this is translated in an incident neutron energy uncertainty that varies from 10^{-5}% in thermal energies up to 1% in the MeV region, as can be seen in fig. 4.2.

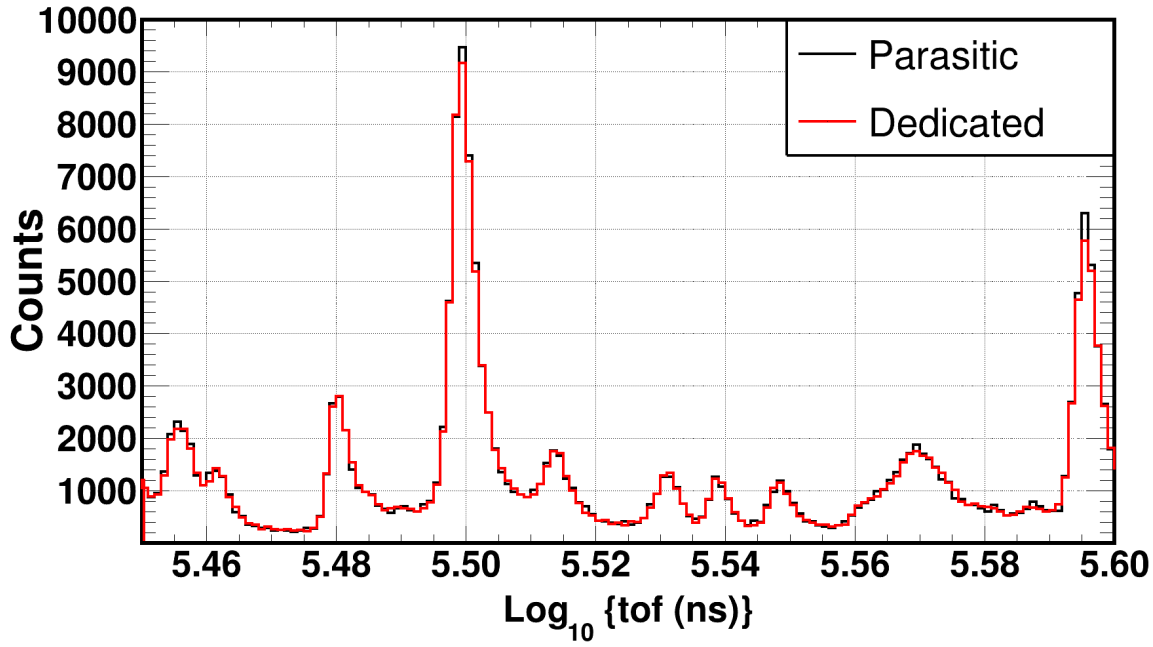

(a) Low incident neutron energy

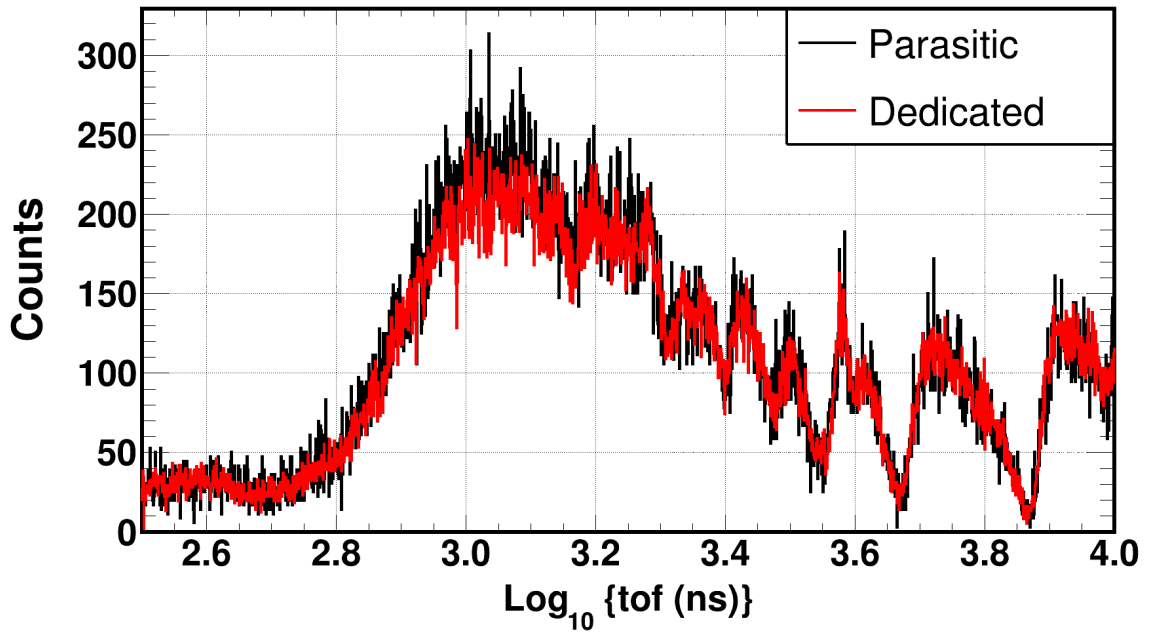

(b) High incident neutron energy

Figure 4.1: *Reconstructed time-of-flight spectra from the ^{235}U sample during the $^{237}Np(n,f)$ campaign. The alignment in time of prominent structures such as the resonances in the ^{235}U (n,f) cross-section (a) and the oxygen dips in the neutron flux (b) in parasitic and dedicated mode, indicate that there were not systematic uncertainties introduced in the time-of-flight determination, due to the reconstruction routine.*

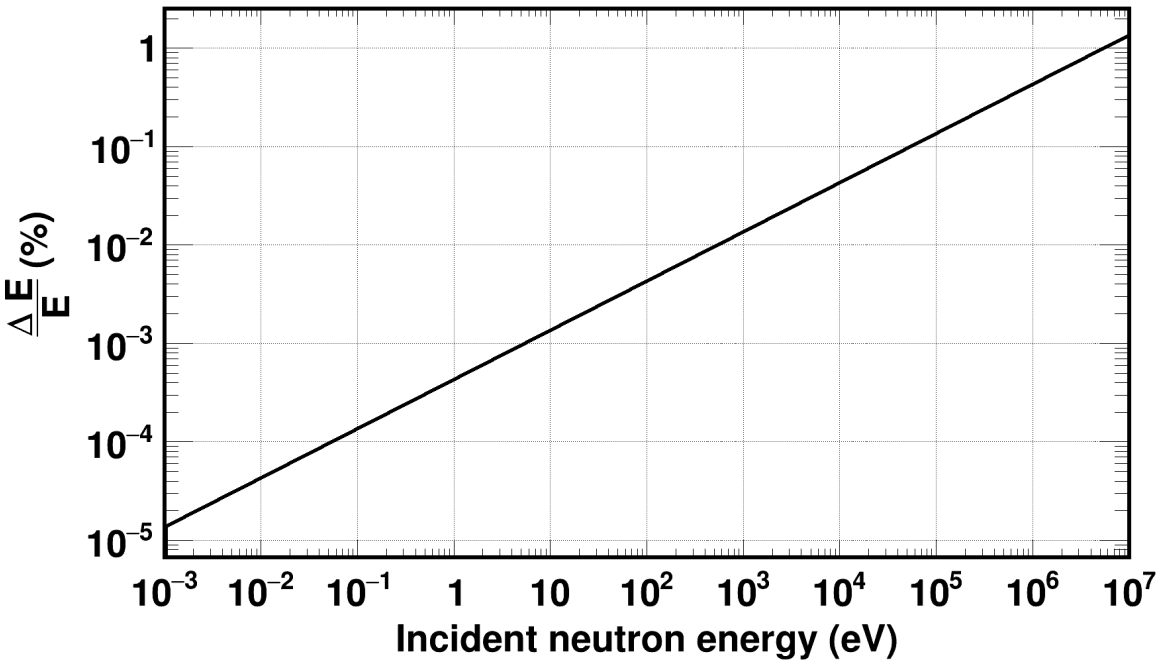

Figure 4.2: *Total estimated uncertainty in the incident neutron energy reconstruction, assuming an effective flight path of* 19.5 *m and a* 6 *ns uncertainty in the time-of-flight determination.*

4.4 Determination of the neutron flight path

An important parameter in the incident neutron energy calculation, is the determination of the neutron flight path. Two different and independent methodologies were used to retrieve this information using well known resonances in the fission cross-section of ^{235}U and Monte Carlo simulations that include the response function of the facility.

4.4.1 Estimation of an effective flight path: The resonance method

A means of estimating the neutron flight path, without prior knowledge of the response function of the time-of-flight spectrometer, is based on the use of well known low incident neutron energy resonances in the fission cross-section and the reconstructed time-of-flight spectrum. More specifically, the time-of-flight spectra of ^{235}U were analysed in both campaigns and high time-of-flight resonances $(1, 2, 3, \ldots$ from right to left), seen in fig. 4.4a, were matched with the corresponding low energy ones$(1, 2, 3, \ldots$ from left to right), seen in fig. 4.4b, in the ^{235}U (n,f) ENDF/B-VIII.0 cross-section.

The experimental time-of-flight t is related to the incident neutron energy E through the non-relativistic relation shown in eq. (4.13) where m is the neutron mass and L the neutron flight path. The relation therefore between the resonance energy obtained from ENDF/B-VIII.0 $E_{\text{ENDF/B-VIII.0}}$ and the square of the inverse of time-of-flight t^{-2} is expected to be linear, whereas the slope is related to the flight

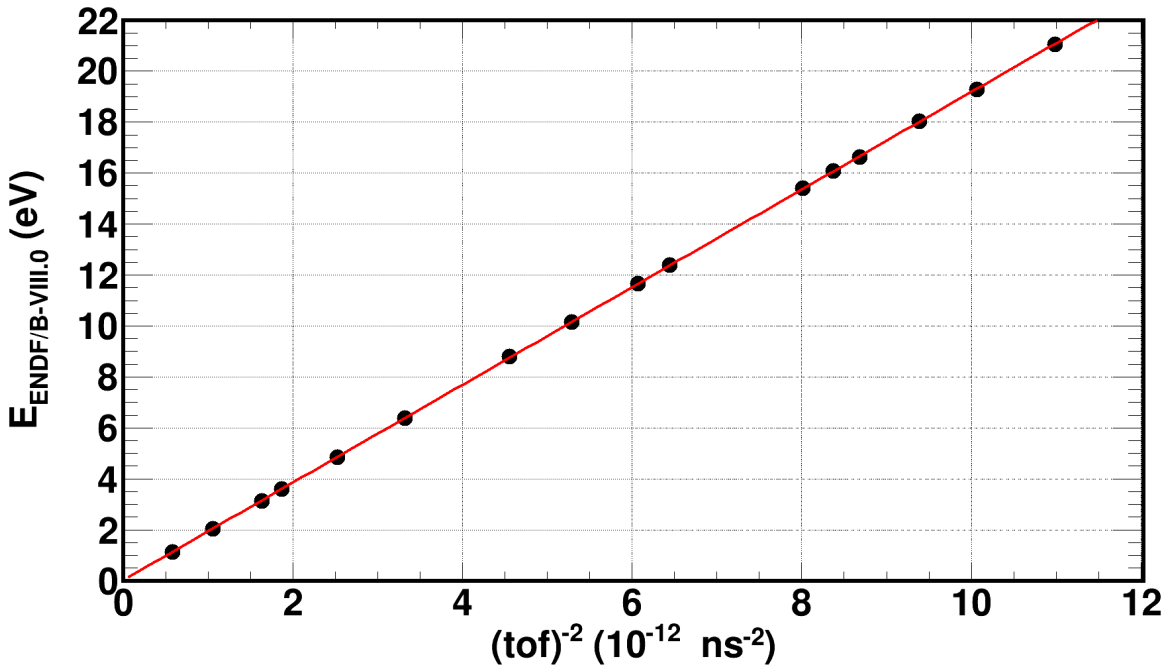

Figure 4.3: *Resonance energy of the ^{235}U (n,f) cross-section with respect to the ^{235}U time-of-flight resonance in the $^{240}Pu(n,f)$ experiment. The relation between resonance energies and the corresponding time-of-flight was expected to be linear which was confirmed by the experimental data. The slope of the fit provides an estimation of the effective neutron flight path.*

path L. This linearity was used to extract the path L by fitting $(t^{-2}, E_{\text{ENDF/B-VIII.0}})$ data as seen in fig. 4.3.

$$E = \frac{mL^2}{2}\frac{1}{t^2} \tag{4.13}$$

Seventeen resonances in total, were used up to a neutron energy of 21 eV, which was a sufficient quantity of data points to perform the fits. Higher energy resonances up to 50 eV were also used without significantly affecting the extracted flight path, however, since in higher energies the response function of the time-of-flight spectrometer could have a significant effect, it was decided to extract a flight path using a small energy range.

As seen in fig. 4.3, where the data was obtained from the ^{235}U sample on the $^{240}Pu(n,f)$ measurement, the linear relation between resonance energies and the corresponding time-of-flight was confirmed. Linear fits were therefore performed, in the ^{235}U samples from both experimental campaigns and the flight paths L were estimated to be 19.5 m in both measurements. The uncertainty of the fit was less than 0.1%, therefore it was considered negligible.

As illustrated in fig. 1.21, the ^{235}U foils were placed at the beginning of the sample stacks with respect to the neutron beam, in both experimental campaigns. The distances between the components of the stack, such as the spacing between each detector-sample modules and the drift gap, as well as the thickness of all materials that were housed within the fission chamber were measured with a caliper therefore are accurately known. Subsequently, the flight paths for the remaining actinide foils in both campaigns, were calculated by adding the known geometrical

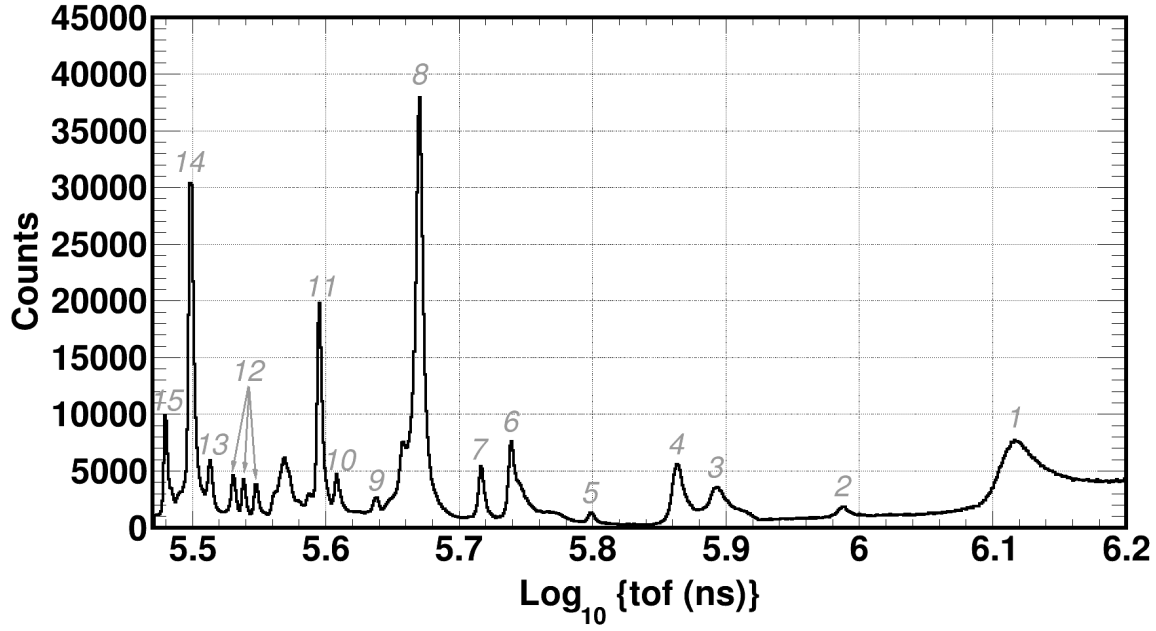

(a) ^{235}U *time-of-flight spectrum recorded during the* $^{240}Pu(n,f)$ *experiment*

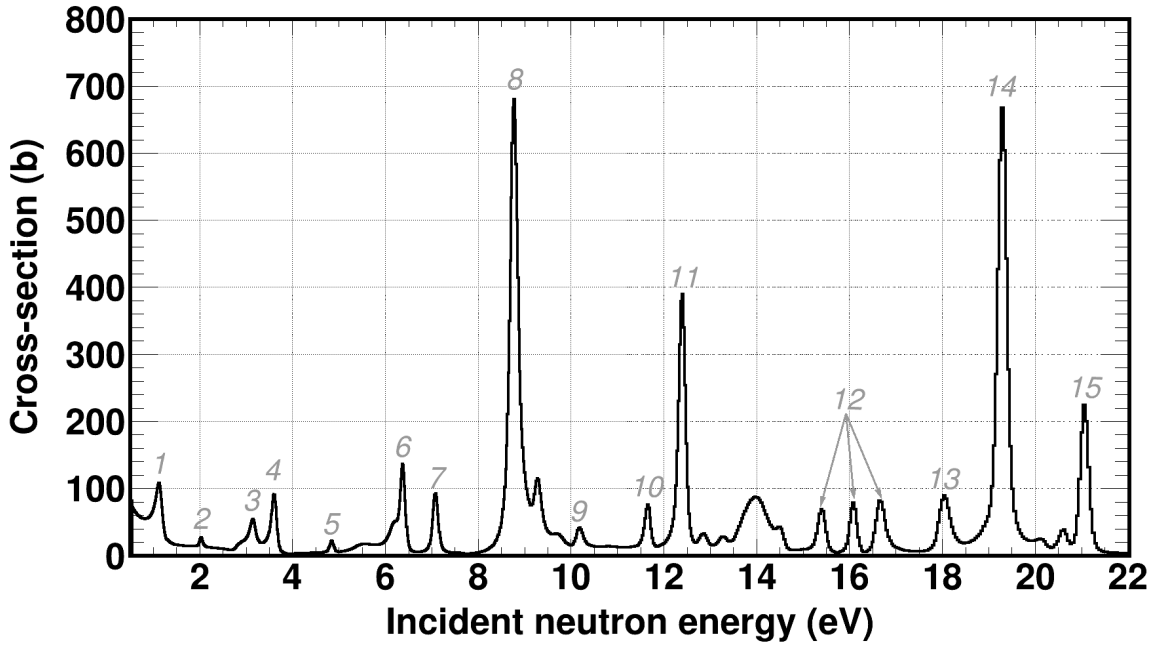

(b) The evaluated ENDF/B-VIII.0 neutron induced fission cross-section of ^{235}U

Figure 4.4: *Matching well-known resonance energies found in the evaluated cross-section of a reaction with the corresponding position in the experimental time-of-flight spectrum, can provide an estimation of the neutron flight path, by means of fitting these data-sets using the non-relativistic relation between energy and time.*

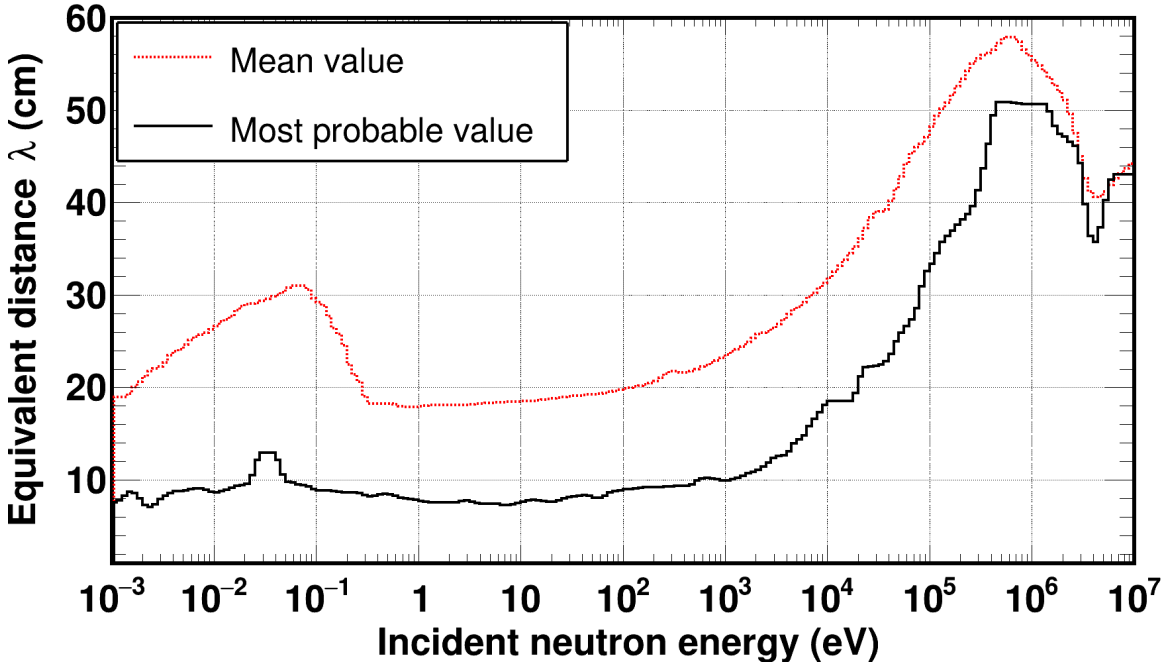

Figure 4.5: *Mean and most probable equivalent distance λ of the EAR2 response function $R(\lambda, E)$ as calculated from Monte Carlo simulations. The behavior of the time-of-flight spectrometer was considered smooth in the energy range from 1 eV - 1 keV, therefore the resonance method can be safely applied.*

distances to the extracted effective flight path.

4.4.2 Ascertainment of the effective flight path: The resampling method

The method described previously provides an effective flight path estimation, which is certainly accurate in the energy range within the energy region of the selected resonances. In addition, in the case where the response function of the time-of-flight spectrometer is unknown, but is not expected to show prominent structures, such as the one for n_TOF EAR2, which is seen in fig. 4.5, the aforedescribed methodology can be proven to be reliable. However, in higher neutron energies the equivalent distance neutrons travel inside the target-moderator assembly increases dramatically, therefore a different approach is necessary. In this context a methodology was developed by Dr. V. Vlachoudis at CERN which is based on Monte Carlo simulations and an optical transport from the scoring plane to the position of the detection system.

More specifically, the spallation process was replicated via Monte Carlo simulations using the FLUKA code and neutrons were scored at a distance of 37.2 cm from the center of the lead target on their way to EAR2, as seen in fig. 4.6. From the moment each neutron was generated in FLUKA with a production energy E_{prod}, it was monitored within the target-moderator assembly until it reached the scoring plane after a time t_m, with an energy E, which is smaller or equal to E_{prod}. The moderation time t_m, which is predicted by the Monte-Carlo simulations, can be

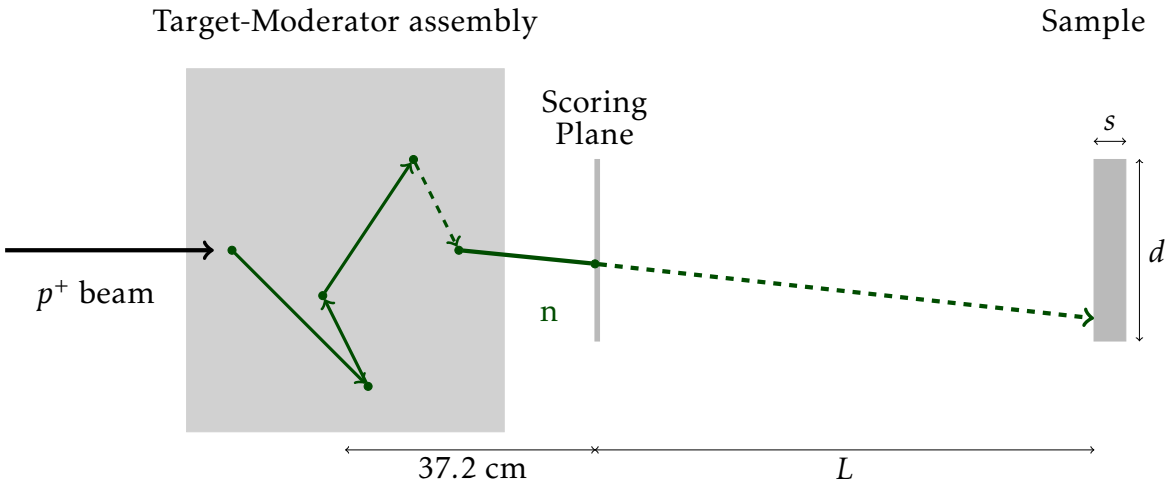

Figure 4.6: *Graphical layout of the principle of the resampling method. Neutrons are scored after the spallation target and then optically propagated to the fission foil. The flight path L was left as a free parameter which was determined by matching the resonance positions over a broad energy range.*

converted to an effective length for each simulated neutron as it was described in 1.2.1 and seen in fig. 1.12.

At the position of the scoring plane, apart from the neutron energy E that will potentially cause fission, the directional cosines are given which were used afterwards during the optical propagation towards the actinide sample. The optical propagation or neutron resampling was based on a user defined angular acceptance θ, which was dictated by the collimation system and had a value of 10° in both campaigns. Neutrons with trajectories that did not fulfil the collimation conditions defined by this angle, were discarded. The characteristics of the fission foil (mass, size, shape and material) are external user parameters while the distance from the scoring plane L is left as free parameter to calculate the expected reaction rate in the time-of-flight or energy domain, depending on the user request, at the distance L for a given sample and reaction based on ENDF/B-VIII.0 evaluations.

The simulated time-of-flight spectrum includes the effect of the resolution function on the reaction yield, therefore it can be directly compared to the experimental one. It was empirically proven that a unitary distance L indeed existed, such that the position of all resonances and dips in the simulated and experimentally measured time-of-flight spectra, was aligned over a broad energy range from eV ($\sim$ 1.5 ms) up to 2 MeV ($\sim 1\mu$s), as can be seen in fig. 4.7 in the case of ^{235}U during the $^{240}Pu(n,f)$ experimental campaign. This distance was found to be 19.5 m in the case of both experimental campaigns.

It has to be noted that this methodology does not provide deconvoluted time-of-flight spectra, therefore the conversion from time to energy using the flight path L still includes effects of the response function on the reaction yield. In view of this, the provided cross-section, which is not an observable itself but rather a calculated quantity based on a model as will be explained in the text, will not be provided in the so-called "true neutron energy", since this would require a deconvolution from the response function which is an ill-posed mathematical problem and beyond the

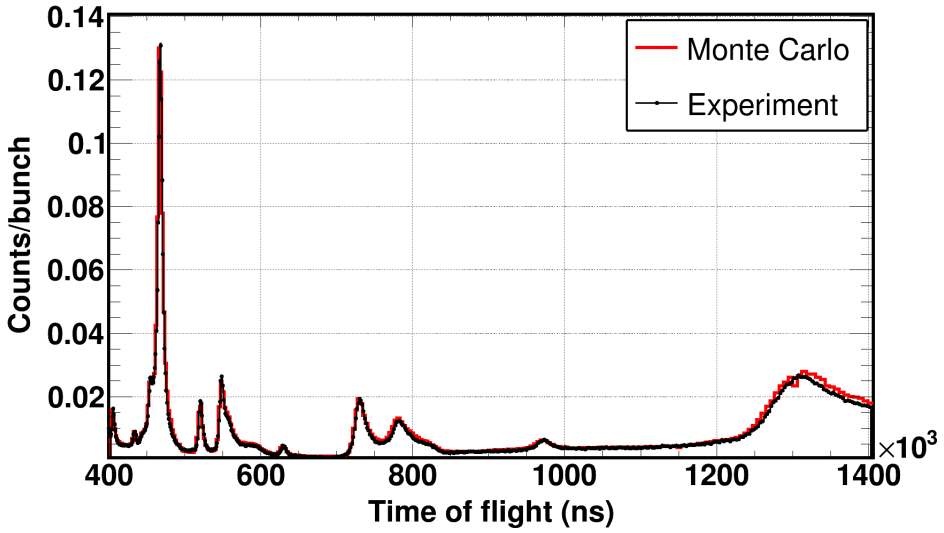

(a) 1 – 12 *eV*

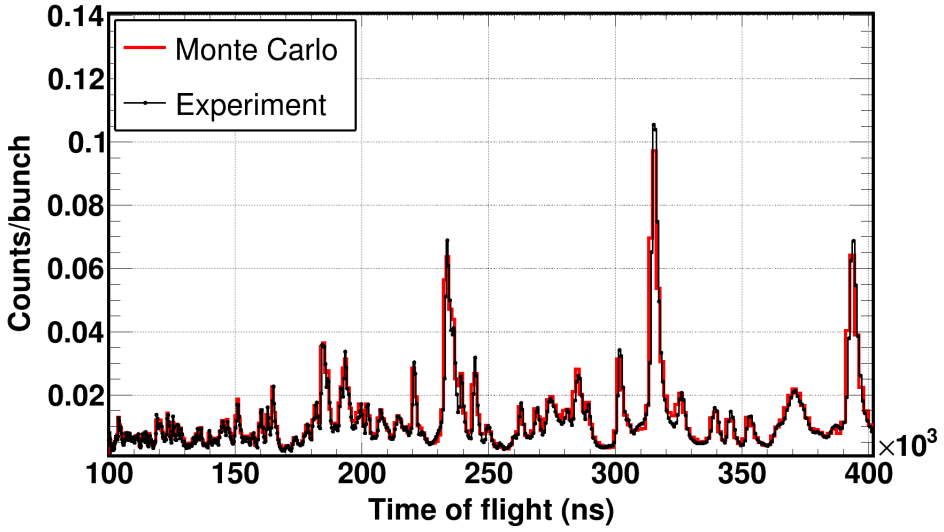

(b) 12 – 200 *eV*

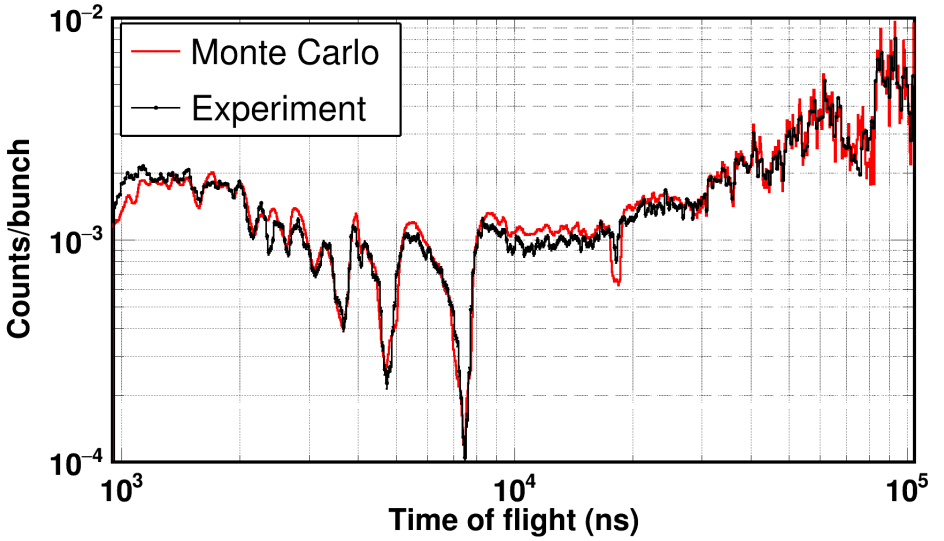

(c) 200 *eV* - 2 *MeV*

Figure 4.7: *Expected time-of-flight spectrum as calculated by the resampling routine in the case of ^{235}U (n,f) reaction at a distance of $L = 19.5$ m from the centre of the lead spallation target in comparison to the recorded one during the $^{240}Pu(n, f)$ campaign. The matching in the resonance position is very satisfactory over a wide energy range from 1 eV up to 2 MeV.*

scope of the current research.

Furthermore, the effect of the response function is far more dramatic in regions where appreciable variations exist, therefore the provided cross-section above the effective fission threshold was not expected to be far from truth. In the case of the resolved resonance region, the provided resonance parameters that were extracted from R-Matrix calculations, took into account the response function by means of a numerical convolution on the theoretical cross-section performed by the SAMMY code.

Finally, the compilation in the EXFOR database and evaluation of neutron time-of-flight data does not require a reaction cross-section given in the true neutron energy, as long as the response function of the time-of-flight spectrometer is provided.

4.5 Amplitude threshold and self-absorption corrections

As described previously in ch. 2, Monte Carlo simulations were performed to estimate the self absorption of fission fragments within the foils as well as the fraction of rejected fission signals due to the introduction of an amplitude threshold in the analysis. The simulations incorporated a nominal description of the fission foil composition (i.e. no additional moisture was considered) and the detection medium, as described in detail in ch. 2.

4.5.1 Self-absorption

To estimate the fraction of fission fragments that were absorbed within the sample volume, the Monte Carlo simulations described in ch. 2 were implemented. The estimation was based on scoring the energy deposited by the fission fragments on the gas and gating at zero entries. A zero energy deposition implied that the specific fission fragment never managed to reach the gas and was most probably absorbed.

In addition, a zero deposition could occur when the fission fragment was emitted perpendicularly to the axis of the gas volume (i.e. at an angle of 90°), and although this probability is much smaller, it was also taken into account.

The estimated correction factors for the self absorption f_{abs} were estimated to be less than 0.1% for all fission foils in both experimental campaigns, therefore they were considered to be negligible. Likewise, since the `FLUKA` code is considered to be a standard tool for the propagation of charged particles in matter, the estimated uncertainty was also considered to be negligible.

4.5.2 Amplitude cut

To avoid contaminating the time-of-flight spectrum with either α-particle events or residuals from the γ-flash subtraction, an amplitude threshold was introduced in

the analysis. This threshold was chosen in a way to completely reject the aforementioned parasitic contributions to the fission yield so that the time-of-flight spectra consisted only of true fission events as seen in fig. 4.8, therefore a proper correction ought to have been applied and was based on Monte Carlo simulations.

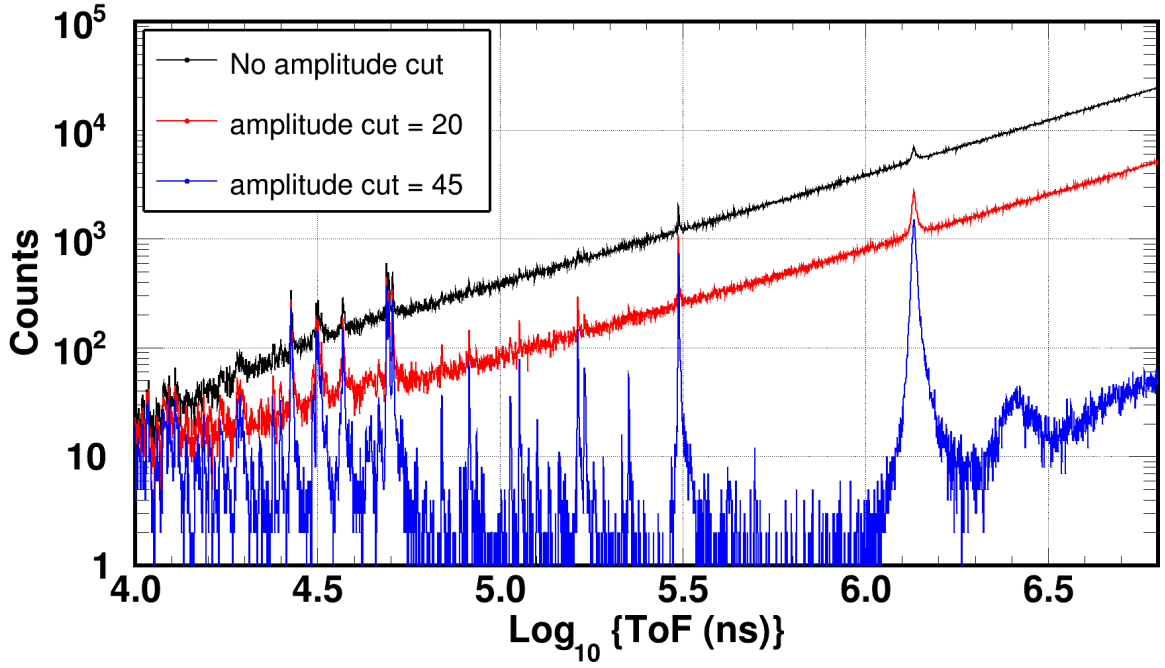

Figure 4.8: *The introduction of an amplitude threshold in the analysis aided in rejecting non-fission events and therefore revealing resonance structures in the time-of-flight spectra. The image shown in the present figure concerns the time-of-flight spectrum of a* ^{240}Pu *sample (#3) in the incident neutron energy region between* 50 *meV and* 20 *keV.*

More specifically, the reproduction of the experimental amplitude spectra, made possible the estimation of the expected fission counts that lied below the applied amplitude threshold. According to the followed strategy, as explained previously in the text, energy independent thresholds were applied, therefore the experimental amplitude spectra were constructed from the full time-of-flight range.

The estimation of the correction factors f_{amp} was based on the ratio calculation between the amplitude spectrum integral that lies below the amplitude threshold to the total one. It has to be stressed that the aforementioned calculations were performed on the simulated spectra.

To study the sensitivity of the amplitude cut correction, several thresholds were applied and the corresponding correction factors f_{amp} were estimated. As seen in a typical amplitude spectrum from a ^{240}Pu sample in fig. 4.9, the thresholds were applied above the separation valley between the α-particle and fission fragment parts of the spectrum. In addition, to ensure that the contribution of α-counts to the fission yield is practically zero, the thresholds were applied above the point where the tails of the beam-off amplitude spectra ended, as illustrated in fig. 3.25. As seen in fig. 4.9, the fraction of rejected fission signals was of the order of 10%.

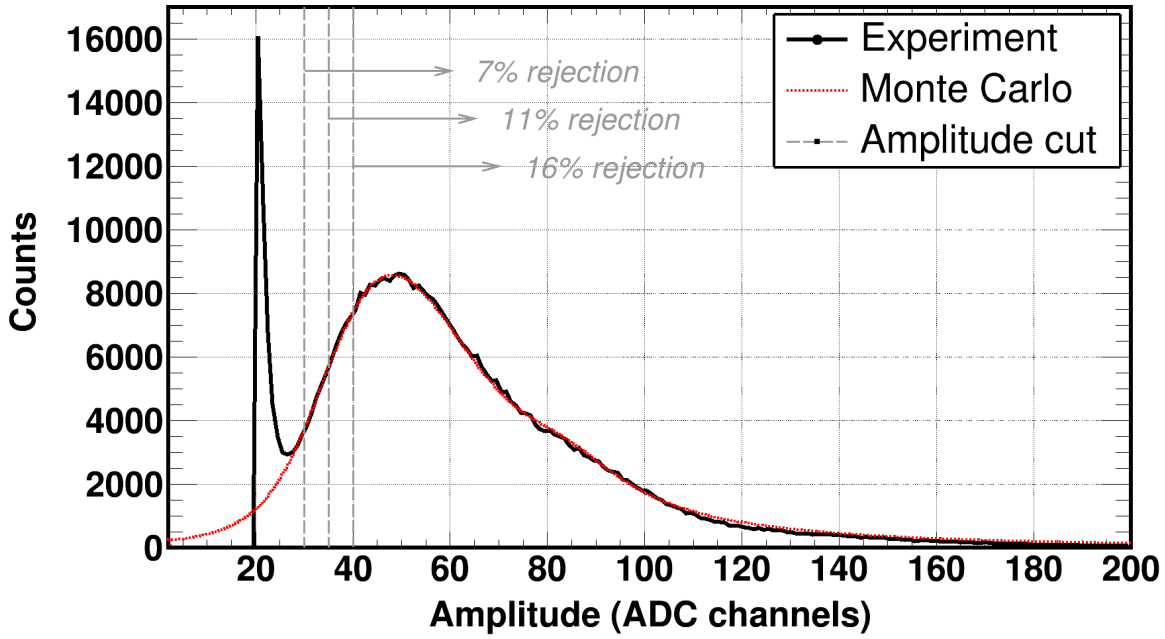

Figure 4.9: *Experimental and simulated amplitude spectra obtained from a ^{240}Pu sample (#5). The amplitude cut was applied above the α-particle and fission fragment separation valley to ensure that no α-counts contributed to the fission yield. Three different thresholds along with the corresponding fraction of rejected fission events are shown.*

To estimate any possible systematic effects on the correction factors, firstly the simulated and experimental integrals above the several amplitude thresholds were put to comparison and a satisfactory agreement was observed within 0.1%.

In addition, as described in subsec. 2.4.3, the ^{238}U amplitude spectra were used to estimate any possible systematic effects in the low amplitude part of the spectra. A constant extrapolation tail was considered for amplitudes smaller that the applied ADC threshold in order to estimate the fraction of rejected fission signals on the experimental amplitude spectra and compare it to the corresponding simulated one. Any deviation between the two correction factors indicated systematic effects which had a linear dependency to the applied threshold as seen in fig. 4.10 thus the systematic uncertainty was reduced with the introduction of a higher amplitude threshold.

The information shown in fig. 4.10, regards the sensitivity study performed on the ^{238}U sample from the $^{240}Pu(n,f)$ campaign. Since neither the detectors in each campaign were operated on the same gains nor the ADC resolution used in both campaigns was the same, the systematic uncertainty could not be propagated to the rest of the detectors. However, the ratio between the most probable amplitude found in an amplitude distribution to the different amplitude threshold applied provided a means of propagating the systematic uncertainties on the rest of the detectors.

It has to be noted that since the derived cross-section was determined relevant to the reference $^{235}U(n,f)$ reaction, the systematic uncertainties cancelled out, however the discussion that took place practically resulted in a proposed methodology to estimate such systematic effects.

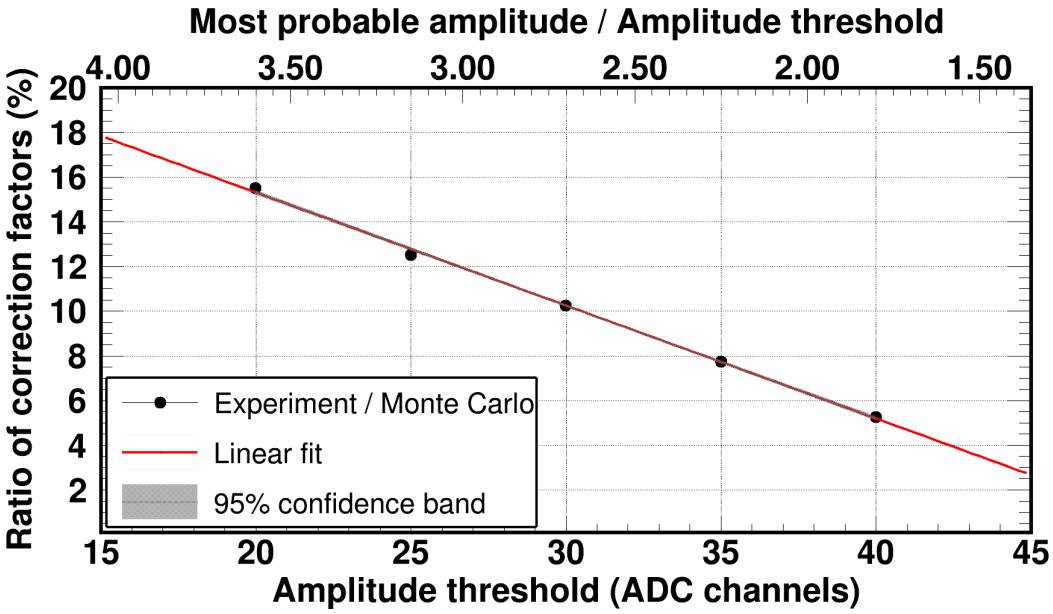

Figure 4.10: *The ratio of the correction factors between the experimental and the simulated amplitude spectra was found to be disproportionate to the applied threshold, indicating that for high amplitude thresholds the systematic uncertainty was reduced. The ratio between the most probable amplitude to the applied amplitude threshold provided a propagation of the systematics to detectors operating at different gains and/or read by ADCs with different resolutions.*

Table 4.1: *Applied amplitude thresholds along with the estimated correction factors and the corresponding uncertainties for the samples used in both experimental campaigns.*

Sample		Threshold (ADC channels)	Correction (%)	Uncertainty (%)
$^{240}Pu(n,f)$ campaign				
^{235}U		20	4.0	5
^{240}Pu	(#5)	30	7.0	5
^{240}Pu	(#4)	50	11.5	10
^{240}Pu	(#3)	45	9.0	10
^{238}U		20	2.0	15
$^{237}Np(n,f)$ campaign				
^{235}U		50	0.5	10
^{238}U	(#2)	150	6.5	7
^{237}Np	(#3)	150	58	15
^{237}Np	(#4)	100	7.0	9
^{237}Np	(#5)	100	10.0	15
^{237}Np	(#6)	300	3.0	10
^{238}U	(#8)	150	3.0	10
^{237}Np	(#9)	200	5.5	10

Finally, in table 4.1 the applied thresholds and the corresponding correction factors are provided accompanied by the estimated uncertainties which were extracted through the means of the variation of the smoothing parameters in eq. (2.8), within their uncertainties.

4.6 Contribution of contaminants

As illustrated in tables 1.3 and 1.4, despite the high purity of the samples, contaminants and impurities did exist, whose contribution on the recorded fission yield was taken into consideration.

In both campaigns, the contribution of impurities was taken into account by "weighting" the ENDF/B-VIII.0 evaluated (n,f) cross-section $\sigma^{(i)}$ of each contaminant found in the samples to its reported atomic abundance $f^{(i)}_{\text{abun}}$, as seen in eq. (4.14).

$$\sigma^{(i)}_{w} = f^{(i)}_{\text{abun}} \cdot \sigma^{(i)} \tag{4.14}$$

Subsequently, since the correction factors f_{imp} were applied point-wise in terms of the incident neutron energy E, the "weighted" cross-sections $\sigma^{(i)}_{w}$ were summed at each energy point. Finally, the energy dependent correction factors for the contribution of impurities $f_{\text{imp}}(E)$ were calculated as the ratio of the "weighted" cross-sections between the sample in study to the sum of the isotopes found in the sample (including the isotope under study), as seen in eq. (4.15), where the correction factor for the ^{240}Pu samples is shown, as an example.

$$f_{\text{imp}} = \frac{\sigma^{^{240}Pu}_{w}}{\sum_i \sigma^{(i)}_{w}} \tag{4.15}$$

4.6.1 Correction factors for the $^{240}Pu(n,f)$ campaign

The ^{240}Pu samples used were 99.89% pure, however even a small amount of fissile isotopes (i.e. ^{239}Pu) was enough to dwarf the recorded fission yield attributed to ^{240}Pu , as illustrated in fig. 4.11, where the "weighted" cross-sections $\sigma^{(i)}_{w}$ of the several contaminants (i) found in the samples is shown. It has to be noted that the higher "weighted" cross-section of an isotope, the higher the corresponding yield.

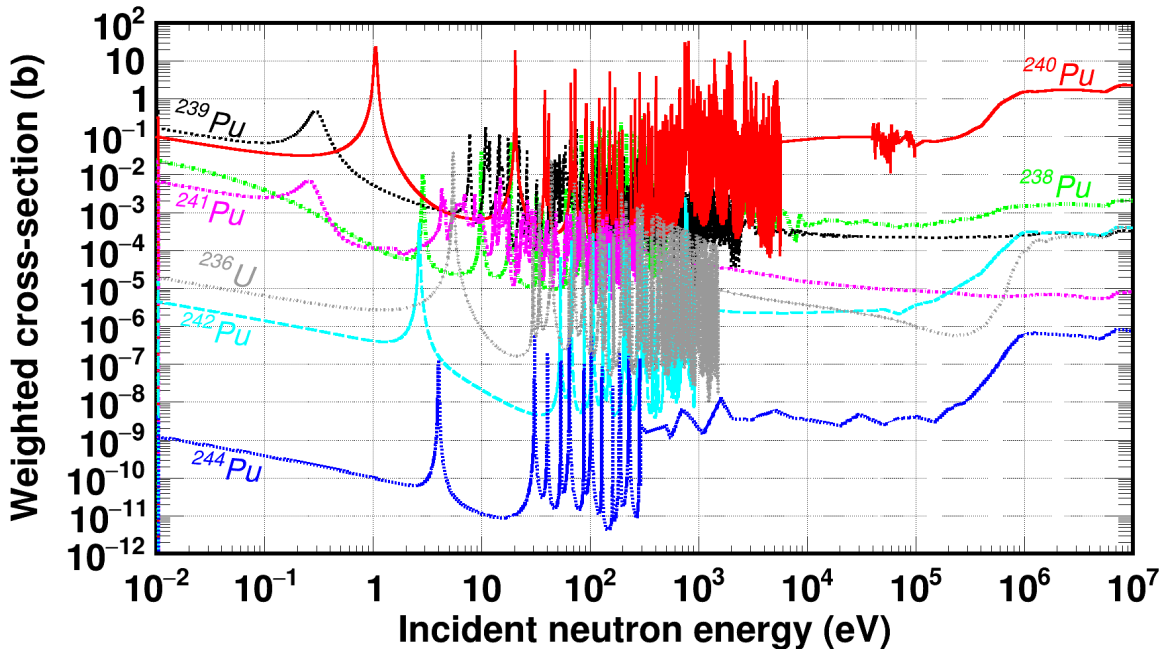

Figure 4.11: *Weighted fission cross-sections for the isotopes present at the ^{240}Pu samples at the time of the measurement. The higher the weighted cross-section for a given isotope, the higher the expected fission yield, therefore at lower energies the contribution of parasitic reactions is significantly higher than the one under study. The presence of ^{236}U is justified due to the decay of the parent ^{240}Pu .*

A closer examination of fig. 4.11 would reveal that apart from the several plutonium isotopes, seen also in table 1.3, the weighted cross-section of ^{236}U was also calculated since it is the daughter nucleus formed when ^{240}Pu decays through the emission of an α-particle. Given the 6541 years half life of ^{240}Pu and the 3.5-year period elapsed from the samples' characterisation to the measurement, 0.04% of the initial nuclei had decayed to ^{236}U at the time of the experiment, which was the estimated level of the ^{236}U contamination on the ^{240}Pu samples.

Finally, the formula seen in eq. (4.15) was applied point-wise and the common correction factor for the ^{240}Pu samples was calculated from thermal energies up to 10 MeV, as seen in fig. 4.12 and applied to the recorded counting spectra. In fig. 4.13, where two counting spectra are shown before and after the correction concerning the #3 ^{240}Pu sample, it is evident that at higher energies the correction is negligible as opposed to lower ones, where at specific resonance energies, the recorded counts were mainly attributed to contaminants.

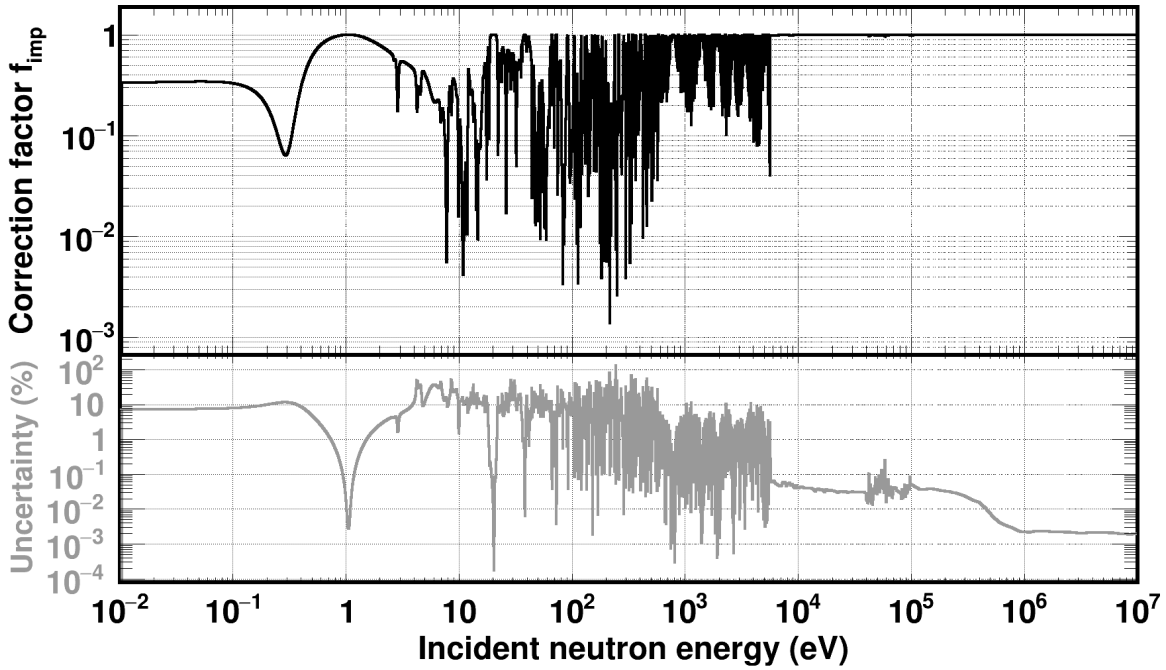

Figure 4.12: *Correction factor f_{imp} (top panel) that was applied to the ^{240}Pu recorded counting spectra. The correction was significant in the thermal region and in the resonances of contaminants. The bottom panel shows the total estimated uncertainty of the correction factor f_{imp}.*

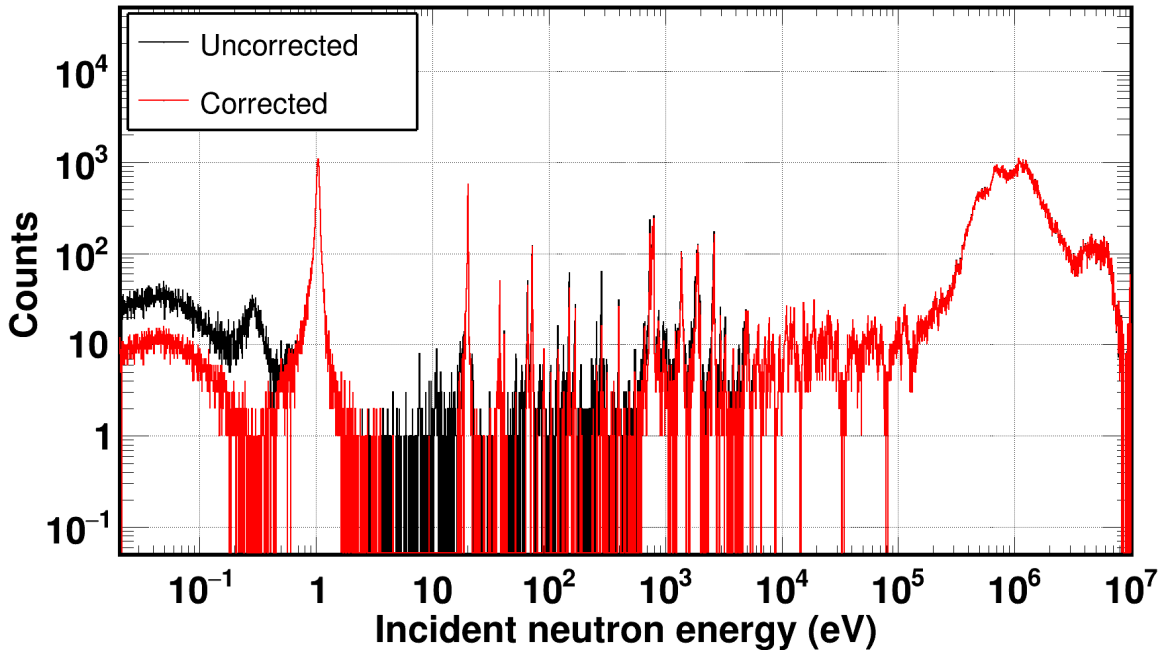

Figure 4.13: *Counting spectra prior and after the correction due to impurities concerning the ^{240}Pu #3 sample. It is evident that the contribution of contaminants is significant at resonance energies in their corresponding fission cross-sections.*

It has to be noted that since impurities were also present on the ^{235}U sample, the weighted cross-sections were calculated as well and as seen in fig. 4.14, the

$^{235}U(n,f)$ weighted cross-section was found to be at least two orders of magnitude higher that the corresponding cross-sections of the reported contaminants, therefore the correction was considered negligible.

Similarly to the ^{240}Pu isotope, the decay of ^{235}U to ^{231}Th, with a half-life of 7.038×10^{8} y was considered, however, its long half-life and much higher (n,f) cross-section compared to the ^{231}Th one, made the correction negligible as well.

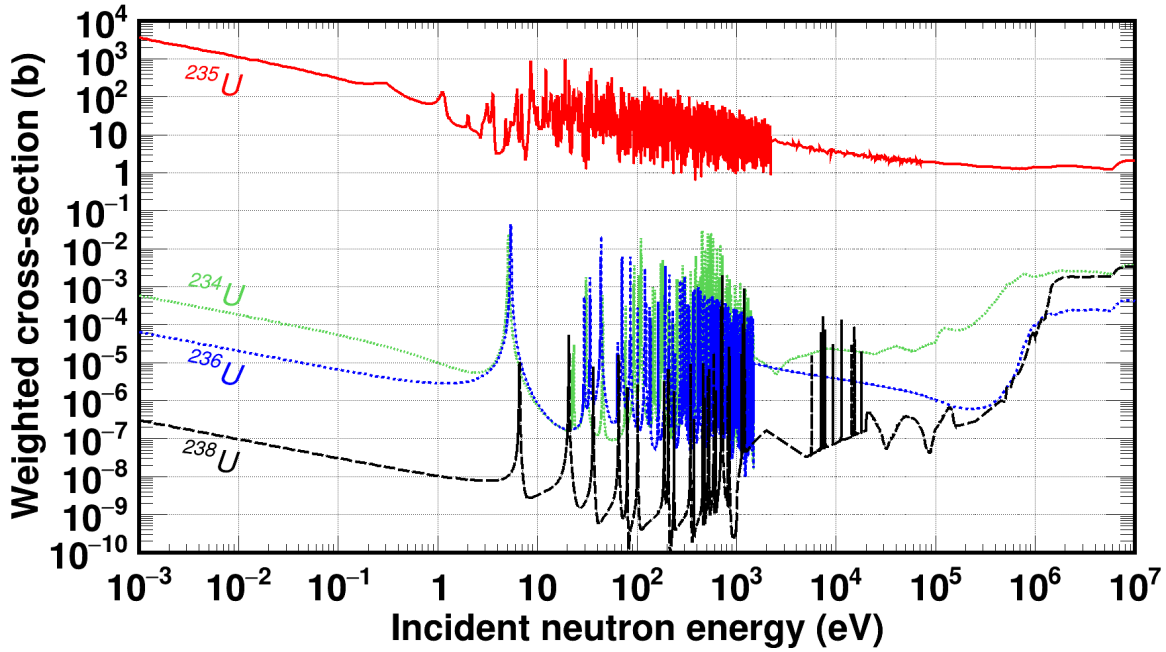

Figure 4.14: *Weighted fission cross-sections regarding the ^{235}U sample from the $^{240}Pu(n,f)$ campaign. It is evident that the contribution of parasitic counts to the fission yield of ^{235}U , is negligible.*

4.6.2 Correction factors for the $^{237}Np(n,f)$ campaign

Similarly to the $^{240}Pu(n,f)$ case, the counting spectra were corrected in terms of contribution of parasitic reactions to the fission yield. In this case, however, the ^{237}Np samples provided by JRC-Geel were rather oddly reported to be 100% pure, therefore no correction was applied. As will be explained later in the text, contaminants were proven to be present, however they are not quantified up to present. The ^{237}Np sample provided by IPN-Orsay, was reported to have plutonium contaminants, therefore the corresponding weighted cross-sections were calculated and seen in fig. 4.15.

In both reference samples, impurities were reported, therefore the weighted cross-sections and the corresponding correction factors were calculated. In the ^{235}U case, the contribution of parasitic counts was negligible as expected and seen in fig. 4.16 whereas for the ^{238}U samples, the thermal and resonance regions were dominated by the fission reaction on the fissile ^{235}U , as illustrated in fig. 4.17. Finally, the correction factor f_{imp} applied to the ^{237}Np (IPN-Orsay) sample along with the estimated uncertainty, explained in 4.6.3 can be seen in fig. 4.18.

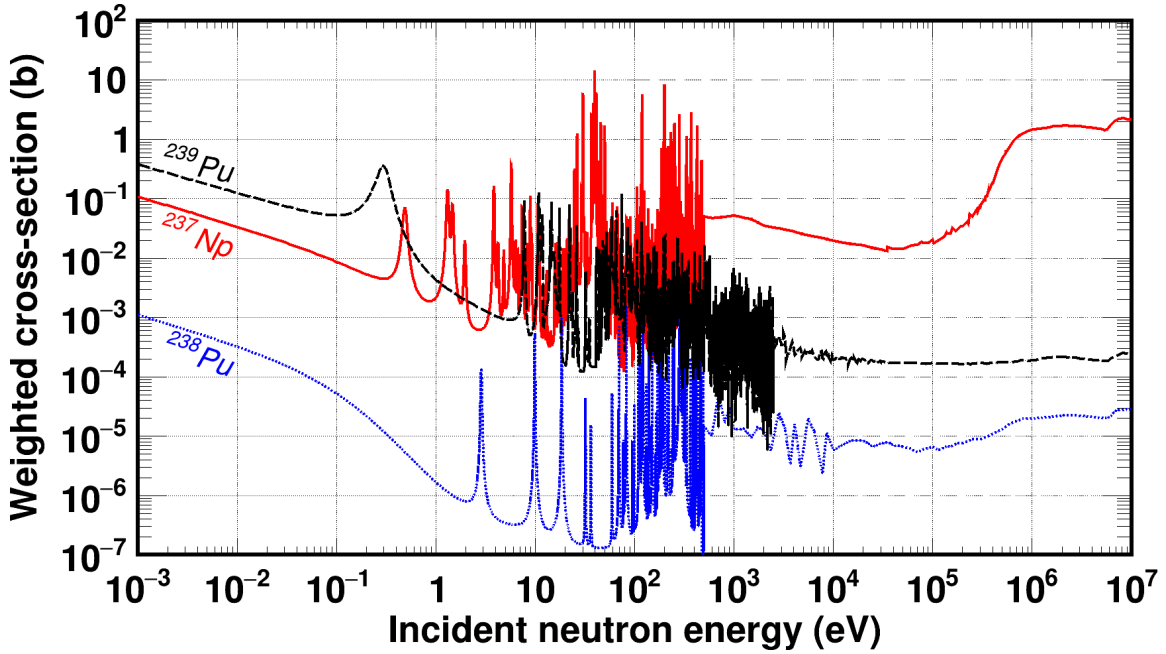

Figure 4.15: *Weighted fission cross-sections regarding the ^{237}Np sample provided by IPN-Orsay. It is evident that the contribution of parasitic counts was mainly attributed to the fissile ^{239}Pu and was significant in the thermal region.*

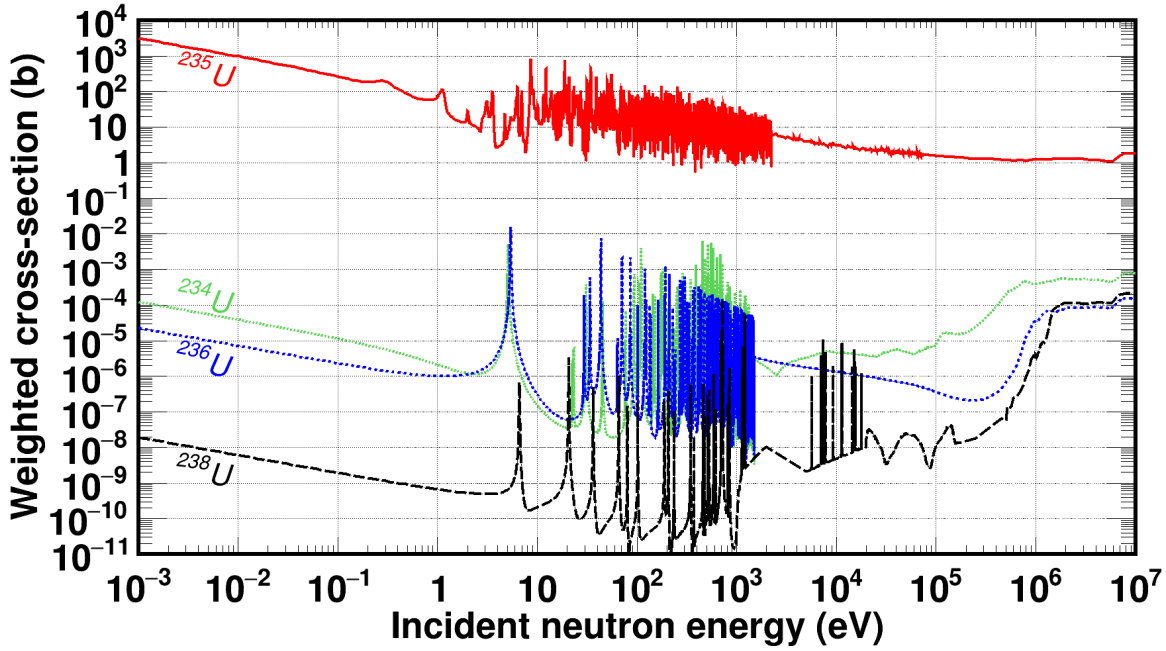

Figure 4.16: *Weighted fission cross-sections regarding the ^{235}U sample provided by JRC-Geel. The contribution of parasitic counts to the fission yield of ^{235}U , is negligible.*

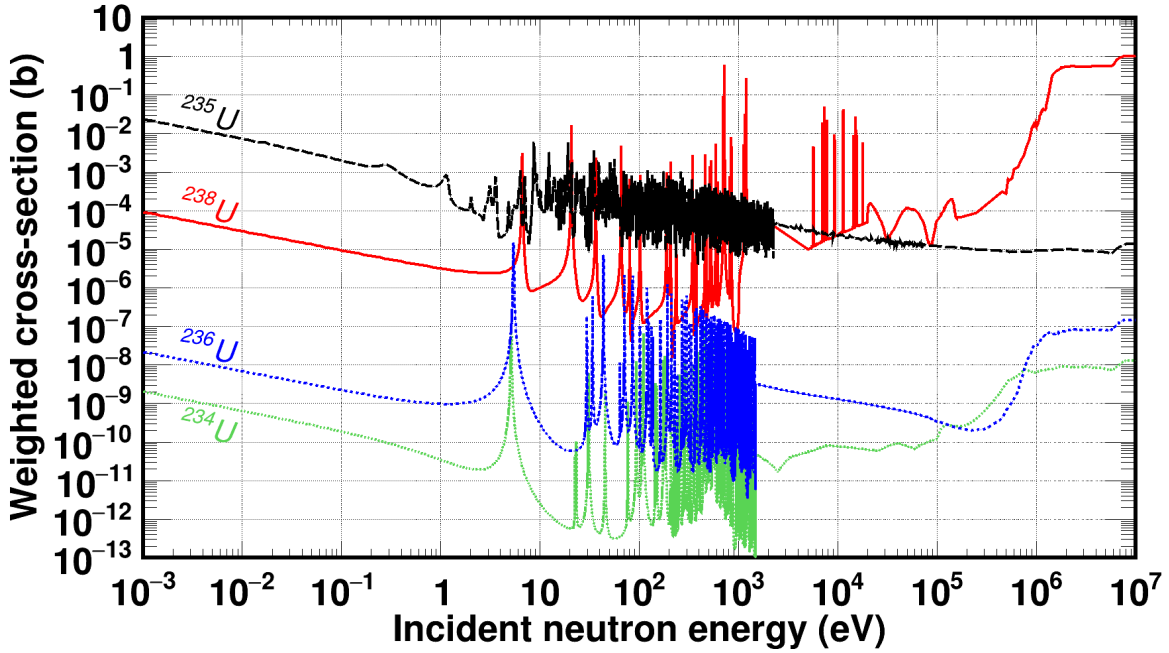

Figure 4.17: *Weighted fission cross-sections regarding the ^{238}U sample provided by JRC-Geel. The contribution of parasitic counts was mainly attributed to the fissile ^{235}U and was quite significant in the thermal and resonance regions, therefore, practically, ^{238}U can be useful only above 100 keV.*

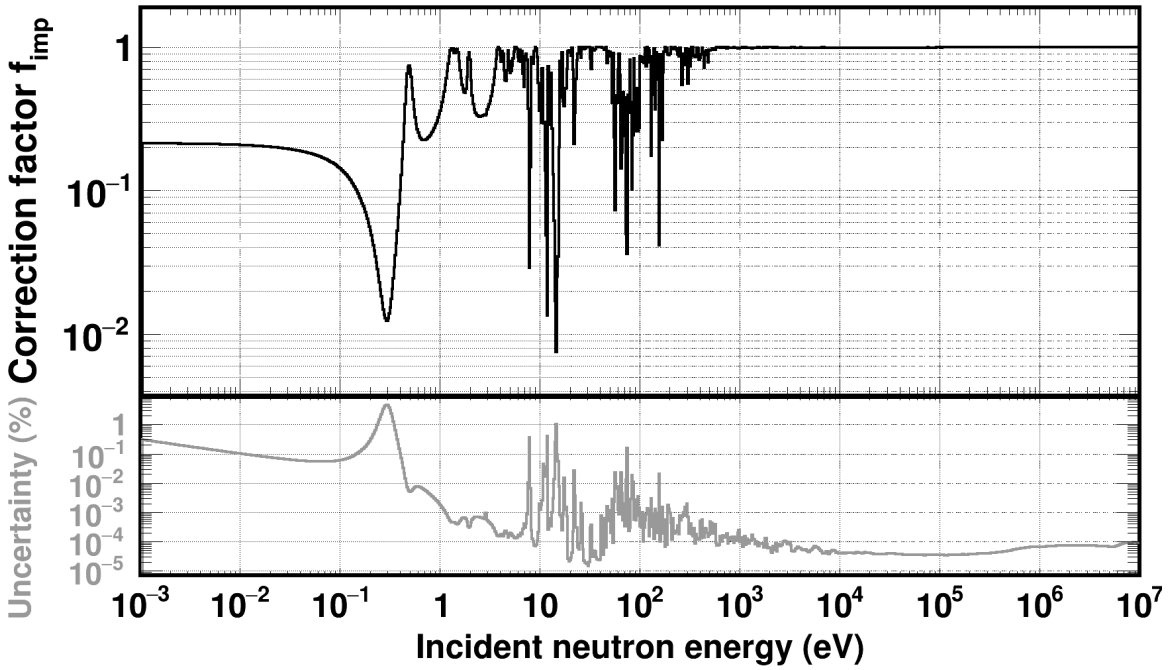

Figure 4.18: *Correction factor f_{imp} (top panel) that was applied to the ^{237}Np -IPN recorded counting spectra. The correction was significant in the thermal region and in the resonances of the two plutonium contaminants. The bottom panel shows the maximum estimated uncertainty of the correction factor f_{imp}.*

4.6.3 Estimation of uncertainties

The proper estimation of uncertainties can be accomplished via full covariance propagation in which the covariance matrices of the parameters seen in eq. (4.14) and (4.15) are needed. In the case of the $^{240}Pu(n,f)$ measurement, the covariance and correlation matrices for the cross-sections could be retrieved by the evaluations themselves, however they were both considered to be negligible compared to the provided covariances of the atomic abundances which can be seen in tables 4.2 and 4.3.

Although the distinctive steps to apply a full covariance propagation will be described in Appendix A, a rather short discussion will follow on the calculation of the uncertainty in the correction factor f_{imp} along with its correlation matrix.

The correlation matrix was provided by JRC-Geel along with the uncertainties of the atomic abundances. The (i^{th}, j^{th}) covariance matrix element $\text{cov}(i,j)$ had to be derived from the corresponding correlation matrix element $\text{cor}(i,j)$ according to the formula seen in eq. (4.16) and the provided uncertainties σ.

$$\text{cov}(i,j) = \text{cor}(i,j) \cdot \sigma_i \cdot \sigma_j \tag{4.16}$$

Table 4.2: *Correlation matrix provided by JRC-Geel concerning the correlations between the atomic abundances on the ^{240}Pu samples. Only the lower part of the symmetric matrix is shown. The "e-notation" is used to describe exponents to the power of ten. The gray cells contain the mass number of the plutonium isotope present in the samples.*

	238	239	240	241	242	244
238	1					
239	-4.40e-3	1				
240	-0.1531	-0.9466	1			
241	-8.00e-4	0	-0.1671	1		
242	-1.20e-3	-9.00e-4	-0.2201	-2.00e-4	1	
244	-2.00e-4	0	-0.0475	0	0	1

Table 4.3: *Calculated covariance matrix concerning the covariances between the atomic abundances on the ^{240}Pu samples. Only the lower part of the symmetric matrix is shown. The "e-notation" is used to describe exponents to the power of ten. The gray cells correspond to the mass number of the plutonium isotope present in the samples.*

	238	239	240	241	242	244
238	8.41e-12					
239	-2.30e-13	3.24e-10				
240	-7.99e-12	-3.07e-10	3.24e-10			
241	-7.19e-15	0	-9.32e-12	9.61e-12		
242	-1.43e-14	-6.64e-14	-1.62e-11	-2.54e-15	1.68e-11	
244	-5.10e-16	0	-7.52e-13	0	0	7.74e-13

The sensitivity matrix G was then calculated using eq. 4.17 where i denotes the incident neutron energy and j the corresponding plutonium isotope. The covariance matrix is finally calculated in order to estimate the uncertainties on the correction factor as well as the correlations of the corrections concerning the incident neutron energies.

$$G(i,j) = \left.\frac{\partial f_{\text{imp}}}{\partial f_{\text{abun}}^{(j)}}\right|_{E_i} \tag{4.17}$$

The relative estimated uncertainty can be seen in the bottom panel of fig. 4.12 and the correlation matrix can be seen in fig. 4.19 where a linear correlation was deduced between the correction factors at each energy. This behavior was expected since an increase of the correction factor would be associated with an increase in the mass of ^{240}Pu which in turn should affect the correction over the whole energy region.

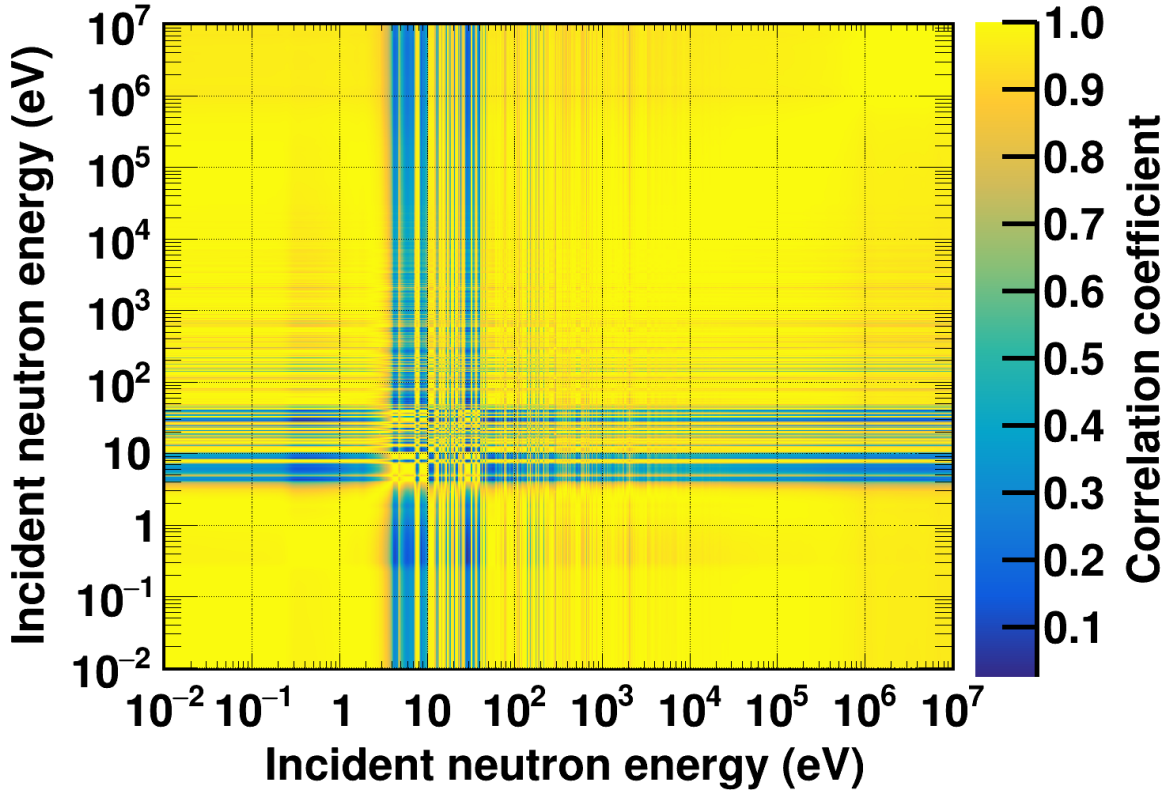

Figure 4.19: *Correlation matrix for the correction factor f_{imp} applied to the plutonium samples. An almost positive correlation was deduced throughout the entire energy range.*

Since a covariance matrix was not provided for the ^{237}Np -IPN sample, a different approach had to be considered. In this, the most significant correction occurring from the neutron induced fission of the ^{239}Pu impurity was taken into account, which is considered to be a neutron standard up to 1 GeV [179, 180] and is known with an uncertainty of less than 2% in the thermal region where the correction was much more significant as can be seen in fig. 4.18.

To estimate the maximum uncertainty, the provided atomic abundances were

increased within their reported uncertainties and a new correction factor was estimated. The difference of the two correction factors (bottom panel, fig. 4.18) provided the maximum estimated uncertainty of the applied correction factor (top panel, fig. 4.18).

As mentioned previously, since the most significant uncertainties occurred from the reported impurities which did not come along with a covariance matrix, correlations regarding the correction factor f_{imp} could not be estimated.

4.7 Contribution of neutron self-shielding

The term neutron self-shielding is used to describe the beam attenuation when it is transmitted through matter. The materials that contributed to the attenuation between consecutive fission foils, taking into account the propagation direction, were:

- The 5 mm in thickness gas that was present in the drift region.
- The Micromegas detector which consisted of three foils in total namely: 5μm natural copper (micromesh), 50μm Kapton and 3μm natural copper (anode).
- The 5 mm-thick gas that was present between the pad and the aluminium backing of the next fission foil.
- The 0.25 mm in thickness aluminium sample backing.
- The fission foil itself.

To calculate the neutron self-shielding or beam attenuation, the Beer-Lambert law was used, seen in eq. (4.2) along with the JEFF-3.3 evaluated (n, tot) cross-sections and the following assumptions: (a) The gas was neglected since its surface density and (n, tot) was so small that the neutron absorption is practically negligible, (b) The Kapton present in the detectors was assumed to be pure carbon since given its total neutron cross-section and mass fraction, which was reported to be 70% [181], its neutron absorption was the most significant and (c) The neutron absorption on the ^{235}U sample was neglected since the correction was of the order of 10^{-2}%.

In addition, the surface densities n (in atoms/barn) were calculated using the mass densities ρ, since all the materials present in the detectors were industrial metals and therefore no deviations from the reported densities were expected. The areal densities n were then calculated using eq. (4.18)

$$n[\text{atoms/barn}] = 10^{-24} \cdot \rho[gr/cm^3] \cdot \tau[cm] \frac{N_A}{A} \tag{4.18}$$

where τ denotes the provided thickness of each material, N_A is the Avogadro constant and A is the mass number of the material. For the fission foils an average $100\,\mu\text{gr/cm}^2$ areal density was used, while for the natural copper that consists of two stable isotopes, the surface density was weighted according to the isotopic abundance f_{iso}, which was 69.15% and 30.85% for ^{63}Cu and ^{65}Cu respectively. It has to be noted that the contaminants found in the fission foils were neglected as neutron absorbers in the context of the present correction.

The final configuration of the absorbers that were considered to have an effect on the attenuation of the neutron beam, can be seen in fig. 4.20. According to this configuration, the beam with intensity I_0, that exits the first sample, which in both campaigns was a ^{235}U , would suffer successive losses described by the ratio of the self-shielding factors seen in eq. (4.19) which was applied to the recorded fission yields of the ^{240}Pu , ^{237}Np and ^{238}U samples.

$$\frac{f_{\text{shield}}}{f_{\text{shield}}^{(\text{ref})}} = \exp\left\{\sum_i n_i \cdot \sigma_{tot,i}\right\} \tag{4.19}$$

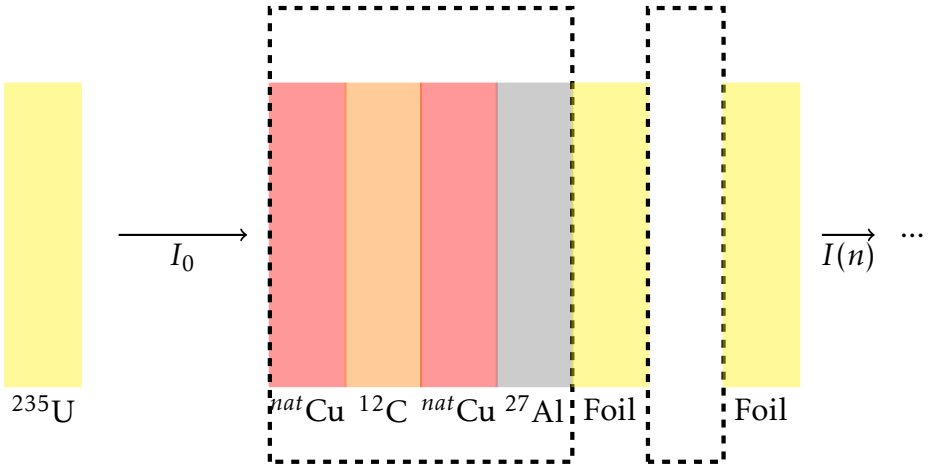

Figure 4.20: *Part of the configuration of the neutron absorbers that were considered in the neutron self-shielding correction. The dashed rectangle is used to describe the sequence of the ^{nat}Cu-^{12}C-^{nat}Cu-^{27}Al stack.*

In fig. 4.21 the most significant attenuation factors are shown, in which it is visible that the neutron self-shielding is mostly dominated by the aluminium backings of the fission foils and strong resonances present in the total neutron absorption cross-sections of surrounding materials. Typical correction factors, calculated for the fission foils in the $^{240}Pu(n,f)$ campaign are seen in fig. 4.22.

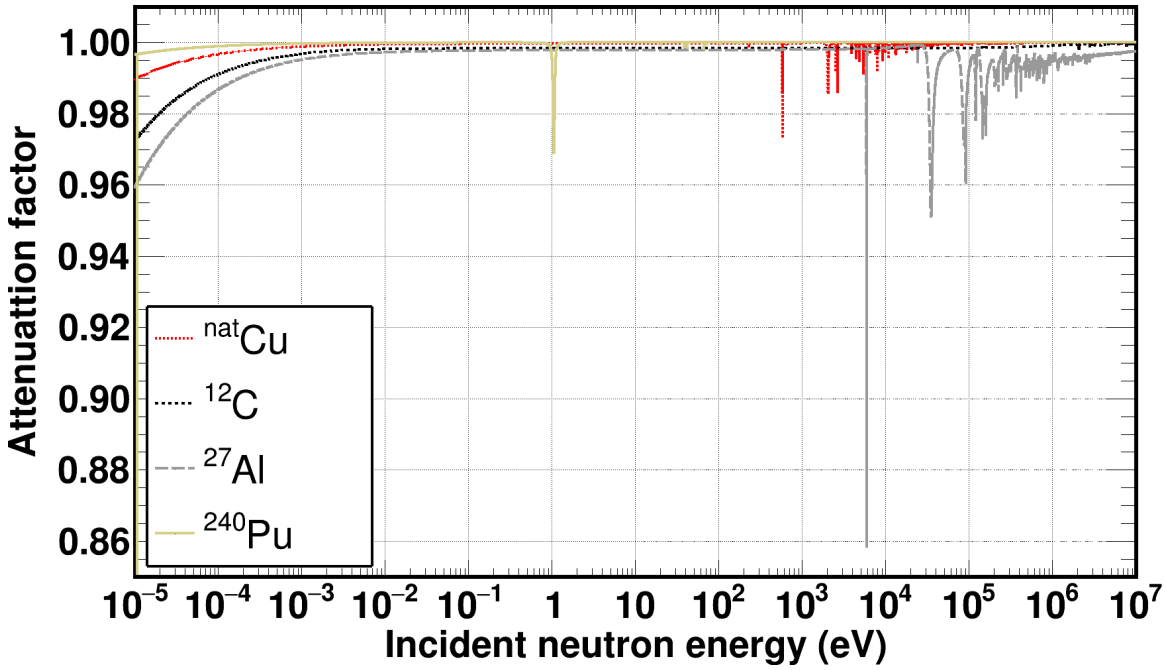

Figure 4.21: *Attenuation coefficients of a beam that is propagated through the foils present in the experimental campaigns. The four more significant attenuation factors are shown.*

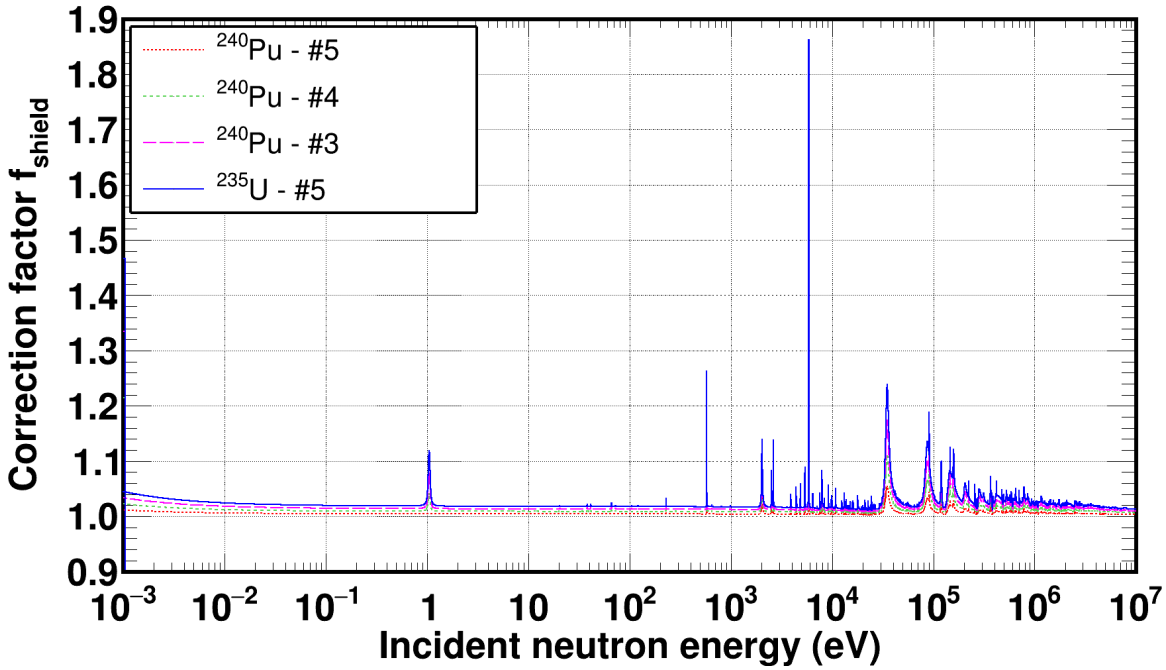

Figure 4.22: *Self-shielding correction factors applied on the recorded fission yields of the* $^{240}Pu(n,f)$ *measured fission samples.*

4.7.1 Estimation of uncertainties

The main sources of uncertainties, occurred from the cross-sections used in eq. 4.19 since the thickness of each material was accurate within industry standards, which are usually quite strict.

As mentioned previously, the JEFF-3.3 cross-sections were used, since other evaluation libraries did not provide any information on the uncertainties. Even JEFF-3.3 though, did not report sufficient information. As seen in fig. 4.21, the most significant absorption occurred from the aluminium in the 8 keV - 1 MeV incident neutron energy region, however the evaluation provided uncertainty data from 1.8 MeV onwards, which was of the order of 5%. In this energy region, the correction due to the presence of the backings was estimated to be of the order of less than 0.5%, therefore the uncertainty of the correction was considered negligible.

In addition, in the energies were resonances in the (n,tot) reaction were strong (i.e. 1.05 eV, ^{240}Pu and 579 eV, ^{63}Cu) the absorption is of the order of $2-3\%$ and the uncertainties in the JEFF-3.3 evaluation were reported to be of the order of 2%, therefore also practically negligible.

Finally, to estimate the dependence on the selected evaluation library, the corrections were estimated using the ENDF-B/VIII.0 evaluation as well and the new correction factors were in agreement within less than 1% to the ones obtained from JEFF-3.3 therefore, practically, the final estimated uncertainty of the self-shielding correction factor to the recorded fission yield was considered to be known within 5% and independent of the incident neutron energy which is an overestimation, however with a negligible impact on the derived cross-sections.

4.8 Parasitic counts from photo-fission induced events

It was already mentioned that the spallation process was accompanied by an intense burst of γ-rays that reached the experimental area in about 67 ns after the collision of the proton bunch on the lead target. Apart from the aforementioned burst, the so-called γ-flash which promptly occurred, an additional delayed photon spectrum arrived at the experimental hall, which was generated by neutron capture mainly on the target surrounding materials.

Both the prompt and the delayed photon spectra could have potentially induced fission events through the means of photo-fission reactions on the actinide foils, therefore a relevant study was performed making use of the previously mentioned optical transport code, the pool of FLUKA simulations and the ENDF/B-VIII.0 (γ, f) evaluated cross-sections of ^{235}U , ^{238}U , ^{237}Np and ^{240}Pu which can be seen in fig. 4.23.

The coupled use of the FLUKA simulations and the optical transport code, made the study of the photon spectrum that reached the experimental area at the level of the fission samples, i.e. roughly 19.5 m above the centre of the spallation target, possible. More specifically, the arrival time and incident energy distributions were extracted (fig. 4.24) and then used to estimated the photo-fission reaction rate rel-

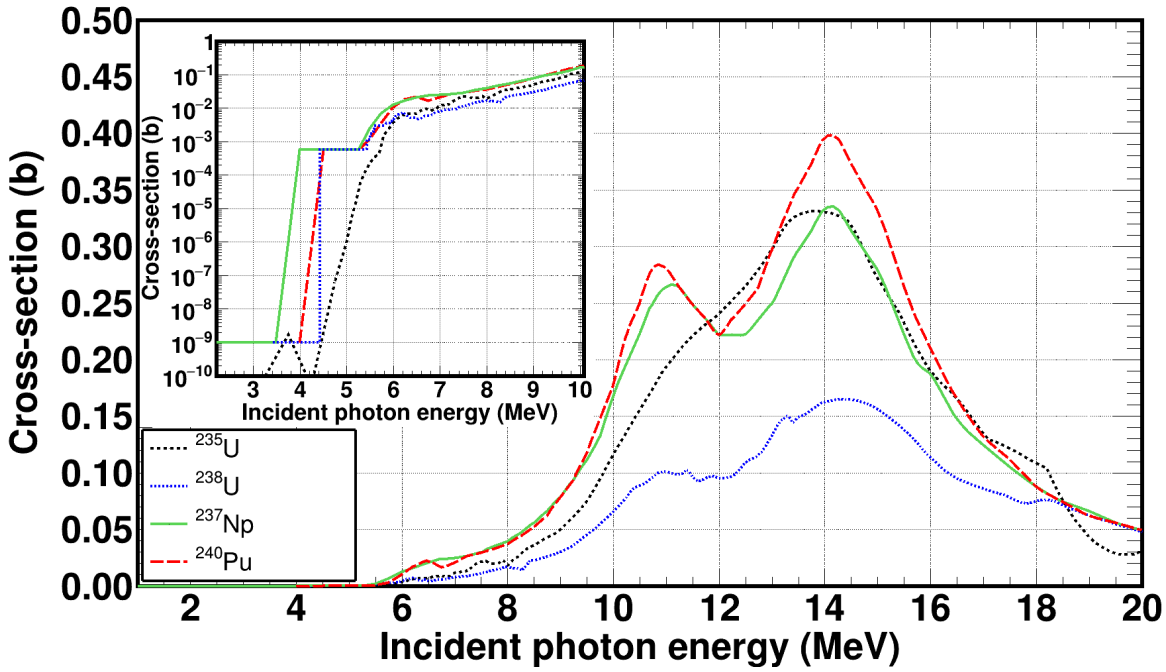

Figure 4.23: *Photon induced fission cross-sections obtained from the latest ENDF/B-VIII.0 evaluations regarding the ^{235}U , ^{238}U , ^{237}Np and ^{240}Pu isotopes. The inset contains the cross-sections for incident photon energies in the $1-10$ MeV range, where the EAR2 n_TOF photon spectrum spans across.*

evant to the time-of-flight.

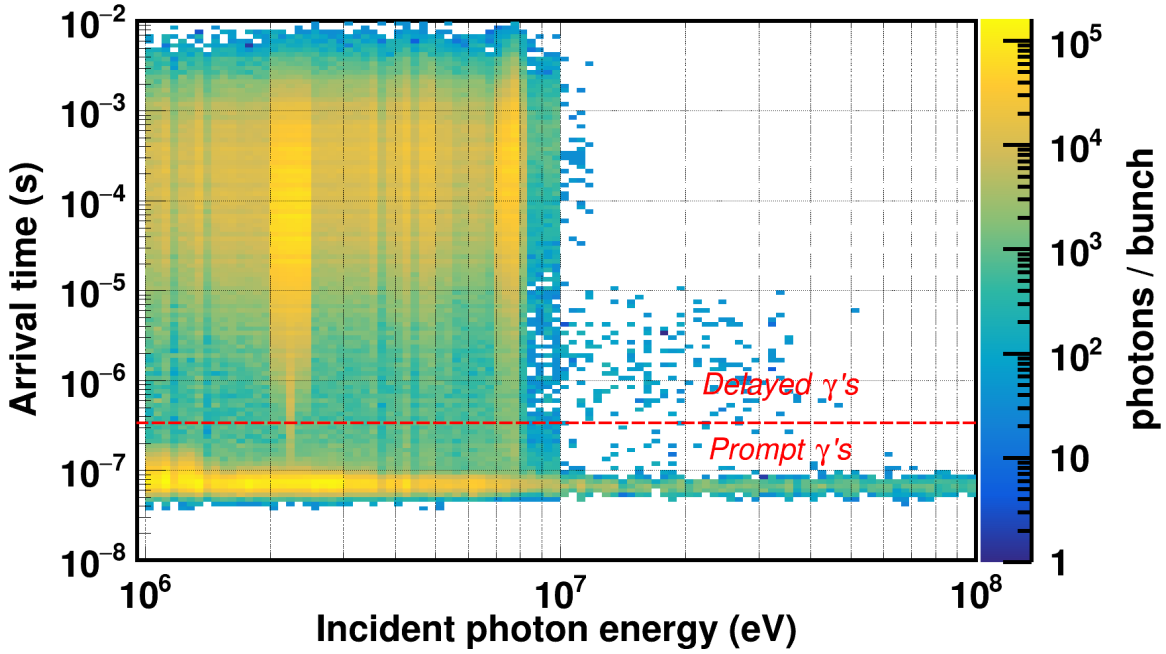

Figure 4.24: *Distribution of arrival time and incident energy of the photon spectrum 19.5 m above the centre of the spallation target. The distribution was obtained from the combined use of the FLUKA simulations and the optical transport code.*

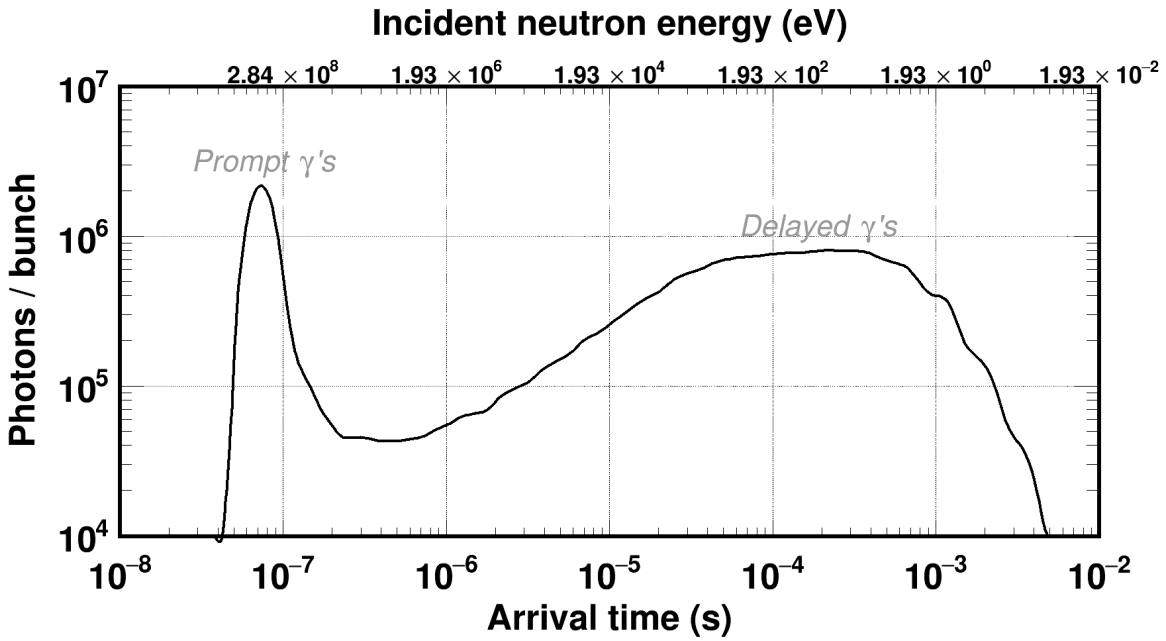

Figure 4.25: *Time distribution of the photon spectrum which arrived in the experimental area at a distance of* 19.5 *m above the centre of the spallation target. The spectrum can be divided into a prompt and a delayed component. The equivalent incident neutron energy is also shown.*

The arrival time distribution of the photon spectrum shown in fig. 4.25 can be divided into two components: the prompt which lasted for about 200 ns and the delayed one that extended up to 5 ms. Due to the fact that the prompt component was rather fast and corresponded to incident neutron energies above 50 MeV, in practice it did not contribute to the recorded fission yield. On the contrary, the delayed component spanned from 200 ns up to about 5 ms and therefore triggered photo-fission reactions that were mixed with neutron induced fission ones.

To estimate the fraction of the (γ, f) reactions to the (n,f) ones, the photo-fission reaction rate $\mathrm{RR}_{\gamma f}$ was calculated in terms of the time-of-flight, as seen in eq. (4.20)

$$\mathrm{RR}_{\gamma f}(tof) = m \int \Phi_{\gamma}(tof, E_{\gamma})\, \sigma_{\gamma f}(E_{\gamma})\, \mathrm{d}E_{\gamma} \tag{4.20}$$

where Φ_{γ} describes the photon flux that arrived at EAR2, m the mass of each sample while $\sigma_{\gamma f}$ denotes the (γ, f) cross-section. The total integrated photon flux per bunch can be seen in fig. 4.26 for the prompt and delayed component of the photon spectrum. It has to be noted that the prompt spectrum did not indicate any particular structures, which was expected from the nature of the spallation process. On the other hand, prominent γ-ray peaks were observed at the delayed spectrum resulting from neutron capture reactions on the materials of the target's vessel, the moderation circuit, as well as from the lead target itself. In addition, the major portion of the delayed component, carried photons with energies up to around 10 MeV while in the prompt one photons with 100 MeV incident energy were predicted.

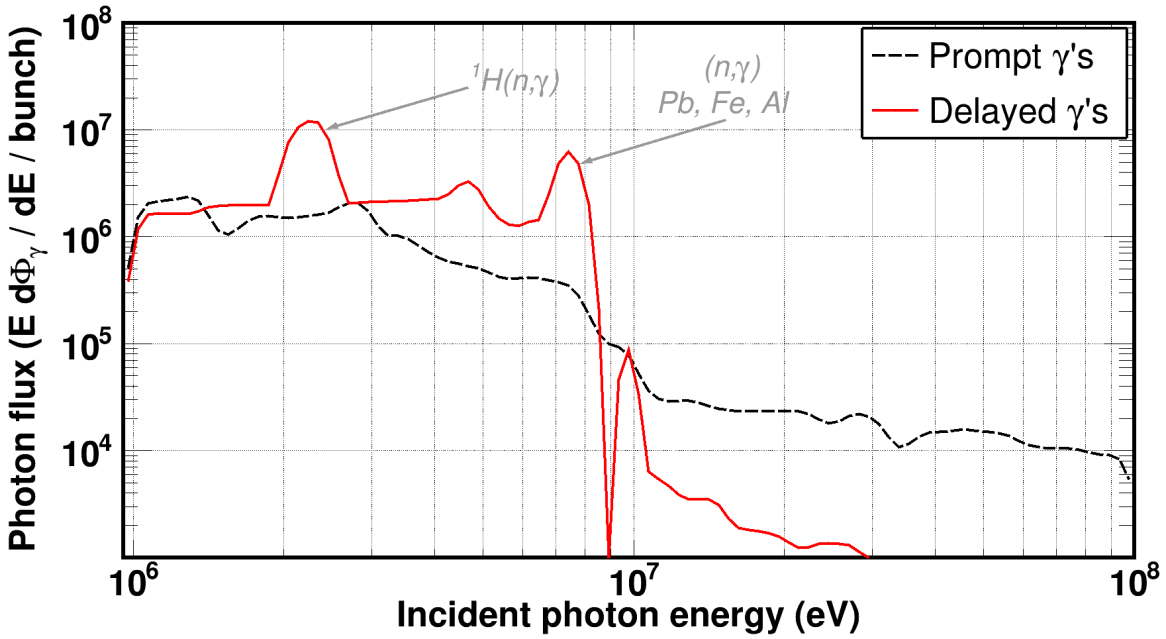

Figure 4.26: *Energy distribution of the photon spectrum that arrived in the experimental area at a distance of* 19.5 *m above the centre of the spallation target. The photon flux is shown for the delayed and the prompt component as well. Photon peaks were observed resulting from neutron capture on the materials around the spallation target.*

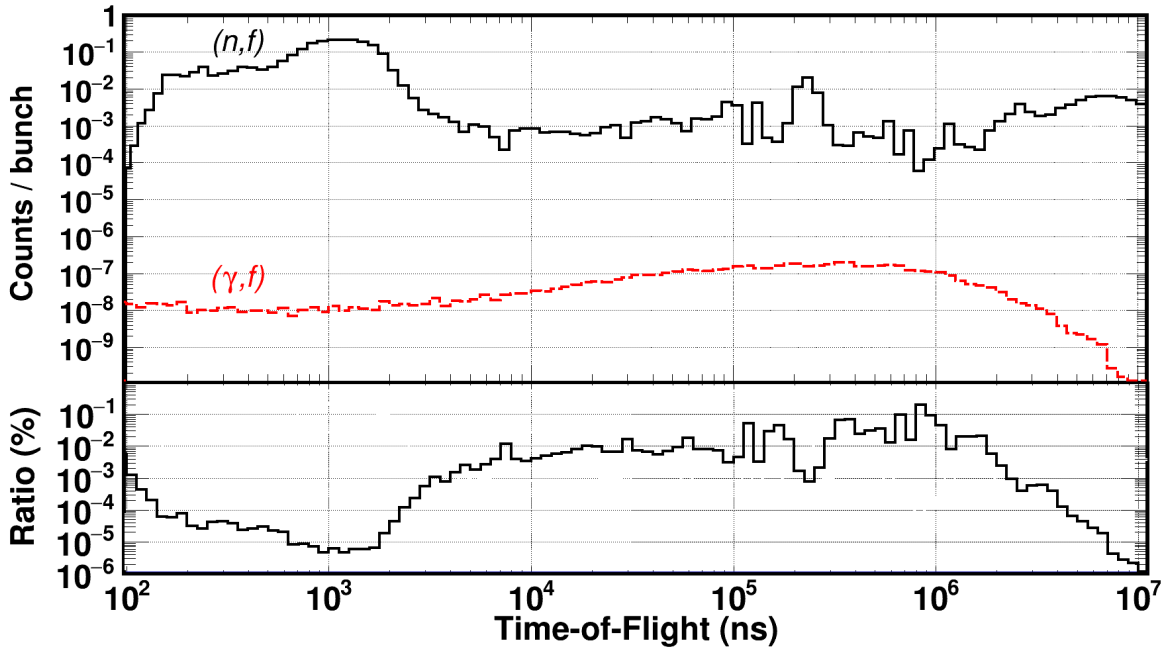

Figure 4.27: *Experimental and calculated reaction rate for neutron induced and photo-fission reactions, respectively (top panel) for the* ^{237}Np *sample provided by IPN-Orsay. The ratio was found to be less than* 0.3%*, which was the highest ratio among the actinide samples in both campaigns, therefore the correction was practically negligible.*

To estimate the contribution on the recorded fission yield or similarly the correction factor $f_{\gamma f}$, the expected counting spectrum from photon induced fission was divided with the experimental one, recorded during the campaign. In fig. 4.27, the worst case scenario is shown which was accounted for the ^{237}Np sample provided from IPN-Orsay. It is evident that the parasitic events due to photo-fission can be neglected since they were estimated to be less than 0.3%. Regarding the uncertainty of the correction factors, it has to be noted that covariance data did not exist in the evaluation libraries, therefore the aforementioned methodology was considered as uncertain as the maximum discrepancies among the evaluation libraries that provided photo-fission cross-sections (ENDF/B-VIII.0, JENDL/PD-2016 and IAEA/PD-1999) which were of the order of 15%.

4.9 Corrections on the incident neutron flux

Although the neutron beam that was delivered at EAR2 was considered to be parallel, the beam attenuation due to the collimation system was studied. As discussed previously, the collimation system, consisted of two collimators which acted similarly to a pin-hole camera whose focal point lied at the entrance of the fission chamber, 19.24 m above the centre of the spallation target.

Above the focal point, on which the narrowest beam profile rested, as neutrons travel towards the beam dump, the neutron beam diverges and although it still consisted of the same total integrated flux, the interception with the fission foils becomes smaller. It is therefore crucial to study the beam interception factor as well as the rate with which the neutron flux dropped from sample to sample.

4.9.1 Profile and beam interception factor

In cases when the samples are smaller than the incident particle beam, the analysis should take into account the portion that intercepts them, the so-called beam interception factor (BIF). Although this was not deemed mandatory in the present work, a study was performed to estimate whether dramatic changes on the beam profile were to be expected or not.

Firstly, the transport code was used to project the neutron beam profile at the altitude of the ^{235}U samples and as seen in fig. 4.28 the beam size was indeed larger than the diameter of the samples and practically only the beam halo did not intercept the foils. It has to be mentioned that the trapezoidal shape of the beam spot was attributed to the entrance window when entering in the vacuum chamber that leads to the experimental area.

To understand how the beam was diverging, the profiles were calculated and projected along the z-axis at distances ranging from 19.5 to 19.7 m covering the detector-samples set-ups in both campaigns. In fig. 4.29 four typical projections are shown along with an arrow that indicates the diameter of the fission foils.

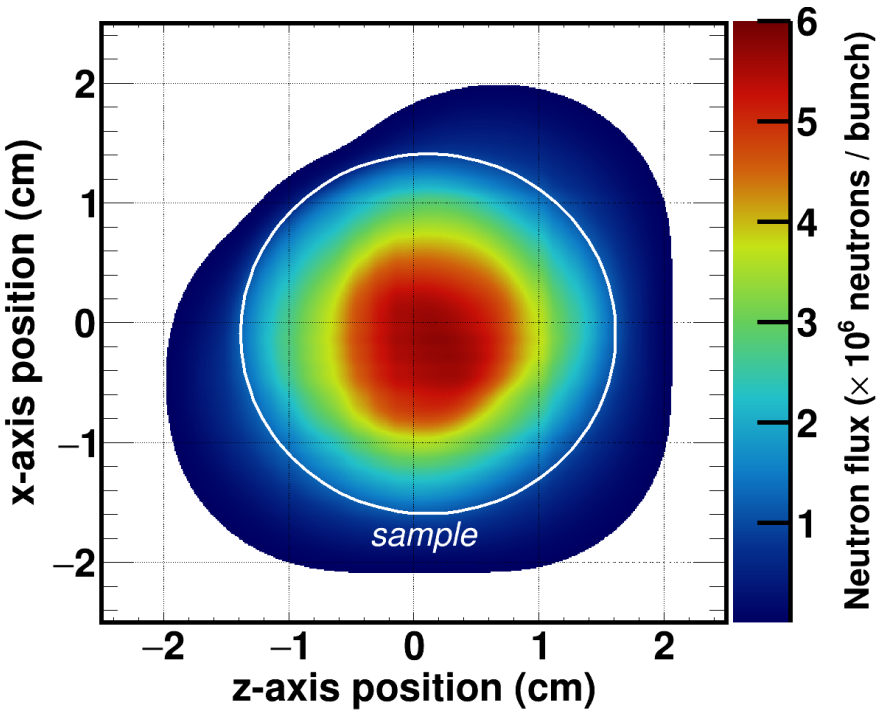

Figure 4.28: *Neutron beam profile at a* 19.5 *m distance above the centre of the spallation target, calculated through the use of the transport code. For comparison purposes, a circle with a* 3 *cm diameter, which corresponds to a sample diameter, is drawn and therefore it is evident that there was a high fraction of interception with the beam. The trapezoidal shape was attributed to the exit window from the lead target to the experimental area.*

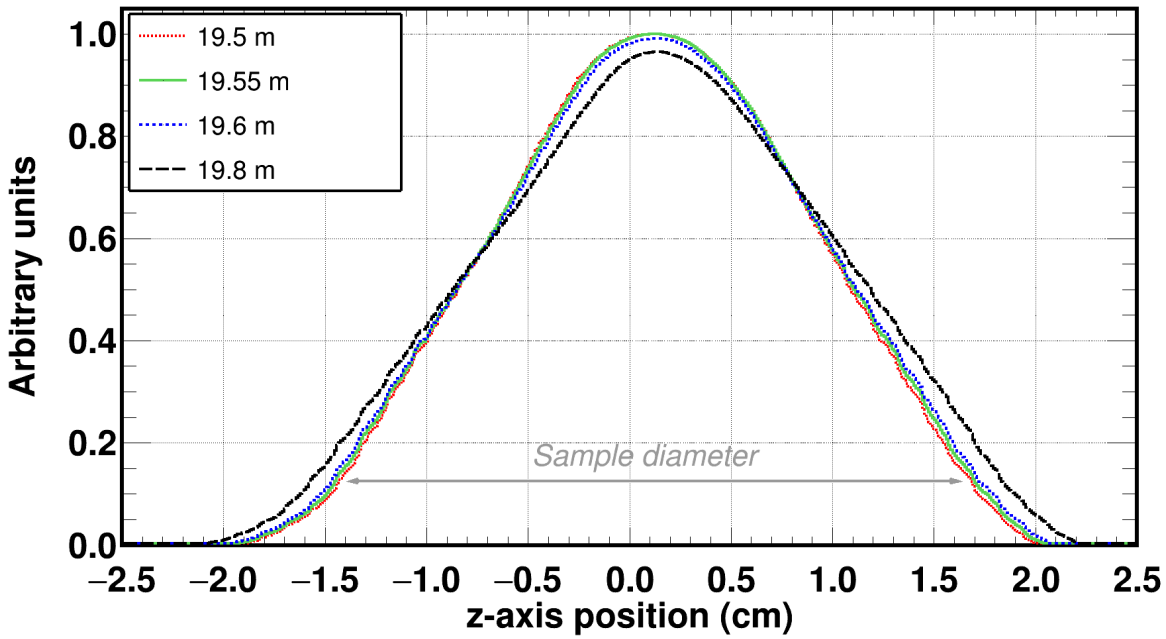

Figure 4.29: *Neutron beam profile, projected along the z-axis for several distances above the centre of the lead target. The projections were normalised to the most probable value of the* 19.5 *m distribution. The double-head arrow indicates the diameter of the fission foils.*

Table 4.4: *Evolution of the FWHM and the BIF when moving towards the beam dump. The reference values at* 19.5 *m correspond to the position of the* ^{235}U *foils in both campaigns.*

Distance (m)	FWHM (cm)	Ratio to 19.5 m (%)	BIF (%)	Ratio to 19.5 m (%)
19.50	1.93	-	97.5	-
19.55	1.95	1.0	97.0	0.5
19.60	1.98	2.5	96.0	1.5
19.70	2.01	4.0	95.0	2.6
19.80	2.11	8.5	94.0	3.6

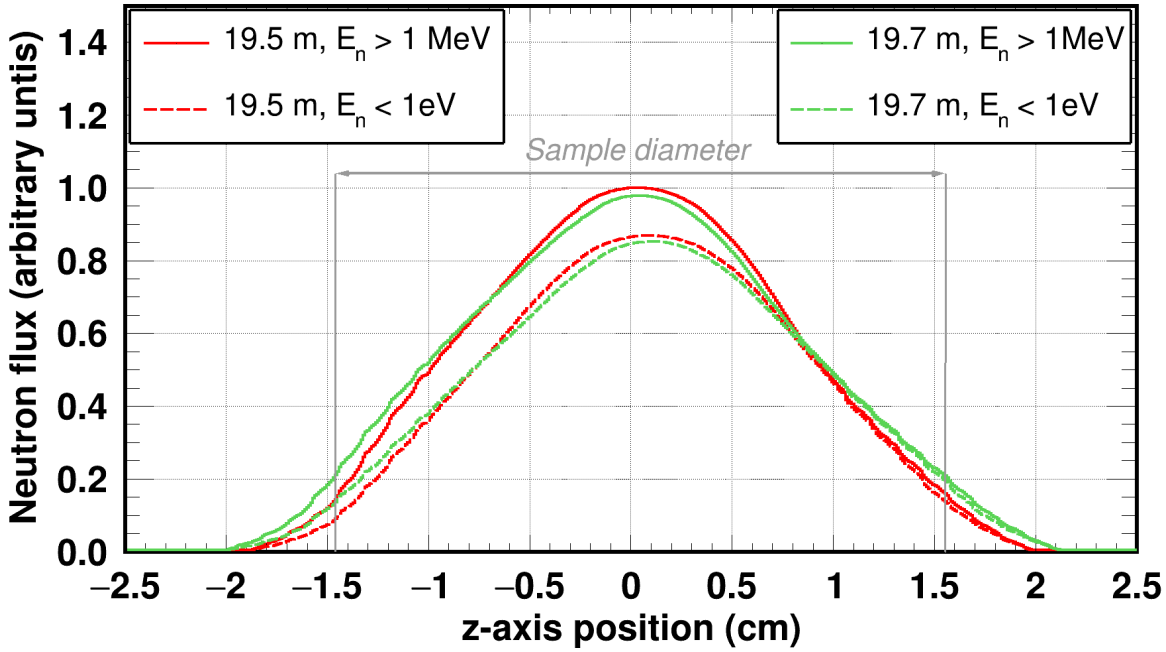

Figure 4.30: *Neutron beam profile, projected along the z-axis at* 19.5 *and* 19.7 *m for neutron energies up to* 1 *eV and above* 1 *MeV. In all four cases a high interception factor above* 95% *was observed, while no significant offset between the distributions was recorded.*

In table 4.4 it can be seen that the BIF, which is the ratio of the neutrons that hit the sample to the total neutrons arriving at its plane and was calculated by integrating the $2D$ profiles assuming a perfect alignment, did not vary significantly within the 20 cm length of the detector set-up, thus a correction from sample to sample need not be considered. It has to be noted that in the previous studies, no cuts were applied to the incident neutron energy.

To investigate the possibility of a significant difference in terms of beam coverage between different neutron energy ranges, the profiles were projected at 19.5 and 19.7 m for incident energies up to 1 eV and above 1 MeV. As seen in fig. 4.30, MeV neutrons were predicted to be more forward peaked, hence the significantly narrower profile than the thermal ones. In addition, both neutron groups covered the surface of the fission foils at a fraction above 95% depending on the distance from

the spallation target, thus no significant offsets were observed, neither in greater distances, nor within the two neutron energy groups.

The aforementioned studies were performed on the profile projections along the z-axis. The exact same conclusions could be drawn from the z-axis projections, since as seen in fig. 4.31, the projections did not vary significantly in therms of the fwhm, the full width and the beam interception factor for a 3 cm in diameter sample, therefore for the sake of simplicity only the z-axis projections were discussed.

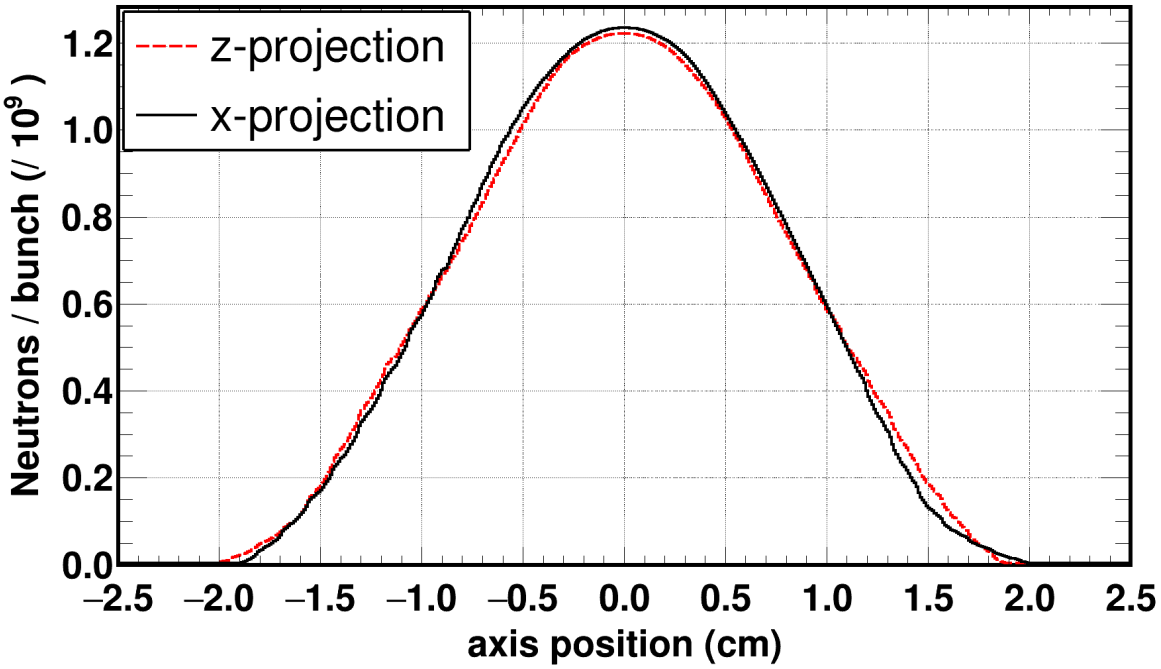

Figure 4.31: *Projections of the simulated neutron beam profile at* 19.5 *m along the z and x axes. It is evident that no significant differences were observed on the FWHM and the overall beam coverage for a sample of* 3 *cm in diameter. Both projections are aligned to 0, for comparison purposes.*

To experimentally validate the simulations, the only available means was by utilising the gafchromic foils used during the alignment of the fission chamber. It was previously mentioned that the gafchromic foils were exposed to the neutron beam, then scanned with the use of a typical image scanner and then edited photowise to get the neutron beam spot revealed in order to quantify the offset from the centre of the beam.

The gafchromic foils could additionally be used though, to experimentally estimate the beam profile in both campaigns. To do so, the scanned images were further edited in a way to enhance the contrast, then de-satured (i.e. converted to black and white) and finally the colours were inverted in such a way that the beam spot was white. A C++ code was developed to import the processed images on ROOT6 in order to convert them to 2D-histograms (fig. 4.32, gafchromic from the $^{240}Pu(n,f)$ campaign) and get the beam profiles, which as shown in fig. 4.33, provided the same full width as the ones predicted by the simulations at 19.8 m above the spallation target and therefore the simulations were considered solid in terms of extracting information on whether the fission foils were fully covered by

the beam. It has to be noted that the shapes of the gafchromic projection should not be taken into full consideration, since they were heavily affected by the quality of image processing, the scanning device, as well as, the exposure time on the neutron beam, however these factors did not affect the estimated value of the full width of the beam size.

Finally, for consistency purposes the neutron spectrum was compared to the photon one at the level of the gafchromic position, since these passive foils are rather sensitive to γ-rays. As seen in fig. 4.34, the neutron beam profile was similar to the photon one in terms of the full width, therefore the comparison made between the profile from the gafchromic foil and the simulated one was valid, at least at a first order approximation.

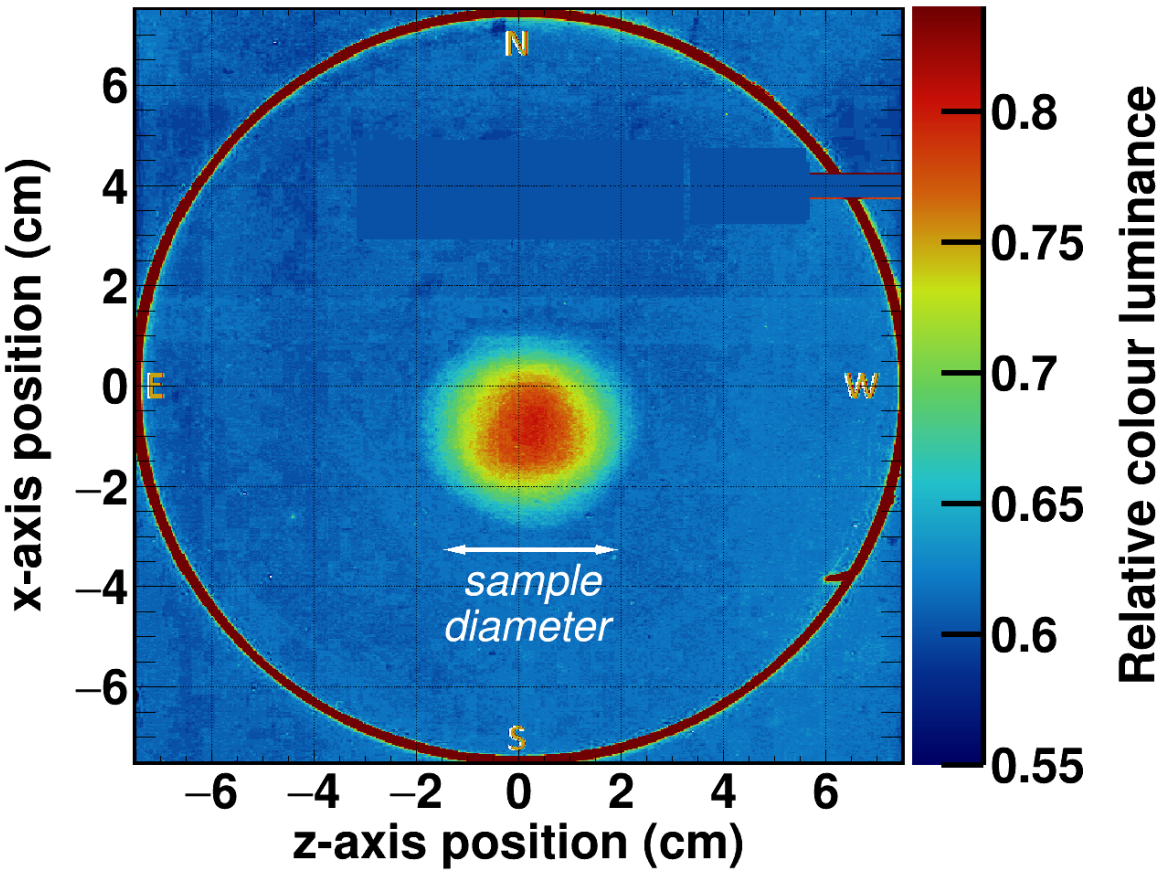

Figure 4.32: *The scanned and post-processed copy of the gafchromic foil from the $^{240}Pu(n,f)$ measurement was converted into a 2D histogram. High luminescence values corresponded to white areas on the processed image. The beam spot is visible at the center of the figure. The red circle corresponded to the fission chamber's window. Orientation markings are also visible along with a measure of the sample's size. The trapezoidal shape of the beam was also quite distinguishable.*

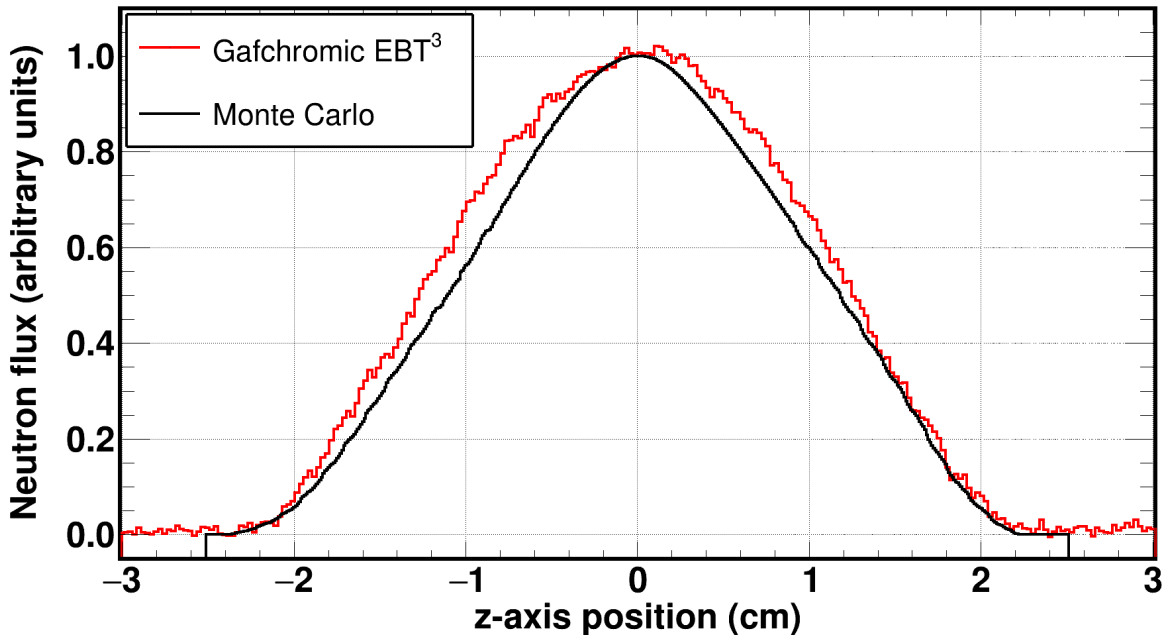

Figure 4.33: *The comparison between the simulated and gafchromic profiles along the z-axis indicated a very good agreement on the full width of the neutron beam. The gafchromic profile was constructed from the corresponding foil on the* $^{240}Pu(n,f)$ *experiment. Both projections are aligned to 0, for comparison purposes.*

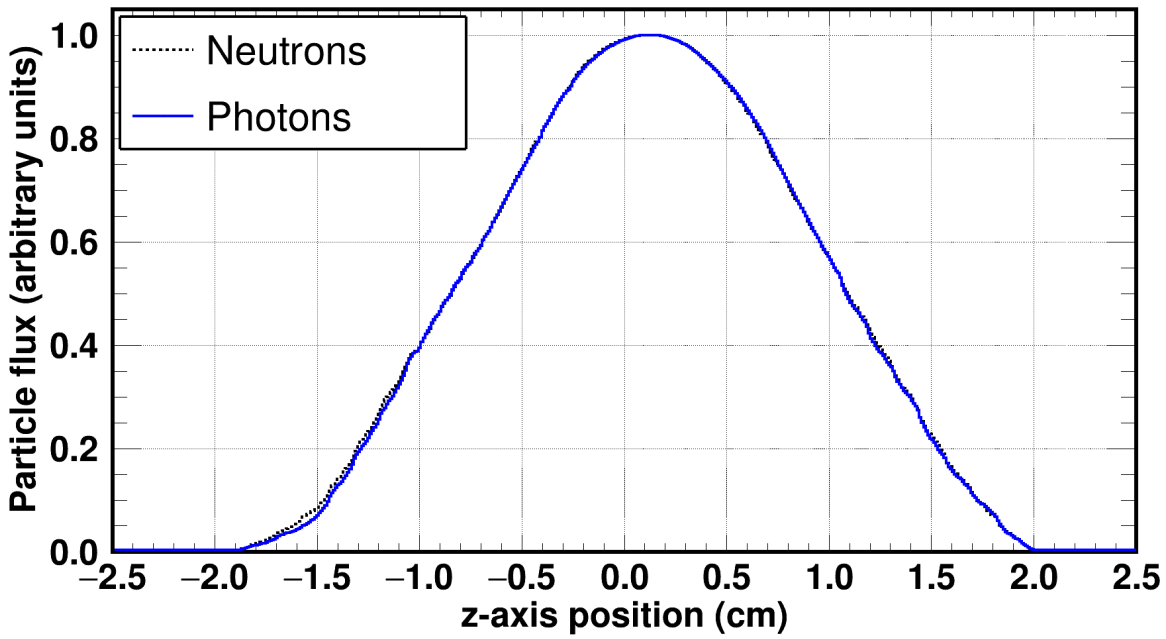

Figure 4.34: *Comparison between the photon and neutron beam profiles that arrived at* 19.8 *m above the centre of the spallation target. Both spectra are in very good agreement and were normalised to their most probable values.*

4.9.2 Incident neutron flux propagation

Although the previous methodology can be used to determine the beam interception factor, which in principle is a correction on the incident neutron flux, it seemed more appropriate to calculate directly the incident neutron flux on each sample using the available pool of FLUKA simulations. However the information extracted previously is equally important, because it assisted in proving that the simulations could be used to draw general conclusions on the beam profile, as well as, the alignment and the coverage of the samples.

Prior to bluntly using the simulations to correct the ratio of the recorded fission yields, a sensitivity study was performed. First and foremost, the neutron flux was experimentally estimated using the SiMon2 detector as well as the uranium foils at the level where each sample rested. The term estimation is used here, because the analysis performed was qualitative rather than quantitative and its goal was to determine to which extent the simulations could be used; thus the procedure that will be described should not be confused or related to the challenging task of experimentally determining the neutron flux.

The recorded reaction yields were corrected in terms of mass, dead-time (see sec. 4.11) and amplitude cut. Additional corrections were performed regarding the detection efficiency in the case of the SiMon2 detector [145]. Finally, since the reference foils were placed at different distances with respect to the centre of the spallation target, the SiMon2 flux was normalised to the ^{235}U one, at the thermal point. The ^{238}U flux, was left unnormalised in order to estimate the difference of the neutron flux as the beam was propagated.

As seen in fig. 4.35 different energies were covered. The γ-flash was blinding the silicon detectors down to an energy of 100 keV, while the statistics for ^{238}U was usable only above 2 MeV. For the ^{235}U samples, since a convolution of the standard $^{235}U(n,f)$ cross-section or a deconvolution of the recorded fission yield could not be performed regarding the resolution function, the resonance region between 1 eV and 1 kev was discarded. The very good agreement, within 10%, between the three fluxes in the overlapping energy regions indicated firstly, a consistent analysis procedure (SiMon2, ^{235}U) and secondly, a small effect on how the neutron flux changes within the chamber (^{235}U , ^{238}U).

The estimated values were then compared to the evaluated flux ones, which were also normalised at the thermal point. As seen in fig. 4.35, a quite good agreement was observed between the experimentally estimated fluxes and the evaluated flux of EAR2 over a broad energy region that spanned from 10 meV up to a few MeV. This agreement indicated that the experimentally estimated fluxes were not too far from the truth and therefore could be used to experimentally determine flux ratios.

It has to be noted that SiMon2 and evaluated fluxes were in a perfect agreement in the energy regime from thermal up to a few keV, therefore the evaluated flux could be used to determine the cross-sections in the resolved resonance region, in the absence of a reference foil within the fission chamber with a smooth reaction (i.e. $^{10}B(n,\alpha)$).

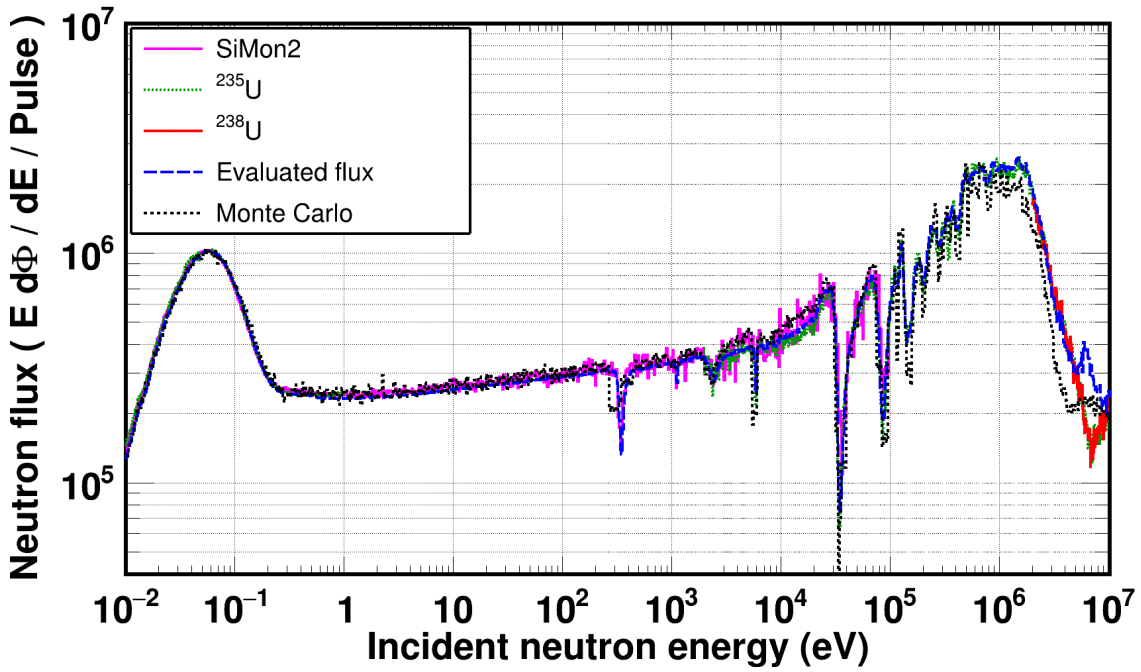

Figure 4.35: *The neutron flux was estimated using the neutron monitor and the uranium samples and compared to the evaluated and simulated one. As shown the agreement that was achieved was quite reasonable. The incident neutron fluxes were normalised at the thermal point.*

Finally, the incident neutron flux at the level of the ^{235}U sample was simulated using the pool of FLUKA simulations and the transport code. Although the shape of the flux was predicted quite well, systematic discrepancies that reached 20% were observed above 100 keV. Their origin is not quite well understood, however, as it will be explained right shortly, they did not affect the present correction methodology.

To determine whether the simulations can be used to draw conclusions on the incident neutron flux and its variation from sample to sample or not, the simulated and experimental flux ratios between the ^{235}U and ^{238}U samples were calculated in the MeV region and then fitted with a constant function. The ratio of the simulated fluxes was 1.58(48)% while for the experimental ones 1.34(26)% and therefore both ratios were found to be in excellent agreement and as a result the simulations could be used to deduce the corrections on the flux ratios from sample to sample.

In this respect, the fluxes were simulated at 19.5 and 19.517 m from the centre of the spallation target, distances which correspond to the position of the ^{235}U samples and the consecutive fission foil, respectively. To estimate an energy-dependent correction factor, the flux ratio seen in fig. 4.36, was fitted with a constant function at each individual energy decade. A set of constant functions was used since the uncertainty was too high. In table 4.5 the constant fitting values are reported, along with the corresponding uncertainties which were assigned as the maximum deviation between the fitting value and the experimental point.

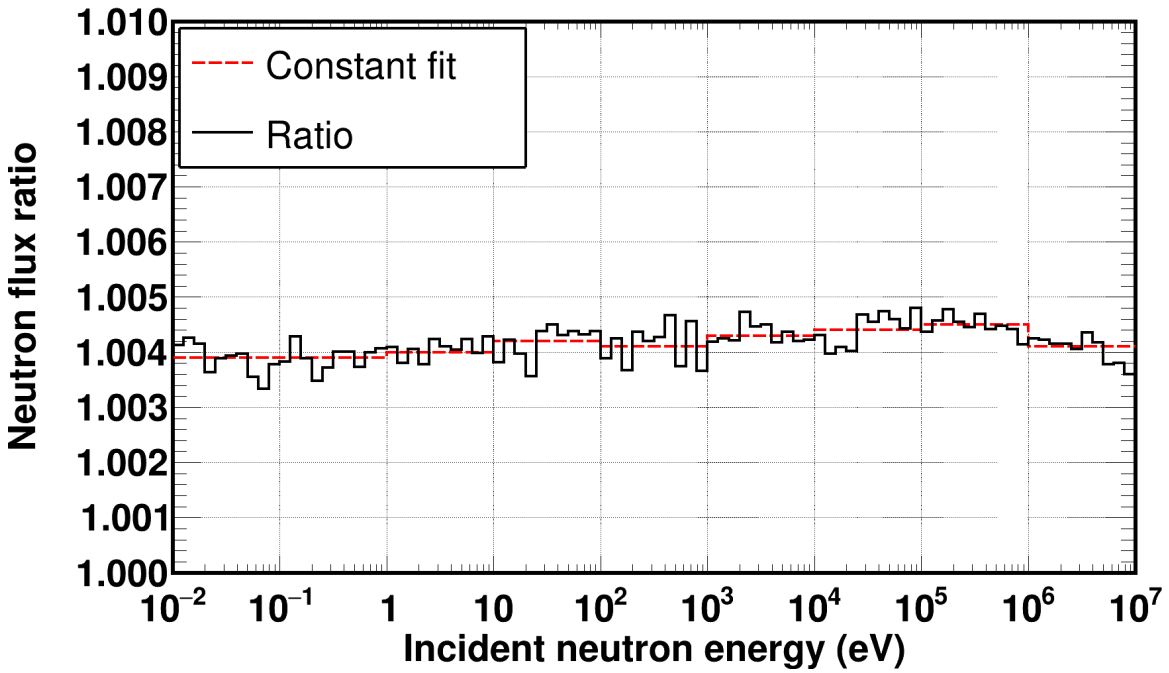

Figure 4.36: *Ratio of the simulated incident neutron fluxes between* 19.5 *and* 19.517 *m. The ratio was fitted with a constant fitting function, individually per energy decade. An average correction factor for the full energy range can also be considered.*

It has to be noted that since the correction factors per energy decade did not appreciably vary and given the order of 10% uncertainties, a constant energy independent correction factor can be applied, by calculating the weighted mean $\bar{x}$ of the individual correction factors x_i, using eq. (4.21a) with an uncertainty $\sigma_{\bar{x}}$ shown in eq. (4.21b), where σ_i denotes the absolute individual uncertainties. The constant correction factor that was eventually applied from sample to sample was estimated to be 0.41(1)% and although it seems negligible, in certain cases, such as the $^{237}Np(n,f)$ experiment, when multi-stacks are present, the correction can reach a few percent in samples that are relative far (i.e. > 10 cm) from the first one.

$$\bar{x} = \frac{\sum_i x_i \sigma_i^{-2}}{\sum_i \sigma_i^{-2}} \tag{4.21a}$$

$$\sigma_{\bar{x}} = \sqrt{\frac{1}{\sum_i \sigma_i^{-2}}} \tag{4.21b}$$

Table 4.5: *Constant fit values per energy decade for the ratio of fluxes at the distances of* 19.5 *and* 19.517 *m. The uncertainties were assigned as the maximum deviation from the fitting value to the experimental point.*

Energy range (eV)			Ratio (%)	Uncertainty (%)
10^{-2}	-	10^{-1}	0.39	14
10^{-1}	-	10^{0}	0.39	9
10^{0}	-	10^{1}	0.40	6
10^{1}	-	10^{2}	0.42	15
10^{2}	-	10^{3}	0.41	13
10^{3}	-	10^{4}	0.43	14
10^{4}	-	10^{5}	0.44	9
10^{5}	-	10^{6}	0.45	8
10^{6}	-	10^{7}	0.41	11

Finally, in an attempt to provide a rule of thumb for such a correction that will be valid within 20 cm, it can be said that the incident neutron flux decreased by 0.24% per cm, when moving along with the beam.

4.10 Spontaneous fission and cluster decay

Recorded fission events during the experiments consisted, apart from neutron and γ induced ones, from spontaneous fragments, as well as, proton-neutron clusters depositing higher energy than the α particles from the corresponding decays. The contribution of both spontaneous mechanisms was considered to correct the recorded fission yields.

4.10.1 Spontaneous fission

The spontaneous fission rate of ^{240}Pu was reported to be $5.7 \times 10^{-6}(2)\%$ which in principle was not expected to create a significant number of parasitic events. Indeed, as seen in fig. 3.25, in the worst case, the recorded rate of events that could be attributed to spontaneous fission was less than 6×10^{-3} counts/bunch while the total fission events were of the order of 1.6 counts/bunch, therefore the contribution of spontaneous fission events was considered negligible in the case of ^{240}Pu .

In the case of ^{237}Np , it was reported that the spontaneous fission rate was less than $2 \times 10^{-10}\%$, thus significantly smaller than the corresponding ^{240}Pu one and therefore parasitic contributions on the fission yield were also considered negligible.

4.10.2 Cluster decay

A decay mode of nuclei with atomic numbers above 40 is the emission of a proton-neutron cluster which is larger than an α particle but lighter than a fission fragment. An example of such a decay is the emission of ^{34}Si from ^{240}Pu at a rather insignificant branching ratio smaller than 6×10^{-15} [182].

An additional example is the cluster decay of ^{237}Np , which is accompanied by the emission of ^{30}Mg at a branching ratio smaller than 8.0×10^{-14} [182] therefore quite insignificant as well.

Despite the quite small branching ratios, the detection of clusters would be difficult, since the detectors were operated at a rather small gain, optimised for the detection of much heavier nuclei. However, it was considered mandatory to check the branching ratios prior to deciding on whether a special treatment was necessary or not.

4.11 Dead-time and pile-up correction

The dead-time/pile-up correction is the last correction on the recorded fission yield, which was the last one left to be described since it proved to be the most crucial. Although up to about 1 MeV incident neutron energy, no significant counting losses were observed, above the fission threshold fission signals were not recorded to a great extent for reasons that will be explained later in the text. To accommodate for these vast counting losses, a dedicated methodology was developed which was successfully applied [17].

4.11.1 Introduction

To apply such corrections, the calculation of the recorded reaction yield was deemed necessary. In time-of-flight spectra, where an isolethargic binning is frequently used, the effective experimental rate R_{exp} is used instead, which can be described as the ratio between the events N_{exp} observed in a time window $\Delta(\text{tof})$ to the time window, as shown in eq. (4.22)

$$R_{\text{exp}}(\text{tof}) = \frac{N_{\text{exp}}(\text{tof})}{\Delta(\text{tof})} \tag{4.22}$$

Several methodologies can be applied in tof spectra which can be divided into two main categories: (a) extendable (paralyzable) and (b) non-extendable (non-paralyzable). The former models treat a detection system in such a way, that the intrinsic resolving/dead time is extended whenever a new event is detected within the specific dead-time, therefore new events can be registered. On the contrary, a non-paralyzable detector cannot be paralyzed, therefore once an event is registered, the dead-time is not extending, thus no additional events can be recorded during the dead-time period.

The two models, which were initially developed for continuous sources, pro-

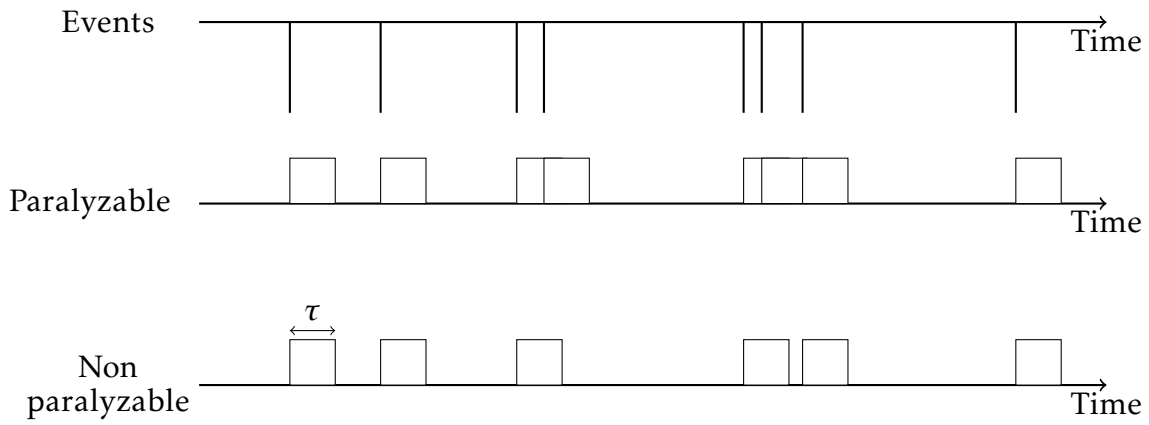

Figure 4.37: *Illustration of the paralyzable and non-paralyzable behaviour of a detection system. Events that arrive within the resolving (dead) time τ cause an extension of the acquisition in the paralyzable case, while in the non-paralyzable one during the dead-time no additional events can be registered.*

vide analytical expressions to estimate the true reaction rate R_{true} given the experimental one R_{exp} and a fixed dead-time τ, and therefore the dead-time correction factor f_{DT} as seen in eq. (4.23a) and (4.23b) for the paralyzable and non-paralyzable, respectively. Over the years, several hybrid models were also developed based on these ones, as described in the review papers by Müller [183, 184]. It has to be noted that when a digital acquisition system is employed and therefore the recorded signals are stored in raw format, both behaviours can be considered, since events can be artificially killed within a fixed time window. In addition, in cases where a pulse shape analysis is used, a detection system can be simultaneously extendable and non-extendable depending on the reconstruction efficiency: In some case pile-up events might be recovered while at others, not.

$$f_{\text{DT}} = \frac{R_{\text{true}}}{R_{\text{exp}}} = \frac{1}{e^{-R_{\text{true}}\tau}} \tag{4.23a}$$

$$f_{\text{DT}} = \frac{R_{\text{true}}}{R_{\text{exp}}} = \frac{1}{1 - R_{\text{exp}}\tau} \tag{4.23b}$$

In time-of-flight experiments where recorded signals occur from pulsed sources which produce beams with intensities that might appreciably vary with a relative variance σ^2, the detector is only periodically triggered during the N_{b} bunches of the experiment and therefore a different approach should be used. The standard generalised analytical expression that is applied on the time-of-flight spectra in each i^{th} tof bin of the recorded counts $N_{\text{exp}}(i)$ is the one described by Moore [18] and is seen in eq. (4.24), where the time difference $\tau = i - i_0$ is the dead-time of the system.

$$N_{\text{true}}(i) = -N_{\text{b}} \frac{\ln\left(1 - \dfrac{N_{\text{exp}}(i)/N_{\text{b}}}{1 - \sum_{j=i_0}^{i-1} N_{\text{exp}}(j)/N_{\text{b}}}\right)}{1 - \sigma \tanh\left\{\sigma \sum_{j=i_0}^{i-1} N_{\text{true}}(j)/N_{\text{b}}\right\}} \tag{4.24}$$

In cases when the beam intensity is considered to be constant with a variance less than 15%, Moore's formula is reduced to eq. (4.25), which is derived from Coates [19] and in modern facilities where the production of neutron beams is rather stable, this model is most commonly used. It has to be mentioned that both models describe in practice a paralyzable detection system, a statement which is very useful in the application of the analytical function.

$$N_{\text{true}}(i) = -N_{\text{b}} \ln\left(1 - \frac{N_{\text{exp}}(i)/N_{\text{b}}}{1 - \sum_{j=i_0}^{i-1} N_{\text{exp}}(j)/N_{\text{b}}}\right) \tag{4.25}$$

4.11.2 Correction below the fission threshold

To decide which model should be applied to the recorded fission yield in the time-of-flight domain, the variation of the beam intensity had to be studied. In both experiments the beam had a quite constant intensity, however there were time periods when variations were observed beyond 15%, as shown in fig. 4.38, where the beam intensity is presented for a small fraction of the recorded runs. In this case two approaches can be used: (a) apply Moore's formula directly on the summed fission yield and (b) divide the experiment in periods (or runs) where the intensity was constant within the formula requirements by Coates.

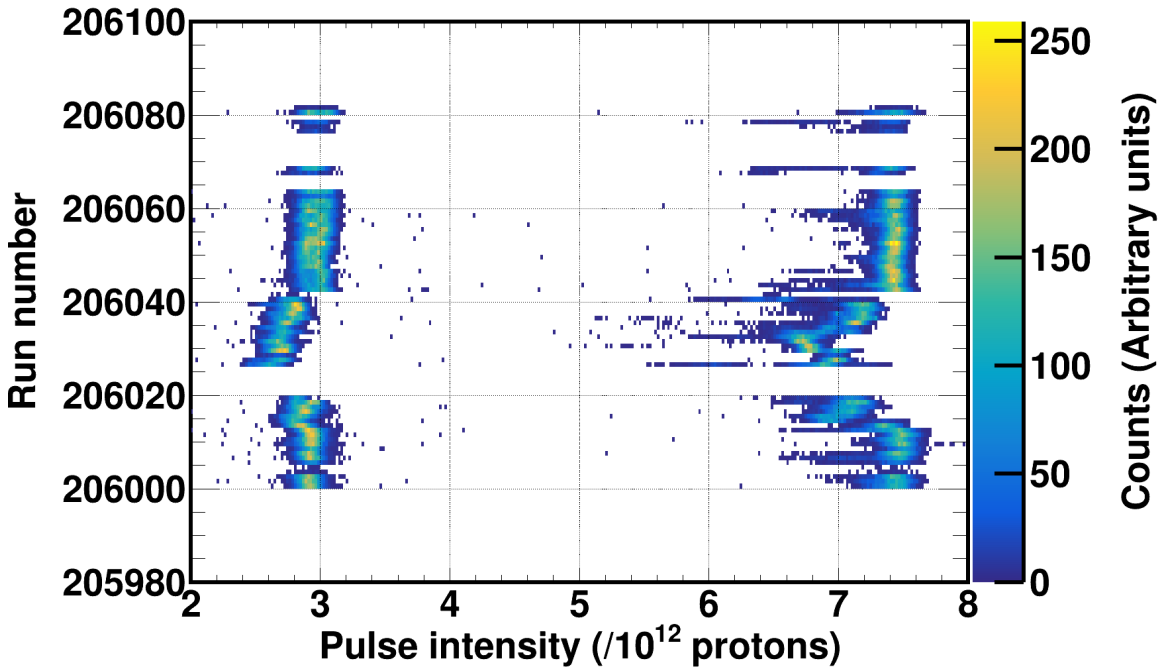

Figure 4.38: *The pulse intensity was constant throughout the vast majority of the campaigns. Runs in which a larger deviation than* 15% *was observed (i.e. 206020 - 206040)), were separately corrected concerning counting losses due to pile-up effects. The image is taken from PKUP during the* $^{237}Np(n,f)$ *experiment and both the dedicated and the parasitic bunches can be seen.*

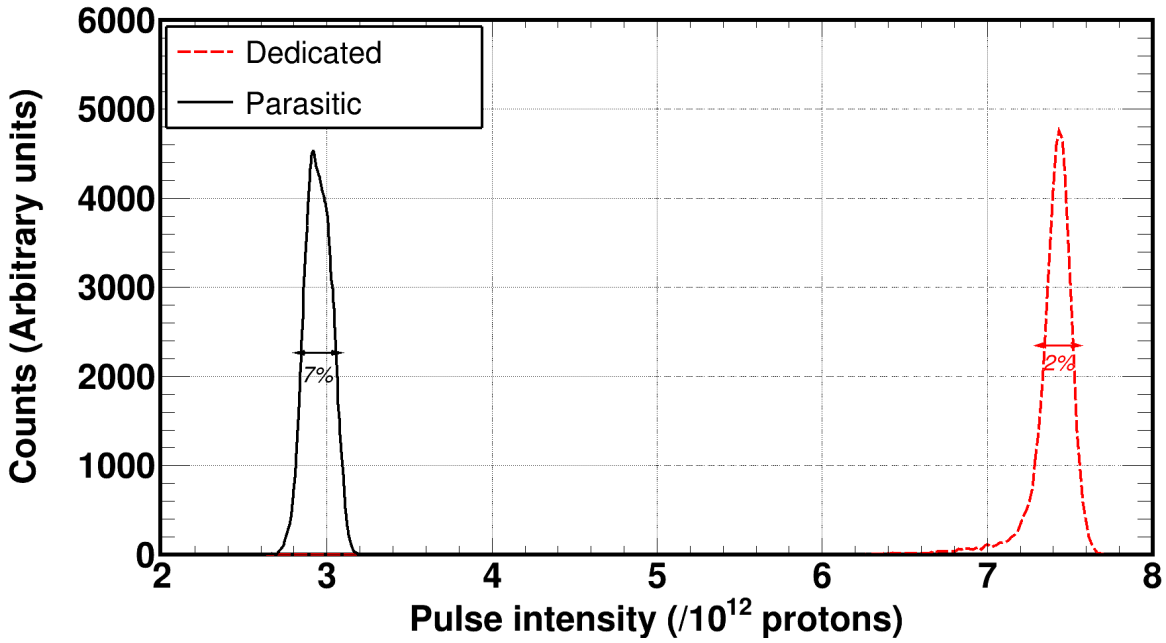

Figure 4.39: *The pulse intensity obtained from PKUP during the* $^{237}Np(n,f)$ *campaign, was considered stable within less than* 7% *(fwhm). Dedicated and parasitic bunches were separately analyzed and the corrected yields were then summed.*

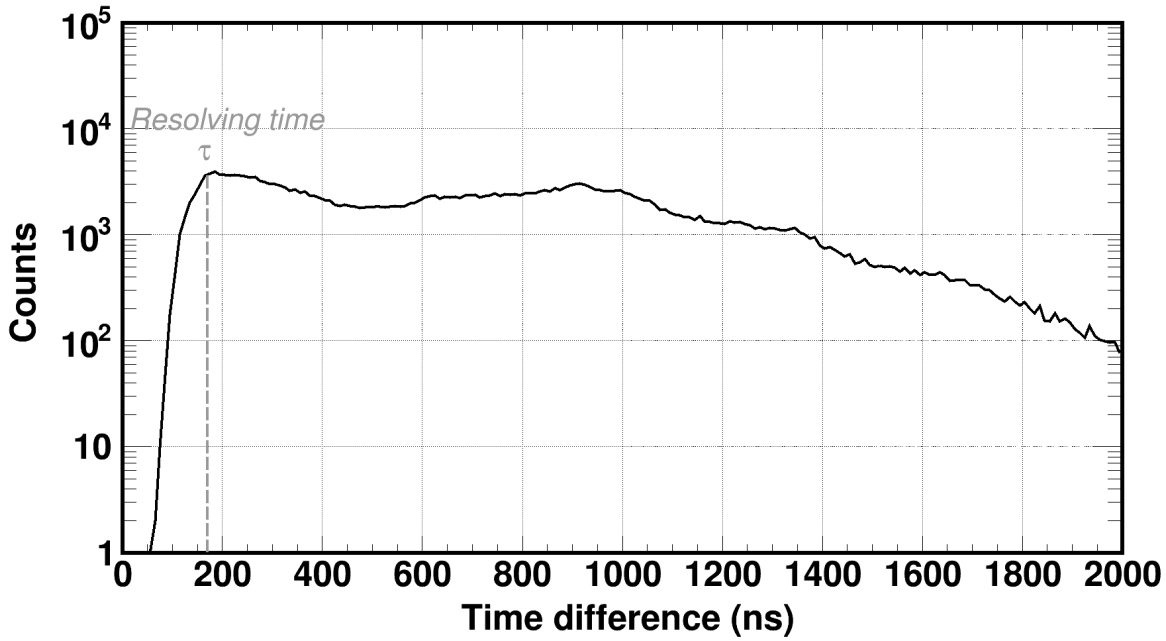

Figure 4.40: *Waiting time distribution for the ^{240}Pu - #3 sample reconstructed for all time of flights. The reconstruction routine became inefficient below $\approx$ 200 ns, a time difference which was considered as the resolving time of the detection system and was assigned as a fixed dead-time value.*

Both approaches worked similarly well, providing the same corrected yield, however, the application of Coates model will be further discussed due to its simplicity in the application. To apply the model, it had to be ensured that the beam intensity did not appreciably vary, which was confirmed from the PKUP detector and as shown in fig. 4.39 the proton beam was considered to be stable with a standard deviation smaller than 3%.

The next step, was to choose a fixed dead-time period during which any signal that was reconstructed would be rejected, treating therefore the detection system as a non-paralyzable one. Although the assignment of a fixed dead-time was not expected to be crucial for reasons that will be explained, the resolving time of the reconstruction routine was chosen to be applied. This was estimated by investigating the waiting time distributions (or similarly the distributions of the time difference between consecutive signals) of the detectors and determining the time difference τ where the efficiency of the reconstruction significantly dropped, as seen in fig. 4.40 and indicated with the dashed line.

To properly apply any non-paralyzable model in cases where reconstruction routines are used, the raw experimental time-of-flight spectra must be appropriately altered in such a way that upon the reconstruction and detection of a signal, any other that falls within the dead-time period should be artificially rejected, even if it is successfully reconstructed. Such an example is shown in fig. 4.41, where five in total signals were reconstructed, however only three (marked with blue squares) will be parsed in the time-of-flight spectrum, because the ones marked with red squares happened to arrive within the assigned dead-time τ period and therefore should be rejected.

This procedure was applied in all raw spectra and resulted in new ones which

consisted of fission events which would be produced from a truly non-paralyzable detection system, therefore Coates' formula could be applied. Figure 4.42 shows an example case of the correction applied on the ^{235}U sample of the $^{240}Pu(n,f)$ campaign in the energy region around the 8.8 eV resonance of the $^{235}U(n,f)$ reaction.

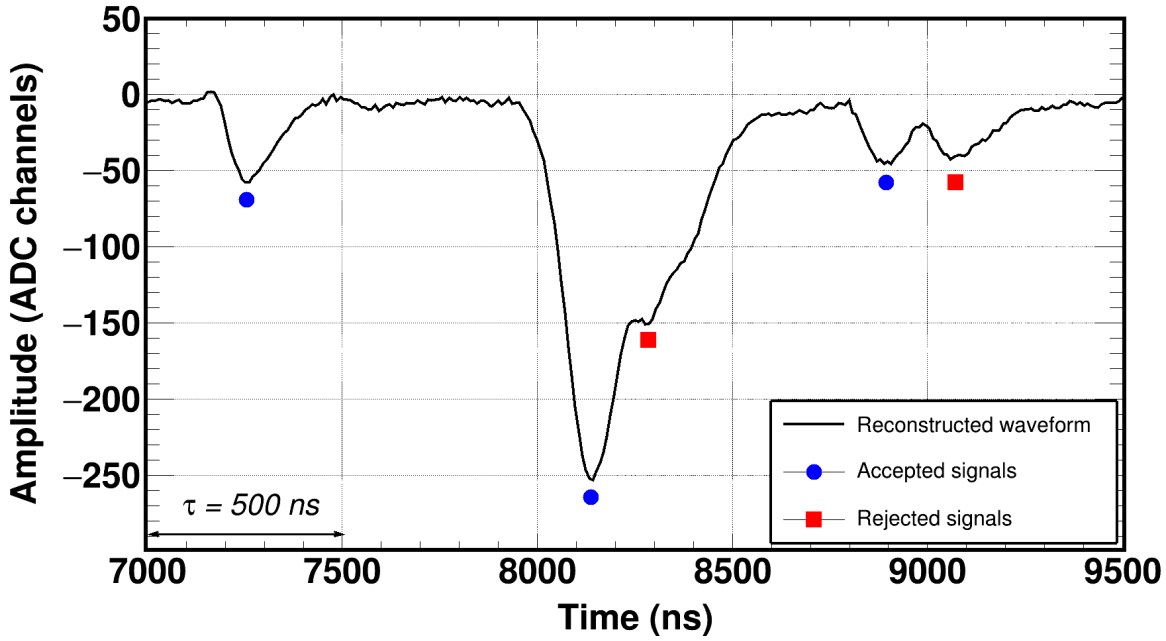

Figure 4.41: *Signals that arrived within the assigned dead-time period, were rejected in order to allow for the detection system to behave as a non-paralyzable one and apply Coates's formula for the dead-time correction.*

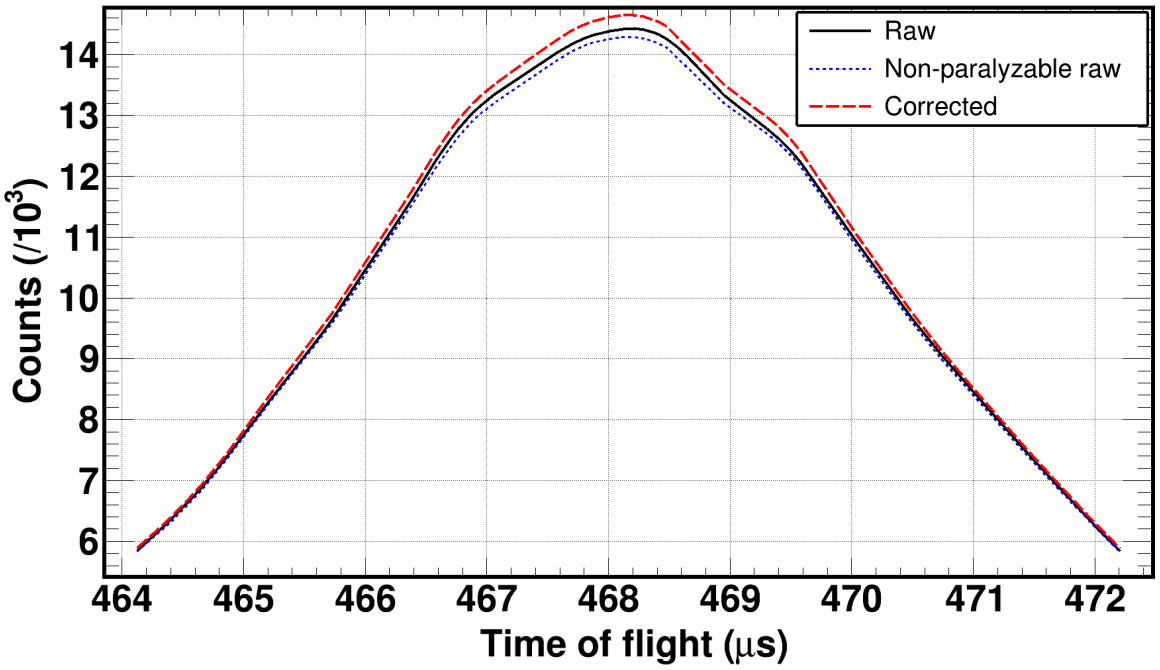

Figure 4.42: *The raw tof spectra (black solid line) were converted into the corresponding ones of a non-paralyzable system (blue dotted line), which were in turn corrected (red dashed line) using Coate's formula.*

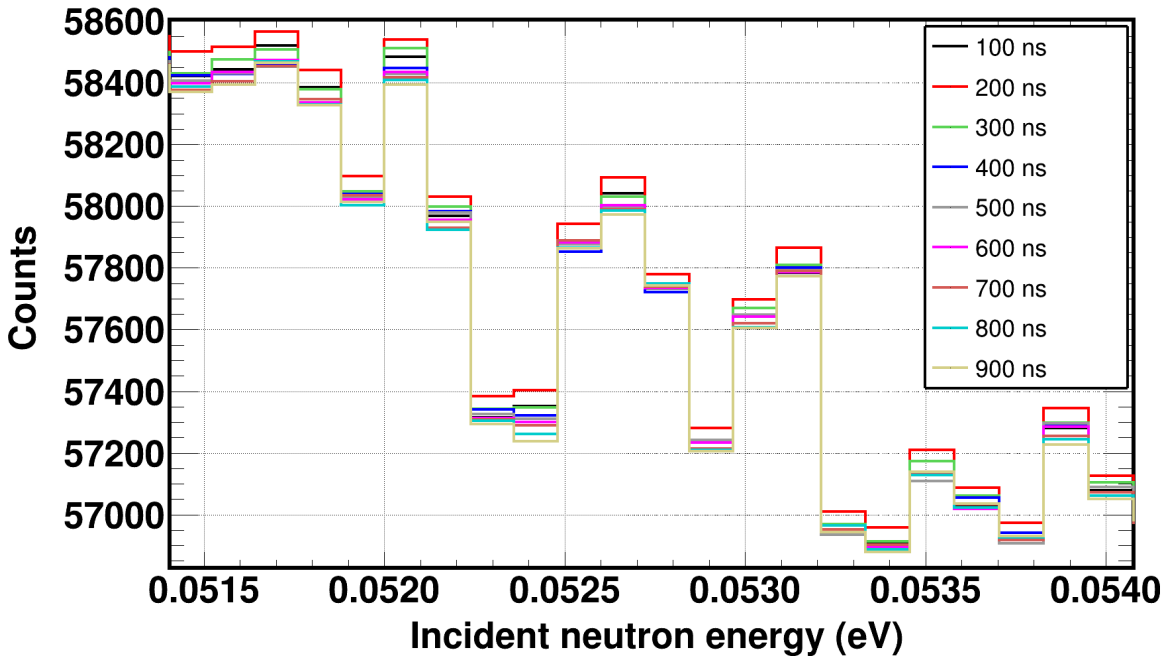

Figure 4.43: *The tof spectra were corrected introducing several fixed dead-time periods ranging from* 100 *to* 900 *ns. The corrected spectra were found to be consistent within less than* 0.3% *up to at least* 1 *MeV. The corrected spectra for the* ^{235}U *sample of the* $^{240}Pu(n,f)$ *campaign are shown at thermal neutron energies.*

To test the sensitivity of the model with respect to the selection of the fixed dead-time, the correction was applied for different dead-times ranging from 100 to 900 ns. Consistent corrected spectra - to a certain extent even for unrealistically large dead-times - would provide an indication of a trusted correction methodology. Indeed, as seen in fig. 4.43, where the corrected spectra of the ^{235}U sample in the $^{240}Pu(n,f)$ campaign in thermal neutron energies are shown, an excellent agreement was achieved within less than 0.3%. This can be an estimate of the uncertainty of the correction which is in perfect agreement with the one stated in [185]. A similar agreement was observed for incident neutron energies up to 1 MeV in all cases. Above that energy, a special treatment was needed in cases where a large counting rate was observed, as will be explained in the next subsection.

Finally, the correction factor of the ^{235}U sample in the $^{240}Pu(n,f)$ campaign can be seen in fig. 4.44. It has to be noted that only this particular correction factor f_{DT} is shown, because it was the highest in the incident neutron energy region from thermal up to 1 MeV.

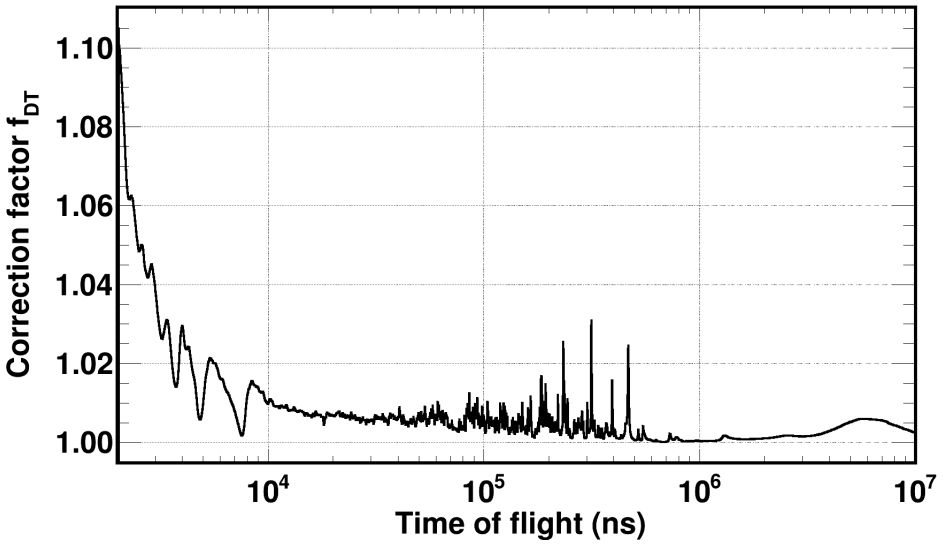

Figure 4.44: *Estimated dead-time correction factor for the ^{235}U sample in the $^{240}Pu(n,f)$ campaign from thermal neutron energies up to 1 MeV. This particular factor was found to be the highest of all the corresponding ones.*

4.11.3 Correction above the fission threshold

The available dead-time models were able to provide realistic corrections below the MeV region where the expected counting rates were significantly smaller than the corresponding ones above the effective fission threshold. In this energy region, a different approach was deemed necessary for the following reasons:

1. The correction factors were significantly inconsistent when applied for different fixed dead-times, as illustrated in fig. 4.45 where the dead-time corrected spectra of ^{235}U from the $^{240}Pu(n,f)$ experiment is shown. The corrections were estimated using Coates' model.
2. The most common models for dead-time corrections in time-of-flight experiments (i.e. Coates and Moore) which are applied in non-paralyzable systems are able to efficiently estimate losses in moderately small counting rates. As discussed in [186], these analytical models often fail to correctly estimate true counting rates, even in cases where the recorded reaction rate is seemingly low. In the case of both experiments, the instant expected counting rates were in the order of MHz, as calculated using the ENDF/B-VIII.0 evaluations for the ^{235}U , ^{238}U and ^{240}Pu -#3 samples in the $^{240}Pu(n,f)$ campaign as well as for the ^{237}Np -#5 and ^{237}Np -IPN in the $^{237}Np(n,f)$ one. The calculations can be seen in fig. 4.46 for a wide energy range from thermal to MeV.
3. Finally, the need for a special approach in the MeV region was justified upon deriving the experimental cross-sections especially in the case of $^{240}Pu(n,f)$, where the samples had similarly big masses, as shown in fig. 4.47 and 4.48. The $^{237}Np(n,f)$ campaign played a key role in confirming the quite significant effect of the reaction rates in time-of-flight experiments. The massive ^{237}Np sample provided from IPN-Orsay, suffered appreciably large counting losses and as shown in fig. 4.48, the application of an analytical model led

to a significant underestimation of the cross-section, similar to the $^{240}Pu(n,f)$ case. On the other hand, the samples provided by JRC-Geel had a proper mass thus providing a realistic cross-section. In addition, the ^{237}Np rates were similar to the ^{235}U one, indicating that in reference measurements the important parameter is not only the absolute rate, but their ratio.

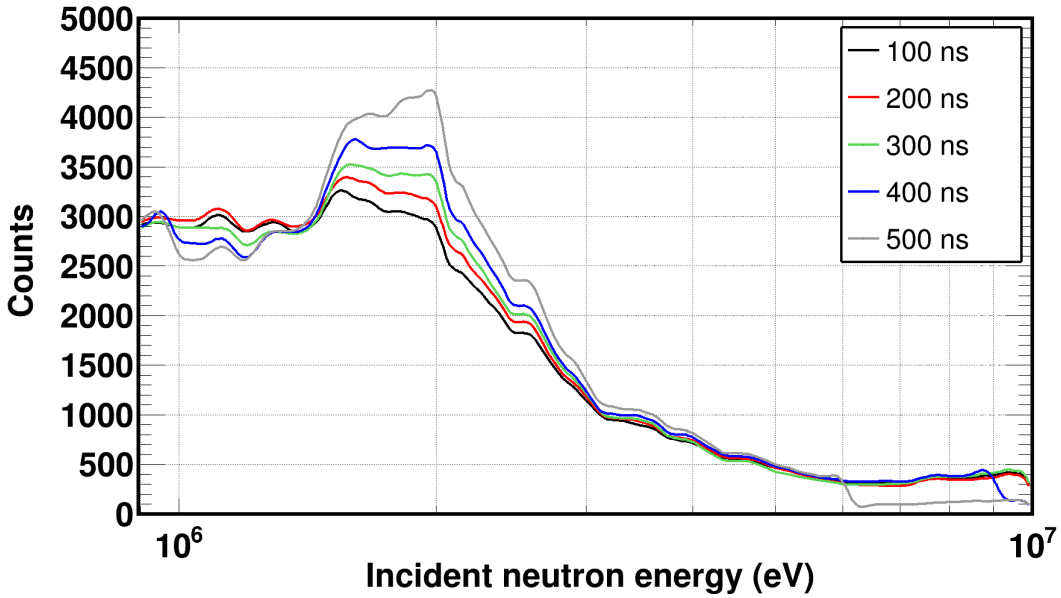

Figure 4.45: *Dead-time corrected counting spectra in the MeV region concerning the ^{235}U sample in the $^{240}Pu(n,f)$ campaign. Significant discrepancies were observed that reached up to 30%, indicating the weak predictive power of counting losses in that energy region.*

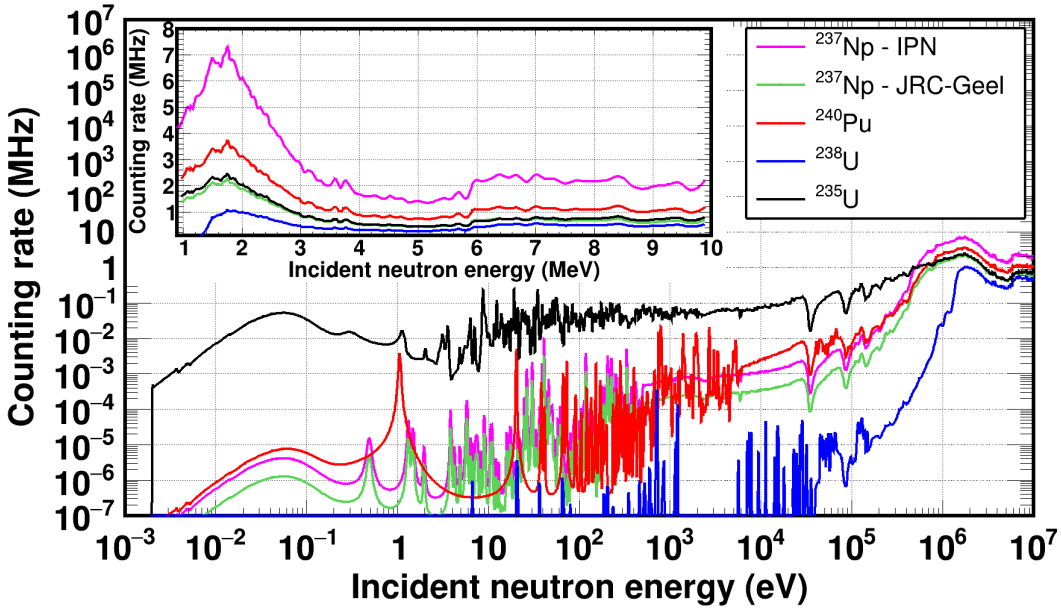

Figure 4.46: *Calculated instantaneous fission rates for the heavier samples in both campaigns using the ENDF/B-VIII.0 evaluations. It is evident that for high incident neutron energies above 1 MeV (the expected rates shown in the inset), significantly higher counting rates of the order of MHz were expected compared to lower energies.*

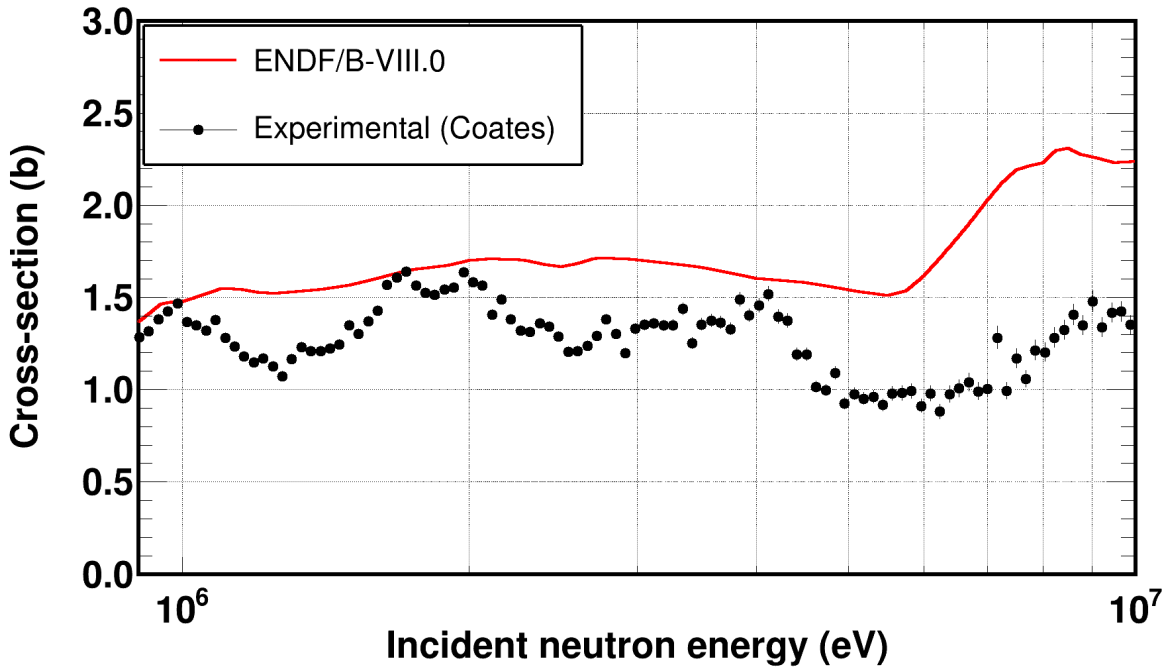

Figure 4.47: *Neutron induced fission cross-section, as calculated for a single ^{240}Pu sample using the model proposed by Moore in comparison to the ENDF/B-VIII.0 evaluation. The effect of the significant amount of counting losses is quite visible.*

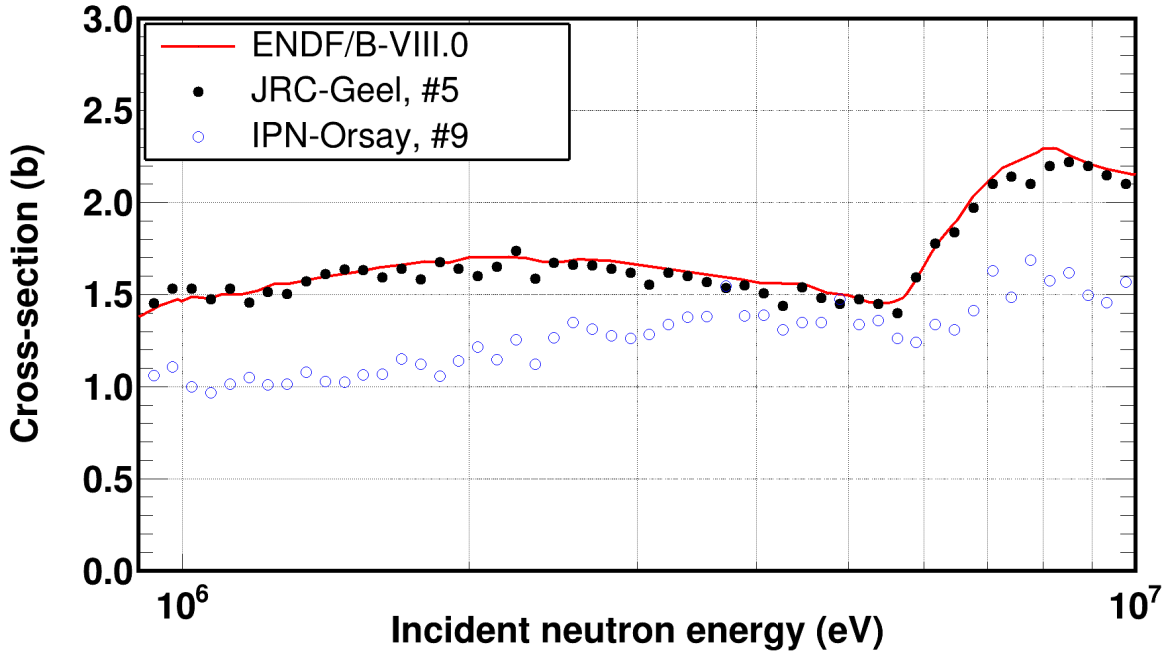

Figure 4.48: *Neutron induced fission cross-section, as calculated for a ^{237}Np sample with appropriate mass (#5) and the one provided from IPN-Orsay in comparison to the ENDF/B-VIII.0 evaluation. Both cross-sections were derived using the model proposed by Moore. The discrepancies observed, indicated that high counting rates led to high counting losses which could not be addressed by analytical expressions.*

For the previous reasons, the challenging issue of significant losses had to be addressed through the means of a general approach, regardless of the nature of the source (continuous or pulsed), with the use of waiting time distributions and detector emulation devices.

4.11.3.1 Waiting time distributions

The proposed methodology to estimate counting losses when high counting rates are expected lied on the intrinsic characteristic of counting experiments, which can be efficiently described by Poissonian statistics. In occasions where a constant counting rate R is expected, the time difference between consecutive events, is proven (see. Appendix in [17]) to follow an exponential decay distribution as seen in eq. (4.26) where $\mathrm{d}P/\mathrm{d}t$ describes the probability density to detect two consecutive signals.

$$\frac{\mathrm{d}P}{\mathrm{d}t} = R\,e^{-Rt} \tag{4.26}$$

This intrinsic characteristic can be used to estimate the counting losses occurring in a counting experiment with a constant counting rate R as illustrated in fig. 4.49. This feature is generally valid and can be used in all cases, as long as the counting rate is constant or in the approximation that it does not appreciably vary.

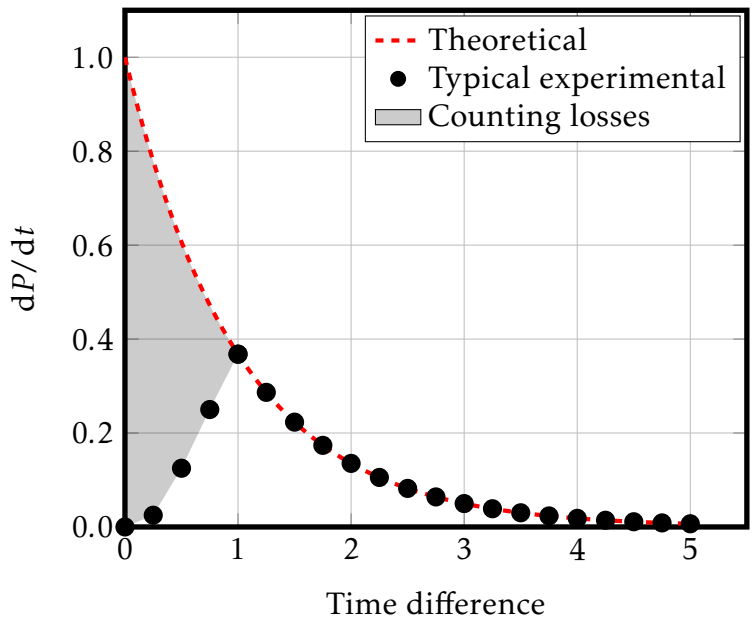

Figure 4.49: *Illustration of counting losses in the waiting time distribution. For time differences below the resolving time of the detection system, the experimental counts are less than the expected ones which follow an exponential decay distribution, due to counting losses occurring during the experiment.*

A counting spectrum, either in tof or energy, can consist of narrow enough regions, where the counting rate can be considered constant, as shown in fig. 4.49 for incident neutron energies above 1 MeV. In addition, these regions have to be wide enough to provide waiting time distributions with sufficient statistics in order to apply an exponential decay fitting function to the experimental points and estimate the counting loses.

More specifically, to quantify these losses and therefore calculate the correction factor f_{DT} in each proper sub-region of the counting spectrum of each isotope, the experimental waiting time distributions per region were fitted using eq. (4.26). The ratio between the integral of the fitted curve, extrapolated until it intercepts the y-axis and the experimental points, provided an estimation of the correction factor f_{DT}, as expressed in eq. (4.27).

$$f_{\mathrm{DT}} = \frac{\text{Extrapolated Fitted Integral}}{\text{Experimental Integral}} \tag{4.27}$$

The aforementioned methodology worked seemingly well in the case of fission cross-section time-of-flight measurements, as as described in the following discussion. A typical waiting time distribution can be seen in fig. 4.50, where the time difference between consecutive events was constructed in the case of the ^{240}Pu -#4. The similarities that were observed with the theoretical case illustrated in fig. 4.49 were quite encouraging.

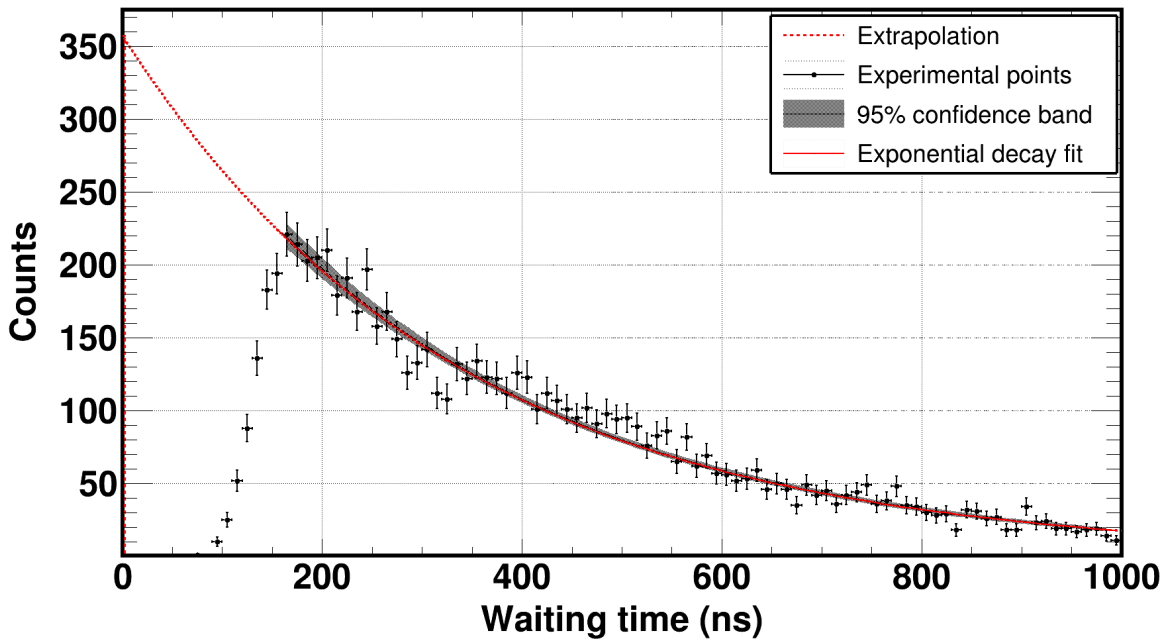

Figure 4.50: *Exponential decay fit of the waiting time distribution of the ^{240}Pu -#4 sample for signals that arrived in time-of-flights that corresponded to 2 - 2.2 MeV incident neutron energies. Apart from the experimental points, the fitting function and its extrapolation, the confidence band at 95% confidence level is shown. The similarities with the theoretical case in fig. 4.49 were quite encouraging.*

Finally, the construction of waiting time distributions and their exponential decay fits was applied to the ^{240}Pu , ^{238}U , ^{235}U and ^{237}Np -IPN-Orsay samples, in which the counting losses were significant, due to their masses and therefore could not be properly estimated with the application of the available analytical methodologies. As evidenced in fig. 4.54, where the $^{238}U(n,f)$ cross-section was derived with reference to the ^{235}U one, a systematic overestimation was observed, which was attributed to the underestimation of the dead-time correction on the ^{235}U reference sample using Coates/Moore formulas. On the other hand, the fits of the waiting time distributions, provided realistic corrections leading to a proper reproduction of the standard $^{238}U(n,f)$ cross-section within less than 5%, thus providing solid proof that such a methodology can be successfully applied.

It has to be mentioned that the waiting time distributions extend up to practically the end of the acquisition window, however the fits were applied in a rather small region (i.e. $\sim 4-5$ times the resolving time), in order to avoid interference from prominent structures attributed to the reaction rate (i.e. resonances in the cross-section, dips in the flux etc). For this reason, each distribution was fitted in several different ranges in the resolving time neighborhood and the difference of the corresponding correction factors provided an estimation of the uncertainty which was found to be not greater than 10%.

4.11.3.2 Detector emulation

Supplementary to the fitting methodology, the prediction of the true counting rate (R_{true}) in an experiment, given the recorded experimental one (R_{exp}) can be made possible through the use of detector emulation devices providing a hardware estimation of the occurring counting losses. The fundamental idea lied in the generation of signals that featured the same attributes to the ones of the actual detection system (i.e. width, rise-time etc) at given frequencies that represent R_{true}. These signals were afterwards fed to the acquisition system of the experimental campaign and were analyzed using the exact same reconstruction routines and methodologies as in the real experimental data that suffered from counting losses, in an attempt to calculate the R_{exp}. The ratio between R_{true} and R_{exp} practically represents the dead-time correction factor f_{DT} for each input frequency, as expressed in eq. (4.28). In addition to individual correction factors per frequency, this methodology has the ability to provide a correction function $R_{true} = f(R_{exp})$, derived by fitting the emulated data, which can later be used to estimate the R_{true} at given counting rates R_{exp} recorded in a similar experiment in which the same detection system was employed.

$$f_{DT} = \frac{R_{true}}{R_{exp}} \tag{4.28}$$

Experimental set-up

The correction function $R_{true} = f(R_{exp})$ was estimated through the use of a dual-channel CAEN DT5800 digital detector emulator. This particular module provided

the possibility to emulate user-defined signals at frequencies specified by the user. The sampling of these signals in time is also a parameter of the system and various standards or user-defined distributions can be accepted, such as the Poisson distribution, which was the one used in the present study. The input signals that were used were the ones derived from the $^{240}Pu(n,f)$ campaign in which the challenging issue of significant counting losses was initially observed.

The goal of this study was to quantify the counting losses due to the finite resolution of the detector signals and possible inefficient offline signal reconstruction. Firstly, to better understand the nature of the counting losses with respect to the reaction rate which is emulated by the generation frequency, a constant amplitude of 1 V was chosen as an output of the emulator instead of a more realistic fission amplitude distribution. This choice assisted in pinpointing cases where an unrecoverable pile-up took place, as will be explained later in the text.

Micromegas signals were generated following the realistic Poisson distribution at various frequencies, ranging from 20 kHz up to 1.9 MHz. The output was then sent to the acquisition system which was allowed to record about $\sim 10^6$ emulated signals, thus minimizing the statistical uncertainty of the recorded counts. The standard procedure of data handling, selection and storage, similar to the one described in previous chapters, was used.

Notes on data analysis

As mentioned previously, signals of a constant amplitude were generated and then analyzed by the standard reconstruction techniques. A typical signal reconstruction can be seen in fig. 4.51 in which three prominent categories of signal reconstruction are shown:

(a) Signals marked with green diamonds: Normal reconstruction occurring when the routine successfully recognized the raw signal
(b) Signal marked with a magenta triangle: High counting rates can result in poor performance of the reconstruction routine and consequently in the signal discard. It has to be noted that since the reconstruction routine used a set of user-defined parameters, the unrecovered signals can be recognized as true events with a different set of parameters. The method proposed in this work takes also into account such cases and can provide corrections for an inefficient use of the reconstruction routine, since this leads to counting losses as well.
(c) Signals marked with gray triangles: Prominent examples of unrecoverable pile-up. Although the routine was able to successfully reconstruct the waveform, it could not distinguish signals that arrived very close to each other and resulted in the formation of a bigger signal similar in shape to the input one. The initial choice of a constant amplitude in the input signals assisted in pinpointing these cases since the signal amplitude is higher than 100 channels by a factor of 2, 3, etc.
(d) Signals marked with blue squares: Example cases of recovered pile-up in which, despite the small proximity of events, the reconstruction routine was

able to distinguish them.

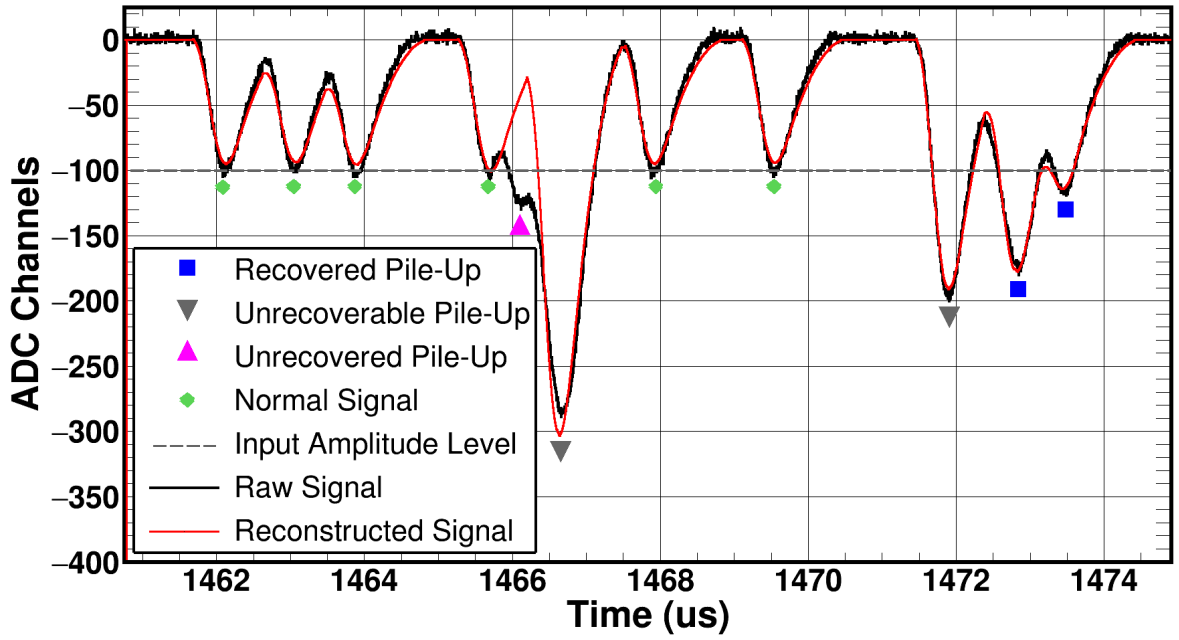

Figure 4.51: *Typical signal reconstruction from emulated signals recorded at* 1 *MHz. Apart from the raw and the reconstructed signals, different pile-up cases which are marked with symbols, are shown. See text for further details.*

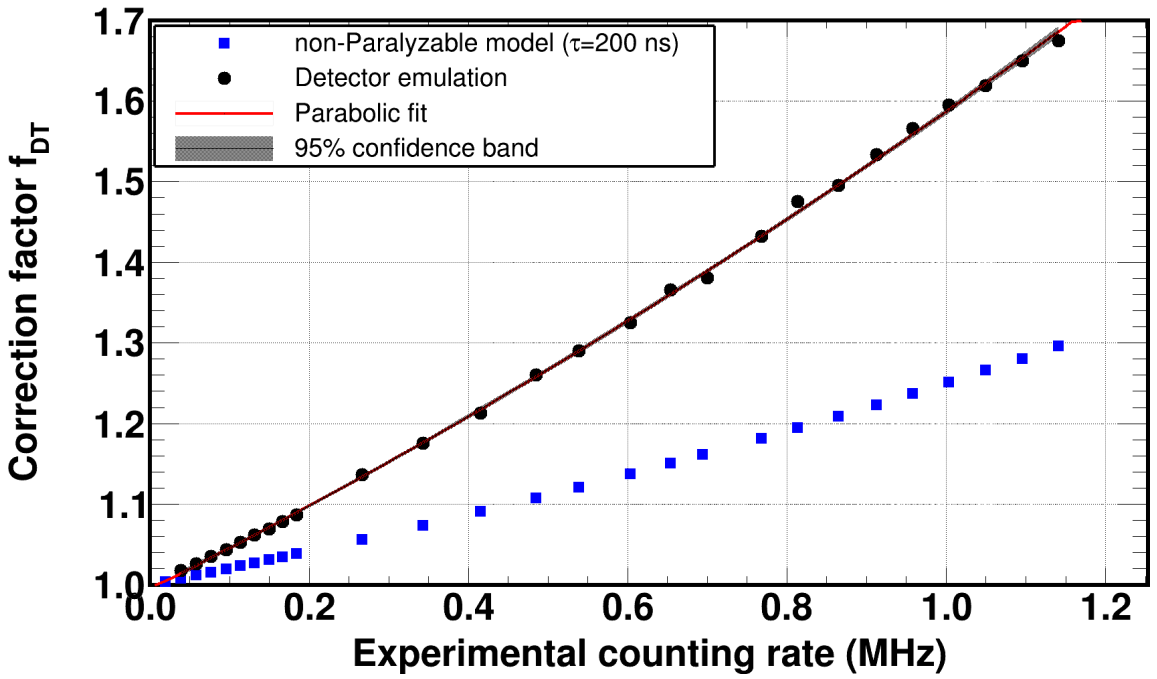

Figure 4.52: *The correction factor f_{DT} extracted from the detector emulation technique showed a parabolic relation to the experimental counting rate. The fitting function can be used to predict correction functions in the bandwidth from* 20 *kHz up to* 1.2 *MHz. The correction factors predicted from the non-Paralyzable are also shown for comparison.*

The signal reconstruction was followed by data analysis and the calculation of the experimental counting rate which was smaller than the one produced by the emulator. The application of eq. (4.28) provided a correction factor for each recorded frequency in the bandwidth from 20 kHz up to 1.9 MHz. As seen in fig. 4.52, the correction factors presented a parabolic behaviour. In addition, the comparison to the correction factors predicted by the standard non-Paralyzable model, indicated that the $\sim 20\%$ discrepancy seen in the $^{238}U(n,f)$ cross-section in fig. 4.54, can be attributed to the $\sim 20\%$ discrepancy of the correction factors estimated by the two methodologies.

To validate that the correction factors predicted by the detector emulation technique, the waiting time distributions were used. For each frequency, the methodology presented in the previous subsection was applied, by fitting the waiting time distributions with an exponential decay function. As seen in fig. 4.53 in the 1 MHz frequency, the behaviour was the expected exponential one, validating the requested Poissonian nature of the module and the correction factors calculated through the application of eq. (4.26) were in perfect agreement to the corresponding ones from the emulation methodology, within less than 1%, which can be considered as the uncertainty of the methodology in the frequency bandwidth in which it can be applied.

Finally, the validation of the methodology was achieved by applying the correction function that was estimated, to the experimental counting rates of ^{238}U and ^{235}U samples in the $^{240}Pu(n,f)$ campaign. The quite efficient reproduction of the standard $^{238}U(n,f)$ cross-section shown in fig. 4.54, indicated the accuracy of the developed methodology.

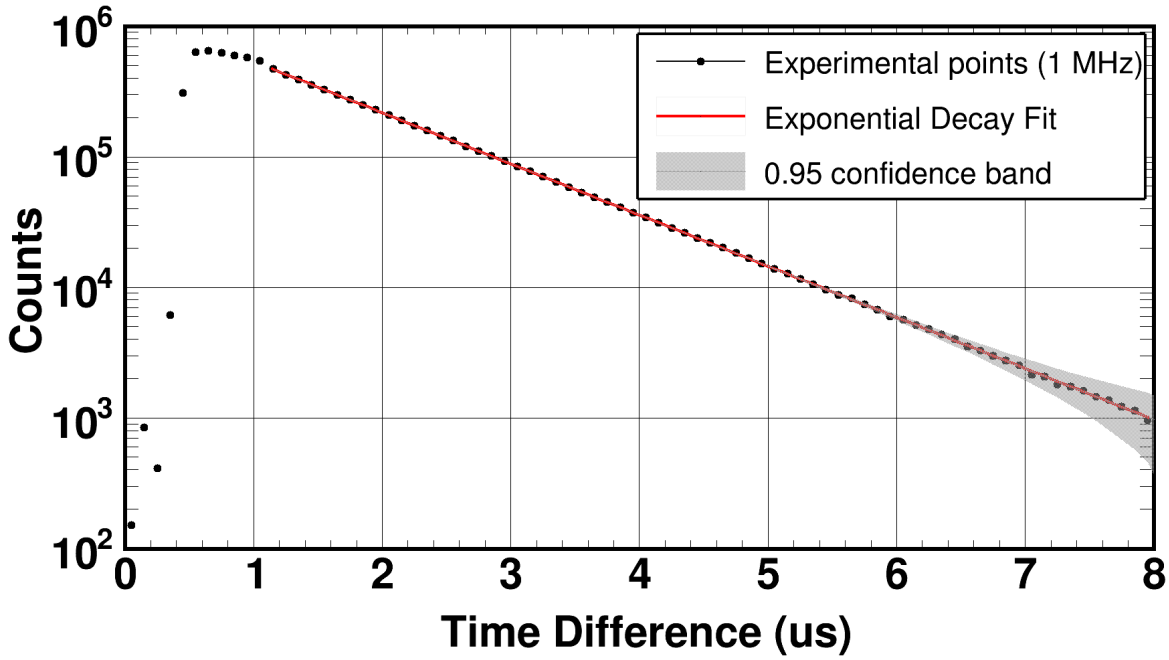

Figure 4.53: *Exponential decay fit of the waiting time distribution in the case of* 1 *MHz. Apart from the experimental points and the fitting function, the confidence band at* 95% *confidence level is shown.*

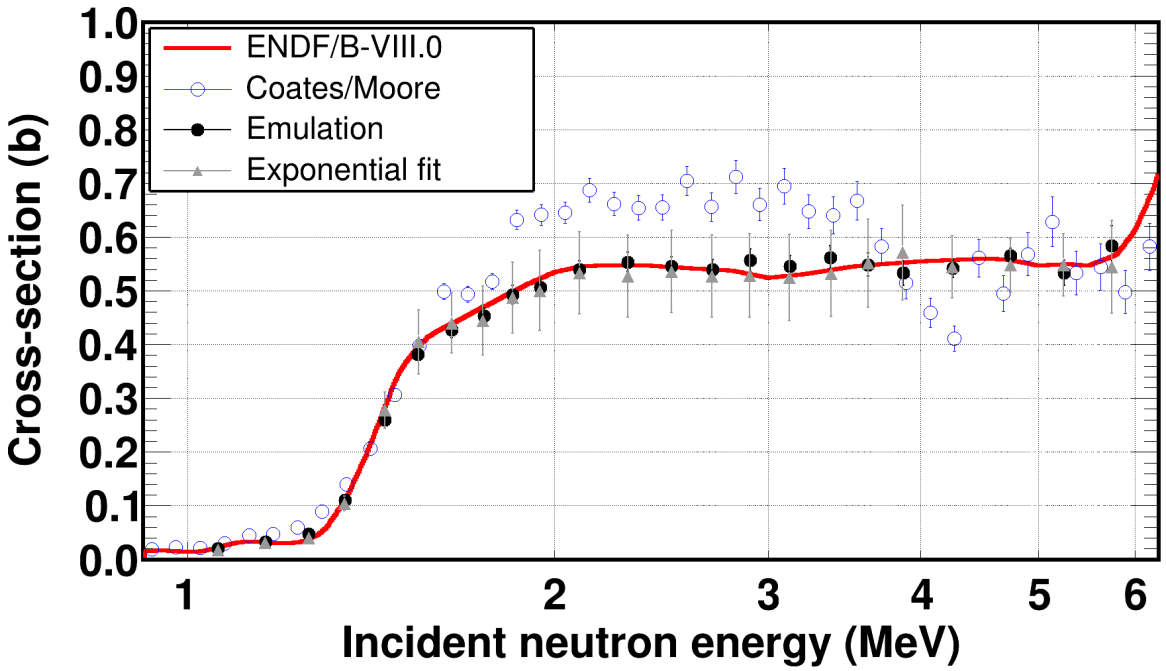

Figure 4.54: *Neutron induced fission cross-section of ^{238}U which was derived from the $^{240}Pu(n,f)$ experiment data. It was evident that the estimated dead-time corrections from Coates/Moore overestimated its value. The application of the proposed methodologies made possible the reproduction of the standard cross-section with less than 5% discrepancies.*

Notes on the level of paralysis of the detection system

As discussed previously, a detection system that is described by a fixed dead-time can be considered either paralyzable, non-paralyzable or a mixture of both, in which case it is described by a paralysis parameter p. In a paralyzable system the paralysis parameter is 1 while for a non-paralyzable one, is 0. In all intermediate cases p gets a value in between.

Although a fixed dead-time can be assigned as the resolving time, the level of the paralysis is very difficult to be estimated. This becomes even more difficult in cases where a pulse shape fitting is applied, in which case the paralysis parameter can vary within a small time interval, depending on the success of the reconstruction routine to properly reproduce the input waveforms. As illustrated in fig. 4.51, the signal marked with a magenta triangle was not reconstructed although it arrived relatively close to the resolving time.

In addition, it was observed that for various frequencies the resolving time is not constant, therefore a fixed dead-time model might not always be proper to account for severe counting losses. To illustrate the aforementioned problems, the emulated data was fitted with the paralyzable and non-paralyzable model.

In the paralyzable case, the fitting function seen in eq. (4.30) was used to parametrize the experimental counting rate R_{exp} as a function of R_{true}. The A parameter is for normalization purposes while τ will directly provide the dead-time of the detection system. As shown in fig. 4.55 the paralyzable model can reproduce the shape of the emulated data with quite a large margin, while it predicted a dead-

time of $\tau = 250$ ns, which was about 40% higher than the 150 ns resolving time.

$$f(x) = A\,\frac{x}{1 - x\tau} \tag{4.29}$$

Similarly, in the non-paralyzable case, the fitting function seen in eq. (4.29) was used to parametrize the experimental counting rate R_{true} as a function of R_{exp}. Note the reverse relation with respect to the paralyzable case. Again, the A parameter is for normalization purposes, while τ provides the fixed dead-time of the system. As shown in 4.56 the paralyzable model can successfully reproduce the shape of the emulated data, however it predicted a dead-time of $\tau = 320$ ns, which was more than a factor of two higher than the actual 150 ns resolving time.

$$f(x) = A\,x\,e^{-x\,\tau} \tag{4.30}$$

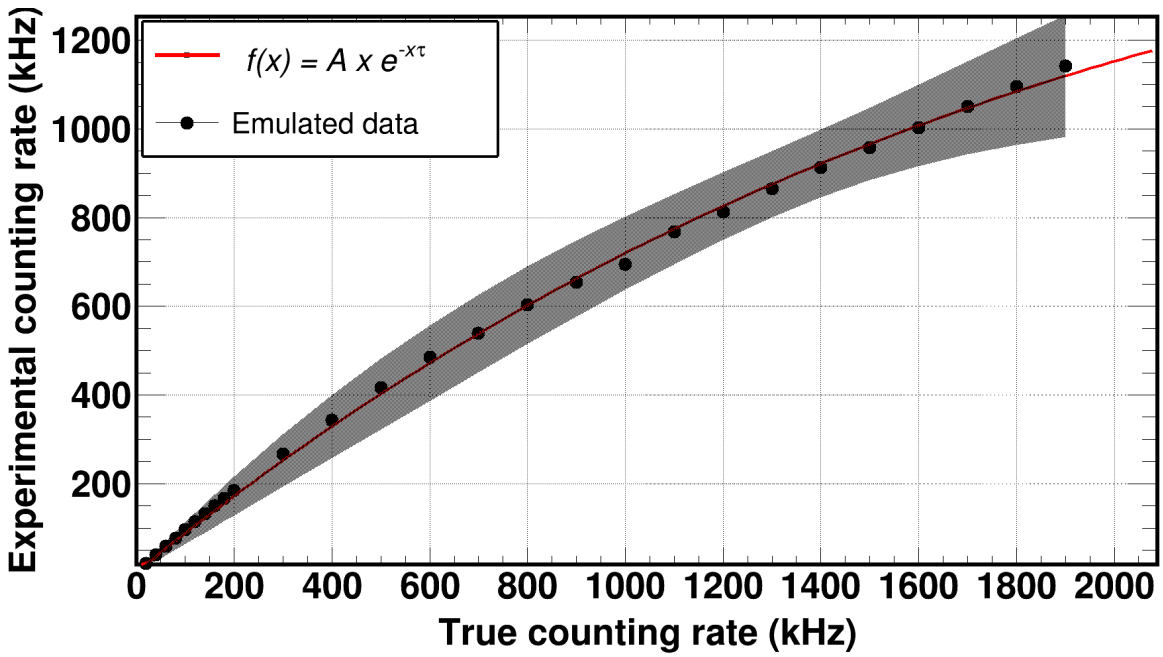

Figure 4.55: *The emulated results were fitted with the paralyzable model and great uncertainties were observed as indicated by the* 95% *confidence band. In addition, the model yielded a fixed dead-time of* 250 *ns,* 40% *higher that the* 150 *ns resolving time.*

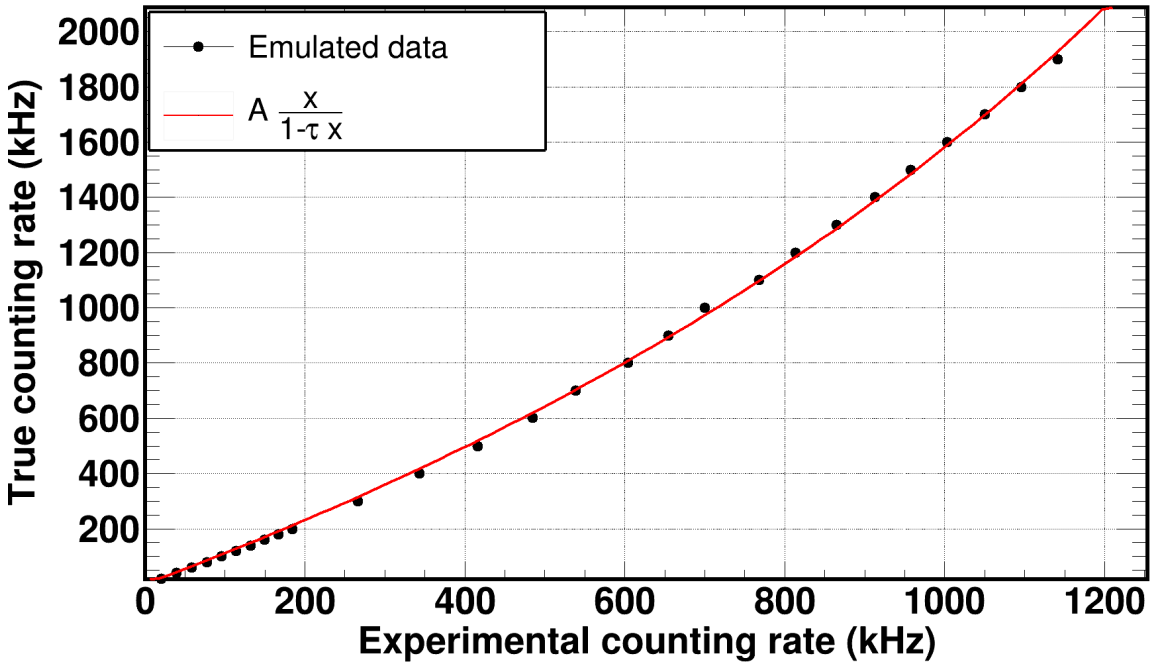

Figure 4.56: *The emulated results were fitted with the non-paralyzable model which, although able to reproduce the shape, yielded a fixed dead-time of* 320 *ns, more than two times greater than the* 150 *ns resolving time.*

On the uncertainty and limitation of the methodologies

The application of the fitting methodology of waiting time distributions in the experimental time-of-flight data was able to predict correction factors which, when applied to the fission yield, reproduced the $^{238}U(n,f)$ cross-section within a quite reasonable extent. However, the uncertainty of this method depended on the quality of the fits in the waiting time distributions. Since these distributions were calculated by making compromises between the statistics, the variation of the reaction yield and an adequate binning to reproduce the cross section, an uncertainty of the order of 15% could be justified.

On the other hand the use of emulation devices provided a correction function, which when applied to the fission yields of ^{238}U and ^{235}U , a better reproduction of the $^{238}U(n,f)$ was achieved with discrepancies less than 3%. At the same time, a parabolic function was quite representative of the data regression, therefore correction factors were estimated with minimal uncertainties, for the specific bandwidth 20 kHz - 1.9 MHz. However, the application of such a method required the use of additional hardware devices, which might not always be available.

All in all, the combined use of both methodologies, which advantageously rely only on experimental techniques rather than on simulations or analytical models, was proven to be a good asset in deriving realistic estimates of the counting losses that occurred during a high instantaneous data collection rate. It goes without saying, that the use of such a methodology is not limited to fission experiments, but can be used in a plethora of applications, as long as its requirements are met.

4.12 Validation of the corrections on the recorded fission yield

The validation of the numerous applied corrections to the recorded fission yield is considered to be of vital importance prior to deriving the fission cross-sections. Several methodologies and techniques were used to prove not only the coherence of the analysis among the several fission foils, but the good quality of the corrections as well. The validation was based on comparisons between the corrected fission yields, the reproduction of standard reactions such as the $^{238}U(n,f)$, the calculation of the incident neutron flux along with the comparison to simulations and evaluations, which was already mentioned and discussed and last but not least the consistency of the corrected yield in different experimental conditions, such as for high and low counting rates.

4.12.1 Comparison of the corrected fission yields

The derivation of the fission cross-sections was based on the calculation of the weighted average of the individual cross-sections derived from the each sample. An essential prerequisite, however, was that the quantities the weighted average was calculated from had a reasonable agreement.

To confirm this, the Z-score ζ was calculated between all possible combinations of the fission yields in each campaign, based on eq. (4.31) which describes the calculation of ζ between two experimental quantities x and y which are accompanied by their uncertainties u_x and u_y, respectively.

$$\zeta = \frac{x - y}{\sqrt{u_x^2 + u_y^2}} \tag{4.31}$$

In both campaigns, the corrected fission yields were found to be in a quite satisfactory agreement, within less than 1σ mostly in the vast majority of the incident neutron energies, as illustrated in fig. 4.57 for the ^{240}Pu samples from thermal up to Mev energies (top figure) and the ^{237}Np ones in the MeV region (bottom figure).

In the ^{240}Pu foils, a systematic deviation from zero was observed for incident neutron energies above 6 MeV, which in fact defined the upper limit of the reported data. This upper energy limit was attributed to the limitation of the γ-flash subtraction technique that was described in a previous chapter.

On the contrary, the ^{237}Np samples are in an excellent agreement up to ~ 14 MeV, above which systematic discrepancies were observed. This significantly higher upper energy limit was attributed to the narrower γ-flash pulse, which in combination to the appreciably reduced γ-flash ringing on the ending tail allowed for the γ-flash subtraction to be more efficient, thus reaching a significantly higher neutron energy.

A similar comparison could be simply made by investigating the derived cross-sections for each sample and determining how good the agreement between each derived cross section was. This comparison was additionally made and in the case

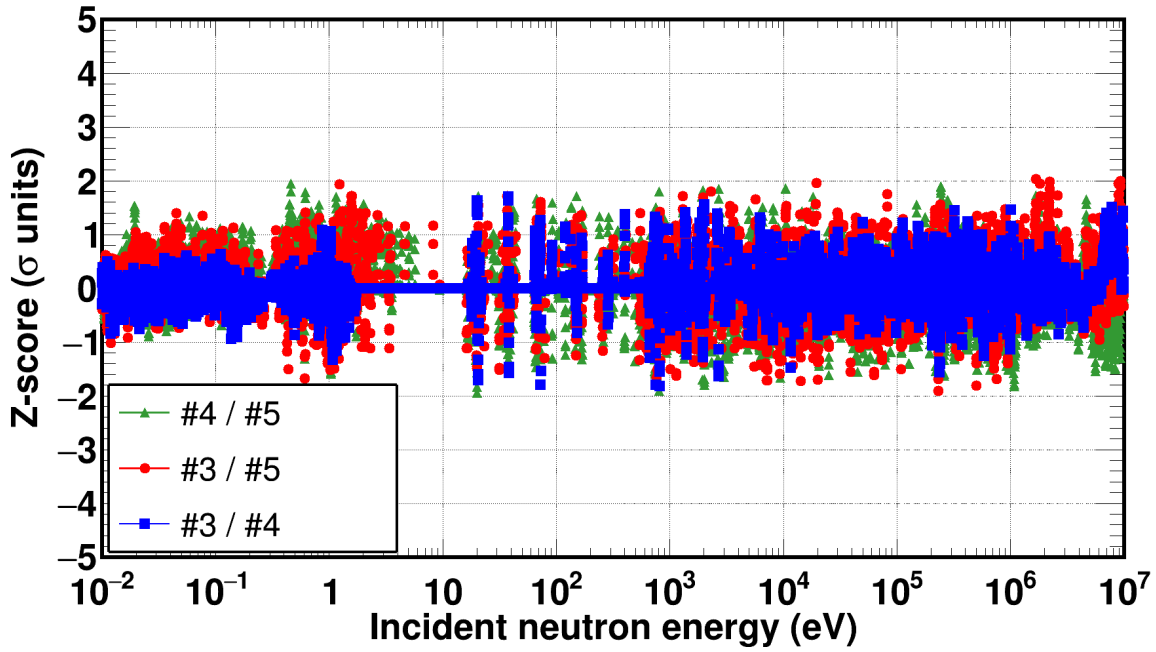

(a) ^{240}Pu *samples*

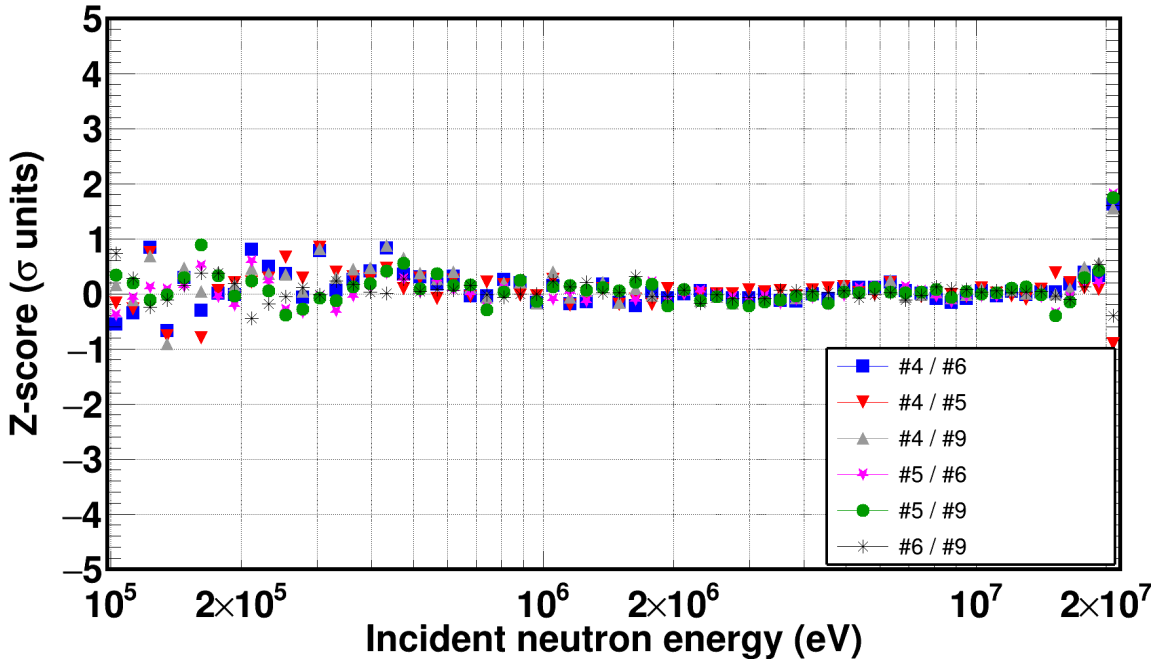

(b) ^{237}Np *samples*

Figure 4.57: *To confirm the good agreement between the corrected fission yields, the Z-factor was calculated between all possible combinations of samples. The fission yields were found to be in a quite satisfactory agreement with less than* 1σ *in most cases.*

of the ^{237}Np samples revealed a systematic effect. In fig. 4.58 the individual cross sections are shown for each sample along with the only experimental point found in literature by Kozharin et al. [83] and the current evaluations. It is evident that the cross sections derived from the JRC-Geel samples, although in very good agreement between them, were about twice as high as the corresponding one from IPN-Orsay which was in overall agreement with both the experimental points and the current evaluations.

In this rather bizarre situation, systematic effects due to the analysis were excluded since all the cross-sections were derived with reference to the same standard. In addition, an issue with the analysis, would also be reflected in all the samples, something which was not observed in the present case. A possible explanation would be the presence of an unknown and common fissile contaminant in the JRC-Geel samples which, as discussed previously, could only affect the thermal region. A contact with JRC-Geel revealed that there was indeed a small amount of plutonium (< 0.5 ppm) in the raw material, however it has not yet been characterised, therefore the cross section will only be derived in the threshold region.

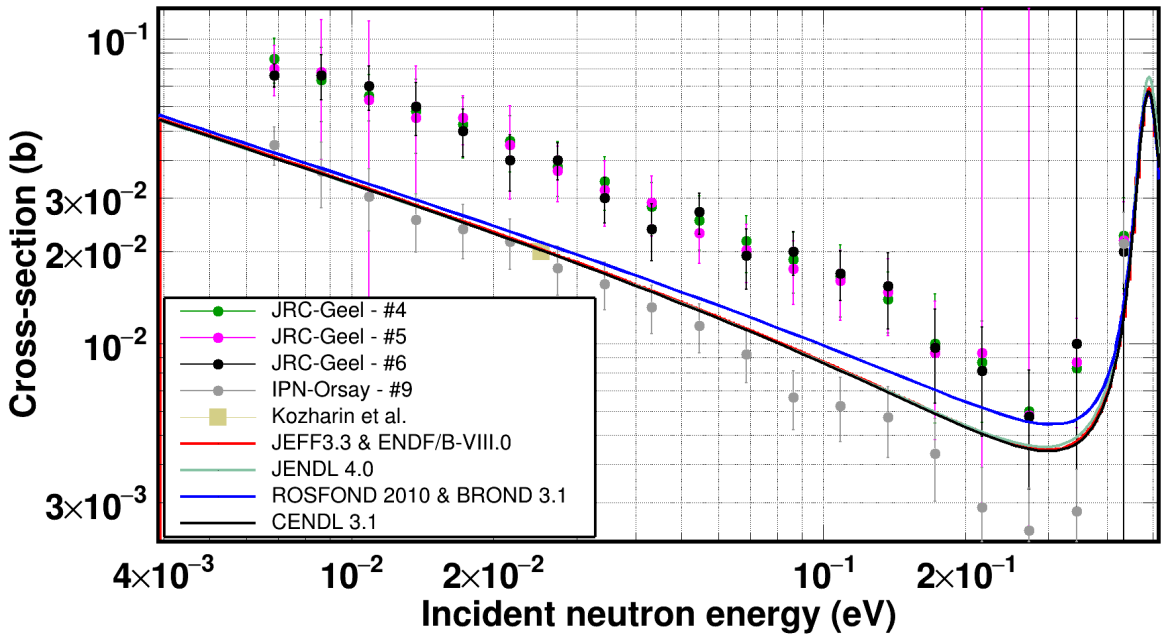

Figure 4.58: *The derived cross sections in the thermal region revealed a systematic effect on the JRC-Geel samples. A contamination of unknown quantity of a plutonium isotope was eventually present in the samples, which postponed the analysis at lower energies until the full sample characterisation is accomplished.*

4.12.2 Comparison between high and low counting rates

The dead-time correction of the fission yield is sensitive to the intensity of the incident neutron beam. Although different correction factors were estimated for dedicated and parasitic bunches, the corrected rate had to be the same within a reasonable margin.

Although the present data quality check is essential for a measurement, it could

only be applied to the fission foils from the $^{237}Np(n,f)$ campaign, since as previously explained, during the $^{240}Pu(n,f)$ experiment, the data acquisition system was not properly configured to digest parasitic bunches.

All in all, the parasitic and dedicated yields were compared in order to detect any possible inconsistencies in the analysis. As an example, the normalised to the number of bunches corrected time-of-flight spectra of the ^{235}U sample will be shown, since it was the foil with the highest correction. As seen in fig. 4.59 the agreement between dedicated and parasitic pulses in the energy region from thermal up to MeV energies was quite satisfactory within less than 7% at worst.

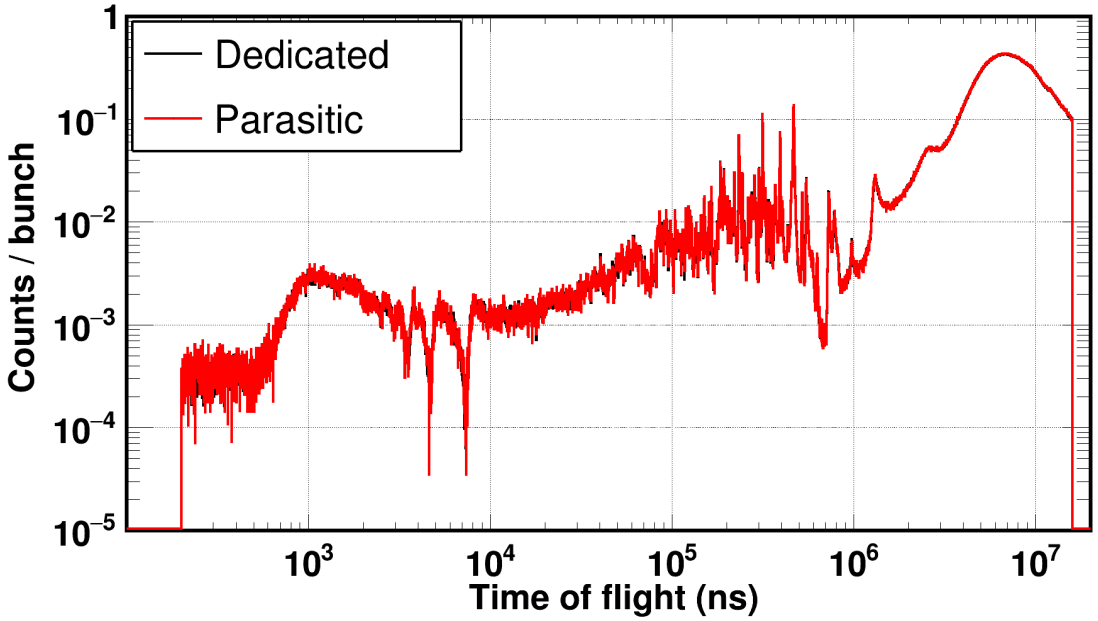

(a) Full energy range

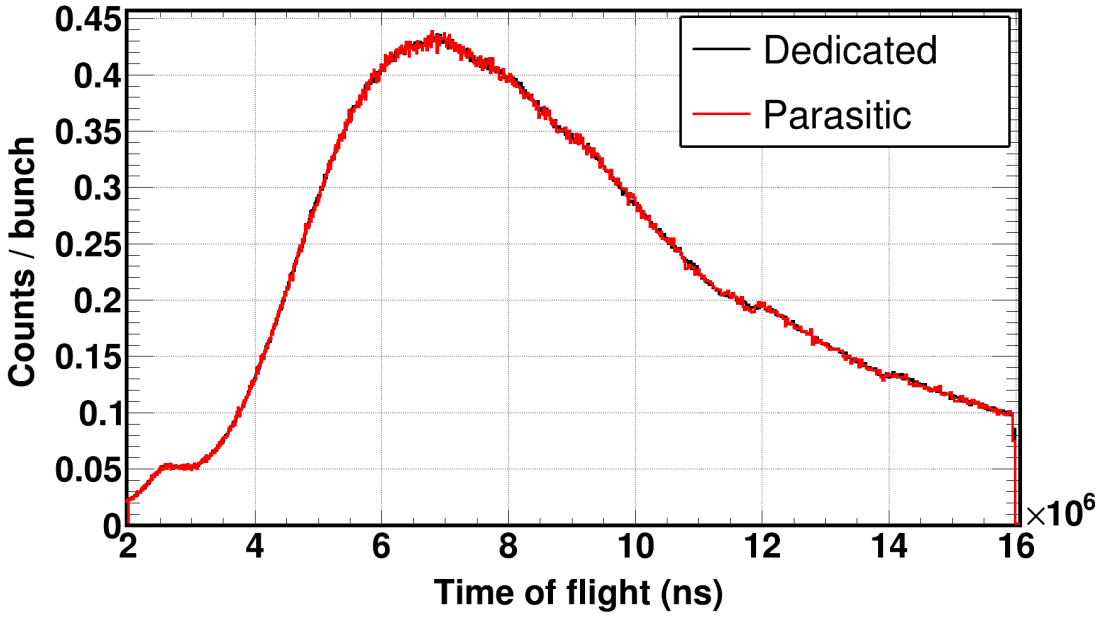

(b) Thermal region

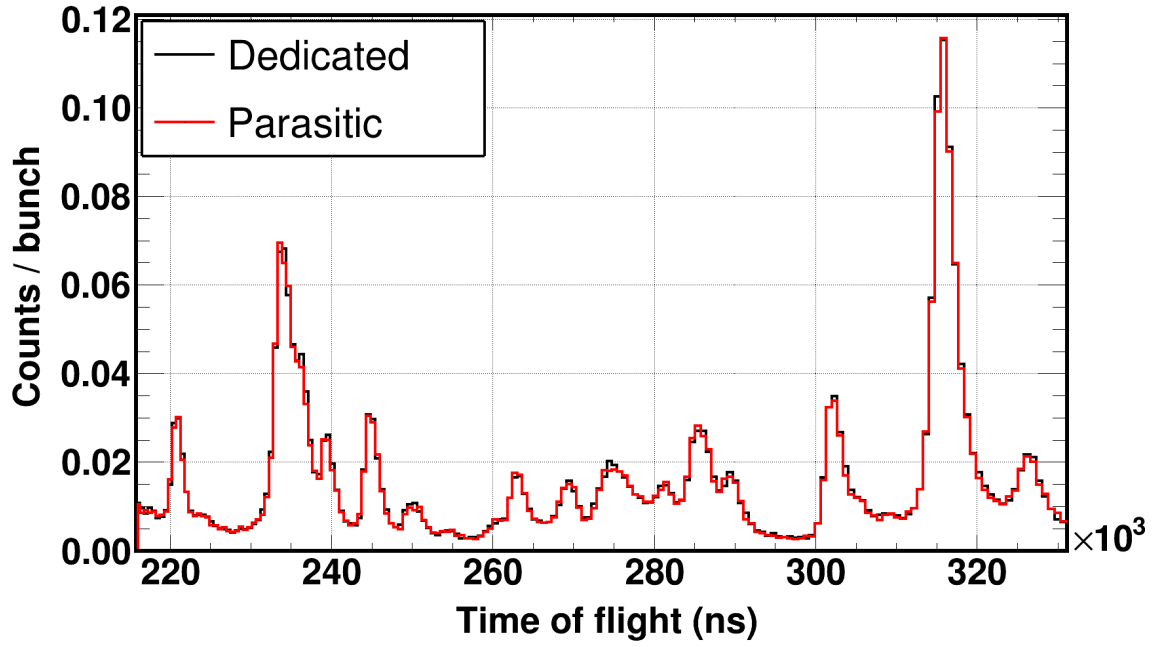

(c) Resonance region

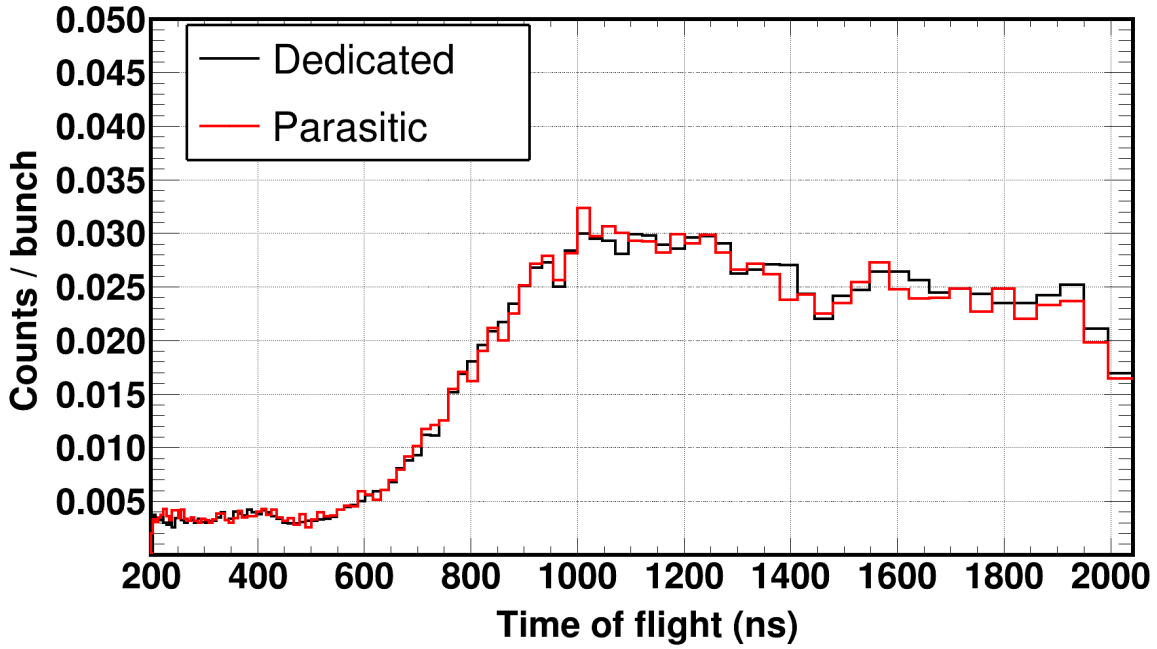

(d) MeV region

Figure 4.59: *Corrected and bunch normalised time-of-flight spectra for dedicated and parasitic intensities concerning the ^{235}U sample in the $^{237}Np(n,f)$ campaign. The agreement is quite satisfactory and indicated that the dead-time correction was self-consistent.*

It has to be mentioned that the difference between the dedicated and parasitic corrected counting spectra was considered to be an estimate of the uncertainty of the dead-time correction.

4.12.3 Reproduction of neutron standards

The final conclusive evidence that the analysis was able to produce reliable data was the reproduction of a neutron standard. In both measurements a a ^{235}U sample was housed in the fission chamber along with a single ^{238}U foil in the $^{240}Pu(n,f)$ campaign and a set of two in the $^{237}Np(n,f)$ one.

The ^{238}U samples were used for this particular reason: A problematic reproduction of the $^{238}U(n,f)$ cross-section with reference to the $^{235}U(n,f)$ one, would indicate issues in the fission yields and therefore further investigation would be required.

It was already shown in fig. 4.54 that for the $^{240}Pu(n,f)$ measurement, the $^{238}U(n,f)$ cross section was properly reproduced up to 6 MeV with discrepancies that did not exceed 5%.

In the $^{237}Np(n,f)$ data, a similarly good reproduction was achieved for both ^{238}U samples with the exception that a higher energy limit was achieved, as illustrated in fig. 4.60 where the cross-section could be reproduced up to 12 MeV, with discrepancies that did not exceed 5%. This energy region can be extended up to 15 MeV, however the discrepancies rise up to 10% which could still be considered acceptable.

It was already mentioned that higher energies were able to be reached due to the faster electronics employed and the elimination of the heavily oscillatory baseline that followed the γ-flash , making the developed methodology of the average γ-flash subtraction substantially more efficient.

It has to be mentioned that the foil closer to the floor is denoted as "front" while the other one as "back".

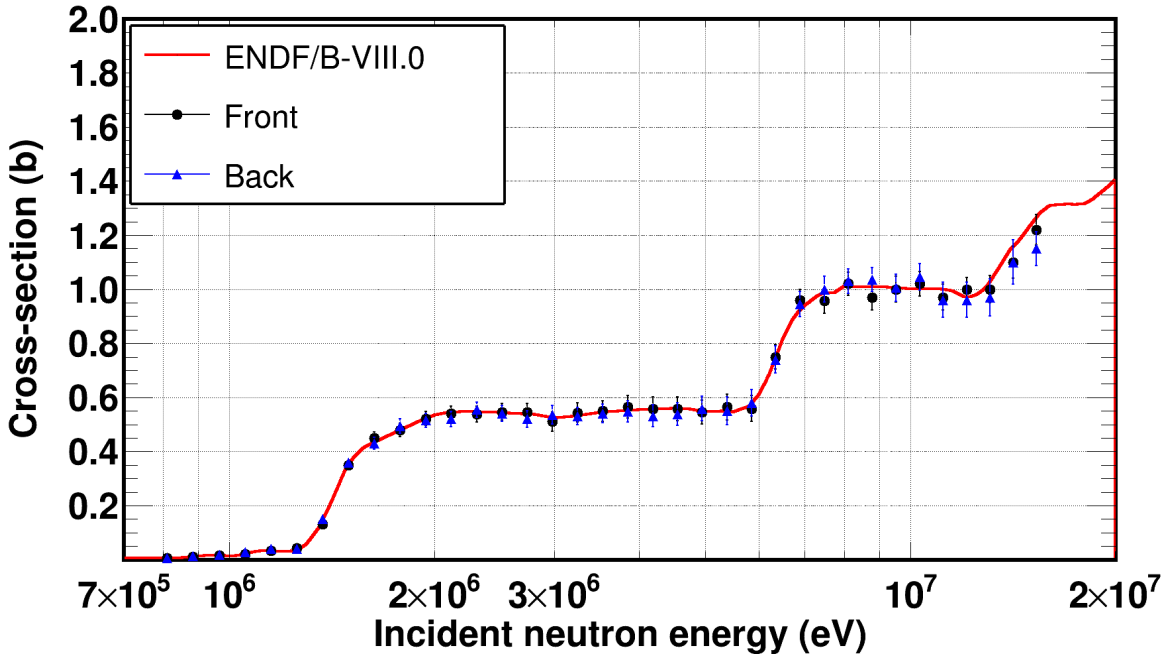

Figure 4.60: *The neutron induced cross-section of ^{238}U was properly reproduced by both fission foils up to 12 MeV within 5%. An extension can be considered, if a less than 10% reproduction can be considered adequate enough.*

4.13 Neutron induced cross-sections of ^{240}Pu and ^{237}Np

The proper signal handling and rejection of noise, accompanied by realistic and highly controlled data analysis can provide reliable and accurate estimates of the cross-section, whose calculation was based on eq. (4.8) for both experiments. Each data-set will be discussed separately in the following subsections.

4.13.1 The $^{240}Pu(n,f)$ cross-section

The data analysis of the first experiment performed in the new experimental area EAR2 at n_TOF facility at CERN, led to the derivation of the $^{240}Pu(n,f)$ cross-section in a large energy range that spanned over eight orders of magnitude in incident neutron energy, from 9 meV up to 6 MeV. In fig. 4.61 an overview of the derived cross-section is shown, along with the evaluations and experimental data found in literature. For illustration purposes, the legend was removed, however the cross-section will be shown and discussed in detail, in the forthcoming lines.

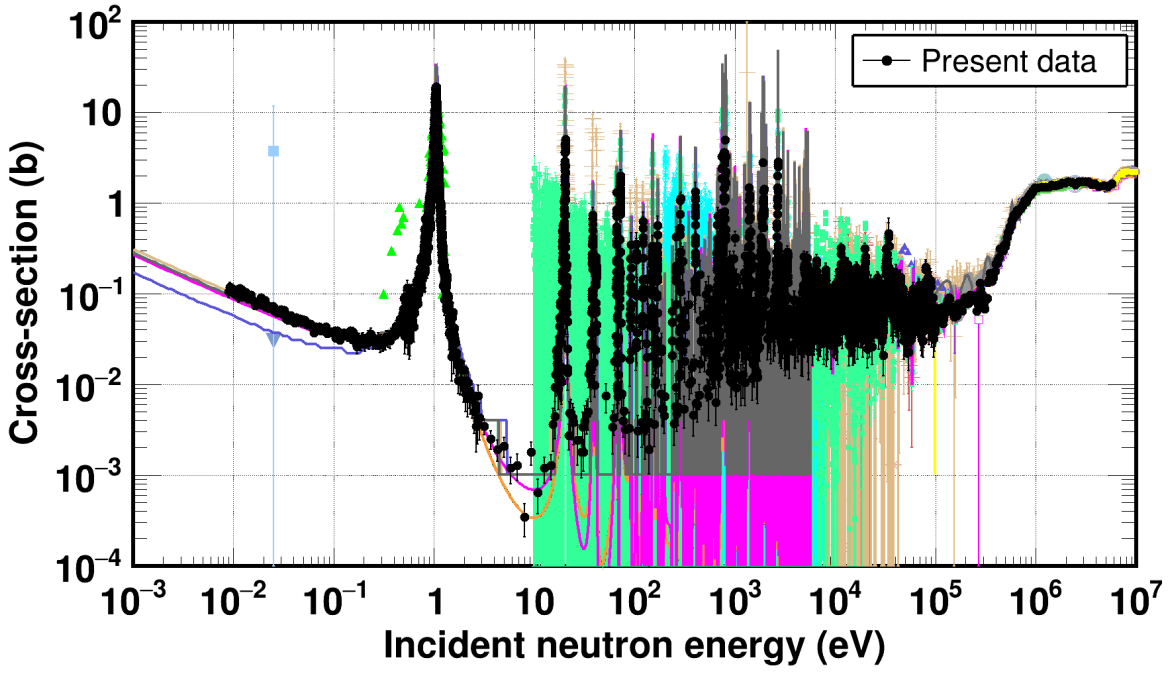

Figure 4.61: *The neutron induced fission cross-section of ^{240}Pu was calculated in a wide energy that spanned from 9 meV up to 6 MeV. The derived data is shown along with the current evaluations and the existing experimental data.*

Prior to proceeding to the presentation of the derived cross section, it has to be noted that a direct comparison between the present data and evaluations, especially

in the resonance region is not considered proper since a deconvolution must be performed, concerning the response function in each time-of-flight spectrometer. The same principle applies to the existing experimental data. However, a proper argumentation can be made in the $1/v$ and MeV region. Nonetheless, the data will be presented since straightforward conclusions can be drawn. In the next chapter, a proper comparison in the resonance region, will be performed.

4.13.1.1 Cross-section in the 1 meV - 0.4 eV range

Apart from the present data, only three datasets exist in the energy region from 9 meV to 0.5 eV, as evidenced in fig. 4.62. Eastwood et al. [70] and Prat et al. [72] reported the cross-section at the thermal point. It is apparent that these datasets are not only quite discrepant but rather uncertain as well, whereas the present ones provide the only time-of-flight measurement in the $1/v$ region, justifying the excellent characteristics of EAR2 for such measurements.

In addition, an overall agreement with the current evaluation libraries was observed. Below 300 meV, however, JENDL-4.0 underestimated the cross section whereas from 300 meV and onwards, the present data confirm the evaluations. Up to 60 meV, ENDF/B-VIII.0 and JEFF-3.3 were underestimating the cross section at about 3%, while in higher energies there was an excellent agreement with the present data.

The data by Leonard Jr. [124], will be discussed in the next section.

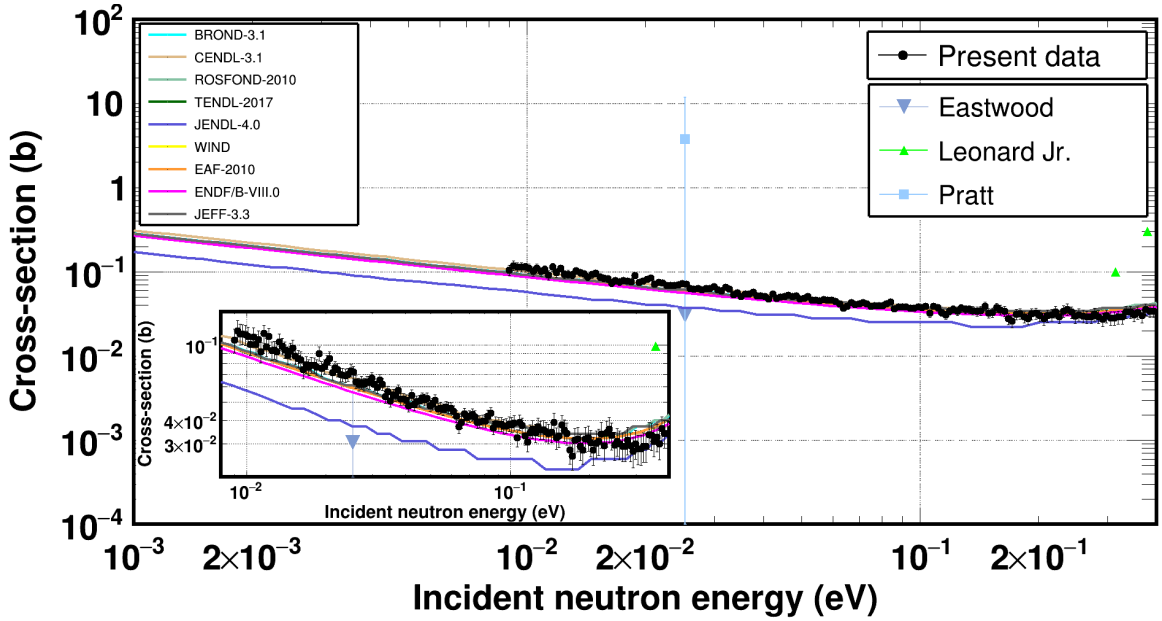

Figure 4.62: *The $^{240}Pu(n,f)$ cross section in the 1 meV - 0.4 eV energy range. The cross-section from 9 meV up to 0.4 eV is shown in the inset. Consult text for further details.*

4.13.1.2 Cross section in the 0.8 – 1.30 eV range

The region that will be discussed concerns the energy range where the first (n,f) resonance lies. Apart from the present data, only a single dataset was found in the EXFOR library. In the current situation, large discrepancies were observed between the present data and the cross section reported by Leonard Jr. [124], as seen in fig. 4.63. The present data, are of significantly better resolution and statistics which was attributed to the quite well balanced combination of good resolution and high flux of EAR2, thus providing the first data-set suitable for an evaluation of the $^{240}Pu(n,f)$ cross-section.

The comparison with the evaluations, although inadequate, since a resonance is heavily affected by the response function of the spectrometer, indicated that most libraries overestimate the fission width on this particular resonance, however a comparison can only be performed through the resonance parameters that will be reported in the next chapter.

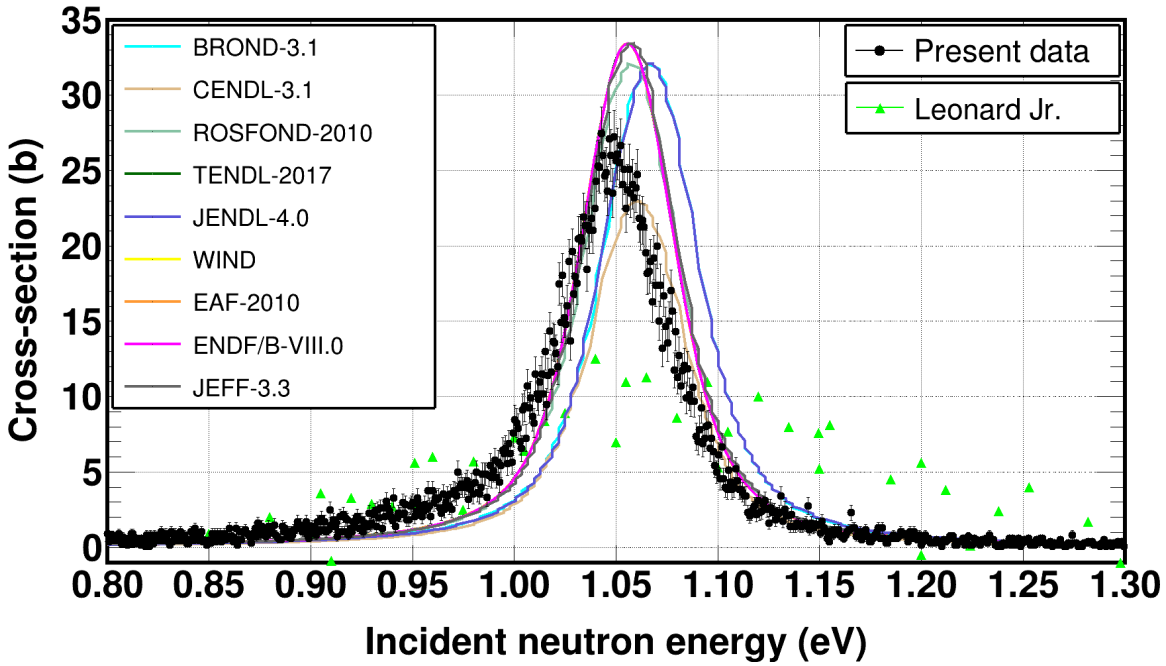

Figure 4.63: *The $^{240}Pu(n,f)$ cross section in the 0.8 – 1.3 eV energy range. Consult text for further details. The present dataset is the only one available with high resolution.*

4.13.1.3 Cross section in the 10 – 100 eV range

In the current region two datasets were found by Weston [49] and Byers et al. [65]. The former are of very good resolution recorded at Oak-Ridge National Laboratory, while the latter was obtained through a nuclear explosion, thus are considered of poor quality given the availability of a time-of-flight data-set, hence it will not be included in the following discussion.

In this energy region it is evident that the kernels between the evaluations themselves and the present work are in a reasonable agreement, however the resonance

analysis that will follow would make a direct comparison possible, therefore no comparison can be made in the resolved resonance region between unbroadened evaluations and broadened experimental data. In the same spirit, a direct comparison between experimental data which suffer from different broadening components is only possible through the resonance parameters estimated from ℜ-Matrix calculations, that will follow.

However, the evaluations are plotted in this region to show that they were based solely on the dataset by Weston [49], therefore any additional time-of-flight data such as the present one, will provide useful information for future evaluations and justifies the inclusion of $^{240}Pu(n,f)$ in the high priority request list [11].

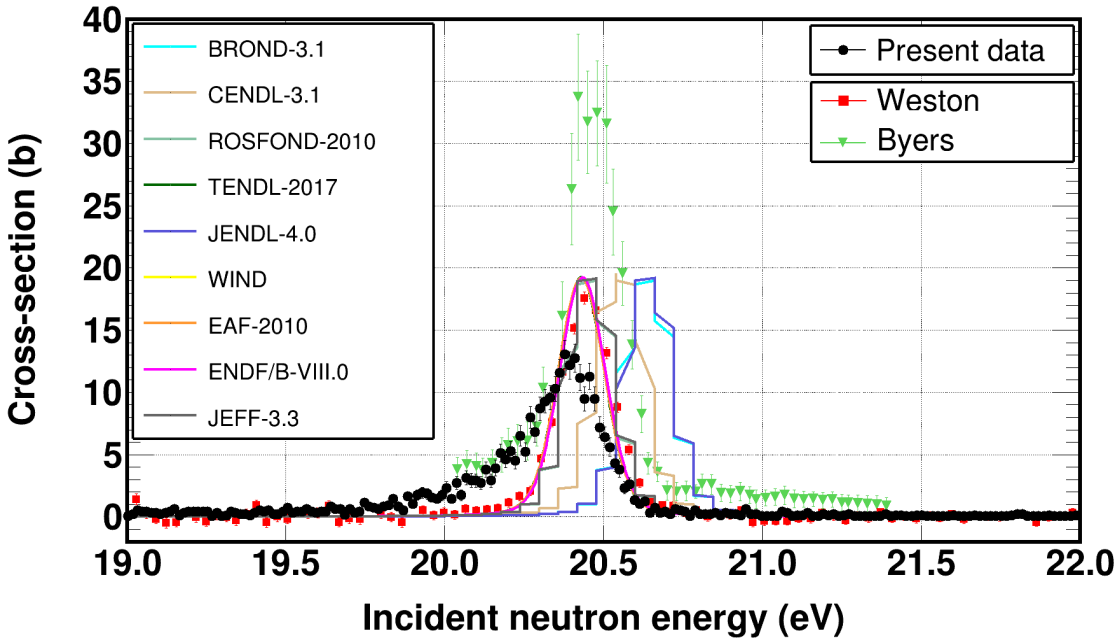

(a) *19 - 22 eV*

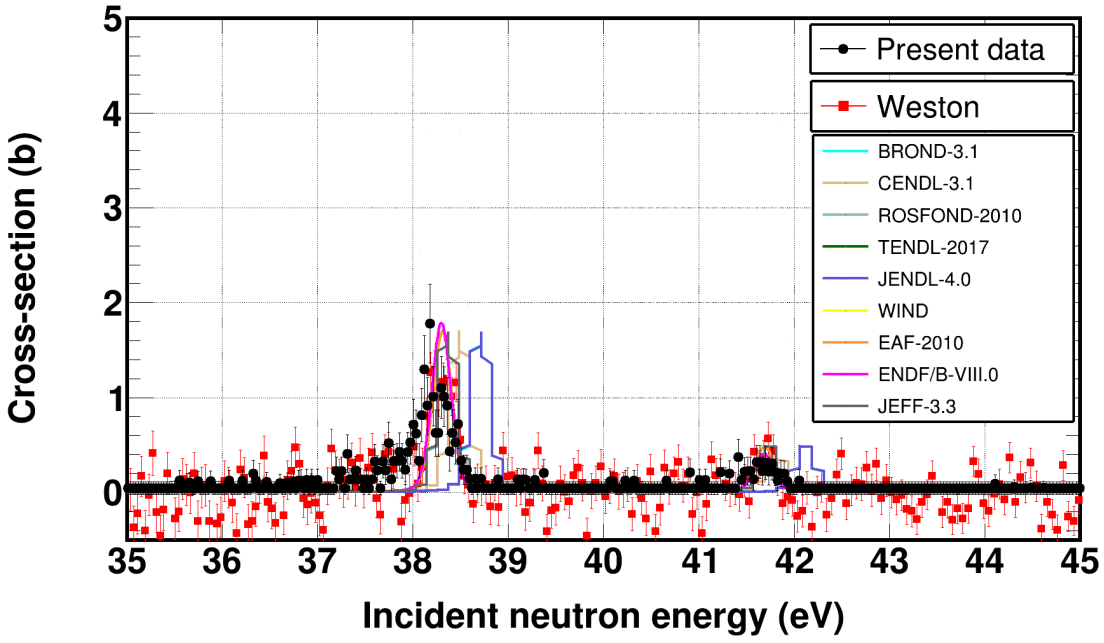

(b) *35 - 45 eV*

4.13.1.4 Cross section in the 100 eV - 100 keV range

In this region that includes the resolved and unresolved resonance regime, quite a lot of resonances were resolved up to at least a few keV, above which resonance-like structures were still present. All these resonances, up to 10 keV were characterised using the $\mathfrak{R}$-Matrix formalism, as will be discussed in the next chapter.

The resonances that were resolved above 1 keV and up to a few tens of keV, were also observed by Weston [49], therefore the possibility of being artefact was appreciably reduced. The evaluation of ^{240}Pu neutron cross-sections in the resolved resonance region performed by Bouland et al. [187] was solely based on the data by Weston, therefore the present cross-section can provide useful additional information for future evaluations.

It has to be mentioned that an additional data-set was found in EXFOR by Migneco et al. [63], however after the private communication with Dr. Peter Schillebeeckx from JRC-Geel, it was concluded that this particular data-set was mistakenly disseminated as a cross-section; it should have been compiled as a fission yield instead. In addition, it can be seen in fig. 4.65a that resonances attributed to a ^{239}Pu contamination were present in the reported data, thus this data-set will be excluded from the present discussion.

Above 10 keV, an additional data-set was reported in EXFOR, by Tovesson et al. [46]. Although this data-set is quite important in the MeV region, below the fission threshold the resolution is quite poor compared to the present data and the one by Weston, therefore it will also be excluded in the present discussion.

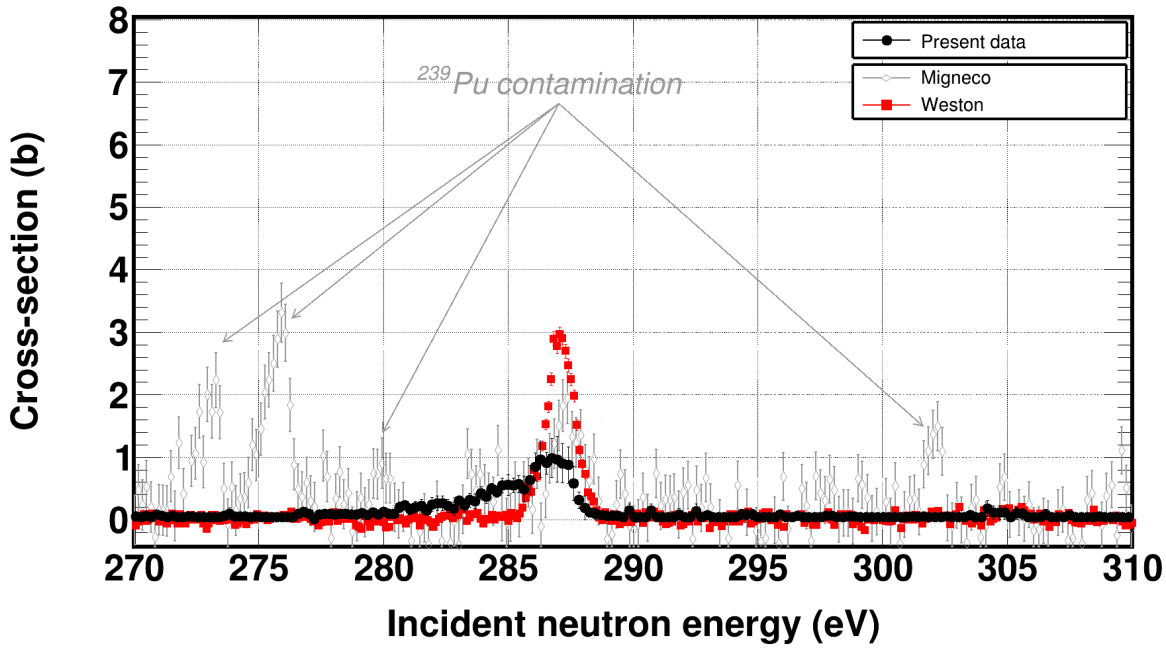

(a) 270 - 310 eV

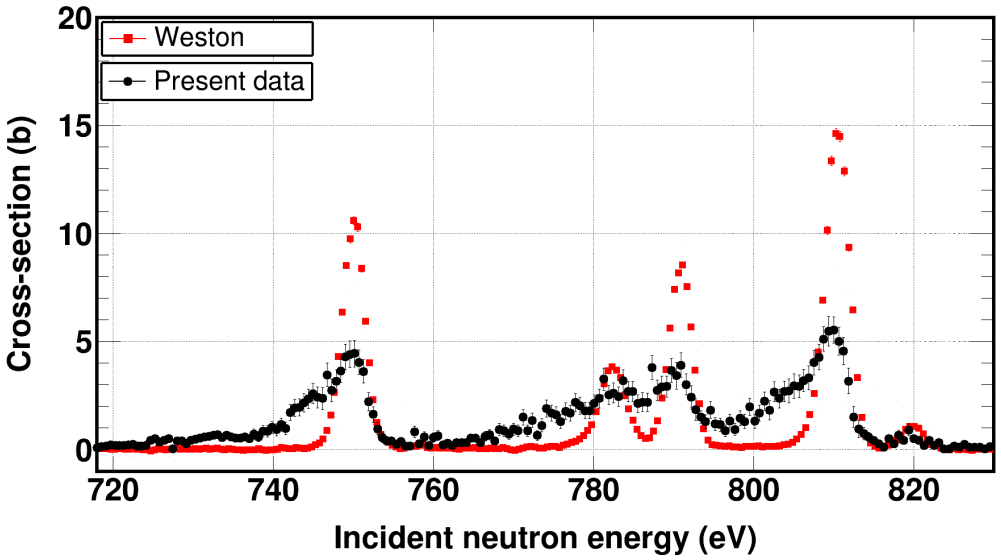

(b) 720 - 830 eV

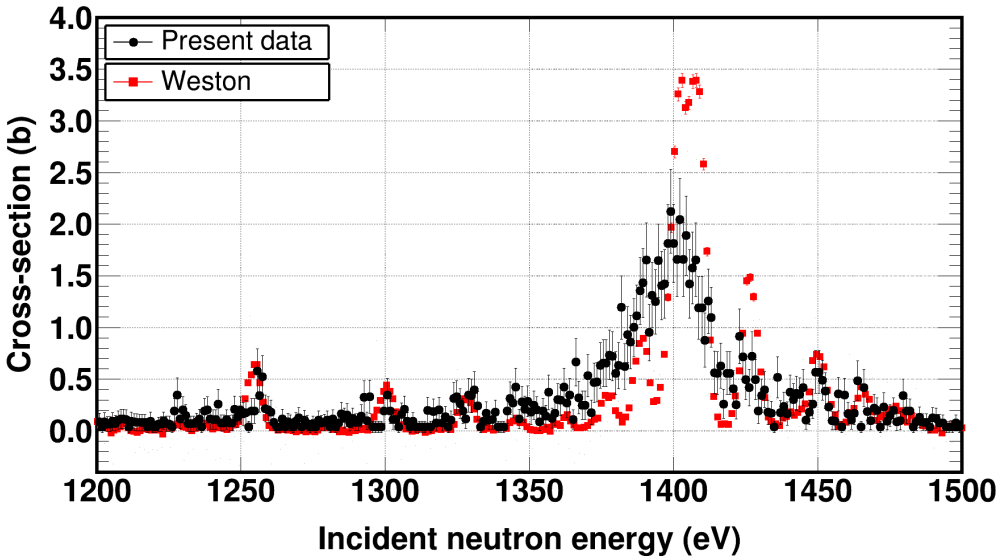

(c) 1200 - 1500 eV

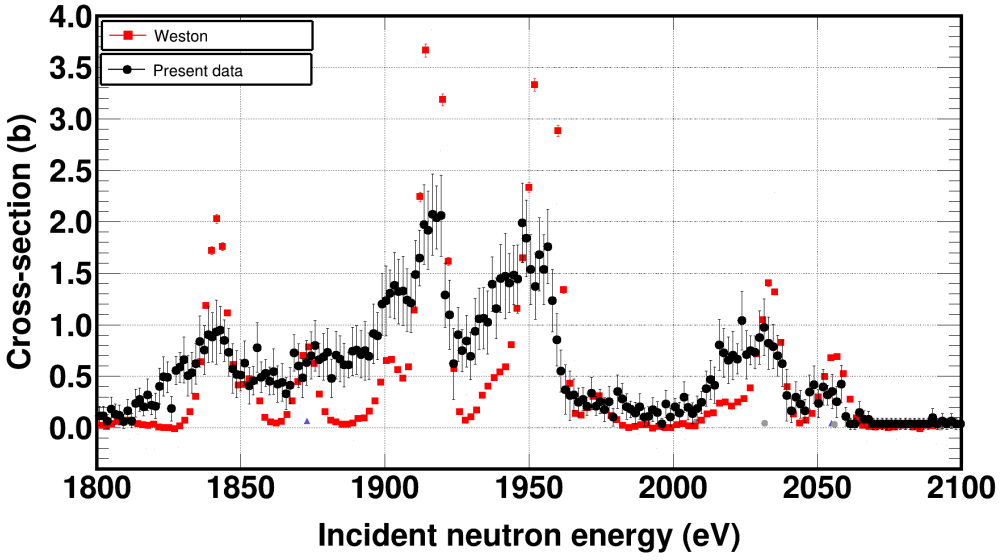

(d) 1800 - 2100 eV

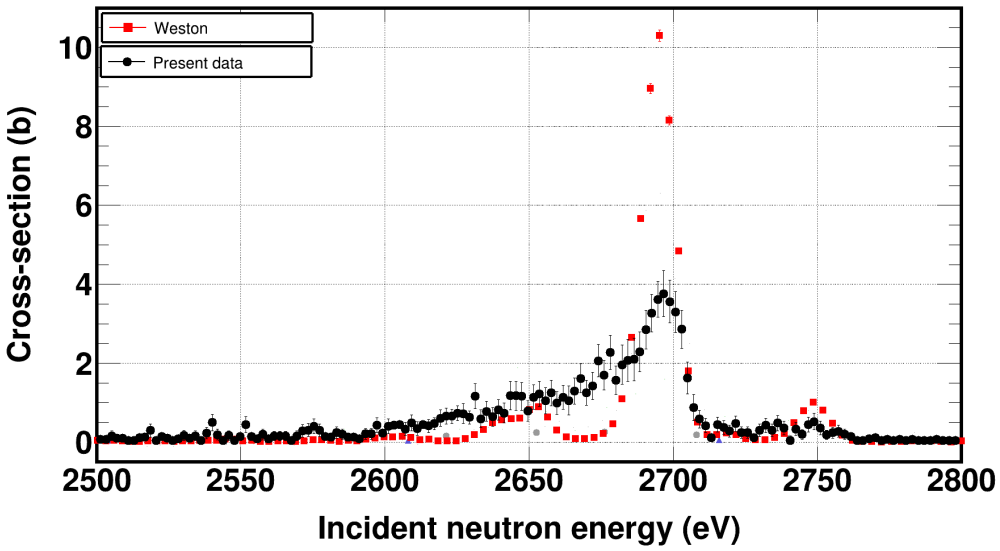

(e) 2500 - 2800 eV

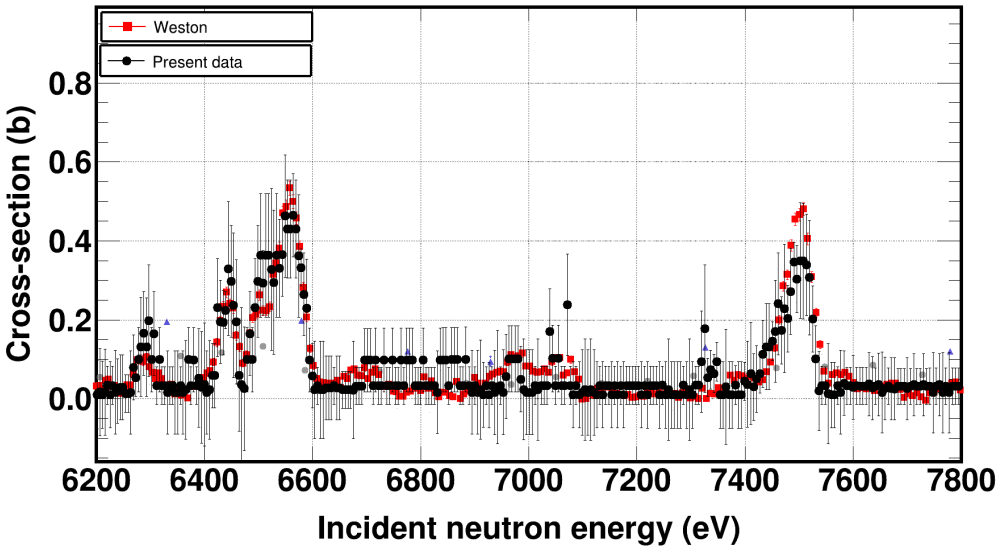

(f) 6200 - 7800 eV

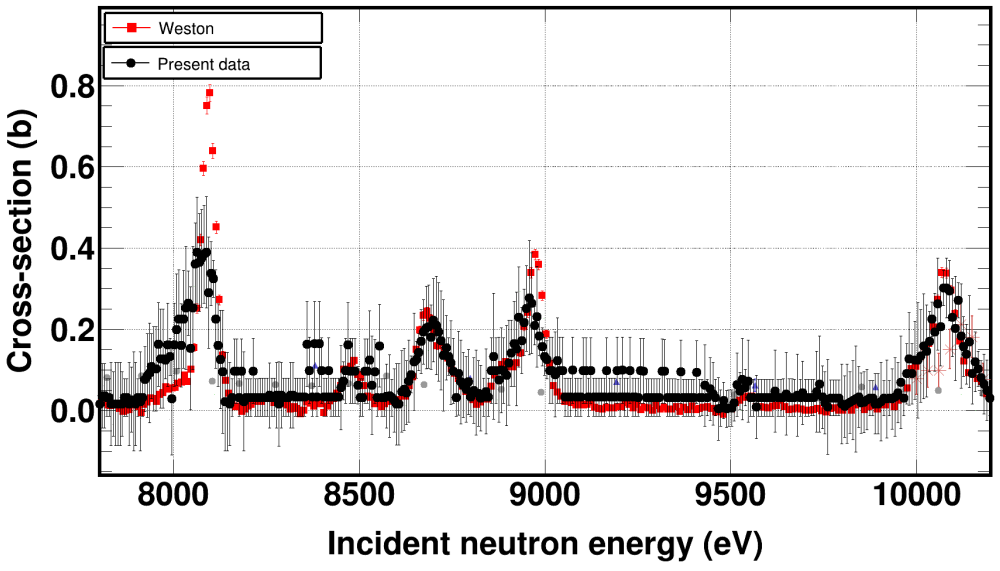

(g) 7750 - 10200 eV

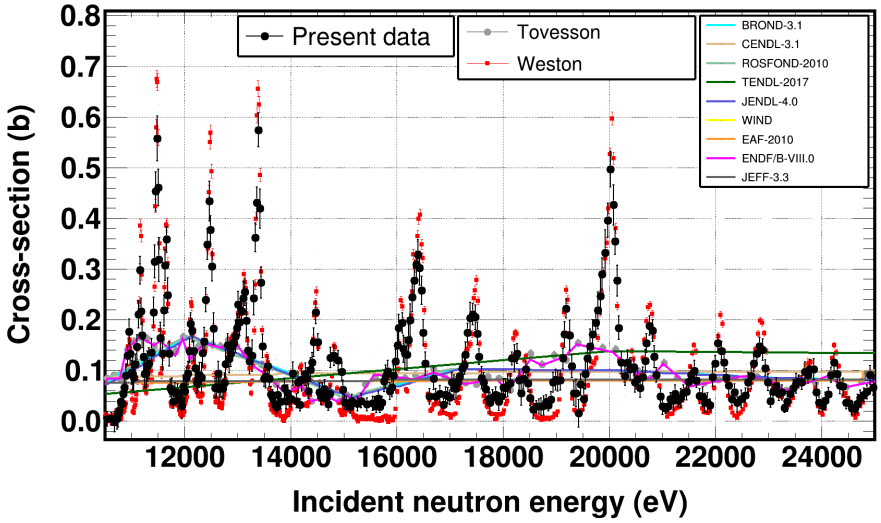

(h) 11 - 25 keV

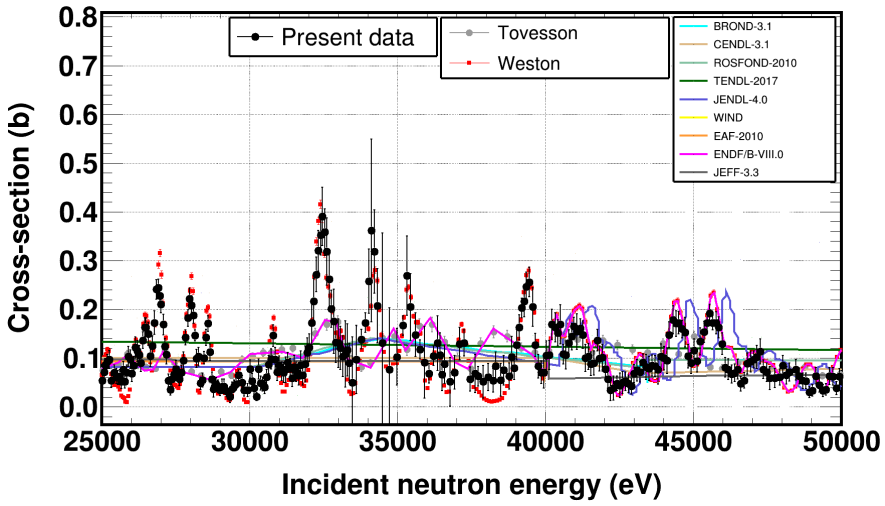

(i) 25 - 50 eV

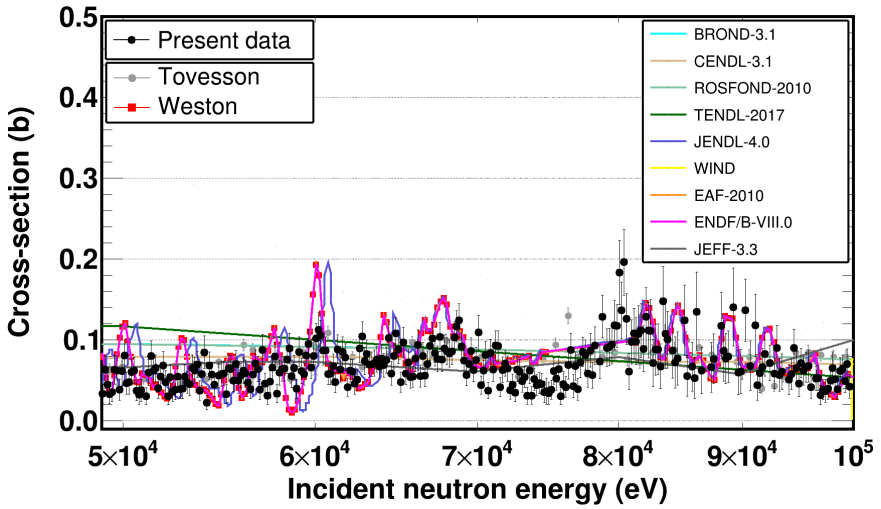

(j) 50 - 100 keV

Figure 4.65: *The $^{240}Pu(n,f)$ cross section in the 100 eV - 100 keV energy range. The only useful data-set, apart from the present one, was reported by Weston up to about 10 keV, above which an additional data-set with much poorer resolution by Tovesson et al. was reported.*

4.13.1.5 Cross section in the 100 keV - 6 MeV range

Finally, the cross section was derived up to 6 MeV, due to limitations from the γ-flash . The present data is in overall agreement with the available dataset found in literature, however, a systematic discrepancy was observed in this region with the data provided by Tovesson et al. [46] and Byers [65], which overestimate the $^{240}Pu(n,f)$ cross-section. The data by Tovesson et al. in particular, which is the most recent time-of-flight data up to the present time, exhibited an almost constant overestimation of the order of 5% up to 2.5 MeV.

On the region around the fission threshold an agreement was observed between the time-of-flight data by Laptev et al. [47], as well as the most recent data by Salvador-Castineira et al. [45]. Discrepancies were observed between the evaluation libraries which reached up to 15%, while overall they overestimate the cross section with respect to to the present data.

On the first chance fission plateau, an absolute agreement was observed between the data by Laptev and the present one, while the data by Salvador-Castineira is in agreement within uncertainties, which was also the case with the data by Kari et al. [60].

Above 3 MeV, the discrepancies between JEFF-3.3 and the other evaluations is quite significant and reached up to 10%. The experimental data presented in this work, confirm the general trend of the other evaluations and disagree with JEFF-3.3. In the same sub-region, above 3 MeV, several datasets exist with large uncertainties, which are all in agreement within uncertainties with the present one.

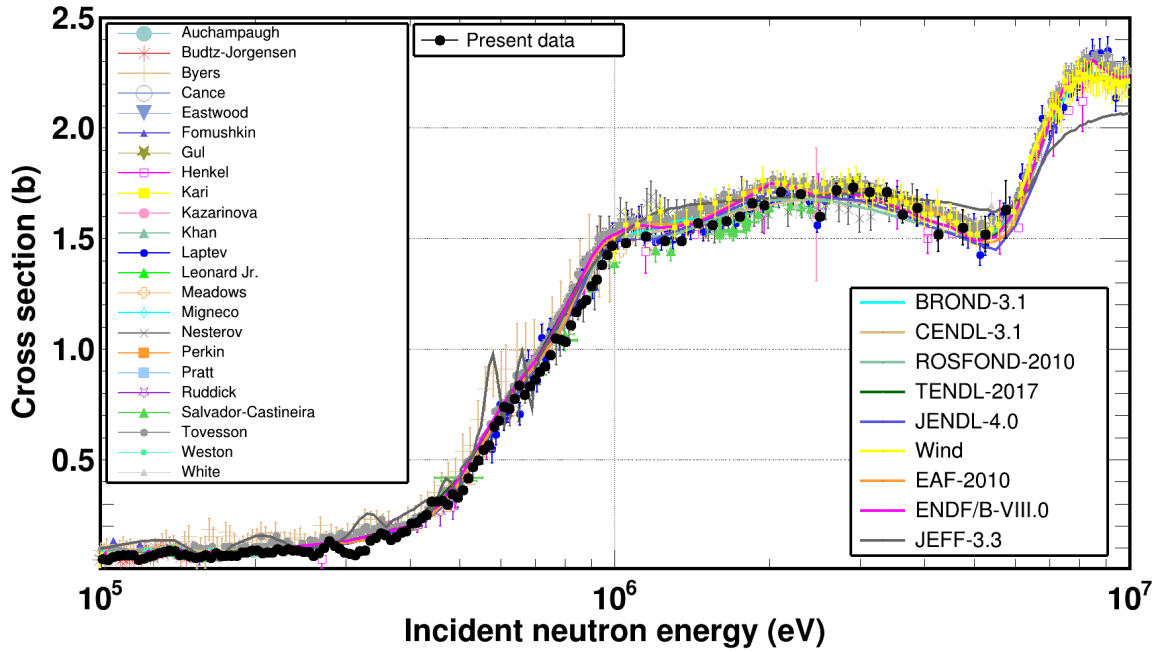

Figure 4.66: *The $^{240}Pu(n,f)$ cross section in the 100 keV - 6 MeV energy range. Consult text for further details.*

4.13.2 The $^{237}Np(n,f)$ cross section

The experience and knowledge gained from the $^{240}Pu(n,f)$ measurement, was used to further profit from the experimental capabilities of EAR2. Although similar results over a wide energy range could be obtained, a contamination in the vast majority of the samples postponed the data analysis for energies below the fission threshold. Nevertheless, regardless of how useful and challenging it is to report cross sections in thermal and resonance energies, the region of interest for this measurement was the range between 200 keV and 20 MeV, which is a region that overlapped the present measurement.

The neutron induced fission cross section of ^{237}Np was derived in the energy region from 200 keV up to 15 MeV covering a large fraction of the requested range, as demonstrated in fig. 4.67. Overall, the derived cross section was in agreement with the evaluations and the experimental data-sets found in EXFOR. A discussion will follow with comparison of the derived cross section in smaller energy regions.

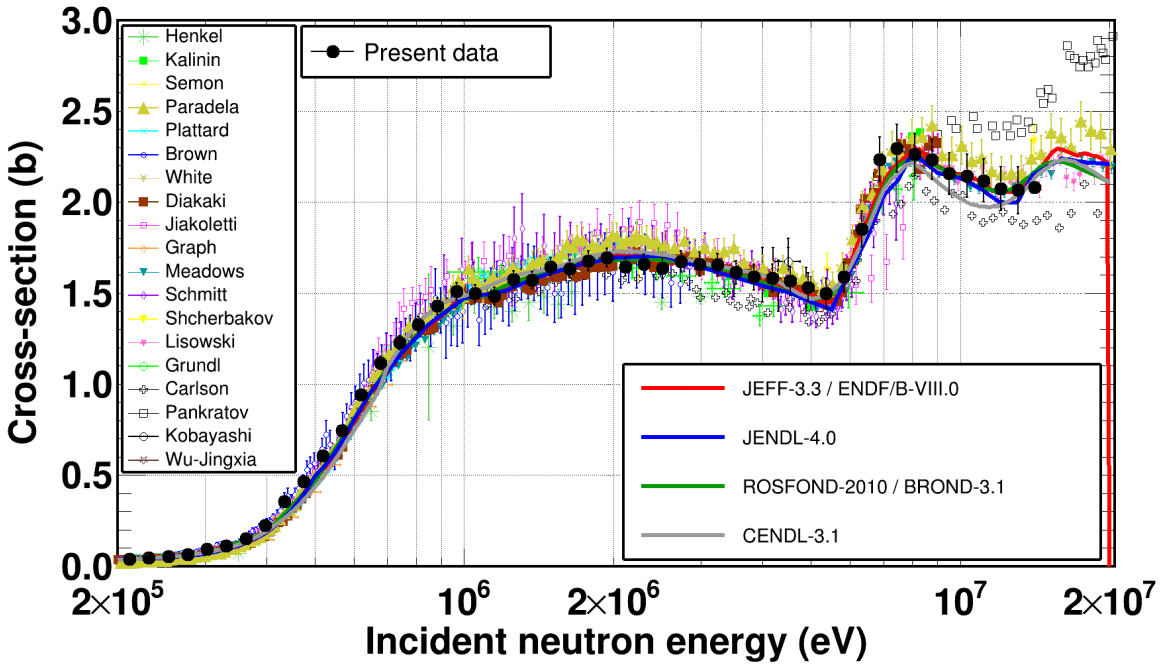

Figure 4.67: *The $^{237}Np(n,f)$ cross section derived at EAR2 of the n_TOF facility at CERN, covering an incident neutron energy range from 200 keV up to 15 MeV.*

4.13.2.1 Cross section in the 200 keV - 1 MeV range

In the region around the fission threshold, discrepancies were observed between the evaluations and the experimental data that exceeded 20%. In the region from 200 to 350 keV the data by Paradela et al. [44] and Shcherbakov et al. [74] underestimated the $^{237}Np(n,f)$ cross-section and discrepancies of the order of 20% were observed with respect to the present data.

From 350 to 550 keV a very good agreement with the data by Brown et al. [114, 115] was observed while there is an agreement with all the available datasets within

uncertainties.

As shown in fig. 4.68, there is an overall agreement within uncertainties with the latest time-of-flight measurements, performed at the n_TOF facility as well, by Diakaki et al. [41–43] and Paradela et al. It is quite remarkable that the three datasets right before the fission plateau, presented a very nice agreement within less than 3% in the region from 800 keV up to 1 MeV.

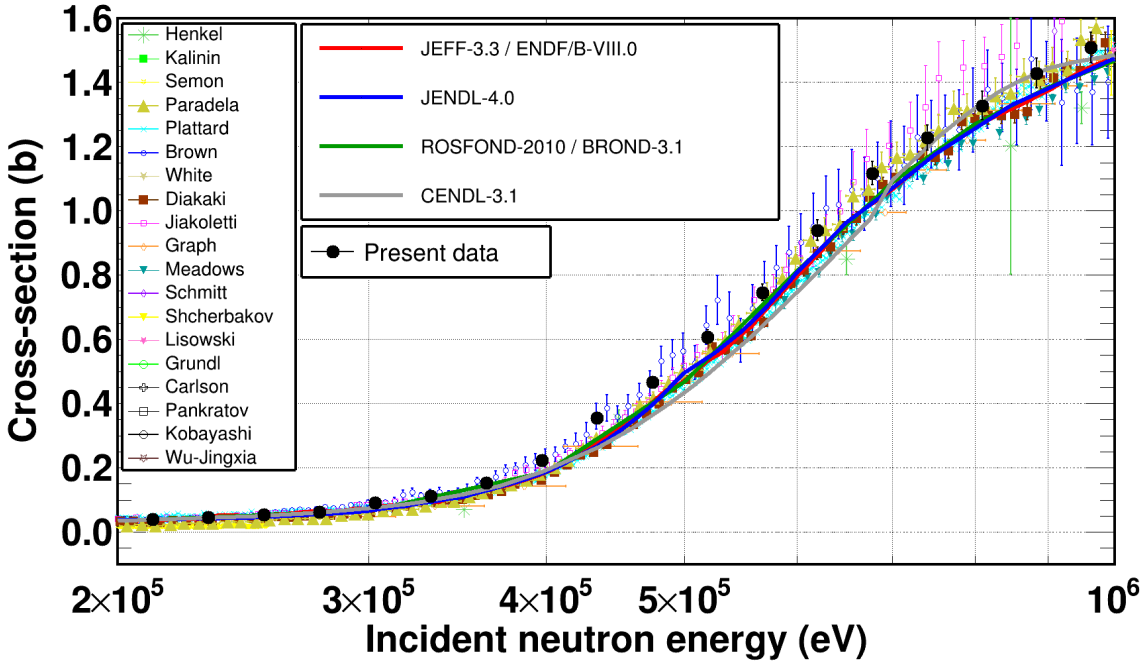

Figure 4.68: *The $^{237}Np(n,f)$ cross section in the 200 keV - 1 MeV energy range. Consult text for further details.*

4.13.2.2 Cross section in the 1 - 6 MeV range

On the first chance fission plateau, up to 4 MeV, the most recent time-of-flight measurements by Diakaki et al. and Paradela et al. provided cross sections which, as seen in fig. 4.69, were discrepant within up to 7%. Such a disagreement is considered crucial for this particular reaction, since it is practically used as a reference. On an attempt to resolve the aforementioned discrepancies, the derived cross section from the present work favors the results reported by Diakaki et al., although there is an agreement with all three datasets within uncertainties.

The evaluations in the present energy region, are in a reasonable agreement within a few percent. This agreement was also confirmed by the present data, which in turn is in agreement within less than 3% at worst with the major evaluated libraries.

Above 4 MeV, the present data is in absolute agreement with the data by Diakaki et al. and Paradela et al. An agreement within a few per cent was also observed with the evaluated libraries.

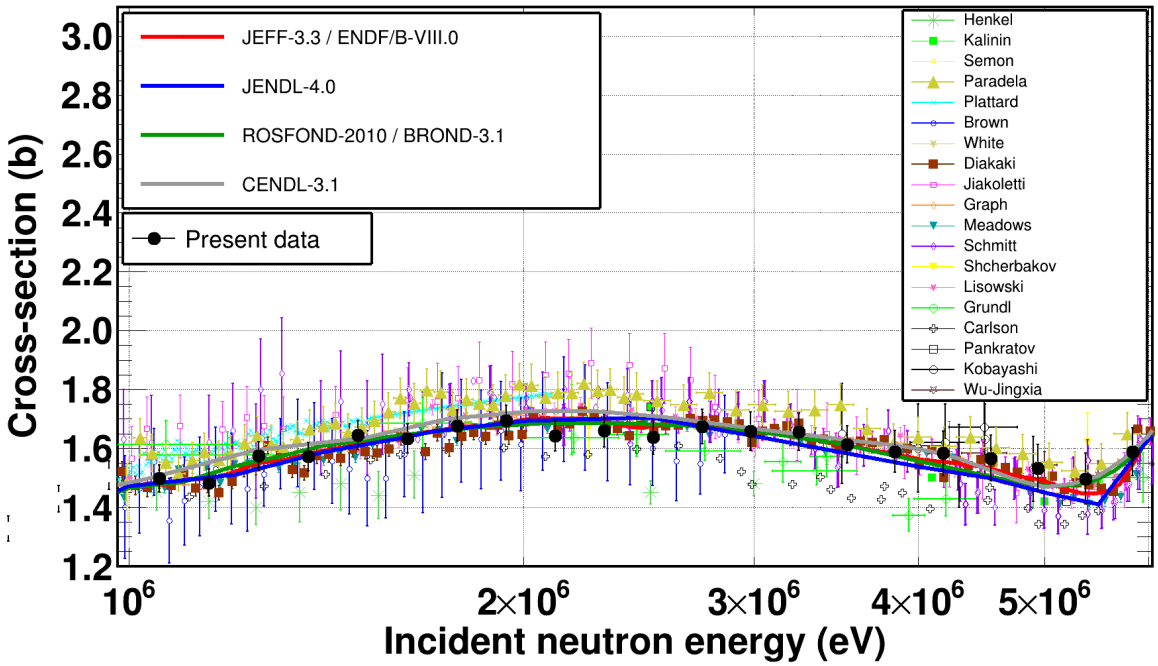

Figure 4.69: *The $^{237}Np(n,f)$ cross section in the 1 - 6 MeV energy range. Consult text for further details.*

4.13.2.3 Cross section in the 6 - 15 MeV range

In the remaining energy region, at the second chance fission threshold the derived cross section was about 3 – 5% higher than the corresponding one provided by the evaluations. However, the very good agreement between the time-of-flight data by Diakaki et al. and Paradela et al., indicates that the evaluations suffered from a systematic underestimation of the cross section on the second chance fission threshold.

On the plateau, on the other hand a very good agreement was observed with the majority of evaluations, with the exception of CENDL-3.1, which underestimated the cross section in the energy region from 10 to 14 MeV. The comparison to the data by Paradela et al. revealed a systematic discrepancy of the order of 3 – 5%, although both datasets agree within their corresponding uncertainties.

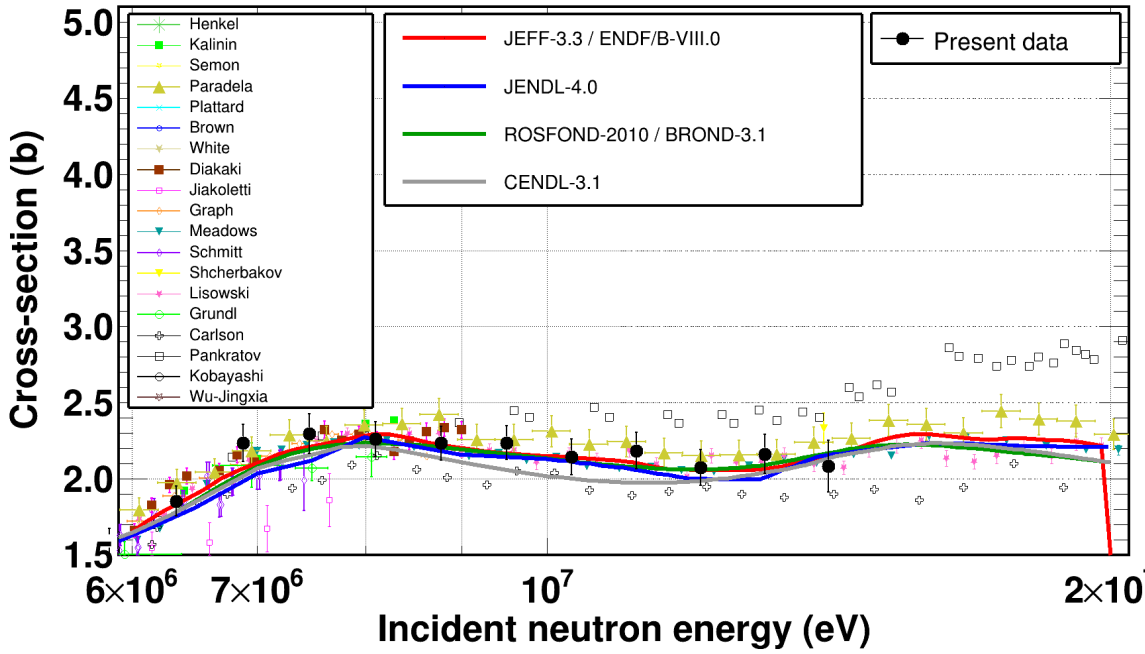

Figure 4.70: *The $^{237}Np(n,f)$ cross section in the 6 - 14 MeV energy range. Consult text for further details.*

CHAPTER 5

^{240}Pu(n,f) cross section: Theoretical investigation

Following the analysis of the experimental data, a thorough theoretical investigation was conducted on the scope of providing a parametrisation of the derived $^{240}Pu(n,f)$ cross section from 9 meV up to 20 keV through the means of resonance analysis using the `R-Matrix` formalism. Auxiliary statistical model calculations were performed in the 100 keV - 6 MeV regime in an attempt to investigate whether the two most commonly used contemporary codes, namely `TALYS-1.9` and `EMPIRE-3.2` , were able to reproduce the behaviour of the fission cross section along with all the other competing channels, over the entire energy range. It has to be noted that a resonance analysis could not be performed for the $^{237}Np(n,f)$ cross section since no cross section data could be deduced at energies below the fission threshold due to the presence due the presence of uncharacterized contaminants.

5.1 Nuclear fission: A concise description

In the very beginning of the present thesis, it was mentioned that nuclear fission was discovered through the detection of Barium isotopes in the course of neutron bombardment of natural Uranium. The discovery of this surprising segregation of nuclear matter gave rise to numerous efforts to explain and describe this phenomenon, starting from the contemporary at the time Liquid Drop Model (LDM) and continuing with the development of fission specialised nuclear potentials.

5.1.1 The Liquid Drop Model of fission

The first extensive theoretical description of fission was performed by Bohr and Wheeler [30] and was based on the Liquid Drop Model proposed by Gamow according to which the binding energy E_b of a nucleus depends on its volume (E_v), surface (E_s), electrostatic (or Coulomb) repulsion between its protons (E_c) and its specific composition of nucleons (E_a), as seen in eq. (5.1).

$$E_b = E_v - E_s - E_c - E_a + \delta(A,Z) \tag{5.1}$$

Liquid drop model and simple deformations

To transform the aforementioned generalised LDM of a spherical liquid drop, in a proper model to describe fission, a simple yet important observation is ought to be made: The splitting of nuclear matter is only possible through the involvement of deformations so that the total binding energy is increased thus allowing the nucleus to be divided. This implies that the nuclear sphere will be transformed to a spheroidal or ellipsoidal with the same volume, when considering relatively small arbitrary deformations when moving towards the scission point (i.e. the configuration the nucleus is at, right before fission occurs).

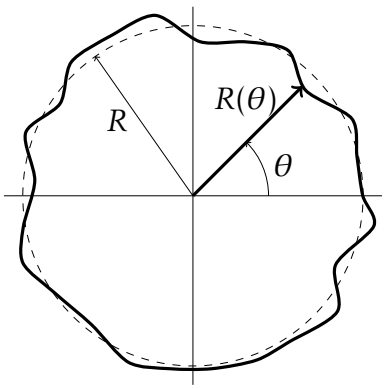

Figure 5.1: *The process of fission is accompanied by arbitrary deformations of the initially undistorted circular nuclear drop (dashed circle with radius R). The distorted sphere can be described by expressing its radius R(θ), through the means of Legendre polynomials (consult text for further information).*

Such small deformations were originally described by Bohr and Wheeler [30] by expanding the nuclear radius R in Legendre polynomials. More specifically, the initially undistorted nuclear sphere (fig. 5.1, dashed line), begins to randomly deform once the neutron gets captured and the compound nucleus is formed, as illustrated in fig. 5.1 with its radius depending on the angle θ. The shape of the nucleus can be simply described with an expansion of the radius $R(\theta)$ in Legendre series as seen in eq. (5.2) where $P_n(cos\theta)$ is the n-th order Legendre polynomial and the α_n coefficients represent the deformation of the nucleus. According to

Bohr and Wheeler [30], the leading coefficients are α_2 and α_4, which correspond to quadrupole and octapole deformations thus describing an ellipsoid. In fig. 5.2, typical deformations are shown for different values of the α_2 and α_4 coefficients.

$$R(\theta) = R\left[1 + \sum_{n=1} \alpha_n P_n(cos\theta)\right] \tag{5.2}$$

It has to be noted that the previous expansion is a simplistic one, since it assumes an azimuthal symmetry. A proper description would be possible by expressing the radius in spherical harmonic coordinates including both the polar and azimuthal angles θ and ϕ thus expanding the nuclear radius using the associate Legendre polynomials $P_n^m(cos\theta)$, as seen in eq. (5.3). In the context of the present concise description, however, an azimuthal symmetry will be considered which does not affect the general conclusions of the LDM for fission.

$$R(\theta,\phi) = R\left[1 + \sum_{n,m} \alpha_{nm} \Upsilon_{nm}(\theta,\phi)\right] = R\left[1 + \sum_{n,m} \alpha_{nm} e^{im\phi} P_n^m(cos\theta)\right] \tag{5.3}$$

Since nuclear matter is practically incompressible, the volume terms which are proportional to the atomic number A, are not affected by deformations, therefore only the surface and Coulomb energies contribute to the change of the binding energy. As a result, the surface energy will be expressed as

$$\begin{aligned} E_s(\theta) &= 4\pi r_0^2 \Omega R^2(\theta) \\ &= E_s^0 \left[1 + \sum_{n=1} \alpha_n P_n(cos\theta)\right]^2 \end{aligned} \tag{5.4}$$

where E_s^0 denotes the surface energy $4\pi r_0^2 \Omega R^2$ of the undistorted drop. The electrostatic energy will change to

$$\begin{aligned} E_c(\theta) &= \frac{3}{5} \frac{1}{4\pi\epsilon_0} \frac{(Ze)^2}{R(\theta)} \\ &= E_c^0 \left[1 + \sum_{n=1} \alpha_n P_n(cos\theta)\right]^{-1} \end{aligned} \tag{5.5}$$

with E_c^0 denoting the electrostatic energy of the spherical nucleus.

Fissility parameter and the single humped potential

For small quadrupole deformations, Bohr and Wheeler [30] proved that the sum of surface and Coulomb energies E_{s+c} can be written as

$$\begin{aligned} E_{s+c} &= E_s^0 \left(1 + \frac{2}{5}\alpha_2^2\right) + E_c^0 \left(1 - \frac{1}{5}\alpha_2^2\right) \\ &= E_{s+c}^0 + \frac{2}{5} E_s^0 \left(1 - \frac{E_c^0}{2E_s^0}\right) \alpha_2^2 \end{aligned} \tag{5.6}$$

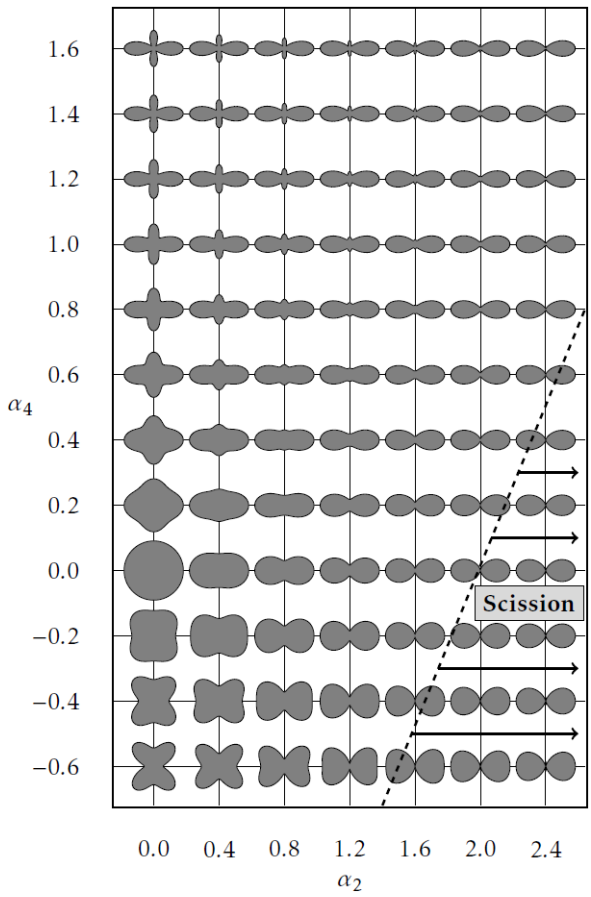

Figure 5.2: *Typical surface shapes of a spherical nucleus when considering quadrupole (α_2) and octapole (α_4) deformations. Scission occurs for extreme deformations which lie right of the dashed line. (Scission line calculated by Cohen and Swiatecki [188].)*

From this expression it can be seen that the term $\chi \equiv E_c^0/2E_s^0$, commonly referred to as the *fissility parameter*, defines whether the binding energy of the distorted sphere will increase, decrease, or remain constant. The fissility parameter, is a characteristic of the nucleus and is equal to $Z^2/50A$. Typical values of χ are 0.72, 0.71, 0.73 and 0.73 for ^{236}U, ^{239}U, ^{238}Np and ^{241}Pu respectively.

In particular, when $\chi > 1$, which corresponds to an oblate deformation with respect to the rotation axis of the nucleus, the surface and Coulomb energies of the distrorted sphere decrease, and the nucleus cannot be stable against fission even for small deformations. For $\chi < 1$, which corresponds to a prolate shape, larger deformations are required for the nucleus to fission which can be mathematically exploited by allowing higher order terms in the Legendre expansion of the nuclear radius, as expressed in eq. 5.2. Minimising E_{s+c}[1], which is now proportional to all the higher order terms, so that it is expressed as a function of α_2, results in an expression for the difference ΔE_{s+c} in binding energy (in MeV) between the distorted E_{s+c} and undisorted E_{s+c}^0 energies with respect to the deformation parameter α_2 described by Cohen and Swiatecki [188] and seen in eq. (5.7).

[1] $\mathrm{d}E_{s+c}/\mathrm{d}\alpha_i = 0,\ i = 2, 3, \ldots$

$$\Delta E_{s+c} = 0.568\left[2.333\alpha_2 - 1.226\alpha_2^2 + 9.500\alpha_2^3 - 8.051\alpha_2^4\right]^2 \tag{5.7}$$

The interpretation of the aforedescribed mathematical treatment, is a competition between the surface and Coulomb energies with increasing deformation. Up to a certain deformation, which corresponds to the saddle point of the potential, the surface energy contributes towards the stability of the nucleus. Beyond the saddle point the Coulomb repulsion becomes more significant than the surface attraction, therefore the nucleus fissions. As seen in fig. 5.3, the net energy which is calculated as the difference between the surface and Coulomb energies, results in a single humped potential that the nuclear system has to overcome in order to fission.

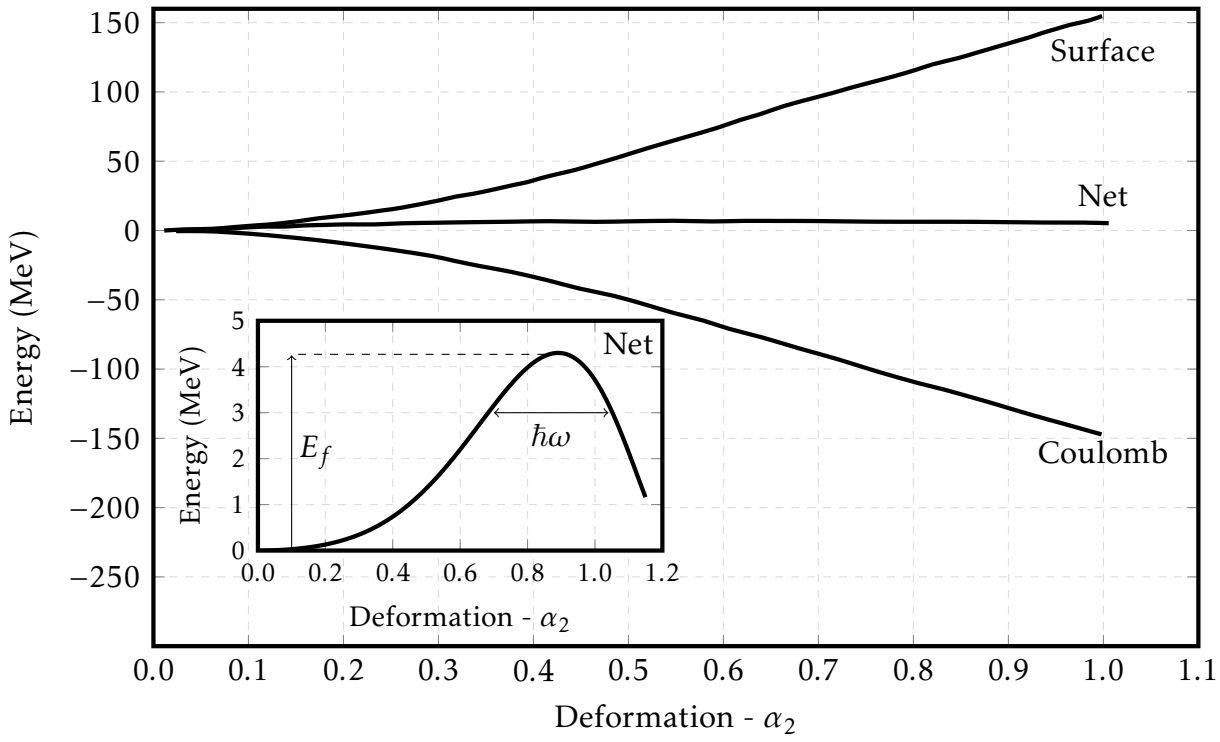

Figure 5.3: *The expansion in higher order Legendre polynomials of the difference between the sum of the surface and Coulomb energies of the distorted and undistorted spheres, results in a single humped fission potential (inset) due to the cancellation of the surface and Coulomb energies. The energy of the saddle point or the fission barrier E_f is shown along with the barrier frequency $\hbar\omega$ which is connected to the transmission coefficient in the Hill-Wheeler approximation.*

Implications of LDM for fission

A single humped potential for fission, introduced by Bohr and Wheeler [30], provides a rather qualitative and macroscopic description of the process. Its main conclusions are summarised below.

1. The extraction of a single-humped potential, when $\chi < 1$ was based on the assumption that nuclei are spherical with no deformations, which implies that the ground state of a fissioning nucleus corresponds to a local minimum and a spherical configuration.
2. For $\chi > 1$, the nucleus is spontaneously deforming itself until it fissions, a process which is known as *spontaneous fission*.
3. For $0.7 \lesssim \chi \leqslant 1$, the deformation energy ΔE_{s+c} exhibits a saddle point with positive energy E_f with respect to the ground state that can be calculated using the calculations performed by Cohen and Swiatecki [188] using the expression seen in (5.8)

$$E_f(MeV) \approx 0.83 E_s^0 (1-\chi)^3 = 14.774 A^{2/3} \left(1 - \frac{Z^2}{50A}\right)^3 \tag{5.8}$$

   Typical values for the LDM fission barrier of some nuclei can be seen in table 5.1, taken from [189].
4. For $\chi > 0.39$, only the terms α_{n0} in eq. (5.3) with n even, are different from zero, which corresponds to a constant deformation energy against rotationally symmetric ($m \neq 0$) and mirror (left/right) asymmetric (n odd) deformations, therefore the LDM predicted a symmetric mass split pass the scission point.
5. The fission process can be described as the interaction of a fictive particle with mass m with an inverted parabolic potential of curvature $\hbar\omega$ and height E_f. The solution of the Schrödinger equation seen in eq. (5.9), leads to the famous Hill-Wheeler transmission coefficient T_f seen in eq. (5.10)

$$-\frac{\hbar^2}{2m}\frac{\mathrm{d}^2\Psi}{\mathrm{d}\alpha_2} + \left(E_f - \frac{1}{2}m\omega^2\alpha_2^2\right)\Psi = E\Psi \tag{5.9}$$

$$T_f = \left[1 + exp\left(2\pi\frac{E_f - E}{\hbar\omega}\right)\right]^{-1} \tag{5.10}$$

5.1.2 The Strutinsky hybrid model

Although the LDM, can qualitatively describe the fission process, it failed to predict fission observables such as[2]:

1. Typical values of the fissility parameter χ of actinides are between $0.7 - 0.8$. Most of these nuclei have non-spherical shapes in their ground states.
2. Spontaneous fission was observed for actinides at significant rates and as mentioned previously, χ values lie below unity.
3. The experimental fission barrier values seen in table 5.1, were found to be about half of the corresponding LDM predictions.
4. Experimental distributions of the fission fragment masses revealed an asymmetric character, which is rather the rule than the exception, contradicting the symmetrical fission predicted by LDM.

[2]The enumeration follows the implications of the LDM described in the previous section

5. The shape of the potential itself cannot justify the observation of the first fission isomer of ^{234m}Pa discovered as early as 1921 by Otto Hahn, let alone the very long lived ^{180m}Ta which has a half-life of the order of 10^{15} y, much larger than Earth's age ($\sim 4.5 \times 10^9$ y). In addition, the resonance structure firstly observed in the $^{240}Pu(n,f)$ [63] and $^{237}Np(n,f)$ [190] cross sections in the keV region where resonances appeared in well-defined clusters could not be justified, a phenomenon also observed in the present experimental work as seen in fig. 5.4 in comparison to the total neutron capture cross section where the resonance grouping is prominent.

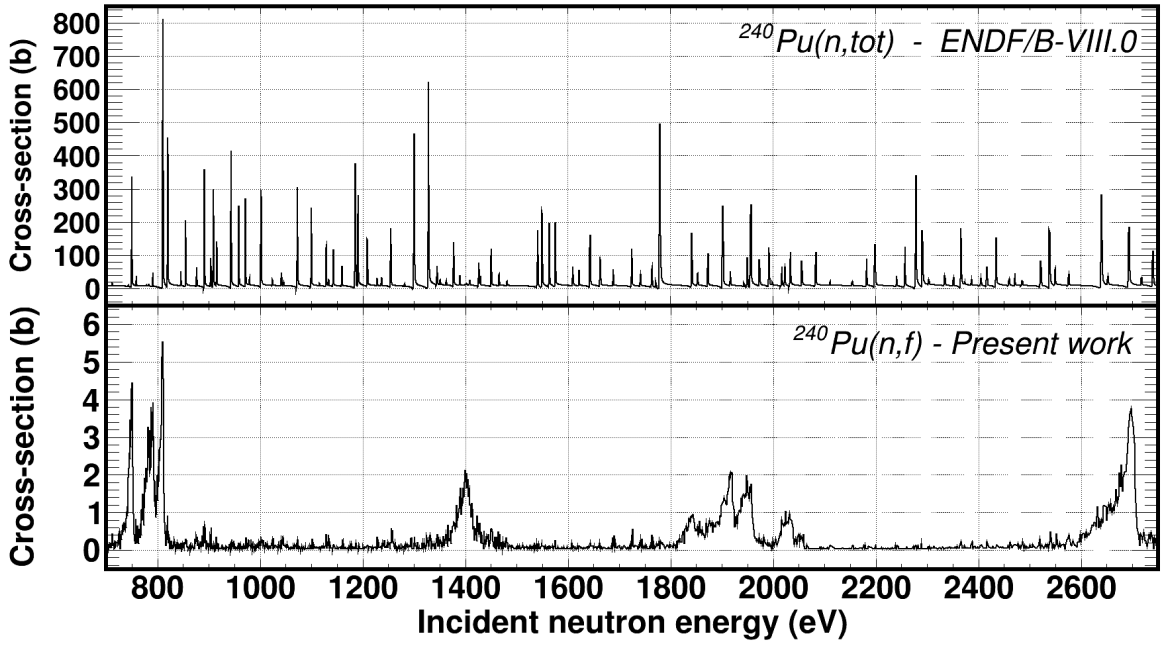

Figure 5.4: *Comparison between total neutron absorption (top) and neutron induced fission (bottom) indicates a prominent resonance grouping and spacing in the fission cross section which was historically discovered in ^{240}Pu . Such a behaviour, which could not be justified from the LDM potential, is attributed to the coupling of class-I and class-II states in a double-humped potential.*

The Single Particle Model

The aforementioned inconsistencies of the LDM predictions and fission observables gave rise to several formalisms to describe the phenomenon, the most important of which is the Single Particle Model (SPM) in which every nucleon in a nucleus with A nucleons, interacts with a potential V that is the average field caused by the remaining $(A-1)$ nucleons similar to the atomic Hartree approximation. The Hamiltonian $\hat{\mathcal{H}}$ of such a system with wavefunction Ψ and eigenstates E can be simply described by summing the individual Hamiltonians $\hat{\mathcal{H}}_i$ (eq. (5.11)) of the nucleons, as expressed in eq. (5.12)

$$\hat{\mathcal{H}}_i \Psi = \left[\sum_{i=1}^{A} \hat{T}_i + \sum_{i=1, j>i}^{A} \hat{\mathcal{V}}_{ij} \right] = E\Psi \tag{5.11}$$

where $\hat{\mathcal{T}}_i$ and $\hat{\mathcal{V}}_{ij}$ correspond to the kinetic and potential energy operators, respectively between the i-th and j-th nucleons.

$$\hat{\mathcal{H}} = \sum_{i=1}^{A} \left[\hat{\mathcal{T}}_i + \frac{1}{2} \hat{\mathcal{V}}_i \right] \tag{5.12}$$

Here, $\hat{\mathcal{V}}_i$ denotes the potential that each nucleon i interacts with, within the nuclear matter, which can be approximated to a Fermi gas. The 1/2 factor was added since the potential $\hat{\mathcal{V}}_{ij} = \hat{\mathcal{V}}_{ji}$, therefore it should not be counted twice.

Table 5.1: *Liquid drop model and experimental fission barriers for several nuclei [189]. It is evident that the LDM fission barriers are greater by a factor of two on average with respect to the experimental ones, indicating the weakness of the LDM to predict fission observables.*

Nucleus	χ	LDM barrier (MeV)	Experimental barrier (MeV)
^{233}Th	0.694	15.58	6.44
^{232}Th	0.697	15.08	5.95
^{239}U	0.707	13.51	6.15
^{238}U	0.710	13.06	5.80
^{232}Ra	0.713	12.68	6.18
^{237}U	0.713	12.63	6.40
^{235}U	0.719	11.79	5.75
^{233}U	0.725	10.96	5.49
^{238}Np	0.725	10.92	6.04
^{237}Np	0.729	10.53	5.49
^{239}Pu	0.738	9.39	5.48

Shell correction and double-humped fission potential

Strutinsky [191], combined the macroscopic LDM and the microscopic SPM and put forward a "macroscopic-microscopic" approach in which shell effects were taken into account. The initial binding energy of the LDM E_{LDM}, seen in eq. (5.1) was changed to the one seen in eq. (5.13) with the addition of a shell correction term δU. It has to be noted that in this approach the N neutrons were treated separately than the Z protons

$$E_b = E_{LDM} + \sum_{N,Z} \delta U \tag{5.13}$$

The shell correction term δU is the difference between the sum of two single particle energies calculated with a different perspective: The energy U of a realistic shell model that includes discrete single-particle level densities and the energy $\tilde{U}$ that conversely is calculated by assuming a uniform distribution of level densities. The application of such a correction, ensures the cancellation of systematic effects

that arise from the difficulty to calculate single particle energies since they heavily depend on the potential $\hat{\mathcal{V}}_{ij}$ used to solve the Schrödinger equation seen in eq. (5.11). Quite conveniently, effects that are attributable to the shell structure itself for any given value of the deformation parameters are the only ones that survive, thus providing a potential that predicts two saddle points, as schematically seen in fig. 5.5 [13].

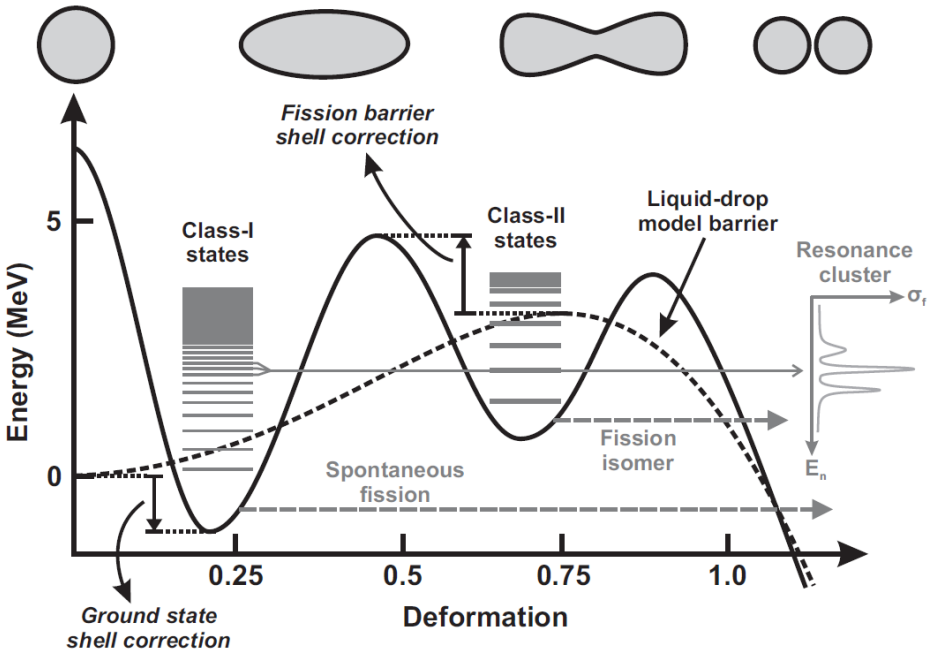

Figure 5.5: *The addition of a shell term in the LDM binding energy, results in a double-humped fission potential. States that reside in the first and second well are designated as class-I and class-II respectively, the coupling of which results in the modulation of fission resonances below the fission threshold which is commonly referred to as resonance clustering. An indicative elongation is shown in the top of the figure. The corresponding single-humped potential is also shown. Courtesy of A. Tsinganis [13].*

The double-humped potential, was a breakthrough in better understanding the fission process and explaining the experimental observables, previously described. An extensive description is provided by Bjørnholm and Lynn [32]. Briefly, a few implications of the shell correction include:

1. A double-humped fission barrier, predicts a non-zero deformation energy for the ground state, which corresponds to a non-spherical nucleus shape.
2. Predicted half-lives of spontaneously fissioning nuclei are in agreement with experimental ones.
3. The predicted fission barriers are in better agreement with experimental data than the LDM ones.
4. The asymmetric mass distribution can be qualitatively described.
5. The fission potential consists of two wells: one in small deformations and another in larger ones. Each well is occupied by states which are designated as class-I and class-II ones for small and large deformations, respectively. Class-

I states are denser and lie in a narrower well, while class-II ones are more sparsely spaced and reside in a much wider well, hence their larger lifetime that can explain the existence of fission (or shape) isomers.

6. A matching of class-I and -II states, spin and parity-wise results in the modulation of fission resonances: Each resonance cluster seen in fig. 5.4 can be attributed to the coupling between a group of class-I states and the corresponding class-II state.

5.2 Neutron-induced reaction cross sections

The absorption of an incident neutron from a nucleus in the actinide region ${}^{A}_{Z}X_{N}$ which consists of N neutrons, Z protons and $A = Z + N$ nucleons, typically results in the formation of a compound system ${}^{A+1}_{Z}X_{N+1}$ for low energy neutrons. During such a process, the nuclear system is excited and has several paths to release the given energy, typically through the emission of γ-rays (radiative neutron capture, (n,γ)), the re-emission of the absorbed neutron with the same or different energy (elastic scattering, (n,n) and inelastic scattering (n,n'), respectively) and through the fission process.

5.2.1 Characteristics of neutron cross sections

As seen in fig. 5.6, where the most important neutron induced reaction cross sections are shown for ^{237}Np , the (n,γ) channel dominates for neutron energies up to a few keV, featuring a general decrease with increasing energy. The elastic scattering cross section on the other hand, can be considered to be much smoother and relatively constant throughout a large energy domain. Neutron induced fission is usually much insignificant for energies up to a few hundreds of keV (where the effective fission threshold is situated at) resonances notwithstanding, above which it becomes a significant reaction for fast neutrons.

Apart from the different tendencies observed in the cross sections, some similarities can also be seen. The reaction likelihood smoothly decreases from cold energies up to the epithermal region and is proportional to $1/v$ (or similarly $\sim 1/\sqrt{E_n}$) since the higher the neutron energy E_n, hence its velocity v, the less time it spends inside the nucleus. This behaviour is commonly referred to as the $1/v$ law. At higher neutron energies, resonances appear which correspond to excited states of the compound nucleus, that lie above the neutron separation energy. This region is commonly referred to as the "*Resolved Resonance Region (RRR)*". Finally, when the level spacing of the compound nucleus is significantly smaller than the resolving capabilities of the apparatus, typically from intermediate and higher neutron energies, i.e. the so-called "*Unresolved Resonance Region (URR)*", resonances can no longer be resolved thus resulting in a smooth behaviour of the cross section.

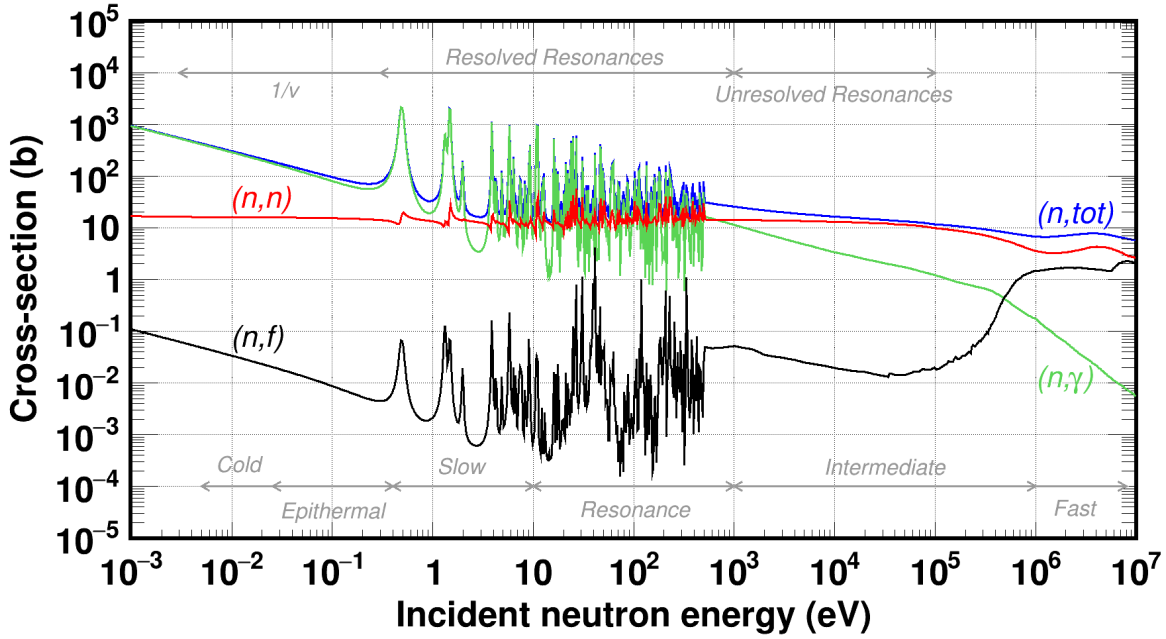

Figure 5.6: *Most important neutron induced reaction cross sections for ^{237}Np obtained from the ENDF/B-VIII.0 evaluation library. An incident neutron energy classification is shown on the bottom part of the graph while on the top, the $1/v$ along with the resolved and unresolved resonance regions are indicated. Both classifications are indicative.*

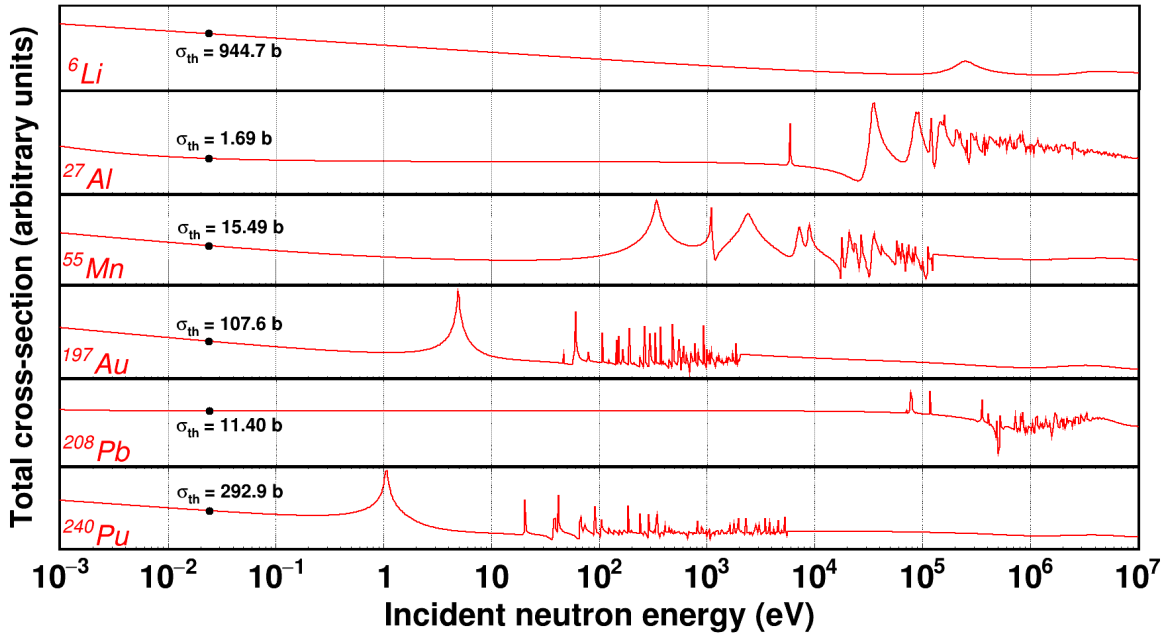

Figure 5.7: *Total neutron induced evaluated cross sections for nuclei from ^{6}Li up to ^{240}Pu , obtained from ENDF/B-VIII.0 library. With increasing mass, typical level spacing becomes smaller, hence more resonances appear towards the bottom of the plot, except when closed shells exist, as in the case of ^{208}Pb. The cross sections σ_{th} at the thermal point, which corresponds to ~ 25 meV, are also shown.*

A general tendency of the likelihood for a nucleus to interact with a neutron, can be seen in fig. 5.7 where with increasing mass, resonances appear at lower energies. This observation lies on the fact that, the heavier the nucleus, the smaller its level spacing becomes. However, for ^{208}Pb, the first resonance appears at about 100 keV, which is attributed to its closed shells since it is a magic nucleus and prefers to maintain its closed shell configuration.

In fig. 5.7, the cross section σ_{th} at the thermal point ($\sim$ 25.3 meV) is also indicated. A general trend is quite visible according to which, the heavier a nucleus gets, the higher the probability to absorb a neutron becomes, since such an absorption results in a smaller perturbation for neutron-rich nuclei. Two exceptions are seen though, for ^{6}Li and ^{208}Pb. In the former case, the absorption of a neutron results in the formation of ^{7}Li which is much more abundant than ^{6}Li (92.5% as opposed to 7.5%) hence the extremely high cross section, while in the latter case the closed-shell configuration results in a stable nucleus, difficult to be perturbed, hence the small cross section.

5.2.2 Neutron induced fission cross sections

The general characteristics of a neutron induced fission cross section have already been discussed in the previous sections. What needs to be addressed as well is the quite high probability for specific nuclei to fission. As seen in fig. 5.8, the ^{235}U fission cross section is appreciably larger that the corresponding $^{238}U(n,f)$ one and practically does not feature any effective threshold at all.

As can be seen in fig. 5.9, the neutron separation energy S_n (i.e. the energy required to remove the last neutron from a nucleus[3]) of ^{236}U is 6.5 MeV [192]; 300 keV larger than the energy required to activate fission E_f (i.e. the fission barrier). This can be visualised as an occasion in which the nuclear system, lowers its ground state. On the contrary, in the $^{238}U(n,f)$ case, the neutron separation energy is 1.8 MeV lower than the fission barrier for ^{239}U, therefore fission is not that probable for incident neutron energies, smaller than this value. The former case describes a "fissile" nucleus, whereas the latter a "fissionable" one.

The previously described difference in the cross section is attributed to shell effects. The pairing term of the LDM (eq. (5.1)) can explain that the neutron capture from a nucleus with odd A in the $^{235}U(n,f)$ case, results in the formation of an even-even configuration and therefore in the lowering of the total binding energy by a value of δ_0. On the other hand neutron capture from ^{238}U , an even-even nucleus hence more stable, results in the formation of a system with an odd mass number A, therefore its total binding is increased by δ_0.

[3]The neutron separation energy of the compound nucleus ${}^{A+1}_{Z}X_{N+1}$ has the same value as the Q-Value of the $n + {}^{A}_{Z}X_N \rightarrow {}^{A+1}_{Z}X_{N+1}$ for a zero incident neutron energy.

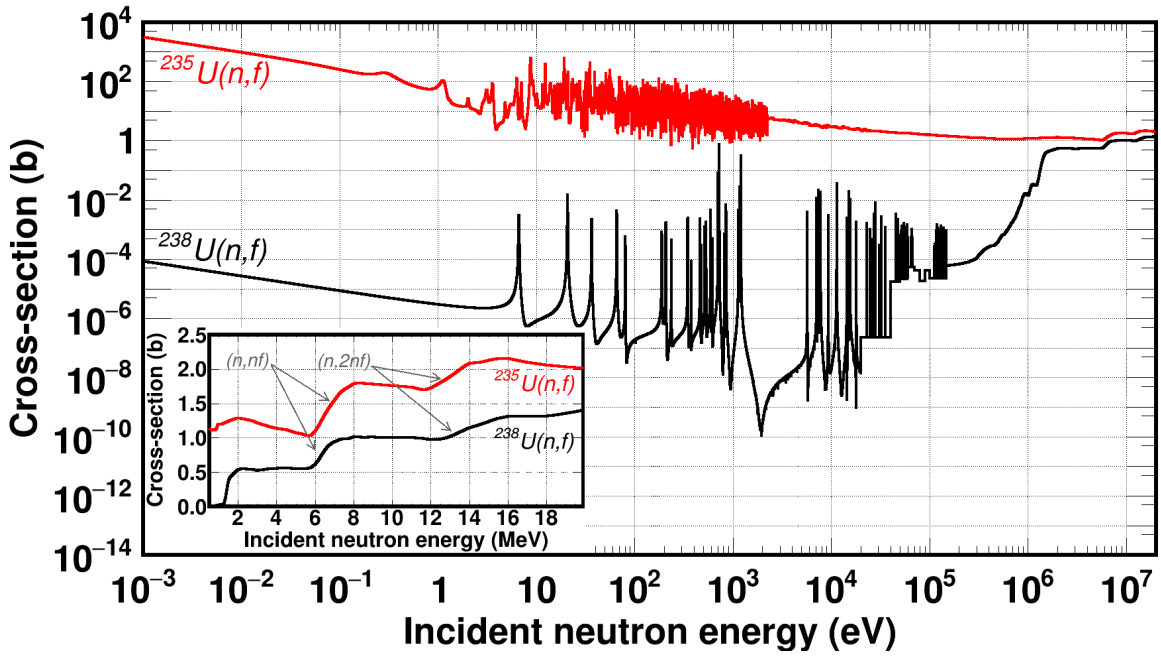

Figure 5.8: *Neutron induced fission cross sections for ^{235}U and ^{238}U , obtained from the ENDF/B-VIII.0 evaluation library. The appreciably higher cross section of $^{235}U(n,f)$ is attributed to the pairing effect. The inset shows the cross section in the MeV region in which the emission of pre-equilibrium neutrons (n, xnf), prior to fission is possible.*

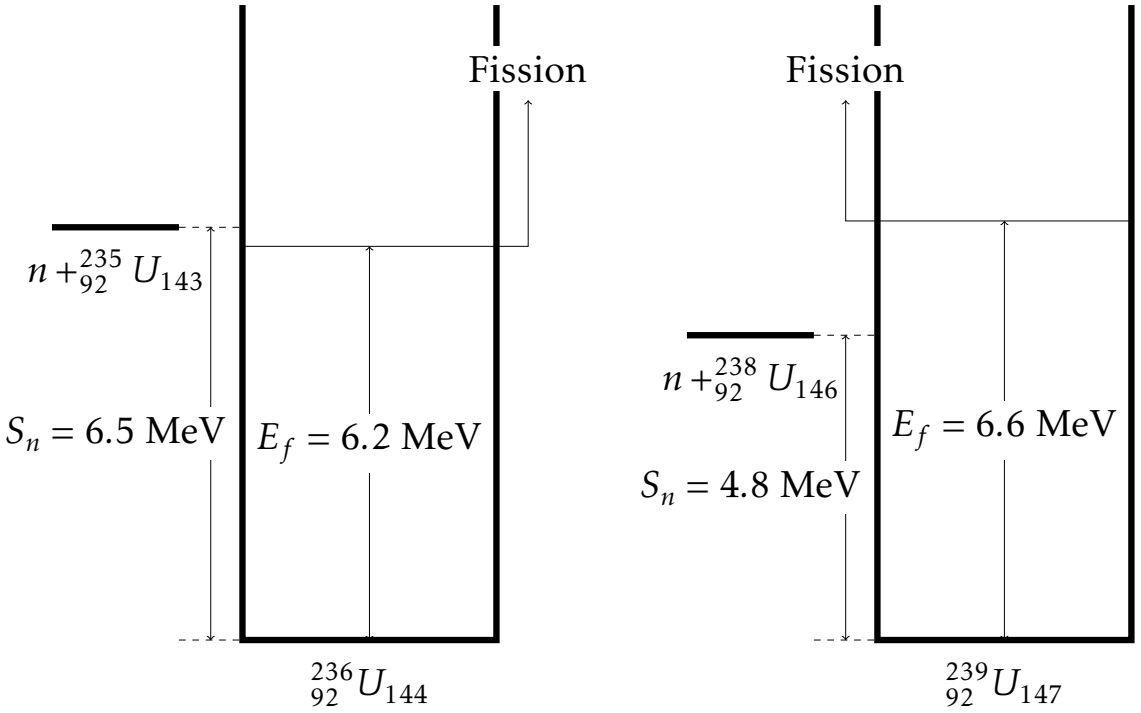

Figure 5.9: *Energy diagrams of neutron capture in ^{235}U and ^{238}U . In the former case, the neutron separation energy is higher than the fission barrier (fissile actinide), while in the latter, lower (fissionable actinide).*

An additional feature of neutron induced fission cross sections, regardless of

fissile or fissionable nuclei, is the prominent steps seen in the inset of fig. 5.8 at incident neutron energies above ~ 5 MeV. These structures correspond to multiple-chance fission (n,xnf), in which an x number of pre-equilibrium neutrons is emitted prior to fission. As the incident neutron energy increases, so does the probability for the formed compound nucleus to emit one ((n,2nf), second-chance fission), two ((n,3nf), third-chance fission) etc., neutrons. Such emissions occur before the nucleus reaches an equilibrium state suitable for fission, therefore the time-scale of this process is much shorter than the corresponding one of the standard fission.

5.2.3 Neutron resonances and the compound nucleus

Neutron absorption for incident energies in the ev - keV region, results in the formation of the compound nucleus. For zero incident energy, the compound is formed at an excited state, which typically lies ~ 5 – 6 MeV above its ground state, as illustrated in fig. 5.10 for ^{241}Pu.

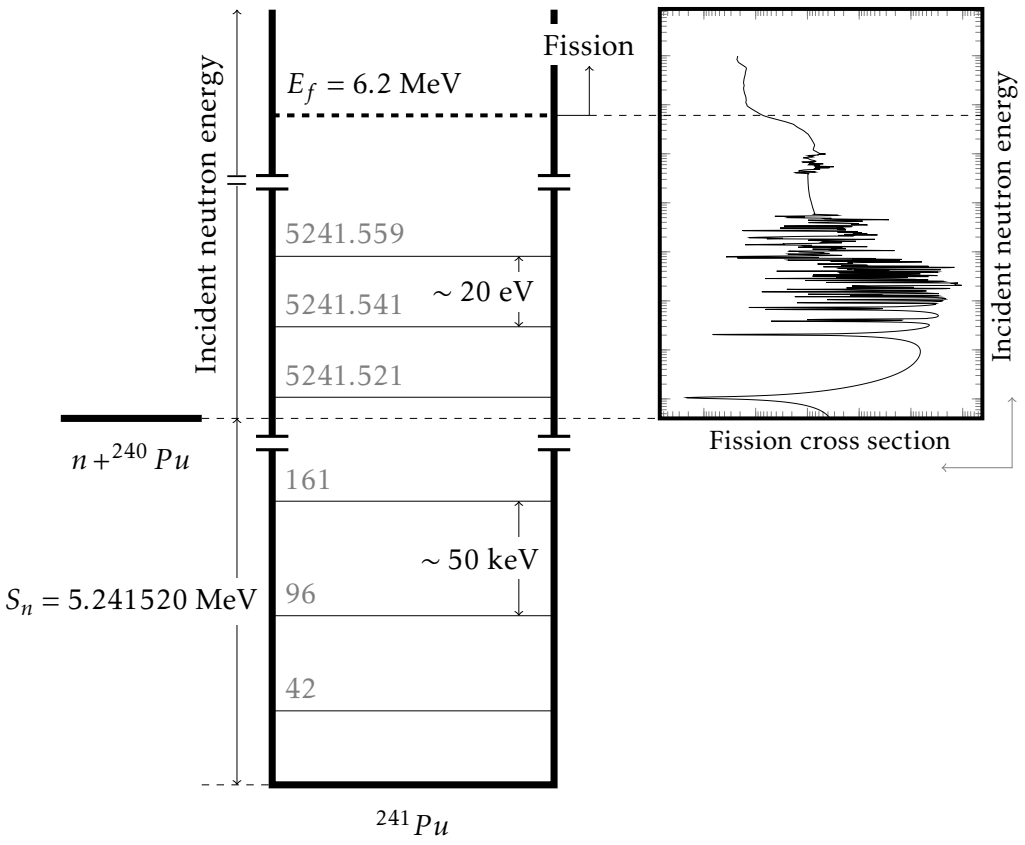

Figure 5.10: *Schematic representation of neutron capture from ^{240}Pu . A zero-energy neutron absorption is followed by the formation of the compound ^{241}Pu nucleus, ~ 5.2 MeV above its ground state. Resolved resonances with ~ eV spacing in the (n,f) cross section correspond to levels of the compound nucleus above the neutron separation energy. The first three levels of ^{241}Pu are shown along with the first three ones above the neutron separation energy. Units are in eV, unless otherwise specified.*

The level spacing of the compound nucleus if of the order of 50 keV close to the ground state and is reduced to about three orders of magnitude, when it gets excited from neutron absorption. The neutron in its absence of charge, can easily penetrate the nucleus and transfer its energy to the nucleons. At specific energies a complex quasi-stationary configuration is formed, which corresponds to a level of the compound nucleus which is characterised by its half-live τ, energy E, spin J and parity π. This matching, between class-I and class-II states can also be seen in fission cross sections in the form of resonances.

The observed resonances in neutron induced cross sections, can be approximately described by a Breit-Wigner shape [193] which requires a resonance energy E_0, a total and a partial width Γ and Γ_i, respectively. The partial width is related to the decay channels (Γ_γ for (n,γ), Γ_n for (n,n) and Γ_f for (n,f)) of the compound nucleus, therefore the total width Γ is the sum of all the possible partial widths. Typical values of the total width are of the order of eV, hence the half-life τ of the nuclear state can be calculated by Heisenberg's uncertainty principle according to which $\tau = \hbar/\Gamma$, resulting in a half life of the order of $\sim 10^{-16}$ s.

The energy profile $I(E)$ of a resonance (eq. (5.15)), which corresponds to a Breit-Wigner shape and can be seen in fig. 5.11, occurs by a Fourier transform of the time-dependent wave-function $\Psi(t)$ (eq. (5.14)) of a nuclear level with lifetime τ. In the description of the wave-function, Ψ_0 corresponds to the amplitude of the wave-function.

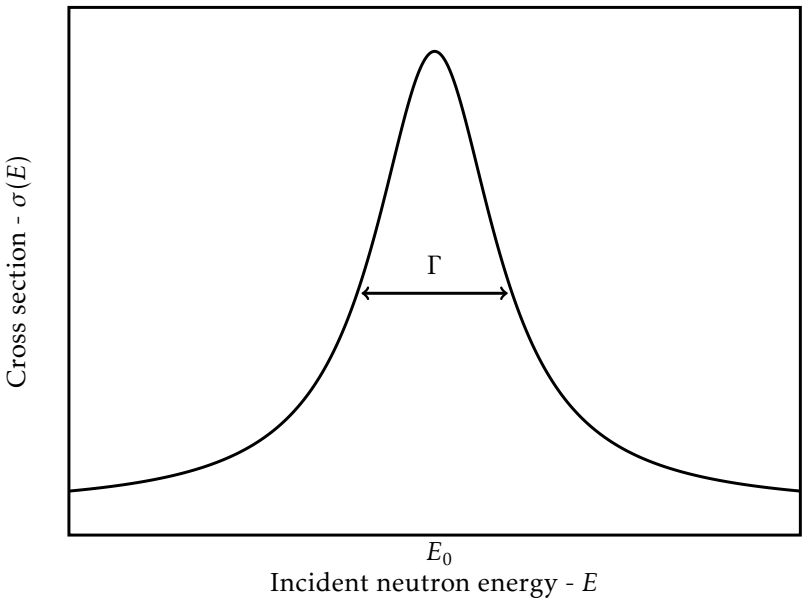

Figure 5.11: *Schematic representation of an isolated resonance, which is characterised by a total width* Γ *and an energy* E_0*, described by a Breit-Wigner shape.*

$$\Psi(t) = \Psi_0 \exp\left\{-i\left(\frac{E_o t}{\hbar} + \frac{t}{2\tau}\right)\right\} \tag{5.14}$$

$$I(E) = \frac{1}{2\pi}\frac{\Gamma}{(E-E_0)^2 + \Gamma^2/4} \tag{5.15}$$

The analysis of resonances in a reaction yield, i.e. the estimation of their properties (E_0, Γ_i, J^π) can reveal information about the nuclear system and it is possible by implementing the ℜ-Matrix formalism, which will be described in the next section.

5.3 The ℜ-Matrix formalism

A neutron-nucleus reaction can be described by assuming that the neutron beam is a plain wave with mass m, described by its wave-function Ψ, incident at the target nucleus which is represented by a potential well, as schematically shown in fig. 5.12. The neutron interacts with the potential well and then is scattered radially in space. In this scenario, the incident and outgoing wave-functions could be calculated by solving the Schrödinger equation of the system in order to extract the probability currents j_{inc} and j_{out} (i.e. eq. (5.16) for the incident plain wave) and hence the cross section $\sigma(\Omega)$ in the solid angle Ω (eq. (5.17)), through the conservation of probability density.

$$j_{inc} = \frac{\hbar}{2mi}(\Psi^*\nabla\Psi - \Psi\nabla\Psi^*) \tag{5.16}$$

$$\sigma(\Omega) = r^2 \frac{j_{out}(r,\Omega)}{j_{inc}} \tag{5.17}$$

In the aforementioned situation the potential is generally unknown, therefore the interaction process can be described either by calculating the potential or by using its eigenstates. The former approach can be used for high excitation energies, where the compound nucleus that is formed is excited in the continuum , through the means of optical model calculations, based on the Hauser-Feshbach formalism. The latter approach, is used for small excitation energies, where the compound nucleus is excited at discrete levels, yet its analytical description is quite complicated. The use of the eigenstates, therefore, makes the description much simpler, through the ℜ-Matrix formalism that was initially introduced by Wigner and Eisenbud [194] in 1947. Extensive overviews were published by Lane and Thomas [195] in 1957 and Fröhner [196] in 2000.

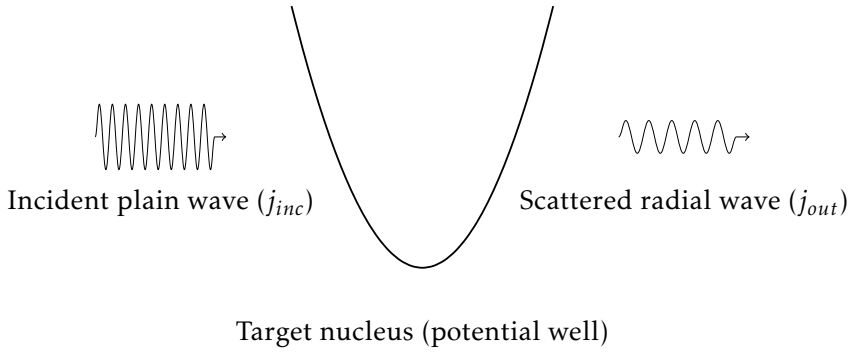

Figure 5.12: *Schematic representation of a neutron-nucleus interaction. The neutron beam can be described as a current of plain waves that interact with the target nucleus, which is represented as a potential well. The interaction results in a set of scattered radial waves.*

5.3.1 Internal and external reaction regions

It has already been mentioned that a neutron-nucleus reaction results in the formation of a compound nucleus at an excited state. Despite the fact that the wave function of the compound nucleus is rather difficult to be mathematically described, an expansion in its eigenstates is possible.

The formation of the compound nucleus takes place at a geometrical distance $r = a_c$ between the neutron and the target nucleus, where r describes the separation distance between the incident particle and the target nucleus. The parameter a_c can be considered to have a value equal to the radius of the compound nucleus i.e. $a_c = r_0(A+1)^{1/3}$, with $r_0 = 1.25$ fm. The nuclear interaction takes place in three simple steps, as schematically represented in fig. 5.13:

(a) Entrance channel: The neutron approaches the target nucleus ($r > a_c$) therefore both particles are well separated hence the Schrödinger equation is solvable.
(b) Compound nucleus formation: The neutron is absorbed by the target when $r = a_c$ and while $r < a_c$ the wave function is an expansion of its eigenstates.
(c) Exit channel: The compound nucleus is disintegrated and the product particles form a system of solvable Schrödinger equations. To simplify the description, the exit channel will be composed of two particles with a separation distance $r > a_c$, similar to neutron scattering.

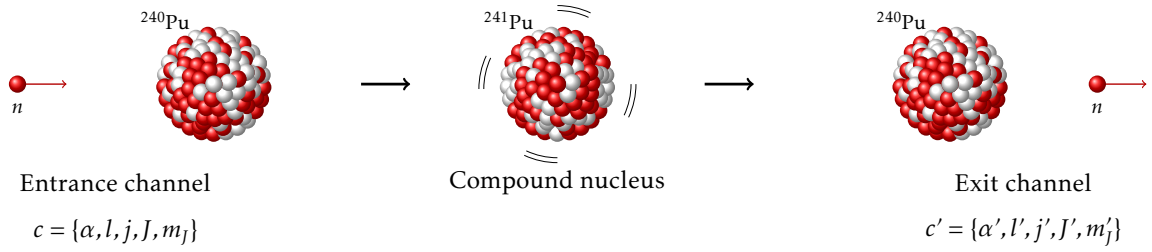

Figure 5.13: *Schematic representation of the stages involved during a neutron-nucleus interaction. The entrance and exit channels, which correspond to the external region, can be described by the quantum numbers $\{\alpha, l, j, J, m_J\}$ (see text for details). The compound nucleus stage, which corresponds to the internal region, can be described with its eigenstates.*

The three previous steps, can be further classified based on the separation distance, assuming that both the entrance (c) and exit (c') channels are composed of two particles with spin i and I. When $r > a_c$, which is denoted as the *external region*, the particles involved in the reaction can be described using nuclear scattering theory, as opposed to the *internal region* which concerns the compound nucleus. Each channel, can then be represented by a set of quantum numbers, namely:

- α: Spin and excitation state of the individual interacting particles and can be considered as a set of the natural parameters of the interacting particles.
- l: Orbital angular momentum of the two-particle system
- j: The spin of the channel, which is the quantum sum of the individual spins, $|i - I| < j < i + I$

- J: The total angular momentum of the system, $|j-l| < J < j+l$
- m_J: The projection of J on the z-axis.

It has to be noted, that the primed quantum numbers correspond to the exit channel.

The particular case of incident chargeless particles, has been addressed by Blatt and Biedenharn [197] who solved the non-relativistic Schrödinger equation assuming an incident plain wave and an outgoing spherical one, as illustrated in fig. 5.12 and deduced that the cross section $\sigma_{cc'}$ is given by eq. (5.18),

$$\sigma_{cc'} = \pi \lambda\!\!\!^{-2}_c \, g_J \, |\delta_{cc'} - \mathcal{U}_{cc'}|^2 \tag{5.18}$$

where $\lambda\!\!\!^{-}_c$ is the reduced de Broglie wavelength of the incident particle in channel c, $\delta_{cc'}$ is the Kronecker delta, $\mathcal{U}_{cc'}$ is the collision matrix whose physical meaning will be explained later and g_J is the spin factor which describes the probability of having an angular momentum J upon the occurring interaction (i.e. in the entrance channel). More specifically, the total number of possible total angular momentum combinations is $(2i+1)(2I+1)(2l+1)$, however only $(2J+1)$ combinations can add to J and can be described as follows:

$$g_J = \frac{2J+1}{(2i+1)(2I+1)} \tag{5.19}$$

5.3.1.1 Wave functions in the external region

The wave function $\Psi(r,\theta,\phi)$ in the external region can be calculated by solving the Schrödinger equation and factorising the solutions in spherical coordinates i.e. $\Psi(r,\theta,\phi) = R(r)\Theta(\theta)\Phi(\phi)$. Since the particles interact through a central potential $V(r)$, only the radial part $R(r)$ depends on it, therefore the solution of the angular part is typically given by the spherical harmonics $Y_{lm_l}(\theta,\phi)$ with the appropriate coefficients.

This leaves only the radial part of the Schrödinger equation, seen in eq. (5.20), where μ_c is the reduced mass of the channel c.

$$\left[\frac{\mathrm{d}^2}{\mathrm{d}r^2} - \frac{l(l+1)}{r^2} - \frac{2\mu_c}{\hbar^2}\Big(V(r) - E\Big)\right] R(r) = 0 \tag{5.20}$$

The potential $V(r)$ in the case of an incident charged particle is a Coulomb one, whereas in the case of low energy neutrons at maximum resonant energies (i.e. s-wave neutrons) it can be considered that $V(r) = 0$, thus eq. (5.20) is reduced to the so called spherical Bessel equation, whose solution is a linear combination of the incident and outgoing waves, $I_l(r)$ and $O_l(r)$, respectively, where l describes all the waves that survive in the channel wave-packet and x_l, y_l correspond to the wave amplitude. Both waves can be described by the spherical Bessel functions of first and second kind[4], $j_l(\rho)$ and $n_l(\rho)$ respectively, as seen in eq. (5.21)

$$R_l(r) = y_l I_l(r) + x_l O_l(r) \tag{5.21}$$

[4]The Bessel functions of second kind $n_l(\rho)$ are most commonly referred to as Neumann functions.

where the solution is expressed in wave-number units $\rho = kr$ as seen in equations (5.22a) and (5.22b), where it is evident that $O_l = I_l^*$. A schematic representation of a few waves that can be part of the incident wave-packet can be seen in fig. 5.14 where the four first Bessel functions of the first kind are shown.

$$I_l(r) = -i\rho\Big[j_l(\rho) - in_l(\rho)\Big] \tag{5.22a}$$

$$O_l(r) = \quad i\rho\Big[j_l(\rho) + in_l(\rho)\Big] \tag{5.22b}$$

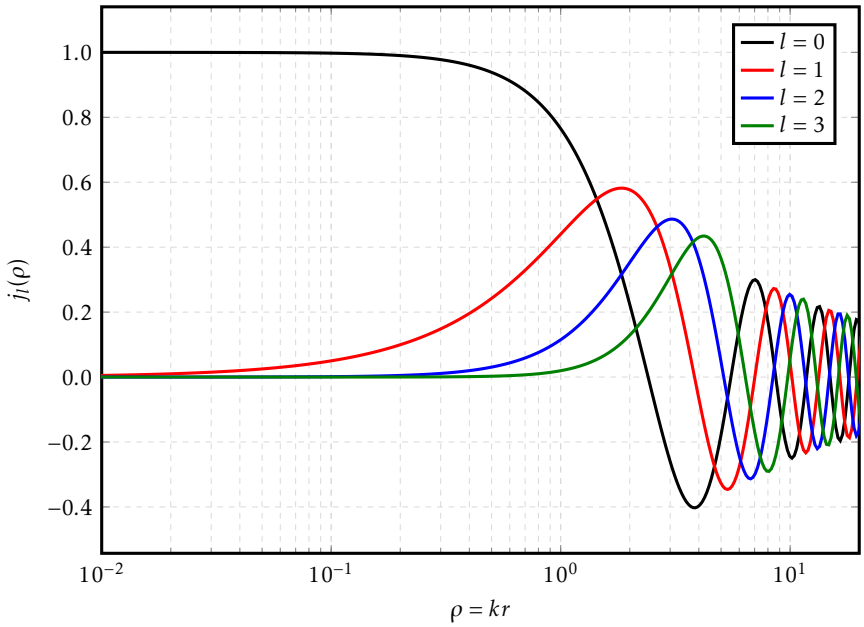

Figure 5.14: *The first four Bessel functions of first kind $j_l(\rho)$ are shown with respect to the separation radius r that measures the distance of the incident (or outgoing) neutron from the center of the compound nucleus in wave-length units $\rho = kr$.*

In addition, the scattered neutron can be described as a radial wave that is propagated infinitely in space, as seen in fig. 5.15, where j_0 is shown from $r = a_c$, which corresponds to $(x, y) = (0, 0)$, up to three wavelengths away from the interaction.

The previous discussion took into account only a single number of a channel c and the radial part, however the interaction involves several channels that can be simultaneously occurring, as well as their angular solutions. Consequently, the total wave function $\boldsymbol{\Psi}$ can be expressed as a linear combination of all channels and solutions, as seen in eq. (5.23)

$$\boldsymbol{\Psi} = \sum_c y_c \mathcal{I}_c + \sum_{c'} x_{c'} \mathcal{O}_{c'} \tag{5.23}$$

with ϕ_c describing the phase shift of channel c in a hard-sphere collision and $\mathcal{I}_c$ and $\mathcal{O}_c$ are described in equations (5.24a) and (5.24b).

$$\mathcal{I}_c = \frac{1}{r} I_c \phi_c i^l Y_{lm_l}(\theta, \phi) \tag{5.24a}$$

$$\mathcal{O}_c = \frac{1}{r} O_c \phi_c i^l Y_{lm_l}(\theta, \phi)\Big] \tag{5.24b}$$

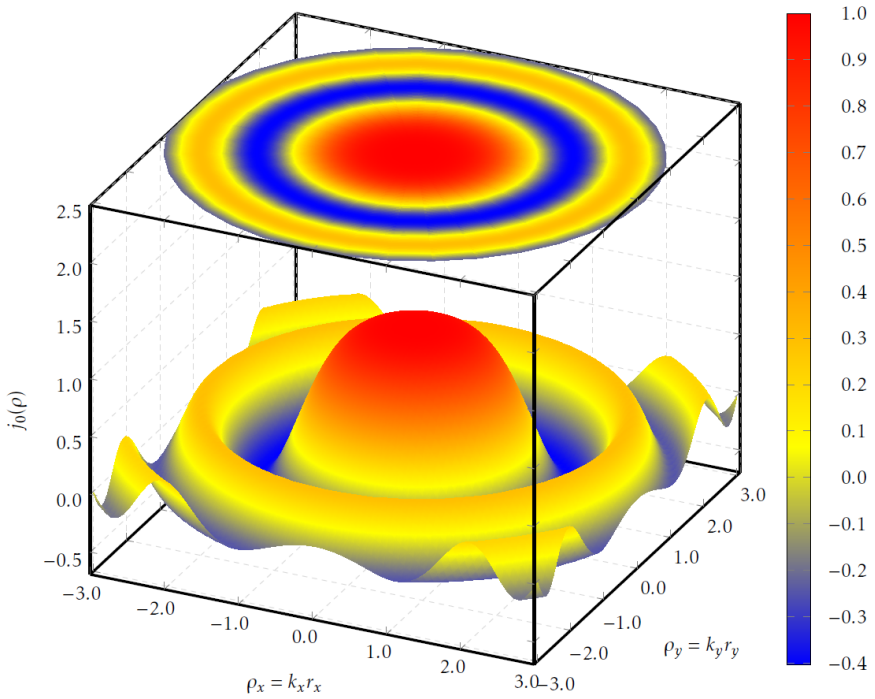

Figure 5.15: *The zero-order Bessel function of the first kind $j_0(\rho)$ is shown with respect to the separation radius r that measures the distance of the incident (or outgoing) neutron from the center of the compound nucleus in wave-length units of $\rho = kr$ in the x and y direction.*

The coefficients y_c and $x_{c'}$ practically describe in which way the incident wave is modified and is altered to the outgoing one. The outgoing coefficients, heavily depend on the details of the reaction, which can be observed in the cross section. The incident coefficients y_c are known since they are chosen from the experiment, while the observed cross section can provide information on the $x_{c'}$, which practically describes the nature of the interaction. A convenient way to express $x_{c'}$ in terms of y_c is through the introduction of the collision matrix $\mathcal{U}_{cc'}$, as seen in eq. (5.25).

$$x_{c'} \equiv -\sum_{cc'} \mathcal{U}_{cc'} y_c \tag{5.25}$$

Finally, the wave-function can be expressed in terms of the collision matrix and the incident coefficients, as seen in eq. (5.26) where the collision matrix $\mathcal{U}_{cc'}$ can be deduced from the observed cross section, seen in eq. (5.18).

$$\boldsymbol{\Psi} = \sum_{c} y_c \left(\mathcal{I}_c - \sum_{c'} \mathcal{U}_{cc'} \mathcal{O}_{c'} \right) \tag{5.26}$$

5.3.1.2 Wave functions in the internal region

Solving eq. (5.20) within the internal region is not a straightforward process, therefore a mathematical trick needs to be applied. Apart from the wave function $\Psi_l(E,r)$, the eigenvectors $\Psi_l(E_\lambda,r)$ are also solutions, therefore they satisfy the exact same

equation but for the specific energy E_λ, as seen in equations (5.27a) and (5.27b) where the mass m of the compound nucleus is used instead of the reduced mass.

$$\left[\frac{\mathrm{d}^2}{\mathrm{d}r^2} - \frac{l(l+1)}{r^2} - \frac{2m}{\hbar^2}\Big(V(r) - E\Big)\right]\Psi_l(E,r) = 0 \tag{5.27a}$$

$$\left[\frac{\mathrm{d}^2}{\mathrm{d}r^2} - \frac{l(l+1)}{r^2} - \frac{2m}{\hbar^2}\Big(V(r) - E_\lambda\Big)\right]\Psi_l(E_\lambda,r) = 0 \tag{5.27b}$$

This trick requires the expansion of the wave function $\Psi_l(E,r)$ in its eigenvectors, as seen in eq. (5.28) with the proper coefficients $A_{l\lambda}$ which have to be defined. Here λ is the number of possible eigenstates found in the compound nucleus and in practice it is directly related to each individually observed resonance.

$$\Psi_l(E,r) = \sum_\lambda A_{l\lambda}\Psi_l(E_\lambda,r) \tag{5.28}$$

It has to be noted that both equations must be finite at $r = 0$, since they represent a physical system. In addition, to avoid singularities at the interface of the interaction, the logarithmic derivatives of the eigenvectors must be constant as seen in eq. (5.29), where B_l is a real parameter that can be freely chosen.

$$\left|\frac{\mathrm{d}\Psi_l(E_\lambda,r)}{\mathrm{d}r}\right|_{r=a_c} = \frac{1}{a_c}B_l\Psi_l(E_\lambda,a_c) \tag{5.29}$$

The eigenvectors $\Psi_l(E_\lambda,r)$ can be conveniently chosen so as to form an orthonormal basis set so that

$$\int_{r=0}^{a_c}\Psi_l(E_\lambda,r)\Psi_l(E'_\lambda,r)\,\mathrm{d}r = \delta_{\lambda\lambda'} \tag{5.30}$$

and the $A_{l\lambda}$ coefficients can be expressed as shown in eq. (5.31)

$$A_{l\lambda} = \int_{r=0}^{a_c}\Psi_l(E_\lambda,r)\Psi_l(E,r)\,\mathrm{d}r \tag{5.31}$$

The only obstacle up to the present point is eliminating the potential $V(r)$, which can be achieved by multiplying equations (5.27a) and (5.27b) with $\Psi_l(E_\lambda,r)$ and $\Psi_l(E,r)$, respectively, subtracting the resulting equations and integrating between $r = 0$ and $r = a_c$. This results in an expression for $\Psi_l(E_\lambda,r)\Psi_l(E,r)$, hence the $A_{l\lambda}$ coefficients can be calculated using eq. (5.32)

$$A_{l\lambda} = \frac{\hbar^2}{2m}\frac{1}{(E_\lambda - E)}\left[\Psi_l(E_\lambda,r)\frac{\mathrm{d}\Psi_l(E,r)}{\mathrm{d}r} - \Psi_l(E,r)\frac{\mathrm{d}\Psi_l(E_\lambda,r)}{\mathrm{d}r}\right]_{r=a_c} \tag{5.32}$$

The last step is to ensure that the wave functions and their derivatives within the internal region match the corresponding ones in the external one, for both channels c and c' at $r = a_c$. This leads to the expression for the wave function Ψ_l regarding the c channel, seen in eq. (5.33)

$$\Psi_l(E,a_c) = \frac{\hbar^2}{2ma_c}\sum_\lambda\left[\frac{\Psi_c(E_\lambda,a_c)\Psi_c(E_\lambda,a_c)}{E_\lambda - E}\right]\Big(D_c - B_l V_c\Big) \tag{5.33}$$

The constants V_c and D_c represent the value of the wave-function $\Psi_l(E,r)$ and its derivative at $r = a_c$. Since the wave functions of both channels c and c' should match at the nuclear surface, it can be shown that for all the possible channels c the following expression holds:

$$V_{c'} = \sum_c \mathcal{R}_{cc'}\Big(D_c - B_l V_c\Big) \tag{5.34}$$

where $\mathcal{R}_{cc'}$ is the so-called $\mathfrak{R}$-Matrix and contains the physical properties E_λ and $\gamma_{\lambda c}$ which represent the eigenstate and its probability of forming the level λ of the compound nucleus, as seen in eq. (5.35)

$$\mathcal{R}_{cc'} = \frac{\gamma_{\lambda c}\gamma_{\lambda c'}}{E_\lambda - E} \tag{5.35}$$

with

$$\gamma_{\lambda c} = \sqrt{\frac{\hbar^2}{2ma_c}}\Psi_c(E_\lambda, a_c) \tag{5.36}$$

representing the reduced width of the resonance, with E_λ being the energy at the resonance peak.

5.3.2 Approximations to the $\mathfrak{R}$-Matrix formalism

Combining and rearranging equations (5.34) and (5.33), the collision matrix $\mathcal{U}$ can be written as a function of the $\mathfrak{R}$-Matrix , as seen in eq.

$$\mathcal{U} = \mathbf{\Omega}\mathcal{P}^{1/2}\Big[\mathcal{I} - \mathcal{R}(\mathcal{L} - \mathcal{B})\Big]^{-1}\Big[\mathcal{I} - \mathcal{R}(\mathcal{L}^* - \mathcal{B})\Big]\mathcal{P}^{-1/2}\mathbf{\Omega} \tag{5.37}$$

where the diagonal $\mathbf{\Omega}, \mathcal{P}, \mathcal{L}$ matrices describe the fraction of outgoing with respect to ingoing waves at $r = a_c$, the penetrability of the ingoing particle inside the target nucleus and the rate of attenuation of the outgoing wave, respectively. The matrix $\mathcal{I}$ corresponds to the unitary matrix. A full description of the reported expansion can be found in the review manuscripts that have already been mentioned.

It is important to mention that all the matrices involved in eq. (5.37) correspond to quantities that are experimentally known, however the difficulty in calculating the collision matrix $\mathcal{U}$ lies in the inversion of the $\mathcal{I} - \mathcal{R}(\mathcal{L} - \mathcal{B})$ matrix. Several approximations have been made, however only three of them, relevant to the present work, will be briefly discussed. All based on Wigner's idea, who introduced the so-called level matrix $\mathcal{A}$ whose ij elements, are given by eq.

$$\left(\mathcal{A}^{-1}\right)_{ij} = (E_\lambda - E)\delta_{ij} - \sum_c (\gamma_{ic}L_{0c}\gamma_{jc}) \tag{5.38}$$

5.3.2.1 Single Level Breit Wigner approximation

The single level Breit-Wigner (SLBW) approximation is useful in isolated resonances, where all the matrices involved in eq. (5.37) contain a single element. The

formation of the compound nucleus occurs through the elastic scattering, which is considered to be the entrance channel and is described by the neutron width Γ_n. The exit channel reaction r, is represented by Γ_r and for neutron reactions at incident energies up to several tenths of keV comprises only radiative capture (Γ_γ) and fission (Γ_f). The total width Γ is the sum of all the partial widths i.e. $\Gamma = \Gamma_n + \Gamma_\gamma + \Gamma_f$.

The reaction cross section σ_r can be therefore expressed through Γ_n, Γ_r and Γ, the resonance energy E_λ and a shift Δ_λ which results from the boundary condition, as seen in eq. (5.39)

$$\sigma_r = \pi \lambda\!\!\!^{-2} g_J \frac{\Gamma_n \Gamma_r}{(E - E_\lambda - \Delta_\lambda)^2 + \Gamma^2/4} \tag{5.39}$$

5.3.2.2 Multi Level Breit Wigner approximation

When multiple levels are close to each other so that they overlap, the cross section can be calculated as the sum of SLBW resonances, seen in eq. (5.39). Therefore, the Multi-Level Breit Wigner (MLBW) approximation uses a sum over all the available levels in the collision matrix $\mathcal{U}$.

The non-diagonal elements of the level matrix $\mathcal{A}$ are omitted, which implies that any possible interference between channels is not taken into account. However, the interference between the compound nucleus levels is not ignored.

5.3.2.3 Reich-Moore approximation

This approximation (RM) proposed by Reich and Moore [198] was initially developed to address the asymmetry observed in low energy fission resonances which was attributed to interferences between resonance levels.

In addition, the large number of open channels (mainly γ-de-excitation) that are present in interactions where middle and heavy nuclei are involved, makes the calculation of the level matrix quite complicated. Since the behaviour of the heavy compound nucleus is chaotic, the reduced widths $\gamma_{\lambda c}$ follow a Gaussian distribution with zero mean, which is the so-called Gaussian Orthogonal Ensemble. These channels can be conveniently neglected, leading to the RM $\mathfrak{R}$-Matrix , seen in eq. (5.40).

$$\mathcal{R}_{cc'} = \sum_c \frac{\gamma_{\lambda c}\gamma_{\lambda c'}}{E_\lambda - E - i\Gamma_{\lambda\gamma}/2}, \qquad c \neq \text{photons} \tag{5.40}$$

This approximation is one of the most accurate used and it is considered to be a standard in the resonance analysis of neutron induced reactions, therefore it was the one adopted in the present work.

5.4 Average cross sections

At higher incident neutron energies, the levels of the compound nucleus become so close to each other that are practically indistinguishable from the experimental

point of view. This is due to the fact that the average neutron widths become larger than the level spacing, with increasing energy. At the same time the experimental energy resolution of a time-of-flight spectrometer, typically becomes worse, thus enhancing the resonance overlapping. The resonances are further broadened due to the temperature, as will be explained later, with the Doppler broadening increasing as $\sqrt{E}$.

Therefore an energy limit exists, generally different for each individual nucleus, above which the cross sections cannot be described by individual resonance parameters. An average cross section though can be provided by implementing average parameters, assuming that the neutron will interact with a potential created by a single, semi-transparent medium (nucleus) , similar to the way the light interacts with any such material, hence the terms optical potential and optical model calculation.

This theory was developed by Hauser and Feshbach [199] and relates average cross sections for the available reaction channels, to a few average physical parameters such as level densities and particle strength functions, which are directly related to average widths as it will be shown in the next paragraph.

An average cross section $\langle\sigma_c\rangle$ from the channel c to the c' can be calculated similar to eq. (5.18) by introducing the average collision matrix $\langle\mathcal{U}_{cc'}\rangle$, as seen in eq. (5.41)

$$\langle\sigma_{cc'}\rangle = \pi\lambda\!\!\!^{-2}_c\, g_J\, |\delta_{cc'} - \langle\mathcal{U}_{cc'}\rangle|^2 \tag{5.41}$$

The calculation however of an average collision matrix is tricky, therefore the aforementioned expression can be written for a single channel c as follows

$$\sigma_c = \pi\lambda\!\!\!^{-2}_c\, g_J\, (1 - |\mathcal{U}_{cc}|)^2 \equiv \pi\lambda\!\!\!^{-2}_c\, g_J\, T_c \tag{5.42}$$

where T_c is the transmission coefficient for the channel c and is related to the average channel width $\langle\Gamma_c\rangle$ and the average level spacing D, as seen in eq. (5.43). An example expression for the transmission coefficient for fission for a Hill-Wheeler potential has already been given in eq. (5.10).

$$T_c = 2\pi\frac{\langle\Gamma_c\rangle}{D} \tag{5.43}$$

The total average cross section $\langle\sigma_{cc'}\rangle$ can now be written in the so-called Hauser-Feshbach formula seen in eq.

$$\langle\sigma_{cc'}\rangle = \underbrace{\langle\sigma_{cc}\rangle\delta_{cc'}}_{\text{Elastic scattering}} + \underbrace{\pi\lambda\!\!\!^{-2}_c g_J \frac{T_c T_{c'}}{\sum_i T_i} W_{cc'}}_{\text{Reaction}} \tag{5.44}$$

where the term $W_{cc'}$ is related to the channel widths as seen in eq. (5.45).

$$W_{cc'} = \left\langle\frac{\Gamma_c\Gamma_{c'}}{\Gamma}\right\rangle \frac{\langle\Gamma\rangle}{\langle\Gamma_c\rangle\langle\Gamma_{c'}\rangle} \tag{5.45}$$

For the (n,n) reaction, the cross section can be written as

$$\sigma_n = \pi\lambda\!\!\!^{-2} g_J \frac{\Gamma_n}{D} \tag{5.46}$$

where $S_J \equiv g_J\Gamma_n/D$ is the neutron strength function and is a measure of how large the cross section is. It can be proven that for s-wave resonances (i.e. $J = 0$) the neutron width can be expressed as seen in eq. (5.47). It has to be noted that for the elastic scattering the so-called reduced width $\Gamma_n^0/\sqrt{E}$ can be considered constant.

$$g_J\Gamma_n^0 = S_0\langle D\rangle\sqrt{E} \tag{5.47}$$

Generally the neutron width for a resonance with spin J can be expressed as follows

$$g_J\Gamma_n^J = S_J\langle D\rangle E^{2J+1} \tag{5.48}$$

5.5 Resonance analysis for the $^{240}Pu(n,f)$ cross section

It has already been shown, that several resonances were resolved in the $^{240}Pu(n,f)$ cross section from ~ 1 eV, up to a few keV. Since only one data-set by Weston [49] was practically adequate to extract fission resonance parameters, as mentioned in the ^{240}Pu evaluation by Bouland et al. [187], a detailed resonance analysis was performed in the present work by means of the SAMMY code [200–202].

5.5.1 The SAMMY code

SAMMY can treat experimental data in the thermal, resolved and unresolved resonance regions, hence it is the standard tool used in nuclear data evaluations over the last decades. It can apply multilevel $\mathfrak{R}$-Matrix fits to neutron data using the Bayesian model. In the RRR, SAMMY can provide resonance parameters using any of the three approximations previously described, depending on user request. Experimental corrections such as Doppler broadening, self-shielding, background subtraction etc., can be addressed upon user request.

In the URR, SAMMY incorporates the FITACS code [203] which uses the Hauser-Feshbach formalism with width fluctuations, leaving the strength functions and average reaction widths as free parameters.

The information required by SAMMY is organised in two files: the input and the parameter one. In the former, information is provided from the user regarding the problem to be solved: The target nucleus, the neutron flight-path, the possible spin configurations, the temperature in which the experiment was performed etc. Additional commands are given concerning the $\mathfrak{R}$-Matrix approximation, the Doppler broadening model and possibly the response function of the time-of-flight spectrometer to be used.

The parameter file contains practically the resonance parameters to be used for each channel (E_λ and the partial widths Γ_i), which, in the case of the present work, were limited to the $(n,n),(n,\gamma)$ and (n,f) reactions. These parameters can be either fixed or left free to be fitted using the generalised least square method, or the so-called Bayesian fit.

5.5.2 Prior considerations

Prior to initialising the resonance analysis, it is helpful to compare available fission widths found in literature to the broadening introduced in the experimental data, in order to ensure whether it is possible to determine Γ_f. If the broadening is larger than the resonance widths, then what can be reported is $g_J\Gamma_f$, which is in principle proportional to the kernel (or area) K of each resonance, equal to $K = g_J\Gamma_n\Gamma_f/\Gamma$. In addition, a useful piece of information is the estimation of the resonance spins.

5.5.2.1 Resonance broadening

The energy profile of a resonance can be given by eq. (5.15) which corresponds to the ideal case (red densely dotted curve, fig. 5.16) . In practice though, a resonance is broadened for two main reasons: (a) The temperature and (b) the fluctuating resolution of the time-of-flight spectrometer which in the present case is a convolution of the time characteristics of the incident proton beam and the neutron transport in the target-moderator assembly.

Usually experiments take place at a non-zero temperature which results in an increasing vibration of the nuclei in the fission foil, with increasing temperature. This causes a broadening in the resonance, as seen in fig. 5.16 (sparsely dotted blue curve) commonly referred to as Doppler broadening (DB). The most common model to describe the aforementioned broadening is the free gas model, which was the one used in the present analysis. An expression of the FWHM of the broadening Δ_{DB} can be seen in eq. (5.49), where $k_B = 8.62\,10^{-5}$ eV/K is the Boltzmann constant, E the neutron energy, T the absolute temperature and m_n and M the masses of the neutron and the target nucleus, respectively.

$$\Delta_{DB} = 2\sqrt{\log 2}\sqrt{\frac{4Ek_BTm_n}{M}} \tag{5.49}$$

It has already been stressed out that the response function of a spectrometer defines its resolution, which in the present case depends on the time distribution of the incident proton beam ($\Delta t/t = 7$ ns) and the neutron transport inside the target-moderator assembly. Both FWHM values have been illustrated in fig. 1.13. SAMMY can convolute a Doppler broadened resonance with a numerical resolution function, similar to the one shown in fig. 1.12, thus produce the dashed grey line seen in fig. 5.16. In this case the response function of EAR2 determined by Monte Carlo calculations was used.

The actual experimental resonance seen in fig. 5.16 with a solid black line, apart from being broadened and shifted, suffers from statistical uncertainty and a background which can be treated and subtracted from SAMMY if requested. In fission resonances where the fission fragments are detected, the most common background contributions originate from impurities and intrinsic activity, both of which were treated prior to the resonance analysis.

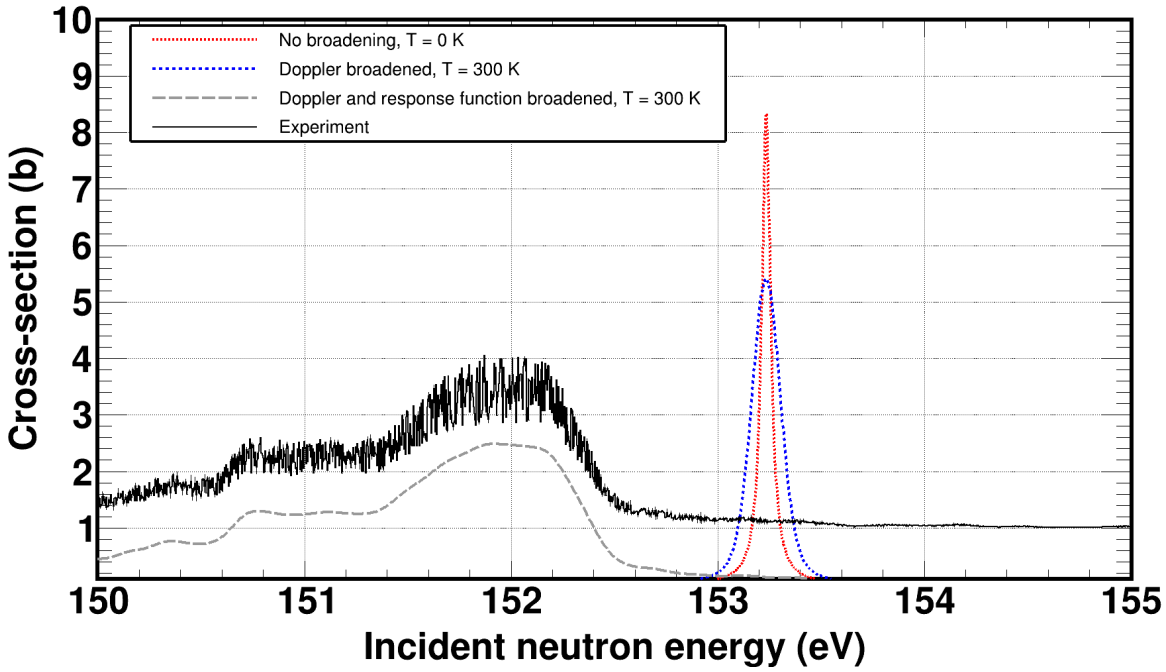

Figure 5.16: *Schematic representation of the broadening introduced in a Breit-Wigner resonance (densely dotted red curve) due to the Doppler effect occurring from the non-zero temperature (sparsely dotted blue curve) and the response function of the spectrometer (dashed grey line). The true experimental cross section can additionally suffer from an induced background (solid black line). The response function of EAR2 was used to broaden the resonance.*

5.5.2.2 Estimation of the resonance spin

To get an estimate of the spin to be assigned to each resonance, the reduced neutron widths found in literature can be of great help. In the case of ^{240}Pu , Bouland et al. [187] made the most recent and complete evaluation in all available channels, practically adopted in JEFF-3.3.

In neutron-induced reactions where the compound nucleus is excited close to its neutron binding energy, it is highly improbable to observe high angular momentum waves. Therefore only s- and p-waves are expected which have a $\sim 1/\sqrt{E}$ and $\sim 1/E^{3/2}$ dependence with energy, respectively. Therefore the reduced widths $\Gamma_n/\sqrt{E}$ are expected to fluctuate around a constant value when s-wave resonances are involved, while a positive linear behaviour is expected for p-waves. As seen in fig. 5.17 a distinctive threshold can be freely selected, above which resonances can be considered as s-waves. This choice is arbitrary and illustrates the usual difficulty in assigning a spin in specific resonances during the process of data evaluation.

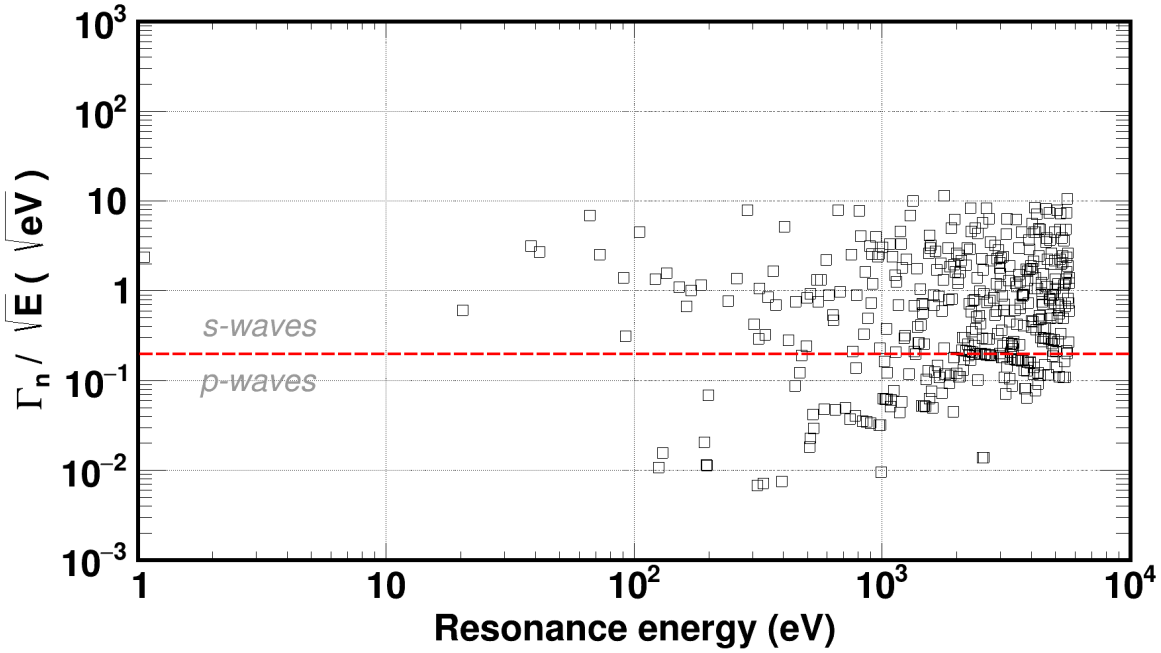

Figure 5.17: *Reduced neutron widths $\Gamma_n/\sqrt{E}$ reported from Bouland et al. [187] can reveal an estimation of the type of a resonance with s-waves having an energy independent relation with energy, while p-waves exhibit a positive linear one due to their $\sim 1/E^{3/2}$ dependence. A threshold can be freely selected above which resonances are considered as s-waves.*

5.5.2.3 Estimation of extracted parameters

The next step is to estimate whether the fission widths Γ_f or the kernels of the resonances $g_J\Gamma_f$ can be determined. If the expected widths are larger than the broadening introduced in the experimental data, then the fission widths can be determined, otherwise only the kernels will be extracted. In addition, an estimate has also to be made regarding the border between the resolved and unresolved resonance regions, as this will define up to which energy resonance parameters can be extracted.

An estimation of the border between the RRR and the URR can be made by constructing the level spacing distribution which theoretically should correspond to the Wigner distribution seen in eq. (5.50). The most probable value of P_W corresponds to the mean level spacing for which resonances can be resolved when P_W is larger than the total broadening of the time-of-flight spectrometer. Such a distribution was constructed by calculating the distance between resonances found in the ENDF/B-VIII.0 library and was fitted with the Wigner function as seen in fig. 5.18, which yielded a mean level spacing of the order of 11 eV.

As seen in fig. 5.19 the vast majority of the resonance widths are significantly smaller than the introduced broadening, therefore their energy profile is broadened due to the Doppler effect and the response of the time-of-flight spectrometer. In the present case the time-of-flight response is indeed the dominant factor. As long as the level spacing remains larger compared to the width of the observed profiles the resonances can be observed, however, what can be determined from the profile

when the resolution dominates is only the resonance area.

$$P_W(x) = \frac{\pi}{2} e^{-\pi x^2/4} \tag{5.50}$$

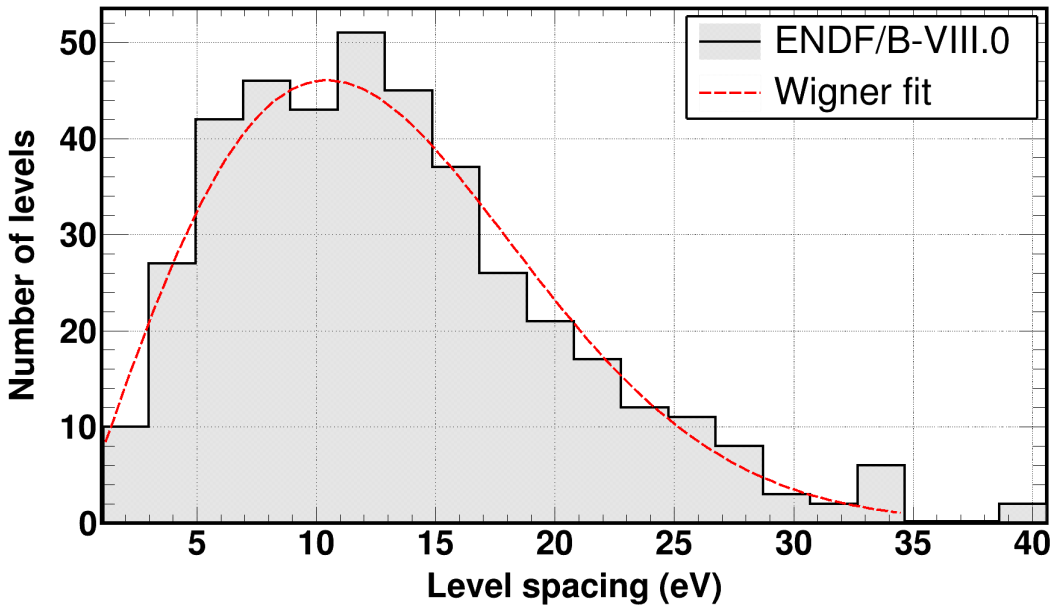

Figure 5.18: *Distribution of the distance between consecutive resonances from parameters found in ENDF/B-VIII.0 library. The data were fitted with a Wigner function, which yielded a mean level spacing of the order of* ~ 11 *eV.*

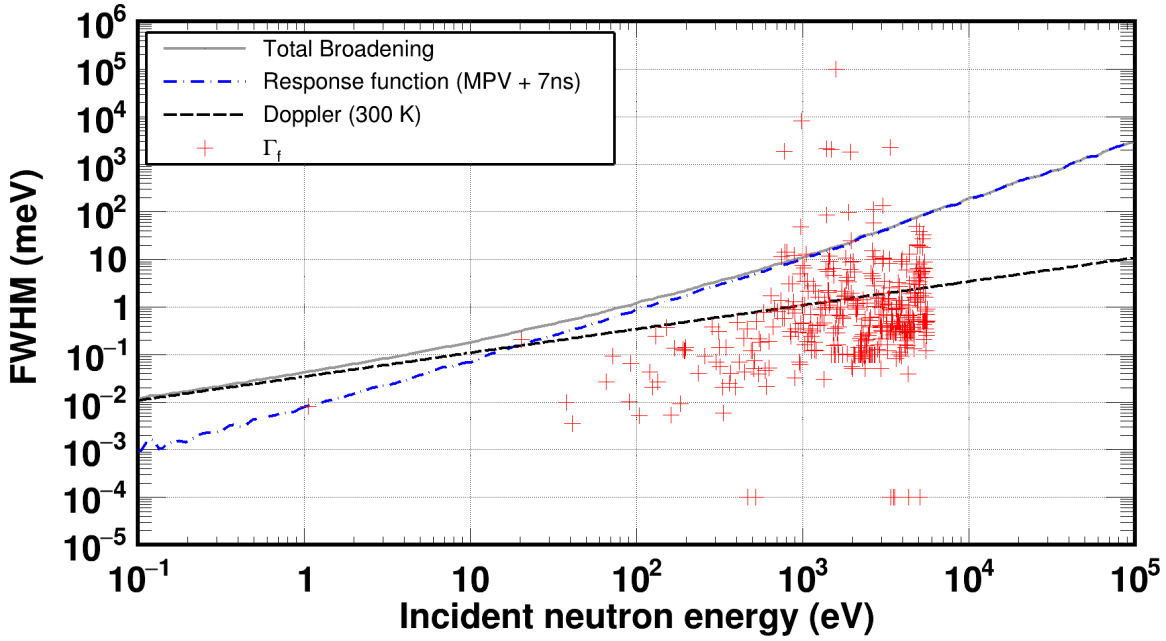

Figure 5.19: *The vast majority of fission widths are below the resolving capabilities of the experiment, therefore only resonance areas can be extracted. Due to the coupling of class-I and -II states, however, stronger resonances appear that could potentially be resolved.*

5.5.3 Benchmarking the response function of EAR2

Although the broadening introduced by the temperature can be fairly easily convoluted in the ideal resonance shape, the broadening occurring from the time-of-flight response is quite difficult to handle, especially in the present case where the response function is not so accurately known.

In order to address this problem, the $^{235}U(n,f)$ cross section found in ENDF/B-VIII.0 was broadened, via the use of the SAMMY code, with the numerical response function seen in fig. 1.12 which, as mentioned, was calculated using the FLUKA code which uses grouped neutron cross sections, hence the accuracy issue mentioned above.

The resonance parameters found in ENDF/B-VIII.0 were left fixed apart from the energy which was varied, by no more than 2%, as to match the resonance peaks. In the following figures, the experimental cross section for $^{235}U(n,f)$ was calculated, by applying the corrections described in the previous chapter on the counting spectrum and by dividing with the flux on the ^{235}U sample. To broaden the cross section, SAMMY was used along with the free gas model at 300 K and the RM formalism.

The results that follow indicate that overall the numerical response function can be adequately used to broaden the ideal resonance profiles. However, there are energy regions where the provided response function is such that the experimental resonance profiles cannot be reproduced. It was notable that small variations in the evaluated widths of the order of $10-15\%$ in the problematic regions could result in a better reproduction of the resonance peaks, at the expense of missing the low energy tails, which is an indication that the response function needs further study and revision.

In fig. 5.21, the results of the broadening of the ENDF/B-VIII.0 $^{235}U(n,f)$ cross-section through the use of SAMMY can be seen, along with the residuals, in σ units, up to an energy of 2 keV which is the maximum energy up to which resonance parameters were found. Finally, the residuals were calculated through the application of eq. (5.51).

$$\text{Residuals} = \frac{\text{Experimental value} - \text{Theoretical value}}{\text{Uncertainty of experimental value}} \tag{5.51}$$

Fortunately, high residuals occurred in energy regions where no strong resonances were observed in the $^{240}Pu(n,f)$ cross section, thus the reported kernels can be considered accurate within 30% which is the total estimated uncertainty coming from the uncertainty in the cross section and from varying the fission widths in the SAMMY fit until the peaks were better reproduced.

It has to be noted that although the reproduction of the ENDF/B-VIII.0 cross section is quite satisfactory, the broadening is too big to allow for the determination of fission widths. A prominent example can be seen in fig. 5.20, where the $^{235}U(n,f)$ ENDF/B-VIII.0 cross sections at 300 K, in the $65-95$ eV energy region are for two cases: broadened by the EAR2 response function and unbroadened. It is evident that, despite the low incident energy, resonances are quite broadened and when small fission widths are involved they even disappear in the tails of preceding or succeeding ones, justifying the decision of reporting kernels rather than widths.

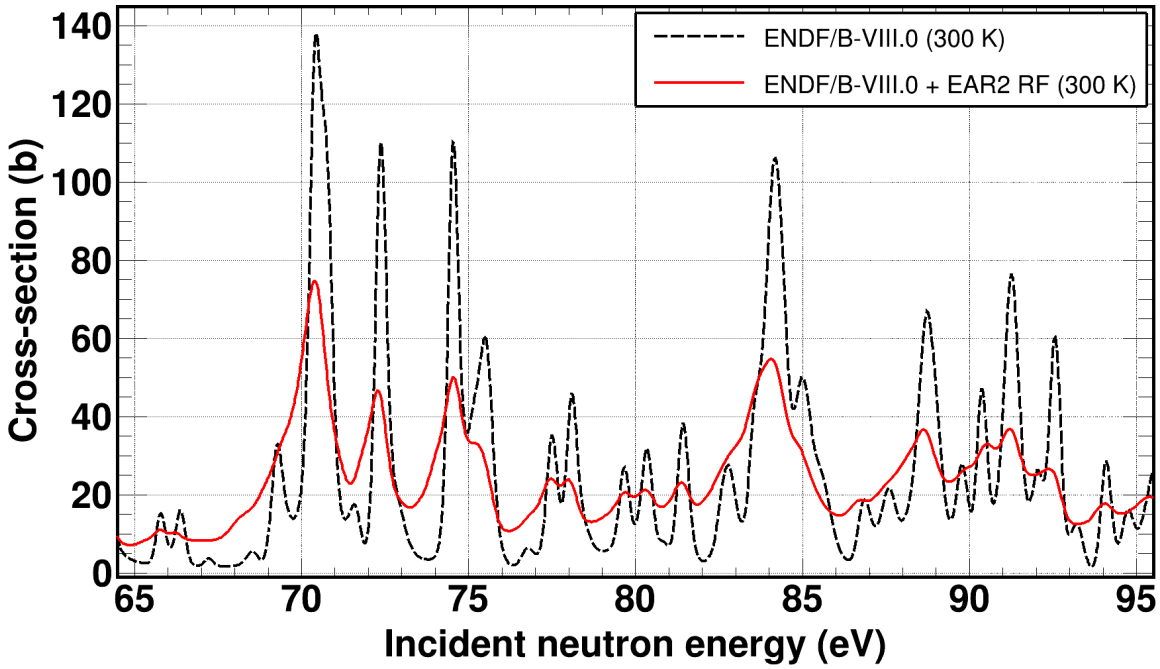

Figure 5.20: *The $^{235}U(n,f)$ ENDF/B-VIII.0 cross section is shown at 300 K, broadened with the EAR2 response function in comparison with the unbroadened one. The broadening induced by the neutron transport within the target-moderator assembly, results in a large resonance broadening, which justifies the decision of reporting resonance kernels rather than fission widths.*

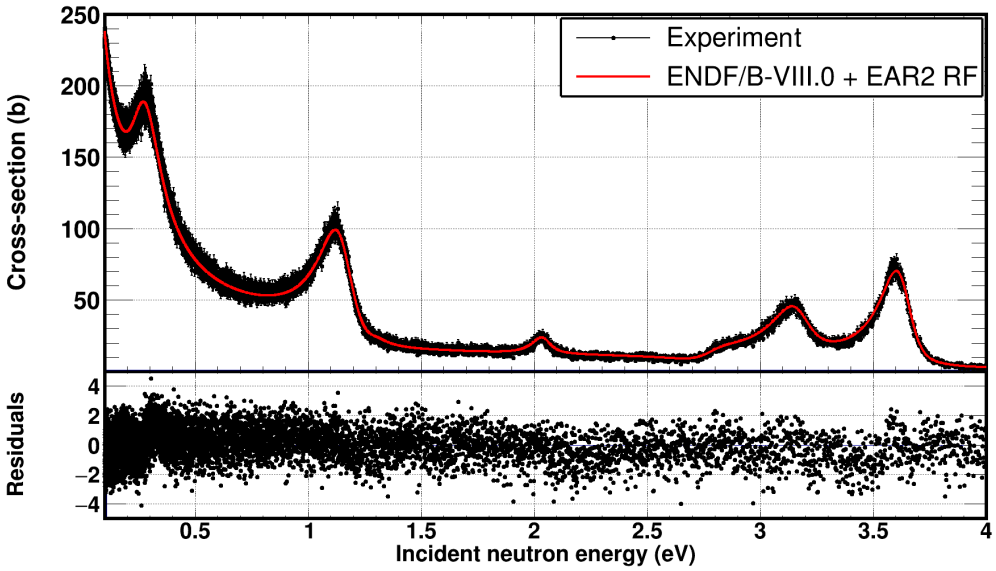

(a) 100 meV - 4 eV

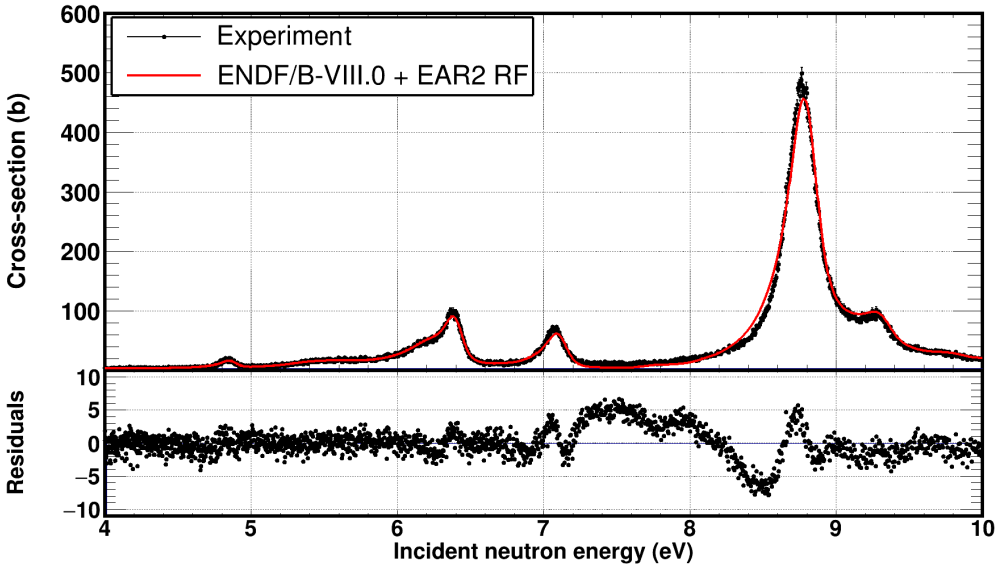

(b) 4 - 10 eV

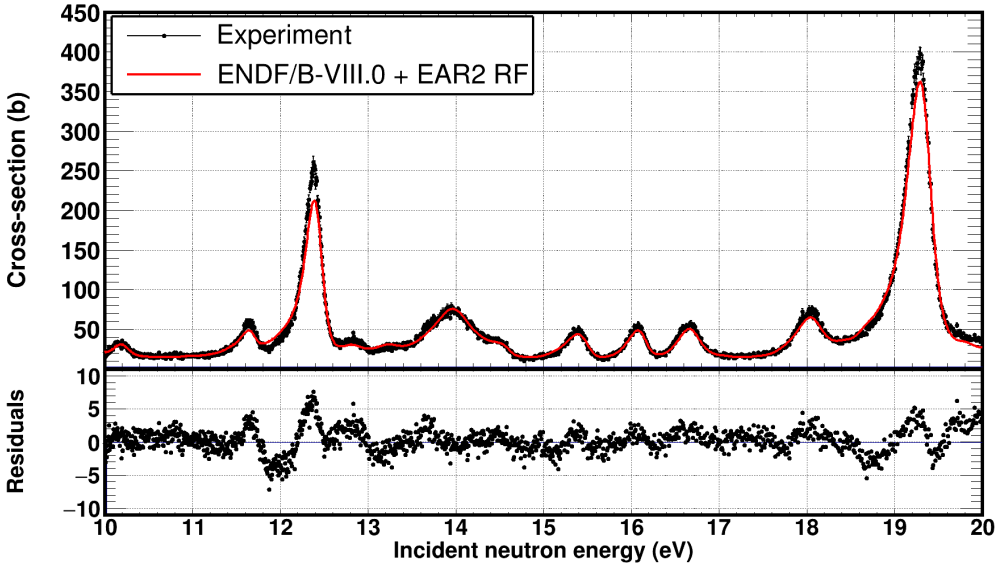

(c) 10 - 20 eV

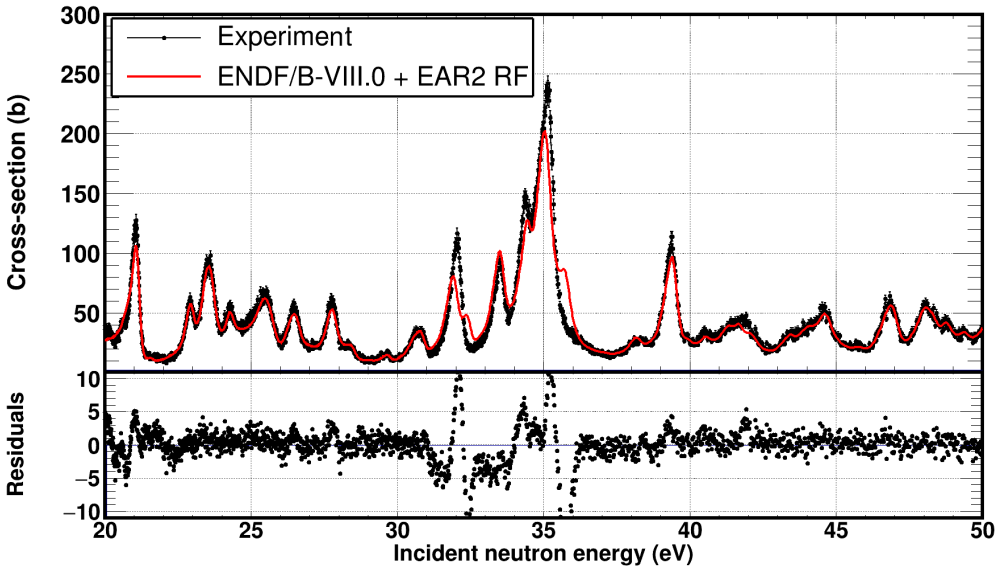

(d) 20 - 50 eV

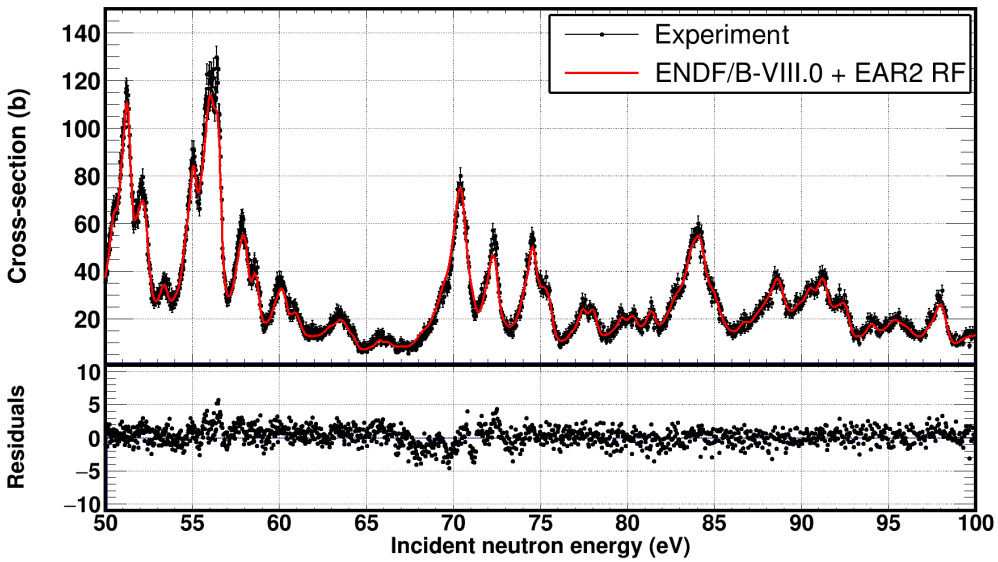

(e) 50 - 100 eV

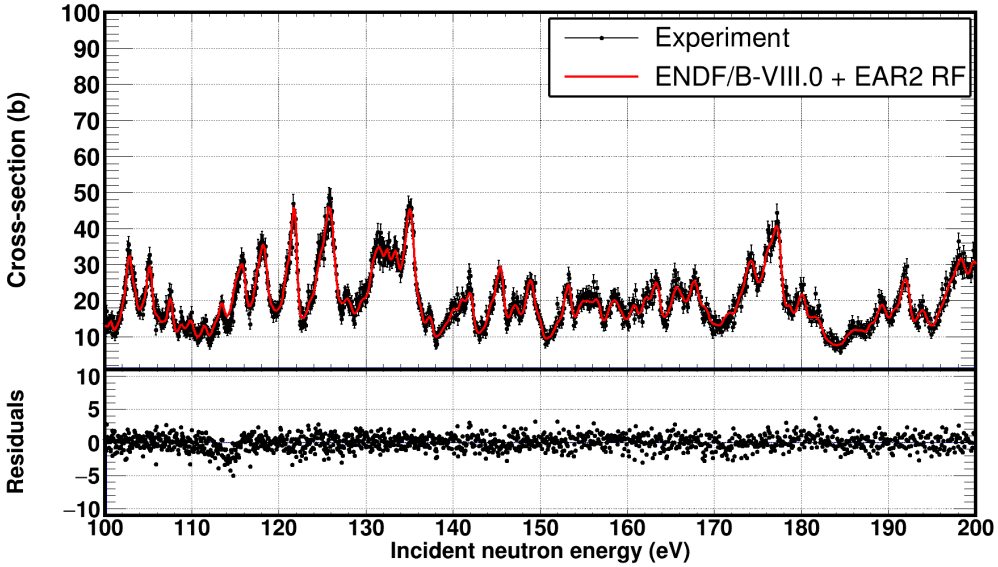

(f) 100 - 200 eV

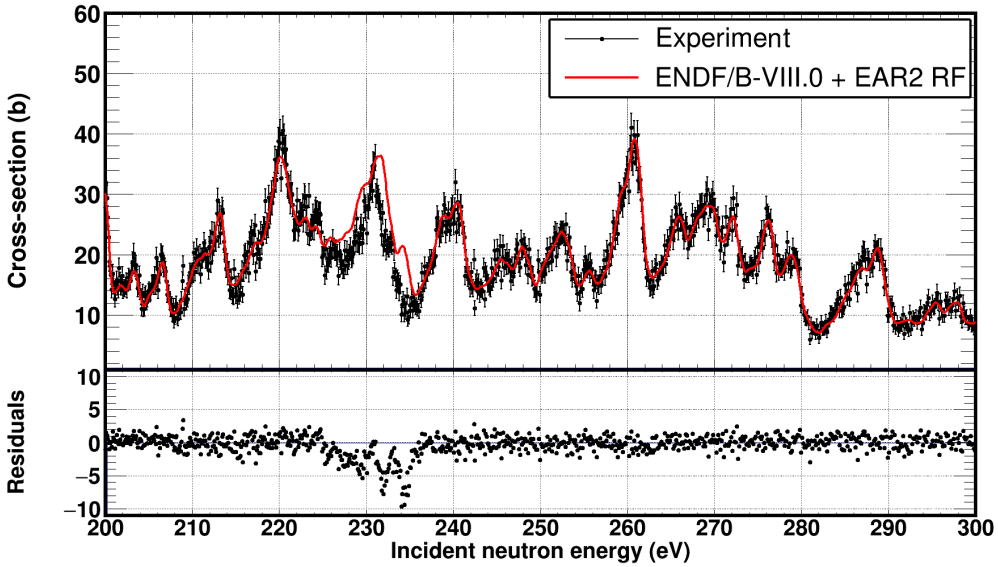

(g) 200 - 300 eV

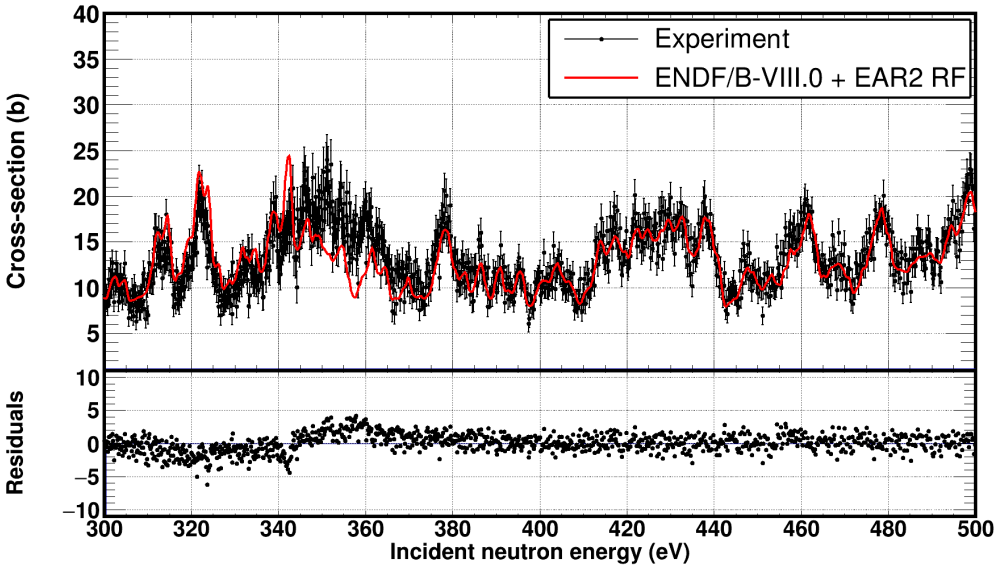

(h) 300 - 500 eV

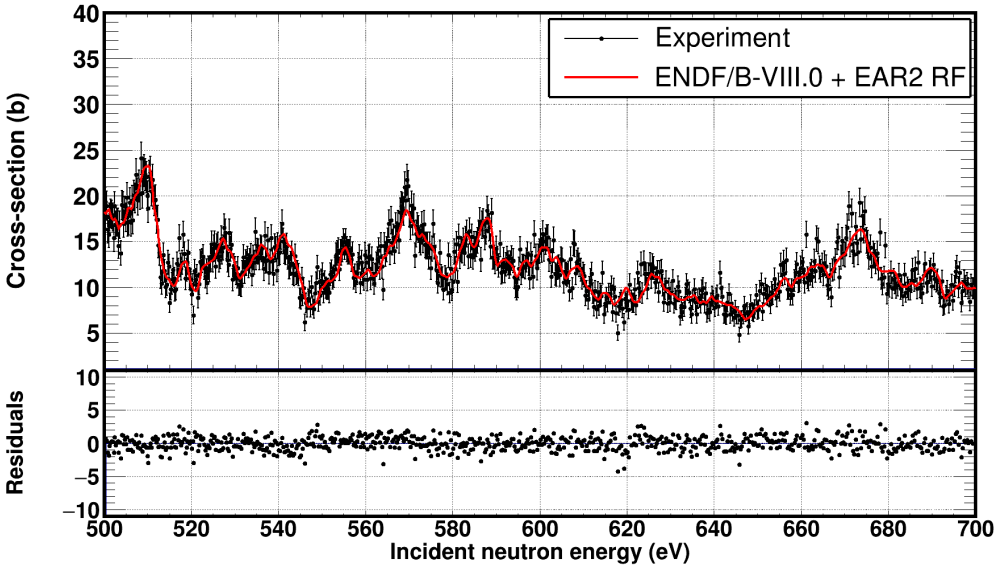

(i) 500 - 700 eV

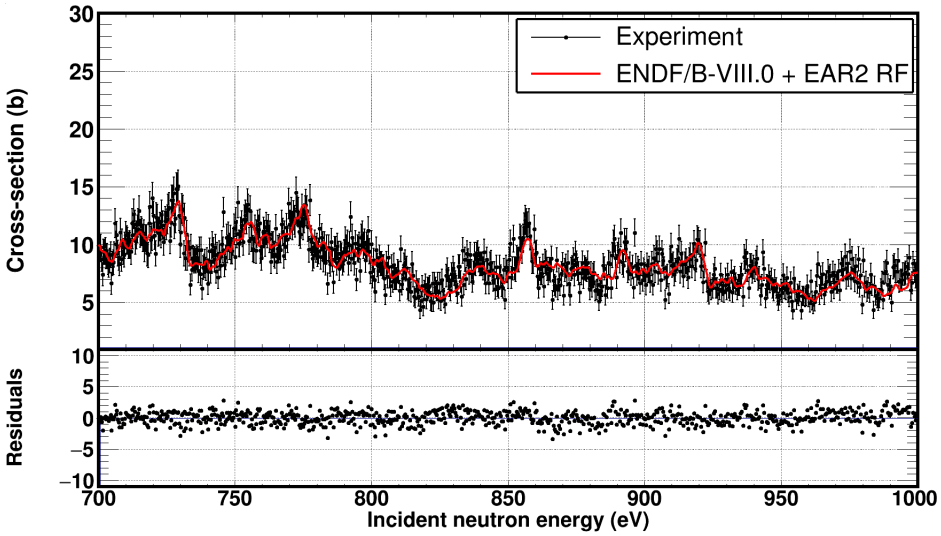

(j) 700 - 1000 eV

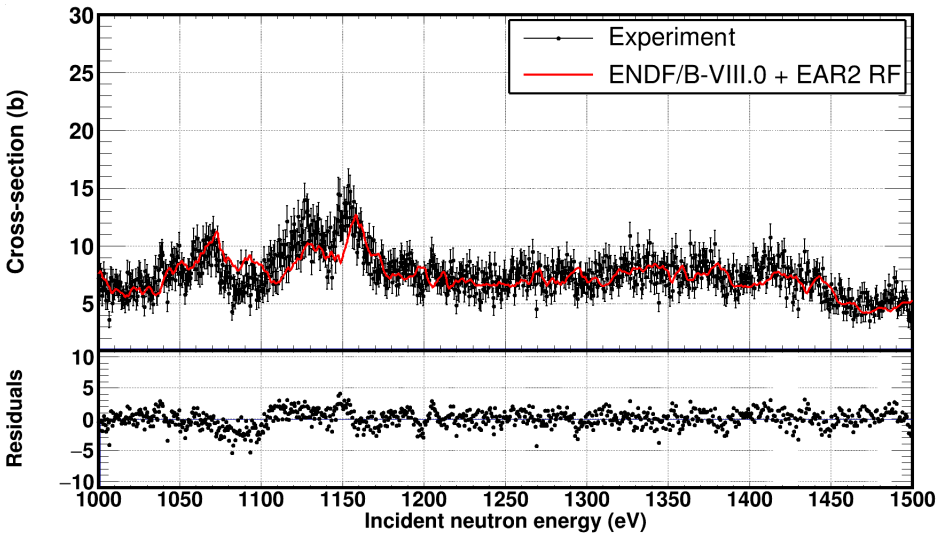

(k) 1000 - 1500 eV

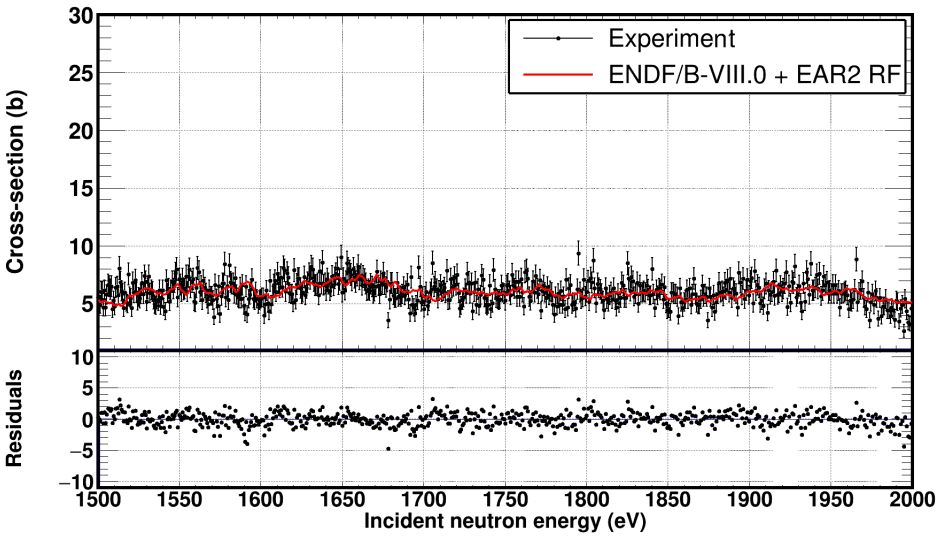

(l) 1500 - 2000 eV

Figure 5.21: *The $^{235}U(n,f)$ ENDF/B-VIII.0 cross section was broadened in terms of the EAR2 response function and compared to the experimental one (top panels), calculated from the ^{235}U reference sample. An overall satisfactory reproduction was observed. In the bottom panels the residuals (in σ units) can be observed. An isolethargic binning of 5000 bin/decade was used.*

5.5.4 Results from the ℜ-Matrix analysis

Following the satisfactory reproduction of the $^{235}U(n,f)$ resonance structure, which proved that the EAR2 response function can be used up to at least 2 keV, an ℜ-Matrix analysis of the $^{240}Pu(n,f)$ cross section was performed from 9 meV up to 10.2 keV using the Reich-Moore formalism. In the energy region above 2 keV, although the response function was not benchmarked, the resonance analysis was performed nevertheless. Moreover, the broadening introduced was large, as previously discussed, therefore only the kernels of the strong resonances will be reported.

During the analysis, the prior knowledge to perform the fits was based on the evaluation of ^{240}Pu from Bouland et al. [187] up to 5.7 keV. Up to this energy regime, Γ_n and Γ_γ were fixed to the values reported by Bouland et al., while the resonance energy and the fission widths were left free.

Above 5.7 keV, in the absenece of resonance parameters in literature, a constant radiation width $\Gamma_\gamma = 31.8$ meV adopted from the ENDF/B-VIII.0 evaluation of $^{240}Pu(n,f)$ was considered, following the standard assumption in such cases that Γ_γ can be considered constant. Values for the neutron widths were also absent in literature, despite the existence of a good resolution transmission data-set by Gwin [204]. In this respect, a constant reduced neutron width was used in the present resonance analysis, which was calculated considering s-wave resonances, a mean level spacing of $\langle D \rangle = 12.06(60)$ eV and the strength function proposed by Bouland et al. [187] $S_0 = 1.032(71)\,10^{-4}$, according to eq. (5.47), thus the estimation of new resonance kernels in the 5.7 – 10.2 keV energy region, was achieved.

A fudge factor of 0.1 = 10% was used for the energy fits, while the fission widths were left completely free to vary using a fudge factor of 10. The Bayesian fits were performed in cycles of five consecutive runs. The final resonance energies were in agreement within a few percent with the evaluated values and convergence was achieved from the first cycle. The fission widths had to be fitted multiple times until a convergence was reached and then varied by hand until the peak was reproduced. The difference between the SAMMY values and the by-hand-adjustment ones, was of the order of 20%, which is the estimated uncertainty in the reported fission widths.

In regions where the reaction rate was low and resonances could not be observed, the parameters of Bouland et al. were used in order to reproduce the cross-section in the $1/v$ region.

Finally, in fig. 5.22, the results of the SAMMY fits are shown along with the corresponding residuals. In table 5.2 the resonance energies along with the fission kernels are reported. In Appendix C the parameters used to reproduce the cross section are reported in ENDF format.

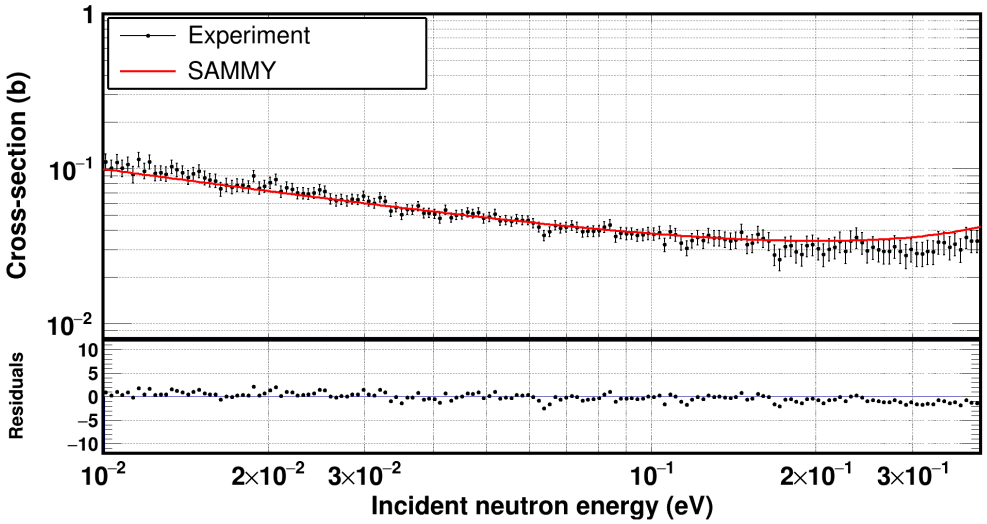

(a) 10 - 400 meV

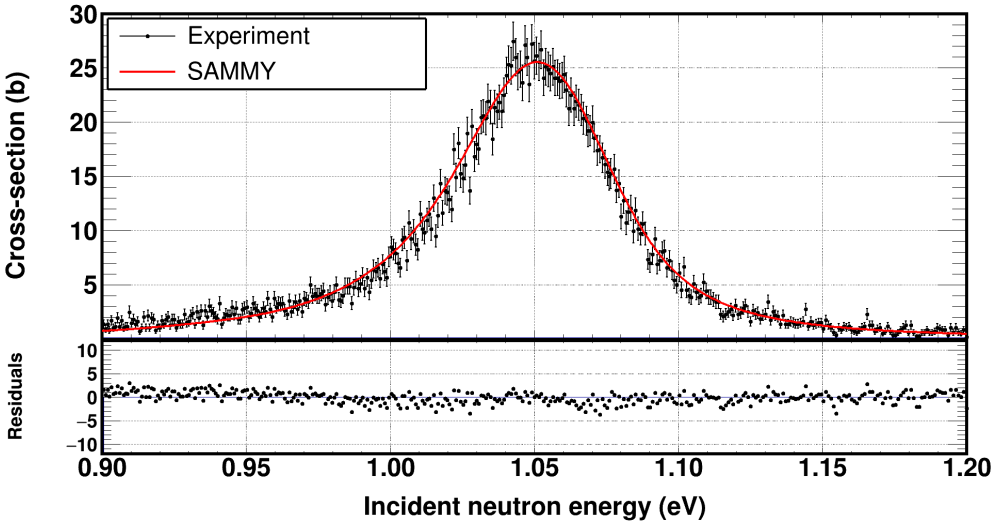

(b) 900 meV - 1.2 eV

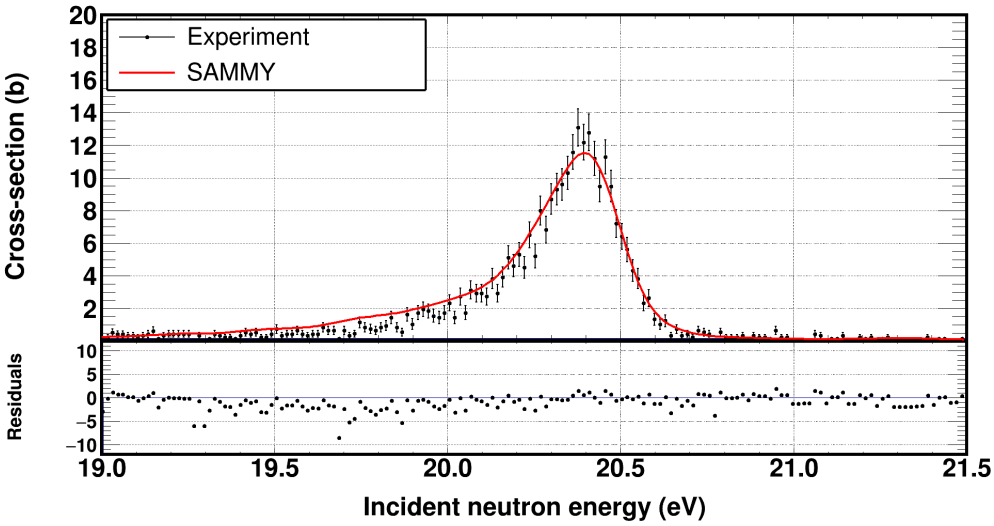

(c) 19 - 21.5 eV

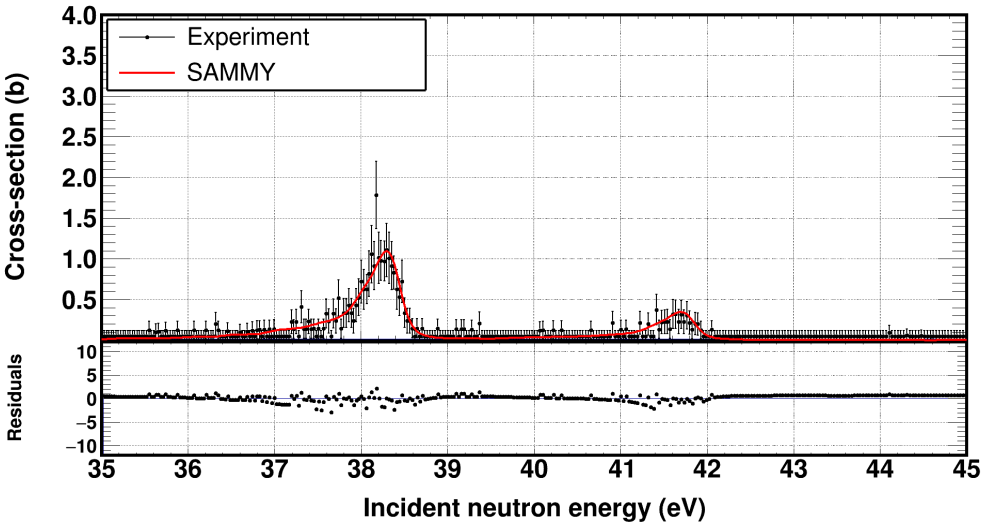

(d) 35 - 45 eV

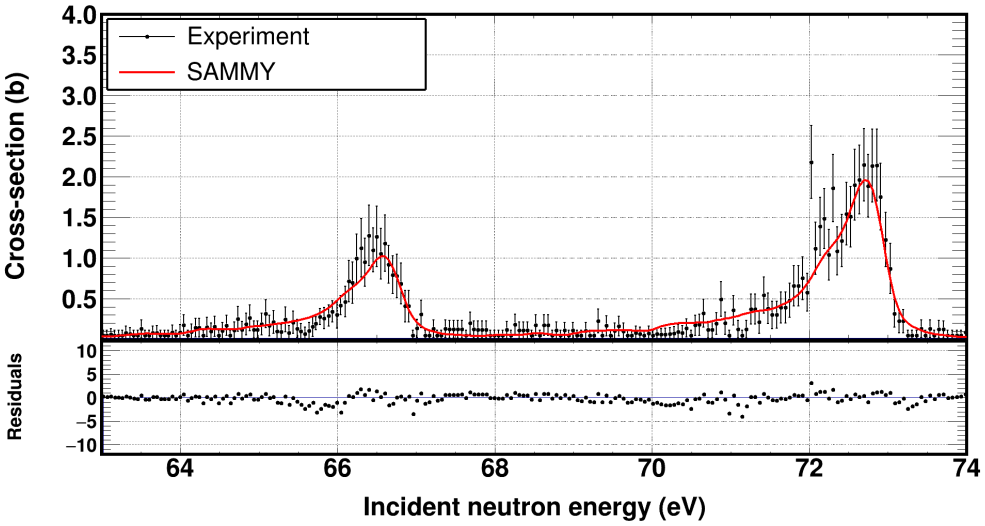

(e) 63 - 74 eV

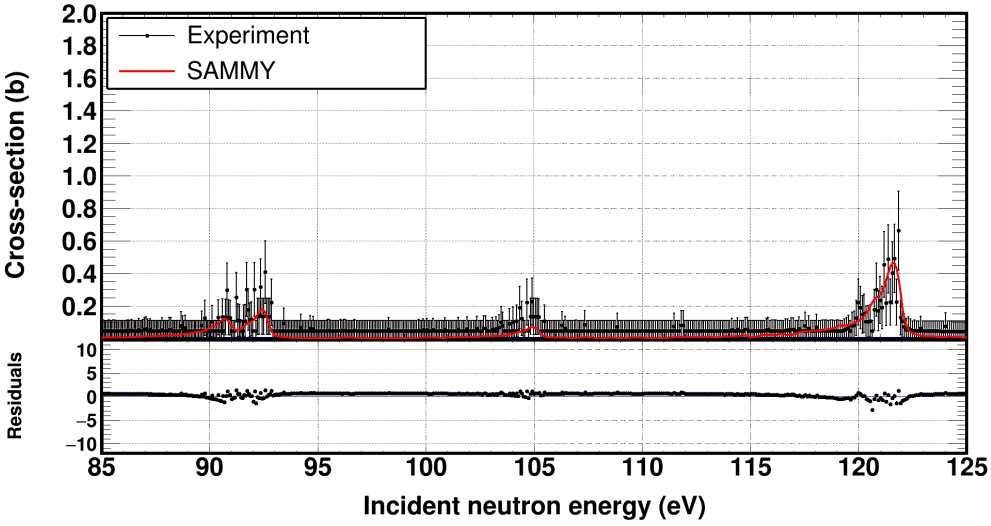

(f) 85 - 125 eV

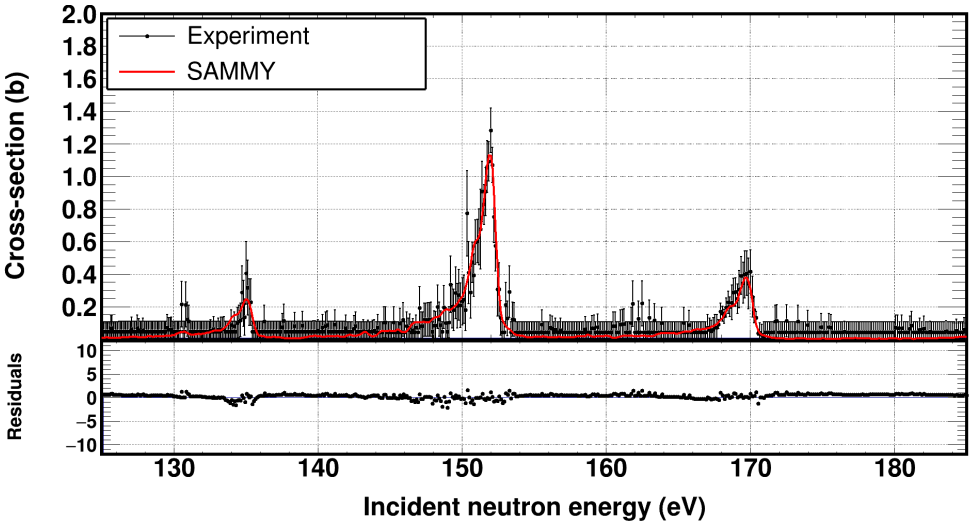

(g) 125 - 185 eV

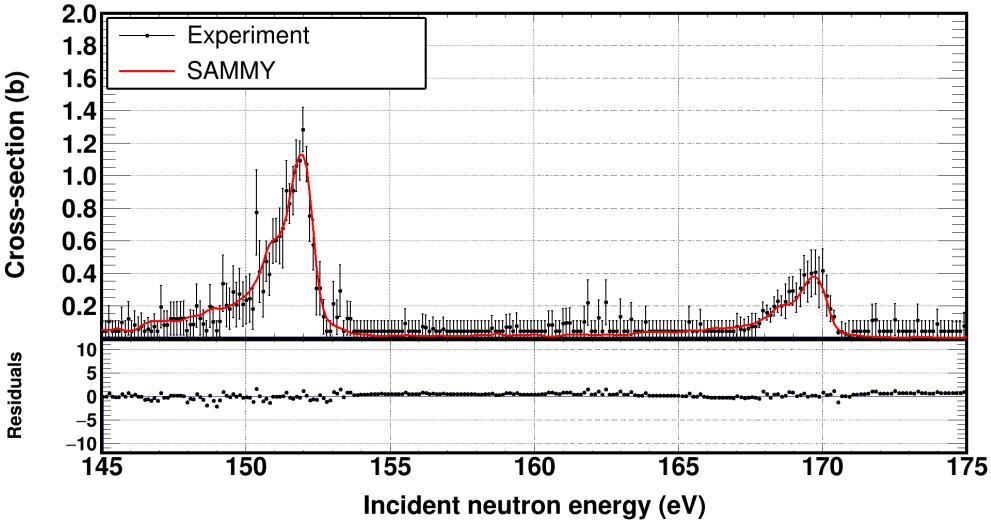

(h) 145 - 175 eV

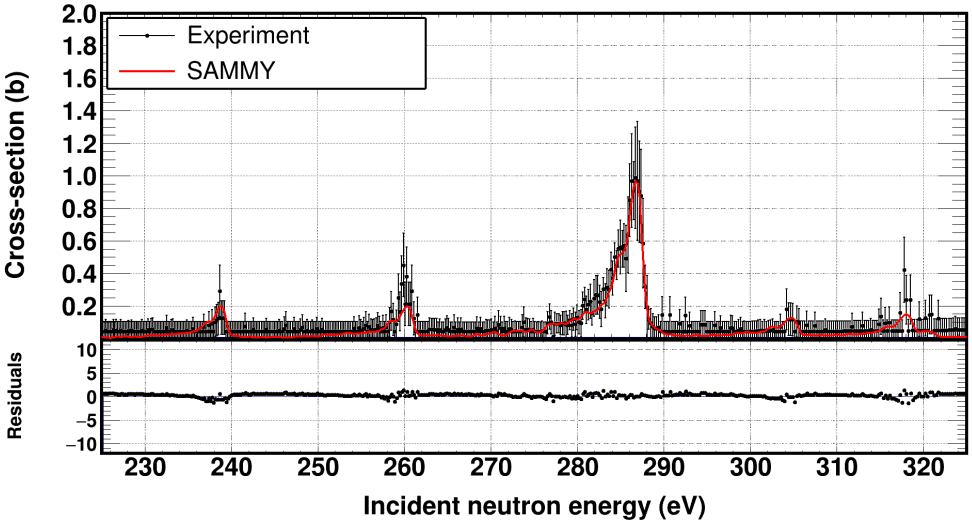

(i) 225 - 325 eV

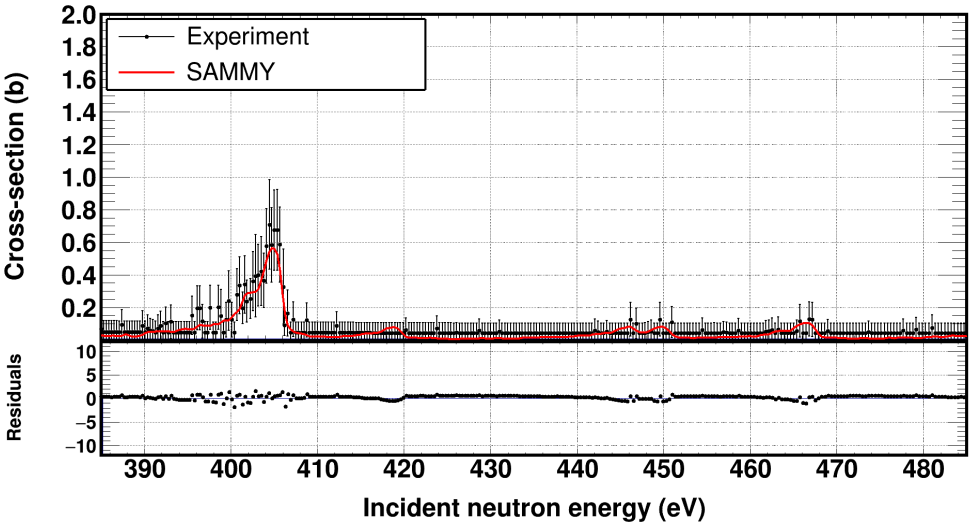

(j) 385 - 485 eV

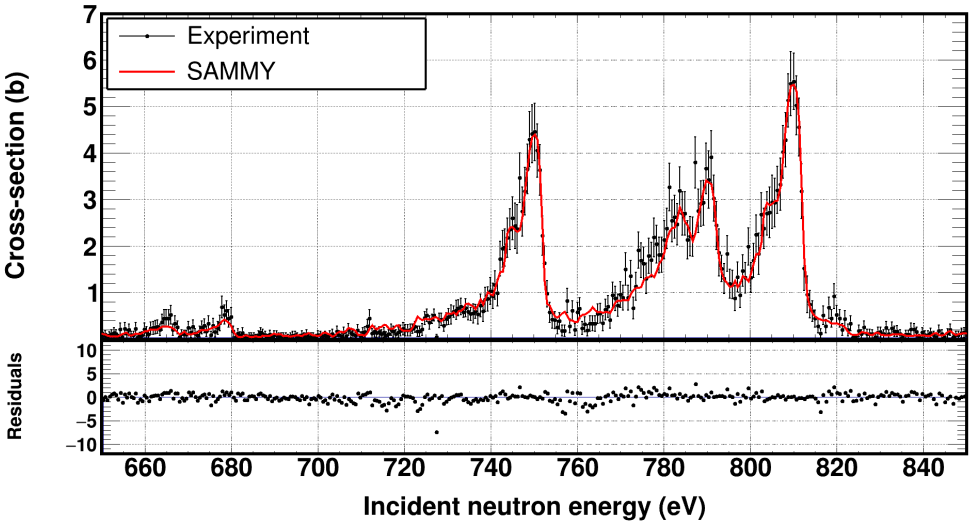

(k) 650 - 850 eV

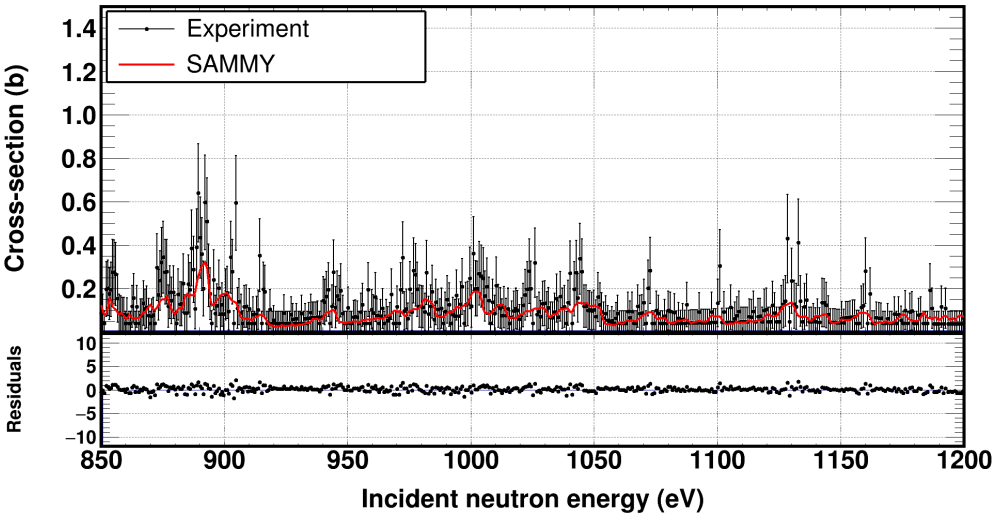

(l) 850 - 1200 eV

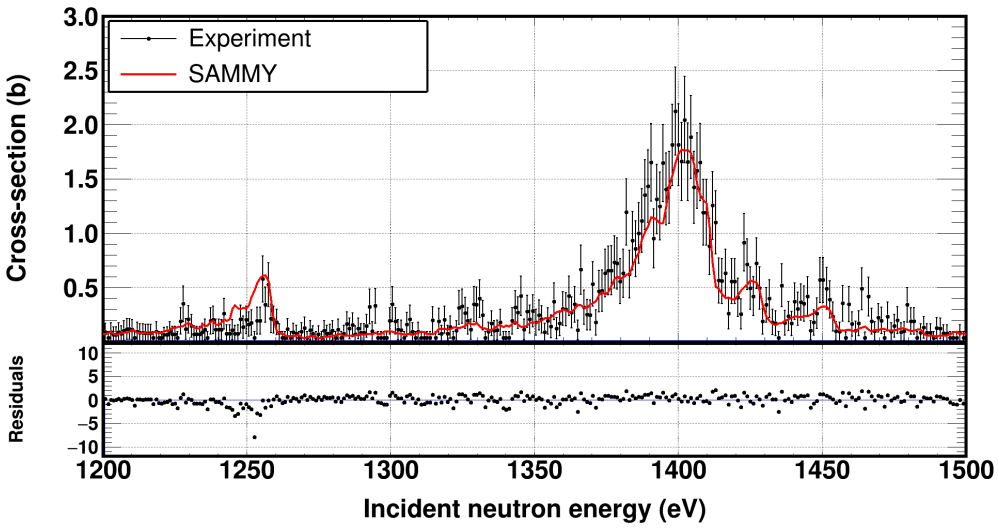

(m) *1200 - 1500 eV*

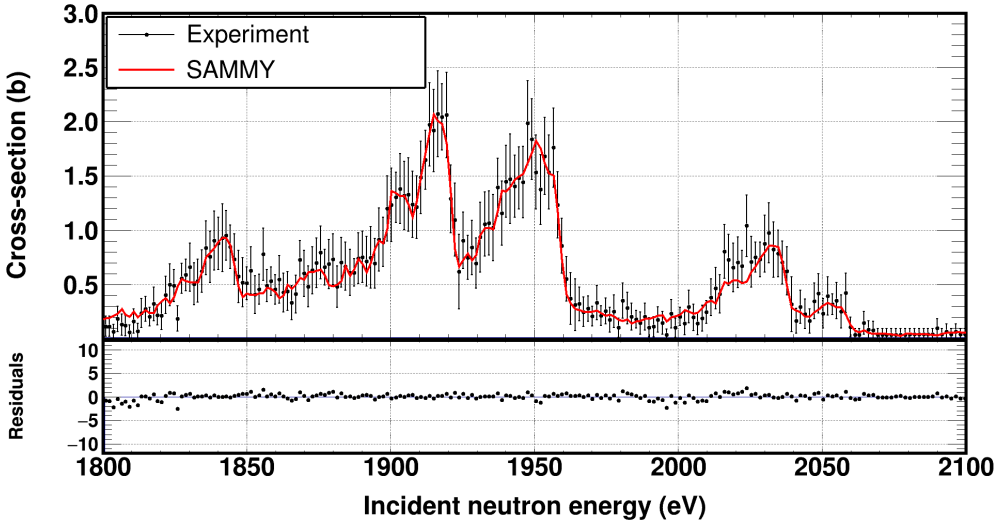

(n) *1800 - 2100 eV*

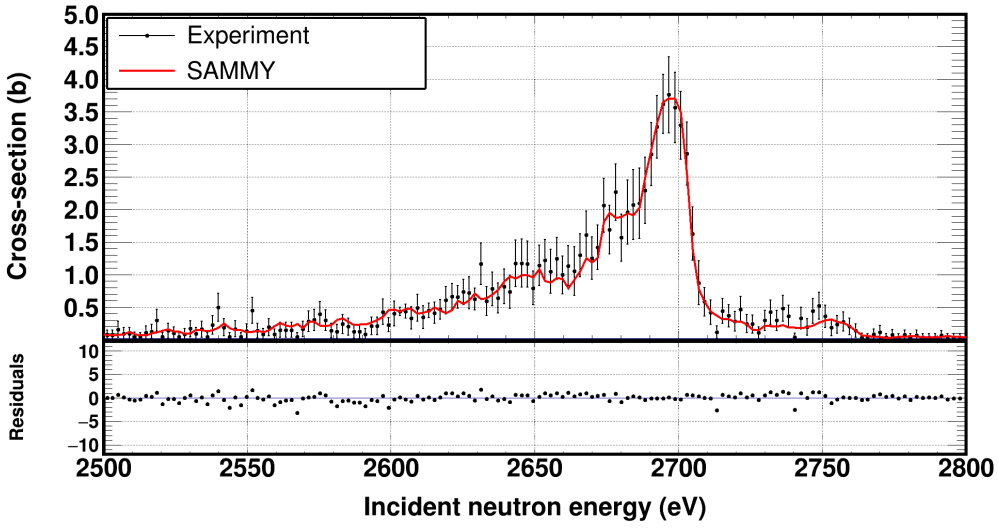

(o) *2500 - 2800 eV*

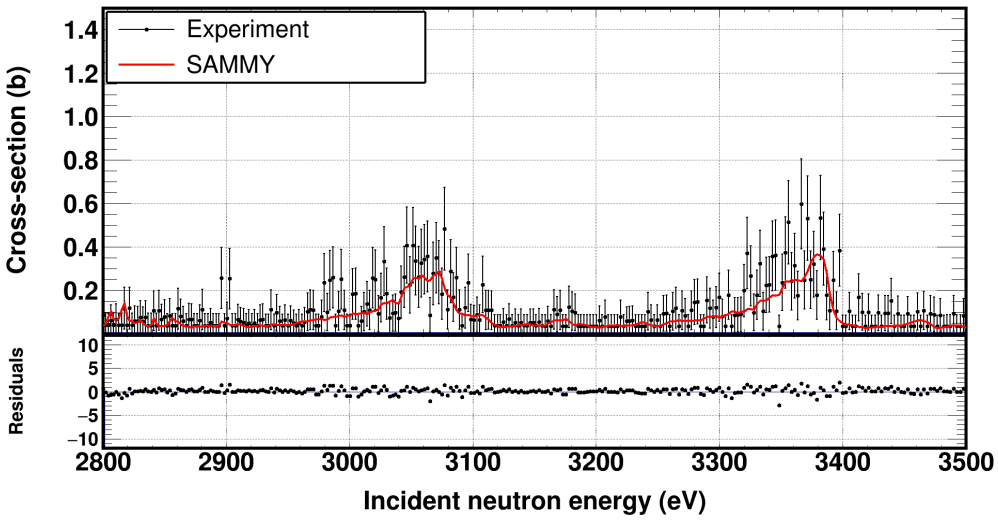

(p) 2800 - 3500 eV

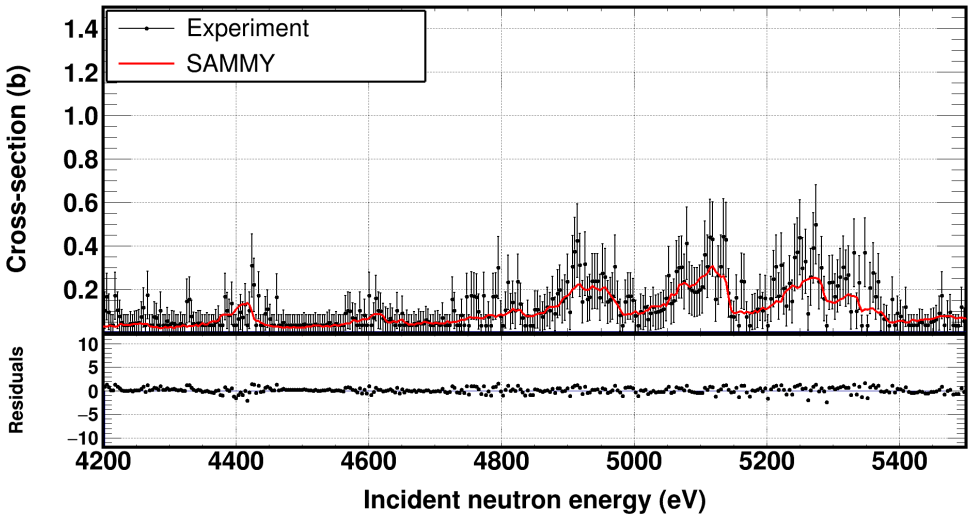

(q) 4200 - 5500 eV

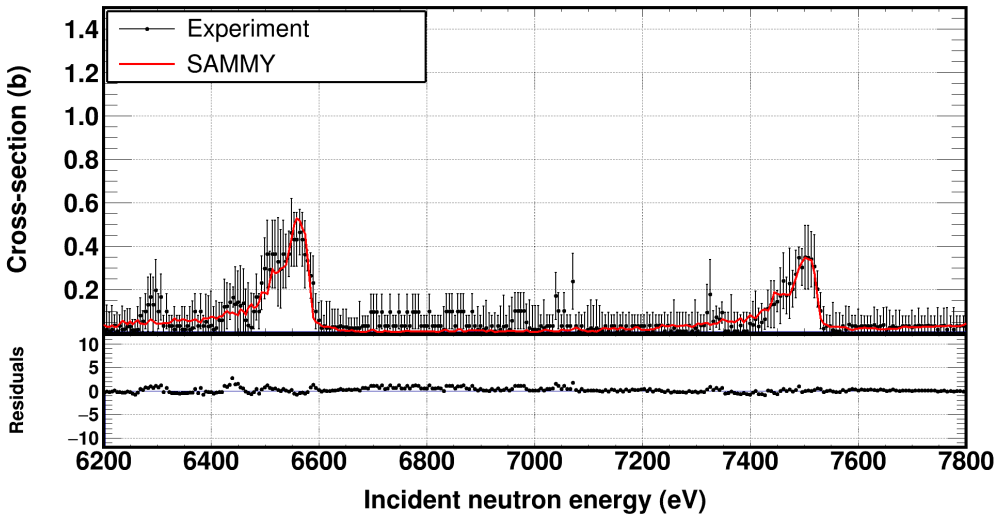

(r) 6200 - 7800 eV

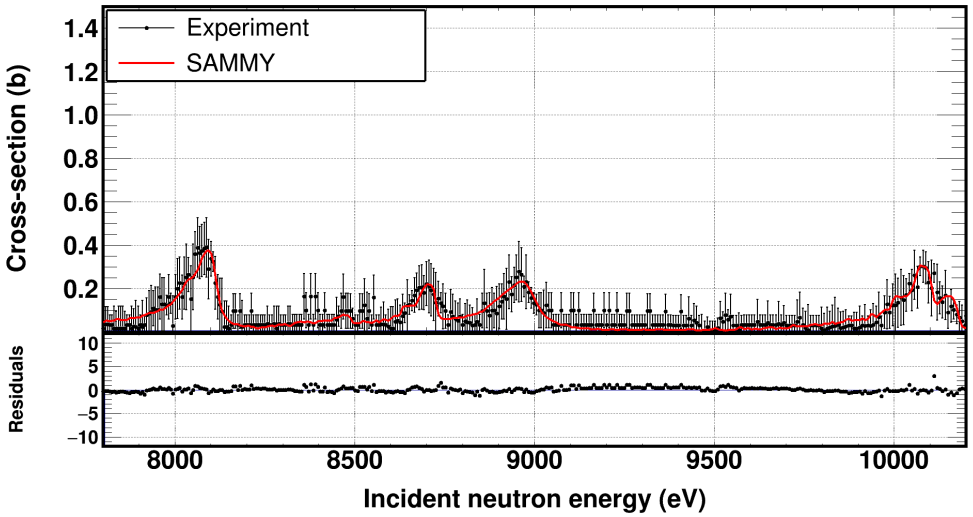

(s) 7800 - 10200 eV

Figure 5.22: *SAMMY fits in the $^{240}Pu(n,f)$ cross section from 10 meV up to 10.2 keV (top panels). In the bottom panels the residuals (in σ units) can be observed. An isolethargic binning of 3000 bin/decade was used.*

Table 5.2: *Resonance parameters extracted from the $\mathfrak{R}$-Matrix analysis of the $^{240}Pu(n,f)$ data. Due to the significant broadening induced by the time-of-flight response function, only the kernels are reported in resonances with sufficient statistics.*

Resonance Energy (eV)	$\Gamma_n\Gamma_f/\Gamma$ (meV)	Resonance Energy (eV)	$\Gamma_n\Gamma_f/\Gamma$ (meV)
1.06	$4.240\,10^{-4}$	1902.74	1.145
20.56	$9.256\,10^{-3}$	1913.20	4.426
38.45	$3.373\,10^{-3}$	1937.75	1.969
41.88	$1.087\,10^{-3}$	1945.34	7.135
66.73	$5.285\,10^{-3}$	1957.29	12.00
73.03	$1.663\,10^{-2}$	2034.24	2.319
122.26	$1.435\,10^{-2}$	2037.75	$1.491\,10^{-2}$
152.00	$1.986\,10^{-2}$	2054.03	3.788
170.09	$2.809\,10^{-2}$	2688.63	33.97
287.92	$5.365\,10^{-2}$	2700.36	3.66
405.31	$1.206\,10^{-1}$	2746.25	5.342
749.93	3.217	6540.00	28.25
795.22	1.197	7460.13	18.42
808.18	4.240	7502.21	19.46
1400.51	8.587	8059.46	20.95
1412.08	1.855	8090.72	20.08
1423.93	2.044	8721.60	18.88
1842.16	1.578	8903.75	20.65
1853.57	1.645	10082.37	47.55
	$\longrightarrow$	10201.16	18.75

5.5.5 Comparison with evaluations and experimental data

It has already been stressed that a comparison of the derived cross section in the resonance region with other experimental data-sets and evaluations, is only possible through the means of the comparison of resonance parameters.

In this context and bearing in mind that only the Kernels were reported due to the broadening issues discussed previously, a comparison of the quantity $\Gamma_n\Gamma_f/\Gamma$ will follow, between the present data and the BROND-3.1, CENDL-3.1 and ENDF/B-VIII.0 evaluation libraries and the resonance parameters reported by Bouland et al. [187], which were basically based on the data by Weston [49], as far as the fission widths are concerned.

It has to be noted that the resonance parameters reported in the JEFF-3.3, JENDL-4.0, ROSFOND-2010 and TENDL-2017 evaluation files, were identical to each other and based on the reported values by Bouland et al. [187].

In table 5.3 the kernels estimated in the present work are reported along with the kernels that were calculated from the resonance parameters found in literature. The differences reported in table 5.3, were calculated with reference to the present work, therefore negative values imply that the kernels in literature are higher than experimental ones and vice versa.

First of all, the first resonance at 1.06 eV, whose characterisation in literature was based on the data by Leonard Jr. et al. [73], appeared to be narrower by about 50% according to the present analysis. The significantly better resolution of the present data, clearly indicates that the evaluated resonance parameters need to be revised.

The agreement varied with the energy region, from very good (0.4%) to significant differences of hundreds %, as illustrated on table 5.3. In general terms, the resonances that were analysed in the present work, were found to be narrower that the ones reported, however the absence of experimental data with good resolution, justifies the need for more data in the resolved resonance region and the inclusion of the $^{240}Pu(n,f)$ in the high priority request list [11].

Table 5.3: *Resonance kernels extracted from the present data in comparison with the corresponding ones found in literature. The kernels reported by Bouland et al. were identical to the ones from JEFF-3.3, JENDL-4.0, ROSFOND-2010 and TENDL-2017, therefore they are not explicitly included in the table. Negative differences indicate a larger kernel with respect to the one reported in the present work.*

Present work		**Bouland et al.**		**ENDF/B-VIII.0**		**BROND-3.1**		**CENDL-3.1**	
Resonance Energy (eV)	Kernel (meV)	Kernel (meV)	Difference (%)	Kernel (meV)	Difference (%)	Kernel (meV)	Difference (%)	Kernel (meV)	Difference (%)
1.06	$4.24\,10^{-4}$	$6.31\,10^{-4}$	−49	$6.32\,10^{-4}$	−49	$6.16\,10^{-4}$	−45	$4.45\,10^{-4}$	−5
20.56	$9.26\,10^{-3}$	$1.89\,10^{-2}$	−104	$1.89\,10^{-2}$	−105	$1.89\,10^{-2}$	−105	$1.96\,10^{-2}$	−111
38.45	$3.37\,10^{-3}$	$4.27\,10^{-3}$	−27	$4.47\,10^{-3}$	−33	$4.27\,10^{-3}$	−27	$4.30\,10^{-3}$	−27
41.88	$1.09\,10^{-3}$	$1.37\,10^{-3}$	−26	$1.17\,10^{-3}$	−7	$1.37\,10^{-3}$	−26	$1.20\,10^{-3}$	−10
66.73	$5.29\,10^{-3}$	$1.62\,10^{-2}$	−207	$1.56\,10^{-2}$	−195	$1.62\,10^{-2}$	−207	$1.67\,10^{-2}$	−216
73.03	$1.66\,10^{-2}$	$4.05\,10^{-2}$	−144	$4.05\,10^{-2}$	−144	$4.06\,10^{-2}$	−144	$4.16\,10^{-2}$	−150
122.26	$1.44\,10^{-2}$	$1.32\,10^{-2}$	8	$1.36\,10^{-2}$	5	$1.32\,10^{-2}$	8	$1.46\,10^{-2}$	−2
152.00	$1.99\,10^{-2}$	$9.38\,10^{-2}$	−372	$1.08\,10^{-1}$	−442	$9.38\,10^{-2}$	−372	$9.99\,10^{-2}$	−403
170.09	$2.81\,10^{-2}$	$4.05\,10^{-2}$	−44	$3.84\,10^{-2}$	−37	$4.05\,10^{-2}$	−44	$4.51\,10^{-2}$	−61
287.92	$5.37\,10^{-2}$	$3.05\,10^{-1}$	−469	$3.01\,10^{-1}$	−462	$3.05\,10^{-1}$	−469	$3.09\,10^{-1}$	−475
405.31	$1.21\,10^{-1}$	$1.44\,10^{-2}$	88	$1.53\,10^{-2}$	87	$3.60\,10^{-1}$	−199	$3.64\,10^{-1}$	−202
749.93	3.22	8.68	−170	8.62	−168	8.68	−170	7.02	−118
795.22	1.20	3.91	426	5.03	520	3.91	426	3.76	−214
808.18	4.24	10.26	−142	9.79	−131	10.26	−142	5.99	−41
1400.51	8.59	10.03	−17	9.03	−5	10.03	−17	9.65	−12
1412.08	1.85	2.88	−56	2.78	−50	2.89	−56	2.73	−48
1423.93	2.04	2.88	−41	2.78	−36	2.88	−41	2.73	−33
1842.16	1.58	1.99	−29	1.83	−16	1.99	−29	1.90	−20
1853.57	1.65	1.99	−21	1.84	−12	1.99	−21	1.90	−15
1902.74	1.15	2.84	−148	2.82	−146	2.85	−149	2.81	−145

Continued on next page

Table 5.3 – *Continued from previous page*

Present work		**Bouland et al.**		**ENDF/B-VIII.0**		**BROND-3.1**		**CENDL-3.1**	
Resonance Energy (eV)	Kernel (meV)	Kernel (meV)	Difference (%)	Kernel (meV)	Difference (%)	Kernel (meV)	Difference (%)	Kernel (meV)	Difference (%)
1913.20	4.43	2.84	36	2.82	36	2.85	−36	2.81	37
1937.75	1.97	2.02	−3	2.04	−4	2.02	−3	1.95	1
1945.34	7.13	6.00	16	5.90	17	6.00	16	4.55	36
1957.29	12.00	23.81	−98	23.69	−97	23.81	−98	20.70	−72
2034.24	2.32	6.62	−185	6.22	−168	6.62	−185	6.67	−188
2037.75	$1.49\,10^{-2}$	$1.36\,10^{-2}$	9	$1.50\,10^{-2}$	−0.4	$1.36\,10^{-2}$	9	–	–
2054.03	3.79	4.10	−8	3.88	−3	4.10	−8	2.87	24
2688.63	33.97	77.05	−127	76.62	−126	77.05	−127	71.89	−112
2700.36	3.66	3.14	14	1.18	68	3.14	14	1.99	46
2746.25	5.34	8.42	−58	8.12	−52	8.42	−58	8.66	−62

5.6 Nuclear model calculations

5.6.1 The EMPIRE-3.2 and TALYS-1.9 codes

An attempt has been made to reproduce the general shape of the fission cross section at higher neutron energies using two standard reaction codes, EMPIRE-3.2 and TALYS-1.9 which are based on the Hauser-Feshbach statistical model. Both codes implement several nuclear reaction models and are widely used for theoretical cross section calculations and data evaluations. The codes incorporate all major reaction mechanisms, such as direct, compound and pre-equilibrium emission using various optical model parameters.

Both codes were used with their default parameters concerning decays schemes, γ-ray strength functions, discrete levels, ground state deformations and nuclear level densities. For the level densities in particular, the Generalised Superfluid Model (GSM) and the Enhanced Generalised Superfluid Model (EGSM) were used in the TALYS-1.9 and EMPIRE-3.2 calculations, respectively. In the TALYS-1.9 runs, the embeded optimised parameters were used regarding the optical model, while in the EMPIRE-3.2 case, a ^{240}Pu dedicated optical model was available [205]. In both cases a double-humped potential was considered.

In both cases the fission barriers and widths were varied and an attempt was made to keep the input parameters in good agreement within a few percent in both codes. For the ^{240}Pu nucleus, whose fission barrier has mainly an effect in the second chance fission region, in the case of the EMPIRE-3.2 calculation the values used for the barrier heights were $V_a = 6.650$ MeV and $V_b = 5.150$ MeV for the first and second well, respectively. The corresponding curvatures were $\hbar\omega_a = 500$ keV and $\hbar\omega_b = 600$ keV respectively. For ^{241}Pu, which is the compound nucleus, the first barrier was $V_a = 6.000$ MeV, while the second $V_b = 5.100$ MeV. The corresponding curvatures were $\hbar\omega_a = 650$ keV and $\hbar\omega_b = 540$ keV.

In the calculations performed with TALYS-1.9 , in the case of ^{240}Pu the first barrier was $V_a = 5.850$ MeV and the second $V_b = 5.100$ MeV. For ^{241}Pu, the first barrier was $V_a = 5.950$ MeV and the second $V_b = 5.400$ MeV. These values are in agreement with the corresponding values in the EMPIRE-3.2 calculations within 1% and 5%, respectively. The curvature $\hbar\omega$ in TALYS-1.9 , had a single value of 700 keV.

5.6.2 Results of the calculations

The calculated cross section values by both theoretical codes reproduce fairly well the experimental data found in EXFOR, concerning the $(n,tot),(n,n),(n,\gamma)$ and $(n,2n)$ reactions, was examined. The parameters used in both calculations were suitable to adequately reproduce the aforementioned reactions, as can be seen in figures 5.23 and 5.24. Unfortunately no experimental data was found for the $(n,2n)$ reaction.

What was observed in both calculations was that although the $(n,tot),(n,el)$ and (n,γ) were reproduced similarly well, big differences were observed in the fission channel. Although both codes succeeded in reproducing fairly well the general

shape of the experimental cross section values, there were distinct differences to be observed between the obtained results. EMPIRE-3.2 could reproduce quite well the general shape of the fission threshold, but the cross section on the sub-threshold region was underestimated. On the other hand, TALYS-1.9 reproduced (on average) better the sub-threshold region, however it overestimated the cross section on the threshold.

It should be stressed here, however, that as it has already been shown, structures were experimentally observed in the sub-threshold fission. These structures are visible in the vicinity of the fission threshold and correspond to overlapping class-II resonances. Moreover, in the present data, additional structures were observed on the threshold itself, which can be attributed to vibrational bumps right before scission occurs, therefore they are related to the second potential well. These structures are not damped, therefore they are expected to be easily detected in doubly even actinides, such as ^{240}Pu , due to the lower level density of class-II states [206]. However, as can be seen in fig. 5.25, in both calculations, the structures seen in the vicinity of the threshold were not reproduced as expected, hence additional models are needed concerning the second well of the fission potential.

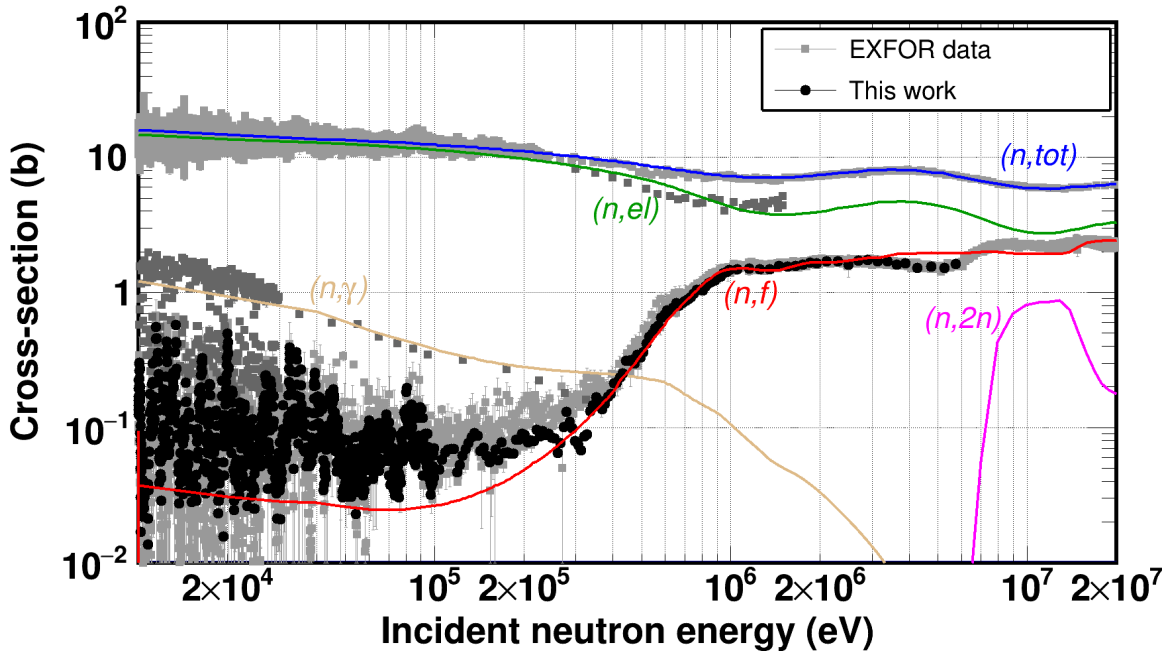

Figure 5.23: *The calculation performed with the* `EMPIRE-3.2` *code, could adequately reproduce the* $(n,tot),(n,el)$ *and* (n,γ) *reactions. In the* (n,f) *case the magnitude of the cross section on the threshold was adequately reproduced, however below* 300 *keV, the calculated one was underestimated.*

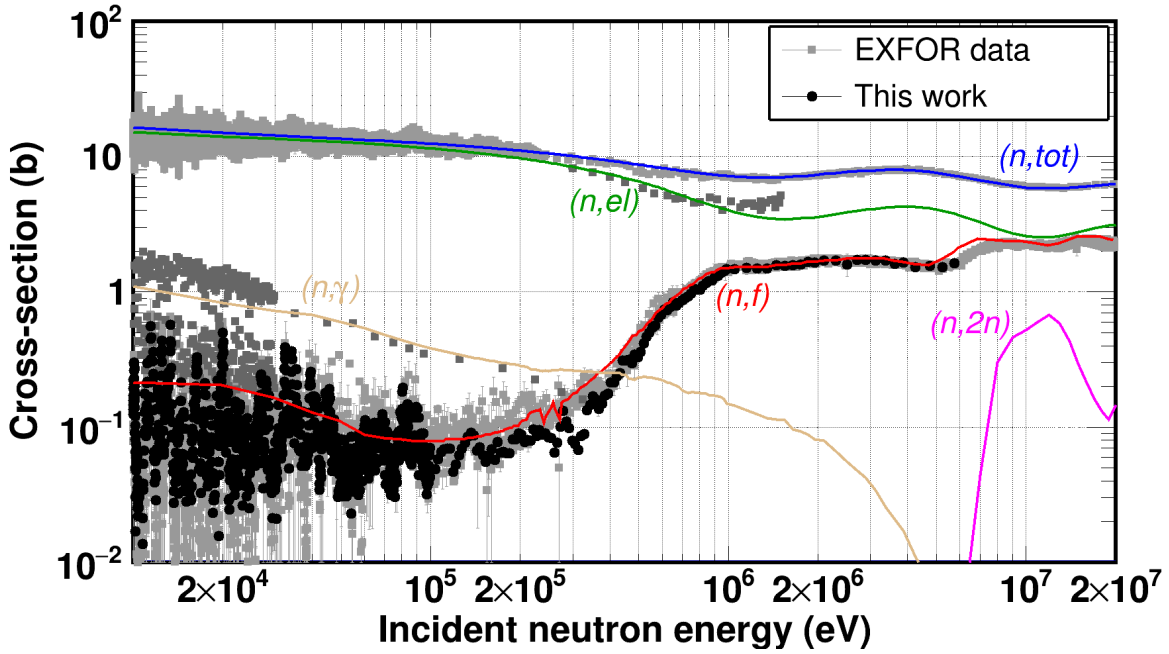

Figure 5.24: *The calculation performed with the* `TALYS-1.9` *code, could adequately reproduce the* $(n,tot),(n,el)$ *and* (n,γ) *reactions. In the* (n,f) *case the magnitude of the cross section on the sub-threshold region was adequately reproduced, however the cross section on the threshold was overestimated.*

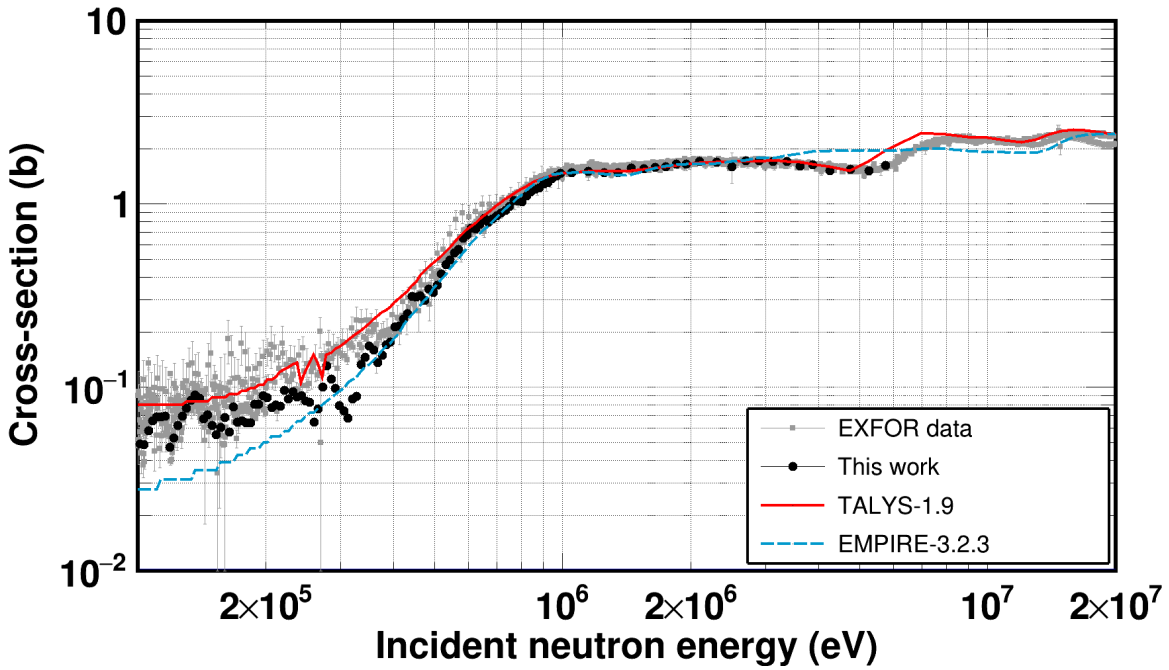

Figure 5.25: *In both fission calculations, the structures seen on and in the vicinity of the threshold could not be reproduced, therefore additional models of discrete states in the intermediate well of the fission barrier are needed.*

Epilogue

Summary

Although fission was discovered about 80 years ago, a comprehensive theoretical description with strong predictive capabilities is still an ongoing project, since it heavily relies on fission observables, while accurately known fission cross-sections are equally important in nuclear modelling.

Despite the lack of such a theoretical descriptive framework, the fission process is used in energy production by nuclear power plants whose efficient operation and reduction of safety margins, also depends on the accuracy of the reported cross-sections.

The use however of nuclear energy, apart from its benefits, includes the non-trivial task of nuclear waste management. The most widely accepted solution is the transmutation of long-lived actinides in advanced nuclear systems, such as Generation-IV reactors and Accelerator Driven Systems (ADS), whose optimal design requires the most accurate possible knowledge of fission cross-sections mainly in the MeV neutron energy region. Among various fission reactions, the $^{240}Pu(n,f)$ and $^{237}Np(n,f)$ ones, are considered to be of high priority, as evidenced by their inclusion in the High Priority Request List (HPRL) [6, 11, 12].

The $^{240}Pu(n,f)$ reaction cross-section is important because ^{240}Pu constitutes about 25% of the total Plutonium output (or about 60 kg annually per thermal reactor unit), hence is considered to be one of the most important among nuclear waste products. On the other hand, the $^{237}Np(n,f)$ cross-section is equally important, since it is frequently used as a reference reaction in feasibility and design studies regarding advanced nuclear systems. In addition, the latest time-of-flight data by Paradela et al. [44] and Diakaki et al. [41], both obtained at n_TOF, revealed a discrepancy of the order of 7% at the first chance fission plateau, which the present work attempted to solve.

Due to the aforementioned reasons, both reactions were experimentally studied at the newly commissioned vertical beam-line at the n_TOF facility at CERN, most commonly referred to as EAR2, which features a high flux/moderate resolu-

tion flight path at ∼ 19 m, above the Pb neutron production target. The apparatus used to detect the fission fragments, consisted of a Micromegas detector assembly exploiting its good time characteristics, high neutron transparency and robust design.

The analysis of the $^{240}Pu(n,f)$ data, which was the first experiment performed in EAR2, was based on pulse shape analysis procedures and on the calculation of average waveforms, which was accomplished by the development of the corresponding routines, which have already been used in other measurements performed within the framework of the n_TOF collaboration. Auxiliary Monte-Carlo simulations were carried out combining the `GEF` and `FLUKA` codes, to estimate the detection efficiency. The extensive and careful data analysis, followed by detailed sensitivity studies, finally yielded a cross-section over a broad energy range from 9 meV up to 6 MeV, spanning over 9 orders of magnitude, as well as a practical guide on how to conduct fission measurements and data analysis in the new experimental area.

The present data-set is the only one with good resolution from sub-thermal energies up to ∼ 20 eV, justifying the justifying the choice of EAR2 for such measurements. In the resolved and unresolved energy regions, only one useful data-set was available in literature, reported by Weston [49], therefore the importance of the present data in future evaluations is quite significant. In support of this claim, resonances were also resolved up to a few keV, which were characterised by means of the $\mathfrak{R}$-Matrix formalism implementing the `SAMMY` code, therefore already providing a parametrisation of the $^{240}Pu(n,f)$ cross-section over a broad range from 9 meV up to 10.2 keV while current evaluations do not go beyond 5.7 keV.

In the MeV region, where the high counting rate caused quite significant counting losses, a new methodology was developed to address similar issues which was based on detector emulation devices and exponential decay fits in the experimental waiting-time distribution. The application of this methodology, yielded a cross section which was in overall agreement with the time-of-flight data by Laptev et al. [47] and the latest ones found in literature by Salvador-Castineira et al. [45] obtained with quasi-monoenergetic beams. The most recent time-of-flight data by Tovesson et al. [46], were found to be about 5% above the present data up to 2.5 MeV.

Additional nuclear model calculations were performed, by means of the `TALYS-1.9` and `EMPIRE-3.2` statistical model codes, which, despite the satisfactory reproduction of the $(n,\gamma),(n,el)$ and (n,tot) exit channels, confirmed the need for the development of discrete class-II state models in the intermediate well of the fission barrier by failing to reproduce prominent structures in the vicinity of the fission threshold.

During the analysis of the $^{237}Np(n,f)$ data, a contamination was found in the samples which has not been characterised up to the present date, therefore results were reported in the vicinity of the fission threshold from 200 keV up to about 15 MeV. An overall agreement with the data by Diakaki et al. [41] was observed, thus supporting this reported cross-section in comparison to the corresponding one by Paradela et al. [44]. An appreciably higher energy limit was achieved compared to the $^{240}Pu(n,f)$ experimental campaign, attributed to the improved electronics and the significantly reduced counting rate due to the smaller sample masses. Both

successful campaigns assisted in designing similar recent experiments, such as the ^{230}Th(n,f) and ^{241}Am(n,f) ones already performed in EAR2.

In this respect, the present thesis proved the impressive capabilities of EAR2, which can be further enhanced by optimising the coupling of the spallation target's exit window to the experimental hall. At the time of the experiments, two non-symmetrical water layers were present, one for moderation and one for cooling purposes, causing a complicated neutron transport towards the experimental area, which resulted in a wide broadening of the resonances observed in the cross-section. The new spallation target and upgrade of the moderation system, during the second long shut-down period at CERN (LS2, 2019-2021), will be of significant importance in improving the resolving capabilities of EAR2.

In addition, the importance of using smooth reference reactions in fission cross-sections measurements in the resolved resonance region was stressed out in the manuscript. The generally small fission cross-section, can be successfully measured in EAR2, by incorporating suitable reference reactions, such as the $^{10}B(n,\alpha)$ and $^{6}Li(n,t)$ ones, and taking advantage of the high neutron flux delivered in EAR2. The resonances which can be resolved, will be subsequently analysed to provide useful information for parametrising cross-sections which can be used either in applications or in nuclear modelling.

Perspectives

Taking the aforementioned conclusions into consideration, EAR2 can prove to be a powerful tool for studying neutron-induced fission reactions over an impressively broad energy range and fully cover cross-section measurements suitable for applications. Such an example is the ^{241}Am(n,f) measurement already performed at EAR2, which is also included in the HPRL, due to its significance in the design of ADS.

In the same framework several other fission cross-sections can be studied in EAR2, namely the ^{245}Cm(n,f) and ^{241}Pu(n,f) ones, both of which are included in the HPRL. The former reaction, although already studied in EAR1, is still included in HPRL since the target uncertainties have not been yet met since the data reported in EXFOR, are discrepant up to 20% in the 500 eV - 6 MeV region. The latter reaction, involves the short-lived beta radioactive ^{241}Pu, which, despite its 14 years half-life, can be measured in EAR2 with the use of Micromegas detectors, which could be operated in convenient gains so as to suppress the contribution of the 5 keV maximum beta kinetic energy.

The resonances that were resolved in the $^{240}Pu(n,f)$ case, provide new important data in literature, therefore a re-evaluation of the corresponding cross-section can be proposed. Especially in the 9 meV - 2 eV energy range, where either quite discrepant or poor resolution data exist, the present work provided the only data set that covers the aforementioned energy regime.

As far as the $^{237}Np(n,f)$ measurement is concerned, a sample characterisation is pending, after which a point-wise cross-section will be reported from 9 meV up to 200 keV, which will be accompanied by a resonance analysis, similar to what has

been presented in the $^{240}Pu(n,f)$ case. Detector optimisation through the means of involving faster gaseous detectors has already proven to further increase the upper reachable energy limits, which can additionally assist in the characterisation of the EAR2 neutron flux. In addition, the use of position sensitive Micromegas detectors, either pixelised or stripped, can contribute to angular distribution studies and therefore provide additional fundamental information on the fission mechanism.

Moreover, the combination of high neutron flux and good resolution can be an asset in exploring sub-threshold fission in the vicinity of the fission threshold, where observed structures can provide useful information on the reaction mechanism of fission. Resonance-like structures, for instance, on the fission threshold can aid in understanding the vibrational character of the nuclear system right before it reaches the scission point.

Furthermore, cross-section studies in the region close to the fission barrier can reveal fine structures of the fission mode and spectroscopic information on the class-II states, especially in the case of doubly even nuclei.

Finally, the nuclear model calculations performed in the $^{240}Pu(n,f)$ case, revealed that a special theoretical modelling treatment is required in neutron energies in the vicinity of the fission barrier. Structures which were repeatedly observed, cannot be reproduced by the current models, which subsequently need to be enriched with discrete class-II levels.

List of relevant publications

1. Stamatopoulos, A., Diakaki, M., Tsinganis, A., Colonna, N., Gunsing, F., Tassan-Got, L., Kokkoris, M., Kalamara, A., Zugec, P., Patronis, N., Sabate-Gilarte, M., Vlastou, R., The n_TOF Collaboration,
An alternative methodology for high counting-loss corrections in neutron time-of-flight measurements
Nucl. Instr. Meth. A 913 (2019), pp. 40-47, 10.1016/j.nima.2018.10.032

2. Stamatopoulos, A., Kanellakopoulos, A., Kalamara, A., Diakaki, M., Tsinganis, A., Kokkoris, M., Michalopoulou, V., Axiotis, M., Lagoyiannis, A., Vlastou, R.
Measurement of the 234U(n, f) cross-section with quasi-monoenergetic beams in the keV and MeV range using a Micromegas detector assembly
European Physical Journal A, 54 (1) (2018), art. no. 7, 10.1140/epja/i2018-12429-2

3. Kalamara, A., Vlastou, R., Kokkoris, M., Chasapoglou, S., Stamatopoulos, A., Patronis, N., Serris, M., Lagoyannis, A., Harissopulos, S.
Ir 191 (n,2n) and Ir 191 (n,3n) reaction cross sections in the 15-21 MeV energy range Physical Review C, 98 (3) (2018) , art. no. 034607, 10.1103/PhysRevC.98.034607

4. Georgali, E., Eleme, Z., Patronis, N., Aslanoglou, X., Axiotis, M., Diakaki, M., Foteinou, V., Harissopulos, S., Kalamara, A., Kokkoris, M., Lagoyannis, A., Nicolis, N.G., Provatas, G., Stamatopoulos, A., Stoulos, S., Tsinganis, A., Vagena, E., Vlastou, R., Vogiatzi, S.M.
The (n,2n) reaction for the lightest stable erbium isotope Er 162 from reaction threshold up to 19 MeV
Physical Review C, 98 (1) (2018), art. no. 014622, 10.1103/PhysRevC.98.014622

5. Kalamara, A., Vlastou, R., Kokkoris, M., Nicolis, N.G., Patronis, N., Serris, M., Michalopoulou, V., Stamatopoulos, A., Lagoyannis, A., Harissopulos, S.

Au 197 (n,2n) reaction cross section in the 15-21 MeV energy range
Physical Review C, 97 (3) (2018), art. no. 034615, 10.1103/PhysRevC.97.034615

6. Stamatopoulos, A., Tsinganis, A., Colonna, N., Vlastou, R., Kokkoris, M., Schillebeeckx, P., Plompen, A., Heyse, J., Zugec, P., Barbagallo, M., Calviani, M., Berthoumieux, E., Chiaveri, The n_TOF collaboration
Measurement of the 240Pu(n,f) cross-section at the CERN n-TOF facility: First results from experimental area II (EAR-2)
EPJ Web of Conferences (2017), 146, art. no. 04030, 10.1051/epjconf/201714604030

7. Zugec, P., Colonna, N., Sabate-Gilarte, M., Vlachoudis, V., Massimi, C., Lerendegui-Marco, J., Stamatopoulos, A., Bacak, M., Warren, S.G.
A direct method for unfolding the resolution function from measurements of neutron induced reactions
Nucl. Instr. Meth. A 875 (2017), pp. 41-50, 10.1016/j.nima.2017.09.004

8. Sabate-Gilarte, M., Barbagallo, M., Colonna, N., Gunsing, F., Zugec, P., Vlachoudis, V., Chen, Y.H., Stamatopoulos, A., Lerendegui-Marco, J., Cortés-Giraldo, M.A., Villacorta, A., Guerrero, C., Damone, L., Audouin, L., Berthoumieux, E., Cosentino, L., Diakaki, M., Finocchiaro, P., Musumarra, A., Papaevangelou, T., Piscopo, M., Tassan-Got, The n_TOF collaboration
High-accuracy determination of the neutron flux in the new experimental area n_TOF-EAR2 at CERN
Eur. Phys. J. A (2017) 53 (10) art. no. 210, 10.1140/epja/i2017-12392-4

9. Tsinganis, A., Kokkoris, M., Vlastou, R., Kalamara, A., Stamatopoulos, A., Kanellakopoulos, A., Lagoyannis, A., Axiotis, M.
Neutron-induced fission cross-section measurement of 234U with quasi-monoenergetic beams in the keV and MeV range using micromegas detectors
EPJ Web of Conferences, (2017) 146, art. no. 04035,
10.1051/epjconf/201714604035

10. Zugec, P., Weiss, C., Guerrero, C., Gunsing, F., Vlachoudis, V., Sabate-Gilarte, M., Stamatopoulos, A., Wright, T., Lerendegui-Marco, J., Mingrone, F., Ryan, J.A., Warren, S.G., Tsinganis, A., Barbagallo, M.
Pulse processing routines for neutron time-of-flight data
Nucl. Instr. Meth. A, (2016) 812, pp. 134-144, 10.1016/j.nima.2015.12.054

11. Tsinganis, A., Stamatopoulos, A., Colonna, N., Vlastou, R., Schillebeeckx, P., Plompen, A., Heyse, J., Kokkoris, M., Barbagallo, M., Berthoumieux, E., Calviani, M., Chiaveri, E, The n_TOF collaboration
Measurement of the 240Pu(n,f) cross-section at the CERN n-TOF facility: First results from EAR-2
Proceedings of the 14th International Conference on Nuclear Reaction Mechanisms (2015), NRM 2015, pp. 23-28, cds.cern.ch/record/2114737

APPENDIX A

Notes on full covariance propagation

In the following pages a brief and practical description will be provided on how to perform a full covariance propagation on experimental observables. The following discussion will not be based on a strict mathematical framework, but on a general example of calculating the covariance and correlation matrices, on a reaction cross section. Several detailed documents can be found, which provide a more in depth understanding of the concepts and importance of calculating covariance and correlation matrices such as the ones by Geraldo and Smith [207], Fröhner [196] and Mannhart [208]. The vast majority of the following lines, was the outcome of fruitful and rather endless discussions with Dr. Peter Schillebeeckx, from JRC-Geel.

A nuclear reaction cross-section experiment, typically involves the measurement of certain observables at different incident energies E such as the number of recorded ejectiles C and projectiles Φ which impinge on a sample with mass m. The reaction cross-section σ can then be calculated using eq. (A.1), where $f(E)$ denotes the correction factors that need to be applied to the number of recorded events C. In the present case only a single correction factor will be considered, but the same ideas can be extended to multiple ones.

$$\sigma(E) = \frac{C(E)\, f(E)}{m\, \Phi(E)} \tag{A.1}$$

The aforementioned cross-section measurement took place at n incident energies therefore the quantities, which are different for each energy E_n, involved in (A.1) can be expressed as follows :

$$\begin{aligned}
\sigma(E) \equiv \overrightarrow{\sigma(E)} &= \Big\{\sigma(E_1), \sigma(E_2), \ldots, \sigma(E_n)\Big\} \equiv \Big\{\sigma_1, \sigma_2, \ldots, \sigma_n\Big\} \\
C(E) &\equiv \quad \cdots \quad \equiv \Big\{C_1, C_2, \ldots, C_n\Big\} \\
f(E) &\equiv \quad \cdots \quad \equiv \Big\{f_1, f_2, \ldots, f_n\Big\} \\
\Phi(E) &\equiv \quad \cdots \quad \equiv \Big\{\Phi_1, \Phi_2, \ldots, \Phi_n\Big\}
\end{aligned}$$

The final goal is to estimate whether the calculated cross section in the i-th energy affects/is affected by the corresponding one in the j-th energy. The first and most important step in achieving the aforementioned estimation is to identify the uncorrelated or fully correlated quantities involved in the measurement. The use of the same sample in all incident energies, for instance, renders the mass m to be a fully correlated quantity, therefore its individual correlation matrix V_m will be an all-ones matrix. On the contrary, uncorrelated quantities, which are accompanied by their uncertainties, will have a covariance matrix with diagonal elements equal to the square of their uncertainties, while the rest elements will be equal to zero. It has to be noted that theses matrices will have $(n \times n)$ elements. An example of such a quantity, is usually the recorded events C, therefore the covariance matrix V_C will be :

$$V_C = \begin{bmatrix} C_1 & & \mathbf{0} \\ & C_2 & \\ \mathbf{0} & & \ddots \\ & & & C_n \end{bmatrix}_{(n\times n)}$$

The covariance matrix of quantities which are derived by fully-correlated and/or uncorrelated parameters, can be estimated by following the methodology that will be described in the following lines. An example of such a quantity might be the incident flux Φ, estimated by the counts observed in a reference reaction.

The second step is to construct the matrix V, which will be composed of the individual covariance matrices calculated in the previous step. In the present case for instance, this matrix will be filled with the covariance matrices V_C, V_f, V_m, V_Φ which correspond to the quantities by which the cross section will be calculated, according to eq. (A.1). This matrix will have in total $(4n \times 4n)$ elements, since the cross section is calculated from four quantities at n incident energies. The covariance matrices V_x will be placed in the main diagonal of V, while the rest elements will be zeros, as shown below :

$$V = \begin{bmatrix} V_C & & \mathbf{0} \\ & V_f & \\ \mathbf{0} & & V_m \\ & & & V_\Phi \end{bmatrix}_{(4n\times 4n)}$$

The next step is to calculate the Jakobian or sensitivity matrix G, whose elements are the first-order partial derivatives of the cross section, at the present example, with respect to the quantities by which it is calculated at each incident energy (i.e. C, f, m, Φ), as shown below :

$$
G = \begin{array}{c}
 \\
\partial\sigma_1 \\
\partial\sigma_2 \\
\vdots \\
\partial\sigma_n
\end{array}
\begin{array}{c}
\begin{array}{ccccccccccccccc}
/\partial C_1 & /\partial C_2 & \dots & /\partial C_n & /\partial f_1 & /\partial f_2 & \dots & /\partial f_n & /\partial m & /\partial m & \dots & /\partial m & /\partial \Phi_1 & /\partial \Phi_2 & \dots & /\partial \Phi_n
\end{array} \\
\left[\begin{array}{ccccccccccccccc}
\partial\sigma_1/\partial C_1 & 0 & \dots & 0 & \partial\sigma_1/\partial f_1 & 0 & \dots & 0 & \partial\sigma_1/\partial m & \partial\sigma_1/\partial m & \dots & \partial\sigma_1/\partial m & \partial\sigma_1/\partial \Phi_1 & 0 & \dots & 0 \\
0 & \partial\sigma_2/\partial C_2 & \dots & 0 & 0 & \sigma_2/\partial f_2 & \dots & 0 & \partial\sigma_2/\partial m & \partial\sigma_2/\partial m & \dots & \partial\sigma_2/\partial m & 0 & \partial\sigma_2/\partial \Phi_2 & \dots & 0 \\
\vdots & \vdots & & \vdots & \vdots & \vdots & & \vdots & \vdots & \vdots & & \vdots & \vdots & \vdots & & \vdots \\
0 & 0 & \dots & \partial\sigma_n/\partial C_n & 0 & 0 & \dots & \partial\sigma_n/\partial f_n & \partial\sigma_n/\partial m & \partial\sigma_n/\partial m & \dots & \partial\sigma_n/\partial m & 0 & 0 & \dots & \partial\sigma_n/\partial \Phi_n
\end{array}\right]_{(n\times 4n)}
\end{array}
$$

The final step in calculating the covariance matrix $\mathtt{cov}(\sigma)$ is to apply the following matrix multiplication :

$$\mathtt{cov}(\sigma)_{(n\times n)} = G_{(n\times 4n)} * V_{(4n\times 4n)} * G^{T}_{(4n\times n)}$$

In the aforementioned expression, G^T denotes the transpose of the sensitivity matrix, while in the subscripts the dimensions of each matrix are shown. The square roots of the diagonal elements $\mathtt{cov}_{ii} \equiv \mathtt{cov}_i$ of the covariance matrix $\mathtt{cov}(\sigma)$, correspond to the total estimated uncertainty $\delta\sigma_i$ of the reported cross section in the i-th energy.

Finally, the elements $\mathtt{cor}_{ij}$ of the correlation matrix $\mathtt{cor}(\sigma)$ can be calculated from the $\mathtt{cov}_{ij}$ elements of the covariance matrix as seen below :

$$\mathtt{cor}_{ij} = \frac{\mathtt{cov}_{ij}}{\mathtt{cov}_i \, \mathtt{cov}_j}$$

APPENDIX B

An ancillary library in covariance matrix calculations

The covariance matrix calculations that have been performed, were based on an ancillary collection of functions combining the C++boost library (Version 1.68.0) [209] and the ROOT6 data analysis framework [178]. The collection of functions, given in the following lines, was written in C++and can be used within ROOT's interpreter.

```
/*****************************************************************
 *                                                               *
 * Fills a symmetric float matrix m_sym,                         *
 * based on values stored in a filler[] array.                   *
 *                                                               *
 *****************************************************************/
boost::numeric::ublas::symmetric_matrix<float> fill_symmetric (boost::
    numeric::ublas::symmetric_matrix<float> m_sym, float* filler, int
    size_FILLER){

   float* in = filler;
   for (size_t i=0; i<m_sym.size1(); ++i)
         for (size_t j = 0; j <= i && in != &filler[size_FILLER+1]; ++j)
            m_sym (i, j) = *in++;

   return m_sym;

}//___fill_symmetric()

/*****************************************************************
 *                                                               *
 * Fills a mapped float matrix m_spar using sparsity.            *
 * The non-zero values are stored in a float array (data[]).     *
 * Its position is stored in the int arrays row[] and col[].     *
```

```
 * The data[i] element is placed on the row[i]-th row and          *
 * col[i]-th column of the m_spar matrix.                          *
 *                                                                 *
 *******************************************************************/
boost::numeric::ublas::mapped_matrix<float> fill_sparse (boost::numeric::
    ublas::mapped_matrix<float> m_spar, int size_DATA, int* row, int* col
    , float* data){

   for (int i=0; i<size_DATA; ++i)
      m_spar( row[i], col[i] ) = data[i];

   return m_spar;

}//___fill_sparse()

/*******************************************************************
 *                                                                 *
 * Fills a diagonal float matrix m_diag.                           *
 * based on values stored in a data[] array.                       *
 *                                                                 *
 *******************************************************************/
boost::numeric::ublas::diagonal_matrix<float> fill_diagonal (boost::
    numeric::ublas::diagonal_matrix<float> m_diag, float* data) {

    for (int i = 0; i < (int) m_diag.size1(); ++i)
      m_diag (i, i) = data[i];

    return m_diag;

}//___fill_diagonal()

/*******************************************************************
 *                                                                 *
 * Reverses the  X-axis of a TH2 histogram                         *
 * in which the covariance/correlation matrix is ploted.           *
 * The use of log axis must be specified (logAxis flag).           *
 *                                                                 *
 *******************************************************************/
void ReverseXAxis (TH2 *h, bool logAxis)
{
   // Remove the current axis
   h->GetXaxis()->SetLabelOffset(999);
   h->GetXaxis()->SetTickLength(0);

   TString draw_option;
   if (logAxis)  draw_option = "G";
   else          draw_option = "+";

   // Redraw the new axis
   gPad->Update();
   TGaxis *newaxis = new TGaxis(gPad->GetUxmax(),
                                gPad->GetUymin(),
                                gPad->GetUxmin(),
                                gPad->GetUymin(),
                                h->GetXaxis()->GetXmin(),
                                h->GetXaxis()->GetXmax(),
                                510, draw_option);
```

```
77    newaxis->SetLabelOffset(0.);
78    if (logAxis)
79          gPad->SetLogx(1);
80
81    newaxis->Draw();
82 }//___ReverseXAxis()
83
84 /*************************************************************
85  *                                                           *
86  * Reverses the  Y-axis of a TH2 histogram                   *
87  * in which the covariance/correlation matrix is ploted.     *
88  * The use of log axis must be specified (logAxis flag).     *
89  *                                                           *
90  *************************************************************/
91 void ReverseYAxis (TH2 *h, bool logAxis)
92 {
93    // Remove the current axis
94    h->GetYaxis()->SetLabelOffset(999);
95    h->GetYaxis()->SetTickLength(0);
96
97    TString draw_option;
98    if (logAxis)  draw_option = "G";
99    else          draw_option = "+";
100
101   // Redraw the new axis
102   gPad->Update();
103   TGaxis *newaxis = new TGaxis(gPad->GetUxmin(),
104                                gPad->GetUymax(),
105                                gPad->GetUxmin()-0.001,
106                                gPad->GetUymin(),
107                                h->GetYaxis()->GetXmin(),
108                                h->GetYaxis()->GetXmax(),
109                                510, draw_option);
110   newaxis->SetLabelOffset(-0.05);
111
112   if (logAxis)
113         gPad->SetLogy(1);
114
115   newaxis->Draw();
116 }//___ReverseYAxis()
117
118 /*************************************************************
119  *                                                           *
120  * Calculates the correlation matrix m_correlation           *
121  * based on the input covariance matrix m_covariance.        *
122  *                                                           *
123  *************************************************************/
124 boost::numeric::ublas::matrix<float> calculate_correlation_matrix (boost
    ::numeric::ublas::matrix<float> m_covariance, boost::numeric::ublas::
    matrix<float> m_correlation){
125
126   for (int i=0; i< (int) m_covariance.size1(); ++i)
127      for (int j=0; j< (int) m_covariance.size2(); ++j)
128         m_correlation(i,j) = m_covariance(i,j)/sqrt(m_covariance(i,i))/
              sqrt(m_covariance(j,j));
129
130   return m_correlation;
```

```
131
132 }//___calculate_correlation_matrix()
133
134 /*****************************************************************
135  *                                                               *
136  * Converts a boost matrix in a graphical representation         *
137  * using a TH2F histogram.                                       *
138  *                                                               *
139  *****************************************************************/
140 TH2F* Matrix_to_Histo(boost::numeric::ublas::matrix<float> matrix, TH2F*
    histo){
141
142    float bin_content = 0.;
143    for (int i=0; i<histo->GetNbinsX(); ++i)
144       for (int j=0; j<histo->GetNbinsY(); ++j){
145          bin_content = matrix(j ,i);
146          histo->SetBinContent(i+1, j+1, bin_content);
147       }
148
149    return histo;
150
151 }//___Matrix_to_Histo()
152
153 /*****************************************************************
154  *                                                               *
155  * Calculates the total estimated uncertainty, based on          *
156  * the input covariance matrix in a TH2F form,                   *
157  * and stores it in a TH1F histogram.                            *
158  *                                                               *
159  *****************************************************************/
160 TH1F* CovarianceHisto_to_Uncertainty(TH1F* uncertainty, TH2F*
    covarianceMatrix){
161
162
163    float bin_content = 0.;
164    int   nbins       = covarianceMatrix->GetNbinsX();
165    if (nbins != uncertainty->GetNbinsX())
166       cout << "***Warning : Dimensions do not agree!***\n";
167    for (int i=0; i<nbins; ++i){
168       bin_content = sqrt( covarianceMatrix->GetBinContent(i,i) );
169       if ( isfinite(bin_content) )
170          uncertainty->SetBinContent(i+1, bin_content);
171       else
172          uncertainty->SetBinContent(i+1, 0.);
173    }
174
175    return uncertainty;
176
177 }//___CovarianceHisto_to_Uncertainty()
178
179 /*****************************************************************
180  *                                                               *
181  * Calculates the power of an array[]'s elements.                *
182  *                                                               *
183  *****************************************************************/
184 float* powerArray(int size_array, float* array, int power){
185
```

```
186     for (int i =0; i<size_array; ++i)
187         array[i] = pow(array[i], power);
188 
189     return array;
190 
191 }//___powerArray()
```

APPENDIX C

Reich-Moore resonance parameters of ^{240}Pu(n,f)

The resonance parameters to reproduce the reported cross section are given in the ENDF-6 format. Each file line in this particular format corresponds to the parameters of one resonance. The first five columns from the left to the right contain the energy, the spin, the neutron width, the radiation width, and the fission width of the resonance, respectively. The first eight fictitious resonances were adopted from Bouland et al. [187] and were used to simulate the contributions of the external resonances.

```
-4.070000+3 5.000000-1 3.550000+4 3.180000+1 3.370000-3 0.000000+09440 2151 6
-1.300000+3 5.000000-1 3.520000+3 3.180000+1-4.310000-2 0.000000+09440 2151 7
-3.050000+2 5.000000-1 2.140000+2 3.180000+1 4.000000-2 0.000000+09440 2151 8
-7.010000+1 5.000000-1 3.090000+2 3.180000+1-4.000000-2 0.000000+09440 2151 9
-3.000000+0 5.000000-1 1.310000+0 3.910000+1 1.000000-3 0.000000+09440 2151 10
 1.058452+0 5.000000-1 2.449860+0 2.914800+1 7.647165-3 0.000000+09440 2151 11
 2.043357+1 5.000000-1 2.749483+0 2.700000+1-2.896727-1 0.000000+09440 2151 12
 3.834652+1 5.000000-1 1.961190+1 2.400000+1 1.736031-2 0.000000+09440 2151 13
 4.174571+1 5.000000-1 1.740953+1 2.550000+1 7.107088-3 0.000000+09440 2151 14
 6.664089+1 5.000000-1 5.551704+1 3.300000+1 3.273883-2 0.000000+09440 2151 15
 7.277471+1 5.000000-1 2.169623+1 2.640000+1 9.775602-2 0.000000+09440 2151 16
 9.078330+1 5.000000-1 1.327000+1 3.079200+1-1.011600-2 0.000000+09440 2151 17
 9.249460+1 5.000000-1 3.004000+0 2.825800+1-6.317000-2 0.000000+09440 2151 18
 1.050100+2 5.000000-1 4.620600+1 2.854900+1-5.097000-3 0.000000+09440 2151 19
 1.216856+2 5.000000-1 1.493247+1 3.356100+1 8.703435-2 0.000000+09440 2151 20
 1.257000+2 5.000000-1 1.200000-1 3.180000+1-2.000000-2 0.000000+09440 2151 21
 1.307780+2 5.000000-1 1.787500-1 3.085700+1 2.413000-1 0.000000+09440 2151 22
 1.351414+2 5.000000-1 1.826245+1 3.289100+1 4.829136-2 0.000000+09440 2151 23
 1.520201+2 5.000000-1 1.349667+1 3.745700+1 3.771223-1 0.000000+09440 2151 24
 1.627153+2 5.000000-1 8.484407+0 2.911200+1 1.579265+0 0.000000+09440 2151 25
 1.698055+2 5.000000-1 1.323762+1 3.103600+1-1.366601-1 0.000000+09440 2151 26
 1.858290+2 5.000000-1 1.578200+1 3.095700+1 8.954000-3 0.000000+09440 2151 27
 1.920270+2 5.000000-1 2.850800-1 3.065000+1-1.284000-1 0.000000+09440 2151 28
 1.955500+2 5.000000-1 1.600000-1 3.180000+1 1.200000-1 0.000000+09440 2151 29
 1.974100+2 5.000000-1 1.600000-1 3.180000+1-1.200000-1 0.000000+09440 2151 30
 1.997070+2 5.000000-1 9.700000-1 2.860000+1 1.373000-1 0.000000+09440 2151 31
 2.389117+2 5.000000-1 1.190574+1 2.873000+1 1.354283-1 0.000000+09440 2151 32
 2.604632+2 5.000000-1 2.225148+1 3.277500+1-1.185314-1 0.000000+09440 2151 33
 2.869340+2 5.000000-1 1.345980+2 3.204100+1-3.694902-1 0.000000+09440 2151 34
```

```
3.048503+2 5.000000-1 7.367736+0 3.387000+1 2.120380-1 0.000000+09440 2151 35
3.135967+2 5.000000-1 1.199994-1 3.180000+1-2.500121-1 0.000000+09440 2151 36
3.181398+2 5.000000-1 5.229059+0 3.218500+1 3.212877-1 0.000000+09440 2151 37
3.207017+2 5.000000-1 1.890885+1 3.488000+1-3.263681-2 0.000000+09440 2151 38
3.326899+2 5.000000-1 1.300000-1 3.180000+1 2.485512-2 0.000000+09440 2151 39
3.383416+2 5.000000-1 5.937988+0 3.138500+1-4.566949-3 0.000000+09440 2151 40
3.458764+2 5.000000-1 1.589930+1 3.391900+1 3.520549-1 0.000000+09440 2151 41
3.635231+2 5.000000-1 3.162209+1 3.883100+1 1.365071-1 0.000000+09440 2151 42
3.719488+2 5.000000-1 1.329041+1 3.036800+1-1.350234-1 0.000000+09440 2151 43
3.930402+2 5.000000-1 1.500000-1 3.180000+1-1.699704-2 0.000000+09440 2151 44
4.050408+2 5.000000-1 1.033676+2 3.241000+1-4.314615-1 0.000000+09440 2151 45
4.188809+2 5.000000-1 5.768944+0 3.090700+1 2.865661-1 0.000000+09440 2151 46
4.456683+2 5.000000-1 1.844683+0 3.136800+1-5.844636-1 0.000000+09440 2151 47
4.497984+2 5.000000-1 1.610510+1 3.218100+1 1.471065-1 0.000000+09440 2151 48
4.666322+2 5.000000-1 2.651139+0 3.290500+1 1.031386+0 0.000000+09440 2151 49
4.732970+2 5.000000-1 4.113400+0 3.070500+1 1.000235+0 0.000000+09440 2151 50
4.937954+2 5.000000-1 5.345616+0 3.152900+1-5.300350-1 0.000000+09440 2151 51
4.989327+2 5.000000-1 1.854077+1 3.632400+1 2.082159-1 0.000000+09440 2151 52
5.099950+2 5.000000-1 4.139980-1 3.180000+1 6.396444-2 0.000000+09440 2151 53
5.124990+2 5.000000-1 5.174995-1 3.180000+1-4.473510-2 0.000000+09440 2151 54
5.144720+2 5.000000-1 2.085088+1 3.360200+1-2.059906-1 0.000000+09440 2151 55
5.262590+2 5.000000-1 9.607400-1 3.180000+1 1.000096+0 0.000000+09440 2151 56
5.307589+2 5.000000-1 6.768164-1 3.180000+1 2.924212+0 0.000000+09440 2151 57
5.463326+2 5.000000-1 3.105819+1 3.989700+1-9.968682-2 0.000000+09440 2151 58
5.534221+2 5.000000-1 1.787541+1 3.478200+1 3.946256-1 0.000000+09440 2151 59
5.665224+2 5.000000-1 3.136153+1 3.381400+1-2.786323-1 0.000000+09440 2151 60
5.843677+2 5.000000-1 1.151834+0 3.180000+1 3.611068+0 0.000000+09440 2151 61
5.966365+2 5.000000-1 5.420325+1 3.716500+1 1.224677-1 0.000000+09440 2151 62
6.080180+2 5.000000-1 2.222384+1 2.914800+1-9.021935-2 0.000000+09440 2151 63
6.321824+2 5.000000-1 1.349694+1 3.243200+1-4.069090-1 0.000000+09440 2151 64
6.375531+2 5.000000-1 1.187997+1 3.059600+1-1.158420-1 0.000000+09440 2151 65
6.498321+2 5.000000-1 1.199937+0 3.180000+1 2.196548+0 0.000000+09440 2151 66
6.656584+2 5.000000-1 2.033903+2 2.738200+1-3.594152-1 0.000000+09440 2151 67
6.788542+2 5.000000-1 2.540811+1 3.203400+1-1.309361+0 0.000000+09440 2151 68
7.120900+2 5.000000-1 1.329991+0 3.180000+1 3.258355-1 0.000000+09440 2151 69
7.433468+2 5.000000-1 1.010032+0 3.180000+1 5.599228-1 0.000000+09440 2151 70
7.502519+2 5.000000-1 6.949741+1 3.248300+1-1.360236+1 0.000000+09440 2151 71
7.588647+2 5.000000-1 5.821591+0 3.202500+1 1.679265-1 0.000000+09440 2151 72
7.782610+2 5.000000-1 1.119496+0 3.180000+1 5.850607-1 0.000000+09440 2151 73
7.829462+2 5.000000-1 3.833237+0 3.122900+1-3.119923+3 0.000000+09440 2151 74
7.904807+2 5.000000-1 2.523830+1 2.316800+1-1.339674+1 0.000000+09440 2151 75
8.102763+2 5.000000-1 2.196445+2 3.728400+1 1.554993+1 0.000000+09440 2151 76
8.200160+2 5.000000-1 1.105578+2 2.980500+1 6.462737-1 0.000000+09440 2151 77
8.332517+2 5.000000-1 1.019970+0 3.180000+1-3.502732+0 0.000000+09440 2151 78
8.455725+2 5.000000-1 9.482834+0 3.356400+1 1.238273-1 0.000000+09440 2151 79
8.550127+2 5.000000-1 4.710073+1 3.467500+1-3.329061-1 0.000000+09440 2151 80
8.679579+2 5.000000-1 1.019975+0 3.180000+1 1.417381+0 0.000000+09440 2151 81
8.763691+2 5.000000-1 1.451541+1 3.285700+1 7.682956-1 0.000000+09440 2151 82
8.917092+2 5.000000-1 9.468625+1 3.225600+1-9.351548-1 0.000000+09440 2151 83
9.000000+2 5.000000-1 1.000000+0 3.180000+1-1.200000+1 0.000000+09440 2151 84
9.040090+2 5.000000-1 2.208300+1 3.477300+1-7.322000-1 0.000000+09440 2151 85
9.089050+2 5.000000-1 7.786600+1 3.219600+1 3.237000-2 0.000000+09440 2151 86
9.152340+2 5.000000-1 3.587900+1 3.482800+1-3.398000-1 0.000000+09440 2151 87
9.435070+2 5.000000-1 1.228200+2 3.274400+1-2.976600-1 0.000000+09440 2151 88
9.584120+2 5.000000-1 7.392300+1 3.097900+1 7.036000-2 0.000000+09440 2151 89
9.700000+2 5.000000-1 1.000000+0 3.180000+1 5.000000+0 0.000000+09440 2151 90
9.713190+2 5.000000-1 7.978700+1 2.989300+1 6.005000-2 0.000000+09440 2151 91
9.792000+2 5.000000-1 7.200000+0 3.180000+1-4.366000-1 0.000000+09440 2151 92
9.830000+2 5.000000-1 1.000000+0 3.180000+1 4.800000+1 0.000000+09440 2151 93
9.918917+2 5.000000-1 2.998325-1 3.180000+1 2.674736+4 0.000000+09440 2151 94
1.002312+3 5.000000-1 9.728192+1 2.978900+1-1.558025+0 0.000000+09440 2151 95
1.012088+3 5.000000-1 1.999988+0 3.180000+1 8.114951+0 0.000000+09440 2151 96
1.024019+3 5.000000-1 5.230772+0 3.180000+1 8.046956-1 0.000000+09440 2151 97
1.028667+3 5.000000-1 2.000065+0 3.180000+1 4.525412+0 0.000000+09440 2151 98
1.037374+3 5.000000-1 1.999975+0 3.180000+1-2.169453+0 0.000000+09440 2151 99
1.041772+3 5.000000-1 1.213925+1 2.973500+1-1.699458-1 0.000000+09440 2151 100
1.045520+3 5.000000-1 3.938692+0 3.180000+1 2.471820+0 0.000000+09440 2151 101
1.050897+3 5.000000-1 2.000282+0 3.180000+1 7.489642+0 0.000000+09440 2151 102
1.072315+3 5.000000-1 1.092296+2 2.909300+1-2.724902-1 0.000000+09440 2151 103
1.077422+3 5.000000-1 1.700018+0 3.180000+1-1.850070+0 0.000000+09440 2151 104
1.085995+3 5.000000-1 1.999996+0 3.180000+1 2.212435+0 0.000000+09440 2151 105
```

```
1.099855+3 5.000000-1 8.003082+1 3.408400+1-3.036769-1 0.000000+09440 2151 106
1.115893+3 5.000000-1 2.571215+0 3.180000+1-5.465667-1 0.000000+09440 2151 107
1.129035+3 5.000000-1 4.979185+1 3.094600+1 6.716840-1 0.000000+09440 2151 108
1.133956+3 5.000000-1 6.965051+0 3.180000+1 3.620806-1 0.000000+09440 2151 109
1.142870+3 5.000000-1 4.220156+1 3.098400+1-4.222007-1 0.000000+09440 2151 110
1.159591+3 5.000000-1 2.378873+1 3.286200+1-6.870245-1 0.000000+09440 2151 111
1.175536+3 5.000000-1 1.500023+0 3.180000+1 4.117688+0 0.000000+09440 2151 112
1.185558+3 5.000000-1 1.587978+2 3.211900+1 1.108575-1 0.000000+09440 2151 113
1.190808+3 5.000000-1 1.140709+2 3.183200+1-1.457607-1 0.000000+09440 2151 114
1.200851+3 5.000000-1 2.000042+0 3.180000+1 1.404001+0 0.000000+09440 2151 115
1.208924+3 5.000000-1 6.254362+1 3.169700+1-3.504050-1 0.000000+09440 2151 116
1.228230+3 5.000000-1 1.038647+1 3.180000+1 9.402248-1 0.000000+09440 2151 117
1.236874+3 5.000000-1 1.118474+1 3.180000+1 7.823147-1 0.000000+09440 2151 118
1.256039+3 5.000000-1 7.989459+1 3.119400+1-4.518973+0 0.000000+09440 2151 119
1.281430+3 5.000000-1 4.200867+0 3.180000+1-1.006939+0 0.000000+09440 2151 120
1.300521+3 5.000000-1 2.491274+2 3.065000+1-2.669134-1 0.000000+09440 2151 121
1.328257+3 5.000000-1 3.675604+2 3.271100+1 5.070223-1 0.000000+09440 2151 122
1.345157+3 5.000000-1 2.491071+1 3.180000+1 1.093861-1 0.000000+09440 2151 123
1.350989+3 5.000000-1 7.739068+0 3.180000+1-2.715013-2 0.000000+09440 2151 124
1.363119+3 5.000000-1 7.311624+0 3.180000+1 2.784838-1 0.000000+09440 2151 125
1.377032+3 5.000000-1 6.613678+1 3.122600+1-1.134817-1 0.000000+09440 2151 126
1.388910+3 5.000000-1 1.466700+1 3.180000+1 6.296000+0 0.000000+09440 2151 127
1.402440+3 5.000000-1 9.830000+0 3.180000+1-2.085500+3 0.000000+09440 2151 128
1.408500+3 5.000000-1 9.910000+0 3.180000+1-8.520300+1 0.000000+09440 2151 129
1.426030+3 5.000000-1 3.908300+1 2.987100+1 5.485200+0 0.000000+09440 2151 130
1.429259+3 5.000000-1 1.568855+1 3.180000+1-1.023209+0 0.000000+09440 2151 131
1.442152+3 5.000000-1 2.000036+0 3.180000+1 6.739917+0 0.000000+09440 2151 132
1.449633+3 5.000000-1 2.691321+1 3.180000+1-1.493385+0 0.000000+09440 2151 133
1.451289+3 5.000000-1 2.741371+1 3.152300+1-2.739115+0 0.000000+09440 2151 134
1.462942+3 5.000000-1 2.179734+1 3.180000+1 3.717479-1 0.000000+09440 2151 135
1.465979+3 5.000000-1 1.999985+0 3.180000+1-2.728332+0 0.000000+09440 2151 136
1.475475+3 5.000000-1 2.000118+0 3.180000+1-4.668645+0 0.000000+09440 2151 137
1.481350+3 5.000000-1 9.762134+0 3.180000+1 2.014349+0 0.000000+09440 2151 138
1.498132+3 5.000000-1 2.000088+0 3.180000+1 4.273911+0 0.000000+09440 2151 139
1.502736+3 5.000000-1 4.000008+0 3.180000+1-1.105880-1 0.000000+09440 2151 140
1.528855+3 5.000000-1 4.999763+0 3.180000+1 3.254678+0 0.000000+09440 2151 141
1.540412+3 5.000000-1 1.024544+2 3.231300+1-1.596319-1 0.000000+09440 2151 142
1.549456+3 5.000000-1 1.616882+2 3.170700+1 4.106222-1 0.000000+09440 2151 143
1.555236+3 5.000000-1 2.500029+0 3.180000+1-3.636942+0 0.000000+09440 2151 144
1.563741+3 5.000000-1 1.180319+2 3.043800+1-1.200554-1 0.000000+09440 2151 145
1.575196+3 5.000000-1 1.264906+2 3.163700+1-5.095096+0 0.000000+09440 2151 146
1.581892+3 5.000000-1 3.000011+0 3.180000+1 1.096347-1 0.000000+09440 2151 147
1.599997+3 5.000000-1 1.999998+0 3.180000+1-1.014115-1 0.000000+09440 2151 148
1.609690+3 5.000000-1 3.598789+1 3.180000+1 7.252641-1 0.000000+09440 2151 149
1.621464+3 5.000000-1 2.796052+1 3.180000+1-3.702969-1 0.000000+09440 2151 150
1.628807+3 5.000000-1 5.000011+0 3.180000+1 8.371193-1 0.000000+09440 2151 151
1.643325+3 5.000000-1 1.110493+2 3.166000+1 9.520456-1 0.000000+09440 2151 152
1.662724+3 5.000000-1 6.912209+1 3.217700+1-7.914254-1 0.000000+09440 2151 153
1.667283+3 5.000000-1 6.000023+0 3.180000+1 1.124609-1 0.000000+09440 2151 154
1.688269+3 5.000000-1 3.526481+1 3.180000+1-1.887533+0 0.000000+09440 2151 155
1.707292+3 5.000000-1 4.499990+0 3.180000+1 1.434991+0 0.000000+09440 2151 156
1.724329+3 5.000000-1 8.441634+1 3.143600+1 1.786533+0 0.000000+09440 2151 157
1.749086+3 5.000000-1 2.999996+0 3.180000+1-9.897855-2 0.000000+09440 2151 158
1.742025+3 5.000000-1 2.484046+1 3.180000+1 7.811418-1 0.000000+09440 2151 159
1.763851+3 5.000000-1 5.548738+1 3.180000+1-2.679878-1 0.000000+09440 2151 160
1.771502+3 5.000000-1 9.730459+0 3.180000+1 9.919709-2 0.000000+09440 2151 161
1.779053+3 5.000000-1 4.871030+2 3.065400+1-4.533043-2 0.000000+09440 2151 162
1.788586+3 5.000000-1 4.999701+0 3.180000+1 8.024958-1 0.000000+09440 2151 163
1.811105+3 5.000000-1 4.999869+0 3.180000+1 7.405383-1 0.000000+09440 2151 164
1.841931+3 5.000000-1 1.282446+2 3.306300+1-1.098214+1 0.000000+09440 2151 165
1.852724+3 5.000000-1 3.392367+1 3.180000+1-1.260800+0 0.000000+09440 2151 166
1.861615+3 5.000000-1 4.000016+0 3.180000+1-1.008620-1 0.000000+09440 2151 167
1.873100+3 5.000000-1 8.065080+1 3.074400+1 4.141161+0 0.000000+09440 2151 168
1.885711+3 5.000000-1 5.000001+0 3.180000+1-2.280639+0 0.000000+09440 2151 169
1.902041+3 5.000000-1 2.180232+2 3.180000+1 3.712492+0 0.000000+09440 2151 170
1.916672+3 5.000000-1 3.519166+1 3.062700+1 8.703864+1 0.000000+09440 2151 171
1.938050+3 5.000000-1 1.981037+0 3.180000+1-2.022380+3 0.000000+09440 2151 172
1.943396+3 5.000000-1 7.930715+0 3.180000+1 1.735735+1 0.000000+09440 2151 173
1.948121+3 5.000000-1 8.583414+1 3.180000+1 1.124522+1 0.000000+09440 2151 174
1.954813+3 5.000000-1 2.761408+2 3.083600+1-2.121080+1 0.000000+09440 2151 175
1.973633+3 5.000000-1 7.159968+1 3.180000+1 1.761466+0 0.000000+09440 2151 176
```

```
1.991434+3 5.000000-1 1.175789+2 3.067300+1-4.790384-2 0.000000+09440 2151 177
1.998876+3 5.000000-1 5.398094+0 3.180000+1 4.758460-2 0.000000+09440 2151 178
2.016797+3 5.000000-1 5.500078+1 3.151400+1-3.976761-1 0.000000+09440 2151 179
2.022934+3 5.000000-1 6.019261+1 2.871300+1 1.825908+0 0.000000+09440 2151 180
2.032972+3 5.000000-1 1.112358+2 3.230200+1 1.458383+1 0.000000+09440 2151 181
2.037536+3 5.000000-1 4.999995+0 3.180000+1 1.160570-1 0.000000+09440 2151 182
2.054392+3 5.000000-1 7.245387+1 2.844300+1-5.762362+0 0.000000+09440 2151 183
2.060777+3 5.000000-1 5.000008+0 3.100000+1 8.565730-2 0.000000+09440 2151 184
2.082973+3 5.000000-1 9.914006+1 3.087900+1-1.529060-1 0.000000+09440 2151 185
2.096839+3 5.000000-1 9.999617+0 3.180000+1 6.938264-1 0.000000+09440 2151 186
2.110794+3 5.000000-1 1.387651+1 3.180000+1-2.396157+0 0.000000+09440 2151 187
2.127115+3 5.000000-1 6.000007+0 3.180000+1-7.716250-1 0.000000+09440 2151 188
2.141995+3 5.000000-1 7.999991+0 3.180000+1-8.846337-1 0.000000+09440 2151 189
2.154595+3 5.000000-1 1.405225+1 3.180000+1 1.360600+0 0.000000+09440 2151 190
2.177350+3 5.000000-1 9.999884+0 3.180000+1 2.641534+0 0.000000+09440 2151 191
2.181900+3 5.000000-1 8.963041+1 3.006200+1 1.200380-1 0.000000+09440 2151 192
2.198245+3 5.000000-1 1.397799+2 3.067200+1-5.089683-1 0.000000+09440 2151 193
2.223435+3 5.000000-1 1.199993+1 3.180000+1-1.398057-1 0.000000+09440 2151 194
2.230372+3 5.000000-1 8.999984+0 3.180000+1 1.165416-1 0.000000+09440 2151 195
2.240618+3 5.000000-1 3.412299+1 3.180000+1-9.162085-1 0.000000+09440 2151 196
2.256669+3 5.000000-1 1.366788+2 3.098600+1 4.206537-1 0.000000+09440 2151 197
2.262685+3 5.000000-1 9.999989+0 3.180000+1-1.170128-1 0.000000+09440 2151 198
2.268460+3 5.000000-1 8.000000+0 3.180000+1 1.044080-1 0.000000+09440 2151 199
2.277959+3 5.000000-1 3.982564+2 3.160100+1 4.623187-1 0.000000+09440 2151 200
2.282838+3 5.000000-1 2.793029+1 3.100500+1 7.643282-1 0.000000+09440 2151 201
2.290749+3 5.000000-1 2.183104+2 3.087700+1-2.358251-1 0.000000+09440 2151 202
2.303391+3 5.000000-1 1.695197+1 3.180000+1-1.003252-1 0.000000+09440 2151 203
2.318130+3 5.000000-1 1.000006+1 3.180000+1-4.828338+0 0.000000+09440 2151 204
2.334391+3 5.000000-1 3.783717+1 3.180000+1 5.528427-1 0.000000+09440 2151 205
2.350998+3 5.000000-1 3.854399+1 3.180000+1 1.293140-1 0.000000+09440 2151 206
2.359620+3 5.000000-1 1.200000+1 3.180000+1-1.270086-1 0.000000+09440 2151 207
2.365789+3 5.000000-1 2.429069+2 3.048300+1 3.844221-1 0.000000+09440 2151 208
2.373255+3 5.000000-1 9.654791+0 3.180000+1-1.029046-1 0.000000+09440 2151 209
2.385989+3 5.000000-1 1.834880+1 3.180000+1 1.338134+0 0.000000+09440 2151 210
2.404739+3 5.000000-1 2.501600+1 3.180000+1-6.171959-2 0.000000+09440 2151 211
2.415783+3 5.000000-1 6.835348+1 3.180000+1 5.860738-1 0.000000+09440 2151 212
2.424812+3 5.000000-1 5.000002+0 3.180000+1 1.041547-1 0.000000+09440 2151 213
2.434102+3 5.000000-1 2.153628+2 3.044200+1 3.002389-1 0.000000+09440 2151 214
2.459363+3 5.000000-1 2.633801+1 3.180000+1-4.299888-1 0.000000+09440 2151 215
2.470454+3 5.000000-1 4.894785+1 3.180000+1-2.102593-1 0.000000+09440 2151 216
2.476850+3 5.000000-1 9.999697+0 3.180000+1-5.154752+0 0.000000+09440 2151 217
2.484478+3 5.000000-1 2.144899+1 3.180000+1 3.392187-1 0.000000+09440 2151 218
2.511802+3 5.000000-1 1.000000+1 3.180000+1-1.132654-1 0.000000+09440 2151 219
2.520792+3 5.000000-1 1.141589+2 3.380100+1 3.504025-1 0.000000+09440 2151 220
2.531340+3 5.000000-1 1.499997+1 3.180000+1-1.035389-1 0.000000+09440 2151 221
2.538203+3 5.000000-1 2.865485+2 3.234200+1 2.097929-1 0.000000+09440 2151 222
2.542701+3 5.000000-1 7.000001-1 3.180000+1 9.879762-2 0.000000+09440 2151 223
2.548838+3 5.000000-1 8.559029+1 3.258000+1-6.546508-1 0.000000+09440 2151 224
2.563200+3 5.000000-1 7.000000-1 3.180000+1-1.001775-1 0.000000+09440 2151 225
2.574794+3 5.000000-1 4.677104+1 3.638300+1-4.838475-1 0.000000+09440 2151 226
2.578207+3 5.000000-1 1.000001+1 3.180000+1 9.502421-2 0.000000+09440 2151 227
2.594956+3 5.000000-1 9.999915+0 3.180000+1-1.122552+0 0.000000+09440 2151 228
2.602375+3 5.000000-1 1.000014+1 3.180000+1 6.668367+0 0.000000+09440 2151 229
2.626698+3 5.000000-1 1.500085+1 3.180000+1-8.146468-2 0.000000+09440 2151 230
2.632733+3 5.000000-1 1.000006+1 3.180000+1 9.232796-2 0.000000+09440 2151 231
2.644784+3 5.000000-1 4.302633+2 3.162000+1-4.590650+0 0.000000+09440 2151 232
2.651599+3 5.000000-1 3.832174+1 3.180000+1 1.356380+1 0.000000+09440 2151 233
2.669595+3 5.000000-1 9.999241+0 3.180000+1-1.022190+1 0.000000+09440 2151 234
2.697695+3 5.000000-1 3.264284+2 3.180000+1 1.204056+2 0.000000+09440 2151 235
2.700209+3 5.000000-1 1.501059+1 3.180000+1 7.561670+1 0.000000+09440 2151 236
2.705951+3 5.000000-1 9.997509+0 3.180000+1-1.965192+1 0.000000+09440 2151 237
2.717850+3 5.000000-1 4.042608+1 3.180000+1 1.973270+0 0.000000+09440 2151 238
2.729087+3 5.000000-1 9.999976+0 3.180000+1-1.017916-1 0.000000+09440 2151 239
2.738982+3 5.000000-1 1.816584+2 3.180000+1 6.708491-1 0.000000+09440 2151 240
2.753986+3 5.000000-1 1.136489+2 2.912900+1 8.326295+0 0.000000+09440 2151 241
2.763699+3 5.000000-1 1.000018+1 3.180000+1 9.799219-2 0.000000+09440 2151 242
2.817270+3 5.000000-1 4.434600+1 3.180000+1-1.596400+0 0.000000+09440 2151 243
2.843590+3 5.000000-1 1.723800+2 3.180000+1-1.277000-1 0.000000+09440 2151 244
2.858230+3 5.000000-1 2.865500+1 3.180000+1 1.522000+0 0.000000+09440 2151 245
2.882230+3 5.000000-1 3.197600+1 3.180000+1-3.500000-1 0.000000+09440 2151 246
2.895860+3 5.000000-1 6.388200+1 3.180000+1 1.600000-1 0.000000+09440 2151 247
```

```
2.904880+3 5.000000-1 1.229000+2 3.180000+1 6.100000-1 0.000000+09440 2151 248
2.923600+3 5.000000-1 1.800000+1 3.180000+1-1.000000-1 0.000000+09440 2151 249
2.938130+3 5.000000-1 1.532200+2 3.180000+1-4.000000-1 0.000000+09440 2151 250
2.968600+3 5.000000-1 9.873400+1 3.180000+1-3.600000-1 0.000000+09440 2151 251
2.980410+3 5.000000-1 1.124700+2 3.180000+1 5.000000-2 0.000000+09440 2151 252
2.986550+3 5.000000-1 1.088700+1 3.180000+1-9.600000-1 0.000000+09440 2151 253
2.994392+3 5.000000-1 6.118310+1 3.180000+1 3.253102-1 0.000000+09440 2151 254
3.003927+3 5.000000-1 8.386441+1 3.180000+1 5.650757-1 0.000000+09440 2151 255
3.017801+3 5.000000-1 1.266507+2 3.180000+1-1.926973-1 0.000000+09440 2151 256
3.029415+3 5.000000-1 2.012692+1 3.180000+1 2.169818+0 0.000000+09440 2151 257
3.040498+3 5.000000-1 9.999997+0 3.180000+1-2.324077-1 0.000000+09440 2151 258
3.048258+3 5.000000-1 9.999997+0 3.180000+1 3.708435-1 0.000000+09440 2151 259
3.054563+3 5.000000-1 4.902183+1 3.180000+1-5.811993+0 0.000000+09440 2151 260
3.069793+3 5.000000-1 1.366908+1 3.180000+1 2.764478+1 0.000000+09440 2151 261
3.078446+3 5.000000-1 1.334092+2 3.180000+1 3.820619+0 0.000000+09440 2151 262
3.088279+3 5.000000-1 3.346105+1 3.180000+1-7.941633-1 0.000000+09440 2151 263
3.092153+3 5.000000-1 1.000007+1 3.180000+1-2.587702+0 0.000000+09440 2151 264
3.106168+3 5.000000-1 6.000201+0 3.180000+1-1.274269+1 0.000000+09440 2151 265
3.112966+3 5.000000-1 3.966110+1 3.180000+1 8.344615-1 0.000000+09440 2151 266
3.139996+3 5.000000-1 3.999997+0 3.180000+1-4.210755+0 0.000000+09440 2151 267
3.172994+3 5.000000-1 2.393388+2 3.180000+1 1.555127+0 0.000000+09440 2151 268
3.184586+3 5.000000-1 7.999994+0 3.180000+1-3.069320-1 0.000000+09440 2151 269
3.192244+3 5.000000-1 3.604414+2 3.180000+1 4.413969-1 0.000000+09440 2151 270
3.209159+3 5.000000-1 1.499997+1 3.180000+1 3.182170-1 0.000000+09440 2151 271
3.237632+3 5.000000-1 7.395925+1 3.180000+1-7.585758-1 0.000000+09440 2151 272
3.258349+3 5.000000-1 5.999999+0 3.180000+1-3.109478-1 0.000000+09440 2151 273
3.265686+3 5.000000-1 2.601802+1 3.180000+1 1.238735-1 0.000000+09440 2151 274
3.268518+3 5.000000-1 1.091200+2 3.180000+1 1.724216-1 0.000000+09440 2151 275
3.291033+3 5.000000-1 1.000004+1 3.180000+1-1.813346+0 0.000000+09440 2151 276
3.305462+3 5.000000-1 1.199993+1 3.180000+1-1.005825+0 0.000000+09440 2151 277
3.317454+3 5.000000-1 1.500005+1 3.180000+1 2.986924-1 0.000000+09440 2151 278
3.331685+3 5.000000-1 1.476297+1 3.180000+1-1.649836+0 0.000000+09440 2151 279
3.339866+3 5.000000-1 1.399972+1 3.180000+1 2.859482+0 0.000000+09440 2151 280
3.345935+3 5.000000-1 5.000026+0 3.180000+1 6.252944+0 0.000000+09440 2151 281
3.360217+3 5.000000-1 1.300042+1 3.180000+1-7.344631+0 0.000000+09440 2151 282
3.381666+3 5.000000-1 1.499970+1 3.180000+1-3.089585-1 0.000000+09440 2151 283
3.381571+3 5.000000-1 1.595099+1 3.180000+1 2.737493+3 0.000000+09440 2151 284
3.389176+3 5.000000-1 1.500001+1 3.180000+1 3.004772-1 0.000000+09440 2151 285
3.423040+3 5.000000-1 3.514200+1 3.180000+1 0.000000+0 0.000000+09440 2151 286
3.440018+3 5.000000-1 1.000003+1 3.180000+1-3.392526-1 0.000000+09440 2151 287
3.458115+3 5.000000-1 7.118754+1 3.180000+1-5.479770-1 0.000000+09440 2151 288
3.465627+3 5.000000-1 3.646335+2 3.180000+1-1.603531+0 0.000000+09440 2151 289
3.487252+3 5.000000-1 2.500001+1 3.180000+1 3.465190-1 0.000000+09440 2151 290
3.493623+3 5.000000-1 6.589960+1 3.180000+1-1.217463+0 0.000000+09440 2151 291
3.500478+3 5.000000-1 1.000004+1 3.180000+1 6.031963-1 0.000000+09440 2151 292
3.514000+3 5.000000-1 1.000000+1 3.180000+1-5.000000-1 0.000000+09440 2151 293
3.538640+3 5.000000-1 1.000000+1 3.180000+1 5.000000-1 0.000000+09440 2151 294
3.555000+3 5.000000-1 9.063000+1 3.180000+1 0.000000+0 0.000000+09440 2151 295
3.567140+3 5.000000-1 1.787900+2 3.180000+1-2.560800-1 0.000000+09440 2151 296
3.580900+3 5.000000-1 1.500000+1 3.180000+1 0.000000+0 0.000000+09440 2151 297
3.595000+3 5.000000-1 4.218000+1 3.180000+1-3.000000-1 0.000000+09440 2151 298
3.609900+3 5.000000-1 7.567000+1 3.180000+1 3.024200-1 0.000000+09440 2151 299
3.613640+3 5.000000-1 3.800000+1 3.180000+1 3.649900-1 0.000000+09440 2151 300
3.647730+3 5.000000-1 1.000000+1 3.180000+1 2.800000-1 0.000000+09440 2151 301
3.657110+3 5.000000-1 2.737100+2 3.180000+1-7.983800-2 0.000000+09440 2151 302
3.665100+3 5.000000-1 5.414400+1 3.180000+1 2.832800-1 0.000000+09440 2151 303
3.681740+3 5.000000-1 1.000000+1 3.180000+1-9.009700-1 0.000000+09440 2151 304
3.701990+3 5.000000-1 5.374400+1 3.180000+1 9.132100-1 0.000000+09440 2151 305
3.711300+3 5.000000-1 2.500000+1 3.180000+1-5.000000-1 0.000000+09440 2151 306
3.723110+3 5.000000-1 5.575500+1 3.180000+1 9.400000-1 0.000000+09440 2151 307
3.742610+3 5.000000-1 8.000000+0 3.180000+1 5.000000-1 0.000000+09440 2151 308
3.765220+3 5.000000-1 5.000000+0 3.180000+1-5.000000-1 0.000000+09440 2151 309
3.777390+3 5.000000-1 5.000000+0 3.180000+1-3.245200+0 0.000000+09440 2151 310
3.800220+3 5.000000-1 1.079500+2 3.180000+1 1.144100+0 0.000000+09440 2151 311
3.822610+3 5.000000-1 8.000000+0 3.180000+1-4.762400-1 0.000000+09440 2151 312
3.833040+3 5.000000-1 4.000000+0 3.180000+1-4.838700-1 0.000000+09440 2151 313
3.843680+3 5.000000-1 8.033000+1 3.180000+1-9.974200-2 0.000000+09440 2151 314
3.853020+3 5.000000-1 1.027100+2 3.180000+1 3.946300-1 0.000000+09440 2151 315
3.858910+3 5.000000-1 1.000000+1 3.180000+1 2.695100+0 0.000000+09440 2151 316
3.872310+3 5.000000-1 4.508000+1 3.180000+1 1.339400+0 0.000000+09440 2151 317
3.885820+3 5.000000-1 1.000000+1 3.180000+1-5.000000-1 0.000000+09440 2151 318
```

```
3.900740+3 5.000000-1 2.296100+2 3.180000+1 1.100000-1 0.000000+09440 2151 319
3.916400+3 5.000000-1 1.825100+2 3.180000+1-2.845100-1 0.000000+09440 2151 320
3.938910+3 5.000000-1 1.000000+1 3.180000+1 9.344700-1 0.000000+09440 2151 321
3.954130+3 5.000000-1 1.091100+2 3.180000+1-9.119800+0 0.000000+09440 2151 322
3.960000+3 5.000000-1 1.000000+1 3.180000+1 1.000000+0 0.000000+09440 2151 323
3.975010+3 5.000000-1 1.189100+2 3.180000+1-1.360500+0 0.000000+09440 2151 324
3.990000+3 5.000000-1 2.900000+1 3.180000+1 9.020000-2 0.000000+09440 2151 325
4.001900+3 5.000000-1 2.500000+1 3.180000+1-9.961700+0 0.000000+09440 2151 326
4.022090+3 5.000000-1 3.546600+2 3.180000+1 1.111600+0 0.000000+09440 2151 327
4.031000+3 5.000000-1 1.130100+2 3.180000+1-3.997600-1 0.000000+09440 2151 328
4.054550+3 5.000000-1 2.900000+1 3.180000+1 3.000000-1 0.000000+09440 2151 329
4.072780+3 5.000000-1 7.500000+0 3.180000+1 3.000000-1 0.000000+09440 2151 330
4.083840+3 5.000000-1 1.352000+2 3.180000+1-3.100000-1 0.000000+09440 2151 331
4.099860+3 5.000000-1 2.899800+2 3.180000+1 4.687400-1 0.000000+09440 2151 332
4.110000+3 5.000000-1 9.000000+0 3.180000+1 3.000000-1 0.000000+09440 2151 333
4.121840+3 5.000000-1 5.421400+2 3.180000+1 1.572500-1 0.000000+09440 2151 334
4.134630+3 5.000000-1 6.788300+1 3.180000+1-3.129600-1 0.000000+09440 2151 335
4.143220+3 5.000000-1 5.000000+0 3.180000+1-3.000000-1 0.000000+09440 2151 336
4.148940+3 5.000000-1 2.913100+2 3.180000+1-2.254200-1 0.000000+09440 2151 337
4.160190+3 5.000000-1 9.028000+1 3.180000+1 1.396200-1 0.000000+09440 2151 338
4.170000+3 5.000000-1 2.400000+1 3.180000+1 3.000000-1 0.000000+09440 2151 339
4.203120+3 5.000000-1 4.607700+2 3.180000+1-3.307900-1 0.000000+09440 2151 340
4.220710+3 5.000000-1 6.891100+1 3.180000+1 5.839100-1 0.000000+09440 2151 341
4.240560+3 5.000000-1 6.000000+0 3.180000+1-5.800000+0 0.000000+09440 2151 342
4.260500+3 5.000000-1 8.000000+0 3.180000+1 7.839200+0 0.000000+09440 2151 343
4.270970+3 5.000000-1 1.593300+2 3.180000+1 1.926700-1 0.000000+09440 2151 344
4.280500+3 5.000000-1 3.100000+1 3.180000+1-3.000000-1 0.000000+09440 2151 345
4.287650+3 5.000000-1 3.229600+2 3.180000+1 1.519000-1 0.000000+09440 2151 346
4.315060+3 5.000000-1 3.500000+1 3.180000+1-2.983200-1 0.000000+09440 2151 347
4.328590+3 5.000000-1 3.189000+2 3.180000+1-3.957000-2 0.000000+09440 2151 348
4.338230+3 5.000000-1 7.500000+0 3.180000+1 3.000000-1 0.000000+09440 2151 349
4.362530+3 5.000000-1 2.000000+1 3.180000+1 5.864800-1 0.000000+09440 2151 350
4.376000+3 5.000000-1 8.200000+1 3.180000+1 0.000000+0 0.000000+09440 2151 351
4.386000+3 5.000000-1 3.200000+1 3.180000+1-6.363900-1 0.000000+09440 2151 352
4.398000+3 5.000000-1 7.800000+1 3.180000+1-1.036200+0 0.000000+09440 2151 353
4.414560+3 5.000000-1 5.000000+1 3.180000+1 1.295500+1 0.000000+09440 2151 354
4.422000+3 5.000000-1 6.100000+1 3.180000+1 3.074400-1 0.000000+09440 2151 355
4.433000+3 5.000000-1 4.700000+1 3.180000+1 3.053700+0 0.000000+09440 2151 356
4.446840+3 5.000000-1 1.800000+1 3.180000+1-3.600000-1 0.000000+09440 2151 357
4.459410+3 5.000000-1 1.028300+2 3.180000+1 6.744200-1 0.000000+09440 2151 358
4.473420+3 5.000000-1 2.500000+1 3.180000+1-3.000000-1 0.000000+09440 2151 359
4.490510+3 5.000000-1 2.000000+1 3.180000+1-3.000000-1 0.000000+09440 2151 360
4.501820+3 5.000000-1 2.000000+1 3.180000+1 3.000000-1 0.000000+09440 2151 361
4.517000+3 5.000000-1 1.000000+1 3.180000+1-1.879200+0 0.000000+09440 2151 362
4.538180+3 5.000000-1 2.600000+1 3.180000+1 3.000000-1 0.000000+09440 2151 363
4.560000+3 5.000000-1 2.000000+1 3.180000+1 3.000000-1 0.000000+09440 2151 364
4.569850+3 5.000000-1 2.352300+2 3.180000+1-3.596500-1 0.000000+09440 2151 365
4.588130+3 5.000000-1 5.498500+2 3.180000+1-3.088900-1 0.000000+09440 2151 366
4.598784+3 5.000000-1 7.539544+1 3.180000+1-5.614500-1 0.000000+09440 2151 367
4.614982+3 5.000000-1 2.645561+2 3.180000+1-4.363012+0 0.000000+09440 2151 368
4.645700+3 5.000000-1 1.520703+2 3.180000+1 2.240361+0 0.000000+09440 2151 369
4.663628+3 5.000000-1 7.999990+0 3.180000+1-2.996507-1 0.000000+09440 2151 370
4.686962+3 5.000000-1 1.999953+1 3.180000+1 3.398869+0 0.000000+09440 2151 371
4.712776+3 5.000000-1 5.600028+1 3.180000+1 4.706654-1 0.000000+09440 2151 372
4.721000+3 5.000000-1 5.100000+2 3.180000+1-9.745793-2 0.000000+09440 2151 373
4.745015+3 5.000000-1 2.525385+2 3.180000+1 3.005902-1 0.000000+09440 2151 374
4.755385+3 5.000000-1 5.469606+1 3.180000+1-1.661954+0 0.000000+09440 2151 375
4.768840+3 5.000000-1 3.725816+1 3.180000+1 1.334395+0 0.000000+09440 2151 376
4.778481+3 5.000000-1 3.420522+1 3.180000+1 6.782374-1 0.000000+09440 2151 377
4.791437+3 5.000000-1 1.370271+2 3.180000+1 9.322650-1 0.000000+09440 2151 378
4.800015+3 5.000000-1 2.000003+1 3.180000+1-4.106988-1 0.000000+09440 2151 379
4.811965+3 5.000000-1 1.811611+2 3.180000+1 2.828342-1 0.000000+09440 2151 380
4.821987+3 5.000000-1 6.337532+1 3.180000+1 5.583407+0 0.000000+09440 2151 381
4.842915+3 5.000000-1 1.801807+1 3.180000+1 7.756411-1 0.000000+09440 2151 382
4.868416+3 5.000000-1 1.300032+1 3.180000+1-1.403479+0 0.000000+09440 2151 383
4.894157+3 5.000000-1 6.281168+1 3.180000+1-9.186264-1 0.000000+09440 2151 384
4.912117+3 5.000000-1 1.500116+1 3.180000+1-3.791428+1 0.000000+09440 2151 385
4.932602+3 5.000000-1 1.999974+1 3.180000+1 1.899192+1 0.000000+09440 2151 386
4.949179+3 5.000000-1 5.168930+1 3.180000+1-8.263581+0 0.000000+09440 2151 387
4.958304+3 5.000000-1 3.197466+2 3.180000+1 4.446390+0 0.000000+09440 2151 388
4.967975+3 5.000000-1 1.537089+2 3.180000+1 5.915738+0 0.000000+09440 2151 389
```

```
4.974461+3 5.000000-1 7.499941+1 3.180000+1-3.670441-1 0.000000+09440 2151 390
4.993989+3 5.000000-1 9.559487+1 3.180000+1-1.209084+0 0.000000+09440 2151 391
5.034547+3 5.000000-1 1.500001+1 3.180000+1 1.474956+0 0.000000+09440 2151 392
5.047408+3 5.000000-1 1.000014+1 3.180000+1-1.511388+0 0.000000+09440 2151 393
5.072447+3 5.000000-1 5.655426+2 3.180000+1-7.530590+0 0.000000+09440 2151 394
5.096787+3 5.000000-1 3.600738+1 3.180000+1 2.335674+0 0.000000+09440 2151 395
5.111238+3 5.000000-1 8.606976+1 3.180000+1 1.585183+1 0.000000+09440 2151 396
5.120038+3 5.000000-1 1.950007+1 3.180000+1-4.450881-1 0.000000+09440 2151 397
5.131007+3 5.000000-1 4.364381+1 3.180000+1-4.909029+1 0.000000+09440 2151 398
5.148000+3 5.000000-1 5.000000+1 3.180000+1 0.000000+0 0.000000+09440 2151 399
5.161316+3 5.000000-1 3.999735+1 3.180000+1 1.337416+0 0.000000+09440 2151 400
5.175515+3 5.000000-1 8.000050+0 3.180000+1-2.020682+0 0.000000+09440 2151 401
5.194332+3 5.000000-1 3.455184+2 3.180000+1 5.557858-1 0.000000+09440 2151 402
5.215771+3 5.000000-1 1.624023+2 3.180000+1-7.146896-1 0.000000+09440 2151 403
5.235239+3 5.000000-1 2.400160+1 3.180000+1 6.373983+0 0.000000+09440 2151 404
5.249963+3 5.000000-1 5.226578+2 3.180000+1-5.942786+0 0.000000+09440 2151 405
5.272240+3 5.000000-1 1.438086+2 3.180000+1 2.211556+1 0.000000+09440 2151 406
5.286427+3 5.000000-1 5.300034+1 3.180000+1 3.982997-1 0.000000+09440 2151 407
5.300664+3 5.000000-1 2.826212+2 3.180000+1 3.455677+0 0.000000+09440 2151 408
5.327483+3 5.000000-1 1.783471+2 3.180000+1-1.279411+1 0.000000+09440 2151 409
5.352917+3 5.000000-1 1.503578+2 3.180000+1 2.377037+0 0.000000+09440 2151 410
5.356532+3 5.000000-1 3.600058+1 3.180000+1-4.458459-1 0.000000+09440 2151 411
5.366948+3 5.000000-1 6.972416+1 3.180000+1-8.585174+0 0.000000+09440 2151 412
5.379978+3 5.000000-1 7.999983+0 3.180000+1 5.985574-1 0.000000+09440 2151 413
5.392743+3 5.000000-1 8.464883+1 3.180000+1 1.056984+0 0.000000+09440 2151 414
5.417321+3 5.000000-1 2.641654+2 3.180000+1 3.209798-1 0.000000+09440 2151 415
5.440165+3 5.000000-1 1.200018+1 3.180000+1-3.745295+0 0.000000+09440 2151 416
5.456347+3 5.000000-1 7.999998+0 3.180000+1-4.687669-1 0.000000+09440 2151 417
5.465372+3 5.000000-1 4.971160+1 3.180000+1 5.486636+0 0.000000+09440 2151 418
5.482731+3 5.000000-1 8.874793+1 3.180000+1-9.135525-1 0.000000+09440 2151 419
5.498468+3 5.000000-1 9.920052+1 3.180000+1 5.233080-1 0.000000+09440 2151 420
5.510731+3 5.000000-1 3.580872+2 3.180000+1-4.833182-1 0.000000+09440 2151 421
5.523453+3 5.000000-1 1.752486+2 3.180000+1 4.936127+0 0.000000+09440 2151 422
5.531004+3 5.000000-1 1.600014+1 3.180000+1-5.520429-1 0.000000+09440 2151 423
5.544599+3 5.000000-1 5.510169+2 3.180000+1-3.502386-1 0.000000+09440 2151 424
5.550976+3 5.000000-1 1.210713+2 3.180000+1-7.062558-1 0.000000+09440 2151 425
5.563842+3 5.000000-1 1.500027+1 3.180000+1 7.604213-1 0.000000+09440 2151 426
5.574033+3 5.000000-1 7.899195+2 3.180000+1 2.264141-1 0.000000+09440 2151 427
5.591885+3 5.000000-1 1.961875+2 3.180000+1 7.614072-1 0.000000+09440 2151 428
5.599974+3 5.000000-1 1.408204+2 3.180000+1-3.321755-1 0.000000+09440 2151 429
5.615278+3 5.000000-1 6.200153+1 3.180000+1 3.547899+0 0.000000+09440 2151 430
5.629116+3 5.000000-1 2.000005+1 3.180000+1-6.239646-1 0.000000+09440 2151 431
5.643606+3 5.000000-1 5.499984+1 3.180000+1 1.261262+0 0.000000+09440 2151 432
5.667208+3 5.000000-1 4.499976+1 3.180000+1-7.492328-1 0.000000+09440 2151 433
5.681704+3 5.000000-1 1.054002+2 3.180000+1-7.032994+0 0.000000+09440 2151 434
5.692000+3 5.000000-1 9.100000+1 3.180000+1 1.000027+0 0.000000+09440 2151 435
5.994698+3 5.000000-1 9.635575+1 3.180000+1-2.742806+2 0.000000+09440 2151 436
5.923546+3 5.000000-1 9.578179+1 3.180000+1-8.719333+4 0.000000+09440 2151 437
5.981289+3 5.000000-1 9.624380+1 3.180000+1-7.386747-2 0.000000+09440 2151 438
5.990482+3 5.000000-1 9.626485+1 3.180000+1 1.701938-2 0.000000+09440 2151 439
6.299134+3 5.000000-1 9.877964+1 3.180000+1-2.380441+0 0.000000+09440 2151 440
6.426918+3 5.000000-1 9.977653+1 3.180000+1 8.489580-3 0.000000+09440 2151 441
6.445962+3 5.000000-1 9.992424+1 3.180000+1 3.216161-1 0.000000+09440 2151 442
6.513047+3 5.000000-1 1.004404+2 3.180000+1 2.576070+0 0.000000+09440 2151 443
6.535046+3 5.000000-1 1.006100+2 3.180000+1 7.008146+0 0.000000+09440 2151 444
6.551090+3 5.000000-1 1.007338+2 3.180000+1 1.872091+1 0.000000+09440 2151 445
6.568036+3 5.000000-1 1.008610+2 3.180000+1 2.854212+2 0.000000+09440 2151 446
7.507561+3 5.000000-1 1.078032+2 3.180000+1 2.078677+2 0.000000+09440 2151 447
8.020528+3 5.000000-1 1.114555+2 3.180000+1 2.984314+0 0.000000+09440 2151 448
8.064305+3 5.000000-1 1.117652+2 3.180000+1 3.126991+0 0.000000+09440 2151 449
8.098083+3 5.000000-1 1.119965+2 3.180000+1 1.915492+4 0.000000+09440 2151 450
8.360702+3 5.000000-1 1.138048+2 3.180000+1 7.803218+0 0.000000+09440 2151 451
8.472107+3 5.000000-1 2.208173+2 3.180000+1 1.603310+1 0.000000+09440 2151 452
8.707761+3 5.000000-1 1.161388+2 3.180000+1 1.024600+2 0.000000+09440 2151 453
8.974843+3 5.000000-1 1.179033+2 3.180000+1 5.585383+4 0.000000+09440 2151 454
1.002034+4 5.000000-1 1.245830+2 3.180000+1 8.644155+0 0.000000+09440 2151 455
1.008386+4 5.000000-1 1.249839+2 3.180000+1 2.688988+2 0.000000+09440 2151 456
1.015438+4 5.000000-1 1.254223+2 3.180000+1 1.160772+2 0.000000+09440 2151 457
1.095698+4 5.000000-1 1.302777+2 3.180000+1 6.890957+1 0.000000+09440 2151 458
1.117811+4 5.000000-1 1.315890+2 3.180000+1 3.608399+2 0.000000+09440 2151 459
1.149523+4 5.000000-1 1.334410+2 3.180000+1 1.272934+4 0.000000+09440 2151 460
```

```
1.165517+4 5.000000-1 1.343622+2 3.180000+1 6.927217+3 0.000000+09440 2151 461
1.214599+4 5.000000-1 1.371651+2 3.180000+1 6.046136+2 0.000000+09440 2151 462
1.251171+4 5.000000-1 1.392123+2 3.180000+1-1.312199+2 0.000000+09440 2151 463
1.313069+4 5.000000-1 1.426168+2 3.180000+1-1.011511+1 0.000000+09440 2151 464
1.340774+4 5.000000-1 1.441134+2 3.180000+1-1.946517+5 0.000000+09440 2151 465
1.357051+4 5.000000-1 1.449953+2 3.180000+1 2.057863+2 0.000000+09440 2151 466
1.404650+4 5.000000-1 1.475058+2 3.180000+1 7.500908+1 0.000000+09440 2151 467
1.450304+4 5.000000-1 1.498805+2 3.180000+1 3.924191+2 0.000000+09440 2151 468
1.446678+4 5.000000-1 1.496948+2 3.180000+1 2.026667+2 0.000000+09440 2151 469
1.602778+4 5.000000-1 1.575665+2 3.180000+1 9.326988+2 0.000000+09440 2151 470
1.643575+4 5.000000-1 1.595591+2 3.180000+1-2.116249+2 0.000000+09440 2151 471
1.747387+4 5.000000-1 1.645211+2 3.180000+1 2.335363+3 0.000000+09440 2151 472
1.822297+4 5.000000-1 1.681745+2 3.180000+1 4.654982+3 0.000000+09440 2151 473
1.844846+4 5.000000-1 1.690464+2 3.180000+1 6.169175+2 0.000000+09440 2151 474
1.921493+4 5.000000-1 1.725227+2 3.180000+1-3.124090+2 0.000000+09440 2151 475
```

Bibliography

[1] International Atomic Energy Agency, Power Reactor Information System (2018).
URL https://www.iaea.org/PRIS/

[2] Generation-IV Internation Forum.
URL https://www.gen-4.org

[3] F. Goldner, R. Versluis, Transmutation capabilities of Generation 4 Reactors, Tech. rep., OECD, NEA (2007).
URL https://inis.iaea.org/search/search.aspx?orig_q=RN:39088792

[4] Accelerator-driven Systems (ADS) and Fast Reactors (FR) in advanced nuclear fuel cycles, Tech. rep., OECD, NEA (2002).
URL https://www.oecd-nea.org/ndd/reports/2002/nea3109.html

[5] A. Stanculescu, Accelerator driven systems (adss) for nuclear transmutation, Annals of Nuclear Energy 62 (2013) 607 – 612. doi:http://dx.doi.org/10.1016/j.anucene.2013.02.006.

[6] The High Priority Request List (HPRL).
URL https://www.oecd-nea.org/dbdata/hprl/

[7] The Nuclear Energy Agency (NEA).
URL http://www.oecd-nea.org/

[8] Organisation for Economic Co-operation and Development (OECD).
URL http://www.oecd.org/

[9] S. Gabriel, A. Baschwitz, G. Mathonnière, F. Fizaine, T. Eleouet, Building future nuclear power fleets: The available uranium resources constraint, Resourses Policy 38 (4) (2013) 458 – 469. doi:https://doi.org/10.1016/j.resourpol.2013.06.008.

[10] W. P. on the Physics of Plutonium Fuels, I. F. C. (WPPR), Plutonium management in the medium term, Tech. rep., OECD, NEA (2002).
URL https://www.oecd-nea.org/ndd/reports/2002/nea3109.html

[11] High priority request ID 37 : $^{240}Pu(n,f)$.
URL https://www.oecd-nea.org/dbdata/hprl/hprlview.pl?ID=457

[12] High priority request ID 44 : $^{237}Np(n,f)$.
URL https://www.oecd-nea.org/dbdata/hprl/hprlview.pl?ID=464

[13] A. Tsinganis, Measurement of the ^{242}Pu(n,f) reaction cross-section at the CERN n_TOF facility, Tech. rep., CERN (2014).
URL http://cds.cern.ch/record/2248465

[14] T. Böhlen, et al., The FLUKA Code: Developments and Challenges for High Energy and Medical Applications, Nucl. Data Sheets 120 (2014) 211 – 214. doi:10.1016/j.nds.2014.07.049.

[15] A. Ferrari, et al., FLUKA: a multi-particle transport code, Tech. rep., CERN-2005-10 (2005).
URL http://www.slac.stanford.edu/pubs/slacreports/reports16/slac-r-773.pdf

[16] K.-H. Schmidt, et al., General fescription of fission observables : GEF model, Tech. Rep. NEA/DB/DOC(2014)1, OECD (2014).
URL https://www.oecd-nea.org/databank/docs/2014/db-doc2014-1.pdf

[17] A. Stamatopoulos, et al., An alternative methodology for high counting-loss corrections in neutron time-of-flight measurements, Nucl. Inst. Meth A 913 (2019) 40–47. doi:10.1016/j.nima.2018.10.032.

[18] M. Moore, Rate dependence of counting losses in neutron time-of-flight measurements, Nucl. Instrum. Meth. 169 (1) (1980) 245 – 247. doi:10.1016/0029-554X(80)90129-9.

[19] P. B. Coates, Pile-up corrections in the measurement of lifetimes, J. Phys. E 5 (2) (1972) 148. doi:10.1088/0022-3735/5/2/018.

[20] H. Becquerel, The radio-activity of matter, Nature 63 (1634) (1901) 396–398. doi:10.1038/063396d0.

[21] J. J. Thomson, Cathode rays, Philos. Mag. 90 (sup1) (1987) 25–29. doi:10.1080/14786431003659214.

[22] E. Rutherford, Retardation of the α particle from radium in passing through matter, The London, Edinburgh, and Dublin Philos. Mag. and Journ. of Sc. 12 (68) (1906) 134–146. doi:10.1080/14786440609463525.

[23] H. Geiger, On the scattering of the α-particles by matter, Proc. of the Royal Society of London A: Math., Phys. and Eng. Sc. 81 (546) (1908) 174–177. doi:10.1098/rspa.1908.0067.

[24] J. Chadwick, The existence of a neutron, Proc. of the Royal Society of London A: Math., Phys. and Eng. Sc. 136 (830) (1932) 692–708. doi:10.1098/rspa.1932.0112.

[25] E. Fermi, et al., Artificial radioactivity produced by neutron bombardment, Proc. of the Royal Society of London A: Math., Phys. and Eng. Sc. 146 (857) (1934) 483–500. doi:10.1098/rspa.1934.0168.

[26] E. Fermi, Possible production of elements of atomic number higher than 92, Nature 133 (3372) (1934) 133898a0. doi:10.1038/133898a0.

[27] O. Hahn, F. Strassmann, Über den nachweis und das verhalten der bei der bestrahlung des urans mittels neutronen entstehenden erdalkalimetalle, Naturwissenschaften 27 (1) (1939) 11–15. doi:10.1007/BF01488241.

[28] H. G. Graetzer, Discovery of nuclear fission, Am. J. Phys. 32 (1) (1964) 9–15, English translation of Hahn and Strassmann, Naturwissenschaften (27) 1 (1939)p. 11 . doi:10.1119/1.1970127.

[29] L. Meitner, O. R. Frisch, Disintegration of uranium by neutrons: a new type of nuclear reaction, Nature 143 (3615) (1939) 239–240. doi:10.1038/143239a0.

[30] N. Bohr, J. A. Wheeler, The mechanism of nuclear fission, Phys. Rev. 56 (1939) 426–450. doi:10.1103/PhysRev.56.426.

[31] K. A. Petrzhak, G. N. Flerov, Spontaneous fission of nuclei, Soviet Phys. Uspekhi 4 (2) (1961) 305.
URL http://stacks.iop.org/0038-5670/4/i=2/a=A10

[32] S. Bjørnholm, J. E. Lynn, The double-humped fission barrier, Rev. Mod. Phys. 52 (1980) 725–931. doi:10.1103/RevModPhys.52.725.

[33] E. Fermi, Experimental production of a divergent chain reaction, Am. J. of Phys. 20 (9) (1952) 536–558. doi:10.1119/1.1933322.

[34] JEFF-3.3: Evaluated Data Library (2017).
URL https://www.oecd-nea.org/dbdata/jeff/jeff33/index.html

[35] IAEA, Thorium fuel cycle - Potential benefits and challenges, Nuclear Fuel Cycle and Materials Section, Vienna (Austria), 2005.
URL https://inis.iaea.org/search/search.aspx?orig_q=RN:37048122

[36] G. Aliberti, et al., Nuclear data sensitivity, uncertainty and target accuracy assessment for future nuclear systems, Ann. Nucl. Ener. 33 (8) (2006) 700–733. doi:10.1016/j.anucene.2006.02.003.

[37] M. Salvatores, International Evaluation Co-operation : Uncertainty and Target Accuracy Assessment for Innovative Systems Using Recent Covariance Data Evaluations, Tech. rep., NEA-OECD (2008).
URL https://www.oecd-nea.org/science/wpec/volume26/volume26.pdf

[38] N. Otuka, et. al., Towards a More Complete and Accurate Experimental Nuclear Reaction Data Library (EXFOR): International Collaboration Between Nuclear Reaction Data Centres (NRDC), Nucl. Data Sheets 120 (2014) 272 – 276. doi:http://dx.doi.org/10.1016/j.nds.2014.07.065.

[39] International Atomic Energy Agency (IAEA).
URL https://www.iaea.org/

[40] Safeguards Implementation Practices Guide on Provision of Information to the IAEA, Tech. rep., IAEA (2016).
URL https://www-pub.iaea.org/MTCD/Publications/PDF/SVS_33_web.pdf

[41] M. Diakaki, for the n_TOF Collaboration, Neutron-induced fission cross section of ^{237}Np in the keV to MeV range at the CERN n_TOF facility, Phys. Rev., C 93 (2016) 034614. doi:10.1103/PhysRevC.93.034614.

[42] M. Diakaki, et al., Determination of the ^{237}Np(n,f) reaction cross section for E_n =4.5-5.3 MeV, using a MicroMegas detector assembly, Europ. Phys. J. A 49 (2013) 62. doi:10.1140/epja/i2013-13062-3.

[43] M. Diakaki, et al., Measurement of the ^{237}Np(n,f) Cross Section with the MicroMegas Detector, Nucl. D. Sh. 119 (2014) 52. doi:10.1016/j.nds.2014.08.016.

[44] C. Paradela, for the n_TOF Collaboration, Neutron-induced fission cross section of ^{234}U and ^{237}Np measured at the CERN Neutron Time-of-Flight (n_TOF) facility, Phys. Rev. C 82 (2010) 034601. doi:10.1103/PhysRevC.82.034601.

[45] P. Salvador-Castineira, et al., Neutron-induced fission cross section of ^{240}Pu from 0.5 MeV to 3 MeV, Phys. Rev. C 92 (2015) 014620. doi:10.1103/PhysRevC.92.014620.

[46] F. Tovesson, T. S. Hill, M. Mocko, J. D. Baker, C. A. McGrath, Neutron induced fission of ^{240,242}Pu from 1 eV to 200 MeV, Phys. Rev. C 79 (2009) 014613. doi:10.1103/PhysRevC.79.014613.

[47] A. B. Laptev, et al., Neutron Induced Fission Cross-Sections of ^{240}Pu and ^{243}Am in the Energy Range 1 - 200 MeV, Nucl. Phys. A 734 (1) (2004) E45. doi:10.1016/j.nuclphysa.2004.03.016.

[48] K. Gul, M. Ahmad, M. Anwar, S. M. Saleem, Measurements of Neutron Fission Cross Sections of ^{237}Np,^{240}Pu,^{241}Pu,^{242}Pu,^{244}Pu,and ^{241}Am at 14.7 MeV, Nucl. Sc. and Eng. 94 (1986) 42. doi:10.13182/NSE86-A17115.

[49] L. W. Weston, J. H. Todd, Subthreshold Fission Cross Section of ^{240}Pu and the Fission Cross Sections of ^{235}U and ^{239}Pu, Nucl. Sci. and Eng. 88 (1984) 567. doi:10.13182/NSE84-A18373.

[50] B.M.Aleksandrov, S.M.Solov'ev, P.S.Soloshenkov, V.B.Funshtejn, S.V.Khlebnikov, The neutron fission cross-sections for Am-241, Pu-238, Pu-240 and Pu-241, Vop. At. Nauki i Tekhn., Ser. Yadernye Konstanty (1/50) (1983) 3, EXFOR entry : 40673004.

[51] B. Aleksandrov, Tech. Rep. 213, USSR report to the I.N.D.C., EXFOR.40673:Ref.2 (1983).

[52] M.Cance, G.Grenier, Absolute measurement of the Pu-240(n,f), Pu-242(n,f) and Np-237(n,f) cross sections at 2.5 MeV incoming neutron energy (In French) , 1982, p. 51, Conf. on Nucl. Data for Sci.and Technol., Antwerp 1982, EXFOR entry : 21821002.

[53] J. W. Meadows, The Fission Cross Section of Plutonium-240 Relative to Uranium-235 from 0.35 to 9.6 MeV, Nucl. Sc. and Eng. 79 (1981) 233. doi:10.13182/NSE81-A27412.

[54] C. Budtz-Jorgensen, H. H. Knitter, Neutron-Induced Fission Cross Section of Plutonium-240 in the Energy Range from 10 keV to 10 MeV, Nucl. Sc. and Eng. 79 (4) (1981) 380. doi:10.13182/NSE81-A21389.

[55] N. A. Khan, et al., A New Approach to Measure Reaction Parameters in the 14.8 MeV Neutron Induced Fission of ^{240}Pu and ^{241}Pu, Nucl. Instrum. Meth. 173 (1980) 137. doi:10.1016/0029-554X(80)90578-9.

[56] N. A. Khan, et al., 14.8 MeV Neutron Induced Fission Studies of ^{239}Pu,^{242}Pu,^{244}Pu and ^{241}Am, Nucl. Instrum. Meth. 173 (1980) 163.

[57] K. Kari, Tech. Rep. 2673, Kernforschungszentrum Karlsruhe Reports, PhD Thesis (1978).

[58] K. Kari, S. Cierjacks, 1978, 3rd Symp. Neutr. Capt. Gamma Ray Spectr., Brookhaven, EXFOR.20786:Ref.2.

[59] K. Kari, S. Cierjacks, Progress Report 192/U, Report from CEC-Countries and CEC to NEANDC, EXFOR.20786:Ref.3 (1978).

[60] K. Kari, S. Cierjacks, private communication, EXFOR.20786:Ref.4 (1978).

[61] G. F. Auchampaugh, L. W. Weston, Parameters of the Subthreshold Fission Structure in ^{240}Pu, Phys. Rev. C 12 (1975) 1850. doi:10.1103/PhysRevC.12.1850.

[62] E. F. Fomushkin, E. K. Gutnikova, G. F. Novoselov, V. I. Panin, The Measurement of Plutonium-240 Fission Cross-Sections for Nuclear-Explosion Neutrons, Atomnaya Energiya 39 (4) (1975) 295.

[63] E. Migneco, J. P. Theobald, Resonance Grouping Structure in Neutron Induced Subthreshold Fission of ^{240}Pu, Nucl. Phys. A 112 (1968) 603. doi:10.1016/0375-9474(68)90081-X.

[64] P. White, G. Warner, The fission cross sections of 233U, 234U, 236U, 238U, 237Np, 239Pu, 240Pu and 241Pu relative to that of 235U for neutrons in the energy range 1 - 14 MeV, J. of Nucl. En. 21 (8) (1967) 671 – 679. doi:10.1016/0022-3107(67)90082-2.

[65] D. H. Byers, B. C. Diven, M. G. Silbert, Capture and fission cross section of ^{240}Pu, Vol. 2, 1966, p. 903(F5), neutron Cross-Section Techn. Conf., Washington 1966.

[66] J. L. Perkin, et al., The fission cross sections of U233,U234,U235,U236, Np237,Pu239,Pu240 AND Pu241 for 24 keV neutrons, J. Nucl. En. A&B (Reactor Sci. and Technol.) 19 (6) (1965) 423. doi:10.1016/0368-3230(65)90051-0.

[67] P. Ruddick, P. H. White, The measurement of the neutron fission cross-section of Pu-240 in the energy range 60-500 keV, J.Nucl. Eng. A&B (Reactor Sci. and Technol.) 18 (1964) 561. doi:10.1016/0368-3230(64)90140-5.

[68] V. G. Nesterov, G. N. Smirenkin, 0.04 - 4.0 Mev neutron fission cross section of Pu240, Sov. J. of Atom. En. 9 (1) (1961) 511 – 515. doi:10.1007/BF01481673.

[69] M. Kazarinova, YU.S.Zamyatnin, V. Gorbachev, Fission cross sections for Th230, Pu240,Pu241 and Am241 by neutrons with energies of 2.5 and 14.6 MeV, Atomnaya Energiya 9 (1) (1960) 16.

[70] T. A. Eastwood, et al., Radiochemical methods applied to the determination of cross sections of reactor interest, Vol. 16, 1958, p. 54(203), second Internat. At.En. Conf., Geneva 1958.

[71] R. L. Henkel, R. A. Nobles, R. K. Smith, Neutron-induced fission cross section of ^{240}Pu, Tech. Rep. 4256, div. of Tech. Info. U.S. AEC (1957).

[72] W. W. Pratt, F. J. Muckenthaler, E. G. Sliver, Thermal-neutron fission cross section of Pu239 and Pu240, Progress Report 2081, oak Ridge National Lab. Reports (1956).

[73] B. R. Leonard Jr, E. J. Seppi, W. J. Friesen, E. M. Kinderman, Slow neutron cross sections of ^{240}pu, Bull. Am. Phys. Soc. 1 (1956) 248(C13).

[74] O. Shcherbakov, et al., Neutron-induced fission of 233U, 238U, 232Th, 239Pu, 237Np, natPb and 209Bi relative to 235U in the energy range 1-200 MeV, Jour. Nucl. Sc. Tech. Suppl. 2 (2002) 230.

[75] A. D. Carlson, B. H. Patrick, ^{237}Np fission cross section measurements in the MeV energy region, 1979, p. 971, conf.on Nucl.Cross Sections F.Techn.,Knoxville 1979.

[76] A. D. Carlson, et al., Measurements of the ^{237}Np(n,f) cross section, 1993, p. 704, 8th Symposium on Reactor Dosimetry, Vail, CO, 1993, EXFOR.14035:Ref.2.

[77] I. Garlea, C. Miron-Garlea, H. N. Rosu, G. Fodor, V. Raducu, Integral Neutron Cross Sections Measured Around 14 MeV, Revue Roumaine de Physique 37 (1) (1992) 19.

[78] 1991, p. 510, Conf. on Nucl. Data for Sci. and Technol., Juelich 1991.

[79] J. W. Meadows, The Fission Cross Sections of ^{230}Th,^{232}Th,^{233}U,^{234}U,^{236}U,^{238}U,^{237}Np,^{239}Pu and ^{242}Pu Relative to ^{235}U at 14.74 MeV Neutron Energy, Ann. Nucl. En. 15 (1988) 421. doi:10.1016/0306-4549(88)90038-2.

[80] P. W. Lisowski, et al., Neutron induced fission cross section ratios for 232Th, 235, 238U, 237Th and 239Pu from 1 to 400 MeV, 1988, p. 97, conf.on Nucl.Data For Sci.and Technol.,Mito 1988.

[81] F. Manabe, et al., Measurements of neutron induced fission cross section ratios of 232Th, 233U, 234U, 236U, 238U, 237Np, 242Pu and 243Am relative to 235U around 14 MeV, Fac. of Engineering, Tohoku Univ. Tech. Report 52 (2) (1988) 97.

[82] K. Gul, M. Ahmad, M. Anwar, S. M. Saleem, Measurements of Neutron Fission Cross Sections of ^{237}Np,^{240}Pu,^{241}Pu,^{242}Pu,^{244}Pu,and ^{241}Am at 14.7 MeV, Nucl. Sc. Eng. 94 (1986) 42. doi:10.13182/NSE86-A17115.

[83] V. V. Kozharin, et al., The Thermal-Neutron Fission Cross Section of ^{237}Np and the Resonant Fission Integral, Atomnaya Energiya 60 (6) (1986) 419.

[84] Vop. At.Nauki i Tekhn.,Ser.Yadernye Konstanty (4) (1986) 19.

[85] Tech. Rep. 268, USSR report to the I.N.D.C., EXFOR.40927 (1986).

[86] G. F. Auchampaugh, et al., Nature of the Coupling in Subthreshold Fission of ^{238}Np, Physical Review, Part C, Nuclear Physics 29 (1984) 174. doi:10.1103/PhysRevC.29.174.

[87] G. F. Auchampaugh, et al., High-Resolution Measurements and R-Matrix Analysis of the Total and Fission Cross Sections of ^{237}Np + n from 1 to 600 eV, Tech. Rep. 9756-MS, los Alamos Scientific Lab. Reports (1983).

[88] Trans. Am. Nucl. Soc. 47 (1984) 425.

[89] Progress Report 36, U.S. D.O.E. Nuclear Data Committee Reports, EXFOR.12910 (1985).

[90] W. Jingxia, R. Chaofan, S. Zhongfa, L. Jingwen, Y. Zongyuan, D. Xinlu, Measurement of fission cross section for Np-237 induced by fast neutrons, Chinese J.of Nuclear Physics (Beijing). 6 (1984) 369.

[91] I. Garlea, C. Miron, D. Dobrea, C. Roth, T. Musat, H. N. Rosu, Measuring of the Integral Cross Sections at 14 MeV, for Reactions ^{115}In(n,n‘), ^{197}Au(n,2n), ^{98}Nb(n,2n), ^{27}Al(n,—a), ^{56}Fe(n,p), ^{239}Pu(n,f), ^{238}U(n,f), ^{232}Th(n,f) and ^{237}Np(n,f), Revue Roumaine de Physique 29 (1984) 421.

[92] J. W. Meadows, The Fission Cross Section of ^{237}Np Relative to ^{235}U from 0.1 to9.4 MeV, Nucl. Sc. Eng. 85 (1983) 271. doi:10.13182/NSE83-A17319.

[93] J. W. Meadows, The Fission Cross Sections of Some Thorium, Uranium, Neptunium and Plutonium Isotopes Relative to ^{235}U, Tech. Rep. 83, argonne National Laboratory Reports, EXFOR.12852:Ref.2 (1983).

[94] V. N. Dushin, et al., Statistical Analysis of Experimential Data on the Cross Sections of ^{233},^{235},^{238}U,^{237}Np,^{239},^{242}Pu Fission by Neutrons of Energy 2.6, 8.5, and 14.5 MeV, Atomnaya Energiya 55 (1983) 218.

[95] V. N. Dushin, et al., Statistical Analysis of Experimential Data on the Cross Sections of ^{233},^{235},^{238}U,^{237}Np,^{239},^{242}Pu Fission by Neutrons of Energy 2.6,8.5, and 14.5 MeV, Atomnaya Energiya 55 (1983) 218.

[96] Soviet Atomic Energy 55 (1983) 656, eXFOR.30475:Ref.5.

[97] 1982, p. 51, Conf.on Nucl.Data for Sci.and Technol.,Antwerp 1982.

[98] Progress Report 2214, Centre d'Etudes Nucleaires, EXFOR.21821:Ref.2 (1981).

[99] R. Arlt, et al., Absolutmessungen von Spaltquerschnitten der Nuklide ^{235}U, ^{238}U,^{237}Np und ^{239}Pu bei einer Neutroneneinschussenergie von 14,7 MeV, Kernenergie 24 (1981) 48.

[100] R. Arlt, et al., Spaltquerschnittsmessungen an ^{238}U,^{239}Pu und ^{237}Np, Progress Report 385, zentralinst. f. Kernforschung Rossendorf Reports, EXFOR.30475:Ref.9 (1979).

[101] D. J. Grady, G. T. Baldwin, G. F. Knoll, Absolute fast fission cross section measurements on np-237, 1979, p. 976, conf.on Nucl.Cross Sections F.Techn.,Knoxville 1979.

[102] 1979, p. 990, Conf. on Nucl. Cross Sections F. Techn., Knoxville 1979, EXFOR.22304:Ref.3.

[103] I. D. Alkhazov, et al., Fission Cross Sections of ^{235}U and ^{238}U to Neutrons with an Energy of 14.7 MeV, Atomnaya Energiya 47 (1979) 416.

[104] M. D. Semon, M. Hoffman, W. M. Sanders, Fission, Scattering and Capture Cross Sections for 237-Neptunium, Bul. Am. Phys. Soc. 21 (1976) 655(JE3).

[105] Vol. 6, 1975, p. 34, 3rd All Union Conf. on Neutron Phys., Kiev, 9-13 Jun 1975.

[106] Conference Report 99, USSR report to the I.N.D.C., EXFOR.20423:Ref.2 (1975).

[107] Ph.D. thesis, thesis of dissertation (1973).

[108] Tech. Rep. 6, Kyoto Univ.,Res.Reactor Inst., Annual Report (1973).

[109] Progress Report 26, Japanese report to EANDC, EXFOR.20300:Ref.2 (1972).

[110] Vol. 2, 1973, p. 254, 2nd Conf. on Neutron Physics, Kiev 1973, EXFOR.20423:Ref.3.

[111] R. J. Jiacoletti, W. K. Brown, H. G. Olson, Fission Cross Sections of Neptunium-237 from 20 eV to 7 MeV Determined From a Nuclear-Explosive Experiment, Nucl. Sc. Eng. 48 (1972) 412. doi:10.13182/NSE72-A22509.

[112] Tech. Rep. 4763-MS, los Alamos Scientific Lab. Reports, EXFOR.10182:Ref.2 (1971).

[113] W. Kolar, J. P. Theobald, G. Lanzano, Fission of ^{237}Np + n Through a Double Humped Fission Barrier, Zeitschrift fuer Physik 248 (1971) 355. doi:10.1007/BF01400549.

[114] W. K. Brown, D. R. Dixon, D. M. Drake, Fission Cross Sections of ^{237}Np from Pommard, Nucl. Phys. A 156 (1970) 609. doi:10.1016/0375-9474(70)90256-3.

[115] Tech. Rep. 4372, los Alamos Scientific Lab. Reports, EXFOR.10060:Ref.2 (1970).

[116] Vol. 2, 1969, p. 289, Nucl. and Solid State Phys. Symp., Roorkee 1969.

[117] J. A. Grundl, A Study of Fission-Neutron Spectra with High-Energy Activation Detectors - Part 1. DEtector Development and Excitation Measurements, Nucl. Sc. Eng. 30 (1967) 39. doi:10.13182/NSE67-A17241.

[118] P. H. White, J. G. Hodgkinson, G. J. Wall, Measurement of fission cross sections for neutrons of energies in the range 40-500 keV., Vol. 1, 1965, p. 219, phys. and Chem. of Fission Conf., Salzburg 1965.

[119] V. Pankratov, Atomnaya Energiya 14 (2) (1963) 177.

[120] V. Pankratov, Soviet Atomic Energy 14 (1963) 167.

[121] V. Pankratov, N. Vlasov, B. Rybakov, Atomnaya Energiya 9 (1960) 399.

[122] V. Pankratov, N. Vlasov, B. Rybakov, Soviet Atomic Energy 9 (1961) 939.

[123] V. Pankratov, N. Vlasov, B. Rybakov, J. Nucl. En. A&B (Reactor Sci. and Technol.) 16 (1962) 494.

[124] B. L. Jr, E. Seppi, Bull. Am. Phys. Soc. 4 (1959) 31(K1).

[125] B. L. Jr, E. Seppi, Progress Report 59126, hanford Reports (1959).

[126] H. W. Schmitt, R. B. Murray, Neutron Induced Fission Cross Section Of Np^{237}, Phys. Rev. 116 (1959) 1575. doi:10.1103/PhysRev.116.1575.

[127] B. Gokhberg, G. Otroshchenko, V. Shigin, Doklady Akademii Nauk 128 (6) (1959) 1157.

[128] A. N. Protopopov, A. Selitskii, M. Solov'ev, Fission cross sections of ^{232}Th and ^{237}Np for 14.6 Mev neutrons, Soviet Atomic Energy 4 (1958) 256. doi:10.1007/BF01587189.

[129] S. P. Kalinin, V. M. Pankratov, Neutron-induced fission cross sections of Th232 and U238 in the energy range 3-11 MeV and U233, U235, Np237 and Pu239 in the energy range 3-8 MeV, Vol. 16, 1958, p. 136(2149), second Inter. At. En. Conf., Geneva 1958.

[130] Tech. Rep. 1495, los Alamos Scientific Lab. Reports (1952).

[131] E. D. Klema, The Fission Cross Section Of Np^{237}, Phys. Rev. 72 (1947) 88. doi:10.1103/PhysRev.72.88.

[132] J. Revol (Ed.), The TARC experiment (PS211) : neutron-driven nuclear transmutation by adiabatic resonance crossing, CERN, 1999. doi:10.5170/CERN-1999-011.

[133] A. Abánades, et al., Results from the TARC experiment: spallation neutron phenomenology in lead and neutron-driven nuclear transmutation by adiabatic resonance crossing, Nucl. Instrum. Meth. A 478 (3) (2002) 577 – 730. doi:https://doi.org/10.1016/S0168-9002(01)00789-6.

[134] C. Rubbia, A high gain energy amplifier operated with fast neutrons, AIP Conf. Proc. 346 (1) (1995) 44–53. doi:10.1063/1.49069.

[135] C. Rubbia, et al., Conceptual design of a fast neutron operated high power energy amplifier, Tech. Rep. CERN-AT-95-44-ET, CERN (1995).
URL http://cds.cern.ch/record/289551

[136] C. Rubbia, Resonance enhanced neutron captures for element activation and waste transmutation, Tech. Rep. CERN-LHC-97-004-EET, CERN (1997).
URL http://cds.cern.ch/record/329843

[137] C. Rubbia, et al., A High Resolution Spallation Driven Facility at the CERN-PS to Measure Neutron Cross Sections in the Interval from 1 eV to 250 MeV: a Relative Performance Assessment, Tech. Rep. CERN-LHC-98-002-EET-Add.1, CERN (1998).
URL https://cds.cern.ch/record/363828

[138] F. Gunsing, et al., Nuclear data activities at the n_TOF facility at CERN, Eur. Phys. J. Plus 131 (10) (2016) 371. doi:10.1140/epjp/i2016-16371-4.

[139] F. Gunsing, et al., The measurement programme at the neutron time-of-flight facility n-TOF at CERN, Eur. Phys. J., Web of Conferences 146. doi:10.1051/epjconf/201714611002.

[140] A. Tsinganis, et al., The Fission Programme at the CERN n_TOF Facility, Phys. Proc. 64 (2015) 130 – 139, Scientific Workshop on Nuclear Fission Dynamics and the Emission of Prompt Neutrons and Gamma Rays, THEORY-3. doi:10.1016/j.phpro.2015.04.017.

[141] N. Colonna, et al., The Nuclear Astrophysics program at n-TOF (CERN), EPJ Web of Conferences 165. doi:10.1051/epjconf/201716501014.

[142] J. Praena, et al., Measurement and resonance analysis of the ^{33}S$(n,\alpha)^{30}$Si cross section at the CERN n_TOF facility in the energy region from 10 to 300 keV, Phys. Rev. C 97 (2018) 064603. doi:10.1103/PhysRevC.97.064603.

[143] M. Barbagallo, et al, ^{7}Be$(n,\alpha)^{4}$He reaction and the cosmological lithium problem: Measurement of the cross section in a wide energy range at n-tof at cern, Phys. Rev. L. 117 (15). doi:10.1103/PhysRevLett.117.152701.

[144] T. nTOF Collaboration, F. Gunsing, et al., Nuclear data activities at the n_TOF facility at CERN, Europ. Phys. J. Plus 131 (10). doi:10.1140/epjp/i2016-16371-4.

[145] M. Sabate-Gilarte, et al., High-accuracy determination of the neutron flux in the new experimental area n_TOF-EAR2 at CERN, Eur. Phys. J. A 53 (10). doi:10.1140/epja/i2017-12392-4.

[146] M. H. Dickens, M. T. Hutchings, Inelastic neutron scattering study of the phonon dispersion relation of pbf 2 at 10k, J. of Phys. C 11 (3) (1978) 461. URL http://stacks.iop.org/0022-3719/11/i=3/a=009

[147] M. Mansson, M. Skoulatos, Inelastic Neutron Scattering: Phonon-dispersions and Lattice Dynamics in a Lead (Pb) Crystal, Tech. rep., PSI (2013). URL https://www.psi.ch/lns/TrainingEN/INS_Student_Practicum_PSI.pdf

[148] M. Barbagallo, et al., High-accuracy determination of the neutron flux at n_TOF, Eur. Phys. J. A 49 (12) (2013) 1–11. doi:10.1140/epja/i2013-13156-x.

[149] C. Guerrero, et al., Characterization of the new n_TOF neutron beam: Fluence, profile and resolution, J. Kor. Phys. Soc. 59 (23) (2011) 1624–1627. doi:10.3938/jkps.59.1624.

[150] C. Guerrero, et al., Performance of the neutron time-of-flight facility n_TOF at CERN, Eur. Phys. J. A 49 (2) (2013) 27. doi:10.1140/epja/i2013-13027-6.

[151] C. Weiss, et al., The new vertical neutron beam line at the CERN n_TOF facility design and outlook on the performance, Nucl. Instrum. Meth. A 799 (2015) 90 – 98. doi:10.1016/j.nima.2015.07.027.

[152] P. Salvador-Castineira, A. Tsinganis, et al., Fission cros section measurements for ^{240}Pu,^{242}Pu, Deliverable 1.5 of the ANDES project, Tech. rep., EC-JRC-IRMM (2013). doi:10.2787/81004.

[153] A. Tsinganis, A. Stamatopoulos, et al., Measurement of the 240Pu(n,f) cross-section at the CERN n-TOF facility: First results from EAR-2, 2015, pp. 23–28.
URL http://inspirehep.net/record/1409583/

[154] G. Sibbens, et al., Preparation of 240Pu and 242Pu targets to improve cross-section measurements for advanced reactors and fuel cycles, J. Radioanal. Nucl. Chem. 299 (2) (2014) 1093–1098. doi:10.1007/s10967-013-2668-7.

[155] Y. Giomataris, P. Rebourgeard, J. Robert, G.Charpak, MICROMEGAS: a high-granularity position-sensitive gaseous detector for high particle-flux environments, Nucl. Instrum. Meth. A 376 (1) (1996) 29 – 35. doi:10.1016/0168-9002(96)00175-1.

[156] Y. Giomataris, Development and prospects of the new gaseous detector 'Micromegas', Nucl. Instrum. Meth. A 419 (2) (1998) 239 – 250. doi:10.1016/S0168-9002(98)00865-1.

[157] Y. Giomataris, Micromegas: results and prospects, Tech. rep., CEA/Saclay, DAPNIA.
URL www.slac.stanford.edu/pubs/icfa/fall99/paper1/paper1a.html

[158] A. Oed, Micro pattern structures for gas detectors, Nucl. Instrum. Meth. A 471 (1-2) (2001) 109–114. doi:10.1016/S0168-9002(01)00966-4.

[159] F. Sauli, Micro-pattern gas detectors, Nucl. Instr. Meth. A 477 (1-3) (2002) 1–7. doi:10.1016/S0168-9002(01)01903-9.

[160] L. Shekhtman, Micro-pattern gaseous detectors, Nucl. Instrum. Meth. A 494 (1-3) (2002) 128–141. doi:10.1016/S0168-9002(02)01456-0.

[161] S. Andriamonje, et. al, Development and performance of microbulk micromegas detectors, Journal of Instrumentation 5 (2). doi:10.1088/1748-0221/5/02/P02001.

[162] S. Andriamonje, et. al., A new 2d-micromegas detector for neutron beam diagnostic at n_tof, Journal of the Korean Physical Society 59 (23) (2011) 1601–1604. doi:10.3938/jkps.59.1601.

[163] S. Andriamonje, et. al., Recent developments of a micromegas detector for neutron physics, IEEE Transactions on Nuclear Science 56 (3) (2009) 1076–1082. doi:10.1109/TNS.2009.2015447.

[164] J. F. Ziegler, SRIM-2003, Nucl. Instrum. Meth. B 219 (2004) 1027 – 1036. doi:10.1016/j.nimb.2004.01.208.

[165] J. Ziegler, Stopping and range of ions in matter, SRIM 2013, www.srim.org.

[166] J. Pancin, Détection de neutrons avec un détecteur de type Micromegas: de la Physique nucléaire à l'imagerie, Tech. rep., CERN (2004).
URL http://cds.cern.ch/record/1474098

[167] J. Madson, H. Oskam, Mobility of Argon ions in argon, Phys. Lett. A 25 (5) (1967) 407 – 408. doi:10.1016/0375-9601(67)90727-X.

[168] L. Cosentino, et al., Silicon detectors for monitoring neutron beams in n-TOF beamlines, Rev. Scient. Instrum. 86 (7) (2015) 073509. doi:10.1063/1.4927073.

[169] U. Abbondanno, et al., CERN n_TOF facility: Performance report, Tech. Rep. CERN-SL-2002-053-ECT. INTC-O-011. CERN-INTC-2002-037, CERN (2003).
URL http://cds.cern.ch/record/601511

[170] H. W. Newson, Symmetric and asymmetric fission, Phys. Rev. 122 (1961) 1224–1226. doi:10.1103/PhysRev.122.1224.

[171] E. Segre, H. Staub, H. Bethe, J. Ashkin, Experimental nuclear physics. / volume I, John Wiley and Sons, 1953.

[172] V. Vlachoudis, FLAIR: A Powerful But User Friendly Graphical Interface For FLUKA, 2009, int. Conf. on Mathematics, Computational Methods & Reactor Physics, Saratoga Springs, New York.

[173] I. Ryzhov, et al., Influence of multichance fission on fragment angular anisotropy in the 232Th(n,f) and 238U(n,f) reactions at intermediate energies, Nucl. Phys. A 760 (1) (2005) 19 – 39. doi:10.1016/j.nuclphysa.2005.06.003.

[174] D. Tarrío, et al., Measurement of the angular distribution of fission fragments using a PPAC assembly at CERN n_TOF, Nucl. Instr. Meth. A 743 (2014) 79 – 85. doi:10.1016/j.nima.2013.12.056.

[175] E. Leal-Cidoncha, et al., Fission Fragment Angular Distribution measurements of 235U and 238U at CERN n_TOF facility, EPJ Web of Conferences 111 (2016) 10002. doi:10.1051/epjconf/201611110002.
URL 10.1051/epjconf/201611110002

[176] P. Žugec, et al., Pulse processing routines for neutron time-of-flight data, Nucl. Instrum. Meth. A 812 (2016) 134 – 144. doi:10.1016/j.nima.2015.12.054.

[177] M. Frigo, S. G. Johnson, The design and implementation of FFTW3, Proceedings of the IEEE 93 (2) (2005) 216–231. doi:10.1109/JPROC.2004.840301.

[178] R. Brun, F. Rademakers, ROOT: An object oriented data analysis framework, Nucl. Instrum. Meth. A 389 (1997) 81–86. doi:10.1016/S0168-9002(97)00048-X.

[179] B. Marcinkevicius, S. Simakov, V. Pronyaev, ^{209}Bi(n,f) and ^{nat}Pb(n,f) Cross Sections as a New Reference and Extension of the ^{235}U, ^{238}U and ^{239}Pu(n,f) Standards up to 1 GeV, Tech. rep., IAEA, INDC (2015).
URL https://www-nds.iaea.org/publications/indc/indc-nds-0681.pdf

[180] Neutron cross-section standards (2006) and references (2015) (2015).
URL https://www-nds.iaea.org/standards/

[181] NIST standard reference database 124 (2017).
URL https://physics.nist.gov/cgi-bin/Star/compos.pl?matno=179

[182] R. Bonetti, A. Guglielmetti, CLuster radioactivity : An overview after twenty years, Romanian rep. in Phys. 59 (2) (2007) 301–310.
URL http://www.rrp.infim.ro/2007_59_2/10_bonetti.pdf

[183] J. W. Müller, Dead-time problems, Nucl. Instrum. Meth. 112 (1) (1973) 47 – 57. doi:10.1016/0029-554X(73)90773-8.

[184] J. W. Müller, Some formulae for a dead-time-distorted poisson process: To andré allisy on the completion of his first half century, Nucl. Instrum. Meth. 117 (2) (1974) 401 – 404. doi:10.1016/0029-554X(74)90283-3.

[185] P. Schillebeeckx, et al., Determination of resonance parameters and their covariances from neutron induced reaction cross section data, NDS 113 (12) (2012) 3054 – 3100. doi:https://doi.org/10.1016/j.nds.2012.11.005.

[186] F. Esposito, N. Spinelli, R. Velotta, V. Berardi, Dead time correction of time distribution measurements, Review of Scientific Instruments 62 (11) (1991) 2822–2827. doi:10.1063/1.1142219.

[187] O. Bouland, H. Derrien, N. M. Larson, L. C. Leal, R-Matrix Analysis of the 240Pu Neutron Cross Sections in the Thermal to 5700-eV Energy Range, Nucl. Sc. Eng. 127 (2) (1997) 105–129. doi:10.13182/NSE127-105.

[188] Stanley Cohen and W.J Swiatecki, The deformation energy of a charged drop: IV. Evidence for a discontinuity in the conventional family of saddle point shapes, Annals of Physics 19 (1) (1962) 67 – 164. doi:https://doi.org/10.1016/0003-4916(62)90234-8.

[189] L. Wilets, Theories of nuclear fission, Clarendon Press, 1964.

[190] D. Paya, J. Blons, H. Derrien, A. Michaudon, Structure intermediaire dans les sections efficades de fission du Neptunium-237 et du Plutonium-239 (in English), Second Int. Symp. on physics and chemistry of fission (1969) 307.
URL https://inis.iaea.org/collection/NCLCollectionStore/_Public/45/029/45029008.pdf

[191] V. Strutinsky, Shell effects in nuclear masses and deformation energies, Nucl. Phys. A 95 (2) (1967) 420 – 442. doi:https://doi.org/10.1016/0375-9474(67)90510-6.

[192] G. T. Seaborg, Activation energy for fission, Phys. Rev. 88 (1952) 1429–1431. doi:10.1103/PhysRev.88.1429.2.

[193] G. Breit, E. Wigner, Capture of slow neutrons, Phys. Rev. 49 (1936) 519–531. doi:10.1103/PhysRev.49.519.

[194] E. P. Wigner, L. Eisenbud, Higher angular momenta and long range interaction in resonance reactions, Phys. Rev. 72 (1947) 29–41. doi:10.1103/PhysRev.72.29.

[195] A. M. Lane, R. G. Thomas, R-matrix theory of nuclear reactions, Rev. Mod. Phys. 30 (1958) 257–353. doi:10.1103/RevModPhys.30.257.

[196] F. Fröhner, Evaluation and analysis of nuclear resonance data, Nuclear Energy Agency of the OECD (NEA), 2000.
URL https://inis.iaea.org/search/search.aspx?orig_q=RN:32011631

[197] J. M. Blatt, L. C. Biedenharn, The angular distribution of scattering and reaction cross sections, Rev. Mod. Phys. 24 (1952) 258–272. doi:10.1103/RevModPhys.24.258.

[198] C. W. Reich, M. S. Moore, Multilevel formula for the fission process, Phys. Rev. 111 (1958) 929–933. doi:10.1103/PhysRev.111.929.

[199] W. Hauser, H. Feshbach, The inelastic scattering of neutrons, Phys. Rev. 87 (1952) 366–373. doi:10.1103/PhysRev.87.366.

[200] Sammy website (2019).
URL https://www.ornl.gov/onramp/sammy

[201] Oecd-nea-sammy-8.1.0 (2017).
URL https://www.oecd-nea.org/tools/abstract/detail/psr-0158

[202] N. M. Larson, Updated Users' Guide for SAMMY: Multilevel R-Matrix Fits to Neutron Data Using Bayes' Equations, Tech. rep., ORNL/TM-9179/R8 ENDF-364/R2 (2008).

[203] F. H. Fröhner, Evaluation of the Unresolved Resonance Range of 238U, Nucl. Sc. Eng. 103 (2) (1989) 119–128. doi:10.13182/NSE89-A28501.

[204] R. Gwin, Measurement of Neutron Transmission Through Samples of Pu-240 1.9 and 0.4-cm Thick in the Neutron Energy Range 4 keV to 2 MeV, exfor entry : 14249002 (1982).

[205] R. CAPOTE, S. CHIBA, E. S. SOUKHOVITSKIĭ, J. M. QUESADA, E. BAUGE, A global dispersive coupled-channel optical model potential for actinides, J. of Nucl. Sc. and Tech. 45 (4) (2008) 333–340. doi:10.1080/18811248.2008.9711442.

[206] M. D. Toro, G. Russo, Near threshold neutron-fission cross section, Nucl. Phys. A 284 (2) (1977) 177 – 188. doi:10.1016/0375-9474(77)90115-4.

[207] L. Geraldo, D. Smith, Some thoughts on positive definiteness in the consideration of nuclear data covariance matrices, Tech. rep., Argonne National Lab., IL (USA) (1988).
URL https://inis.iaea.org/search/search.aspx?orig_q=RN:19097979

[208] W. Mannhart, A small guide to generating covariances of experimental data, Tech. rep., International Atomic Energy Agency (IAEA), INDC(NDS)–0588 (2011).
URL https://inis.iaea.org/search/search.aspx?orig_q=RN:42067630

[209] Boost library.
URL https://www.boost.org/